Udvalgte publikationer fra

Rammeprogrammet "Marin Teknik" (STVF)

Møde i Dansk Vandbygningsteknisk Selskab

November 1993

DANSK VANDBYGNINGSTEKNISK SELSKAB

DANISH SOCIETY OF HYDRAULIC ENGINEERING

Indhold:

Andersen, O.H., Juhl, J. and Sloth, P. (1992): Rear side stability of berm breakwaters. 23rd Int. Conf. on Coastal Engineering, Venice, ASCE 1993, Vol. 1, pp. 1020-1029.

Juhl, J. and Jensen, O.J. (1993): Practical experiences with berm breakwaters. Danish Hydraulic Institute, to be published. 16 p.

Fischer, M., Juhl, J. and Rasmussen, E.G. (1992): Numerical modelling of waves and currents with regard to coastal structures. 23rd Int. Conf. on Coastal Engineering, Venice, ASCE 1993, Vol. 1, pp. 170-183.

Burcharth, H.F. and Christensen, C. (1991): On stationary and non-stationary porous flow in coarse granular materials. Laboratoriet for Hydraulik og Havnebygning, Aalborg Universitetscenter, Aalborg, 68 p.

Burcharth, H.F. and Liu, Z. (1992): Design of Dolos armour units. 23rd Int. Conf. on Coastal Engineering, Venice, ASCE 1993, Vol. 1, pp. 1053-1066.

Burcharth, H.F. (1992): Reliability evaluation of a structure at sea. Design of rubble mound breakwaters. Intern. Short Course in connection with Int. Conf. on Coastal Engineering, Venice. 48 pp.

Sumer, B.M., Fredsøe, J. and Christiansen, N. (1992): Scour around vertical pile in waves. J. Waterway, Port, Coastal and Ocean Engineering, ASCE, Vol. 118, No. 1, pp. 15-31.

Fredsøe, J., Sumer, B.M. and Arnskov, M.M. (1992): Time scale for wave/current scour below pipelines. Int. Journal of Offshore and Polar Engineering, Vol. 2, No. 1, pp. 13-17.

Sumer, B.M., Christiansen, N. and Fredsøe, J. (1993): Influence of cross section on wave scour around piles. J. Waterway, Port, Coastal, and Ocean Engineering, ASCE, Vol. 119, No. 5, pp. 477-495.

Sumer, B.M. and Fredsøe, J. (1992): A review of wave/current-induced scour around pipelines. 23rd Int. Conf. on Coastal Engineering, Venice, ASCE 1993, Vol. 3, pp. 2839-2852.

Kozakiewicz, A., Sumer, B.M. and Fredsøe, J. (1992): Spanwise correlation on a vibrating cylinder near a wall in oscillatory flows. J. Fluids and Structures, Vol. 6, No. 3, pp. 371-392.

Deigaard, R., Fredsøe, J. and Brøker Hedegaard, I. (1986): Mathematical model for littoral drift. J. Waterway, Port, Coastal and Ocean Engineering, ASCE, Vol. 112, No. 3, pp. 351-367.

Brøker Hedegaard, I., Deigaard, R. and Fredsøe, J. (1991): Onshore/offshore sediment transport and morphological modelling of coastal profiles. Coastal Sediments 91, Proc. Specialty Conf., Seattle, ASCE 1991, Vol. 1, pp. 643-657.

Brøker Hedegaard, I., Roelvink, J.A., Southgate, H., Pechon, P., Nicholson, J. and Hamm, L. (1992): Intercomparison of coastal profile models. Int. Conf. on Coastal Engineering, Venice, ASCE 1993, Vol. 2, pp. 2108-2121.

Skou, A., Brøker Hedegaard, I., Fredsøe, J. and Deigaard, R. (1991): Applications of mathematical models for coastal sediment transport and coastline development. Proc. 3rd Int. Conf. on Coastal and Port Engineering in Developing Countries, COPEDEC, Mombassa 1991, Vol. 1, pp. 227-236.

Johnson, H.K., Brøker, I. and Madsen, P.A. (1993): Sediment transport behind an offshore breakwater using different wave models. G8 Coastal Morphodynamics, Abstracts-in-depth from the overall MAST workshop, Grenoble 1993, Paper 5.16, 4 p.

Johnson, H.K., Brøker, I., Zyserman, J.A. and Justesen, P. (1993): A new approach to 2DH morphological modelling. G8 Coastal Morphodynamics, Abstracts-in-depth from the overall MAST workshop, Grenoble 1993, Paper 5.10, 4 p.

Johnson, H.K., Brøker, I. and Zyserman, J.A. (1993): Influence of bed roughness on morphological response behind breakwaters. G8 Coastal Morphodynamics, Abstracts-in-depth from the overall MAST workshop, Grenoble 1993, Paper 5.17, 5 p.

Rear Side Stability of Berm Breakwaters

O.H. Andersen, J. Juhl and P. Sloth

Danish Hydraulic Institute
Agern Allé 5
2970 Hørsholm
Denmark

23rd International Conference on Coastal Engineering,
Venice, October 1992

Rear Side Stability of Berm Breakwaters

O.H. Andersen[1], J. Juhl[1] and P. Sloth[1]

Abstract

With the aim of providing improved methods for preliminary design of berm breakwaters, a series of physical model tests and a parameter study with special emphasis on the rear side stability of a trunk section have been carried out at the Danish Hydraulic Institute (DHI). The model tests included different geometries of the berm breakwater profile and a range of wave conditions. For each profile, the wave condition resulting in sea side and/or rear side damage was determined. As a hydrodynamic description of the overtopping waves would be very comprehensive, and at present is not available, a surf similarity approach in combination with a force balance for the armour stones has been chosen. A parametric expression for the rear side stability has been established and found to be in fairly good agreement with the model test results.

Introduction

Existing experience with berm breakwaters provides some insight in the behaviour of the various parts of a berm breakwater. Most research during the last ten years has concentrated on the sea side stability of the trunk section, ie the development of the berm profile. No systematic work on the rear side stability has previously been reported and hence a comprehensive study focusing on the rear side stability of the trunk section was carried out at DHI. As it is still not possible to give an adequate hydrodynamic description of the overtopping phenomenon, eg in the form of a numerical model, it was decided to carry out a series of physical model tests and an associated parameter study.

[1] Danish Hydraulic Institute, Agern Allé 5, 2970 Hørsholm, Denmark

In the present study, the rear side stability is treated as a traditional static stability phenomenon. Emphasis has been put on inclusion of a large number of physical parameters enabling the description to cover a variety of berm breakwater designs: wave height and steepness, crest height, rear side slope, effective sea side slope, stone diameter, relative density and natural angle of repose.

The stability criterion established has been compared to the results of the model tests carried out and in addition to an expression given by Van der Meer and Veldman.

Model setup and procedure

A wave flume with a length of 65 m and a width of 1.8 m was used for model testing in four water depths of 0.67 m, 0.77 m, 0.87 m and 0.97 m. The profile tested is shown in Figure 1. Crushed stones were used both for the core, D_{50} = 0.011 m (50% exceedance), and for the berm and armour layer, D_{n50} = 0.034 m. D_{n50} is the nominal diameter given as $(M_{50}/\rho_s)^{1/3}$, where M_{50} is the mass of the stones (50% exceedance) and ρ_s is the density of the stones. The grading of the berm and armour material equalled D_{n85}/D_{n15} = 1.35 and the relative density equalled Δ = 1.68. The armour layer thickness on the crest and rear side was twice the value of D_{n50}. The model study covered variations in the following parameters:

- w_c, width of the crest, 0.175 m and 0.30 m
- R_c, freeboard of the crest, 0.20 m, 0.30 m and 0.40 m
- f_h, width of the berm, 0.45 m, 0.65 m, 0.85 m and 1.05 m
- f_v, freeboard of the berm, 0.10 m and 0.20 m.

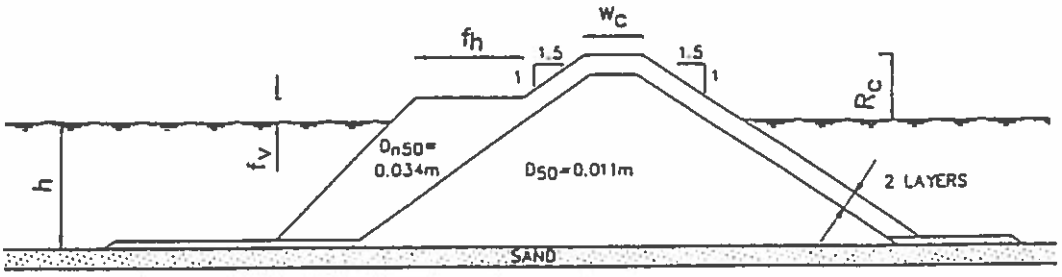

Figure 1. Test profile.

Tests were carried out in test series with successively increasing wave height, H_{mo}, and wave period, T_{02}, from test run to test run, with a fixed fictitious wave steepness $s_{02} = 2\pi H_{mo}/gT_{02}^2$ equal to approximately 0.030 and 0.044 respectively. Each test series consisted of approximately 1,000 irregular waves. The incident wave characteristics in front of the berm breakwater, H_{mo} and T_{02}, and the reflection coefficient were calculated using a multi-gauge technique.

The berm profile was measured after each test run. Damage to the seaward side of the berm breakwater was defined to occur when the entire top of the berm was eroded. Rear side damage was defined as a settlement of the rear side armour layer which in some cases was followed by an exposure of the core.

Table 1 gives an overview of the 23 tested profiles for which rear side damage was observed prior to or coincident with damage of the sea side. The wave conditions, H_{mo} and T_{02}, resulting in rear side damage are also shown in Table 1.

Table 1. Rear side damages.

Note: A is the berm area and tanα the effective sea side slope, as defined below.

wc (m)	Rc (m)	fh (m)	fv (m)	h (m)	A (m^2)	H_{mo} (m)	T_{02} (s)	s_{02}	tanα
0.175	0.2	0.45	0.1	0.97	0.25	0.176	1.67	0.0404	0.39
0.175	0.2	0.85	0.1	0.77	0.59	0.228	1.84	0.0431	0.36
0.175	0.2	0.65	0.1	0.97	0.47	0.211	1.78	0.0427	0.37
0.175	0.2	1.05	0.1	0.77	0.76	0.228	1.84	0.0431	0.29
0.175	0.2	0.85	0.1	0.97	0.68	0.184	2.08	0.0272	0.43
0.175	0.2	1.05	0.1	0.97	0.89	0.202	2.13	0.0285	0.30
0.175	0.3	0.45	0.2	0.77	0.25	0.186	2.06	0.0281	0.45
0.175	0.3	0.65	0.1	0.77	0.41	0.209	2.11	0.0301	0.38
0.175	0.3	0.65	0.1	0.77	0.41	0.219	1.81	0.0428	0.36
0.175	0.3	0.45	0.2	0.87	0.25	0.184	2.00	0.0295	0.42
0.175	0.3	0.65	0.2	0.77	0.44	0.210	2.12	0.0299	0.39
0.175	0.3	0.85	0.1	0.77	0.59	0.228	2.20	0.0302	0.33
0.175	0.3	0.65	0.2	0.87	0.47	0.235	2.17	0.0320	0.37
0.175	0.3	0.85	0.2	0.77	0.64	0.256	1.93	0.0440	0.31
0.175	0.3	1.05	0.1	0.77	0.76	0.232	2.24	0.0296	0.29
0.175	0.3	1.05	0.1	0.77	0.76	0.270	1.99	0.0437	0.29
0.175	0.3	1.05	0.2	0.77	0.83	0.271	1.99	0.0438	0.29
0.3	0.2	0.65	0.1	0.97	0.47	0.207	1.71	0.0453	0.37
0.3	0.2	0.85	0.1	0.97	0.68	0.222	1.78	0.0449	0.32
0.3	0.2	1.05	0.1	0.97	0.89	0.241	1.83	0.0461	0.28
0.3	0.3	1.05	0.1	0.77	0.76	0.238	2.21	0.0312	0.27
0.3	0.3	1.05	0.2	0.77	0.83	0.248	2.19	0.0331	0.30
0.3	0.3	1.05	0.2	0.77	0.83	0.279	1.97	0.0460	0.28

Data Analysis

During the tests, it was observed that the developed sea side profile can be characterised as three slopes: an upper steep slope, a lower slope close to 1:4 or flatter and finally a steep slope intersecting the seabed, see Figure 2. This is a well known observation confirmed by several other researchers.

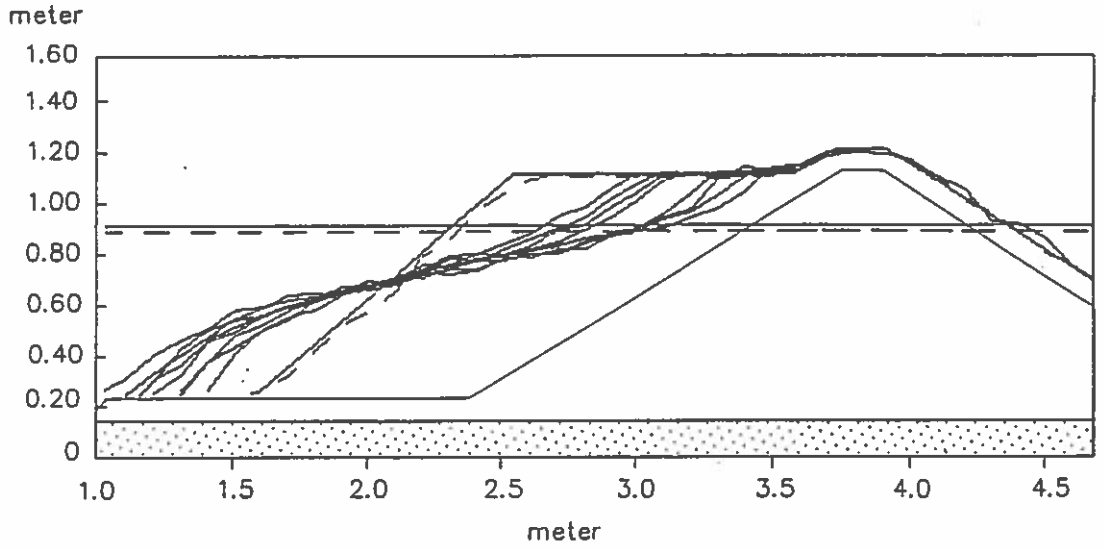

Figure 2. Example of development of sea side profile.

Rear side damage of a trunk section happens at almost fully developed sea side profile. A typical development is that a few stones just above still water level at the rear side are displaced downwards during a series of wave overtoppings (cf Figure 3), and after another few severe wave overtoppings, a settlement of the rear side armour layer occurs, possibly resulting in an exposure of the core.

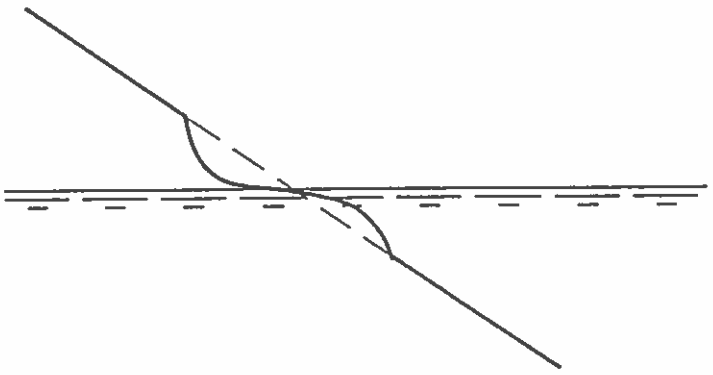

Figure 3. Initiation of rear side damage.

The stability of the rear side depends on the sea side profile, crest height, crest width, rear side slope, stone diameter, relative density and natural angle of repose. It appears from the analysis of the present model test results that a variation with the crest width is not visible. New model tests with larger crest widths are presently being carried out in order to include this parameter as well. The following analysis is considered to be valid for the crests widths in Table 1, and hence w_c is not included in the analysis.

It is assumed that the speed of the overtopping water is the governing factor in determining the rear side stability. The speed at the crest, U_R, is chosen as a reference speed.

U_R can be found by putting the potential at the crest equal to the potential at the still water level at the seaward side:

$$U_R^2 = 2g\ (R_{ui} - R_c) \tag{1}$$

where R_{ui} is the run-up on a hypothetical slope of the sea side, with index i indicating a fraction of the waves. The hydraulic parameters are defined in Figure 4.

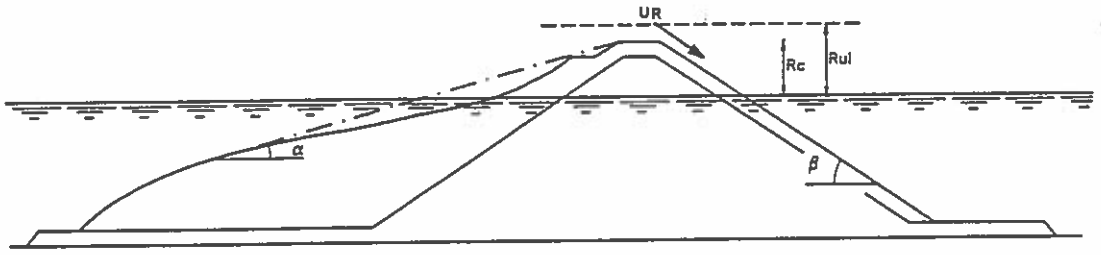

Figure 4. Definition of hydraulic parameters.

Pilarczyk (1990) applied the same reference velocity for the description of the rear side stability of dikes, resulting in a final stability criterion with large resemblance to the criterion derived below.

For the berm breakwater rear side, a traditional static stability criterion is applied. The stability of a single stone at still water level is expressed by a force balance parallel to the rear side slope, cf Figure 5:

$$F_D + W_s \sin\beta - \mu\ (W_s \cos\beta - F_L) < 0 \tag{2}$$

where F_D is the drag force, F_L is the lift force, W_s is the submerged weight, and β is the rear side slope angle. The resistance against rolling and sliding μ can be found as $\mu = \tan\phi$, where ϕ is the natural angle of repose.

This yields:

$$F_D + \mu F_L < W_s\ (\mu\cos\beta - \sin\beta) \tag{3}$$

The submerged weight equals:

$$W_s = \Delta\rho g\ D_{n50}^3 \tag{4}$$

where ρ is the density of water and D_{n50} is the nominal diameter.

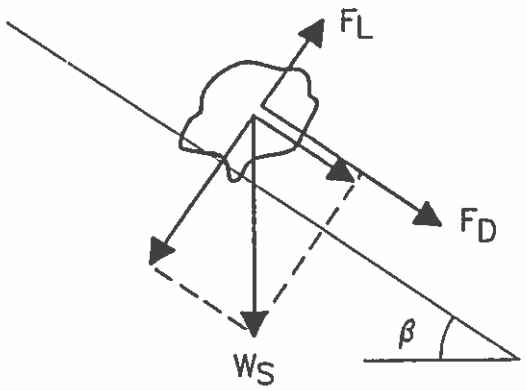

Figure 5. Forces acting on a single stone.

The left side can be expressed as:

$$F_D + \mu F_L = (C_D + \mu C_L) \frac{1}{2} \rho U_R^2 D_{n50}^2 \tag{5}$$

where C_D and C_L are force coefficients. For convenience, the nominal diameter is applied in the above expression. Combining (1), (3) (4), and (5) and re-arranging, the stability criterion now yields:

$$R_c > R_{ul} - \Delta D_{n50} \frac{\mu \cos\beta - \sin\beta}{C_D + \mu C_L} \tag{6}$$

For a relatively flat sea side slope, it is assumed that the run-up can be expressed as a function of the surf similarity parameter, cf CIRIA/CUR (1991):

$$R_{ul} = a \, \xi_{02} \, H_{mo} \tag{7}$$

where ξ_{02} is the surf similarity parameter (Iribarren number) given as:

$$\xi_{02} = \frac{\tan\alpha}{\sqrt{s_{02}}} \tag{8}$$

where $\tan\alpha$ is the effective sea side slope and the factor a is a constant close to 1. In the following, a is kept equal to 1.

The effective sea side slope is for the present purpose defined as a straight line through the toe of the lower slope, where the influence of the breaking waves becomes significant, and up to the seaward face of the crest, cf Figure 4.

In general, the effective sea side slope represents the upper part of the berm area shaped by the incident waves. The effective sea side slope is considered to be

a good measure of the part of the berm area which is active in the wave deformation irrespective of the water depth in front of the structure.

For the specific test programme, the effective sea side slope for the cases with rear side damage has been plotted against the berm area, cf Figure 6. It is observed that the effective sea side slope decreases with the berm area.

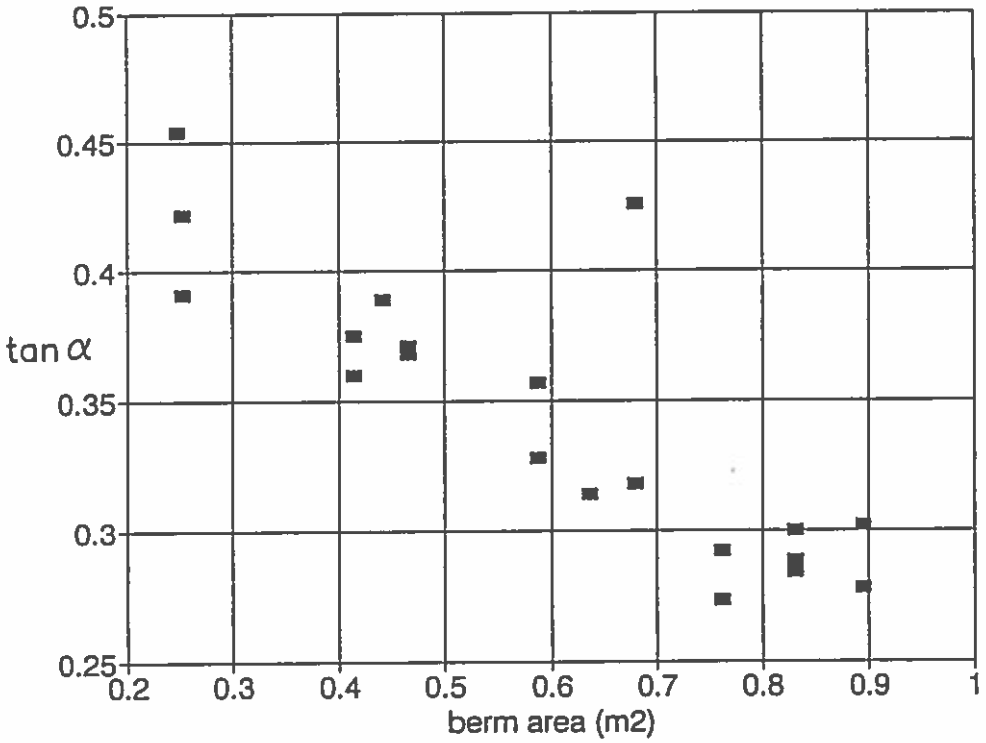

Figure 6. Effective sea side slope vs berm area for the cases with rear side damage.

Combining (6), (7) and (8) gives for the stability criterion:

$$R_c > \tan\alpha \frac{H_{mo}}{\sqrt{s_{02}}} - \Delta D_{n50} \frac{\mu\cos\beta - \sin\beta}{C_D + \mu C_L} \qquad (9)$$

The above expression is made dimensionless by $H_{mo}/\sqrt{s_{02}}$.

$$\frac{R_c}{H_{mo}} \sqrt{s_{02}} > \tan\alpha - \left(\frac{H_{mo}}{\Delta D_{n50}} \frac{1}{\sqrt{s_{02}}} \right)^{-1} \frac{\mu\cos\beta - \sin\beta}{C_D + \mu C_L} \qquad (10)$$

For the observed rear side damages, the effective sea side slopes, $\tan\alpha$, have been divided into three equidistant intervals with the following limits: 0.27, 0.33, 0.39 and 0.45.

For the stone material applied, μ equals 0.9. For this value, the expression (10) has been calibrated to fit the observations. The best agreement was obtained with $(C_D+\mu C_L)$ equal to 0.08. Four different curves representing $\tan\alpha$ = 0.27, 0.33, 0.39 and 0.45 respectively have been drawn in Figure 7. For all curves, the rear side slope equals the value of the actual test programme: $\tan\beta$ = 1:1.5.

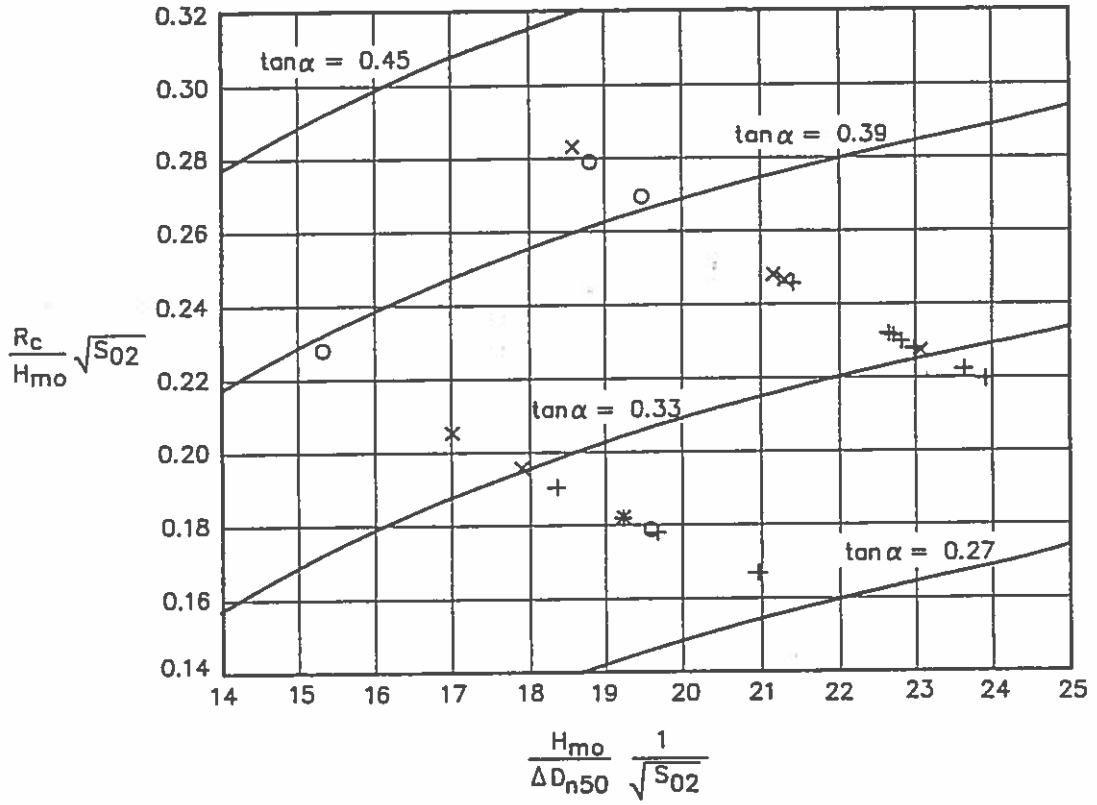

Figure 7. Stability of rear side.

Legend: Measurements: +: 0.27 < tanα < 0.33,
x: 0.33 < tanα < 0.39,
o: 0.39 < tanα < 0.45

Full drawn curves show the stability criterion (10)

It is seen that a fairly good agreement between the measurements and the stability expression is obtained. The measurements show that $R_c/H_{mo}\sqrt{s_{02}}$ increases with $H_{mo}/\Delta D_{n50} / \sqrt{s_{02}}$, which again shows that in the stability expression (10) the $\tan\alpha$ term as well as the term including $H_{mo}/\Delta D_{n50} / \sqrt{s_{o2}}$ are of importance.

For a specified wave condition, the rear side stability can according to (10) be increased in several ways:

- increase of crest height, R_c, which is the most traditional method
- increase of stone diameter, D_{n50}. In Norway, a berm breakwater has been constructed with larger stones on the rear side than on the sea side, cf Tørum et al (1990)

- increase of relative density, Δ
- decrease of rear side slope, $\tan\beta$

However, only the dependency on R_c has been studied experimentally.

The stability expression (10) bears some resemblance to the expression given by Van der Meer and Veldman (1992):

$$\frac{R_c}{H_s} s_{op}^{1/3} = K \qquad (11)$$

H_s is the significant wave height ~ H_{mo}
s_{op} is the fictitious wave steepness based on the peak period
K is a constant, which equals: K = 0.25 for start of damage
K = 0.21 for moderate damage
K = 0.17 for severe damage

The above expression (11) is based on a parameter fitting procedure applied to two different sea side geometries (one of them in two different scale ratios). Comparing to the stability expression (10), the major difference is that in (11), $R_c/H_{mo}\ s_{op}^{1/3}$ is constant, whereas the very similar quantity $R_c/H_{mo}\ \sqrt{s_{02}}$ in (10) depends on $H_{mo}/\Delta D_{n50}\ /\sqrt{s_{02}}$ and the effective sea side slope.

Conclusions

- Model tests with a range of berm breakwater profiles have been carried out at DHI.
- A parametric expression for the rear side stability has been made, cf (10).
- The expression includes the wave height and steepness, crest height, rear side slope, effective sea side slope, stone diameter, relative density and natural angle of repose.
- The measurements show that the rear side stability increases with a decreasing effective sea side slope. A decrease in the effective sea side slope can be obtained by increasing the berm area.
- Applying the surf similarity approach for a bermed profile gives reasonably good agreement between the derived expression for the rear side stability and the model test observations.
- New model tests with different crest widths are being carried out in order to examine the variation of the rear side stability for a wider range of this parameter.

Acknowledgements

The present study was carried out as a part of the research and technological development programme in the field of Marine Science and Technology (MAST) financed by the Commission of the European Communities, Directorate General for Science Research and Development, MAST I, Contract 0032, G6-S, Coastal Structures.

The authors wish to thank Mr Flemming John Andersen, Mr Christian Poulsen, Ms Bettina H. Sørensen and Mr Jakob Johannsen for carrying out the model tests, which were part of their B.Sc. dissertations at the Danish Academy of Engineering.

References

Burcharth, H.F. and Frigaard, P. (1988), '*On Three-Dimensional Stability of Reshaping Breakwaters*'. 21st International Conference on Coastal Engineering, pp 2284-2298.

CIRIA/CUR (1991), '*Manual on the Use of Rock in Coastal and Shoreline Engineering*'. CIRIA Special Publication 83/CUR Report 154.

Jensen, O.J. and Sørensen, T. (1987), '*Hydraulic Performance of Berm Breakwaters*'. Berm Breakwaters: Unconventional Rubble Mound Breakwaters, ASCE, pp 74-91.

Pilarczyk, K.W. (1990), '*Design of Seawalls and Dikes - Including Overview of Revetments*'. In Pilarczyk, K.W. (Ed.), Coastal Protection, Balkema, Rotterdam, pp 197-288.

Tørum, A., Mathiesen, M., Vold, S., Bjørdal, S., and Næss, S. (1990), '*Årviksand Fishing Port Breakwater Extension*'. 27th International Navigation Congress, PIANC, S.II-3, pp 99-105.

Van der Meer, J.W. and Veldman, J.J. (1992), '*Singular Points at Berm Breakwaters: Scale Effects, Rear, Round Head and Longshore Transport*'. Coastal Engineering, 17, pp 153-171.

Practical Experiences With Berm Breakwaters

J. Juhl and O.J. Jensen

Danish Hydraulic Institute
Agern Allé 5
2970 Hørsholm
Denmark

Practical experiences with berm breakwaters

J. Juhl[1] and O.J. Jensen[1]

Abstract

This paper describes the features of berm breakwaters including advantages and drawbacks in comparison to traditional rubble mound structures. A review of selected practical experiences with berm breakwaters from projects actually constructed are described, and two examples of economically advantageous structural variants are presented. Finally, the paper discusses future research needs for berm breakwaters.

Introduction

In principle two different types of rubble mound breakwaters exist, ie conventional rubble mound breakwaters with or without a crown wall and berm breakwaters. The main armour layer of a conventional rubble mound breakwater is designed for limited damage (statically stable), whereas for a berm breakwater the berm reshapes into a flatter and more stable profile. The more stable reshaped profile of a berm breakwater is the basic idea of the S-shaped breakwater, which initially is built with a flatter statically stable slope around the water level. In Figure 1, typical cross-sections of the three mentioned types of rubble mound breakwaters are shown. Further, a number of hybrids of conventional and berm breakwaters exist, eg conventional rubble mound breakwaters with a small berm or increased armour layer thickness.

Berm breakwaters have unconsciously been known since the middle of the nineteenth century, but increasing attention has been paid to this type of breakwater during the last decade. Many of the early breakwater structures were constructed

[1] Danish Hydraulic Institute, Agern Allé 5, 2970 Hørsholm, Denmark

by simply dumping quarried stones, which were available at the site, into the sea. Material was placed until a stable breakwater profile was reached, ie after damage repair was carried out by adding more stone material. A few examples of these early berm breakwaters are shown in Figure 2, of which some still exist.

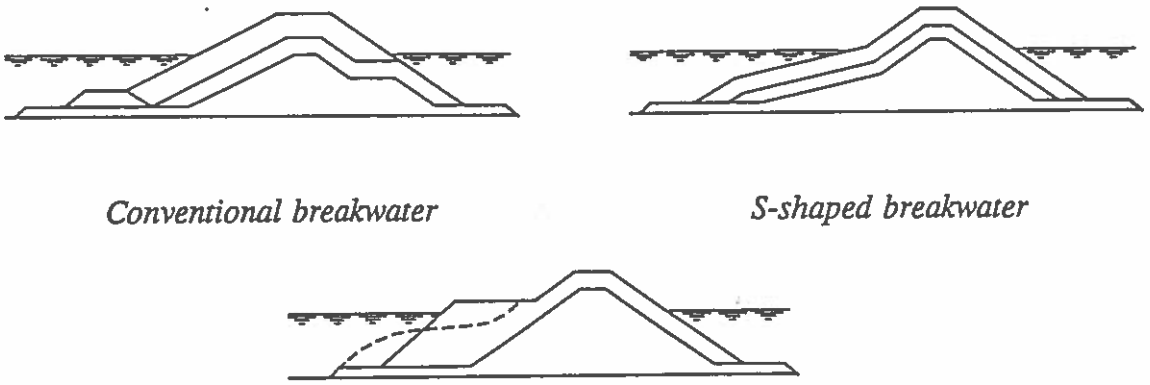

Conventional breakwater *S-shaped breakwater*

Berm breakwater

Figure 1 *Typical cross-sections of three types of rubble mound breakwaters.*

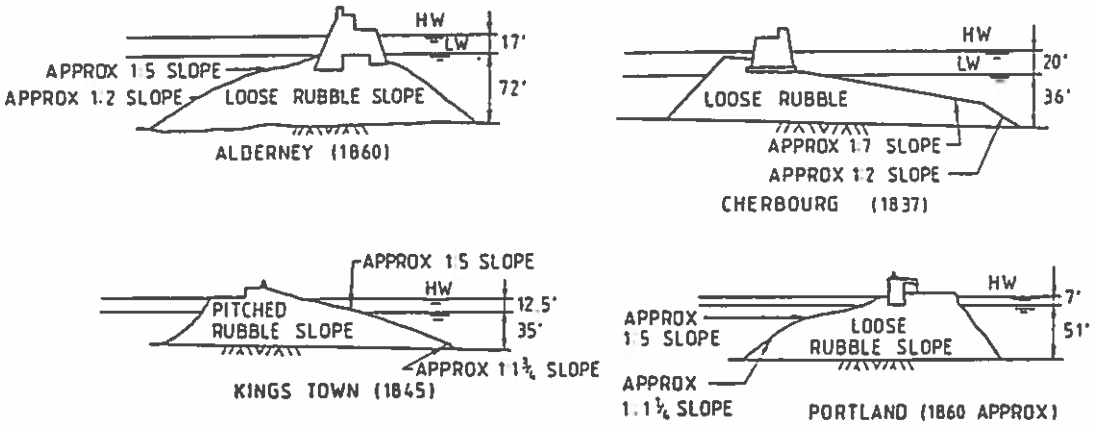

Figure 2 *Examples of historical berm breakwaters (Figure from Hall (1987)).*

In literature, various synonyms have been used for a berm breakwater, ie dynamically stable breakwater, unconventional breakwater, reshaping breakwater, naturally armouring breakwater and mass armoured breakwater. However, it is important to distinguish between berm breakwaters which reshape into a statically stable profile or dynamically stable profile.

The paper describes the features of berm breakwaters and points out both advantages and present drawbacks compared to conventional rubble mound structures. Eight recently constructed berm breakwaters are described in terms of typical cross-sections and key parameters. In a few cases results from model tests are included. In three of the described cases, prototype measurements of the profile development of the berm are available, and for two of these comparison with model measurements

are shown. Finally, the paper includes a discussion on proposed future research on berm breakwaters with the aim of increasing the understanding of the physical processes involved and to establish better design methods.

Features of Berm Breakwaters

A berm breakwater is a rubble mound breakwater with a berm above still water on the seaward side. During exposure to wave action of a certain intensity, the berm reshapes until eventually an equilibrium profile of the stones on the seaward face is reached. A typical berm breakwater profile is shown in Figure 1. Just below the water level the reshaped profile has typically a slope of about 1:5. In front of this flat slope, stones are deposited with a steeper slope. Wave energy is dissipated in the mass of stones in the flat slope resulting in reduced wave run-up above still water level where the natural equilibrium slope is steeper.

Berm breakwaters can be designed to be in either static or dynamic equilibrium in the long term. For a dynamically stable berm breakwater the stones are allowed to move somewhat but with the profile being in equilibrium. In order to ensure long-term stability, berm breakwaters should reshape into a statically stable profile where movements are only occurring in very severe and rare conditions, as frequent stone movements could result in abrasion and fracturing or displacement of stones finally resulting in degradation of the breakwater. The allowance for some displacement of stones on the reshaped profile can imply a certain risk for singular points, where maintenance can be required from time to time in order to ensure the long-term stability.

The average armour rock size needed in a berm breakwater structure is smaller than in a traditional rubble mound structure, because of the flatter final slope of the seaward face on which the breaking wave plunges and dissipates energy, and the higher proportion of wave energy dissipated within the porous mound (reducing the hydrodynamic forces acting on the individual stones). Further, wave action causes consolidation of the breakwater and nesting of the stones by a number of small movements, which increase the stability. Typically stones with a weight two to ten times smaller can be used for construction of the berm compared to the main armour layer of a conventional breakwater.

Especially when a quarry is available near the construction site and it is not possible to produce a sufficient quantity of large armour stones, a berm breakwater can be a feasible solution. Berm breakwaters are presently being considered for more and more applications worldwide, and several berm breakwaters are or have already been constructed. Berm breakwaters can normally be constructed with only two stone gradations as indicated in Figure 1. This reduces the activity of sorting stone material in the quarry.

The smaller stones to be used for berm breakwaters have also an influence on the construction method and equipment to be used. The core can be constructed by end tipping trucks or dumping by barges, whereas the berm can be constructed by cranes with stone grabs, end tipping trucks or excavators. Generally lighter and less specialised construction equipment can be used compared to construction of conventional breakwaters. Even if the construction tolerances are wider for berm breakwater than for conventional rubble mound breakwaters, fulfilment of the specifications to mean weight, gradation, content of fines etc, is strictly required (Sørensen and Jensen (1990) and Jensen and Sørensen (1992)).

Experience with Berm Breakwaters

Berm breakwaters have been designed and model tests have been performed for numerous projects, only a few of which have actually been constructed to date. This section describes eight examples of constructed berm breakwaters. In three cases a profile development in the prototype have been measured. In the following, H_s is the significant wave height, Δ is the relative stone density, $D_{n50} = (W_{50}/\rho_s)^{1/3}$ is the nominal diameter, W_{50} is the median weight, and ρ_s is the stone density.

Norwegian Experience

Two berm breakwaters have been constructed in Norway; one in Årviksand and one in Rennesøy. In order to reduce construction costs, both of these projects included a structural variant to the typical berm breakwater profile. These structural variants are further discussed in the following.

Årviksand

The berm breakwater constructed in Årviksand in northern Norway is an extension of a breakwater for a fishing port. In the design, a significant wave height of $H_s = 6.5$ m and a water level of +3.6 m have been used.

Through model tests it was found economical to use larger stones for the rear side of the breakwater to protect against wave overtopping rather than increasing the crest elevation or extending the berm width. The disadvantage of this solution is an additional stone class to be handled in the quarry. A typical profile of the trunk section including a strengthened rear side is shown in Figure 3. Armour stones with a median weight of 4.4 t was used for the berm, which results in a stability parameter of $H_s/\Delta D_{n50} = 3.4$. The breakwater head was also constructed of stones with an average weight of 4.4 t, but the upper part was armoured with 8 to 14 t stones and the top elevation of the berm increased from +3.6 m to +4.5 m, as shown in Figure 4.

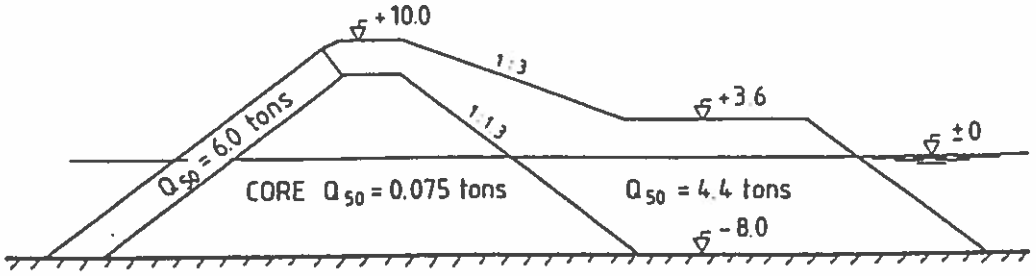

Figure 3 *Extension of breakwater at Årviksand, profile of breakwater trunk section (Figure from Tørum et al (1990)). All measures are in metres.*

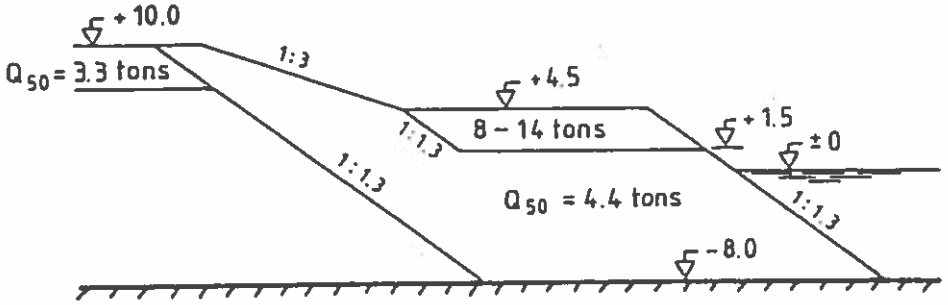

Figure 4 *Extension of breakwater at Årviksand, profile of breakwater head, (Figure from Tørum et al (1990)). All measures are in metres.*

After construction the armour profile has been monitored and new monitoring will be made after major storms in which reshaping of the breakwater has occurred. Fifty of the armour stones have been marked and it is the plan to track their movements after reshaping has taken place. The monitoring of the berm breakwater in Årviksand and similar monitorings of the breakwater in Rennesøy will give valuable prototype experience on profile development.

Rennesøy

A new ferry terminal has been constructed on Rennesøy with a berm breakwater protecting the harbour facilities. From an economical point of view it was desirable to extend the core in under the berm to make better use of the yield from the quarry. Based on results from model tests the profile shown in Figure 5 was selected for the trunk section, whereas the roundhead was designed without extension of the core into the berm. In the design, a significant wave height of approximately H_s = 7.0 m was used and the stability parameter has accordingly been assessed to $H_s/\Delta D_{n50}$ = 3.3.

This structural variant may in many cases be economical due to substitution of berm stones by cheaper core material. The disadvantage of this substitution is lower energy dissipation in the porous berm material and therefore reduced stability of the berm stones.

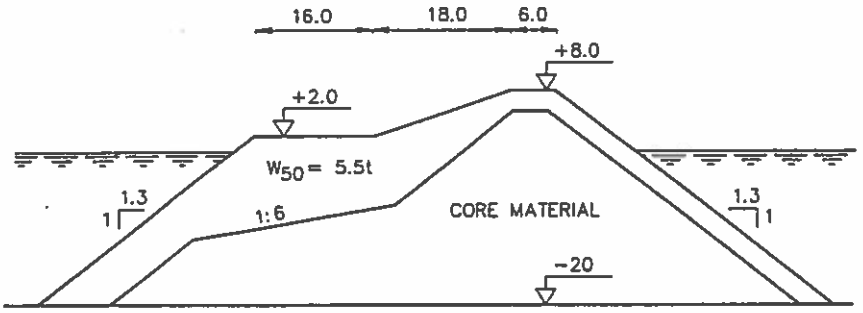

Figure 5 *Typical cross-section for berm breakwater on Rennesøy. All measures are in metres.*

Icelandic Experience

Since 1983, fourteen rubble mound structures of the berm type have been constructed in Iceland. Five of these were new structures, whereas the others were reinforcements or repairs of existing breakwaters (five were built as additional protection on the seaside of old caisson breakwaters, and four are modifications of existing conventional breakwaters). Presently, two berm breakwaters are under construction in Iceland.

The main problem facing construction of rubble mound breakwaters in Iceland is the poor quality of the stones (basalt) and the often associated lack of sufficiently large armour stones. This can be exemplified by results from an inspection of a rubble mound structure built in 1968-69 in one of the most exposed locations in Iceland (Vopnafjordur). The armour layer of the breakwater was originally constructed from stones of 10 to 15 t. An inspection showed that abrasion and splitting of stones had caused deterioration of the breakwater. Weathering took place above the water level, and the estimated loss in diameter was 0.5 to 1.0 cm per year in a 20 years period. This corresponds to a weight loss of 1.8 to 3.4 t for a 10 t stone. This severe problem with abrasion and splitting of stones in Iceland is normally treated by using stones with reduced size in the model tests.

In addition to the normally stated advantages of berm breakwaters, two other factors are mentioned by Viggosson (1990): Local contractors with no special experience in marine work can be used as the tolerances for placement of stones are eased. Shortage of funds often makes it necessary to extend the construction period over two summers with a stop in the winter season (experience in Iceland indicates that a partially completed berm breakwater functions well through the storms of one winter, and repairs are much easier than for a conventional breakwater).

Bakkafjordur

The first berm breakwater in Iceland was built in 1983-84 at Bakkafjordur. The 50 years design wave condition is H_s = 4.8 m and T_p = 12.0 s for a design water

level of +2.5 m. The berm consists of stones in the range from 2.0 to 6.0 t with an average weight of 3.0 t. The stability parameter has been calculated at $H_s/\Delta D_{n50}$ = 2.9. A typical cross-section of the constructed berm breakwater is shown in Figure 6 together with comparisons of prototype measurements and results from model tests. The possible rounding and breakage of the available poor quality stones was included in the model study by testing with reduced stone size. In nature, some deterioration of stones has been observed at the breakwater head.

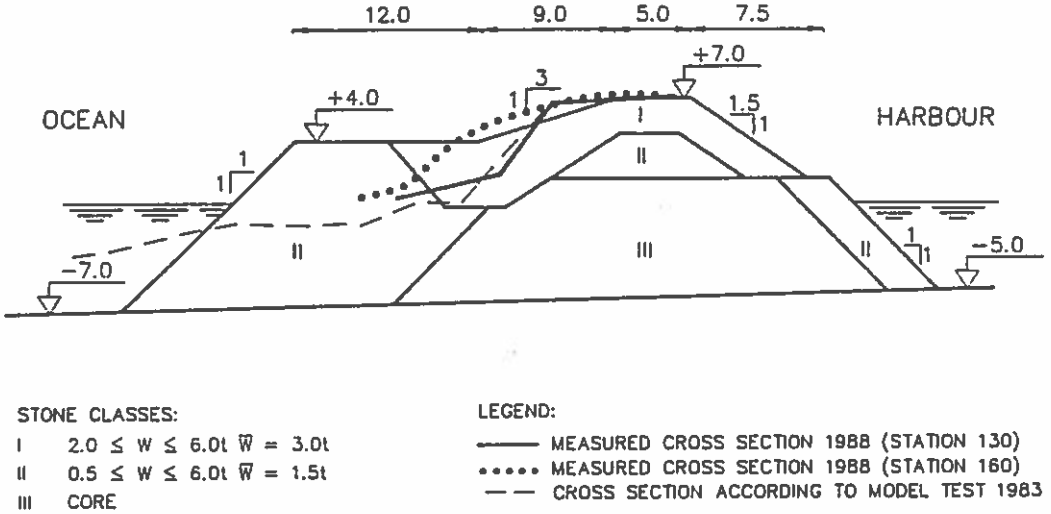

Figure 6 *Measurements of profile reshaping of berm breakwater at Bakkafjordur (based on figures from Viggosson (1990)). All measures are in metres.*

Keflavik (Helguvik)

The berm breakwater project at Keflavik was described by Baird (1987). A typical cross-section of the breakwater is shown in Figure 7. The 50 years design wave condition is H_s = 5.8 m and T_p = 9.6 s with an angle of incidence equal to 45°, and a corresponding design water level of +5.0 m. The berm consists of 1.7 to 7.0 t stones with an average weight of 3.2 to 4.2 t, and the stability parameter has been calculated at $H_s/\Delta D_{n50}$ = 3.2 - 3.5. In the model tests, smaller stones were used in order to take into account possible deterioration of the stones.

Skopun, Faroe Islands

Presently, a berm type breakwater is being constructed in Skopun with the aim of reducing the wave overtopping at the existing harbour and for protection of a reclamation. The design conditions corresponding to a return period of 50 years are H_s = 5.8 m and T_p = 18 s. The design water level is about +1.0 m. A typical cross-section of the berm breakwater is shown in Figure 8. The small berm is constructed

of stones ranging from 5.5 to 12.5 t, with an average stone weight of about 8.3 t. With a stone density of 2.65 t/m³, the stability parameter has been calculated at $H_s/\Delta D_{n50} = 2.5$. Three-dimensional model tests have been carried out as part of the design, and the reshaped profile of the most exposed section of the breakwater is shown in Figure 9.

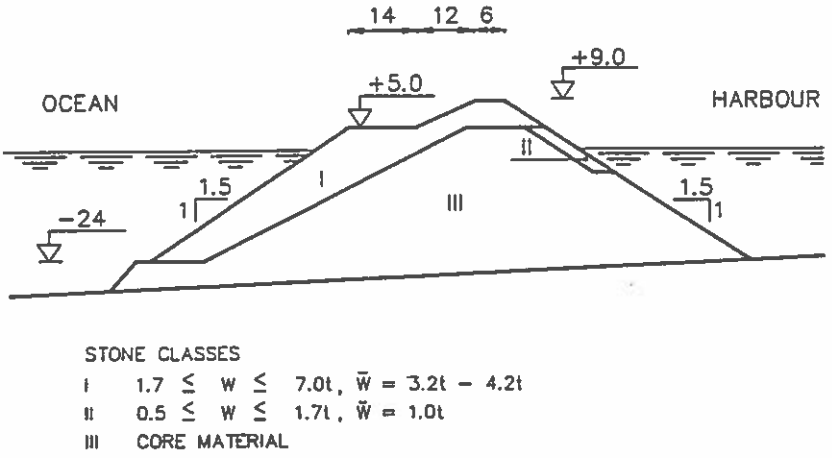

Figure 7 *Cross-section of a berm breakwater at Keflavik. (Based on figure from Baird (1987)). All measures are in metres.*

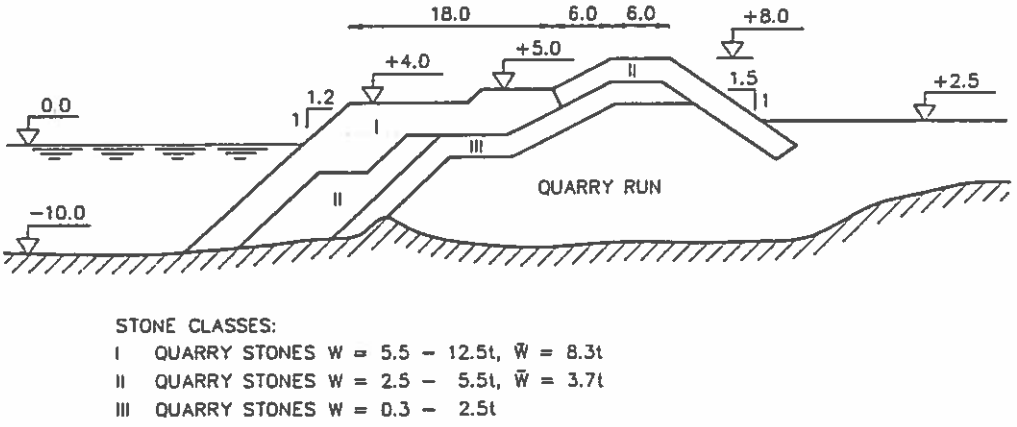

Figure 8 *Typical profile for Skopun harbour (presently under construction). All measures are in metres.*

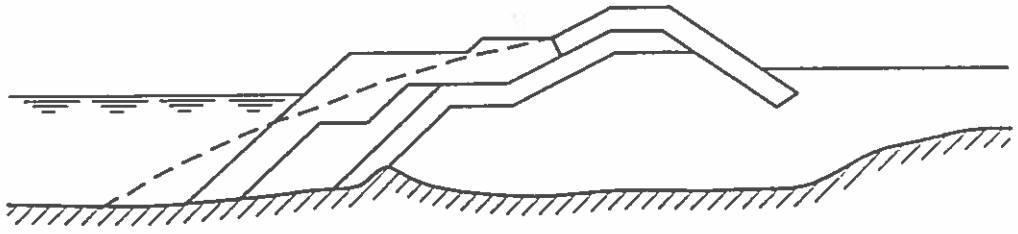

Figure 9 *Reshaped profile after exposure to the design wave conditions (results from model tests). All measures are in metres.*

Hay Point, Australia

For protection of a tug boat harbour, a berm breakwater has been model tested and constructed as described by Bremner et al (1987). Numerical wave modelling has revealed a 100 years significant wave height of H_s = 5.0 m and a corresponding peak period of T_p = 7 s, and a design water level of +4.5 m. The stones used for the berm has a weight of 4.0 to 7.0 t with an estimated average weight of 5.3 t. Applying a stone density of 2.65 t/m³, the stability parameter can be assessed at $H_s/\Delta D_{n50}$ = 2.5. A typical profile of the designed berm breakwater is shown in Figure 10.

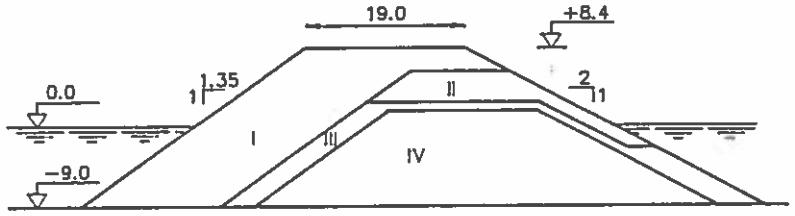

STONE CLASSES:

I	ARMOUR STONES 4–7t
II	ARMOUR STONES 1–2t
III	FILTER STONES 0.25–2t
IV	CORE MATERIAL

Figure 10 Typical cross-section for a berm breakwater at Hay Point. (Based on figure from Bremner et al (1987)). All measures are in metres.

St. George, Alaska, USA

A berm breakwater project on St. George Island has been described by Gilman (1987). The design wave condition is H_s = 10.4 m offshore (and about 6.4 m in front of the breakwater) and T_p = 18.0 s. The harbour layout is shown in Figure 11, and a typical cross-section of the roundhead in Figure 12. The berm for the breakwater roundhead had a top elevation of 16 feet (4.9 m) and a width of 61 feet (18.6 m), and the berm for the trunk section had a top elevation of 12 feet (3.7 m) and a width of 55 feet (16.8 m). The berm of both the trunk and roundhead was constructed of stones with a weight from 1.5 to 9.0 t. The average stone weight is about 4.8 t, and the stability parameter is calculated at $H_s/\Delta D_{n50}$ = 3.3.

Before completion of the breakwater, construction was shut down in late 1986 with the North breakwater roundhead only half completed (30 ft of the horizontal berm was constructed, none of which rose above elevation +12 ft). During the winter of 1986-87, storms occurred which approached the design storm in intensity. Surveys of the breakwater profiles were made before and after the winter storms, showing only minor changes in the profiles. This indicates that the incomplete berm breakwater performed well during these severe wave conditions.

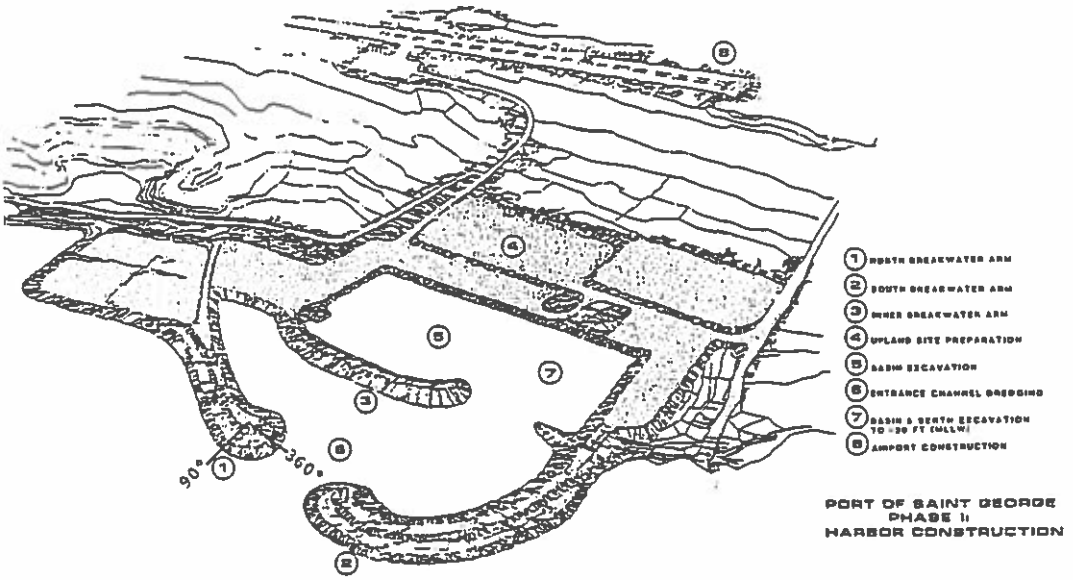

Figure 11 *Harbour layout for St. George. (Figure from Gilman (1987)).*

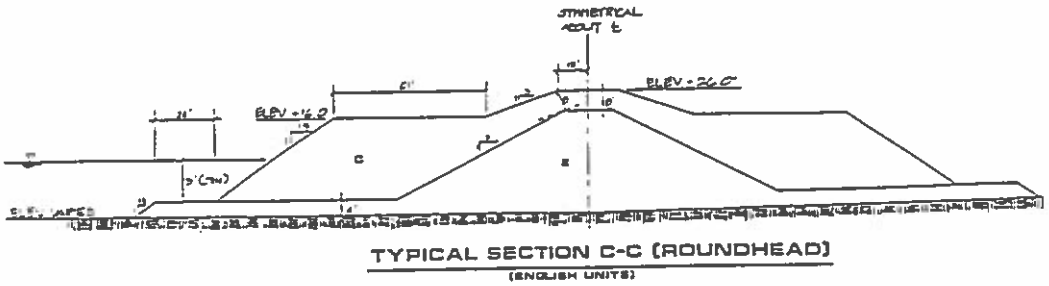

Figure 12 *Typical cross-section of berm breakwater roundhead for St. George. (Figure from Gilman (1987)). All measures are in feet.*

Racine, Wisconsin, USA

The implementation and performance of a berm breakwater design at Racine, Western shore of Lake Michigan, has been described by Montgomery et al (1987). The design conditions, corresponding to a return period of 20 years, are a significant wave height of H_s = 4.4 m, a significant wave period of T_s = 10.0 s and a water level of +1.4 m relative to low water datum. The water depth in front of the breakwater is 6-8 m and a typical cross-section is shown in Figure 13. The width of the berm is 12.2 m at the trunk and 15.2 m at the roundhead. Stones with a weight in the range 0.14 to 3.6 t have been used, which with an average weight of 0.82 t gives a stability parameter of $H_s/\Delta D_{n50}$ = 4.1.

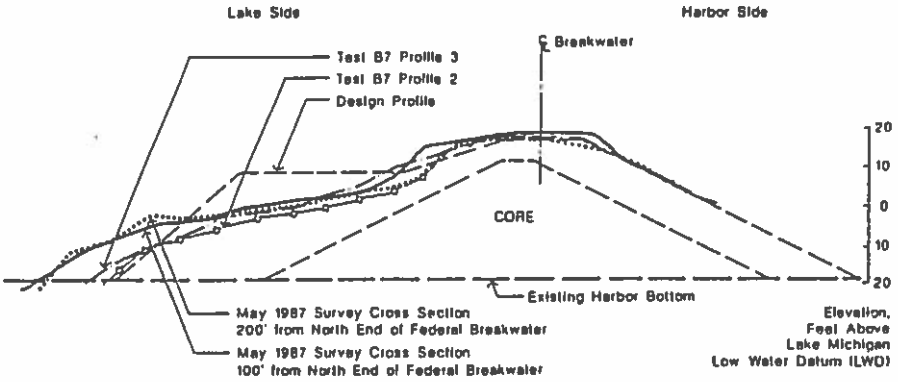

MODEL AND PROTOTYPE SECTIONS AT TWO LOCATIONS IN BREAKWATER TRUNK

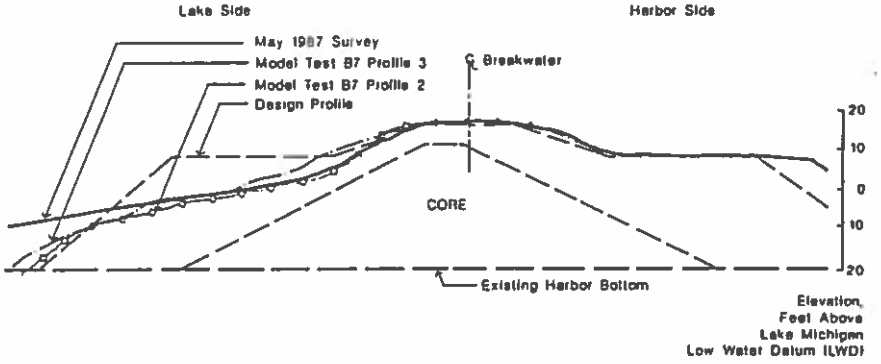

BERM BREAKWATER SECTION NEAR HEAD OF BREAKWATER

Figure 13 Comparison of model tests and prototype measurements. (Figures from Montgomery et al (1987)). All measures are in feet.

After construction, the berm breakwater was levelled and found to be in good agreement with the design. The breakwater was completed in the Autumn of 1986 and was in February and March 1987 exposed to two major storms, which approximated the design conditions. A description of the breakwater performance is summarised below.

Visual, underwater and survey assessments of the berm breakwater were performed after the March storm with the following main observations:

- the berm was reshaped so that it was generally below water along the trunk section, whereas parts of the roundhead was less reshaped
- small rounded cobbles (diameter of 15 to 45 cm) were observed at the water line, indicating breakage of some of the berm stones
- some of the berm stones had moved towards the crest
- the reshaped berm had a typical slope between 1:6 to 1:10
- no evidence of substantial overtopping was observed as the rear side appeared unaffected

A subsequent survey was conducted and indicated that despite the fairly dramatic change in the above-water appearance, the berm breakwater appeared to have behaved similarly to the model tests with respect to berm reshaping. Survey cross-sections and profiles from the modelling study are presented in Figure 13.

Summary of Breakwater Examples

A summary of selected geometrical, wave and stone size data for the presented breakwaters is listed in Table 1.

Table 1 Summary of the data for the described examples of constructed berm breakwaters.

Location	h* (m)	R_c** (m)	H_s (s)	T_p (s)	W (t)	W_{50} (t)	D_{n50} (m)	$H_s/\Delta D_{n50}$	R_c/H_s
Árviksand	11.6	6.4	6.5	~14.0	-	4.4	1.18	3.4	0.98
Rennesøy	-	-	7.0	-	-	5.5	1.28	3.3	-
Bakkafjordur	10.5	4.5	4.8	12.0	2.0-6.0	3.0	1.05	2.9	0.94
Keflavik	29.0	4.0	5.8	9.6	1.7-7.0	3.2-4.2	1.07-1.17	3.2-3.5	0.69
Skopun	11.0	7.0	5.8	18.0	5.5-12.5	8.3	1.46	2.5	1.20
Hay Point	13.5	3.9	5.0	7.0	4.0-7.0	5.3	1.26	2.5	0.78
St. George	8.2	6.4	6.4	18.0	1.5-9.0	4.8	1.22	3.3	1.00
Racine	9.8	3.5	4.4	~10.6	0.14-3.6	0.82	0.68	4.1	0.80

NOTE:

* h is the water depth in front of the structure in the design situation

** R_c is the freeboard, ie the vertical distance from the actual water level to the crest

The listed parameters should be regarded with caution as some of the data are uncertain. For example, is it rarely indicated in the literature if the wave heights refer to offshore or nearshore conditions.

The practical experience with the described berm breakwaters shows that the dimensionless stability parameter, $H_s/\Delta D_{n50}$, is in the range from 2.5 to 4.1, which is in the lower end of the classification of breakwaters made by Van der Meer (1988) quoting: $H_s/\Delta D_{n50}$ = 3-6 for berm breakwaters and S-shaped profiles.

The ratio between the freeboard and the significant wave height, R_c/H_s, varies between 0.7 and 1.2, which is smaller than for conventional rubble mound breakwaters as the porous berm reduces wave run-up and overtopping.

Future Research

Before the research programme MAST I, the knowledge about berm breakwaters was mainly based on results from site specific studies, limited prototype experience, parameter tests of the berm reshaping, and a limited number of three-dimensional model tests.

Within MAST I, the above-mentioned scattered experience with berm breakwaters was reviewed and the following subjects were studied in order to supplement the knowledge:

- numerical modelling of flow on and in berm breakwaters
- numerical modelling of berm reshaping (individual rock unit scale)
- parameter tests on rear side stability
- measurements of water particle velocities and wave forces on a single stone
- movements of individual stones on a berm breakwater

For berm breakwaters, special measures have to be taken for the breakwater roundhead as compared with traditional rubble mound breakwaters. If stone displacements occur on a roundhead, the stones will be moved in the wave direction and will loose most of their stabilising effect. A point of special concern is whether, and under which conditions, a berm breakwater roundhead after some initial reshaping may develop into a statically stable shape that is not subject to continued erosion, or at least such slow erosion that it may be acceptable for a permanent structure. The present experience with berm breakwater roundheads is from a limited number of berm breakwater applications and a few tests performed with the aim of studying the effect of oblique waves.

A berm breakwater trunk section exposed to oblique waves has to be designed with stones larger than a certain critical size in order to avoid continued movements of stones in the wave direction (longshore transport).

Research is required on the influence of three-dimensional effects on berm breakwater stability, ie stability of trunk sections exposed to oblique wave attack and berm breakwater roundheads. Further, research is needed in understanding the physics of berm breakwaters (flow on and in berm breakwaters, forces on single stones and the berm reshaping and stone nesting processes, etc), and in structural details of berm breakwaters (geometrical layout of the profile, stability of toe protection and scour protection, etc).

A few prototype measurements of the berm profile development have been carried out, but a well documented comparison between prototype monitorings, model tests and general experience with berm breakwaters will be desirable.

Conclusions

A berm breakwater is a rubble mound breakwater with a berm above still water on the seaward side, which under wave exposure reshapes into an equilibrium profile with a slope of approximately 1:5. Depending on the stability parameter the reshaped profile will be statically or dynamically stable, the latter indicating that the individual stones will move but the profile will be in equilibrium.

In summary, the most important advantages and drawbacks of berm breakwaters compared to conventional rubble mound breakwaters are:

- Smaller armour stones can be used for a berm breakwater (two to ten times smaller weight), resulting in more quarries capable of supplying the required armour stones.
- Normally only two stone classes are required for construction of a berm breakwater, ie the small stones are used as core material and bed protection and the larger stones for the berm and armour layers on the crest and rear side. If well designed, the entire quarry output can be used.
- The use of smaller stones implies that lighter equipment can be used for construction of berm breakwaters. Wider tolerances can be allowed during construction, giving the contractors the possibility of using end tipping trucks or excavators. However, also for berm breakwaters, fulfilment of the specifications to mean weight, gradation, content of fines, etc, is strictly required.
- The practical experience with berm breakwaters is limited, and the design basis should be improved.
- For a berm breakwater built from two stone classes the stones used for protection of the rear side are relatively small, which means that only limited wave overtopping is acceptable. This leads to the need for increasing the crest elevation of berm breakwaters, or alternatively the introduction of larger stones on the rear side.
- For dynamically stable breakwaters, there is a danger of progressive damage due to oblique wave attack, particularly at the roundhead. Therefore, this type of structure can only be used in cases where continued maintenance is acceptable or for temporary structures. Further, durability of stones may particularly be a problem if frequent stone motion occur.

From the above findings, it can be concluded that berm breakwaters for permanent structures should be designed to reshape into a statically stable profile, ie no continuous stone movements should be allowed.

The practical experience with the eight presented berm breakwaters shows that the dimensionless stability parameter, $H_s/\Delta D_{n50}$, varies between 2.5 and 4.1. In three of the eight presented cases, prototype measurements of the reshaped profile were made, and it was found that the berm breakwaters in question performed well during wave conditions approximating the design conditions. Further, in two of the cases

good agreement for the reshaped profiles were found with measurements from model tests.

Norwegian experience with berm breakwaters has shown that structural variants as compared to the typical profile can be economically advantageous. Two variants have been studied and applied in practice, ie protection of the rear side by larger stones and substitution of a part of the berm stones with core material.

By construction of a berm breakwater on a sandy seabed it is required to include a filter layer beneath the berm in order to prevent settlements of berm stones into the seabed.

The overall objective of research on berm breakwaters is to arrive at a better design basis, which will bring the design standards of berm breakwaters up to the level of design standards for other civil engineering structures. This objective can be reached by establishing an understanding of the physics of berm breakwaters, studies of three-dimensional effects and improved knowledge on design aspects.

Acknowledgements

The present study was carried out as part of the research and technological development programme in the field of Marine Science and Technology (MAST I). The study was financed by the Commission of the European Communities, Directorate General for Science, Research and Development through contract 0032, G6-S, Coastal Structures and by The Danish Research Council.

References

Baird, W.F. and Woodrow, K. *The development of a design for a breakwater at Keflavik, Iceland.* Seminar on Berm Breakwaters: Unconventional Rubble-Mound Breakwaters, Ottawa (1987).

Bremner, W. et al. *The Design and Construction of a Mass Armoured Breakwater at Hay Point, Australia.* Seminar on Berm Breakwaters: Unconventional Rubble-Mound Breakwaters, Ottawa (1987).

Gilman, J.F. *Performance of a Berm Roundhead in the St. George Breakwater System.* Seminar on Berm Breakwaters: Unconventional Rubble-Mound Breakwaters, Ottawa (1987).

Hall, K.R. *Experimental and Historical Verification of the Performance of Naturally Armouring Breakwaters.* Seminar on Berm Breakwaters: Unconventional Rubble-Mound Breakwaters, Ottawa (1987).

Jensen, O.J. and Sørensen, T. *Hydraulic Performance of Berm Breakwaters*. Seminar on Berm Breakwaters: Unconventional Rubble-Mound Breakwaters, Ottawa (1987).

Jensen, O.J. and Sørensen, T. *Hydraulic performance of berm breakwater heads*. Journal of Hydraulic Research, Vol 29, No 6 (1992).

Montgomery, R.J.; Hofmeister, G.J. and Baird, W.F. *Implementation and Performance of Berm Breakwater Design at Racine*. Seminar on Berm Breakwaters: Unconventional Rubble-Mound Breakwaters, Ottawa (1987).

Sørensen, T. and Jensen, O.J. *St. Paul Breakwater, Phase 1*. Coastal Engineering, Delft, 1990.

Tørum, A. et al. *Årviksand Fishing Port, Breakwater Extension*. PIANC, Osaka (1990).

Van der Meer, J.W. *Rock Slopes and Gravel Beaches under Wave Attack*. Ph.D. thesis Delft University of Technology (1988).

Viggosson, G. *Rubble Mound Breakwaters in Iceland*. Journal of Coastal Research (Spring 1990).

Numerical Modelling of Waves and Currents with regard to Coastal Structures

M. Fischer, J. Juhl and E.B. Rasmussen

Danish Hydraulic Institute
Agern Allé 5
2970 Hørsholm
Denmark

23rd International Conference on Coastal Enginering,
Venice, October 1992

Numerical Modelling of Waves and Currents with regard to Coastal Structures

M. Fischer
J. Juhl
E.B. Rasmussen[1]

Abstract

This paper describes a two-dimensional numercial model capable of simulating non-stationary flows. Special emphasis has been put on wave motion on and in porous structures, e.g. a rubble mound breakwater. Comparisons of numerical simulations with analytical solutions and model test results have confirmed the applicability of this model for studies of waves and currents with regard to coastal structures.

Introduction

In the past coastal structures such as breakwaters mainly have been studied by means of physical modelling and simplified numerical calculations. Recent developments in numerical techniques and methods, however, have implied that advanced numerical tools may be adopted in such studies. These numerical models dedicated to coastal structures are still in their infancy but likewise other branches of the hydraulics it is envisaged that numerical models will play an increasing role in future studies.

In the present paper, a special 2D (x-z) version of Danish Hydraulic Institute's three-dimensional model is described. Details on the three dimensional model

---

[1] Danish Hydraulic Institute, Agern Allé 5, DK-2970 Hørsholm, Denmark

adapted here are given in Rasmussen et al. The x-z version is designed especially for flow with regard to coastal structures and porous media. The numerical model is based on the Reynolds-averaged Navier-Stokes equations and the equation for conservation of mass. The equations are discretized into a finite difference scheme imposed on a rectangular, space-staggered grid. The finite difference equations are solved through a non-iterative ADI (Alternating Directions Implicit) technique using the artificial compressibility method.

The energy loss due to both laminar and turbulent effects in porous media is included through the Forchheimer equation. Furthermore, an inertia term has been included in the Forchheimer equation for the case of non-stationary flow.

The free surface boundary in the model has been described applying a subgrid modelling in which the instantaneous position is calculated for each time step by use of linearized momentum equations and kinematic boundary conditions. This implies that the computational domain varies from time step to time step.

The numerical model is applicable to a large range of both dynamic and stationary flow problems with regards to coastal structures such as flows in breakwaters consisting of layers with different porosity, flows through and/or beneath dams and stability of slopes etc. protected by impermeable surface layers likewise.

Model simulations have been compared with both analytical solutions and physical model tests.

Description of Flows in Porous Media

It is common to apply a macroscopic point-of-view of a porosity layer by describing the porous matrix through characteristic constants. These properties are related both to the fluid and to the granular material in order to describe the penetration of the fluid. This implies that the basic problem is reduced to establish a relation between the pressure gradient and the bulk velocity.

It can be argued as to whether this description is suitable or a microscopic point-of-view is needed. However, such an approach would imply the necessity of a description of each stone with connected geometry and roughness factors. Furthermore, highly sophisticated

turbulence descriptions would be required. This leads to unrealistic demands to both model set-up for a simulation of flow in porous media and to the performance of the model itself, since the computational grid should be very fine in order to produce the required resolution of the geometry.

A breakwater normally consists of three porous layers, i.e. core, filter, and armour layer. This implies the necessity of a porosity description, in which multiple layers with different properties can be specified. Physical model tests have shown the necessity of a description of the energy dissipation including both laminar and turbulent flow as well as energy dissipation due to dynamic effects.

The relation between the bulk velocity, u, and the pore velocity, V, is given by

$$u = V \cdot n$$

where n is the porosity.

Forchheimer equation

The Forchheimer equation consists of two terms expressing the hydraulic gradient due to both laminar and turbulent flow, respectively

$$i = a \cdot u + b \cdot u^2$$

where,

- i is the hydraulic gradient
- a is the laminar dissipation factor
- b is the turbulent dissipation factor

Since the linear term, a, accounts for the laminar effects, it depends on the viscosity. The non-linear term, b, represents the fully turbulent flow and is only dependent on the granular matrix material.

Several relationships of a and b have been proposed in the literature, of which many have been based on a dimensional analysis. In the presented model the relationship proposed by Engelund has been adopted. The laminar and turbulent dissipation terms are described by the constants a and b:

$$a = \alpha \cdot \frac{(1-n)^3 \cdot \nu}{n^2 g d^2}$$

$$b = \beta \cdot \frac{(1-n)}{n^3 g d}$$

where
- ν is the viscosity of the fluid
- g is the gravity
- d is the stone diameter
- α is an empiric constant
- β is an empiric constant

The formulation of the hydraulic gradient presented above is only valid for a steady state flow. A model for unsteady flow would be to add a time dependent term to the Forchheimer expression

$$i = a \cdot u + b \cdot u^2 + c \cdot \frac{\partial u}{\partial t}$$

The factor c can be expressed in the following way:

$$c = \frac{\left(1+\gamma \cdot \frac{(1-n)}{n}\right)}{g}$$

where γ is the inertia coefficient.

Implementation of porosity description

The model presented solves the Reynolds-averaged Navier-Stokes equations and the continuity equation in a staggered finite difference grid. The prognostic variables are the three velocity components together with the fluid pressure. The adopted porosity description is based on macro parameters of porosity, stone size and dissipation factors. The implementation of this macro scale porosity description involves two changes to the original balance equations

1) Redefinition of terms including velocity with respect to the influence of the porosity.

2) Adding of dissipation terms due to the microscopic flow resistance, i. e. flow between stones. The expression given by Forchheimer together with an additional term for the dynamic effect is applied.

The continuity equation reads

$$\frac{1}{\rho \cdot c_s^2} \cdot \frac{\partial p}{\partial t} + \nabla \cdot V_i = 0$$

where,

ρ	is the density
c_s	is the speed of sound
p	is the excess pressure
V	is the pore velocity

The momentum equation reads after introduction of the bulk velocity:

$$c \cdot \frac{\partial u_i}{\partial t} + \frac{1}{n^2} \cdot u_j \cdot \frac{\partial u_i}{\partial x_j} =$$

$$-\frac{1}{\rho} \cdot \frac{\partial p}{\partial x_i} - g_i - g \cdot a \cdot u_i - g \cdot b \cdot |u_i| u_i + \frac{1}{n} \cdot \frac{\partial}{\partial x_j} \left(E \cdot \frac{\partial u_i}{\partial x_j} \right)$$

where E is the eddy viscosity

Free Surface Description

The applied free surface description of waves is presented in the following. The method is inspired by the VOF method proposed by Nichols and Hirt but splits the volume fraction into space increment fractions in the three coordinate directions, and can as such be considered as a surface tracking method rather than a volume tracking method.

The presented description includes three dependent variables in addition to the velocity components and the fluid pressure. The variables noted α, β and γ represent fractions of space increments in the x-, y- and z-direction, respectively, and thus describe the location of the free surface within the current grid cell, see Fig. 1. In the present model the instantaneous position of the water is directly calculated, which is the main difference to the VOF method. The fraction of volume in each cell can be found as

$$V = \alpha \cdot \beta \cdot \gamma$$

A free surface cell is identified as a cell containing a non-zero value of V and having at least one neighbouring cell that contains a zero value of V. Cells with zero V values are empty cells whereas cells with non-zero V values are treated as full or interior fluid cells.

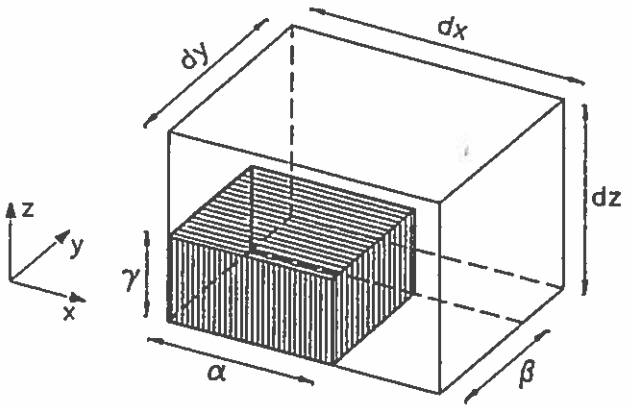

Fig. 1 Description of the free surface by a fraction of volume of fluid technique. The corners represent pressure nodes. For the two-dimensional description β = dy.

Briefly, the basic procedure for advancing a solution in time consists of three steps:

1) From the previous time step the dependent variables form the basis for a new discretisation of the conservation of mass and the conservation of momentum equations. The system is solved implicitly taking into account closed boundaries, open boundaries and free surface boundaries.

2) By use of the fractions calculated in the previous time step and on the basis of the newly found dependent variables the fractions α, β and γ are computed.

3) Finally, the fractions defining fluid regions must be used to update the fluid location taking into account the fluid in the adjacent cells and the boundaries of the computational domain.

The theory presented in the following is developed in three dimensions. For reasons of simplicity the implementation of the free surface into the three-dimen-

sional model has been done in two dimensions only - one horizontal and one vertical direction.

The Continuity Equation

In general the continuity equation reads

$$\frac{\partial \rho}{\partial t}+\frac{\partial}{\partial x}(u\rho)+\frac{\partial}{\partial y}(v\rho)+\frac{\partial}{\partial z}(w\rho) = 0$$

where ρ is the density and u, v and w are the velocity components.

In order to obtain a hyperbolicly dominated system the pressure is introduced into the continuity equation through an equation of state.

$$\frac{1}{\rho c_s^2}\cdot\frac{\partial p}{\partial t}+\frac{\partial u}{\partial x}+\frac{\partial v}{\partial y}+\frac{\partial w}{\partial z} = 0$$

where c_s is the speed of sound and p the excess pressure. In the top layer of the computational domain a cell may not be full of fluid. To obtain the continuity equation for the computational cell at the surface an integration over the fraction of fluid volume is done:

$$\frac{1}{\alpha\ \beta\ \gamma}\int_0^{\gamma}\int_0^{\beta}\int_0^{\alpha}\left(\frac{1}{\rho c_s^2}\cdot\frac{\partial p}{\partial t}+\frac{\partial u}{\partial x}+\frac{\partial v}{\partial y}+\frac{\partial w}{\partial z}\right) dx\ dy\ dz = 0$$

The result of this integration is the continuity equation described in terms of the fractions of volume

$$\frac{1}{\rho c_s^2}\cdot\frac{\partial p}{\partial t}+\frac{\partial u}{\partial \alpha}+\frac{\partial v}{\partial \beta}+\frac{\partial w}{\partial \gamma} = 0$$

The compressibility of the fluid is expressed by the speed of sound c_s. In order to make the coefficient matrix of the system diagonally dominanted, an artificial value of c_s should be used.

The Momentum Equations

The conservation of momentum reads:

$$\frac{\partial u_i}{\partial t} + \frac{\partial (u_i \cdot u_j)}{\partial x_j} = -\frac{1}{\rho} \cdot \frac{\partial P}{\partial x_i} + g_i + \frac{\partial}{\partial x_j}\left(E \cdot \frac{\partial u_i}{\partial x_j}\right)$$

where u is the velocity, P the total pressure, ρ the density, g the gravity and E the eddy viscosity of the fluid.

For reasons of simplicity regarding the space and time discretisation only the linear momentum equations are modelled in the surface cells.

The applied momentum equation for a cell containing a free surface in the x-direction reads

$$\frac{\partial u}{\partial t} = -\frac{1}{\rho} \cdot \frac{\partial}{\partial x}(p + \rho g h)$$

where h is the local, vertical distance to the surface.

Wave Boundary Condition

In order to make simulations of wave impacts on coastal structures an open boundary condition forming propagating waves in the simulation area has been developed. The wave boundary is a mixture of the general Dirichlet type boundary conditions of velocity and level boundaries in the sense that both the level and the velocity are specified. This is presently done by applying a first order wave theory.

Verifications and Simulations

A number of simulations have been performed in order to verify and study the applicability of the model. A few examples are shown in the following:

Simulation of Steady State Flow in Porous Media

Verification of the porosity description in the case of steady state flow is carried out by a comparison to experimentals made by Burcharth. The characteristic flow properties, such as the hydraulic gradient and the discharge velocity, have been measured in the case of penetration of water through three different gravel materials. For all three cases the principle model set-up both for the experimentals and for the numerical simulations is shown in Fig. 2.

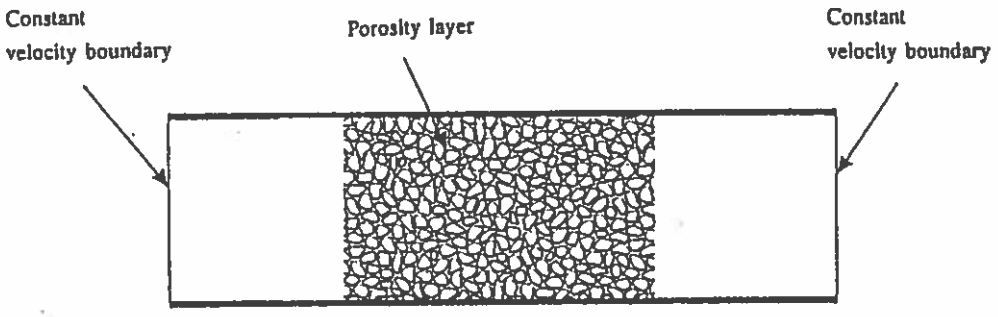

Fig. 2 Model set-up for steady state flow through a porous layer.

The comparison is done in accordance with the following description:

1) Since the hydraulic gradient is given as

$$i = a \cdot u + b \cdot |u| \cdot u$$

where,

- i is the hydraulic gradient
- a is the laminar dissipation factor
- b is the turbulent dissipation factor
- u is the bulk velocity

a straight line is expected when (i/u) is plotted against u. The slope of the line equals b and the intersection with the (i/u)-axis equals a.

2) For the experimentals a and b are deduced as described above. In accordance with the Forchheimer expression and by use of the properties of the gravel material measured by Burcharth the dissipation factors α and β are deduced. For the case of steady state flow the dynamic dissipation term equals zero.

3) With the properties of the gravel material and the fluid, simulations of the flow through a porous layer is carried out. Velocity boundaries with a constant value are imposed at both ends of the model area. For each of the three gravel materials the boundary velocity is varied in order to obtain a suitable number of points. The simulations are made with "full slip" closed boundaries, which implies that the pressure gradient is zero outside the porous layer. For all the simulations the kinematic viscosity of the fluid equals $1.34 \cdot 10^{-6}$

m^2/s, which is in accordance with the viscosity of the water used by Burcharth.

4) The comparisons of the experimentals and the numerical simulations for two of the gravel materials are shown in Fig. 3.

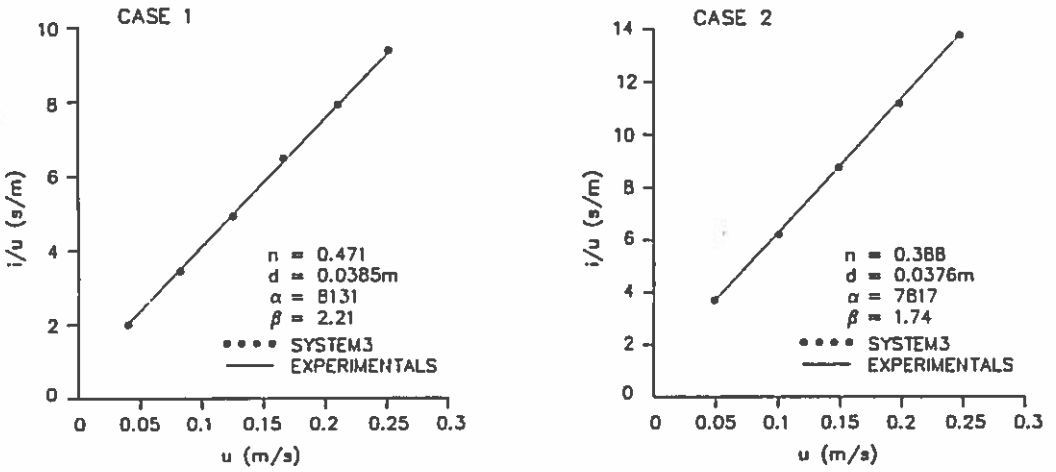

Fig. 3 Comparisons of experimentals and numerical simulations for two cases of steady state flow.

The comparisons show that the model, including a bulk description of the porosity layer, is able to reproduce the measurements for the case of steady state flow.

Simulation of a dam break

Testing of the free surface description is done by simulation of a dam break. Initially a column of water is confined between two vertical walls. When the calculation starts the right wall is removed, and gravity forces the fluid to propagate along the dry floor.

At the beginning of the simulation the fluid is described by 20x20 cells with a size of 0.1 m in both the vertical and horizontal direction. The applied time step is 0.01 sec. Examples of results showing the fluid position and the velocity is presented in Fig. 4.

Experimental results for a dam break test case have been reported by Martin and Moyce and form a basis for a comparison to the model generated results.

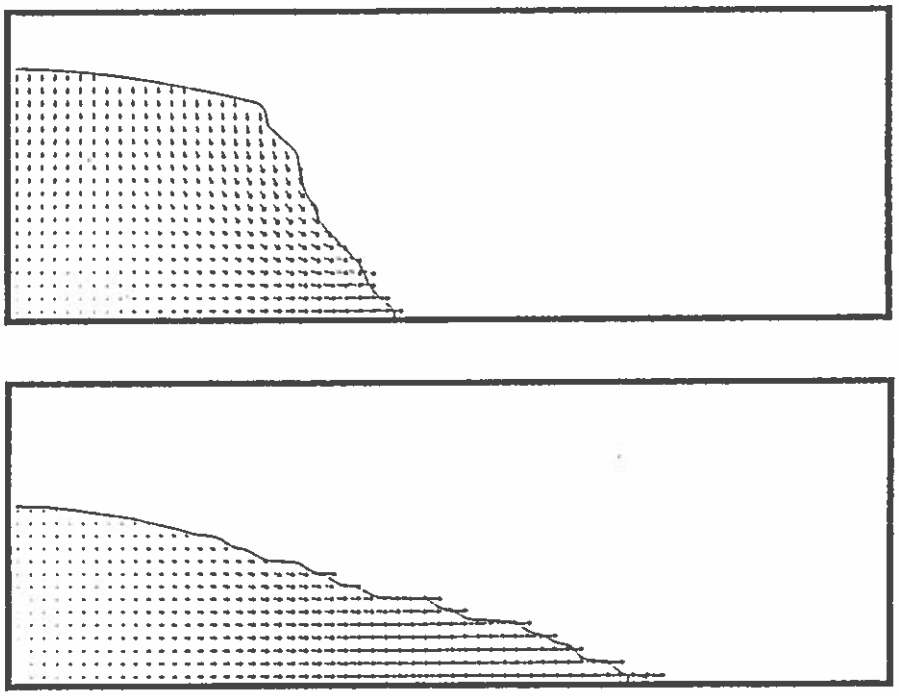

Fig. 4. Example of results for the dam break test. The plots represent the surface location and the velocity for each grid node at time 0.3 sec. and 0.7 sec.

A comparison between model generated results and the experimental results of the toe position vs time is shown in Fig. 5. The largest deviation from the experimental results is everywhere less than one grid spacing.

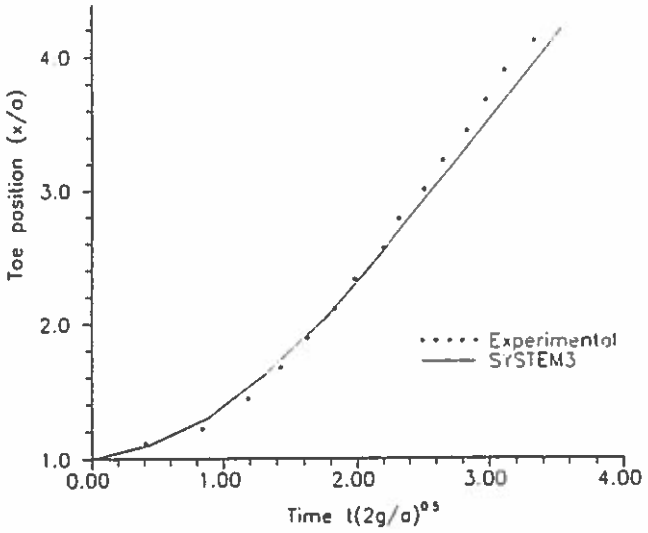

Fig. 5 Comparison of a numerical simulation with experimental data for a dam break.

Wave Run-Up on a Permeable Structure

The combination of porosity layers and a free surface is tested by simulation of wave run-up on a rubble mound breakwater. The breakwater has a sea side slope of 1:2.0 and consists of three porosity layers with the following characteristics:

a = 14.4, 4.9, 2.0 s/m
b = 1820.0, 109.0, 50.0 (s^2/m^2)
c = 0.0, 0.0, 0.0
n = 0.35, 0.37, 0.39

The model grid consists of 100 x 3 x 50 nodes and the general parameters of the simulation are:

$\Delta x = \Delta y = \Delta z = 0.015$ m
$\Delta t = 0.002$ sec

At the right end of the model area a wave boundary is applied with the following parameters:

H = 0.06m, T = 1.0s

The still water depth for the simulation is 0.3 m.

An example from a model simulation is shown in Fig. 6. Time series plots of horizontal velocities in three points (as defined in Fig. 6) are shown in Fig. 7.

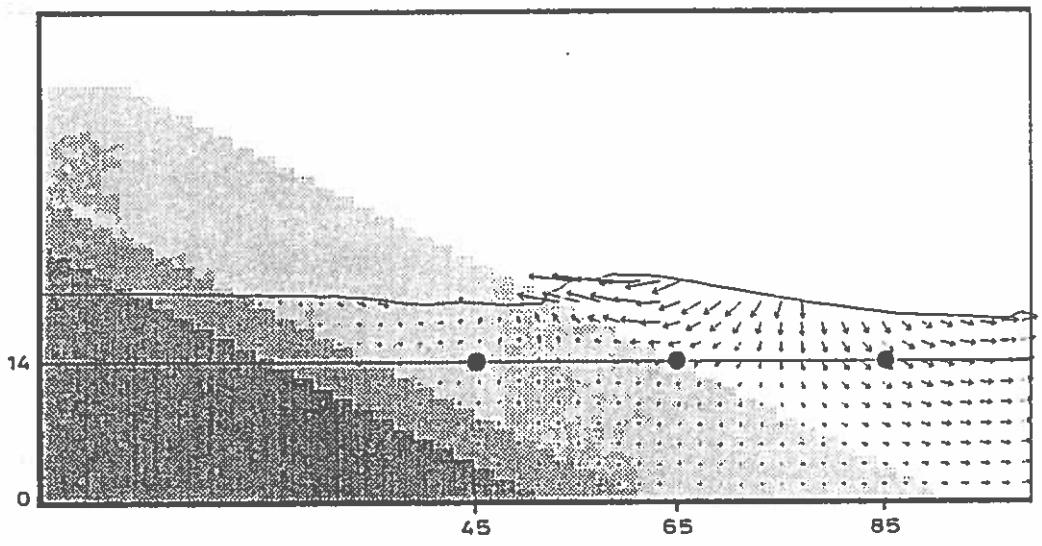

Fig. 6 Example of surface position and velocities during wave run-up on a permeable breakwater. After t = 1.8 s.

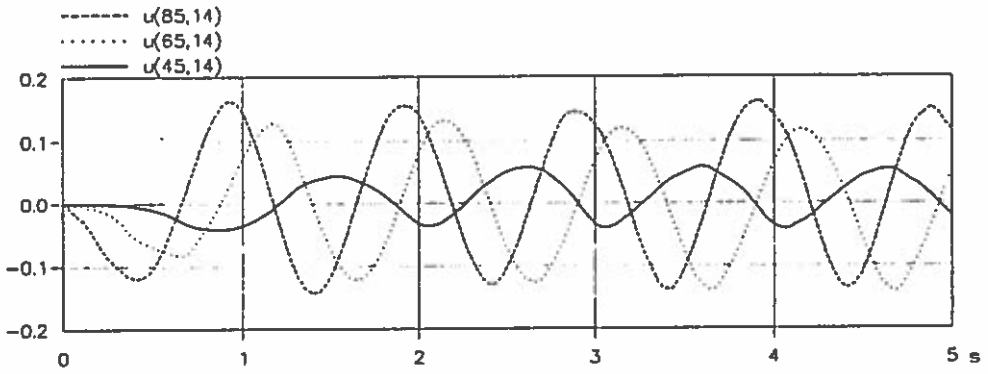

Fig. 7 Time series of horizontal velocities (m/s) at three locations, one outside the breakwater, one at the edge of the breakwater and one in the coarsest porosity layer as shown in Fig. 6.

Conclusions

A 2D (x-z) numerical model has been developed for description of flows on and in coastal structures. The model includes a description of the energy loss in porous media taking into account both laminar and turbulent effects as well as the inertia effect. Comparisons with analytical solutions and measurements from physical model tests with waves and currents have shown promissing results.

In order to correctly simulate the flow on and in porous coastal structures, it will be necessary to establish a better knowledge of the coefficients involved in the energy loss equation and to describe the energy loss due to wave breaking on a slope which implies a formulation of the hereby induced air entrainment.

Acknowledgement

The research project which started in 1988 has been funded by the Danish Council of Technology through grant no. 880440. The verification of the porosity description has partly been co-sponsored by the Commission of the European Communities under the MAST-programme, contract 0032.

References

Burcharth, H.F. & Christensen, C.
"On stationary and non-stationary porous flow in coarse granular materials", University of Aalborg, Denmark (1991).

Engelund, F.
"On the laminar and turbulent flows of ground water through homogenous sand", Trans. Danish Academy Tech. Science, Vol. 3 (1953).

Martin, J.C. & Moyce, W.J.
"An experimental study of the collapse of liquid columns of a rigid horizontal plane", Phil. Trans. Roy. Soc. London A244, 312 (1952).

Nichols, B.D., Hirt, C.W., Hotchkiss, R.S.
"SOLA-VOF: A solution algorithm for transient fluid flow with multiple free boundaries", Los Alamos Scientific Laboratory Report LA-8355 (1980).

Rasmussen, E.B., Vested, H.J., Justesen, P. & Ekebjærg, L.C. "System 3 - A Three-dimensional Hydrodynamic Model", Danish Hydraulic Institute, Denmark (1990).

On stationary and non-stationary porous flow in course granular materials

H.F. Burcharth and Claus Christensen

University of Aalborg
Denmark

Statens Teknisk Videnskabelige Forskningsråd
Rammeprogrammet MARIN TEKNIK 1989 - 92.

MAST G6S PROJECT I
WAVE ACTION ON AND IN COASTAL STRUCTURES

H.F. Burcharth and Claus Christensen

On stationary and non-stationary porous flow in coarse granular materials

May 1991

DEPARTMENT OF CIVIL ENGINEERING
AALBORG UNIVERSITY
SOHNGAARDSHOLMSVEJ 57 DK-9000 AALBORG DENMARK
TELEPHONE +45 98 15 85 22 TELEFAX +45 98 14 25 55 TELEX 69523 auciv dk

CONTENTS

On stationary and non-stationary porous flow in coarse granular materials

by

H.F. Burcharth [1] and Claus Christensen [2]

1. INTRODUCTION AND SUMMARY

Traditionally the hydrodynamic response of rubble mound structures are studied in physical models scaled according to the Froude scaling law which neglects viscous forces. This introduces scale effect because the inherent length scaling of the stone diameters creates laminar flow in regions which in prototypes are dominated by turbulent flow. Numerical modelling of the flow do not have this draw back and is therefore attractive. One important part of a numerical model is the basic description of the non stationary wave generated flow in the porous structure of the breakwater. This flow differs from ground water flow in that fairly large accelerations and velocities are present. The present paper deals with the description of this kind of flow.

A critical discussion based on physical considerations is given of the mathematical description of steady flow. It is argued that the conventional use of the Forchheimer equation is not suitable in case of fully turbulent flow, which is the relevant flow regime for rubble mound breakwaters.

The relationship between the bulk velocity and the pressure gradient in steady and non-steady flow was studied in U-tube permeameter tests for various stone sizes and gradations.

Moreover, a mathematical model of the non-stationary flow in the U-tube permeameter was established in order to provide more insight in the sensitivity of the system to variations in the parameters. In this way also the experimental limitations of the U-tube permeameter technique was explored.

---

[1] Professor of Marine Civil Engineering, University of Aalborg, Denmark.

[2] M.Sc., University of Aalborg, Denmark. The experimental test results presented in this paper are from the M.Sc. dissertation "Hydrodynamic performance of rubble mound breakwaters" April 1990, by Claus Christensen.

Results from stationary flow tests confirmed an apparent validity of the Forchheimer equation but demonstrated also the inconsistency in using this equation when extrapolating results from one flow regime to another. A proposal is given for a formula covering the fully turbulent flow range relevant to flows in breakwaters including the effect of the surface characteristics of the stones.

Results from unsteady flow tests were related to a generalized Forchheimer equation which includes an inertia term. However, it was not possible with the technique used to determine the related added mass coefficient with reasonable accuracy within the tested range of accelerations. Thus the general importance of the inertia effect is still a question although the present research indicate the effect to be marginal. It is concluded that answer to this question demands a different experimental technique where the period of large acceleration are increased compared to present tests.

2. STEADY FLOW. THEORETICAL AND EXPERIMENTAL BACKGROUND

The approach used in the research presented in this paper was macroscopic in the sense that a relationship between the bulk (discharge) velocity, V, and the hydraulic pressure gradient, I, was investigated. Related to this approach there are two theoretically sound models which are generally used for the steady flow case.

2.1 The friction factor model

This model, which is one form of the general exponential form $I = a\, v^m$, is based on the general force balance equation

$$I = f \frac{v^2}{2gR} \quad , \tag{1}$$

where v is a characteristic velocity, e.g. $v = V/n$, where n is the porosity. R is a characteristic length (e.g. the hydraulic radius $R = d/$ in case of pipe flow, and $R = \frac{dn}{6(1-n)}$ for granular materials, cf. eq. (5)), and f is a friction factor which is dependent on of the granular body and on a Reynolds' number, e.g. $Re = VR/\nu$, where ν is the kinematic viscosity.

The problem is to establish an analytical expression for the variation of f. A rather complicated expression is to be expected because it must cover the whole range from laminar flow through the transition to fully turbulent rough flow. Moreover, it must include the relevant characteristics of the granular system. The latter presents a real problem because the hydraulic resistance is sensitive to changes

valid for smooth pipe flow, is an example of this type of expression, but is relatively simple due to the fact that the geometry of the system can be given only by two parameters namely the pipe diameter and the pipe surface roughness.

Although the character of porous flow is different from pipe flow there are similarities with respect to the flow regimes commonly recognised in the literature. Consequently, it might be illustrative to show the well explored but rather complicated variation of f with Re in pipe flow, shown in Figure 1.

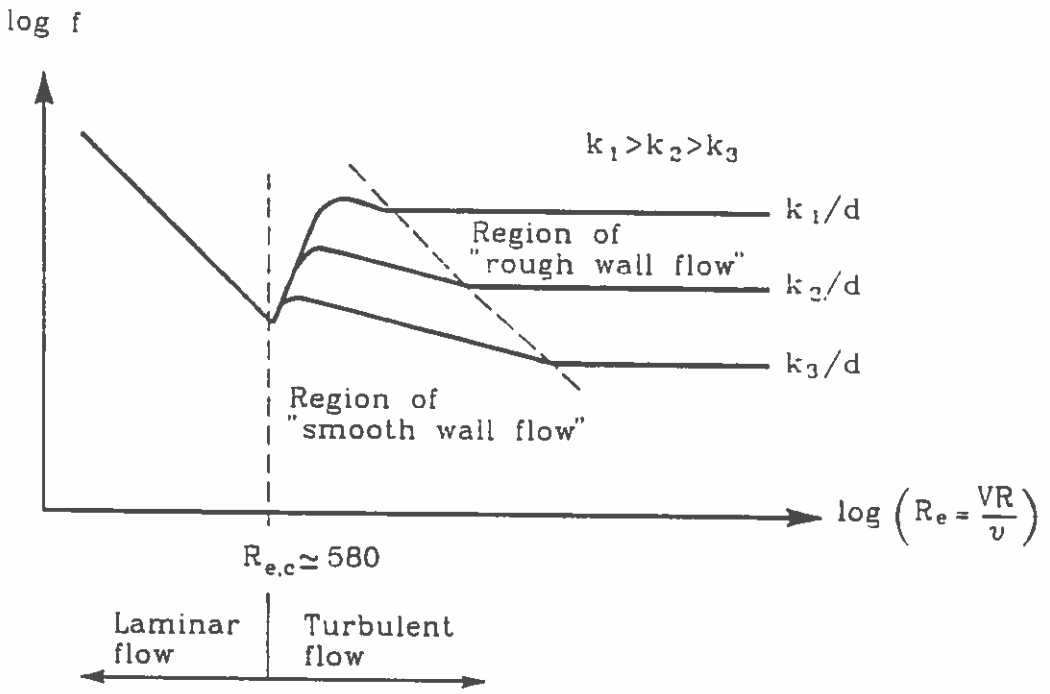

Fig. 1. Variation of the friction factor f with the Reynolds number in pipe flow.

Using the hydraulic radius $R = \frac{d}{4}$ as characteristic length the transition Reynolds number Re_c between the laminar and the smooth wall turbulent region is app. 580. The smooth flow occurs when the wall roughness elements are covered by a laminar boundary layer, but the main flow is turbulent. In this range f is weakly dependent on Re or viscosity. The rough flow corresponds to turbulent boundary layer, i.e. the laminar boundary layer thickness is reduced to a thin film following the surface of the wall roughness elements which then protrude into the turbulent flow. In this range the friction factor f will be influenced only by the relative roughness k/d and not by the viscosity or Re. The Reynolds number range for the smooth wall turbulent flow depends on the relative roughness of the pipe, i.e. the

smooth wall turbulent flow depends on the relative roughness of the pipe, i.e. the ratio between the surface roughness, k and the pipe diameter. The larger the value of k/d, the smaller the Reynolds number range for smooth flow. For very rough pipes this range is almost insignificant and consequently the transition Reynolds number between smooth and rough flow is close to 580.

Several researchers have tried the friction factor model approach for porous flow but generally without much success (Bakhmeteff 1937, De Lara 1955, Rumer 1966, Barends 1978).

2.2 The Forchheimer model

The model is given by a two term series expression

$$I = aV + bV^2 \tag{2}$$

where V is the bulk velocity and a and b are supposed to be constants for a given fluid viscosity and granular body geometry. Eq. (2) is often denoted the Forchheimer equation because Forchheimer (1901) was probably the first to suggest this type of equation.

The general interpretation of the equation is that the linear term constitutes the contribution from the laminar flow, for which reason the factor a depends on the viscosity. The nonlinear term represents the fully turbulent flow contribution, i.e. the factor b is independent on the viscosity. It is an open question to which degree eq. (2) can describe the transition between laminar and turbulent flow, because the variation of I in the transition is most probably dependent on the surface charactersistic of the grain matrix, cf. the well known variation of f (in eq. (1)) in pipe flow. The nonlinear second term in eq. (2) signifying the turbulent flow contribution has the same character as eq. (1), but is different in that b depends only on the granular matrix geometry while f is dependent also on a Reynolds' number, i.e. the viscosity, because eq. (1) covers also the laminar and the transition regions.

If the nonlinear term is neglected we obtain the Darcy equation for laminar flow.

2.3 Flow regimes and related Reynolds number ranges

A conventional way of relating eq. (2) to the various flow regimes is depicted in Fig. 2 for one specific porous matrix and viscosity.

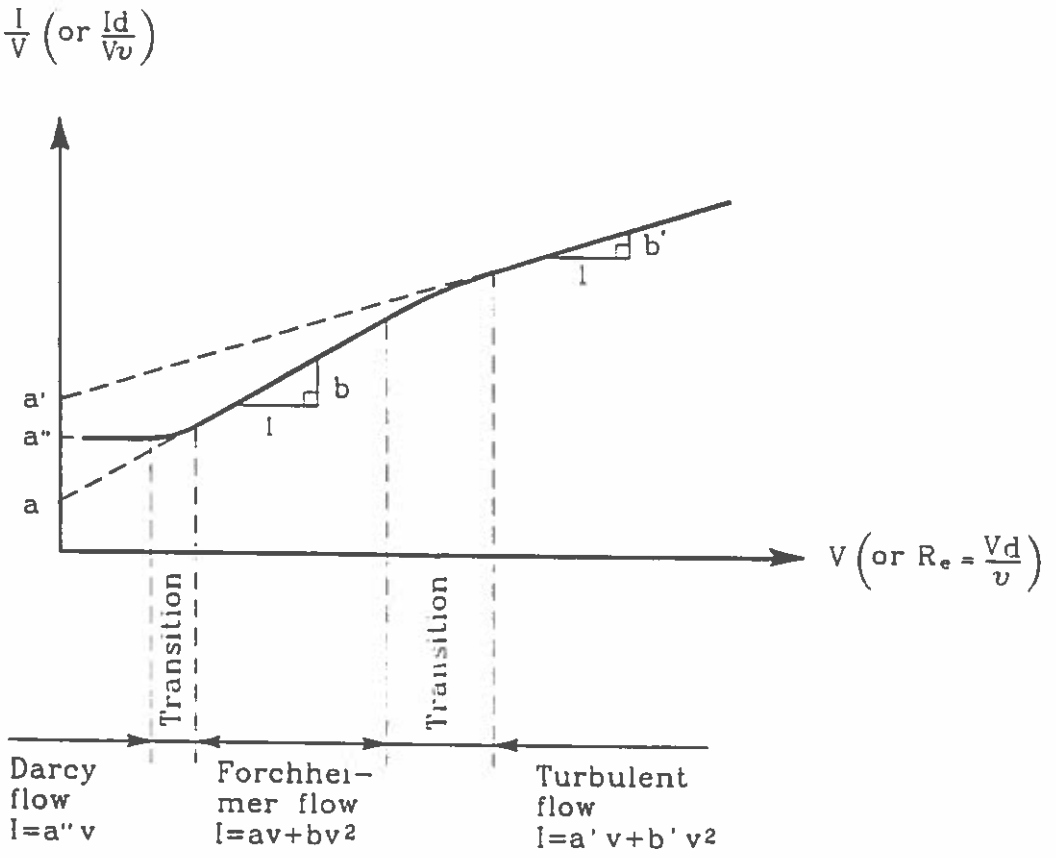

Fig. 2. Conventional representation of flow regimes for porous flow based on a Forchheimer equation analysis. Values of a , a' and a'' depend on the granular matrix and the viscosity. Values of b and b' depend on the granular matrix.

The Reynolds numbers corresponding to the transitions between the various regimes were studied by Fand et al., 1987. Based on experiments with uni-size and mixed-size glass spheres they found the ranges of the diameter - Reynolds number given in Table 1. The applied definition of the Reynolds number is

$$Re = \frac{Vd}{\nu} \tag{3}$$

where d is the sphere diameter in case of uni-size spheres. In case of mixed-size spheres d is a weighted "mean" diameter defined as

$$d = \frac{1}{\sum_{i=1}^{n} \frac{F_i}{d_i}} \tag{4}$$

where F_i is the mass fraction for particles having the diameter d_i and n is the total

number of fractions applied to the sample. Eq. (4) assumes that all particles have the same density.

Table 1. Diameter - Reynolds number ranges for various flow regimes. Results of experiments by Fand et al. (1986) with 2, 3, and 4 mm glass spheres.

	uni-size	multi-size
Darcy flow	$Re \leq 2.3$	$Re \leq 1.6 - 2.1$
Forchheimer flow	$5 \leq Re \leq 80$	$2.7 - 3.7 \leq Re \leq 55 - 74$
Turbulent flow	$Re \geq 120$	$Re \geq 120$

It should be noticed that the Re-range for turbulent flow was found identical for uni-size and multi-size media when the definitions eqs. (3) and (4) are used.

Dybbs et al. (1975) found on the basis of tests with plexiglass spheres in a hexagonal packing the Reynolds number regimes shown in Table 2. They use the "pore-size" Reynolds number based on average pore size and average pore velocity as characteristic length and velocity, respectively.

Table 2. Pore-size-Reynolds number ranges for various flow regimes. Results of experiments by Dybbs et al. (1975) with plexiglass spheres in hexagonal packing.

Darcy flow	$Re < 1 - 10$
Forchheimer flow	$1 - 10 < Re \leq 200$
Turbulent flow	$Re > 350$

When considering the ratio of characteristic grain diameter to characteristic pore diameters to be in the order of 2 - 3 and the ratio between bulk velocity and average pore velocity to be in the order of 4 it is seen that the results given in Tables 1 and 2 are rather consistent, the values in Table 1 being somewhat on the low side. Test results for stone samples indicate higher values than those given for spheres.

The relationship between the diameter Reynolds number and the pore-size-Reynolds number might be explored by considering an analogy between the flow in a pipe with large roughness, cf. Fig. 1., and the porous flow.

For the porous flow, like in pipe flow, a relevant characteristic length in the Reynolds number might be a hydraulic radius, R, which for pipe flow is $\frac{D}{4}$, where D is the pipe diameter. For porous flow R is often defined as the ratio of the pore volume to the total surface area of the grains within a unit volume. If we consider a sample of uni-size spheres we get

$$R = \frac{\text{pore volume}}{\text{number of spheres} \times \text{area of a sphere}} = \frac{n}{\frac{1-n}{\frac{1}{3}\pi\left(\frac{d}{2}\right)^3} \cdot 4\pi\left(\frac{d}{2}\right)^2} = \frac{d\,n}{6(1-n)} \qquad (5)$$

where n is the porosity and d the sphere diameter.

For samples of uni-size spheres having $n \simeq 0.36$ we obtain $R \simeq 0.1d$. By comparing this to $R = \frac{D}{4}$ used for pipe flow it is seen that on "equivalent pipe diameter" for porous flow would be $0.4d$, since $R = \frac{0.4d}{4} = 0.1d$. This might support the use of an average "pore" size of $0.4d$ as characteristic length in the Reynolds number, cf. the discussion given above of the results by Dybbs et al. It might then be concluded that the diameter Reynolds number range for the transition between Forchheimer flow (smooth wall flow) and the turbulent flow (rough wall flow) in the case of spheres is in the range $80 < Re < 120$. A wider range is to be expected for real stone samples. Moreover, it is to be expected that the shape and the relative surface roughness influences the various transition values of the Reynolds number in the non-Darcy flow ranges.

Engelund (1953) argues that a conventional Reynolds number like the one defined by eq. (3) cannot adequately describe the ratio between the inertial and the viscous forces because it is not dependent on the porosity and the shape of the grains. As a logic solution to this problem Engelund uses a Reynolds number defined as

$$\xi = \frac{bV}{a} \quad , \qquad (6)$$

i.e. the ratio between the turbulent and the laminar terms in eq. (2). As an example Engelund found $\xi \simeq 0.07$ for the transition between Darcy and Forchheimer flow.

The definition (6) works very well in the Forchheimer flow regime but is very difficult to use for the turbulent regime because a is ill-determined as a very small quantity compared to bV.

Consequently, it is recommended to use the Reynolds number definition given by eq. (3) for turbulent flow in breakwaters. The argument by Engelund is not so important in this case because the influence of the normal variations in the porosity and the shape of the grains will not cause significant changes in Re. Alternatively a Reynolds number defined by $Re = \frac{VR}{\nu}$, where R is given by eq. (5) could be used.

In the following sections Re means the diameter-Reynolds number given by eq. (3).

2.4 Evaluation of the factors in the Forchheimer equation

Many researchers have tried to develop generally applicable empirical or semi-empirical expressions for a and b (Lindquist 1933, Carman 1937, Muskat 1946, Ergun 1952, Engelund 1953, Irmay 1958, Scheidegger 1960, Ward 1964, Ahmed et al., 1969, Hanoura et al., 1978).

2.4.1 Dimensional analysis

A rational approach is to use dimensional analysis.
From eq. (1) it is seen that

$$I = I\left(\frac{V}{n}\ ,\ \nu\ ,\ g\ ,\ R\ ,\ \text{geometry}\right) \tag{7}$$

The geometry might be expressed partly by a surface roughness element height, k characterizing the surface characteristics of the grains and partly by a gradation parameter, G. In case of laminar flow the surface roughness element height k can be neglected and for the turbulent flow the viscosity ν can be neglected. Thus by dimensional analysis

$$I_{lam} = I_{lam}\left(\frac{\nu}{gR^2}\frac{V}{n}\ ,\ G\right) \tag{8}$$

$$I_{turb} = I_{turb}\left(\frac{\left(\frac{k}{R}\right)^N}{gR}\left(\frac{V}{n}\right)^2\ ,\ G\right) \qquad \text{for all } N \tag{9}$$

If for R eq. (5) is applied we obtain

$$I_{lam} = I_{lam}\left(\frac{(1-n)^2\nu}{n^3gd^2}V\ ,\ G\right) \tag{10}$$

$$I_{turb} = I_{turb}\left(\frac{1-n}{n^3gd}V^2\left(\frac{1-n}{n}\cdot\frac{k}{d}\right)^N\ ,\ G\right) \tag{11}$$

The most simple interpretation of (10) and (11) would be

$$I_{lam} = \alpha\frac{(1-n)^2}{n^3}\frac{\nu}{gd^2}V \tag{12}$$

$$I_{turb} = \beta\frac{1-n}{n^3}\frac{1}{gd}V^2 \tag{13}$$

and consequently the Forchheimer equation (2) becomes

$$I = \alpha\frac{(1-n)^2}{n^3}\frac{\nu}{gd^2}V + \beta\frac{1-n}{n^3}\frac{1}{gd}V^2 \tag{14}$$

in which case α depends only on the gradation, G and β depends both on the relative surface roughness, $\frac{k}{d}$ and the gradation, G.

Another way of deriving an equation for the turbulent drag term is by considering the total drag force on the grains within a sample of volume $dy\,dx\,dz$. The force on each grain is $\approx \frac{1}{2}\rho\left(\frac{V}{n}\right)^2 d^2$ where $\approx$ means proportional to. The number of grains within the volume is $\approx \frac{1-n}{d^3}\,dx\,dy\,dz$. The total force of grains is then $\approx \frac{1-n}{d}\,dx\,dy\,dz\,\rho\,\frac{V^2}{n^2}$. This force is balanced by (equal to) the differential pore water pressure force in two consequtive sections spaced dx in the bulk velocity direction, i.e. $\approx \Delta p\,dy\,dz$ where the full cross section area must be used. Using $I = \frac{\Delta p}{\rho\,g\,dx}$ we arrive at, $I \approx \frac{1-n}{n^2 g\,d}\,V^2$, which is different from eq. (13). This, however, does not imply that eq. (13) is wrong because a dimensionless quantity like n can always be multiplied on the parameters.

One or both of the simple expressions given by eqs. (12) and (13) have been used by several researchers, e.g. Ergun (1952), Lindquist (1933), Fand et al. (1987), Dudgeon (1966).

Table 3 lists examples of experimental values of α and β related mainly to the Forchheimer flow Reynolds number range. α and β are often denoted shape factors, because researchers generally explain α and β as dependent on the geometry of the granular medium. However, no distinction is made between the α- and the β-dependency as explained by the above given dimensional analysis.

Table 3. Examples of α and β values (defined by eq. (14)) covering mainly the Forchheimer flow range.

Researcher	Particles	Porosity	Diameter range or d_{50} mm	Re	α	β
Fand et al. 1987	uniform glass spheres	0.360	2-4	5-80	~ 182	~ 1.92
Lindquist *) 1933	shot	0.383	1-5	4 - 263	184	1.82
Dudgeon **) 1966	uniform glass spheres	0.415	16	< 400	164	1.7
	— " —	0.385	29	< 180	193	2.4
	river gravel	0.367	16	< 85	329	4.7
	— " —	0.406	110	< 7000	922	2.0
	angular rock	0.455	16	< 400	622	5.4
	— " —	0.515	14	< 200	479	4.0
	— " —	0.438	25	< 400	425	5.3
	— " —	0.483	37	< 500	92	10.8
Engelund 1953	flinty, calcareous sand and of uniform size	0.395	1.4-2.6	25-150	335	3.57

*) Data taken from Ahmed et al., 1969.

**) Data calculated from Dudgeon's graphs, not from the data points.

2.4.2 Engelund coefficient

Engelund (1953) used eq. (13) but proposed an alternative to eq. (12), namely

$$I_{lam} = \alpha_E \frac{(1-n)^3}{n^2} \frac{\nu}{g d_E^2} V \tag{15}$$

where the indices E stands for Engelund. The characteristic diameter d_E is defined as the diameter of a sphere which has a volume equal to the average volume of the grains. Using eq. (15) the Forchheimer equation reads

$$I = \alpha_E \frac{(1-n)^3}{n^2} \frac{\nu}{g d_E^2} V + \beta \frac{1-n}{n^3} \frac{1}{g d_E} V^2 \tag{16}$$

Engelunds argument for recommending this expression was a better fit to the experimental data available to him (data of Franzini (1951) with uniform spheres covering the porosity range $n = 0.27 - 0.48$ and data by Rose (1945)). However, it should be noticed that for what might be regarded the relevant porosity range for rubble mound structures, $n = 0.37 - 0.48$, there is no significant difference between eqs. (12) and (15) as the corresponding ratio between the porosity factors $\frac{(1-n)^3}{n^2} / \frac{(1-n)^2}{n^3} = n(1-n)$ only varies between 0.233 and 0.250. Moreover, because Engelund's semi-empirical expression eq. (15) was based mainly on experiments with small particles it is recommended to prefer the theoretically better founded eq. (12), especially when dealing with breakwaters where extrapolation to much larger particle diameters is needed.

The α and β values recommended by Engelund are given in Table 4.

Table 4. The Engelund coefficients (defined by eqs. (16).

	α_E	β
Uniform, spherical particles	~ 780	~ 1.8
Uniform, rounded sand grains	~ 1000	~ 2.8
Irregular, angular grains	up to 1500 or more	up to 3.6 or more

Engelund pointed out that the recommended values of β are based only on very few experiments (by Lindquist, 1933, Givan, 1934 and Chardabellas, 1940).

The Engelund α-coefficients can be transformed to the α value defined by eq. (12) by multiplying with $(1-n)n \simeq 0.24$, cf. Table 5.

Table 5. Engelund coefficients transformed to fit eq. (14).

	α	β
Uniform, spherical particles	~ 190	~ 1.8
Uniform, rounded sand grains	~ 240	~ 2.8
Irregular, angular grains	up to 360 or larger	up to 3.6 or larger

2.4.3 Shih coefficients

Very recently and after the completion of tests presented in this paper Shih (1990) proposed the following expressions for α and β, based on regression analyses of steady flow permeameter test results for single size and wide grade samples of chrushed limestone with stone diameters of up to 75 mm, respectively 40 mm. The values are to be applied in eq. (16) with $d = d_{15}$, i.e. the diameter that 85% of the sample exceeds.

Single size sample:
(Tested ranges: $d_{85}/d_{15} \simeq 1.3$, $5mm < d_{15} < 55mm$)

$$\alpha = 1684 + 3.12 \cdot 10^{-3} \left(\frac{g}{\nu^2}\right)^{2/3} d_{15}^2 \tag{17}$$

$$\beta = 1.72 + 1.57\ exp\left[-5.10 \cdot 10^{-3} \left(\frac{g}{\nu^2}\right)^{1/3} d_{15}\right] \tag{18}$$

Wide grade sample:
(Tested ranges: $2 < d_{85}/d_{15} < 5$, $4mm < d_{15} < 17mm$)

Eqs. (16), (17) and (18) are used with d_{15} replaced by

$$d_* = d_{15} \left(\frac{d_{15}}{d_{60}}\right)^{-1.11} \left(\frac{d_{50}}{d_{85}}\right)^{0.52} \tag{19}$$

The shape of the limestones and the porosities of the samples used by Shih are not specified.

The tested Reynolds range is app. $50 \leq Re \leq$ app. 6,000, i.e. mainly the fully turbulent range and as such relevant to flow in rubble mound breakwaters, but for the small diameter samples (6 and 10mm, cf. Table 14) Re did not reach the turbulent range.

Apart from not being stringent in accordance with the dimensional analysis, cf. eqs. (8) - (11), eqs. (17) and (18) demonstrates an unexpected dependency of α and β on the grain diameter, cf. eqs. (12) - (14). Fig. 3 shows the experimental results by Shih (1990).

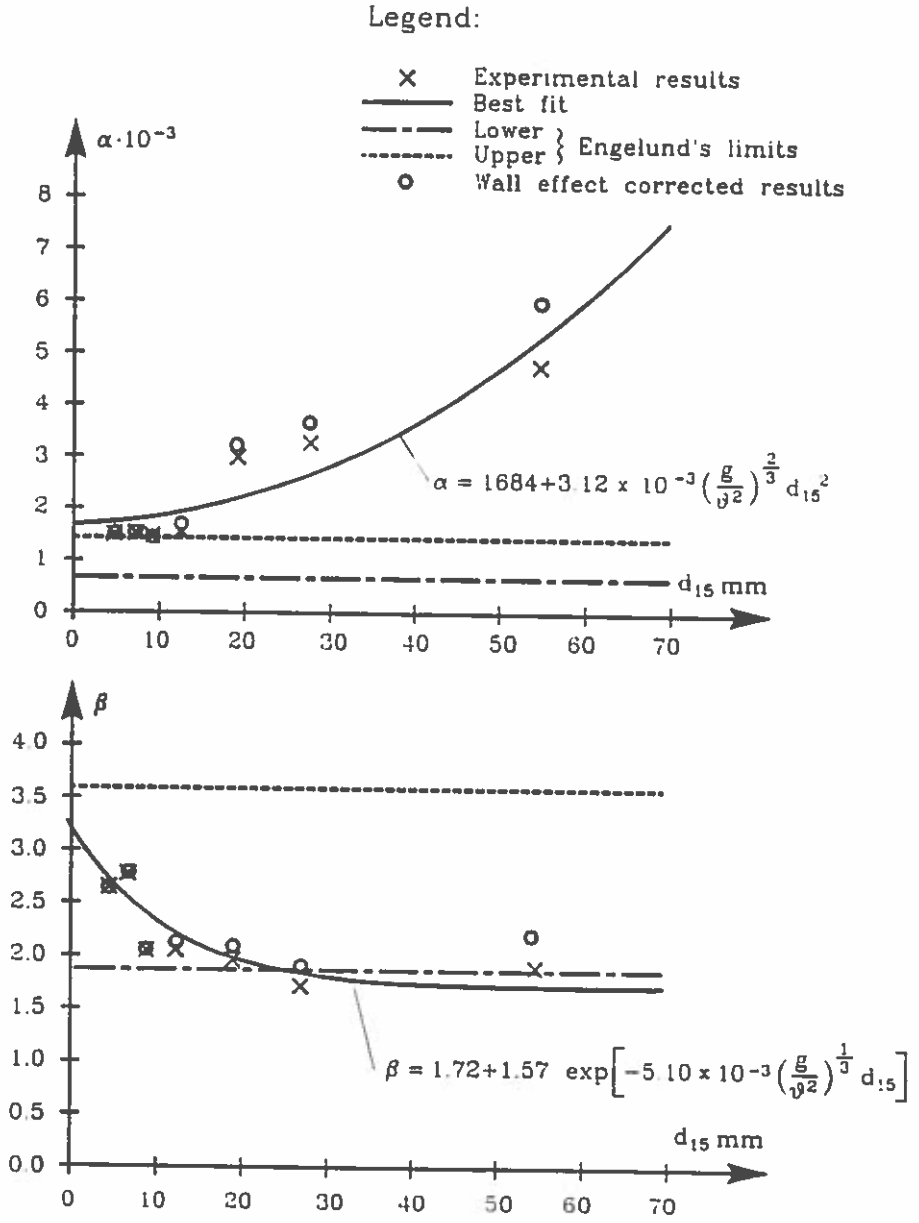

Fig. 3. Experimental results by Shih (1990). Corrections for wall effects according to Fig. 18 also shown.

The surprising but theoretically uncorrect trend of α increasing with the diameter is also observed in the experimental results presented in this paper if a conventional fit to the Forchheimer equation is used, cf. section 9. A similar analysis of the test results by Fand et al. shows the same trend.

The use of the Shih formulae for large size materials, e.g. extrapolation to a real breakwater situation, implies a considerable overestimation of the laminar flow resistance.

A discussion of the appearence of this fictive variation of α and β with the diameter is given in section 2.4.4.

Because of a relative large ratio between the stone diameter and the permeameter diameter in some of the test series by Shih (1990) a correction for wall effects should be made. The circles in Fig. 3 shows the experimental results corrected for wall effects using the correction factors presented in section 8.

2.4.4 Critical review of conventional fit of the Forchheimer equation to experimental data.

It is seen from Fig. 2 that for a given granular matrix the values of the coefficients a and b in the Forchheimer equation generally vary with Re. Only within certain ranges (denoted Darcy, Forchheimer and Turbulent) they attain constant (but different) values. Consequently, the asymptotic values of a and b, depends on the Re-range covered by the underlaying experimental results.

Taking the α-value as an example it will depend on the lower limit of the Re-values applied in the specific test series. Fig. 2 demonstrates clearly that an α-value corresponding to a Forchheimer range Re-value is smaller than an α-value corresponding to an upper transition range Re-value.

In permeameter tests with samples of different grain diameters the upper and lower Re limits usually depend on the diameter. This is due to normal experimental limitations. For example in the case of small diameter samples the max obtainable Re-value is smaller than for a large diameter sample and vise versa for the minimum obtainable Re-value. Thus the experimental Re-range increases with the grain diameter as in the case for almost all published permeameter test results, including the results by Shih. In some cases there might not even be an overlap in the Re-ranges for the finest and the coarsest materials applied in one set of published results.

The drastic increase in α with the diameter seen in Fig. 3 can most probably be explained by this effect. This is because the lowest Re-values, which are related to the smallest diameter samples, correspond to the upper limit of the Forchheimer flow range where α obtains minimum values, while the larger Re-values, which are related to the larger diameter samples, correspond to the fully turbulent flow range characterized by larger α values, cf. Fig. 2.

In this way also the large values of β for small diameter samples seen in Fig. 3 can be explained because the β-values decreases when moving from the Forchheimer flow range to the fully turbulent range, cf. Fig. 2.

It is concluded that it can be very misleading to use Forchheimer equation coefficient values (or α amd β values) outside the Re range corresponding to the underlaying test results.

Correct asymptotic values of the coefficients $a"$, $a-b$, $a'-b'$ in Fig. 2 can only be found from set of test results completely within each of the related Re-ranges. Simple extrapolation from one Re-range to another is not possible.

2.5 Proposal for a turbulent flow equation

For prototype rubble mound breakwaters exposed to design waves the flow regime will be turbulent almost without exception.

The discussion in section 2.4.4 shows that exrtapolation of permeameter data from Forchheimer and/or the transitions regions into the turbulent region is not possible. Consequently to arrive at data corresponding to prototype turbulent flow only permeameter data covering the turbulent range can be used.

It follows from the dimensional analysis that for fully turbulent flow it is not correct to use a series expression consisting of both a linear term and a quadratric term, although this is generally the conventional approach, cf. Fig. 2. A more correct approach is depicted in Fig. 4.

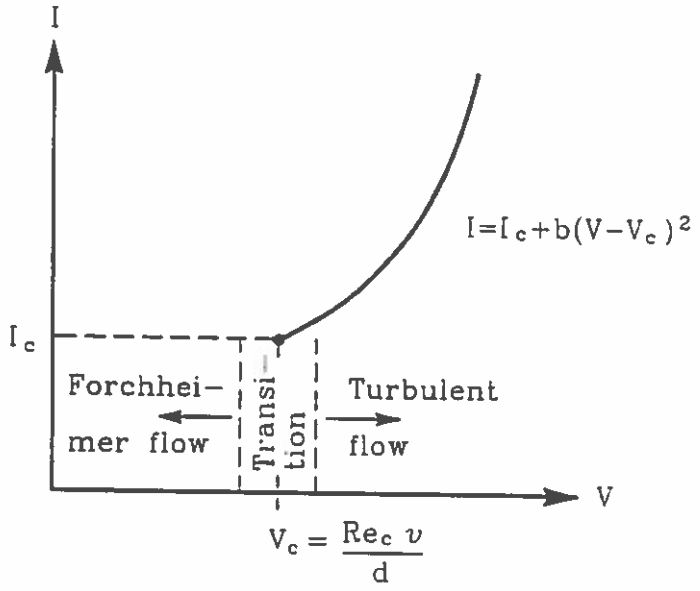

Fig. 4. Representation of the turbulent flow equation.

Re_c is in principle the critical Reynolds number signifying a lower value for the turbulent flow regime and V_c is the corresponding bulk velocity. According to the previous discussion the Reynolds number range for the transition between the Forchheimer flow and the turbulent flow is rather narrow, $80 \leq Re \leq 120$ for spherical particles. For this case it can be assumed as a close approximation that $Re_c = 100$ separates the Forchheimer flow range and the turbulent range. For stone samples the corresponding Reynolds number range are wider and a larger value of Re_c must be chosen, e.g. 300.

The turbulent flow equation is given by

$$I = I_c + b(V - V_c)^2 \tag{20}$$

I_c can be calculated from the Forchheimer flow equation with V equal to

$$V_c = \frac{Re_c \nu}{d} \tag{21}$$

Inserting eq. (21) into eq. (14) we obtain

$$I_c = Re_c \alpha_F \frac{(1-n)^2}{n^3} \frac{\nu^2}{gd^3} + Re_c^2 \beta_F \frac{1-n}{n^3} \frac{\nu^2}{gd^3} \tag{22}$$

or

$$I_c = \frac{\nu^2}{gd^3} \frac{1-n}{n^3} \left[\alpha_F (1-n) Re_c + \beta_F Re_c^2\right] \tag{23}$$

where α_F and β_F correspond to the Forchheimer flow range and to the related definition of the characteristic diameter, d.

In order to evaluate eq. (21) Table 6 shows typical values of I_c and the related V_c calculated for various characteristic grain diameters using $\alpha = 500$, $\beta = 5.0$ and $n = 0.45$, which are approximate values for irregular, angular grains, cf. Table 5. $\nu = 1.14 \cdot 10^{-6}\ m^2/s$ and $Re_c = 300$.

Table 6. Typical values of I_c and V_c.

Characteristic diameter, d	I_c	V_c
m		m/s
0.001	430	0.34
0.01	$43 \cdot 10^{-2}$	0.034
0.03	$1.6 \cdot 10^{-2}$	0.011
0.06	$2.0 \cdot 10^{-3}$	0.006
0.20	$5.3 \cdot 10^{-5}$	0.002

It is seen from Table 6 that for all breakwaters with core material of quarry run ($d > 0.03\ m$) or coarser material I_c will be smaller than app. 10^{-2} and the corresponding critical bulk velocity V_c smaller than app. $10^{-2}\ m/s$. In this case I_c and $V_c \simeq 0$ and eq. (21) reduces to

$$I = \beta \frac{1-n}{n^3} \frac{V^2}{gd} \tag{24}$$

where β depends on the relative surface roughness of the grains and the grading, cf. eq. (11).

For the quasi-steady flow in breakwater sand cores the viscous effects will be present and consequently the Forchheimer equation (14) with the α and the β values given in Table 5 might be used. The very large I_c-value of 430 given in Table 6 for sand with $d = 0.001\ m$ indicates that fully turbulent flow in sand will never occur in a breakwater situation. Even related to permeameter tests such a large hydraulic gradient is extreme.

Considering that eq. (22) is expressing the conditions at transition between Forchheimer flow and fully turbulent flow it is surprising that the laminar and the turbulent terms are of almost the same magnitude. It is to be expected that the laminar term should be negligible. The ratio between the two terms are, cf. also the Engelund Reynolds number equation (6),

$$\xi = \frac{\beta_F\, Re_c}{\alpha_F(1-n)} \simeq 5 \qquad \text{for} \quad Re_c = 300 \tag{25}$$

This indicates that the Reynolds number, $Re^{T,L}$, corresponding to the lower value of the fully turbulent flow regime should be somewhat larger, i.e. $Re_c \simeq 600 - 1000$. However, if this is the case then it can be concluded that the empirically determined α and β values by Engelund and other researchers dealing with sand size grains have not been fitted to results covering the whole regime from Darcy flow to fully turbulent flow, but only the lower Reynolds number range where viscous forces are of importance. Consequently, it is doubtful if the reported small grain β-values by Engelund and others can be taken as the asymptotic values for turbulent flow regime. Instead of this β-values determined from experiments with fully turbulent flow should be used.

As to the α-value = 190 for uniform spherical particles reported by Engelund, cf. Table 5, it represents truly the lower asymptotic value for the Forchheimer flow regime because it is quantitatively identical to the uniform diameter sphere

coefficient, $36\,\kappa = 36 \cdot 5.34 = 192$, given in the Darcy flow equation

$$I = 36\,\kappa\,\frac{(1-n)^2}{n^3}\,\frac{\nu}{gd^2}\,V \tag{26}$$

where κ is the Kozeny-Carman constant, see Fand et al. (1990).

3. UNSTEADY FLOW. THEORETICAL AND EXPERIMENTAL BACKGROUND

A model for unsteady flow in porous media was probably first proposed by Polubarinova Kochina (1962) who generalized the Forchheimer equation by adding a time dependent inertia term

$$I = a\,V + b\,V^2 + C\,\frac{dV}{dt} \tag{27}$$

where a, b and C are taken as constants for a given porous media. However, Polubarinova Kochina did not investigate the inertia term further.

The force F_I corresponding to the inertia term might be formulated as the sum of the contributions from the inertia generated fluid forces on the grains, $F_{I,g}$, and the forces necessary to accelerate the pore water, $F_{I,w}$, i.e. $F_I = F_{I,g} + F_{I,w}$.

$$F_{I,g} = \rho\,v_b\,\frac{dv}{dt} + C_a\,\rho\,v_b\,\frac{dv}{dt} = \rho\,(1+C_a)\,v_b\,\frac{dv}{dt} = \rho\,C_m\,v_b\,\frac{dv}{dt} \tag{28}$$

where ρ is the fluid mass density, v_b is the volume of the grains and v is a characteristic fluid velocity. The first term in (28) is the Froude-Krylov force and the second term is the added mass term.

The pore water inertia term might be formulated as

$$F_{I,w} = \rho\,v_w\,\frac{dv}{dt} \tag{29}$$

where v_w is the pore water volume.

If we consider a sample of length $\Delta\ell$ with a unit area cross section perpendicular to the flow and introduce the volumetric porosity n = void volume/total volume and take the characteristic velocity $v = V/n$, where V is the bulk velocity (Darcy velocity) we obtain

$$F_I \;=\; F_{I,g} + F_{I,w} = \rho\,C_m\,\left(\frac{1-n}{n}\right)\Delta\ell\,\frac{dV}{dt} + \rho\,\Delta\ell\,\frac{dV}{dt}$$

$$= \rho \left(1 + C_m \frac{(1-n)}{n}\right) \Delta\ell \frac{dV}{dt} \tag{30}$$

The force F_I over a unit area corresponds to a difference in pressure Δp_I over the sample length $\Delta\ell$, i.e.

$$F_I = \Delta p_I = I_I \Delta\ell \rho g \quad , \tag{31}$$

where I_I is the gradient corresponding to the inertia forces.

Substituting (31) into (30) we obtain for the last term in (27)

$$I_I = \frac{1 + C_m \left(\frac{1-n}{n}\right)}{g} \frac{dV}{dt} \tag{32}$$

The overall inertia coefficient C_m is expected to be dependent on a Reynolds' number, the shape and the relative surface roughness of the grains. the relative motion of the fluid (usually expressed by a Keulegan-Carpenter number) and the history of the fluid motion.

The complete equation (27) now reads

$$I = aV + bV^2 + \frac{1 + C_m \left(\frac{1-n}{n}\right)}{g} \frac{dV}{dt} \tag{33}$$

The two first terms on the right hand side, which correspond to the drag force, are as an approximation used with values of a and b determined from steady flow tests. Under this assumption it is possible by means of permeameter tests with non-steady flow to determine C_m and thereby explore the significance of the inertia term. Hannoura et al. (1978) used this approach but were not successful in determining consistent values of C_m as they for example found C_m-values in the range $-7 < C_m < 5$ for river gravel of size 1.6 cm. Hannoura et al. used a U-tube permeameter with a 15.2 cm square sample section and a maximum pressure difference corresponding to 150 cm head of water. The fluid velocity (and thus the acceleration) was determined by a TSI laser anemometer in one point a short distance upstream of the sample. The authors explain the reasons for the very large scatter in their results to be partly due to the very short period of "large" acceleration (0.15–0.25 sec) which makes accurate measurements very difficult, and partly due to the use of the steady flow coefficient values of a and b in (23), which might be a bad approximation because the flow regime corresponding to the steady flow Reynolds' number cannot be fully developed during the very short period of fast acceleration starting with the fluid at rest.

In the present study the same approach as used by Hannoura et al. (1978) was applied but with a larger cross section U-tube.

4. EXPERIMENTAL MODEL

The steady and unsteady flow arrangements are shown in Fig. 5.

The unsteady flow tests were performed in a U-tube where compressed air was applied to generate a desired water level difference in the two upright sections. The air was suddenly decompressed through a quick release vent. Maximum pressure difference corresponded to 200 cm head of water.

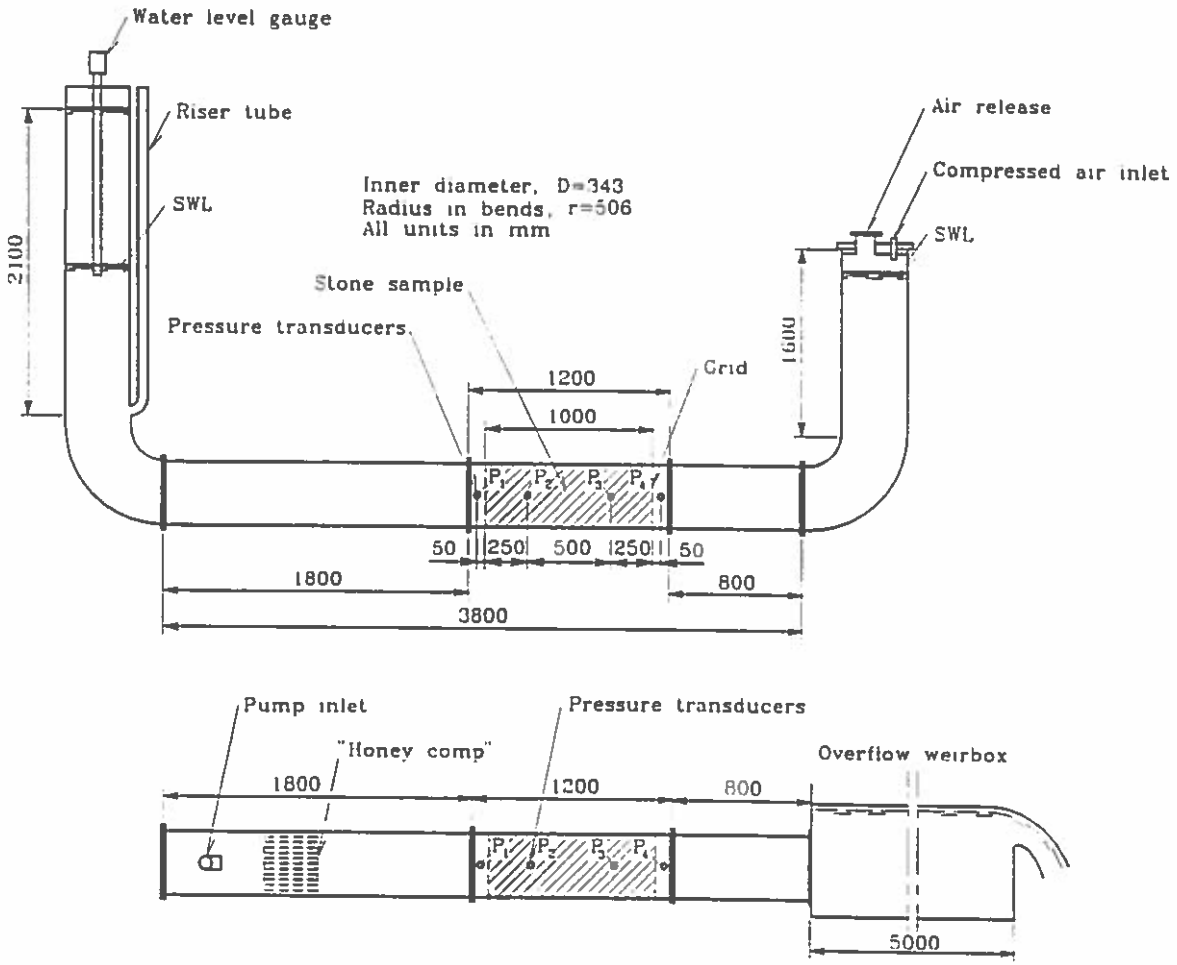

Fig. 5. Experimental set-up.

A water level gauge was used to determine the instantaneous velocity and acceleration by single and double differentiation. A weak non-linearity of the level gauge was corrected for.

The instantaneous pressure difference across the porous media was determined by means of four Wheatstone bridge pressure transducers which were highly linear in the measured range. Two transducers, P_2 and P_3, were placed with a distance

of 500 mm well inside the 1000 mm long stone sample. The transducers P_1 and P_4 were placed just outside the sample. In this way it was possible to compare an internal and an external pressure gradient based on $P_2 - P_3$ and $P_1 - P_4$, respectively. The transducers were mounted in the pipe wall in such a way that an almost smooth inner surface was ensured. In order to investigate if the pressure recorded by the surface mounted transducers were representative for the pressures averaged across the stone sample some series of tests were performed with pressures measured through a perforated tube inserted across the stone sample (this method was also suggested by Allsop and Shih, 1990. It turned out that this approach exhibited the same pressures as the conventional method.

In the steady flow tests only the horizontal part of the U-tube was used, cf. Fig. 5. The water supply was provided by pumps and the discharge was measured by means of a V-notch overflow weir mounted in a 5 meter long weir box. The accuracy is in the order of 1-2%.

Before each test the datachable test section of the pipe was placed in a vertical position and the stone material was placed uniformly over the cross section. No compaction was applied. After filling the test section the surface was levelled and a double grid was placed on the top and bolted tight, see Fig. 6. A similar grid was mounted at the other end of the test section.

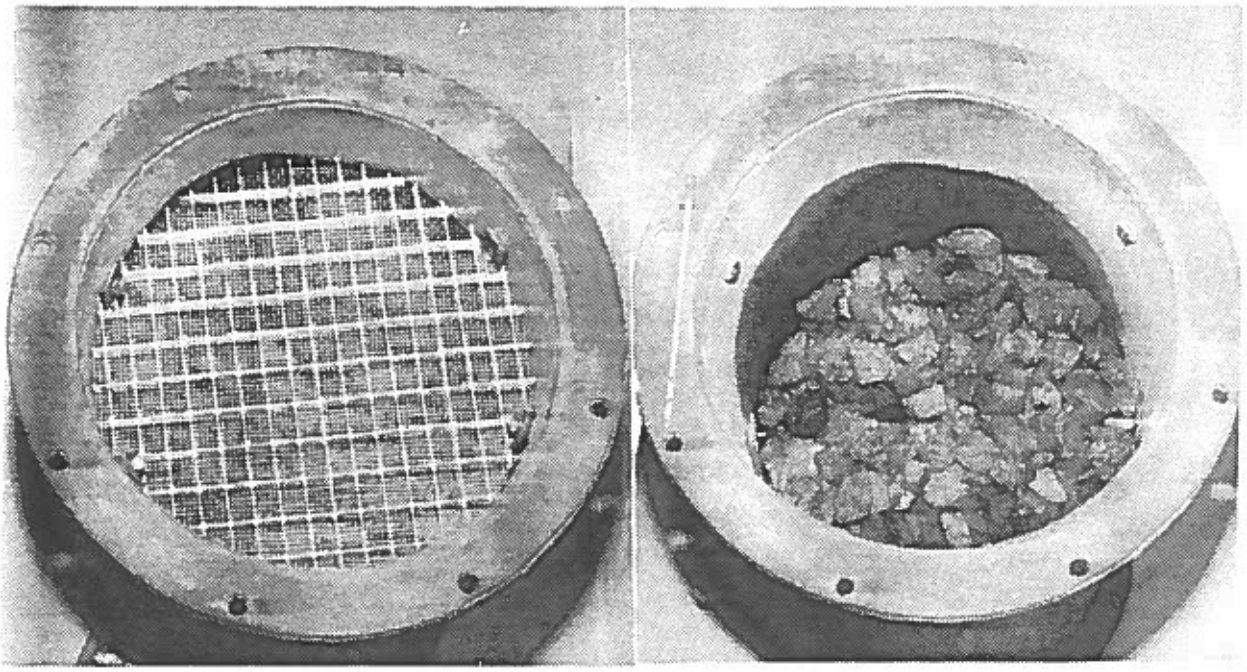

Fig. 6. The double grid constraining the test sample.

In the unsteady flow test series, each containing 5 repeated test runs, 3 initial tests were performed in order to remove the entrapped air. With the same purpose the flow was set running for a period prior to the steady flow tests. The stone sample was not removed and replaced in between the 5 repeated test runs in the unsteady flow tests. Consequently the variability observed in each tests series is due to uncertainty in the measurement system and due to possible natural repositioning of stones within the sample.

Because the steady flow values of a and b is used for the unsteady flow, cf. eq. (33), the stone samples were not removed between the steady and the unsteady tests in order not to introduce extra uncertainty.

5. CHARACTERISTICS OF TESTED STONE SAMPLES

Eight samples of gravel and crushed rock of density 2.5 - 2.7 t/m^3 were used in the tests. For each sample the stone size distribution, the shape parameters and the porosity were determined, see Table 7 and Figures 6 - 13. In the following each test series and test sample are denoted by the same number.

Table 7. Characteristics of stone samples.

Test/ sample	Stone type	d_{15} mm	d_{50} mm	d_{85} mm	$\frac{d_{85}}{d_{15}}$	$\frac{d_{15}}{d_{50}}$	$\frac{d_{50}}{d_{85}}$	grading	shape class	porosity
1	crushed rock	6.6	9.4	11.5	1.7	0.70	0.82	medium	irregular	0.457
2	—	9.8	13.8	17.9	1.8	0.71	0.77	—	—	0.455
3	—	16.0	20.1	25.7	1.6	0.80	0.78	—	—	0.451
4	—	30.9	38.5	50.3	1.6	0.80	0.77	—	—	0.471
5	gravel	13.0	18.1	24.6	1.9	0.72	0.74	—	semi round	0.391
6	—	32.3	37.6	43.8	1.4	0.86	0.86	narrow/medium	very round	0.388
7	crushed rock	31.0	36.8	42.8	1.4	0.84	0.86	—	irregular	0.473
8	—	—	—	—	—	—	—	—	—	0.467

The stone size distribution was determined by a standard sieve apparatus with diameter of 300 mm and mesh widths of 2, 4, 8, 12.5, 16, 25, 32, 45 and 64 mm. The results are drawn as accumulative curves in a log-linear coordinate system and the characteristic diameters are calculated by assuming straight lines between the data points.

The following characterization of the gradations are used (cf. the recommendation in the CIRIA-CUR manual on the use of rock in coastal and shoreline engineering, under preparation)

	d_{85}/d_{15}
narrow or "single size" gradation	1.2 – 1.4
medium width gradation	1.4 – 2.5
wide or "quarry run" gradation	2.5 – > 5.0

As to the shape of stones no generally accepted standard seems to exist. Several systems for defining the gross shape using axial dimensions have been proposed. The one used here is taken from the above mentioned CIRIA-CUR manual and make use of the following definitions:

- z : sieve size, i.e. the smallest square hole that a stone can pass through with optimum orientation.
- ℓ : maximum axial length given by the maximum distance between two points on the stone.
- d : thickness or maximum axial width given by the minimum distance between two parallel straight lines through which the stone can just pass.

The d/z ratio (generally in the order of 0.75) can distinguish tabular from elongate stones. This distinction is of no great significance as the ratio ℓ/d alone can provide the essential degree of departure from the equant form. The ratio ℓ/d is generally in the order of 2.0 - 2.5. In Figs. 7 - 13 are shown the accumulative shape distribution curves and the average values of the ratios ℓ/d and d/z.

A system solely based on the above ratios cannot provide any information on the surface characteristics of the stones and the general type of shape. The CIRIA-CUR definitions of visual shape classes shown in Table 8 are used

Table 8. Definition of shape classes for stones.

	Angular Stones with surface bounded by sharp edges and corners.			Rounded Most corners and edges show clear signs of wear and crushing	
Shape class	Elongate + tabular	Irregular	Equant	Semiround	Very round
	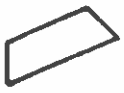	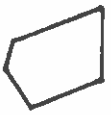			
Typical sources	Columar joints, basalts, bedded sedimentary metamorphic rock	Massive sediment and igneous rocks, some metamorphic rocks	Massive sediment and igneous rocks	Softer sedimentary rocks rounded during wear	Dredged sea stones, glacial and river boulders
Mean aspect ratio l/d	> 3.0	2.0 - 3.0	1.5 - 2.0	1.5 - 3.0	1.0 - 2.5

The porosity is defined as the ratio of the pore volume to the gross volume of a porous media. In general there are two methods to estimate the porosity – either by weighing solids or draining voids. Dudgeon, 1968, has carried out a thourough study of the possible errors affecting the two methods and has compared the results with experiments.

The significant errors affecting both methods are the measurement of the gross volume and weighing errors of which the last should be small. This introduces an error of the magnitude 1-2%. By weighing solids the problem is the estimation of the density for a material that is neither dry nor saturated, surface dry. This problem can partly be overcomed by using an average density. The corresponding problem with draining voids is the error caused by water retention on particle surfaces, particularly in the contact regions. This error can be reduced by trying to measure the amount of water retained on a typical sample and thus correct the result.

Another problem with the estimation of the porosity is that the porosity is higher at the permeameter wall in a zone half a median particle diameter thick. Thus the estimated porosity is an average porosity for the sample in the permeameter. Simple calculations show that the permeability is approximately 1.5% higher in the wall zone.

The errors inherent in both methods amount approximately to 4% and Dudgeon has shown that this agrees with experiments, so no method is on this basis preferable to the other. But the method of weighing solids is usually the easiest in practical application.

An important conclusion by Dudgeon is that the measurement of porosity for large size granular materials can not be carried out with a high degree of accuracy (unless large samples are used).

In the present investigations the porosity was determined by weighing the stone sample contained in the permeameter and subsequent determination of the volume of the stones by dividing by the stone density. The density used complied with the water content of the stone sample when weighing it. The water content corresponded to the mean of dry conditions and saturated, surface dry conditions, ρ_{ssd} as given in Figs. 7 - 13.

MATERIAL PARAMETERS

TEST 1

DENSITY

ρ_{ssd} = 2716 kg/m^3
ρ_0 = 2694 kg/m^3
W_a = 0.8

POROSITY

n = 0.457

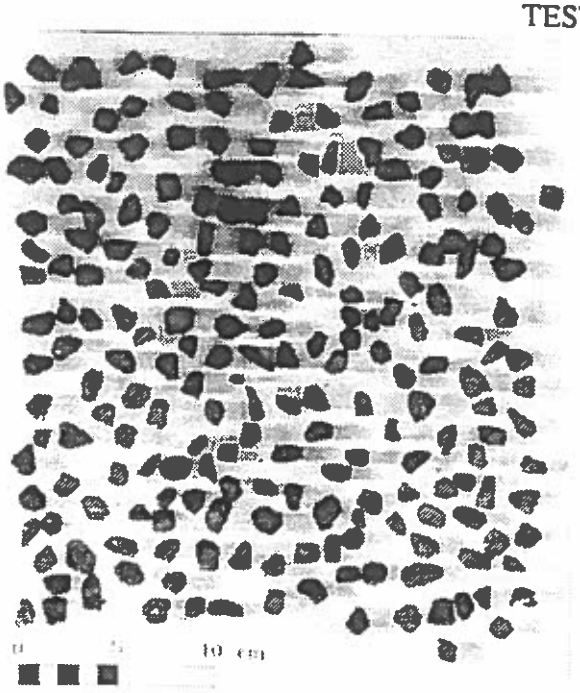

Test 1

STONE SHAPE

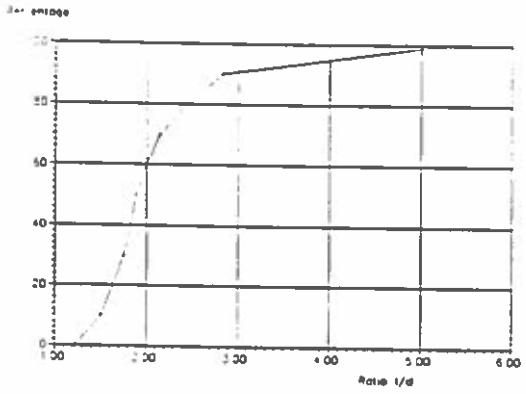

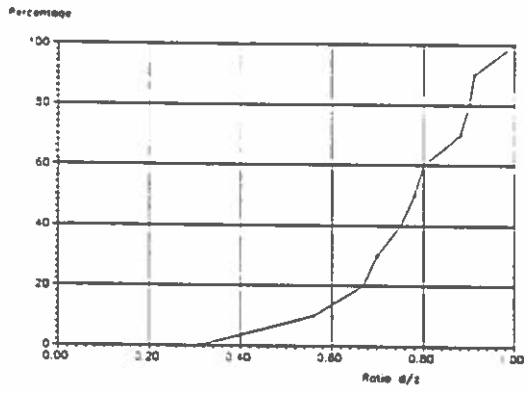

$\overline{z}$ = 10.4 mm, $\overline{l/d}$ = 2.1, $\overline{d/z}$ = 0.76
Shape class : Irregular.

SIZE GRADATION

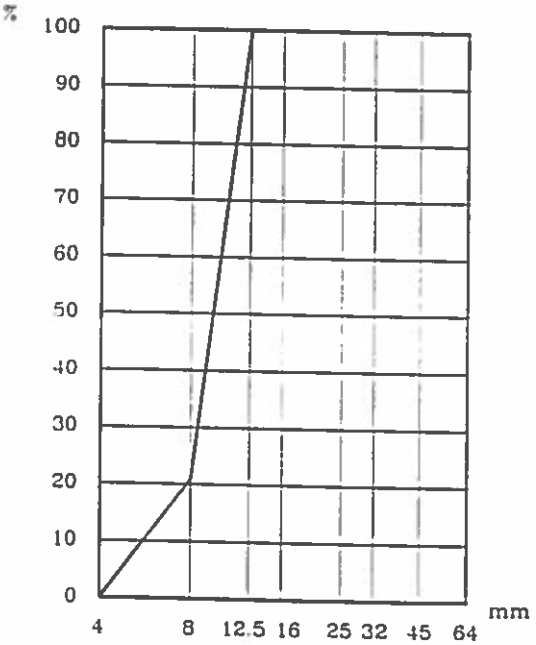

d_{50} = 9.4 mm, d_{15} = 6.6 mm, d_{85} = 11.5 mm.
$\frac{d_{85}}{d_{15}}$ = 1.7, grading: medium.

Fig. 7.

MATERIAL PARAMETERS

TEST 2

DENSITY

ρ_{ssd} = 2680 kg/m^3
ρ_0 = 2667 kg/m^3
W_a = 0.5

POROSITY

n = 0.455

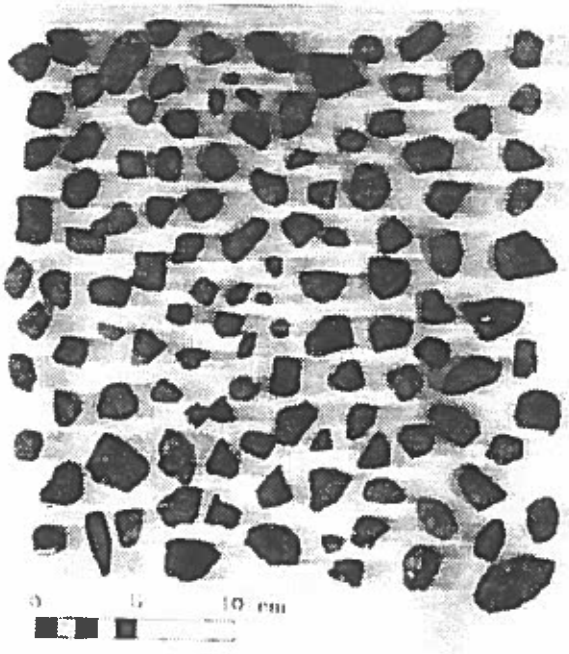

Test 2

STONE SHAPE

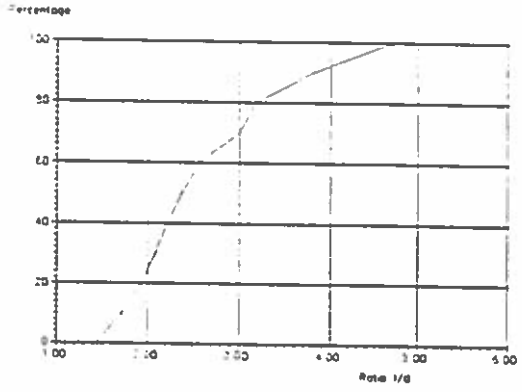

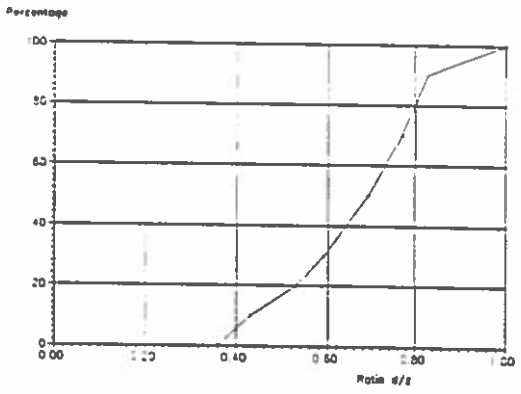

$\overline{z}$ = 13.5 mm, $\overline{l/d}$ = 2.6, $\overline{d/z}$ = 0.66
Shape class : Irregular.

SIZE GRADATION

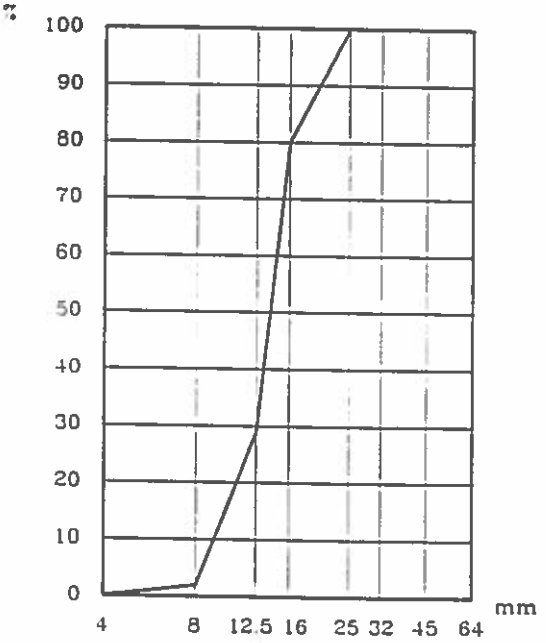

d_{50} = 13.8 mm, d_{15} = 9.8 mm, d_{85} = 17.9 mm.
$\frac{d_{85}}{d_{15}}$ = 1.8, grading: medium.

Fig. 8.

MATERIAL PARAMETERS

TEST 3

DENSITY

ρ_{ssd} = 2623 kg/m^3
ρ_0 = 2602 kg/m^3
W_a = 0.8

POROSITY

n = 0.451

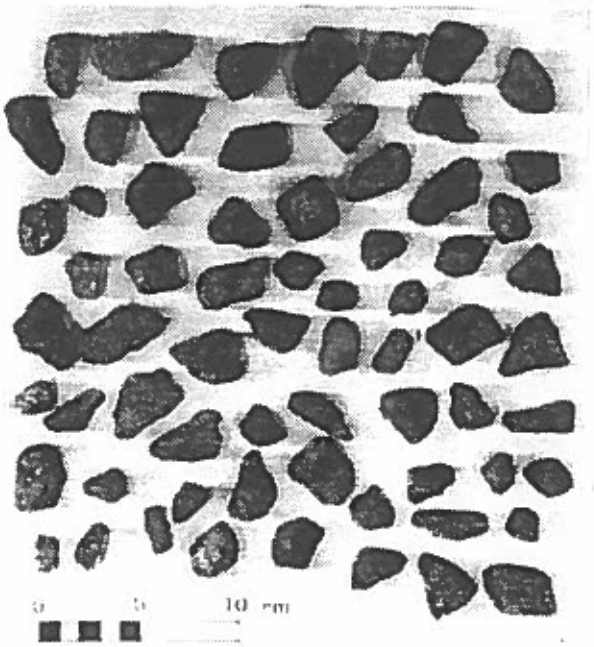

STONE SHAPE

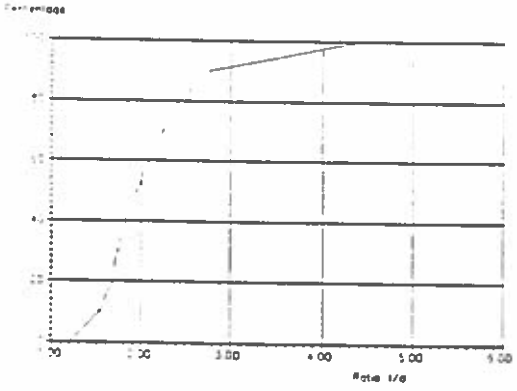

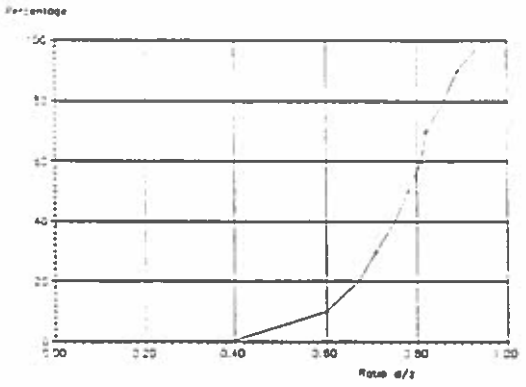

$\overline{z}$ = 22.7 mm, $\overline{l/d}$ = 2.1, $\overline{d/z}$ = 0.76
Shape class : Irregular.

Test 3

SIZE GRADATION

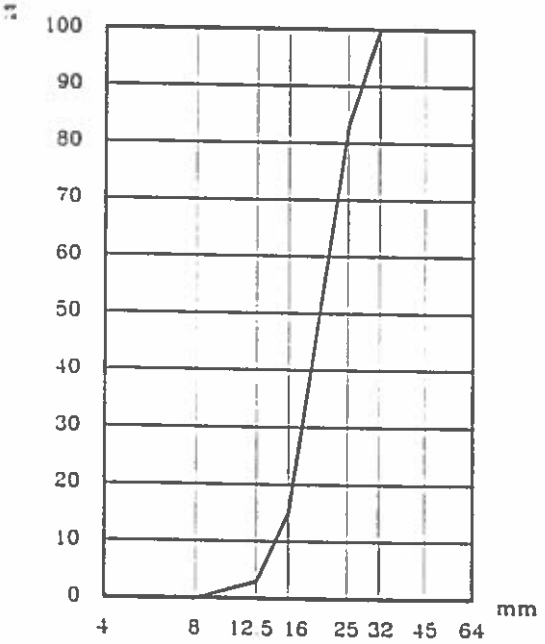

d_{50} = 20.1 mm, d_{15} = 16.0 mm, d_{85} = 25.7 mm,
$\frac{d_{85}}{d_{15}}$ = 1.6, grading: medium.

Fig. 9.

MATERIAL PARAMETERS

TEST 4

DENSITY

ρ_{ssd} = 2679 kg/m^3
ρ_0 = 2669 kg/m^3
W_a = 0.4

POROSITY

n = 0.471

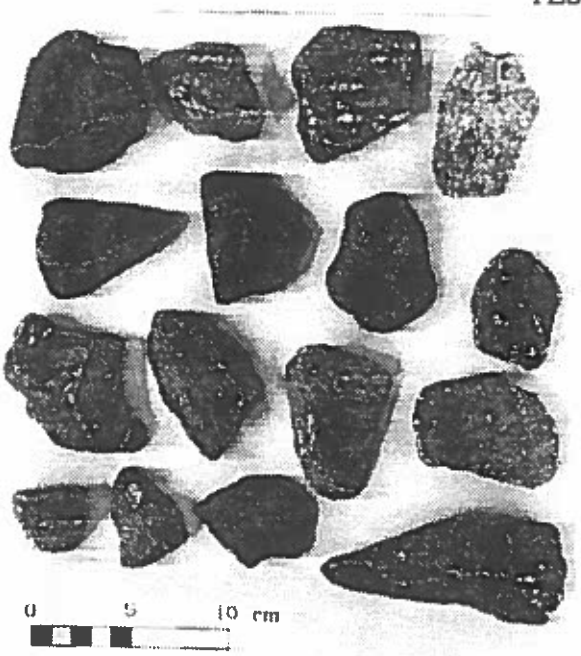

STONE SHAPE

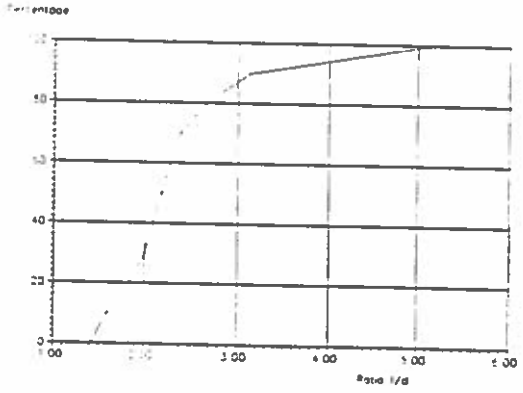

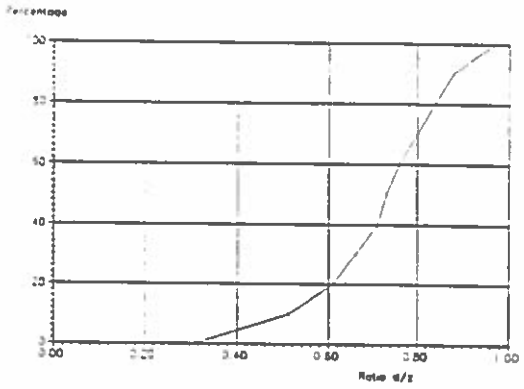

$\overline{z}$ = 41.1 mm, $\overline{l/d}$ = 2.3, $\overline{d/z}$ = 0.72
Shape class : Irregular.

Test 4

SIZE GRADATION

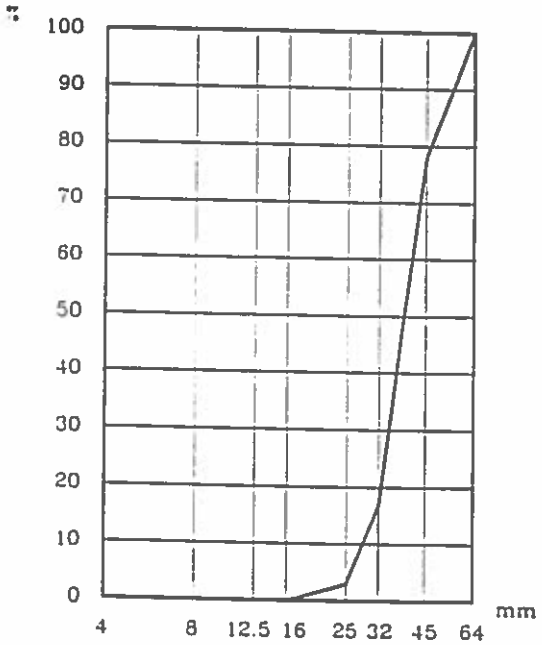

d_{50} = 38.5 mm, d_{15} = 30.9 mm, d_{85} = 50.3 mm,
$\frac{d_{85}}{d_{15}}$ = 1.6, grading: medium.

Fig. 10.

MATERIAL PARAMETERS

DENSITY

ρ_{ssd} = 2525 kg/m^3
ρ_0 = 2476 kg/m^3
W_a = 2.0

POROSITY

n = 0.391

STONE SHAPE

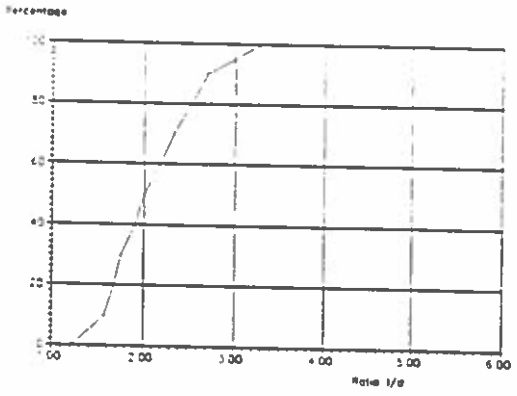

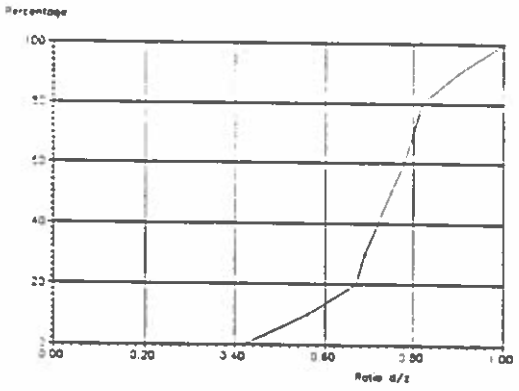

$\overline{z}$ = 17.0 mm, $\overline{l/d}$ = 2.1, $\overline{d/z}$ = 0.74
Shape class : Semi-round.

TEST 5

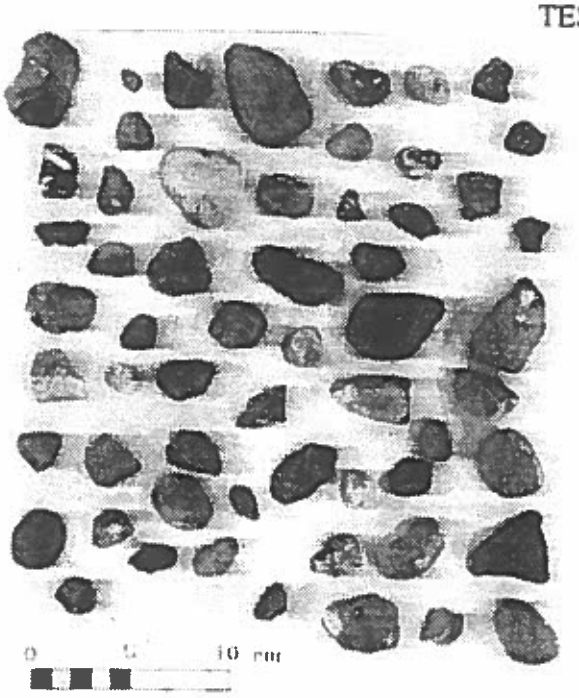

Test 5

SIZE GRADATION

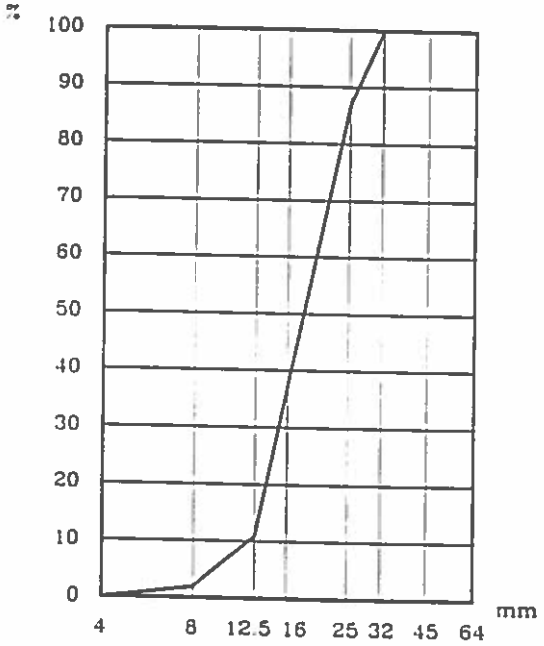

d_{50} = 18.1 mm, d_{15} = 13.0 mm, d_{85} = 24.6 mm.
$\frac{d_{85}}{d_{15}}$ = 1.9, grading: medium.

Fig. 11.

MATERIAL PARAMETERS

TEST 6

DENSITY

ρ_{ssd} = 2594 kg/m^3
ρ_0 = 2579 kg/m^3
W_a = 0.6

POROSITY

n = 0.388

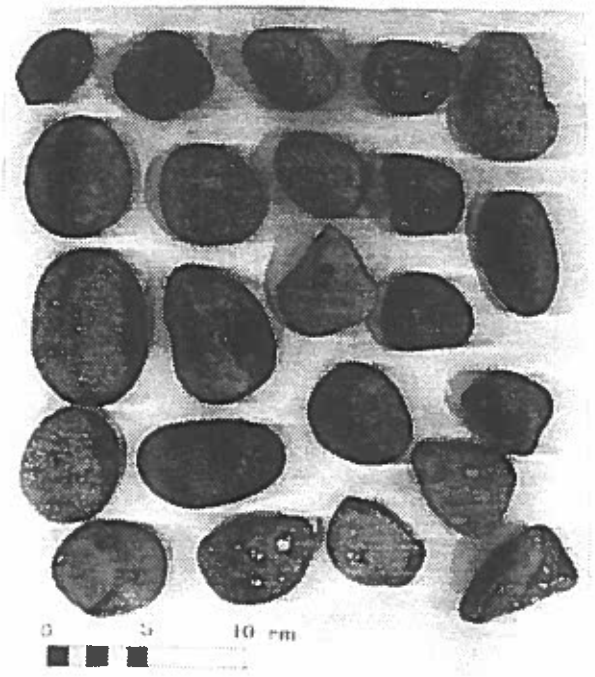

Test 6

STONE SHAPE

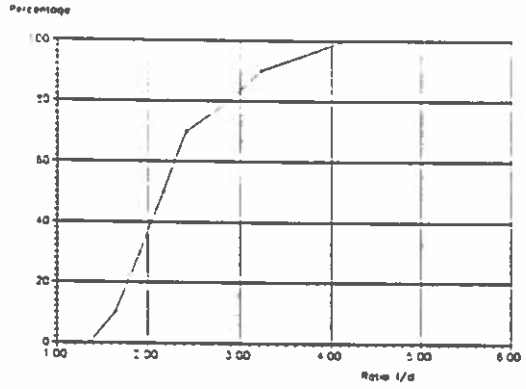

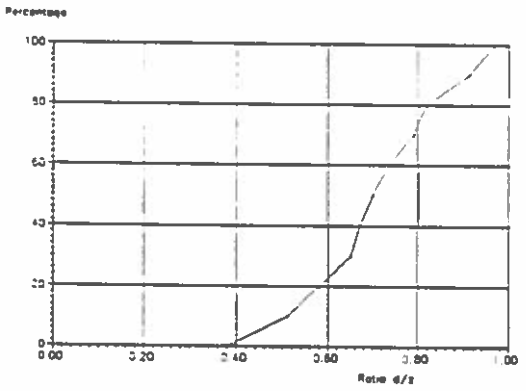

$\overline{z}$ = 38.6 mm, $\overline{l/d}$ = 2.3, $\overline{d/z}$ = 0.70

Shape class : Very round.

SIZE GRADATION

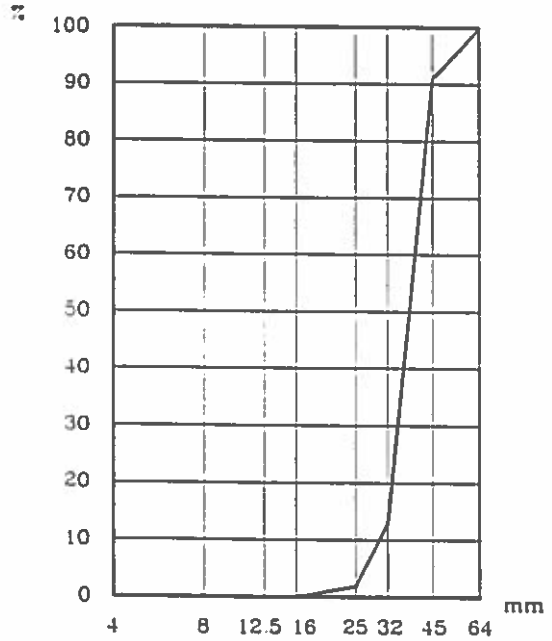

d_{50} = 37.6 mm. d_{15} = 32.3 mm. d_{85} = 43.8 mm.

$\frac{d_{85}}{d_{15}}$ = 1.4. grading: narrow/medium.

Fig. 12.

MATERIAL PARAMETERS

TEST 7

DENSITY

ρ_{std} = 2674 kg/m^3
ρ_0 = 2661 kg/m^3
W_a = 0.5

POROSITY

n_7 = 0.473
n_8 = 0.467

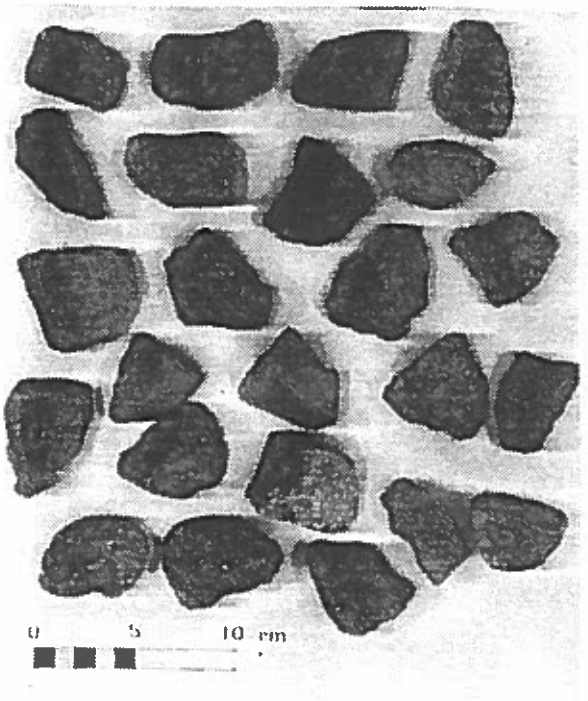

Test 7

STONE SHAPE

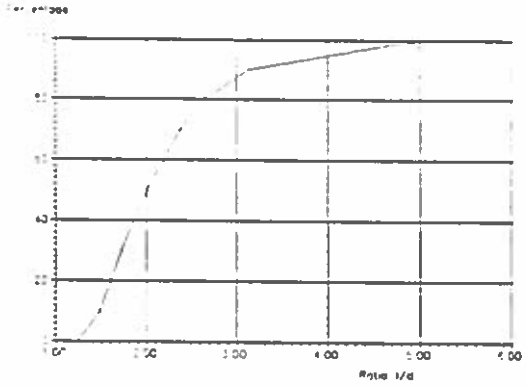

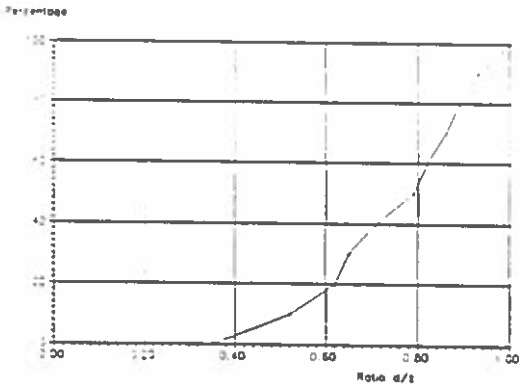

$\bar{z}$ = 38.6 mm, $\overline{l/d}$ = 2.2, $\overline{d/z}$ = 0.75
Shape class : Irregular.

SIZE GRADATION

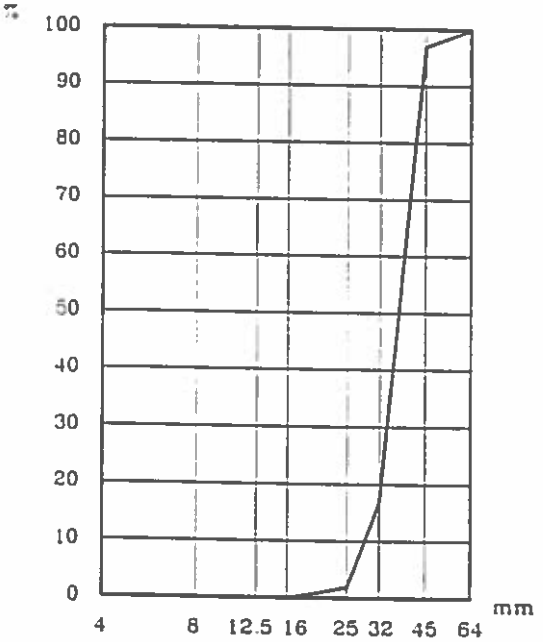

d_{50} = 36.8 mm, d_{15} = 31.0 mm, d_{85} = 42.8 mm.

$\frac{d_{85}}{d_{15}}$ = 1.4, grading: narrow/medium.

Fig. 13.

6. MATHEMATICAL MODEL FOR THE U-TUBE UNSTEADY FLOW

A one-dimensional numerical model of the unsteady flow in the permeameter was established in order to serve as a tool for the design of the permeameter and to obtain parametric insight. Fig. 14 shows the geometrical scheme for the model.

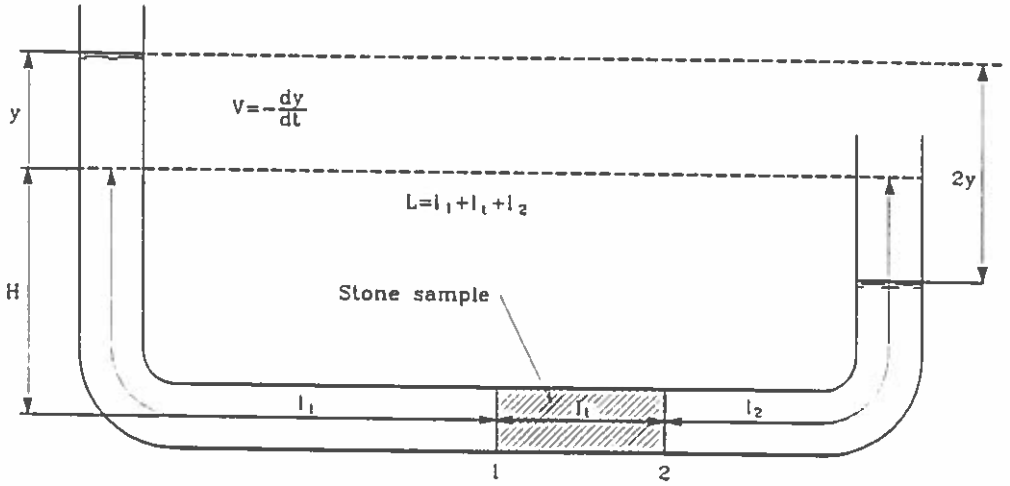

Fig. 14. Geometrical scheme for the numerical model.

The momentum equation is based on the following assumptions:

The flow resistance in the stone sample in the stone sample is given by

(cf. eq. (12))

$$\rho g \ell_t \left(aV + bv^2 + \frac{1 + C'_m \left(\frac{1-n}{n}\right)}{g} \frac{dV}{dt} \right) \tag{34}$$

The flow resistance in the two neighbour pipe sections is as an approximation calculated from the steady flow expressions

$$\rho g (L - \ell_t) f \frac{v^2}{2gR} + 2 \cdot \rho g \zeta \frac{v^2}{2g} + \rho (L - \ell_t) \frac{dV}{dt} \tag{35}$$

where R = the hydraulic radius equal to $D/4$, D = pipe diameter

ζ = the resistance coefficient for losses in the bends

f = the friction factor = $\frac{4}{Re}$ for $Re = \frac{VR}{\nu} < 580$.
For $Re > 580$ f is found from the Colebrook and White formula

$$\sqrt{\frac{2}{f}} = 6.4 - 2.25\ ln\left(\frac{k}{R} + \frac{4.7}{Re\sqrt{f}}\right) \quad ,$$

where k is the pipe roughness.

As the total driving pressure force is $2y\rho g$ the momentum equation reads

$$\frac{d^2y}{dt^2} + \frac{f\frac{L-\ell_t}{2R} + \zeta + b\ell_t g}{L + C_m\ell_t\frac{1-n}{n}}\frac{dy}{dt}\left|\frac{dy}{dt}\right| + \frac{a\ell_t g}{L + C_m\ell_t\frac{1-n}{n}}\frac{dy}{dt} + \frac{2g}{L + C_m\ell_t\frac{1-n}{n}}y = 0 \qquad (36)$$

The hydraulic pressure gradient over the sample length ℓ_t is given by

$$I_t = \frac{(L-\ell_t)}{g\ell_t}\frac{d^2y}{dt^2} + \left(f\frac{L-\ell_t}{2gR\ell_t} + \frac{\zeta}{g\ell_t}\right)\frac{dy}{dt}\left|\frac{dy}{dt}\right| + \frac{2}{\ell_t}y \qquad (37)$$

Numerical solution to the governing equation (36) is obtained with the application of the Runge-Kutta-Nyström method, which is a generalization of the ordinary Runge-Kutta method. Eg. (36) can be written as

$$\ddot{y} = C_1\,\dot{y}\,|\dot{y}| + C_2\,\dot{y} + C_3\,y = f\,(y, \dot{y})$$

where C_1, C_2 and C_3 are constants at a given time step. The method of calculation follows an algorithm in which for each time step four auxiliary quantities A_n, B_n, C_n and D_n are calculated and used for the determination of the next step approximative values y_{n+1} and $\dot{y}_{n+1}$.

Given the time step length h and the number of steps N.

$$k = \frac{1}{2}h$$

for $N = 0$ to $N - 1$ do

$$A_n = k \cdot f\,(y_n,\ \dot{y}_n)$$

$$B_n = k \cdot f\,(y_n + \beta_n, \dot{y}_n + A_n \qquad \text{where } \beta_n = k \cdot \left(\dot{y}_n + \frac{1}{2}A_n\right)$$

$$
\begin{aligned}
C_n &= k \cdot f\,(y_n + \beta_n, \dot{y}_n + B_n) \\
D_n &= k \cdot f\,(y_n + \delta_n, \dot{y}_n + 2C_n) \qquad \text{where } \delta_n = h \cdot (\dot{y}_n + C_n) \\
y_{n+1} &= y_n + h \cdot \left(\dot{y}_n + \frac{1}{3}(A_n + B_n + C_n)\right) \\
\dot{y}_{n+1} &= \dot{y}_n + \frac{1}{3}(A_n + 2B_n + 2C_n + D_n)
\end{aligned}
$$

then y_{n+1} and $\dot{y}_{n+1}$ are approximations to y and $\dot{y}$, respectively at $t_{n+1} = t_0 + h(n+1)$.

$$\ddot{y}_{n+1} = f\,(y_{n+1}, \dot{y}_{n+1})$$

The method is a fourth-order predictor-corrector method, which means that the truncation error per step is of the order h^5. After having solved the governing differential equation the pressures and the gradient are subsequently calculated.

The values of ζ and k used in the numerical calculations were 0.4 and $2 \cdot 10^{-3}$ m, respectively. ζ and k do not need much attention because the hydraulic resistance in the pipe is very small compared to the resistance in the stone sample and to the inertia forces involved.

The ξ-value for the grid was taken as 0.1.

7. SIMULATION OF THE U-TUBE PERMEAMETER PERFORMANCE

In order to study the performance of the permeameter some preliminary numerical simulations using eq. (16) were performed with the following parameter values typical for the experiments:

$$L = 7.60m \;,\; \ell_t = 1.00m \;,\; R = 0.10m \;,\; n = 0.48 \;,$$

$$a = 0.19 \;,\; b = 67 \;,\; c_m = 2$$

According to eq. (16) the initial acceleration is given by

$$\frac{d^2y}{dt^2} = \frac{-2gy_{in}}{L + c_m \ell_t \frac{1-n}{n}} \tag{38}$$

Fig. 15 shows the variation in time of the elevation y, the bulk velocity V, the acceleration $\frac{d^2y}{dt^2}$ and the gradient I for the two initial values $y_{in} = 1.0m$ and $0.5m$.

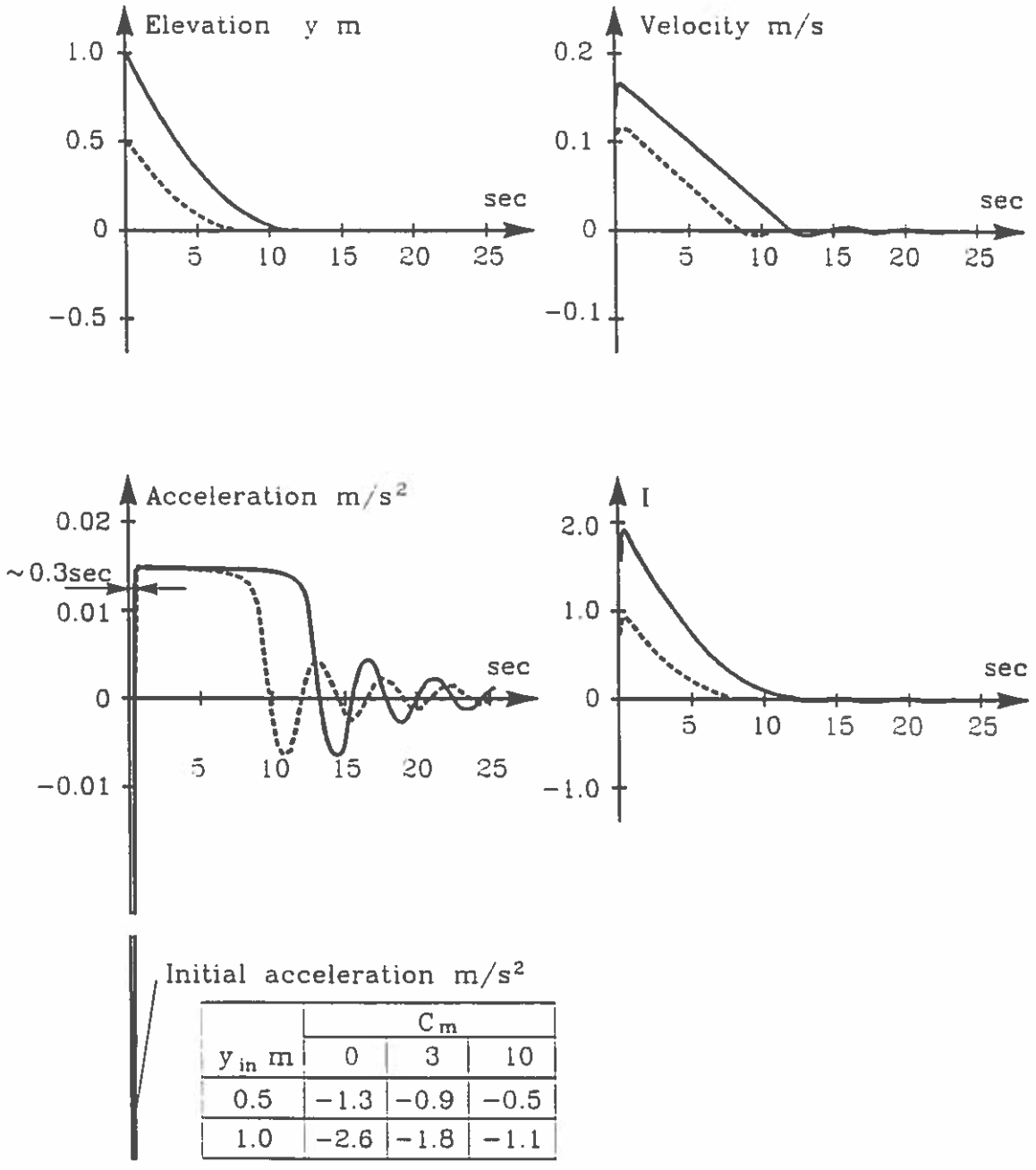

Initial acceleration m/s²

	C_m		
y_{in} m	0	3	10
0.5	−1.3	−0.9	−0.5
1.0	−2.6	−1.8	−1.1

Fig. 15. Preliminary numerical simulation of U-tube flow with typical stone sample, $d_{50} \simeq 25$ mm.

It is seen that the rapid dampening of the flow almost prevents reversal of the flow for which reason oscillatory flow cannot be studied. Much less resistance of the test sample, i.e. a shorter length is needed for such study, but would be impossible due to too large uncertainties related to the measurements of I.

In the first phase of the experiment the accelerations are rather large, covering the expected relevant prototype range of up to app. 0.5 g. Unfortunately, this initial phase is of very short duration, i.e. less than app. 0.3 sec. and is practically independent of the initial elevation, y_{in}. The short duration complicates the experimental determination of C_m for several reasons. Accurate velocity measurements which are needed for reliable calculations of the accelerations are difficult to perform. The very rapid change in accelerations makes fitting difficult. Finally, the assumption of validity of the steady flow values of the Forchheimer equation factors a and b is probably very poor because the flow regime corresponding to the steady flow Reynolds number cannot develop so fast.

In a second phase of app. 5-7 sec. duration the accelerations are almost constant and independent of y_{in}. However, in this phase the accelerations are extremely small, which implies that the inertia forces and the related C_m values are very small and difficult to determine with a reasonable degree of accuracy.

The obtainable values of the gradient I cover the expected prototype range, whereas the obtainable velocities and Reynolds numbers are too small to cover fully the relevant prototype ranges. Consequently extrapolation of the results is necessary.

The possibility of improving the U-tube technique by enlarging the initial elevation y_{in} of up to 10 m was also studied by the use of the numerical model. In this case test-samples 1 (d_{50} = 9.4 mm) and 7 (d_{50} = 36.8 mm) were used with the corresponding steady flow a and b values. Moreover, the influence of C_m was investigated by comparing the two values C_m = 0 and 10. The results are shown in Figs. 16 and 17.

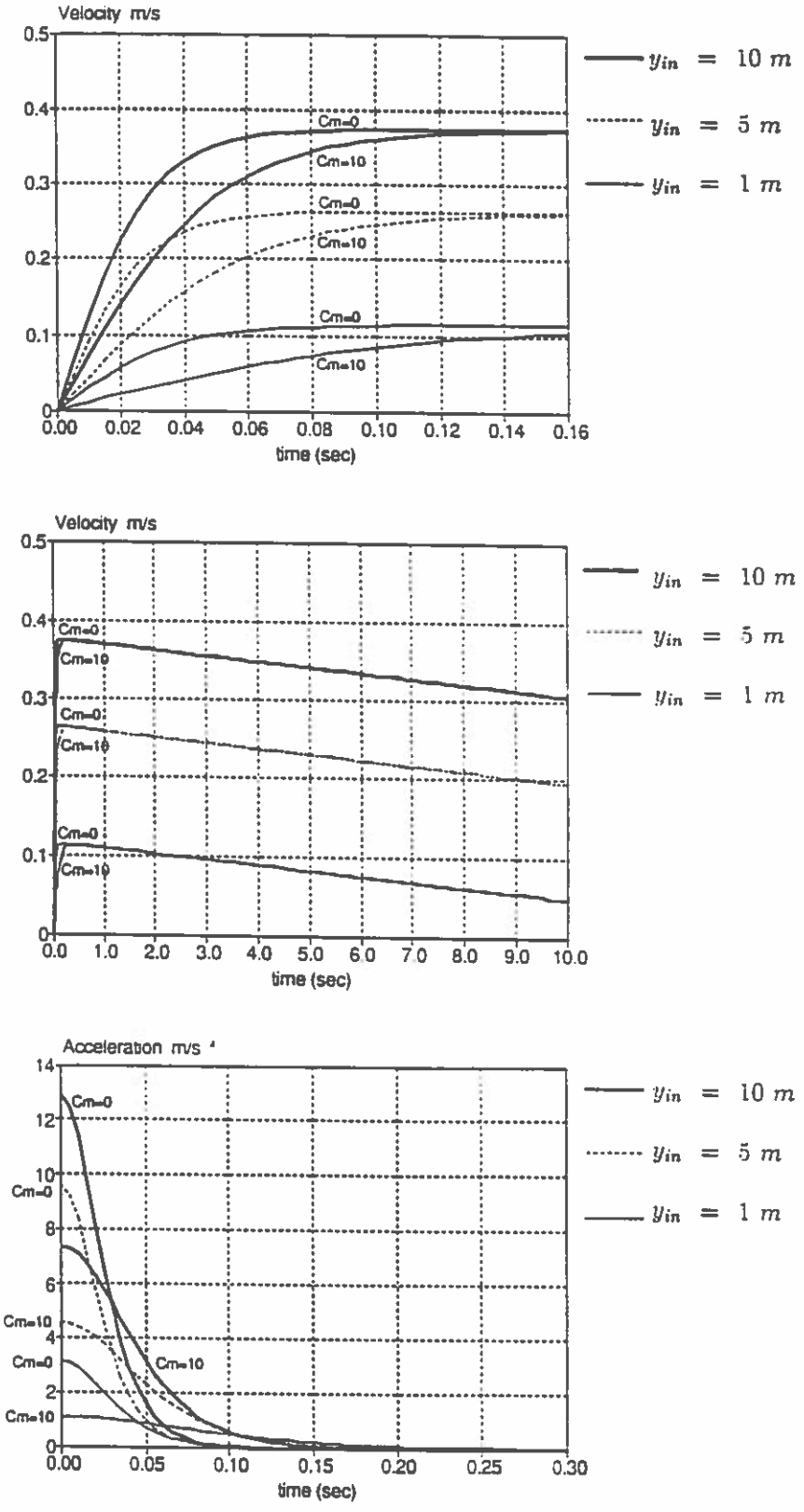

Fig. 16. Numerical simulation of U-tube flow with stone sample 1 ($d_{50} = 9.4mm$).

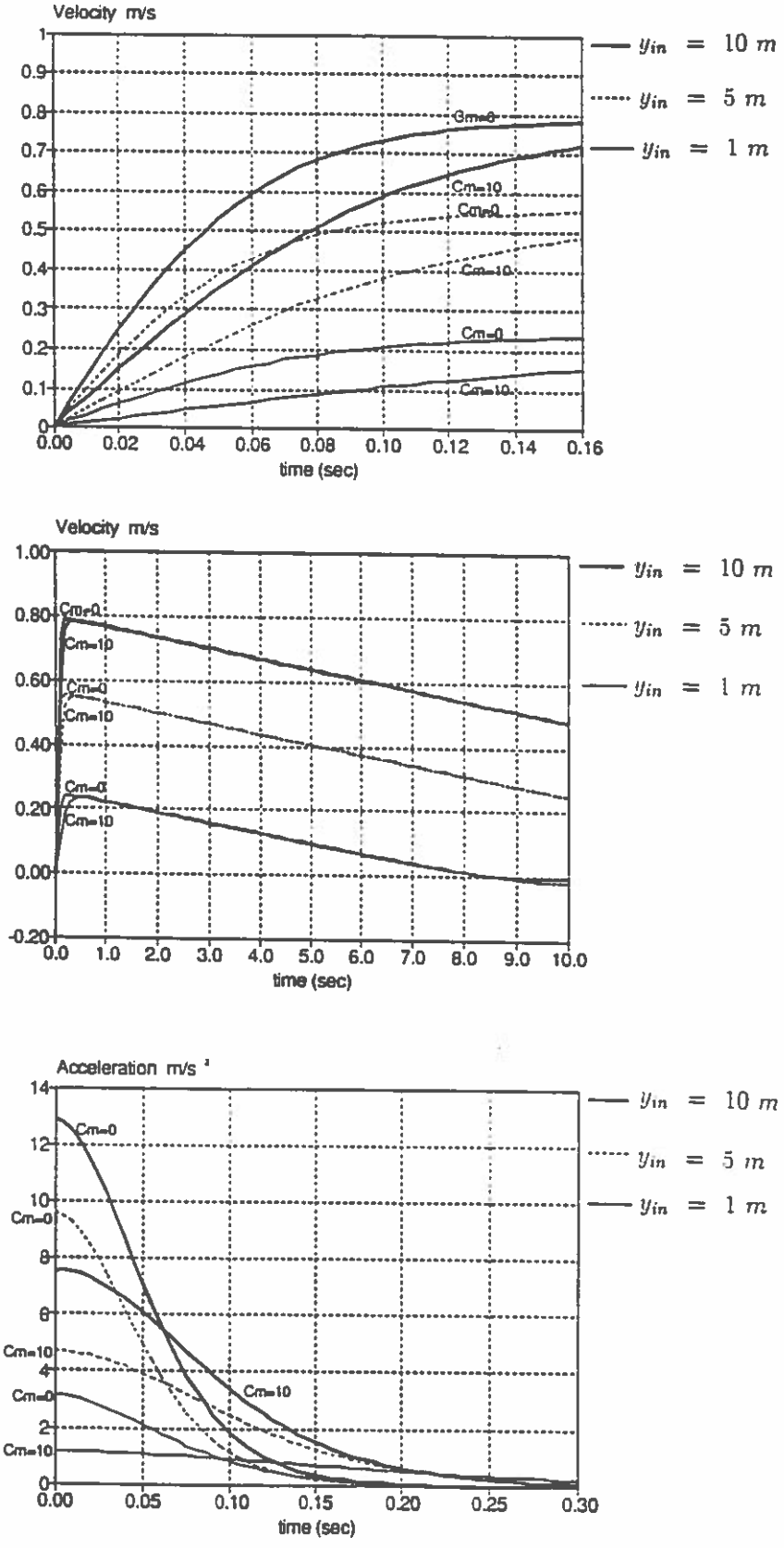

Fig. 17. Numerical simulation of U-tube flow with stone sample 7 ($d_{50} = 36.8mm$).

8. WALL EFFECTS IN PERMEAMETERS

When the ratio of the permeameter diameter D to the particle diameter, d becomes smaller than approximately 50 the observed flow resistance will be reduced compared to the resistance for infinite cross sections. This is due to the effect of the "smooth" confining cylinder wall.

Fig. 18 shows the reduction in the shape parameters α and β as a function of D/d for spherical particles of uniform size in fully turbulent flow, i.e. the flow regime valid for the present tests. It is assumed that the depicted corrections, which are based solely on data by Givan (1934) and Fand et al. (1990), can be applied as an approximation for narrrow graded materials.

In the earlier tests by Fand et al. (1986) no significant wall effect was observed, most probably due to the fact that the minimum value of $\frac{D}{d}$ was 21.

The β-correction curve in Fig. 18 corresponds fairly well to the curve suggested by Rose (1950), valid for Reynolds' numbers larger than app. 1,000. It corresponds also well with the wall effect corrections reported by Dudgeon (1967) for river gravel and uni-size spherical glass marbles.

The present tests are within the range $8.9 \leq \frac{D}{d_{50}} \leq 37$.
The range for the tests by Shih (1990), cf. section 2.4.3, is $9.5 \leq \frac{D}{d_{50}} \leq 111$.

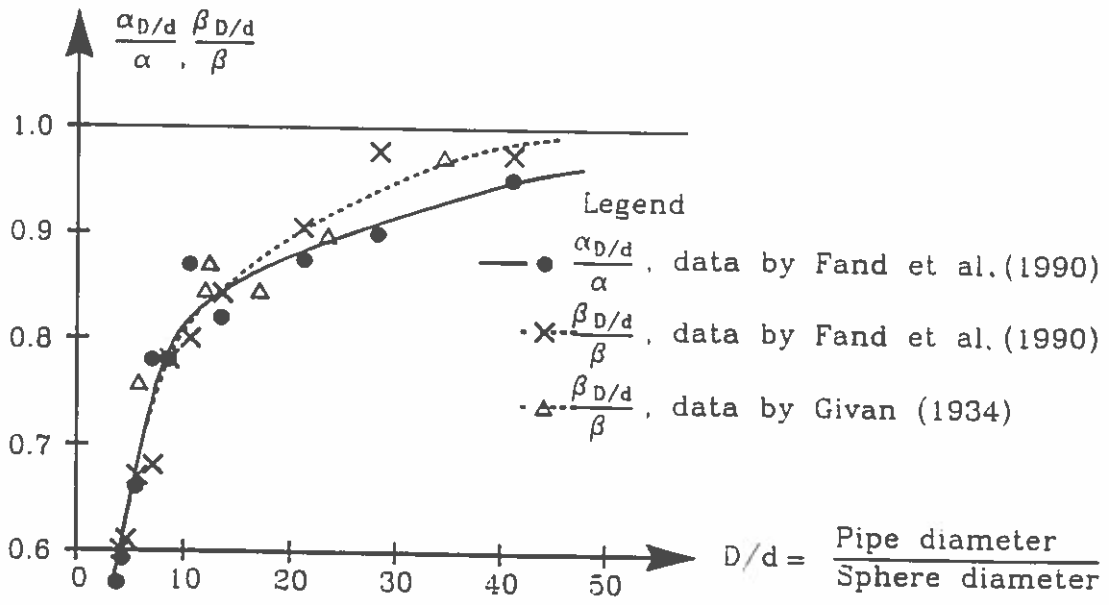

Fig. 18. Wall effect corrections to the shape parameters in the Forchheimer flow equation for spherical particles of uniform size in fully turbulent flow.

9. TEST RESULTS FROM THE STEADY FLOW EXPERIMENTS

9.1 Conventional fitting to the Forchheimer equation

Although the present experiments cover the Reynolds number range, app. 150 < Re < app. 11,200, i.e. the turbulent flow range, and despite the discussions in sections 2.4.4 and 2.5, the conventional fitting to the Forchheimer equation is presented in this section.

The Forchheimer equation $I = aV + bV^2$ can be rewritten as $I/V = a + bV$, i.e. a straight line in a $I/V - V$ diagramme, cf. Fig. 19.

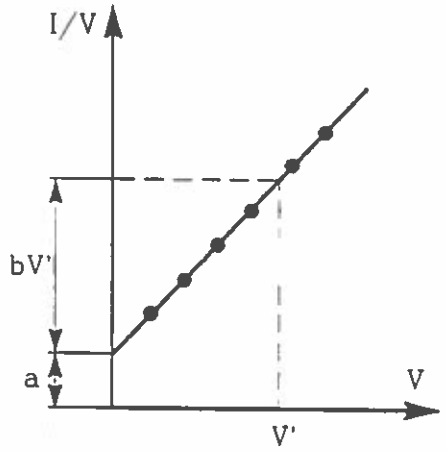

Fig. 19. Sketch indicating test results confirming the Forchheimer type of equation.

The ratio of bV' and a signifies the relative importance of the turbulent and the laminar flow resistance for condition $V = V'$.

The results of the steady flow tests are presented without wall correction in Figs. 20-27.

The results in Fig. 20 are based on the internal pressure transducers P_2 and P_3 in Fig. 5. The results in Fig. 21 are based on the external pressure transducers P_1 and P_4. The characteristics of the stone samples are given in Table 7 and Figs. 7 - 13.

Figs. 20 and 21 clearly indicate that in the flow range tested, the relationship between the bulk velocity and the hydraulic gradient can be fitted to the Forchheimer equation as no indication of a change in the coefficient b which signifies the slope of the straight line is seen for a given stone sample, except at low velocities. These deviations though could to a great extent be due to the larger relative errors involved in the measurement of the related very small velocities and pressures.

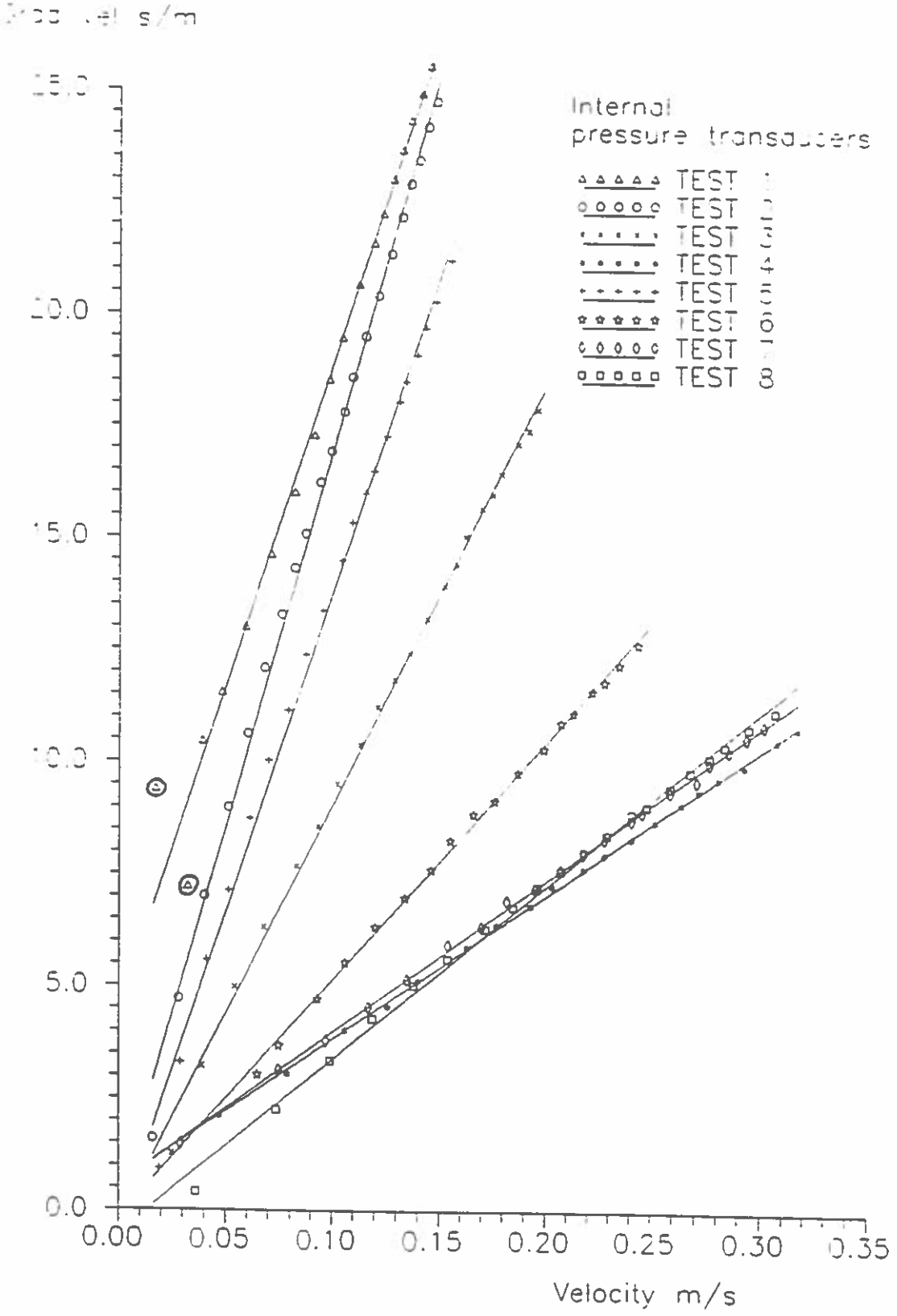

Fig. 20. Results of steady flow tests based on internal pressure transducers.

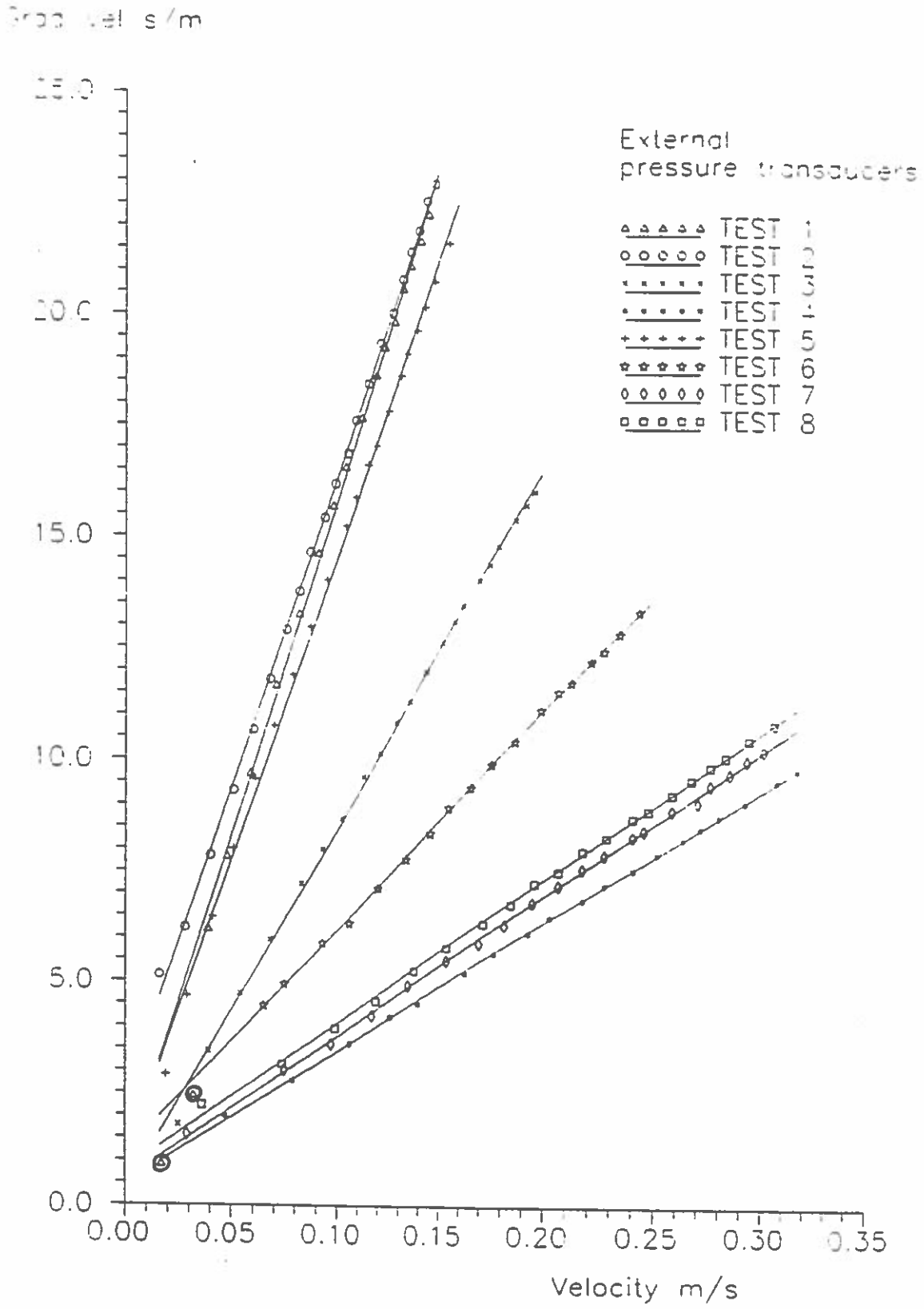

Fig. 21. Results of steady flow tests based on external pressure transducers.

The test results have been fitted both to straight lines, as shown in the Figures 20 and 21, and to two-parameter polynomials using the method of least squares. The results are given in Table 9.

Table 9. Forchheimer equation coefficients for steady flow tests.

Fitting method	External				Internal			
	Linear		Polynomial		Linear		Polynomial	
Steady flow coefficient	a s/m	b s^2/m^2	a s/m	b s^2/m^2	a s/m	b s^2/m^2	a s/m	b s^2/m^2
Test 1*	0.809	149.9	1.350	145.1	4.480	144.5	4.200	146.9
Test 2	2.410	139.3	2.180	141.4	0.182	167.0	0.905	161.5
Test 3	0.289	81.3	0.631	79.2	−0.290	93.6	0.186	90.5
Test 4	0.491	29.4	0.435	29.7	0.600	32.2	0.690	31.9
Test 5	0.986	135.3	1.630	129.9	−0.428	142.1	0.571	133.6
Test 6	1.170	49.9	1.150	50.0	−0.157	53.1	0.115	51.6
Test 7	0.558	32.1	0.501	32.4	0.572	34.0	0.642	33.7
Test 8	0.784	32.8	0.713	33.1	−0.500	38.7	−0.043	36.8

* The first two points in test 1 are obmitted.

As seen there are deviations between results obtained from the internal and the external pressure transducers. This fact has not been reported by other researchers and the the authors' knowledge no other experiments have included both internal and external pressure measurements.

In order to shed some more light on the observed deviations some measurements of the internal pressures were performed with perforated tubes inserted into the test sample in order to obtain an average presure across the sample. However, no significant deviations from the result based solely on the surface mounted pressure cells were found.

Other sources of error related to the use of the external pressure transducers are the energy loss due to the double grids and the definition of the effective sample length, the latter of which will depend weakly on Re due to the variations in the wake length. However, the influence of these factors are small and cannot fully explain the observed differences.

The relative deviation between the gradients, I_{int} and I_{ext}, measured with the internal and the external pressure transducers, respectively, are shown in Figs. 22

and 23 as function of the Reynolds numbers ξ_{int} and ξ_{ext}, cf. eqs. (6) and the Engelund expressions for a and b given by eq. (16). Because ξ depends on the ratio b/a, which again depends on the pressure transducers used, we can define two Reynolds numbers ξ_{int} and ξ_{ext} which in the range of the tests are quite different, mainly due to the large variations in a, cf. Table 9. This large variation is expected because the laminar term, aV, in the Forchheimer equation generally is small compared with the turbulent term, bV^2, for the tested range of the relatively coarse material and consequently the quantity a is rather ill-determined as a small difference between two large quantities. However, a is highly dependent on the method of extrapolation to the limit, $V = 0$. This means that ξ as a Reynolds number for coarse materials will not be, in practice, an accurate indicator of the flow regime. It is seen from Figs. 22 and 23 that the sensitivity of the hydraulic gradient to the position of the applied pressure cells is small. This corresponds to the rather small deviations in b, cf. Table 9.

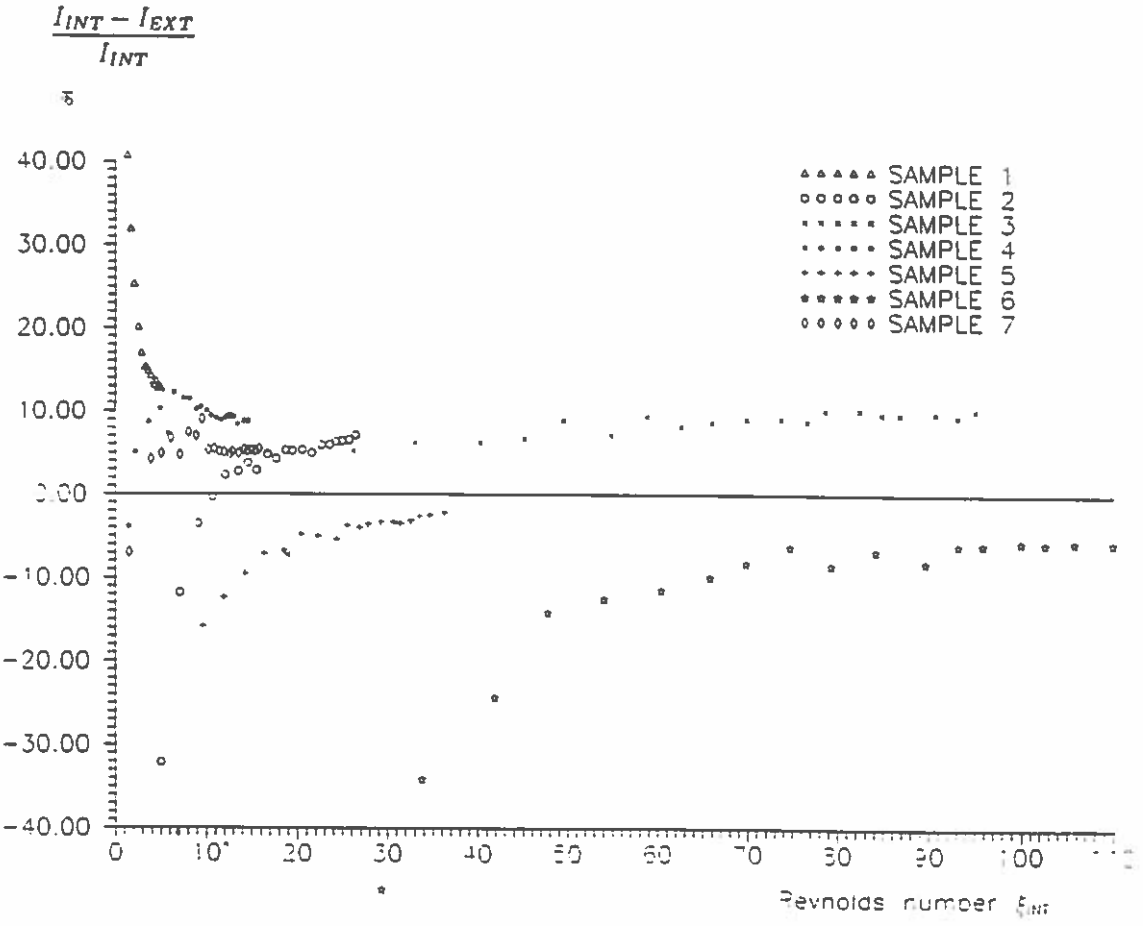

Fig. 22. Relative deviations between gradients measured with internal and external pressure transducers as function on ξ_{INT}.

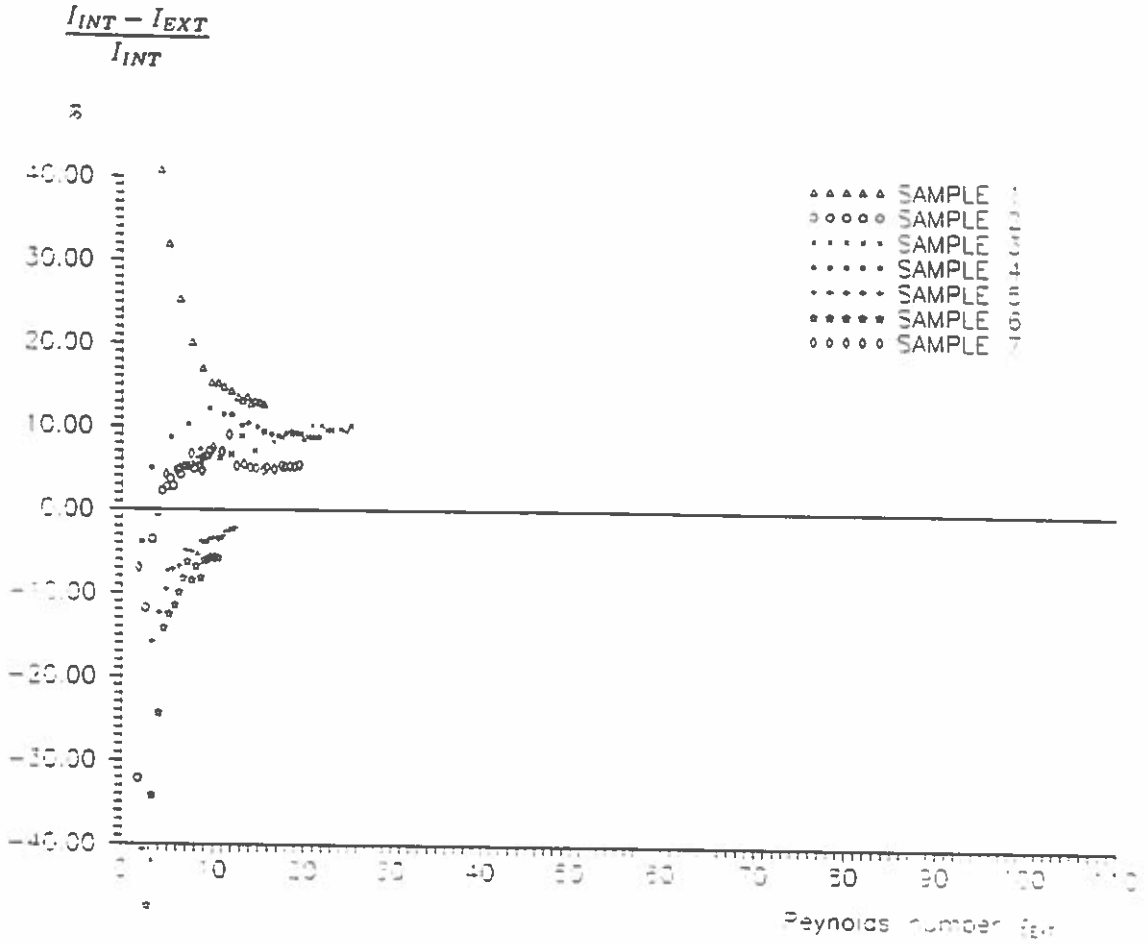

Fig. 23. Relative deviations between gradients measured with internal and external pressure transducers as function on ξ_{EXT}.

Tables 10 and 11 show the Engelund shape parameters α and β defined by eq. (16) with the use of d_{15} and d_{50} as characteristic diameter and based on a and b determined by the external pressure transducer measurements. The ν-values used correspond to the measured water temperature in each test.

Table 10. Shape parameters based on external pressure transducer measurements. No wall effect correction.

Test No.	d_{15}	d_{50}	d_{85}	$\frac{d_{85}}{d_{15}}$	$\frac{d_{15}}{d_{50}}$	Polynomial based on d_{15} α	Polynomial based on d_{15} β	Polynomial based on d_{50} α	Polynomial based on d_{50} β	Linear based on d_{15} α	Linear based on d_{15} β	Linear based on d_{50} α	Linear based on d_{50} β	shape class
1	6.6	9.4	11.5	1.7	0.70	6.49	1.7	1311	2.4	389	1.7	784	2.4	irregular
2	9.8	13.8	17.9	1.8	0.71	19.31	2.3	3823	3.2	2135	2.3	4227	3.2	—
3	16.0	20.1	25.7	1.6	0.80	1412	2.1	2231	2.6	666	2.1	1052	2.6	—
4	30.9	38.5	50.3	1.6	0.80	4591	1.8	7716	2.2	5182	1.8	8032	2.2	—
5	13.0	18.1	24.6	1.9	0.72	1365	1.6	2648	2.2	825	1.7	1600	2.4	semi round
6	32.3	37.6	43.8	1.4	0.86	5946	1.5	8057	1.7	6049	1.5	8196	1.7	very round
7	31.0	36.8	42.8	1.4	0.84	5428	2.0	7653	2.4	6046	2.0	8525	2.4	irregular
8	31.0	36.8	42.8	1.4	0.84	7447	1.9	10500	2.3	8189	1.9	11550	2.3	—

The steady flow data were also corrected for the influence of the permeameter wall.

Table 11 shows the correction factors $\frac{\alpha_{D/d}}{\alpha}$, $\frac{\beta_{D/d}}{\alpha}$ and the corrected shape parameters. The applied correction factors are taken from Fig. 18 with the use of d_{50} as characteristic particle diameter.

Table 11. Wall effect corrected shape parameters based on external pressure transducers.

Test No.	d_{15} mm	d_{50} mm	d_{85} mm	$\frac{d_{85}}{d_{15}}$	$\frac{d_{15}}{d_{50}}$	$\frac{D}{d_{50}}$	$\frac{\alpha_{D/d}}{\alpha}$	$\frac{\beta_{D/d}}{\beta}$	Polynomial based on d_{15} α	Polynomial based on d_{15} β	Polynomial based on d_{50} α	Polynomial based on d_{50} β	shape class
1	6.6	9.4	11.5	1.7	0.70	37	0.94	0.98	690	1.75	1395	2.45	irregular
2	9.8	13.8	17.9	1.8	0.71	25	0.90	0.93	2144	2.5	4248	3.45	—
3	16.0	20.1	25.7	1.6	0.80	17	0.86	0.88	1642	2.4	2594	2.95	—
4	30.9	38.5	50.3	1.6	0.80	8.9	0.80	0.80	5739	2.25	9645	2.75	—
5	13.0	18.1	24.6	1.9	0.72	19	0.88	0.89	1551	1.8	3009	2.45	semi-round
6	32.3	37.5	43.8	1.4	0.86	9.1	0.80	0.80	7433	1.9	10070	2.15	very round
7	31.0	36.8	42.8	1.4	0.84	9.3	0.81	0.81	6701	2.45	9448	2.95	irregular
8	31.0	36.8	42.8	1.4	0.84	9.3	0.81	0.81	9194	2.35	12963	2.85	—

The values of α and β in Tables 10 and 11 corresponding to the polynomial fitting are plotted against d_{15}, d_{50} and d_{85}/d_{15} in Figures 24 - 27.

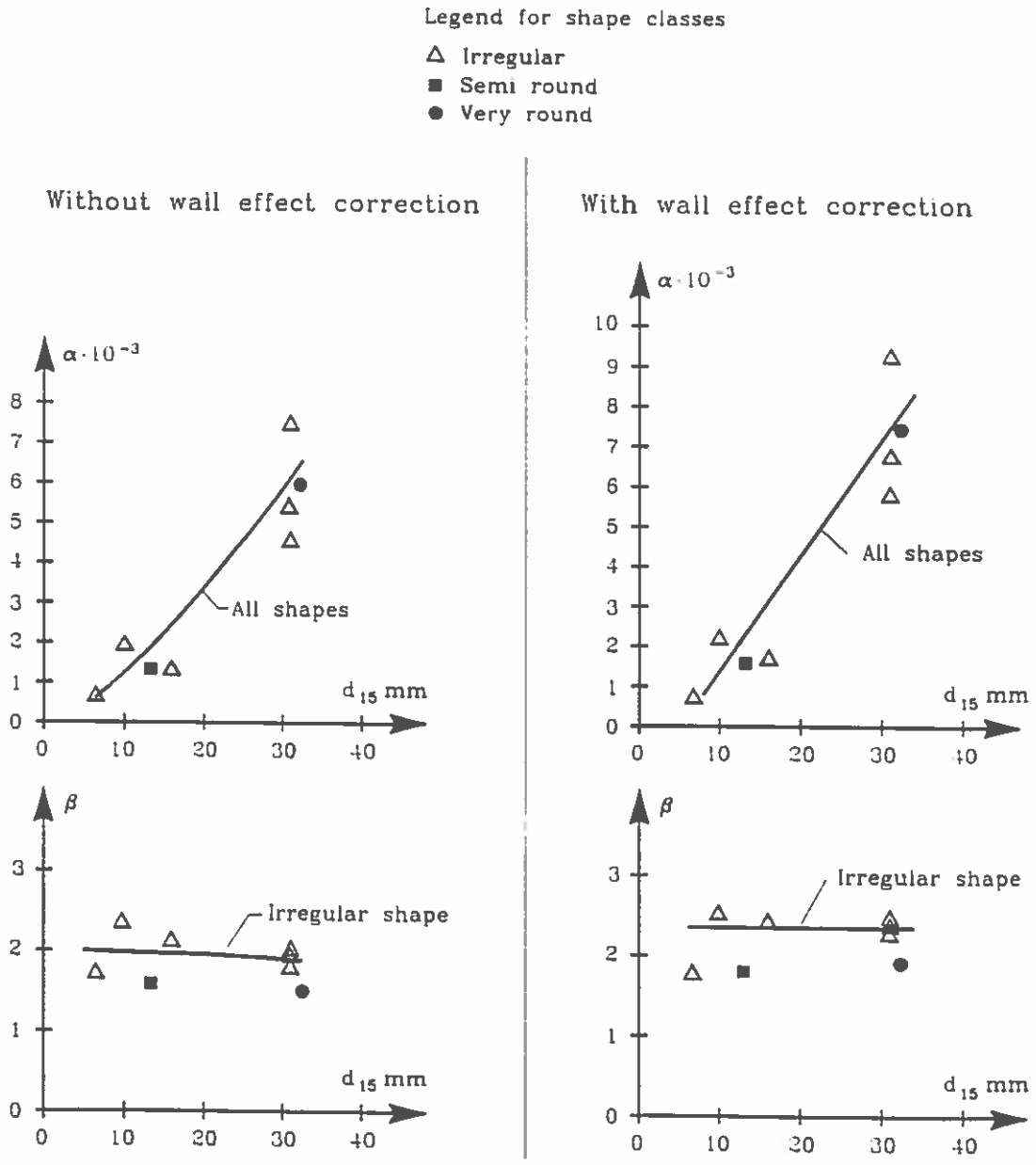

Fig. 24. Variation of α and β with d_{15} and shape classes.

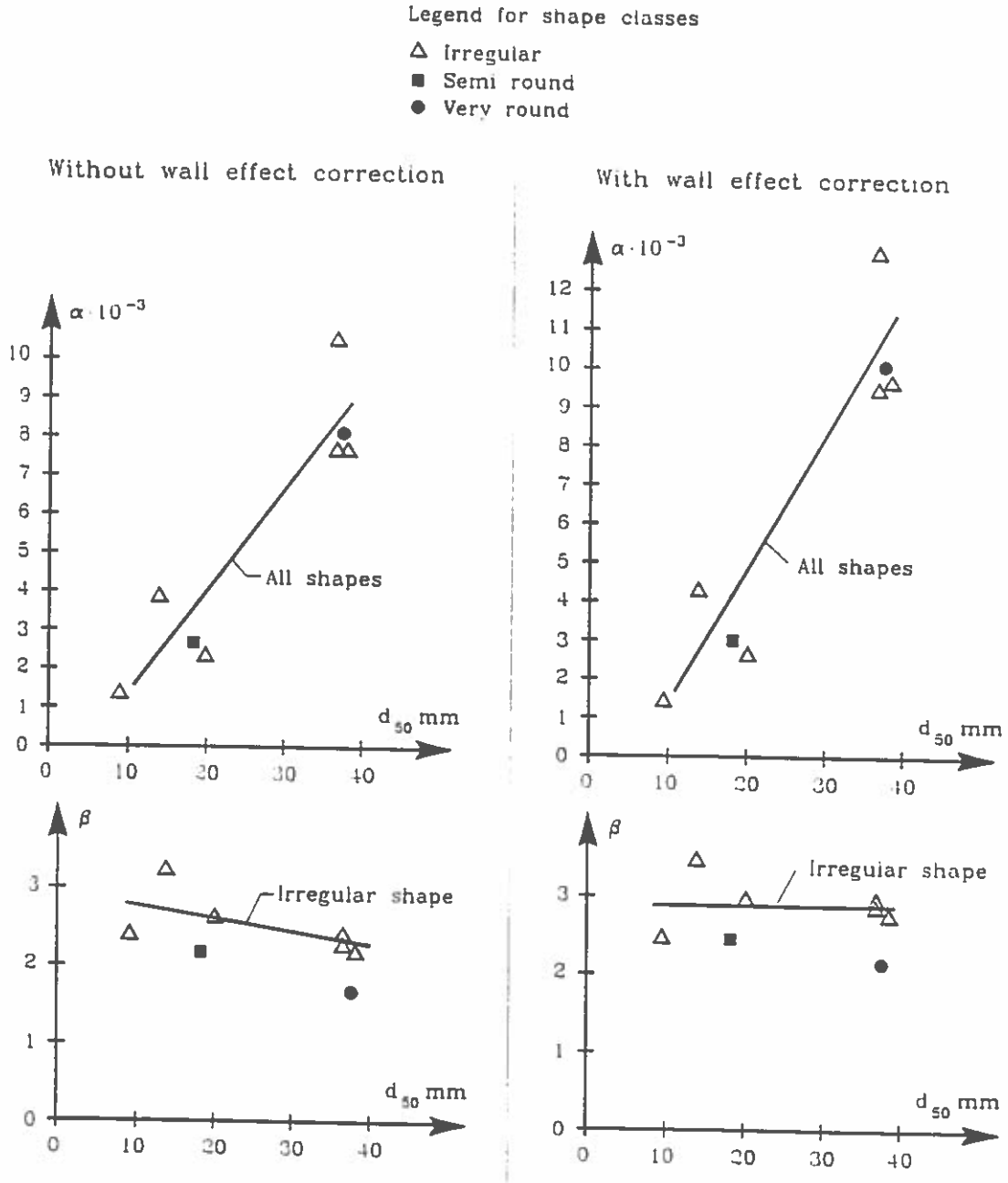

Fig. 25. Variation of α and β with d_{50} and shape classes.

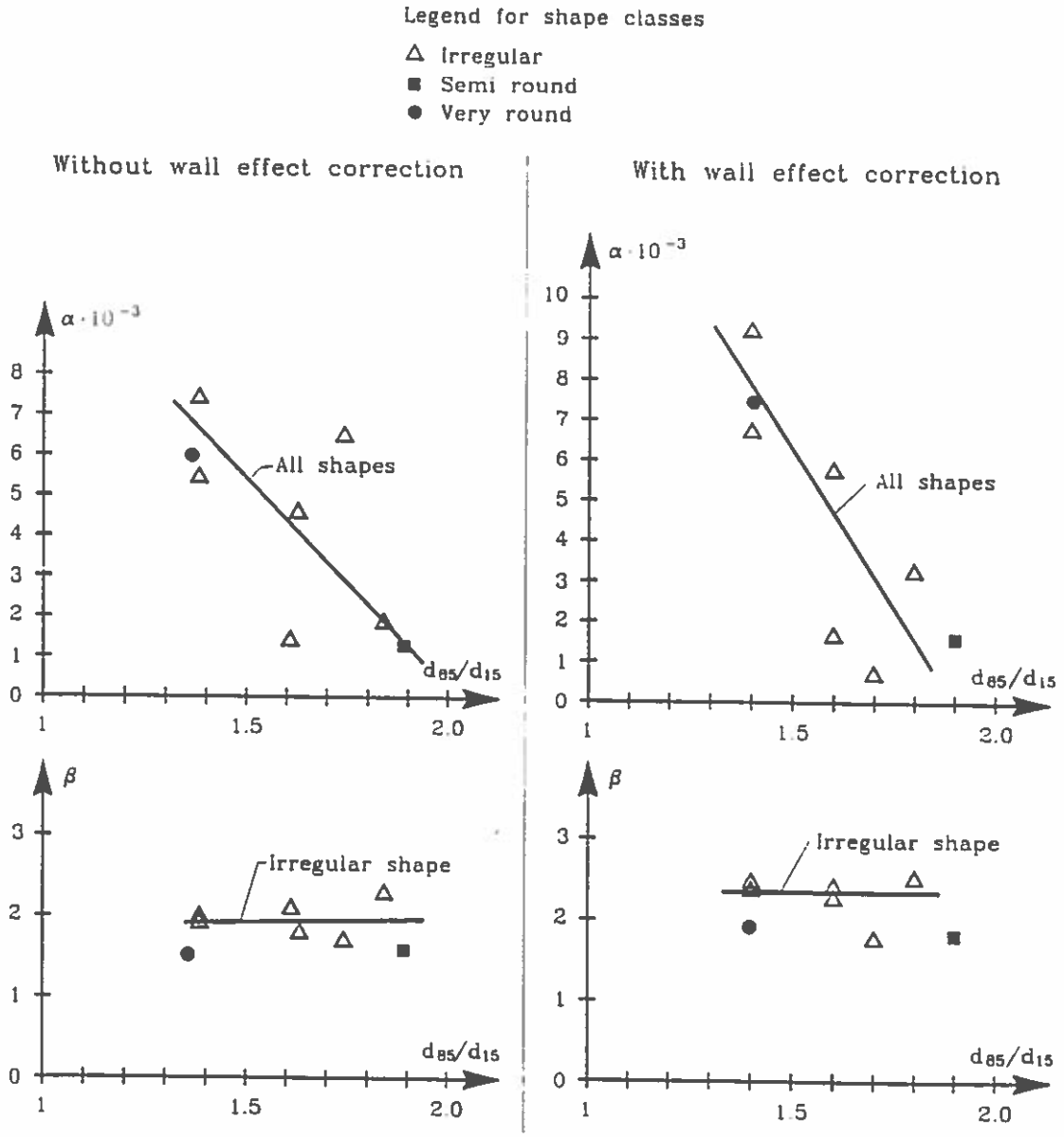

Fig. 26. Variation of α and β (based on d_{15}) with d_{85}/d_{15}.

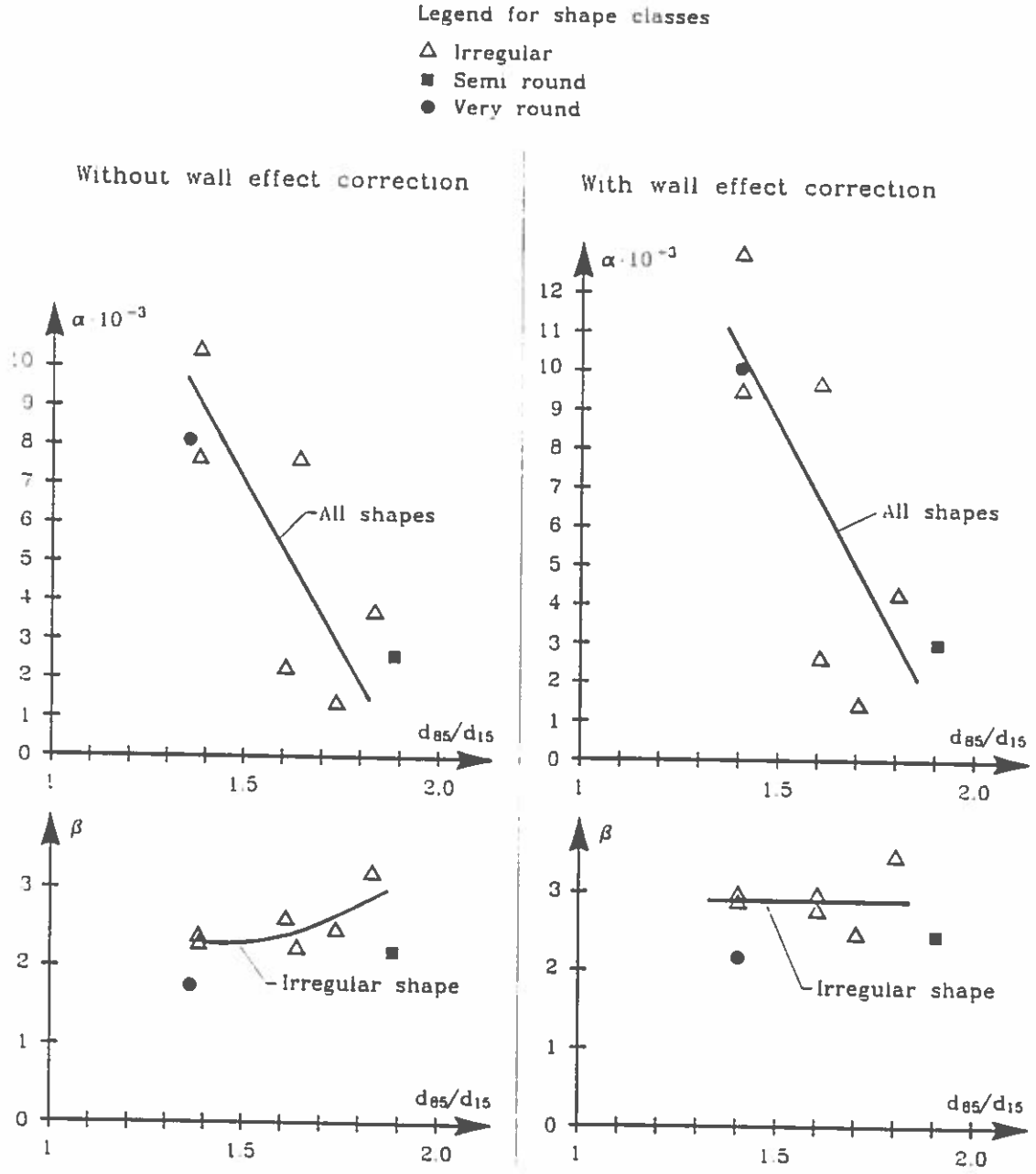

Fig. 27. Variation of α and β (based on d_{50}) with d_{85}/d_{15}.

It is seen from Figs. 24 and 25 that α seems to vary rather consistent and significantly with the characteristic diameters d_{15} and d_{50}, although such a variation is not to be expected according to the basic theoretical considerations behind the expression for α. However, no conclusion can be drawn from these plots because the applied conventional analysis of fitting a Forchheimer equation to data covering more than one flow region (in this case transition and fully turbulent regions) is inconsistent, cf. sections 2.4.4 and 2.5.

For the same reason no conclusions can be drawn with respect to the variation of α with the gradation ratio d_{85}/d_{15} shown in Figs. 26 and 27. In any case, because of the limited gradation range $1.4 \leq d_{85}/d_{15} \leq 1.9$ and because of presence of some correlation between d_{85}/d_{15} and d_{15} or d_{50} in the test samples, it will not be possible to reach conclusions on this matter solely based on the present tests. However, by combining the present results with the test results of Shih (1990) covering the gradation ranges $1.27 \leq d_{85}/d_{15} \leq 1.37$ and $2 < d_{85}/d_{15} < 5$ and by using a Reynolds number based analysis, as discussed in the foregoing sections, valid conclusions with respect to gradings can be reached.

Despite of the applied analysis the plots in Figs. 24 and 25 indicate that α does not depend on the shape of the grains. This finding, which is contradictionary to Engelund's findings given in Table 4, could be explained if the tests covered also a flow regime dominated by laminar flow where the flow resistance is only slightly influenced by the surface characteristic (relative roughness) of the solid boundaries. But actually, the tests covered the turbulent flow dominated regions.

As to the β values it is seen from the wall effect corrected data presented in Figs. 24 B and 25 B that β seems independent of the characteristic diameter, but seems to attain smaller values for rounded stones.

This is to be expected because β, also in the applied analysis, signifies the turbulent flow regime where the flow resistance is dependent on the relative roughness.

Figs. 26 B and 27 B show no consistent variation of β with the gradation ratio d_{85}/d_{15}. Moreover, the average β values, shown with a straight line, correspond to those shown in Figs. 24 B and 25 B.

The β-values for the turbulent flow region are given in Table 12.

Table 12. β-values for turbulent flow.

Shape class	d_{85}/d_{15}	β based on d_{15}	β based on d_{50}
very round	1.4	1.9	2.1
semi round	1.9	1.8	2.4
irregular	1.4 - 1.8	2.3	2.9

As to the general influence of the gradation the same comments holds as stated above in relation to the α-values.

9.2. Fitting of data to the turbulent flow equation

In Figs. 28-35 the results of the present experiments are plotted according to the diagram shown in Fig. 3 and analysed in accordance with the discussion in section 2.5. The β-values for the fully turbulent range are listed in Table 13 together with the corresponding Reynolds number ranges. Where clearly seen from the data plots the Reynolds number value, $Re^{T,L}$, corresponding to the lower end of the fully turbulent flow range is indicated.

Table 13. Shape parameter β for fully turbulent flow based on d_{50} and external pressure transducer measurements.

Test No.	d_{15}	d_{50}	d_{85}	$\frac{d_{85}}{d_{15}}$	$\frac{d_{15}}{d_{50}}$	β no wall-effect correction	β wall-effect corrected	$Re^{T,L}$	Re-range	shape class
1	6.6	9.4	11.5	1.7	0.70	2.34	2.39	600	600-1300	irregular
2	9.8	13.8	17.9	1.8	0.71	3.28	3.53	250	250-1300	—
3	16.0	20.1	25.7	1.6	0.80	2.61	2.97	900	900 - 3050	—
4	30.9	38.5	50.3	1.6	0.80	2.21	2.76		< 2000 - 10300	—
5	13.0	18.1	24.6	1.9	0.72	2.39	2.69	800	800-2100	semi round
6	32.3	37.6	43.8	1.4	0.86	1.76	2.20		< 2100 - 8050	very round
7	31.0	36.8	42.8	1.4	0.84	2.31	2.85		< 900 - 9700	irregular
8	31.0	36.8	42.8	1.4	0.84	2.28	2.81		< 2000 - 10100	—

For the angular material the average β-value is $2.89 \simeq 2.9$. For the very round and the semi-round materials the β-values are 2.2 and 2.7, respectively.

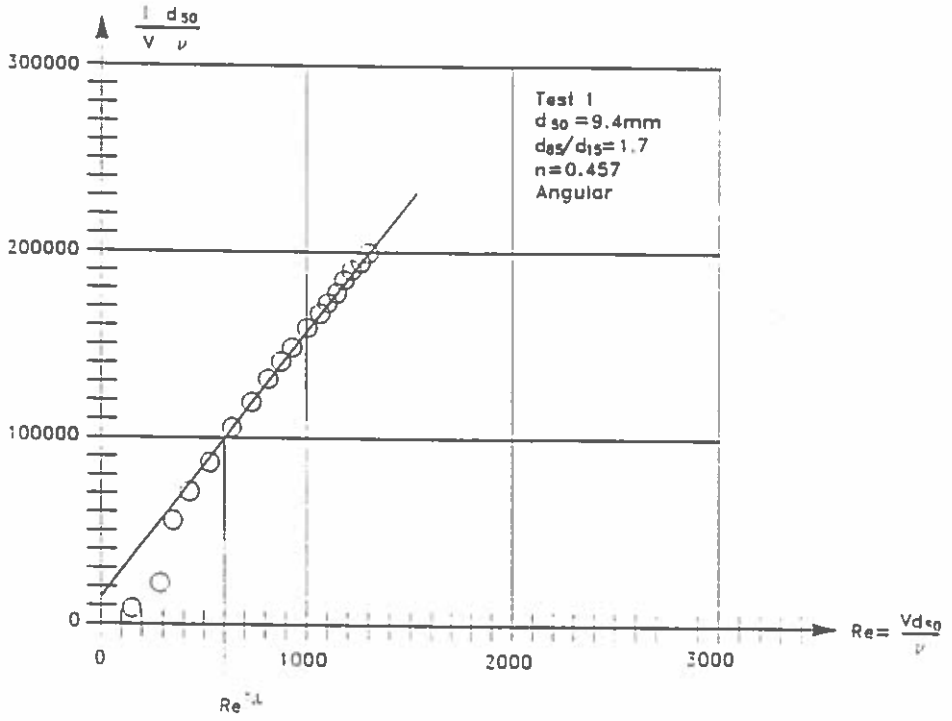

Fig. 28. Results of steady flow tests no. 1, based on external pressure transducer measurements. No wall effect correction.

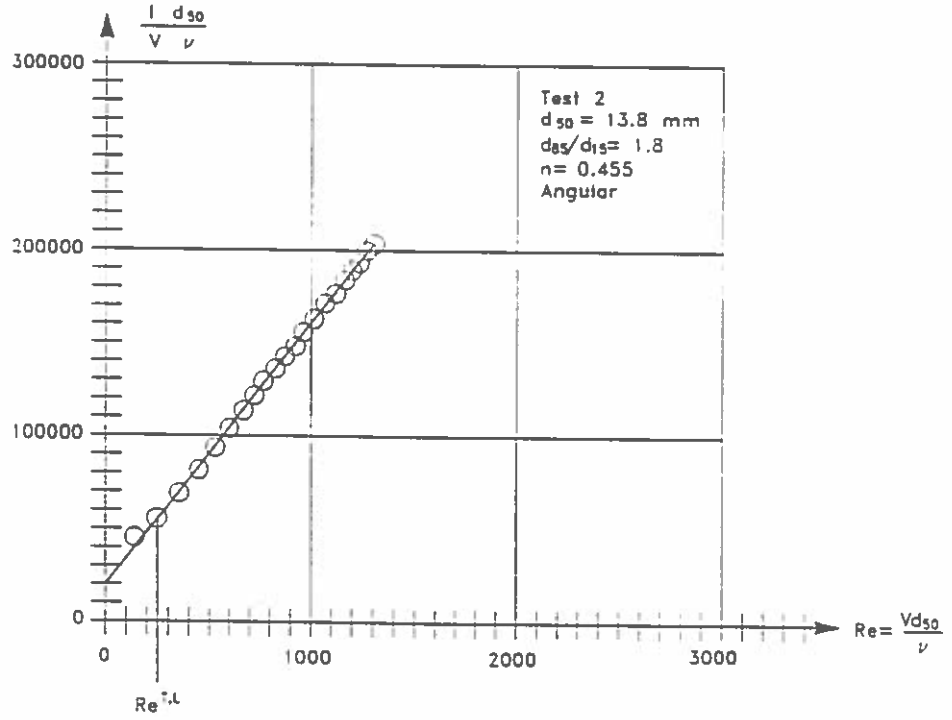

Fig. 29. Results of steady flow tests no. 2, based on external pressure transducer measurements. No wall effect correction.

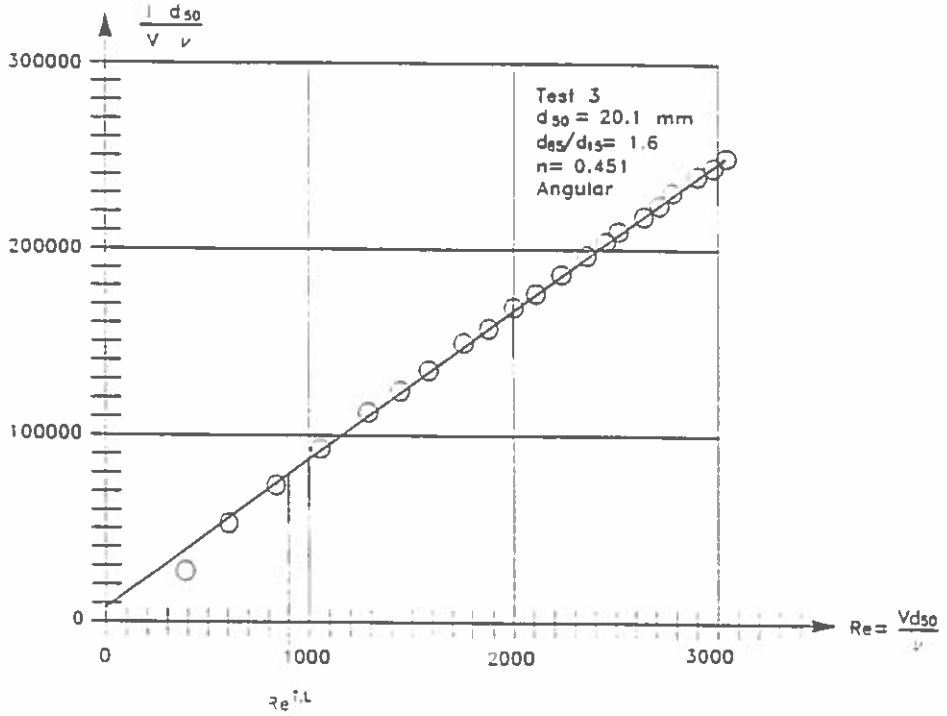

Fig. 30. Results of steady flow tests no. 3, based on external pressure transducer measurements. No wall effect correction.

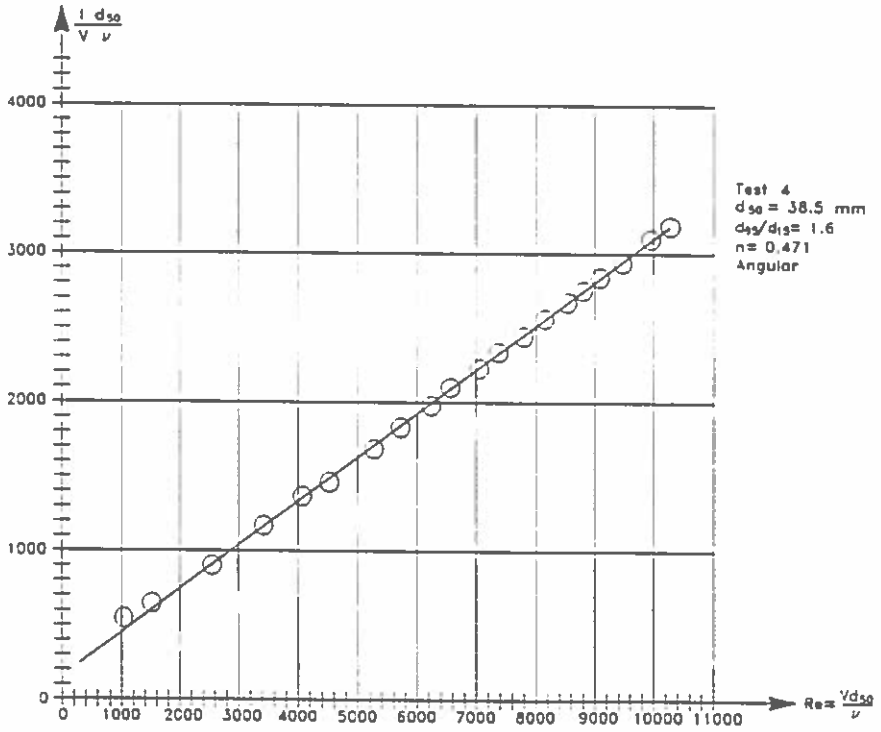

Fig. 31. Results of steady flow tests no. 4, based on external pressure transducer measurements. No wall effect correction.

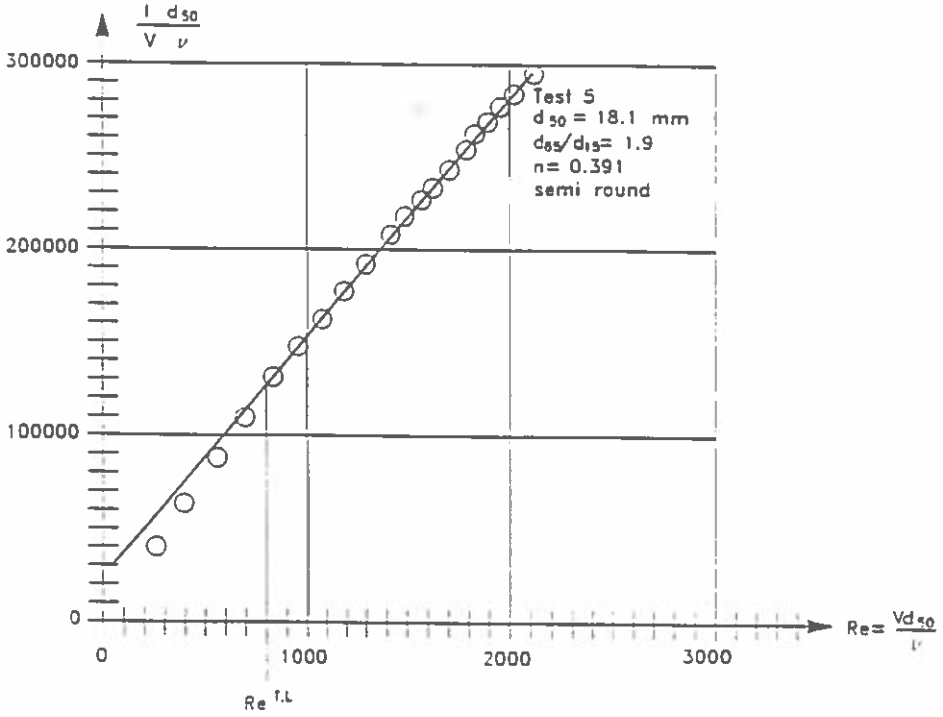

Fig. 32. Results of steady flow tests no. 5, based on external pressure transducer measurements. No wall effect correction.

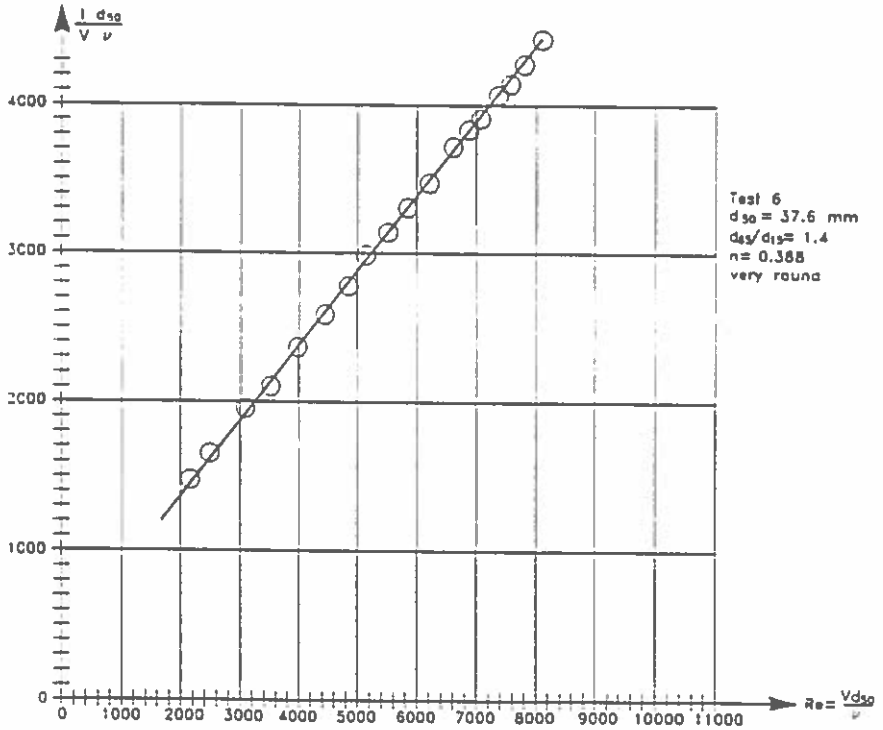

Fig. 33. Results of steady flow tests no. 6, based on external pressure transducer measurements. No wall effect correction.

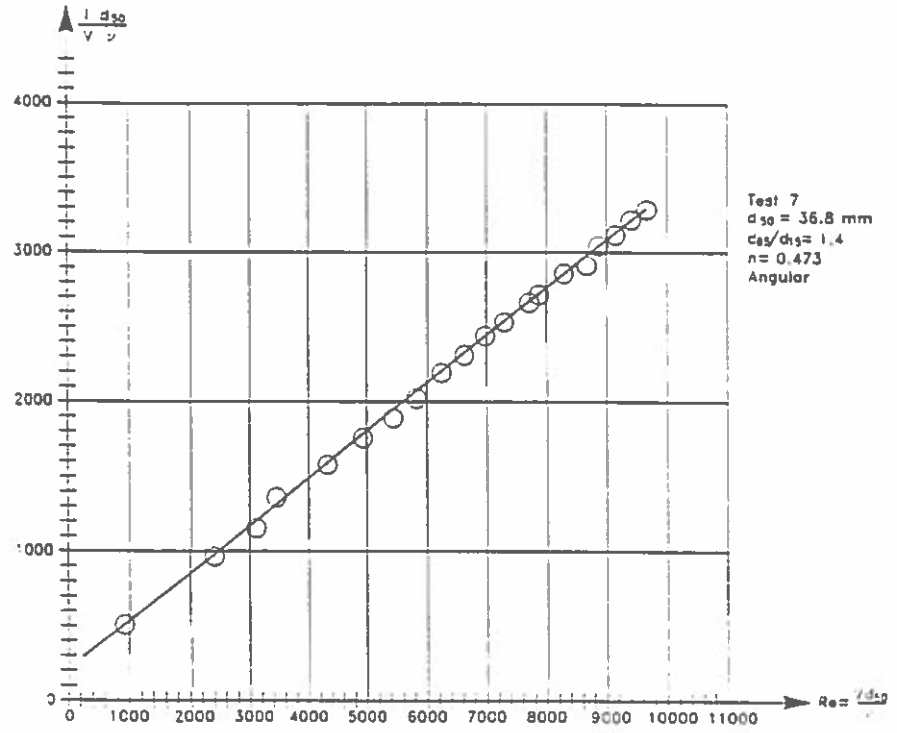

Fig. 34. Results of steady flow tests no. 7, based on external pressure transducer measurements. No wall effect correction.

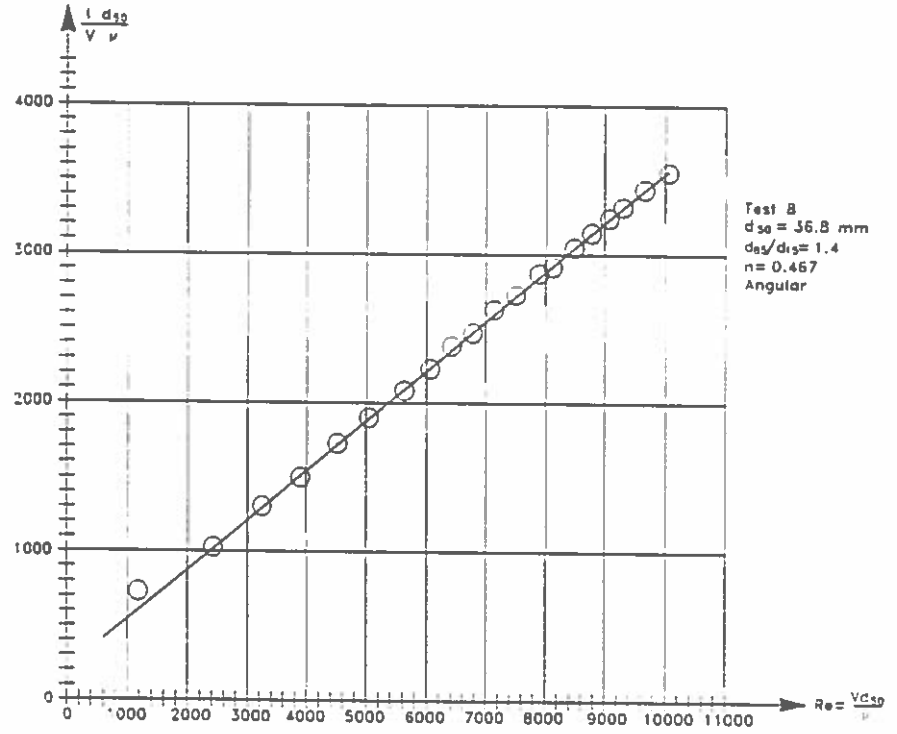

Fig. 35. Results of steady flow tests no. 8, based on external pressure transducer measurements. No wall effect correction.

The results given in Table 13 are almost identical to those given in Table 12 because the data cover almost exclusively the fully turbulent range in which case the conventional Forchheimer equation analysis and the analysis applied in section 9.1 naturally give the same results.

In order to compare the results with others a preliminary analysis of some of the HR permeameter data presented in Shih (1990) was performed including correction for wall effects. The results are given in Table 14.

Table 14. Shape parameter β for single size angular stones with gradation range $1.27 \leq d_{85}/d_{15} \leq 1.37$. HR data, Shih (1990).

d_{50} mm	β (average values) no wall-effect correction	β (average values) wall-effect corrected	approximate range of $Re = \frac{Vd_{50}}{\nu}$	Flow range
6	2.90	2.9	80 - 400	Forchheimer-transition
10	3.37	3.4	150 - 650	transition
14	2.50	2.5	150 - 900	transition - turbulent
20	2.43	2.5	175 - 1225	— " —
28	2.42	2.7	300 - 1900	turbulent
40	2.14	2.5	800 - 2950	— " —
61	2.30	2 .9	1000 - 5700	— " —

It is seen that for the turbulent flow range the average β-value is 2.7, which corresponds very well to the results for the angular stones given in Table 13 when considering the more narrow gradation for the HR single size stone samples.

The data presented by Dudgeon (1966) were analysed in a similar way including correction for wall-effects. Because it was impossible to detect all the data points in the log-log diagrams presented by Dudgeon it was necessary partly to use the graphs instead of the data points. The results are given in Tables 15 and 16.

Table 15. Shape parameter β for angular stones with gradation range $1.56 \leq d_{85}/d_{15} \leq 1.79$. Data by Dudgeon (1966).

d_{50} mm	β no wall-effect correction	β wall-effect corrected	appropriate range of $Re = \frac{V d_{50}}{\nu}$	Flow range
14	4.14	4.2	60 - 2300	Forchheimer - turbulent
14	3.40	3.4	200 - 1500	transition - turbulent
16	3.99	4.1	400 - 3400	turbulent
25	4.22	4.6	400 - 5500	— " —
37	9.49	11.0	520 - 8200	— " —

Table 16. Shape parameter β for river gravel (very rounded stones) with gradation range $1.51 \leq d_{85}/d_{15} \leq 1.81$. Data by Dudgeon (1966).

d_{50} mm	β no wall-effect correction	β wall-effect corrected	appropriate range of $Re = \frac{V d_{50}}{\nu}$	Flow range
16	3.06	3.1	85 - 2400	Forchheimer - turbulent
26	2.76	3.0	1000 - 6000	turbulent
55	2.44	3.0	100 - 3500	Forchheimer - turbulent
	2.11	2.6	3500 - 13500	turbulent
110	1.95	2.9	500 - 7000	— " —
	1.46	2.2	7000 - 36000	— " —

It is seen from Table 15 that the β-values for the angular stones in the turbulent flow range are significantly larger than the corresponding data in Tables 13 and 14. Especially the β-value of 11 for $d_{50} = 37$ mm seems to be completely out of the range. Disregarding this value the average β-value for the turbulent flow range is 4.1 which is 41% higher than the average β-value 2.9 for the present tests and 52% higher than the average β-value of 2.7 for the HR tests.

Also the β-values given in Table 16 for the very rounded stones are somewhat high. The average value for the turbulent flow range is 2.7 which is app. 25% higher than the corresponding β-value of 2.2 for the present tests.

There are no evident explanation for the deviations between the Dudgeon test results and the other results. Although there might be some doubt about the validity of the absolute β-values based on the Dudgeon tests it might be reasonable to use the results for the evaluation of the shape of the stones. Dudgeon also performed tests with uni-size glass spheres. Analysis of his data yields an average β-value for the turbulent flow range of 1.30. If this value is used as reference then we obtain for stone gradation ranges d_{85}/d_{15} of app. 1.7 the following ratios:

$$\frac{\beta_{angular\ stones}}{\beta_{glass\ spheres}} = \frac{4.1}{1.3} = 3.1 \tag{39}$$

$$\frac{\beta_{very\ rounded\ stones}}{\beta_{glass\ spheres}} = \frac{2.7}{1.3} = 2.1 \tag{40}$$

$$\frac{\beta_{angular\ stones}}{\beta_{very\ rounded\ stones}} = \frac{4.1}{2.7} = 1.5 \tag{41}$$

Using the present tests the following ratios can be estimated from Table 13 as follows

$$\frac{\beta_{angular\ stones}}{\beta_{very\ rounded\ stones}} = \frac{2.9}{2.2} = 1.3 \tag{42}$$

$$\frac{\beta_{angular\ stones}}{\beta_{semi\ rounded\ stones}} = \frac{2.9}{2.7} = 1.1 \tag{43}$$

Fand et al. (1987, 1990) also performed permeameter tests with uni-size glass spheres and found for the range $120 \leq Re \leq 410$ an average β-value of 1.57. Fand et al. denote this range as the turbulent flow range. However, it is believed that a slightly smaller β-value might be found for higher Reynolds numbers. The test results indicate a value of 1.5.

Using all presented information and having more confidence in the present results and the HR results for angular stones the β-values given in Table 17 are obtained.

Table 17. Shape parameter β for fully turbulent flow range, $Re = \frac{V d_{50}}{\nu} >$ app. 300.

Particles	Gradation d_{85}/d_{15}	β	$\frac{\beta}{\beta_{glass\ sphere}}$	Data source
Glass spheres	1	1.3 1.5 $\simeq 1.4$	1	Dudgeon, 1966 Fand et al., 1990
Very rounded stones (sea or river gravel)	1.4	2.2	1.6	Present tests
— " —	1.7	(2.7)	(1.9)	Dudgeon, 1966
Semi rounded stones	1.9	2.7	1.9	Present tests
Angular stones (like quarry stones)	1.3 - 1.4	2.7	1.9	HR data, Shih, 1990
— " —	1.4 - 1.8	2.9	2.1	Present tests
— " —	1.6 - 1.8	(4.1)	(2.9)	Dudgeon, 1966

The β-values should be used in the following approximate equation

$$I \simeq \beta \frac{1-n}{n^3} \frac{1}{g d_{50}} V^2$$

or in the more accurate equation

$$I = I_c + \beta \frac{1-n}{n^3} \frac{1}{g d_{50}} (V - V_c)^2$$

where

$$V_c = \frac{Re_c \nu}{d_{50}} \quad , \quad Re_c \simeq 300$$

$$I_c = \frac{\nu^2}{g d_{50}} \frac{1-n}{n^3} \left[\alpha_F (1-n) Re_c + \beta_F Re_c^2 \right]$$

α_F and β_F correspond to the Forchheimer flow range and d_{50} (cf. Table 3).

10. TEST RESULTS FROM UNSTEADY FLOW EXPERIMENTS

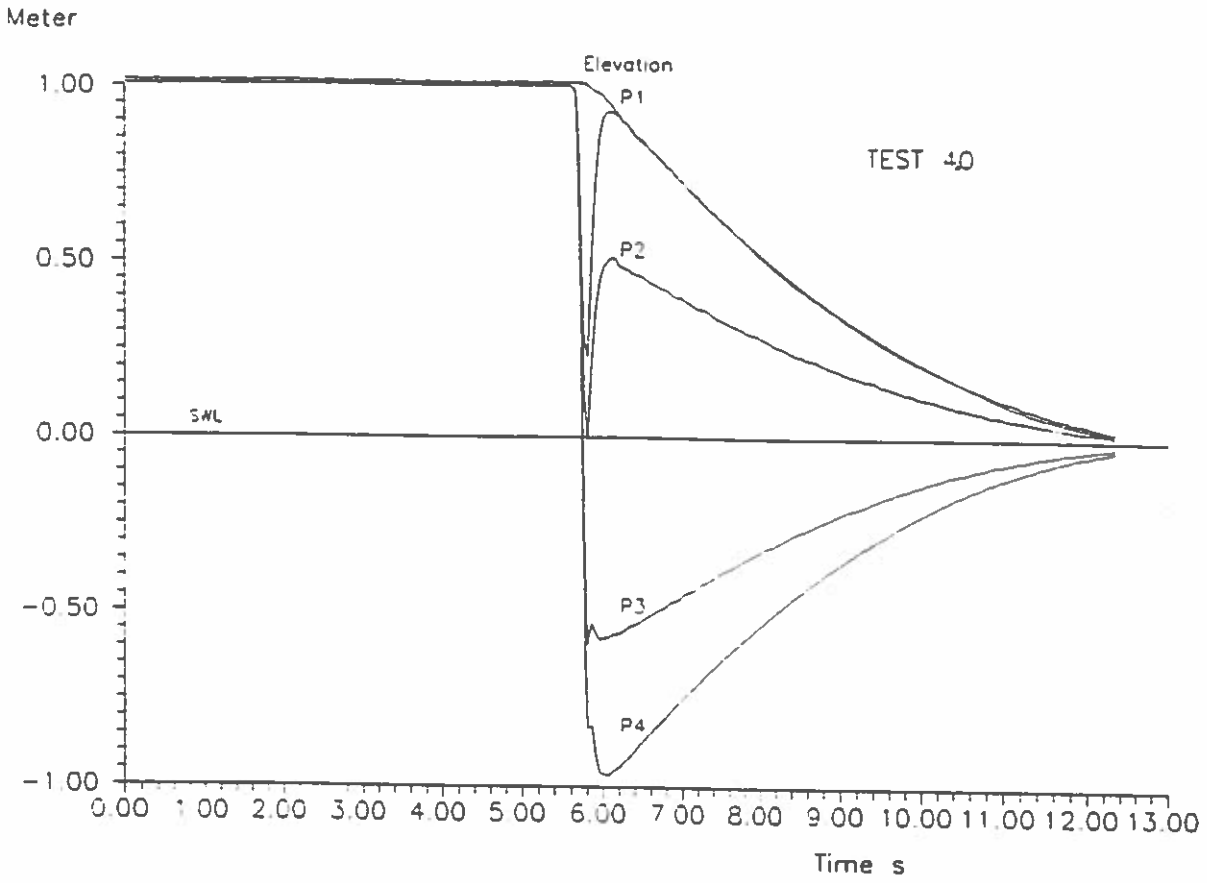

Fig. 36. Typical results from unsteady flow test.

In Fig. 36 typical results from an unsteady flow test are shown. The figure shows relative pressure and elevation relative to the still water level.

Generally an unsteady flow test can be divided into two periods: a short initial period of acceleration typical of the order 0.3 sec. and a long period of deceleration in the range 6-17 sec., depending on the permeability of the test material.

The accelerations in the initial phase were several orders of magnitude larger than in the deceleration phase. Unfortunately, reliable results for the velocities and accelerations were not possible to obtain in the initial phase on the basis of the elevation measurements, cf. the discussion in section 7. This also caused some problems in the deceleration phase, primarily due to the small accelerations. Several trials showed that no method of numerical differentiation yielded results with a high degree of accuracy.

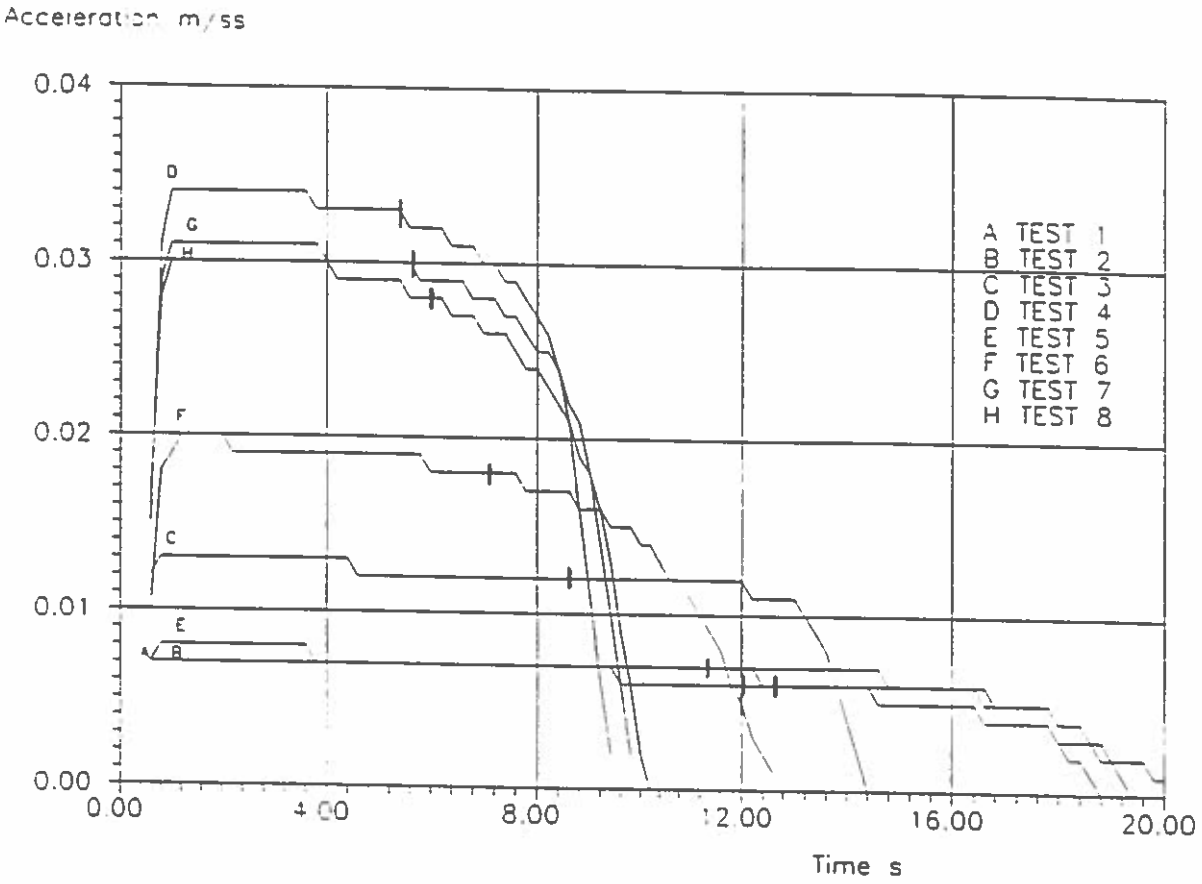

Fig. 37. Accelerations for the unsteady flow tests calculated with the numerical model.

The method chosen was finally to fit a second-order polynomia to the elevation curve and then use this polynomia to estimate the velocities and accelerations. This method was chosen on the basis of the numerical model, which showed that the accelerations in the deceleration phase more or less were constant.

In Fig. 37 accelerations calculated with the numerical model for unsteady flow tests are shown.

The results from the numerical model seem to indicate that the accelerations can be assumed to be constant until the relative elevation reaches a level approximately 0.1 m, indicated by the markers in the figure.

In Fig. 38 the relative elevations and respectively fitted polynomials are shown for test 1 to test 4, which covers the range of the unsteady flow tests. The results in the figure and the accelerations predicted by the numerical model, clearly indicate the accuracy of the method.

In estimating the virtual mass coefficient the following two methods were applied.

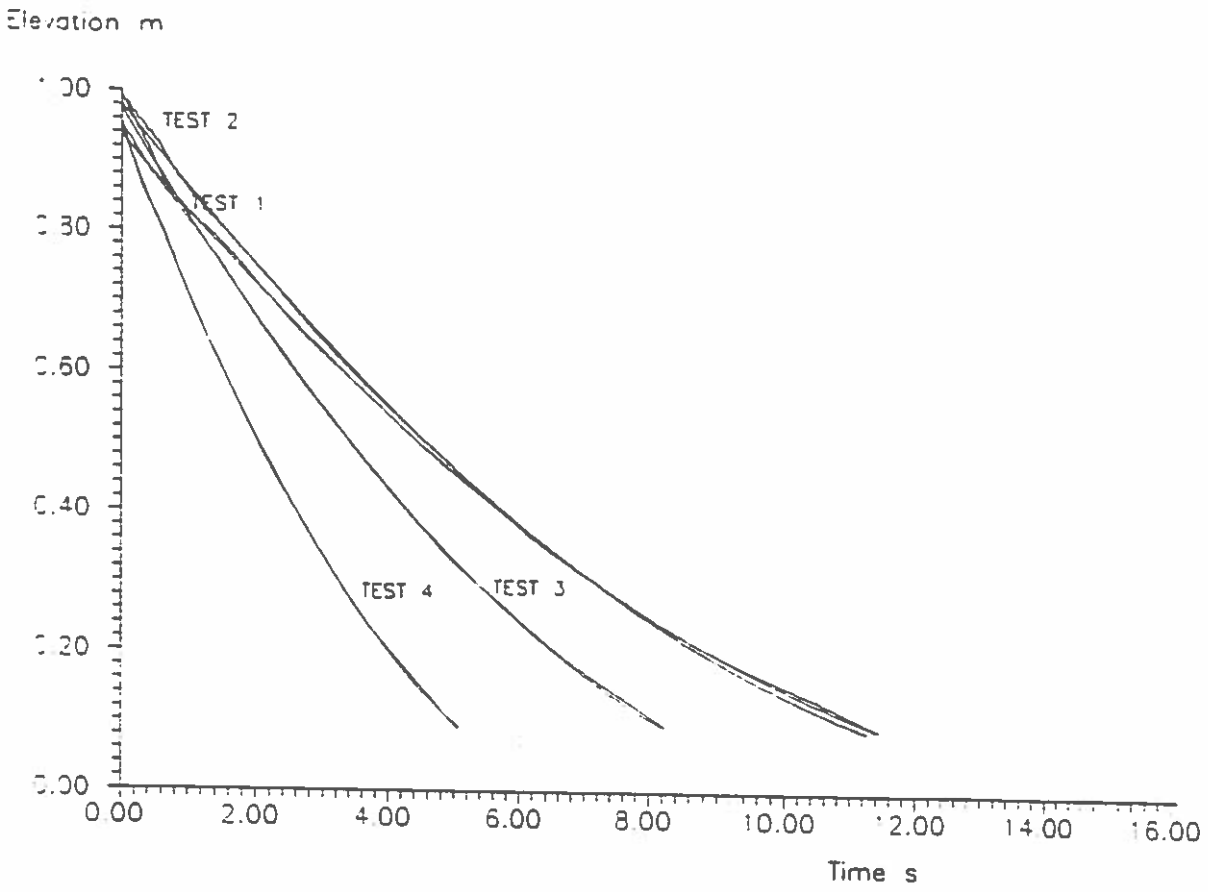

Fig. 38. Comparison of relative elevation and fitted polynomials.

The first method estimates the coefficient with the assumption that the values obtained for the coefficients a and b in the steady flow tests are valid also for the unsteady flow tests. This was done for every time step in order to check if any clear dependence of the Reynolds number was present. This did not seem to be the case and an average value for the coefficient was ultimately calculated for each test run. The reason for the seemingly independence of the Reynolds number could be the small range of Reynold numbers covered by the tests or the uncertainties in the determination of the virtual mass coefficient due to the small accelerations.

The second method estimates all three coefficients a, b and C_m by using the method of least square and calculates average values of all the coefficients. This method proved to give poor results due to the numerical difference, up to two orders of magnitude, between the coefficients.

In Tables 14 and 15 the estimates of the virtual mass coefficients for test 4, 6, 7, and 8 are listed. The estimates from the other tests were omitted due to the poor results.

Table 14. Estimation of average virtual mass coefficients on the basis of the internal pressure transducers.

Internal	Virtual mass coefficient C_m					
Test-run	1	2	3	4	5	$\overline{C}_m$
4	14.48	16.10	14.28	13.00	11.69	13.91
6	14.29	12.13	11.80	8.84	8.37	11.09
7	24.91	25.50	22.93	22.87	22.14	23.67
8	16.60	17.86	20.31	16.53	15.20	17.30

Table 15. Estimation of average virtual mass coefficients on the basis of the external pressure transducers.

External	Virtual mass coefficient C_m					
Test-run	1	2	3	4	5	$\overline{C}_m$
4	9.30	12.03	11.53	12.78	12.89	11.71
6	35.23	34.89	35.88	33.09	34.32	34.68
7	22.54	21.86	23.98	25.02	26.55	23.99
8	33.67	32.55	32.99	32.08	30.96	32.45

As the results show there still seems to be some problems with measurement of the pressures inside the porous media. The results obtained for the external pressure transducers are consistent, especially when considering the many approximations implicated in obtaining the results.

Virtual mass coefficient for a sphere is maximum 1.5, which is considerably smaller than the values obtained above. This could give rise to some concern about the validity of the obtained results. Sarpkaya and Isaacson (1981), however, refers to researchers who theoretically and experimentally have shown that virtual mass coefficients for individual piles, placed in groups, can be significantly larger than 2, which is the maximum value for a cylinder.

Due to the limitations of the U-tube technique no definite conclusions about the magnitude of C_m can be drawn, cf. sections 3 and 7.

12. REFERENCES

Ahmed, N.W.H. and Sunada, D.K. (1969) *Nonlinear Flow in Porous Media.* Journal Hyd. Div., ASCE, HY6, Nov. 1969.

Allsop, N.W.H. and Shih, R.W.K. (1990) *Permeability of Rubble Mound Coastal Structures to Wave Action: Laboratory and Numerical Modelling.* Preliminary article.

Bakhmeteff, B.A. and Feodoroff, N.V. (1937) *Flow through granular Media.* J. of Appl. Mech., 4.A.

Barends, F.B.J. (1978) *Advanced methods in groundwater flow computation.* Delft Soil Mech.lab., LGM-Mededelingen 19.

Carman, P.C. (1937) *Fluid through granular beds.* Frans. Inst. of Chem. Eng., Vol. 15, London.

Chardabellas, Pan. E. (1940) *Durchflusswiderstände im Sand und ihre Abhängigkeit von Flüssigkeits- und Bodenkennziffern.* Mitteilungen der Preussischen Versuchsanstalt für Wasser-, Erd- und Schiffbau, Heft 40, 1940.

CIRIA-CUR manual. *The use of rock in Coastal and Shoreline Engineering.* (In print)

De Lara, G.C. (1955) *Coefficient de perte de charge en milieux poreux basé à l'équilibre hydrodynamique d'un massif.* La Houille Blanche, Vol. 2.

Dudgeon, C.R. (1967) *Wall Effects in Permeameters.* Journ. of the Hydraulics Division, Proc. of ASCE, Vol. 93, No. Hy5. Sept. 1967.

Dudgeon, C.R. (1968) *Relationship Between Porosity and Permeability of Coarse Granular Materials.* Proc. 3rd Australian Conf. on Hydraulics and Fluid Dynamics. 1968.

Engelund, F.A. (1953) *On the Laminar and Turbulent Flows of Ground Water Through Homogeneous Sand.* Akademiet for de Tekniske Videnskaber, København, Danmark, 1953.

Ergun, S. (1952) *Fluid Flow through Packed Column.* Chemical Engineering Progress, Vol. 48, No. 2, 1952, pp. 89-94.

Fand, R.M., Kim, B.Y.K., Lam, A.C.C. and Phan, R.T. (1986) *Resistance to the Flow of Fluids Through Simple and Complex Porous Media Whose Matrices Are Composed of Randomly Packed Spheres.* ASME Journal of Fluids Engineering, Vol. 109, 1987, pp. 268-274.

Franzini, J.B. (1951) *Porosity Factor for Case of Laminar Flow through Granular Media.* Trans. Amer. Geophys. Union, Vol. 32, No. 3, p.443, June 1951.

Givan. C.V. (1934) *Flow of Water through Granular Materials. Initial Experiments with Lead-Shot.* Trans. Amer. Geophys. Union, June 1934, Part II, p. 572.

Hanoura, A.A. and McCorquadale, J.A. (1978) *Virtual Mass of Coarse Granular Media.* Proc. ASCE, Journal Waterway Port, Coastal and Ocean Div., Vol. 104, WW2, May 1978.

Hanoura, A.A. and McCorquadale, J.A. (1978) *Air-water Flow Forces on Rubble-mound Breakwaters.* Journal Hyd. Div., ASCE, Vol. 104, HY7, July 1978.

Irmay, S. (1958) *On Theoretical Derivation of Darcy and Forchheimer Formulas.* A.G.U., Trans., 39, 4, 1958.

Lindquist, E. (1933) *On the Flow of Water through Porous Soil.* Report to the First Congress of Large Dams, Stockholm 1933.

Muskat, M. (1946) *The Effect of Casing Perforations on Well Productivity.* American Institute of Mining and Metallurgical Engineers. Techn. Publ. No. 1528. 1946.

Polubarinova Kochina, P.Ya. (1962) *Theory of Groundwater Movement.* Princeton University Press, Princeton, N.J., 1962.

Rose, H.E. (1945) *Fluid flow through beds of granular materials.* Some Aspects of Fluid Flow, papers presented at a conf. org. by The Inst. of Physics at Leamington Spa 25-28 Oct. 1950. Edward Arnold & Co., London, 1951.

Rumer, R.R. & Drinker. (1966) *Resistance to laminar flow through porous media.* J. of Hyd. Div., ASCE, Vol. 92, HY5. (May)

Sarpkaya, T. and Isaacson, M. (1981) *Mechanics of Wave Forces on Offshore Structures.* Van Nostrand Reinhold Company, New York, N.Y., 1981.

Scheidegger, A.E. (1960) *The Physics of flow through porous media.* Univ. of Toronto Press, 2nd Ed.

Shih, R.W.K. (1990) *Permeability characteristics of rubble material – new formulae.* Proc. ICCE '90 (Int. Conf. on Coastal Eng.), Delft, July 1990.

Ward, J.C. (1964) *Turbulent Flow in Porous Media.* Journal of Hyd. Div., ASCE, Vol. 90, HY5, Sept. 1964.

Design of Dolos armour units

H.F. Burcharth and Zhou Liu

University of Aalborg
Denmark

Design of Dolos armour units

Hans F. Burcharth[1] Zhou Liu[2]

Abstract

The slender, complex types of armour units, such as Tetrapods and Dolosse are widely used. Many of the recent failures of such rubble mound breakwaters revealed that there is an imbalance between the strength (structural integrity) of the units and the hydraulic stability (resistance to displacements) of the armour layers.

The paper deals only with Dolos armour and presents the first design diagrammes and formulae where stresses from static, quasistatic and impact loads are implemented as well as the hydraulic stability. The Dolos is treated as a multishape unit where the thickness can be adjusted to the strength needs.

Introduction

Many of the recent dramatic failures of a number of large rubble mound breakwaters armoured with Dolosse and Tetrapods were caused by breakage of the units. Breakage took place before the hydraulic stability of intact units in the armour layers expired. Thus there was an imbalance between the strength (structural integrity) of the units and the hydraulic stability (resistance to displacements) of the armour layer.

The present paper deals only with Dolosse armour and presents the first design diagrammes and formulae where stresses from static, quasistatic and impact loads are implemented as well as the hydraulic stability. Earlier publications only covered static and quasistatic stresses (e.g. Burcharth et al., 1991). The results are the outcome of a long-term research programme at Aalborg Hydraulic Laboratory (AHL), Aalborg University, which for the last three years has been coordinated with Dolosse research at CERC, Vicksburg.

Dolosse armour was chosen as research object because of its excellent hydraulic stability and because its structural strength can be adjusted by changing the waist ratio, cf. Fig. 1, which shows blocks with the three waist ratios applied in the experiments. By increasing the waist ratio in order to improve the structural behaviour the hydraulic stability will decrease somewhat. This must be taken into account in the design.

[1]Prof. of Marine Civil Engineering, Aalborg University, Denmark.
[2]Research Engineer, Aalborg University, Denmark.

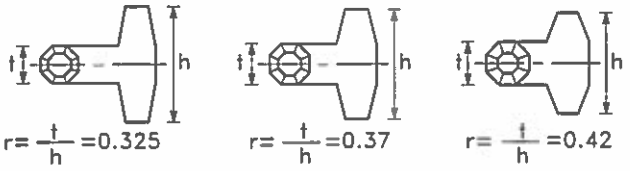

Fig. 1. Applied concrete Dolosse with different waist ratios but with equal mass.

Description of the experiments

A 1 : 1.5 slope armoured with 200 g concrete Dolosse of waist ratios as shown in Fig. 1 was exposed to irregular wave in a wave flume with a foreshore slope of 1 : 20. Fig. 2 shows the layout of the model and the cross section of the breakwater.

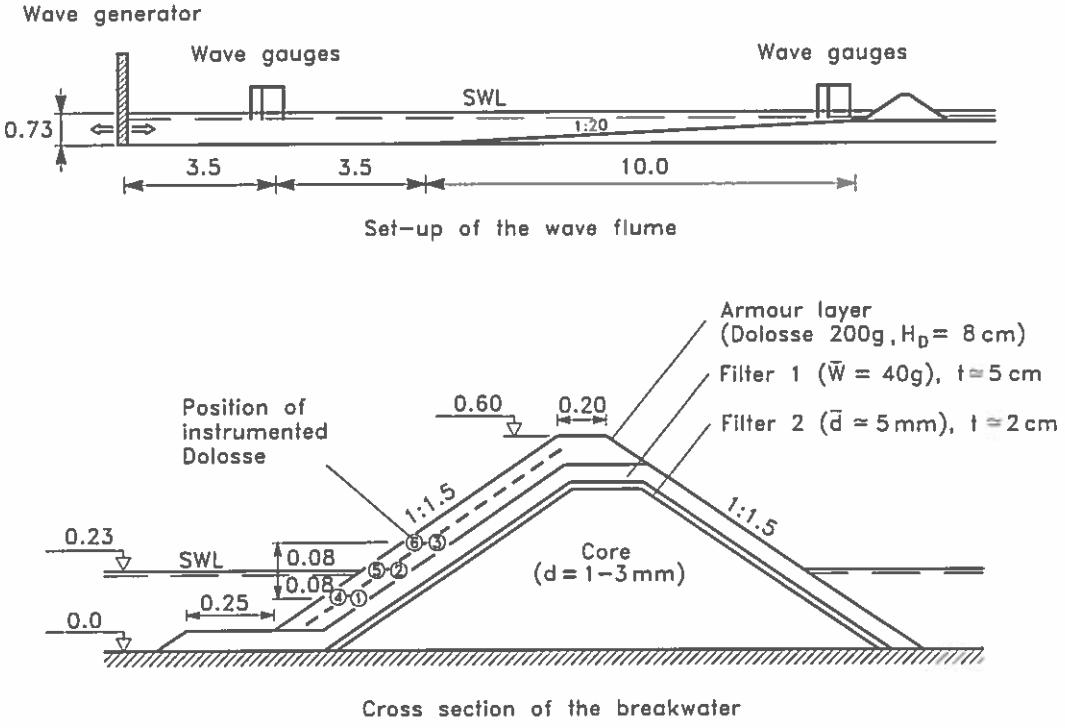

Measures and levels in meter

Fig. 2. Set-up of the wave flume and the cross section of the breakwater. Aalborg Hydraulic Laboratory (AHL) experiments.

To compensate for reflected waves two arrays of three wave gauges were installed. The incident wave spectrum was calculated by the least square method presented by Mansard et al., 1980.

The irregular waves were generated by a piston type paddle according to the five parameter JONSWAP spectrum. Table 1 lists the characteristics of the applied waves propagating towards the breakwater recorded at the paddle and at the toe of the breakwater. T_p is the spectral peak period, $\xi_{mo} = \left(\frac{H^t_{m0}}{L_{p0}}\right)^{-0.5} tan\alpha$, where L_{po} is the deep water wave length corresponding to T_p.

Table 1. H_{m0}, T_p *and* ξ_{mo}.

H^p_{m0}	at the paddle	(cm)	5	-	15
H^t_{m0}	at the toe	(cm)	5.7	-	18.2
T_p	at the paddle	(sec)	1.5	-	3
ξ_{mo}			3.23	-	11.7

The experiments were performed in series in which the wave height was increased step by step. The run time for each step was 5 minutes.

For each combination of H_{m0} and T_p the experiment was repeated 20 times in the study of the hydraulic stability and 3 times for each position of the instrumented Dolosse in the study of the stresses in Dolosse; all with the slope rebuilt.

In order to study the hydraulic stability of the Dolos armour layers a grid was put parallel to the breakwater slope before and after wave attack and photos were taken. All displacements could then be visually registered.

The applied load cells are developed and produced by CERC. The load cell instrumented concrete Dolosse were calibrated for impact loaded conditions using prototype impact test data and were checked for dynamic amplification, cf. Burcharth et al. 1991. They were put in 6 positions on the slope as shown in Fig. 2.

Hydraulic stability of Dolos armour

The following formula for hydraulic stability of Dolos armour on slope 1 : 1.5 is based on the present test results and results by Brorsen et al. 1974, Burcharth et al. 1986, and Holtzhausen et al. 1990.

$$N_s = \frac{H_s}{\Delta D_n} = (47 - 72\,r)\,\varphi_{n=2} D^{1/3} N_z^{-0.1} \qquad (1)$$

where H_s significant wave height in front of breakwater

Δ $(\rho_{concrete}/\rho_{water}) - 1$, ρ is the mass density

D_n length of cube with the same volume as Dolosse

r Dolos waist ratio

$\varphi_{n=2}$ packing density

D relative number of units within levels SWL $\pm$ 6.5 Dn displaced one Dolos height h, or more (e.g. for 2% displacement insert $D = 0.02$)

N_z number of waves. For $N_z \geq 3000$ use $N_z = 3000$.

Fig. 3 shows the case corresponding to damage level of 2% displacement.

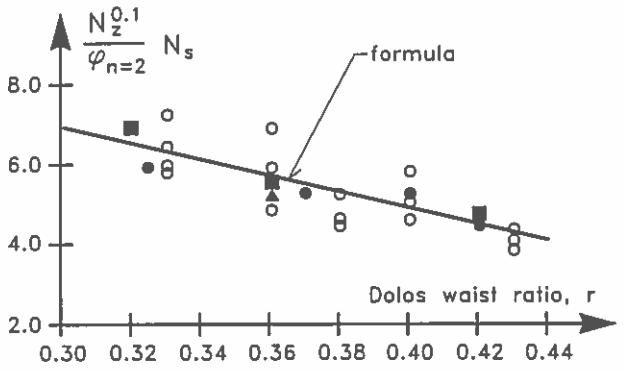

Legend:

Reference	$\varphi_{n=2}$	Repeated No	Duration (min.)	ξ_{mo}
▲ Brorsen et al. (1974)	1 (App.)	2	60	2.49–5.37
■ Burcharth et al. (1986)	0.61–0.7	5 or 15	20	3.04–4.49
o Holtzhausen et al. (1990)	1	3 or 8	60	2.91–7.6
● Burcharth et al. (1992)	0.74	20	5	3.23–11.7

Fig. 3. Hydraulic stability of two layer randomly placed Dolos armour on a slope of 1 : 1.5. *Damage level,* $D = 2\%$ *displaced units within levels SWL* $\pm 6.5 D_n$. *Note that the data points are average of repeated tests, cf. the legend.*

The formula (1) covers both breaking and non-breaking wave conditions, with the limits given by

$$0.32 < r < 0.43$$
$$0.61 < \varphi_{n=2} < 1$$
$$1\% < D < 15\%$$

The uncertainty of the formula is estimated to correspond to a variational coefficient of 0.2. If the PIANC partial coefficient system is used (Burcharth 1991) the design equation reads

$$\frac{1}{\gamma_z}\Delta D_n(47-72\,r)\varphi_{n=2}D^{1/3}N_z^{-0.1} \geq \gamma_{H_s}H_s^T \tag{2}$$

For the calculation of the partial coefficients γ_z and γ_{H_s} the coefficient values $k_\alpha = 0.025$ and $k_\beta = 38$ should be used.

In the following is given a discussion of the dependency of the hydraulic stability of Dolos armour on various parameters.

Test area One of the reasons for the big scatter in the hydraulic stability test results from the various laboratories is the difference in the reference test area. Obviously, the bigger the reference test area, the higher the stability number.

Fortunately, the test areas seem always to be chosen large enough to cover the whole area where units are moving. Therefore the test results can be converted to results corresponding to a certain test area, e.g. to SWL $\pm 6.5 \times D_n$, as is done in the present paper.

Breakwater slope The effect of the slope angle of Dolos armour on hydraulic stability has been one of the most controversial points. Hudson's formula, which was developed for rock armour, where the main resistance to wave-induced movement is due to the gravitational force, cannot represent Dolos armour, the stability of which relies both on weight and interlocking.

With regard to the contribution of Dolos weight to the hydraulic stability, the milder the slope, the bigger the contribution, as expressed in Hudson's formula. But on the other hand, the interlocking ability of Dolos armour builds up with the increase of the slope (before the slope reaches its natural angle of repose, which is found to be around 79°, Gravesen et al. 1978). This means that there is an optimum slope which maximise the stability of Dolos armour as a whole. Price (1979) demonstrated in the on-land static stability test with Dolosse that the resistance to pull-out attained its maximum for slope angles around 28° ($cot\alpha = 2$).

In the hydraulic model tests, Brorsen et al. (1974) reported that the stability number of Dolosse is independent of the slope within the range of slope $1:1 \sim 1:2$. Holtzhausen et al.(1990) concluded that Dolosse stability number decreases with steeper slope, but some of his test results also show the independence of N_s on slope, cf. Fig. 4.

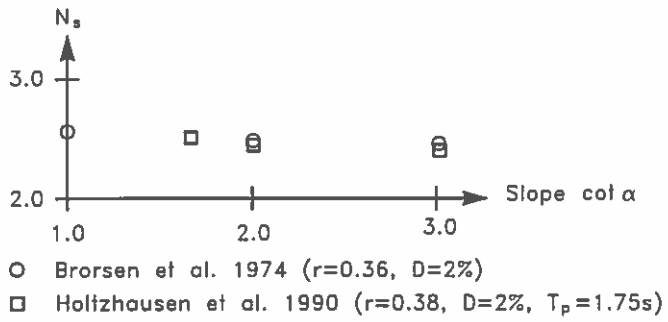

Fig. 4. Influence of slope on N_s.

Wave period The influence of the wave period on the stability of Dolos armour has been the subject of research over the years. HR Wallingford (1970) and Burcharth (1979) found that the stability number decreases with longer wave periods. Burcharth (1979) explained this tendency by *the reservoir effect of the voids* between the units.

The voids are filled with air during wave recession and with water during wave run-up. This reduces not only the wave run-up but also the overflow velocities. Armours with larger porosity, such as Dolosse, exhibit stronger reservoir effect which tributes to the higher hydraulic stability. However, the reservoir effect is reduced in the case of long waves, because such waves carry more water per wave onto the slope and, consequently, relative smaller portion of water can be stored in the voids. The result is higher overflow velocity and lower hydraulic stability of armour and, consequently, a relatively large reduction in stability for armour units with large porosity.

However, there are also some reports which predict increase of the stability number with the wave periods (Holtzhausen et al. 1990).

In the present test results there is no clear tendency about the influence of wave period on the hydraulic stability for which reason the wave period (or wave steepness or ξ) is not included as an independent parameter in formula (1). This treatment of the wave period also reflects the fact that for a given design wave height there will be a range of wave periods anyway. The effect of wave period contributes to the uncertainty of the formula. This, however, is taken into consideration when the partial coefficient method is applied in the design.

Packing density Some research has been carried out previously to study the influence of Dolos packing density on the hydraulic stability.

Carver et al. (1978) collected data from different laboratories and depicted the Hudson formula stability coefficient K_D as a function of the packing density $\varphi_{n=2}$. If $N_s = \frac{H_s}{\Delta D_n}$ is used instead of K_D an almost linear dependency of N_s on $\varphi_{n=2}$ is seen.

Zwamborn (1978) first reported that the Dolos armour with three packing densities ($\varphi_{n=2} = 0.83$, 1 and 1.15) displayed the same stability. But based on tests with a bigger packing density range ($\varphi_{n=2}$= 0.65, 0.83, 0.87, 1, 1.15 and 1.5) Zwamborn et al. (1980) found a rather complicated relation between N_s and $\varphi_{n=2}$, with the general tendency that higher packing density increase the stability number.

A higher packing density gives more neighbour block support and interlocking and hence, fewer displaced units. Therefore, the increase of Dolos stability number with packing density is due to two effects, one is the reduction of displaced units, the other is the increase of total number of units. Eq (1) indicates that the Dolos stability number is linearly proportional to the packing density within the applied range ($\varphi_{n=2} = 0.61 - 1$).

On the other hand a very high packing density ($\varphi_{n=2} > 1$) might reduce the interlocking and the stability because limited space is available for legs to stick in between each other. Therefore, there exists an optimum packing density. SPM (1984) gives $\varphi_{n=2} = 0.83$ while Zwamborn (1980) suggests $\varphi_{n=2} = 1$.

Wave duration (number of waves N_z) In the 50'^{ties} and early 60'^{tics} the storm duration parameter was not considered because the generated waves in laboratories were monochromatic waves, which are the same for every single wave. The equilibrium slope was reached in a short time.

In the case of irregular waves it takes longer time before a possible equilibrium state is reached. Font (1968) studied the effect of storm duration on the stability of rock armoured breakwater. He concluded that for mild wave climates, i.e. relative small $\frac{H_s}{\Delta D_n}$ values, the duration of the storm is not important. However, the duration becomes relevant for more severe exposure.

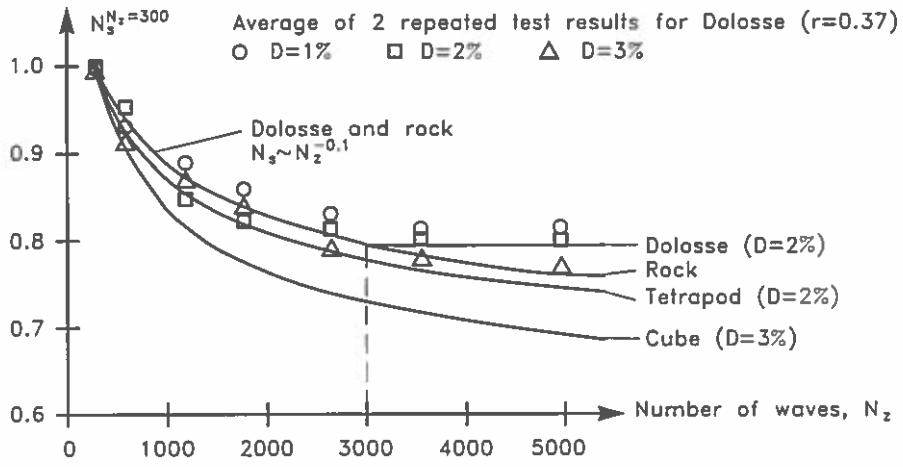

Fig. 5. Influence of wave duration on N_s.

I the present tests two identical tests with 5,000 waves were performed with Dolosse of waist ratio 0.37. Little difference in the ratio $\frac{N_s}{(N_s)_{N_z=300}}$ was found for the damage levels D = 1 %, 2 % and 5 %. Moreover, it was found that the Dolos armour reached an equilibrium state after $N_z = 3,000$. The relationship between N_s and N_z could be approximated by $N_s \sim N_z^{-0.1}$ for $N_z \leq 3,000$.

In Fig. 5 the information on rock, cube and Tetrapod is from van der Meer (1988).

Stresses in Dolosse under wave attack

Sampling frequency The natural frequency of the instrumented Dolosse was found to be app. 1,500 Hz by the impact calibrations. The sampling frequency in the wave flume test was 6,000 Hz, i.e. app. 4 times of the natural frequency of the instrumented Dolosse. Theoretical investigations showed that on average the sampled peak stresses were lower than the real ones by 10% due to the limit of the sampling frequency. This one sided bias has been corrected for in the data processing.

Strain signal processing The recorded strain signals were converted into signals of maximum principal tensile stress by

$$\text{max. principal tensile stress } \sigma_T = \frac{\sigma}{2} + \sqrt{(\frac{\sigma}{2})^2 + \tau^2}$$

$$\text{normal stress } \sigma = \frac{M_c}{W_b}$$

$$\text{combined bending moment } M_c = \sqrt{M_x^2 + M_y^2}$$

$$\text{shear stress } \tau = \frac{T}{W_b/2}$$

where M_x, M_y and T are the measured bending moments and torsion, respectively. W_b is the modulus of the strain-gauged cross section of Dolosse. For more detailed explanation see Burcharth et al. 1991.

The converted max principal tensile stresses were separated into (*static + pulsating*) and *impact* stresses. The static and pulsating stress contributions were converted into a range of prototype Dolos sizes using the valid linear scaling law, while the impact stress contributions were converted into the same prototype ranges using the non-linear scaling law for impinging solid bodies. The signals were then synthesized and a statistical analysis performed.

Stresses from static, pulsating and impact loads in Dolosse The relative importance of static, pulsating and impact stresses depends on the type and the size of the units, the slope angle, the position on the slope and the wave characteristics.

The Dolos stresses are treated as an extreme value problem. No distinction with respect to the Dolos position on slope was made because in practice the same type of units will be used over the whole height of the slope.

Table 2 indicates typical ratios between the various types of stresses for slender and bulky Dolosse on slope 1 : 1.5.

Table 2. Relative contribution to total stress from static, pulsating and impact stresses. 2 % exceedence probability values. Slope 1 : 1.5.

				$\sigma_{total} = \sigma_{static} + \sigma_{pulsating} + \sigma_{impact}$		
Waist ratio	Mass	$\frac{H_s}{\Delta D_n}$	K_D	σ_{static}	$\sigma_{pulsating}$	σ_{impact}
0.325	10t	0.9	0.49	1	0.2	0
		1.8	3.89	1	0.4	0.1
		2.6	11.72	1	0.5	0.4
	50t	0.9	0.49	1	0.2	0
		1.8	3.89	1	0.4	0
		2.6	11.72	1	0.5	0.1
0.42	10t	0.9	0.49	1	0.2	0
		1.8	3.89	1	0.4	0.4
		2.6	11.72	1	0.6	2
	50t	0.9	0.49	1	0.2	0
		1.8	3.89	1	0.4	0.1
		2.6	11.72	1	0.6	1.3

Note that the zeros in the σ_{impact} column does not mean that there is no impacts in the signal. It means that the impact portion of the stresses is smaller than the static+pulsating portion after scaled up to the given size. The tests showed that the variation in the stress ratios with the exceedence probability level is rather weak in the interval 1-5%.

The variation with the slope angle is not known in general. However, because static stresses show only small variations in the slope range 1 : 1.33 to 1 : 2 it is assumed that the stress ratios given in Table 2 are typical for this range of slopes. On the other hand the ratios are probably not valid for very steep slopes as it is known that the static stresses can be up to 100% larger for a 1 : 1 slope than for a 1 : 1.5 slope. For flat slopes of app. 1 : 4 to 1 : 6 it was found from the Crescent City prototype study with 38 t instrumented Dolosse (Howell et al.

1990) that the ratio of the 10 % exceedence probability stress values, σ_{Static} : $\sigma_{pulsating}$, was app. $1 : 0.12$ for $N_s = 1.2 - 1.4$. No impact stresses were recorded in this study, maybe due to the small N_s-values, cf. also the figures given in Table 2.

Design diagrams for Dolosse

In the production of design diagrams, only the maximum value of σ_T for each instrumented Dolos within a test run (150-200 waves) is of interest. There are six instrumented Dolosse and three test runs. This is equivalent to 18 records. If one of the 18 maximum values exceeds the concrete strength, the relative number of broken Dolosse is $\frac{1}{18} = 5.6\%$. Because the maximum stress in Dolosse usually contains significant contributions from impact and because Dolos movement and the related impact stresses occur in the early stage of the wave attack it is believed that the recorded maximum value of σ_T will be very close to the value found in a longer run, e.g. in a design storm of 1,000 waves or more.

In the experiment the instrumented Dolosse cover the area SWL $\pm$ 2.7 D_n. In the design diagram this reference area is expanded to SWL $\pm$ 6.5 D_n, the one for the hydraulic stability formula. The expansion is made based on the principle that no Dolos breakage takes place outside the area SWL $\pm$ H_s.

Only one shank cross section of Dolosse was instrumented, while there are 6 vulnerable sections in a Dolos (4 in the flukes and 2 in the shanks). This model effect has been considered based on the results of the on-land ramp test where the Dolos was instrumented in 2 shank cross sections and 2 fluke cross sections. Therefore, in the design diagram, breakage of a unit is taken as breakage of just one of the 4 legs or as breakage in the shank. The diagrams provide the relationship between all the following properties, expressed in statistical terms where relevant.

Dolos waist ratio
Dolos size
Concrete tensile strength
Incident wave climate
Relative number of broken Dolosse (structural integrity)
Relative number of displaced Dolosse (hydraulic stability).

Fig. 6 shows examples of the design diagrams. The hydraulic stability in terms of displacements is obtained by Eq (1). The amount of rocking is not given explicitly in the design diagrams because the effect of rocking is relevant only to the breakage aspect which is dealt with specifically by the breakage curves.

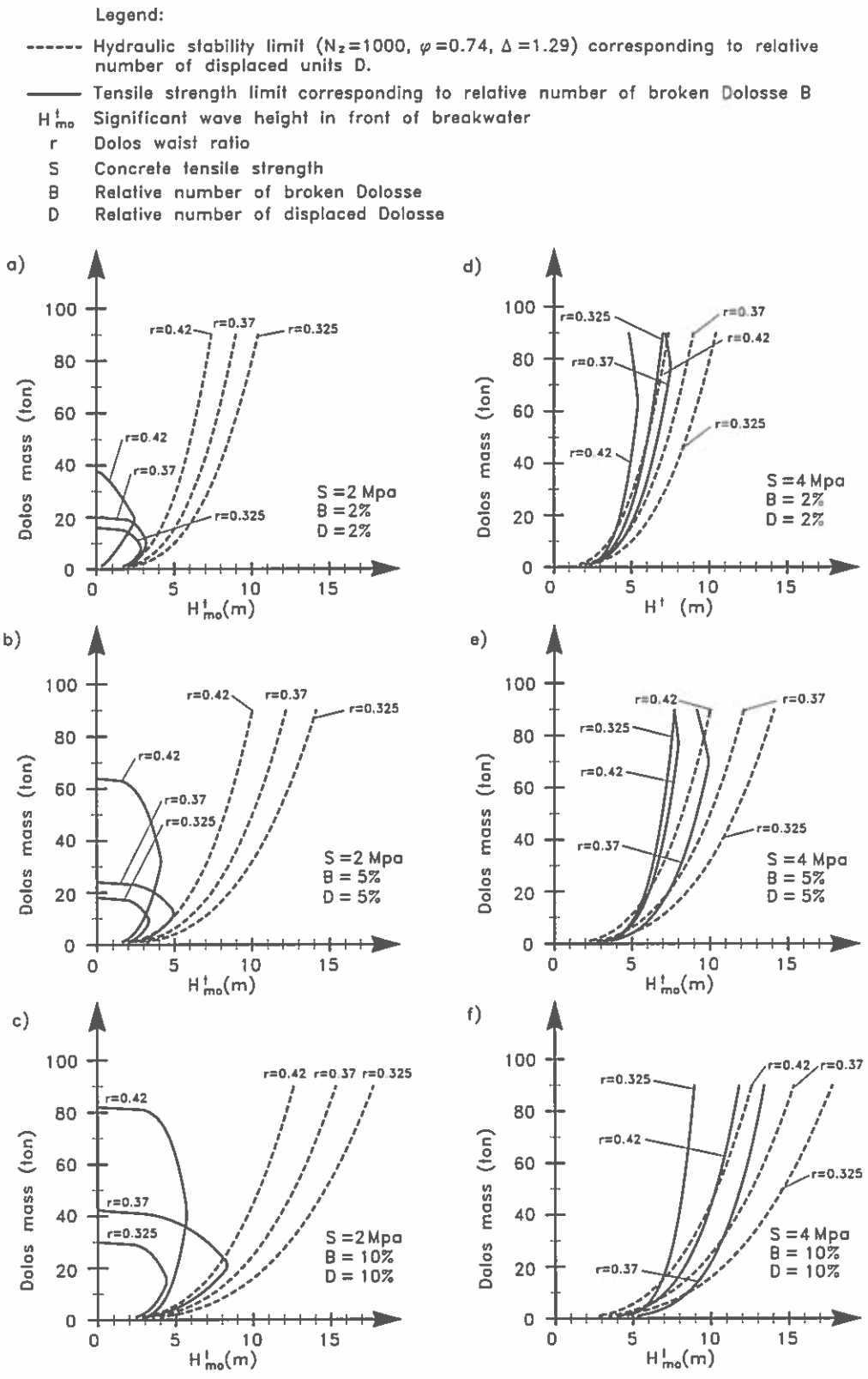

Fig. 6a. Design diagram for structural integrity and hydraulic stability of Dolos armour. Reference area SWL ± 6.5 D_n.

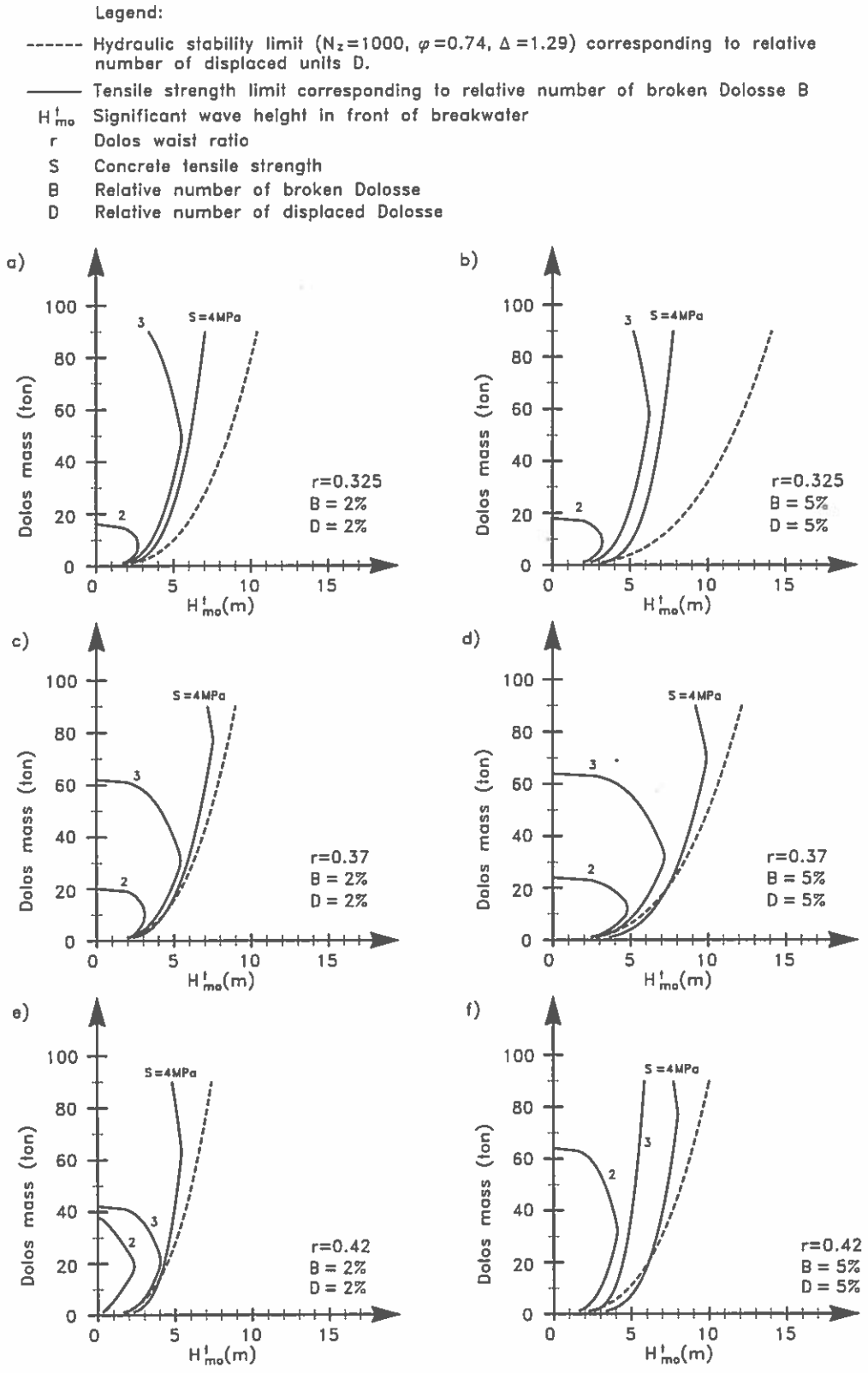

Fig. 6b. Design diagram for structural integrity and hydraulic stability of Dolos armour. Reference area SWL ± 6.5 D_n.

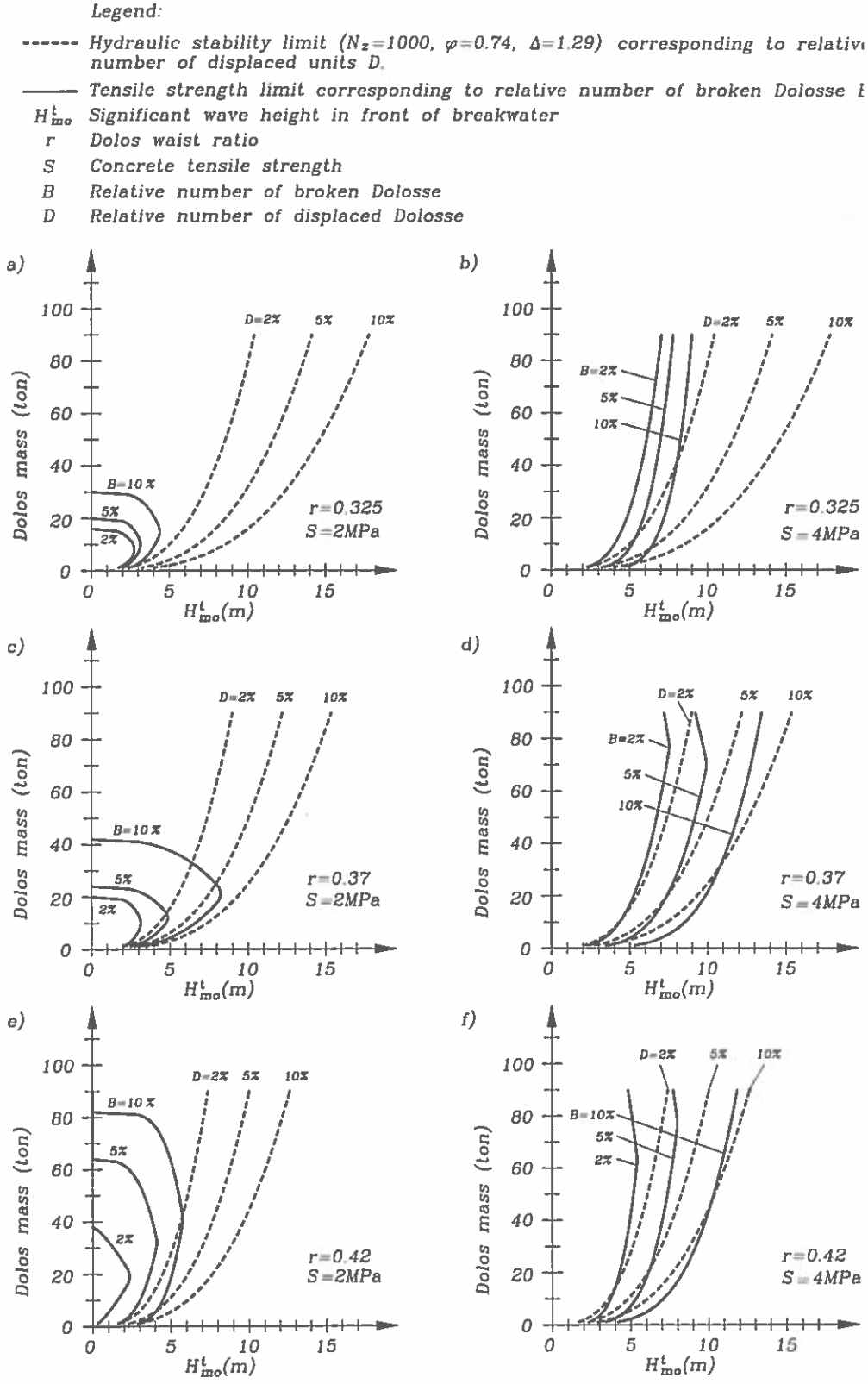

Fig. 6c. Design diagram for structural integrity and hydraulic stability of Dolos armour. Reference area SWL ± 6.5 D_n.

The design diagrams have been checked against observed behaviour of prototype Dolos breakwaters and good agreement was found, cf. Table 3.

Table 3. Prediction of damage of some Dolos breakwaters.

	Crescent City USA	Richards Bay SA	Sines POR
H_s (m)	10.7 (1)	5 (2)	9 (3)
slope	1:4	1:2	1:1.5
Dolos mass (ton)	38	20	42
Waist ratio	0.32	0.33	0.35
Dolos packing density	0.85	1	0.83
Concrete density (kg/m^3)	2500	2350	2400
Elasticity (MPa) (4)	30000	30000	30000
Tensile strength (MPa) (4)	3	3	3
Reported displacement	7.3%		
Reported breakage	19.7%		
Reported displacement+breakage	26.8%	4%	collapse
Predicted displacement	3.6%	0.6%	3.6 %
Predicted breakage	> 10%	5%	> 10%

(1) depth limited in front of breakwater
(2) in front of breakwater
(3) offshore ≈ in front of breakwater
(4) estimated values

Acknowledgements

Part of the study were funded by the Danish Research Council and by the U.S. Army Research, Development and Standardization Group, UK under the Contract DAJA 45-91-C-0010.

References

Brorsen, M., Burcharth, H.F., Larsen,T. (1974) : *Stability of Dolos Slopes.* Proceeding of the 14th International Conference on Coastal Engineering, Copenhagen, Denmark, June, 1974

Burcharth, H.F. (1979) : *The effect of wave grouping on onshore structures.* Coastal Engineering, 2 (1979).

Burcharth, H.F. (1991) : *Introduction of partial coefficients in the design of rubble mound breakwaters.* Coastal structures and breakwaters. Proceeding of the conference organised by the Institution of Civil Engineers, London.

Burcharth, H.F., Brejnegaard-Nielsen, T. (1986) : *The influence of waist thickness of dolosse on the hydraulic stability of dolos armour.* Proceeding of the 20th International Conference on Coastal Engineering, Taipei, Taiwan, 1986.

Burcharth, H.F., Howell, G.L., Liu, Z. (1991): *On the determination of concrete armour unit stresses including specific results related to Dolosse.* Coastal Engineering, Vol. 15, 1991.

Carver, R.D., Davidson, D.D. (1978) : *Dolos-armoured breakwaters: Special considerations.* Proceeding of the 16th International Conference on Coastal Engineering, Hamburg, FRG, July, 1978.

Font, J.B. (1968) : *Effect of storm duration on rubble mound breakwater stability.* Proceeding of the 11th International Conference on Coastal Engineering, London,UK, September, 1968.

Gravesen, H., Jensen, O.J., Sorensen, T. (1978) : *Stability of rubble mound breakwater.* Proceeding of the 16th International Conference on Coastal Engineering, Hamburg, FRG, July, 1978.

Holtzhausen, A.H., Zwamborn, J.A. (1990) : *Stability of Dolosse with different waist thickness for irregular waves.* Proceeding of the 22nd International Conference on Coastal Engineering, Delft, Holland, July 1990.

Price, W.A. (1979) : *Static stability of rubble mound breakwater.* Dock & Harbour Authority. Vol.LX (702), 1979

Van der Meer,J.W. (1988)) : *Stability of cubes, Tetrapods and Accropode.* Proceeding of Breakwaters '88, Eastbourne, UK

Zwamborn,J.A. (1978) : *Dolos packing density and effect of relative block density.* Proceeding of the 16th International Conference on Coastal Engineering, Hamburg, FRG, July, 1978.

Zwamborn, J.A., Bosman, D.E., Moes, J. (1980) : *Dolosse: past, present and future ?* Proceeding of the 17th International Conference on Coastal Engineering, Sydney, Australia, 1980.

Reliability Evaluation of a Structure at Sea

H.F. Burcharth

Professor of Marine Civil Engineering
University of Aalborg
Denmark

RELIABILITY EVALUATION OF A STRUCTURE AT SEA

HANS F. BURCHARTH

Department of Civil Engineering
Aalborg University, Denmark

Contents

1 Introduction

Conventional design practice for coastal structures is deterministic in nature and is based on the concept of a design load, which should not exceed the resistance (carrying capacity) of the structure. The design load is usually defined on a probabilistic basis as a characteristic value of the load, e.g. the expectation (mean) value of the 100-year return period event, however, often without consideration of the involved uncertainties. The resistance is in most cases defined in terms of the load which causes a certain design impact or damage to the structure and is not given as an ultimate force or deformation. This is because most of the available design formulae only give the relationship between wave characteristics and structural response, e.g. in terms of run-up, overtopping, armour layer damage etc. An example is the Hudson formula for armour layer stability. Almost all such design formulae are semi-empirical being based mainly on central fitting to model test results. The often considerable scatter in test results is not considered in general because the formulae normally express only the mean values. Consequently, the applied characteristic value of the resistance is then the mean value and not a lower fractile as is usually the case in other civil engineering fields. The only contribution to a safety margin in the design is then the one inherent in the choice of the return period for the design load.

It is now more common to choose the return period with due consideration of the encounter probability, i.e. the probability that the design load value is exceeded during the structure lifetime. This is an important step towards a consistent probabilistic approach.

A safety factor or a conventional partial coefficient (as given in some national standards) might be applied too, in which cases the methods are classified as Level I (deterministic/quasi probabilistic) methods. However, such approaches do not allow the determination of the reliability (or the failure probability) of the design, and consequently it is neither possible to optimize, nor to avoid over-design of a structure. In order to overcome this problem more advanced probabilistic methods must be applied where the uncertainties (the stochastic properties) of the involved loading and strength variables are considered. Methods where the actual distribution functions for the variables are taken into account are denoted Level III methods. Level II methods comprise a number of methods in which a transformation of the generally correlated and non-normally distributed variables into uncorrelated and standard normal distributed variables is performed and reliability indices are used as measures of the structural reliability. Both Level II and III methods are discussed in the following. Described is also an advanced partial coefficient system which takes into account the stochastic properties of the variables and makes it possible to design to a specific failure probability level.

2 Failure modes and failure functions

Evaluation of structural safety is always related to the structural response as defined by the failure modes. Neglect of an important failure mode will bias the estimation of the safety of the structure.

Fig. 1 illustrates the failure modes for a conventional rubble mound breakwater with a capping wall.

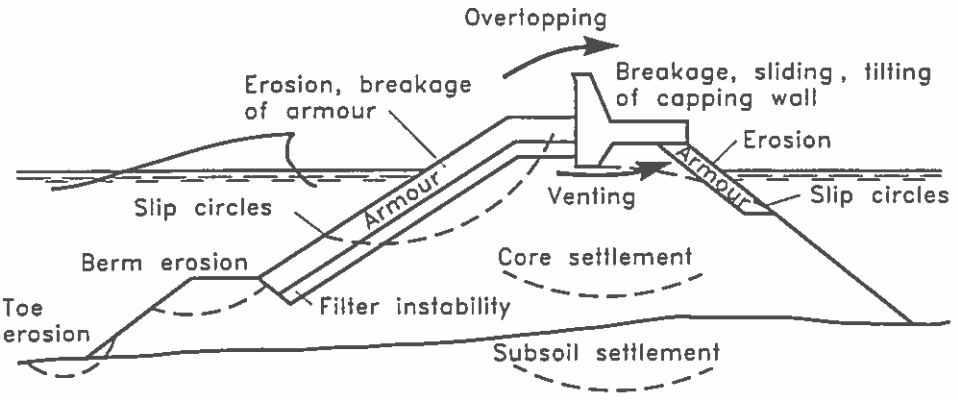

FIG. 1. Failure modes for a rubble mound breakwater.

Each failure mode must be described by a formula and the interaction (correlation) between the failure modes must be known. As an illustrative example let us consider only one failure mode, "hydraulic stability of the main armour layer", described by the Hudson formula

$$D_n^3 = \frac{H_s^3}{K_D \, \Delta^3 \, cot\alpha} \tag{1}$$

where D_n is the nominal block diameter, $\Delta = \frac{\rho_s}{\rho_w} - 1$, where $\frac{\rho_s}{\rho_w}$ is the ratio of the block and water densities, α is the slope angle, H_S is the significant wave height and K_D is the coefficient signifying the degree of damage (movements of the blocks).

The formula can be split into load variables X_i^{load} and resistance variables, X_i^{res}. Whether a parameter is a load or a resistance parameter can be seen from the failure function. If a larger value results in a safer structure it is a resistance parameter and if a larger value results in a less safe structure it is a load parameter.

According to this definition one specific parameter can in one formula act as a load parameter while in another it can act as a resistance parameter. An example is the wave steepness in the van der Meer formulae for rock, which is a load parameter in the case of surging waves but a resistance parameter in the case of plunging waves. The only load variable in eq. (1) is H_s while the others are resistance variables.

Eq. (1) is formulated as a *failure function* (performance function)

$$g = A \cdot \Delta \cdot D_n \, (K_D \, cot\alpha)^{1/3} - H_s \begin{cases} < 0 & \text{failure} \\ = 0 & \text{limit state (failure)} \\ > 0 & \text{no failure (safe region)} \end{cases} \tag{2}$$

All the involved parameters are regarded as stochastic variables, X_i, except K_D, which signifies the *failure,* i.e. a specific damage level chosen by the designer. The factor A in

eq. (2) is also a stochastic variable signifying the uncertainty of the formula. In this case the mean value of A is 1.0.

In general eq. (2) is formulated as

$$g = R - S \tag{3}$$

where R stands for resistance and S for loading. Usually R and S are functions of many random variables, i.e.

$$R = R(X_1^{res}\ ,\ X_2^{res}\ ,\ \ldots\ ,\ X_m^{res}) \quad \text{and} \quad S = S\left(X_{m+1}^{load}\ ,\ \ldots\ldots\ ,\ X_n^{load}\right) \quad \text{or} \quad g = g\left(\bar{X}\right)$$

The limit state is given by

$$g = 0 \tag{4}$$

which is denoted the *limit state equation* and defines the so-called *failure surface* which separates the safe region from the failure region.

In principle R is a variable representing the variations in resistance between nominally identical structures, whereas S represents the maximum load effects within a period of time, say successive T years. The distributions of R and S are both assumed independent of time. The *probability of failure* P_f during any reference period of duration T years is then given by

$$P_f = Prob\ [g \leq 0] \tag{5}$$

The *reliability* $\mathcal{R}$ is defined as

$$\mathcal{R} = 1 - P_f \tag{6}$$

3 Single failure mode probability analysis

3.1 Level III methods

A simple method – in principle – of estimation of P_f is the Monte Carlo method where a very large number of realisations x of the variables X are simulated. P_f is then approximated by the proportion of the simulations where $g \leq 0$.

The reliability of the method depends of course on a realistic assessment of the distribution functions for the variables X and their correlations.

Given f_X as the joint probability density function (jpdf) of the vector $\bar{X} = (X_1\ ,\ X_2\ ,\ \ldots\ ,\ X_n)$ then eq. (5) can be expressed by

$$P_f = \int_{R \leq S} f_X(\bar{x})\ d\bar{x} \tag{7}$$

Note that the symbol x is used for values of the random variable X.

If only two variables R and S are considered then eq. (7) reduces to

$$P_f = \int_{R \leq S} f_{(R,S)}(r,s) dr\, ds \tag{8}$$

which can be illustrated as shown in Fig. 2. If more than two variables are involved it is not possible to describe the jpdf as a surface but requires an imaginary multi-dimensional description.

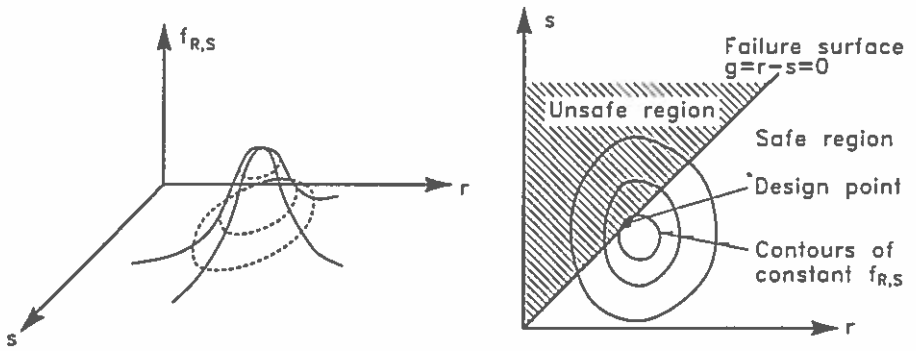

FIG. 2. Illustration of the two-dimensional joint probability density function for loading and strength.

Fig. 2 also shows the so-called *design point* which is the design point on failure surface where the joint probability density function attains the maximum value, i.e. the most probable point of failure.

Unfortunately, the jpdf is seldom known. However, the variables can often be assumed independent (non-correlated) in which case eq. (7) is given by the n-fold integral

$$P_f = \int \int_{R \leq S} \int \ldots \int f_{X_1}(x_1) \ldots f_{X_n}(x_n)\, d\,x_1 \ldots d\,x_n \tag{9}$$

where f_{X_i} are the marginal probability density function of the variables X_i. The amount of calculations involved in the multi-dimensional integration eq. (9) is enormous if the number of variables, n, is larger than say 5.

If only two variables are considered, say R and S, then eq. (9) simplifies to

$$P_f = \int \int_{R \leq S} f_R(r)\, f_S(s)\, dr\, ds \tag{10}$$

which by partial integration can be reduced to a single integral

$$P_f = \int_0^\infty F_R(x)\, f_S(x)\, dx \tag{11}$$

where F_R is the cumulative distribution function for R. Formally the lower integration limit should be $-\infty$ but is replaced by 0 since, in general, negative strength is not meaningful.

Eq. (11) can be explained as the product of the probabilities of two independent events, namely the probability that S lies in the range x, $x+dx$ (i.e. $f_S(x)dx$) and the probability that $R \leq x$ (i.e. $F_R(x)$), cf. Fig. 3.

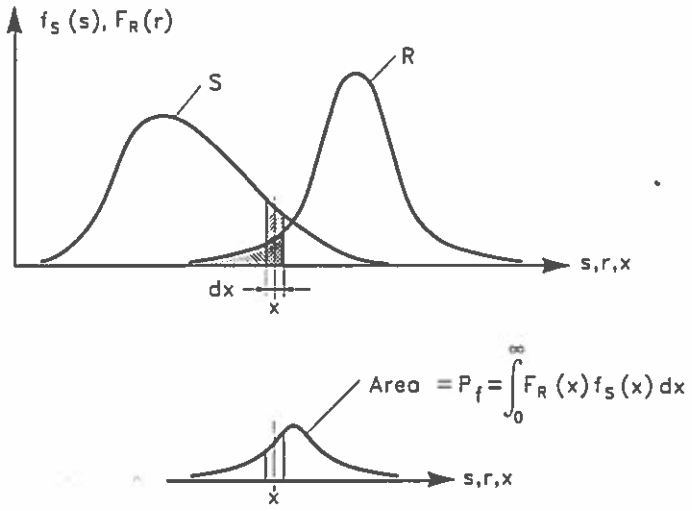

FIG. 3. Illustration of failure probability in case of two independent variables, S and R.

3.2 Level II methods

3.2.1 Linear failure functions of normal-distributed random variables

In the following is given a short introduction to calculations at level II. For a more detailed description see Hallam et al. (1977) and Thoft-Christensen and Baker (1982). Only the so-called *first-order reliability method* (FORM) where the failure surface is approximated by a tangent hyperplane at some point will be discussed. A more accurate method is the *second-order reliability method* (SORM) which uses a quadratic approximation to the failure surface.

Assume the loading $S(x)$ and the resistance $R(x)$ for a single failure mode to be statistically independent and with density functions as illustrated in Fig. 3. The failure function is given by eq. (3) and the probability of failure by eq. (10) or eq. (11).

However, these functions are in many cases not known but might be estimated only by their mean values and standard deviations. If we assume S and R to be independent normally distributed variables with known means and standard deviations, then the linear failure function $g = R - S$ is normally distributed with mean value,

$$\mu_g = \mu_R - \mu_S \tag{12}$$

and

$$\text{standard deviation, } \sigma_g = \left(\sigma_R^2 + \sigma_S^2\right)^{0.5} \tag{13}$$

The quantity $(g - \mu_g)/\sigma_g$ will be unit standard normal and consequently

$$P_f = prob[g \leq 0] = \int_{-\infty}^{0} f_g(x)\, dx = \Phi\left(\frac{0 - \mu_g}{\sigma_g}\right) = \Phi(-\beta) \tag{14}$$

where

$$\beta = \frac{\mu_g}{\sigma_g} \tag{15}$$

is a measure of the probability of failure and is denoted the *reliability index* (Cornell 1969), cf. Fig. 4 for illustration of β. Note that β is the inverse of the coefficient of variation and is the distance in terms of number of standard deviations from the most probable value of g (in this case the mean) to the failure surface, $g = 0$.

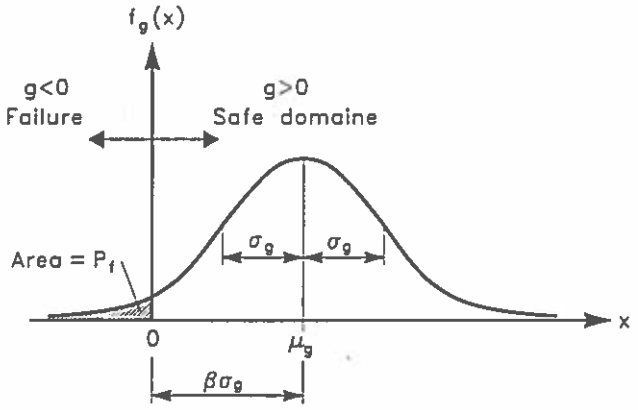

FIG. 4. Illustration of the reliability index.

Some corresponding values of β and P_f are given in Table 1.

Table 1. Corresponding values of β and P_f.

β	$P_f = \Phi(-\beta)$
0.0	0.50
0.5	0.31
1.0	0.16
1.5	0.067
2.0	0.023
3.0	0.0013
4.0	$0.32 \cdot 10^{-4}$
5.0	$0.29 \cdot 10^{-6}$

If R and S are normally distributed and "correlated" then eq. (14) still holds but σ_g is given by

$$\sigma_g = \left(\sigma_R^2 + \sigma_S^2 + 2\rho_{RS}\,\sigma_R\,\sigma_S\right)^{0.5} \tag{16}$$

where ρ_{RS} is the *correlation coefficient*

$$\rho_{RS} = \frac{C_{ov}[R,\ S]}{\sigma_R\,\sigma_S} = \frac{E\left[(R-\mu_R)\,(S-\mu_S)\right]}{\sigma_R\,\sigma_S} \tag{17}$$

R and S are said to be *uncorrelated* if $\rho_{RS} = 0$.

In general, if the failure function $g = g\left(\tilde{X}\right)$ is a *linear* function of the normally distributed basic variables $X_1,\ X_2,\ \ldots\ X_n$, i.e.

$$g = a_o + a_1 X_1 + a_2 X_2 + \ldots + a_n X_n \tag{18}$$

then $\beta = \dfrac{\mu_g}{\sigma_g}$ and P_f can be found from eq. (14) using

$$\mu_g = a_o + a_1\mu_1 + a_2\mu_2 + \ldots + a_n\mu_n \tag{19}$$

and

$$\sigma_g^2 = a_1^2\sigma_1^2 + \ldots + a_n^2\sigma_n^2 + \sum_{i=1}^{n}\sum_{\substack{j=1\\ j\neq i}}^{n}\rho_{ij}a_i a_j \sigma_i \sigma_j \tag{20}$$

where ρ_{ij} expresses the correlation coefficient between any pair of variables, cf. eq. (17).

Besides the illustration of β in Fig. 4 a simple geometrical interpretation of β can be given in case of a linear failure function $g = R - S$ of the independent variables R and S by a transformation into a *normalized coordinate system* of the random variables $R' = (R - \mu_R)/\sigma_R$ and $S' = (S - \mu_S)/\sigma_S$, cf. Fig. 5.

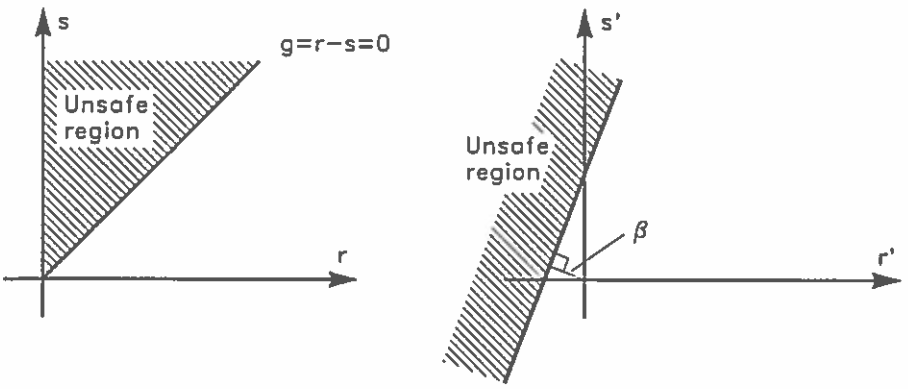

FIG. 5. Illustration of β in normalized coordinate system.

With these variables the failure surface $g = 0$ is linear and given by

$$R'\sigma_R - S'\sigma_S + \mu_R - \mu_S = 0 \tag{21}$$

By geometrical considerations it can be shown that the shortest distance from the origin to this linear failure surface is equal to

$$\beta = \frac{\mu_g}{\sigma_g} = \frac{\mu_R - \mu_S}{(\sigma_R^2 + \sigma_S^2)^{0.5}}$$

in which eqs. (12) and (13) are used.

3.2.2 Non-linear failure functions of normal-distributed random variables

If the failure function $g = g\left(\bar{X}\right)$ is *non-linear* then approximate values for μ_g and σ_g can be obtained by using a *linearized failure function.*

Linearization is generally performed by Taylor-series expansion about some point retaining only the linear terms. If the expansion is performed around the mean values $(X_1, \ \ldots \ , X_n) = \mu_1, \ \ldots \ , \mu_n$ then

$$g \simeq g\left(\mu_1, \ \ldots \ , \mu_n\right) + \sum_{i=1}^{n} \frac{\partial g}{\partial X_i}\left(X_i - \mu_i\right) \ , \tag{22}$$

where $\partial g / \partial X_i$ is evaluated at $(\mu_1, \ \ldots \ , \mu_n)$. The approximate values of μ_g and σ_g are then

$$\mu_g \simeq g\left(\mu_1, \ \ldots \ , \mu_n\right) \tag{23}$$

$$\sigma_g^2 \simeq \sum_{i=1}^{n} \sum_{j=1}^{n} \frac{\partial g}{\partial X_i} \frac{\partial g}{\partial X_j} Cov\left[X_i, \ X_j\right] \tag{24}$$

If the random variables $\bar{X}$ are "uncorrelated", i.e. $\rho_{X_i X_j} = 0$, then e.g. (24) reduces to

$$\sigma_g^2 \simeq \sum_{i=1}^{n} \left(\frac{\partial g}{\partial X_i} \sigma_{X_i} \right)^2 \tag{25}$$

because $Cov\left[X_i, \ X_i\right] = \sigma_{X_i}^2$ and $Cov\left[X_i, \ X_j\right] = 0$ for all i and j, $i \neq j$.

When linearization is performed around the expected mean values the method is often called a *first-order mean value approach* (FMA).

The values of μ_g and σ_g, and thereby also the value of β, depend on the choice of linearization point. Moreover, the value of β defined by eq. (15) will change when different but equivalent non-linear failure functions are used. For example an equivalent failure function to eq. (2) would be

$$g = A^3 \, \Delta^3 \, D_n^3 \, K_D \, cot\alpha - H_s^3 \tag{26}$$

which expresses the Hudson formula as does eq. (2), but will result in different β-values.

In order to overcome these problems a transformation of the basic variables $\bar{X} = (X_1, X_2, \ldots, X_n)$ into a new set of normalized variables $\bar{Z} = (Z_1, Z_2, \ldots, Z_n)$ is performed. For *uncorrelated* normal distributed basic variables $\bar{X}$ the transformation is

$$Z_i = \frac{X_i - \mu_{X_i}}{\sigma_{X_i}} \tag{27}$$

in which case $\mu_{Z_i} = 0$ and $\sigma_{Z_i} = 1$. By this linear transformation the *failure surface* $g = 0$ in the x-coordinate system is mapped into a failure surface in the z-coordinate system which also divides the space into a safe region and a failure region, cf. Fig. 6.

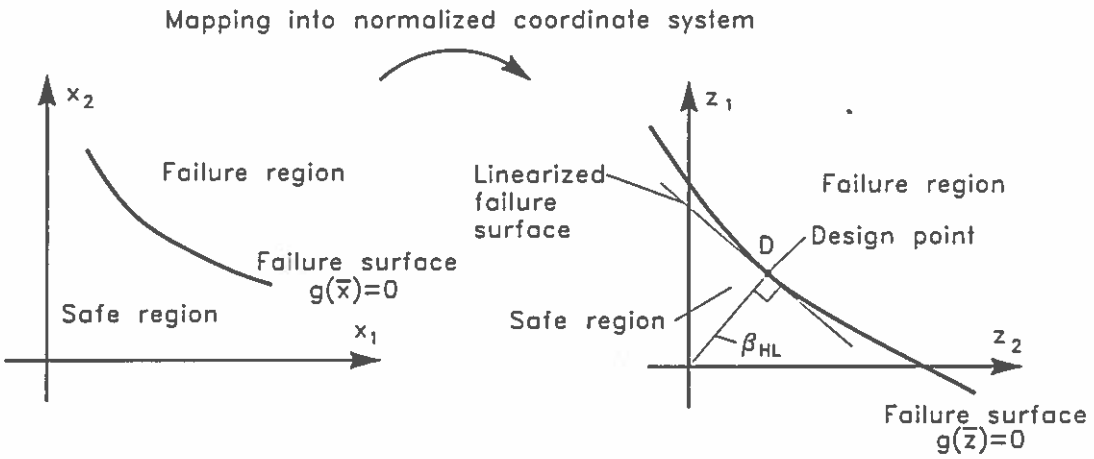

FIG. 6. Definition of the Hasofer and Lind reliability index, β_{HL}.

Fig. 6 introduces the Hasofer and Lind reliability index β_{HL} which is defined as the distance from origo to the nearest point, D, of the *failure surface* in the z-coordinate system. This point is called the *design point*. The coordinates of the design point in the original x-coordinate system are the most probable values of the variables $\bar{X}$ at failure. β_{HL} can be formulated as

$$\beta_{HL} = \min_{g(\bar{z})=0} \left(\sum_{i=1}^{n} z_i^2 \right)^{0.5} \tag{28}$$

The special feature of β_{HL} as opposed to β is that β_{HL} is related to the failure "surface" $g(\bar{z}) = 0$ which is invariant to the failure function because equivalent failure functions result in the same failure surface.

The two reliability indices β and β_{HL} will coincide when the failure surfaces are linear, cf. Figs. 5 and 6. Obviously, this will also be the case if non-linear failure functions are linearized by Taylor Series expansion around the design point.

Linearization around the design point instead of mean values is therefore very much to be preferred, also because the design point is the most probable point of failure, cf. Fig.

2. Linearization around mean values can lead to quite erroneous results but due to the simplicity of the method it might be used to get a first order-of-magnitude impression of the failure probability.

The method where linearization is performed around the design point is often called a *first-order design point approach* (FDA).

The calculation of β_{HL} and the design point coordinates can be undertaken in a number of different ways. An iterative method must be used when the failure surface is non-linear. In the following a simple method is introduced.

Let θ denote the distance from the origin to any point at the failure surface given in the normalized coordinate system

$$\begin{cases} \theta = \left[\sum_{i=1}^{n} z_i^2\right]^{\frac{1}{2}} \\ g(z_1, z_2, \ \dots \ , z_n) = 0 \end{cases} \tag{29}$$

Construct the multiple function (Lagrange function)

$$\begin{aligned} F &= \theta + K_1 g \\ &= \left[z_1^2 + z_2^2 + \ \dots \ + z_n^2\right]^{\frac{1}{2}} + K_1 g(z_1, z_2, \ \dots \ , z_n) \end{aligned} \tag{30}$$

where K_1 is an unknown constant (multiplier).

Maximum or minimum of θ occurs when

$$\begin{cases} \dfrac{\partial F}{\partial z_i} = [z_1^2 + z_2^2 + \ \dots \ + z_n^2]^{-\frac{1}{2}} \cdot z_i + K_1 \dfrac{\partial g}{\partial z_i} = 0 \quad i = 1, 2, \ \dots \ , n \\ g(z_1, z_2, \ \dots \ , z_n) = 0 \end{cases} \tag{31}$$

Assume that only one minimum exists and the coordinates of the design point D are given by

$$\left(z_1^d, z_2^d, \ \dots \ , z_n^d\right) = (\beta_{HL}\alpha_1, \ \beta_{HL}\alpha_2, \ \dots \ , \beta_{HL}\alpha_n) \tag{32}$$

Then

$$\theta_{min} = \beta_{HL} = \left[\sum_{i=1}^{n} (\beta_{HL}\alpha_i)^2\right]^{\frac{1}{2}} \quad \text{and consequently}$$

$$\sum_{i=1}^{n} \alpha_i^2 = 1 \tag{33}$$

Eq. (31) becomes

$$\begin{cases} \beta_{HL}^{-\frac{1}{2}} \cdot (\beta_{HL}\alpha_i) + K_1 \dfrac{\partial g}{\partial z_i} = 0 \quad i = 1, 2, \ \dots \ , n \\ g(\beta_{HL}\alpha_1, \beta_{HL}\alpha_2, \ \dots \ , \beta_{HL}\alpha_n) = 0 \end{cases} \tag{34}$$

or

$$\begin{cases} \alpha_i = \dfrac{-\frac{\partial g}{\partial z_i}}{\frac{\beta_{HL}^{-1}}{K_1}} = \dfrac{-\frac{\partial g}{\partial z_i}}{K} \\ g\left(\beta_{HL}\alpha_1,\ \beta_{HL}\alpha_2,\ \ldots\ ,\beta_{HL}\alpha_n\right) = 0 \end{cases} \tag{35}$$

Inserting eq. (35) into eq. (33) gives

$$K = \left[\sum_{i=1}^{n}\left(\frac{\partial g}{\partial z_i}\right)^2\right]^{\frac{1}{2}} \tag{36}$$

The α-values defined by (32) are often called *sensitivity factors* (or influence factors) because α_i^2 provides an indication of the relative importance on the reliability index β_{HL} of the random variable X_i. If α_i^2 is small it might be considered to model X_i as a deterministic quantity equal to the median value of X_i. In such case the relative change in the reliability index by assuming X_i deterministic can be approximated by

$$\frac{\beta_{HL}\left(X_i\ :\ \text{deterministic}\right)}{\beta_{HL}\left(X_i\ :\ \text{random}\right)} \simeq \frac{1}{\sqrt{1-\alpha_i^2}} \tag{37}$$

The corresponding change in failure probability can be found from eq. (14) or from Table 1. Eq. (37) is used for the evaluation of a simplification of a failure function by reducing the number of random variables.

The sensitivity of β_{HL} to change in the value of a deterministic parameter b_i can be expressed by

$$\frac{d\beta_{HL}}{d\,b_i} = \frac{1}{K}\frac{\partial g}{\partial b_i} \tag{38}$$

where K is given by eq. (36) and the partial derivative of g with respect to b_i is taken in the design point.

Eq. (38) is useful when it is considered to change a deterministic parameter (e.g. the height of wave wall) into a stochastic variable.

EXAMPLE 1

Consider the hydraulic stability of a rock armour layer given by the Hudson equation formulated as the failure function, cf. eqs. (1) and (2)

$$g = A\,\Delta\,D_n\,\left(K_D\,cot\alpha\right)^{\frac{1}{3}} - H_s \tag{39}$$

all the parameters are regarded uncorrelated random variables X_i, except K_D which signifies the *failure criterion*, i.e. a certain damage level here chosen as 5% displacement corresponding to $K_D \simeq 4$. The factor A is also a random variable signifying the uncertainty of the formula.

All random variables are assumed normal distributed with known mean values and standard deviations, cf. Table 2. The normal distribution can be a bad approximation for H_s which is usually much better approximated by an extreme distribution, e.g. a Weibull or Gumbel distribution as will be discussed later. The normal distribution of H_S is used here due to the simplicity involved but might be reasonable in case of depth limited wave conditions.

Table 2. Basic variables.

i	X_i	μ_{X_i}	σ_{X_i}	coefficient of variation σ_{X_i}/μ_{X_i}
1	A	1	0.18	18%
2	D_n	1.5 m	0.10 m	6.7%
3	H_s	4.4 m	0.70 m	16%
4	Δ	1.6	0.06	3.8%
5	$cot\alpha$	2	0.10	5.0%

The failure surface corresponding to the failure function (39) reads for $K_D = 4$

$$A\,\Delta\,D_n\,(cot\alpha)^{\frac{1}{3}}\,1.59 - H_s = 0$$

or

$$X_1\,X_4\,X_2\,X_5^{\frac{1}{3}}\,1.59 - X_3 = 0 \tag{40}$$

By use of the transformation eq. (27) the failure surface in the normalized coordinate system is given by

$$(1 + 0.18\ z_1)\ (1.6 + 0.06\ z_4)\ (1.5 + 0.10\ z_2)\,(2 + 0.10\ z_5)^{\frac{1}{3}}\ 1.59 - (4.4 + 0.70\ z_3) = 0$$

In order to make the calculations in this illustrative example more simple we neglect the small variational coefficients of Δ and $cot\alpha$ and obtain

$$(1 + 0.18\ z_1) \cdot 1.6 \cdot (1.5 + 0.10\ z_2) \cdot 2^{\frac{1}{3}} \cdot 1.59 - (4.4 + 0.70\ z_3) = 0 \tag{41}$$

or

$$0.864\ z_1 + 0.32\ z_2 + 0.058\ z_1 z_2 - 0.70\ z_3 + 0.40 = 0 \tag{42}$$

$$0.864\ \beta_{HL}\alpha_1 + 0.32\ \beta_{HL}\alpha_2 + 0.058\ \beta_{HL}^2\alpha_1\alpha_2 - 0.70\ \beta_{HL}\alpha_3 + 0.40 = 0$$

$$\beta_{HL} = \frac{-0.40}{0.864\,\alpha_1 + 0.32\,\alpha_2 + 0.058\,\alpha_1\alpha_2\beta_{HL} - 0.70\,\alpha_3}$$

By use of eq. (35)

$$\alpha_1 = -\frac{1}{K}(0.864 + 0.058\,\beta_{HL}\alpha_2)$$

$$\alpha_2 = -\frac{1}{K}(0.32 + 0.058\,\beta_{HL}\alpha_1)$$

$$\alpha_3 = \frac{0.7}{K}$$

By eq. (36)

$$K = \sqrt{(0.864 + 0.058\,\beta_{HL}\alpha_2)^2 + (0.32 + 0.058\,\beta_{HL}\alpha_1)^2 + (0.7)^2}$$

The iteration is now performed by choosing starting values for β_{HL}, α_1, α_2 and α_3 and calculating new values until small modifications are obtained. This is shown in Table 3. The convergence is faster if a positive sign is used for α-values related to loading variables and a negative sign is used for α-values related to resistance variables.

Table 3.

	Iteration No.			
	start	1	2	3
β_{HL}	3.0	0.438	0.342	0.341
K		1.144	1.149	1.149
α_1	−0.50	−0.744	−0.747	−0.747
α_2	−0.50	−0.263	−0.266	−0.266
α_3	0.50	0.612	0.609	0.609

The probability of failure is then

$$P_f = \Phi(-\beta_{HL}) = \Phi(-0.341) = 0.367$$

cf. Table 1 for some corresponding values of β and P_f.

The design point coordinates in the normalized z coordinate system are

$$\left(z_1^d,\ z_2^d,\ z_3^d\right) = (\beta_{HL}\alpha_1,\ \beta_{HL}\alpha_2,\ \beta_{HL}\alpha_3)$$

$$= (-0.255,\ -0.091,\ 0.208)$$

Expression (33) $\beta_{HL} = \left(\sum_{i=1}^{3}\left(z_i^d\right)^2\right)^{\frac{1}{2}}$ provides a check on the design point coordinates.

Using the transformation

$$X_i^d = \mu_{X_i} + \sigma_{X_i} z_i^d$$

and the values of μ_{X_i}, σ_{X_i} given in Table 2 the design point coordinates in the original x coordinate system are found to be

$$\left(x_1^d,\ x_2^d,\ x_3^d\right) = (0.954,\ 1.491,\ 4.546)$$

The relative importance of the random variables to the failure probability is evaluated through the α^2-values. Table 4 shows that the uncertainty related to D_n is of minor importance compared to the uncertainties on A and H_s.

Table 4.

i	X_i	α_i	α_i^2 (%)	$\frac{\beta_{HL}(X_i : \text{deterministic})}{\beta_{HL}(X_i : \text{random})} \simeq \frac{1}{\sqrt{1-\alpha_i^2}}$	$\frac{P_f(X_i : \text{deterministic})}{P_f(X_i : \text{random})}$
1	A	−0.747	55.8	1.50 *)	0.831 *)
2	D_n	−0.266	7.1	1.04	0.989
3	H_s	0.609	37.1	1.26 *)	0.899 *)
			100.0		

*) The assumption of validity only for small α-values is not fulfilled

If all 5 parameters in the Hudson formula was kept as random variables with mean values and standard deviations as given in Table 2 then the corresponding values would be as shown in Table 5.

Table 5.

i	X_i	α_i	α_i^2 (%)	$\frac{\beta_{HL}(X_i : \text{deterministic})}{\beta_{HL}(X_i : \text{random})} \simeq \frac{1}{\sqrt{1-\alpha_i^2}}$	$\frac{P_f(X_i : \text{deterministic})}{P_f(X_i : \text{random})}$
1	A	−0.705	49.7	1.41 *)	0.857 *)
2	D_n	−0.275	7.6	1.04	0.986
3	H_s	0.631	39.8	1.29 *)	0.896 *)
4	Δ	−0.154	2.3	1.01	0.999
5	$cot\alpha$	−0.068	0.5	1.00	1.000
			100.0		

*) The assumption of validity only for small α-values is not fulfilled

It is clearly seen why Δ and $cot\alpha$ can be regarded as constants.

If the normally distributed basic variables $\bar{X}$ are *correlated* the procedure given above can be used if a transformation into non-correlated variables $\bar{Y}$ is performed before normalizing the variables.

The correlation between any pair of the random variables $\bar{X}$ is expressed by the covariance matrix

$$\bar{\bar{C}}_{\bar{X}} = \begin{bmatrix} Var[X_1] & Cov[X_1, X_2] & \cdots & Cov[X_1, X_n] \\ Cov[X_2, X_1] & Var[X_2] & & \vdots \\ \vdots & & \ddots & \vdots \\ Cov[X_n, X_1] & & & Var[X_n] \end{bmatrix} \tag{43}$$

If $\bar{\bar{C}}_{\bar{Y}}$ is a diagonal matrix

$$\bar{\bar{C}}_{\bar{Y}} = \begin{bmatrix} Var[Y_1] & \cdots & \cdots & 0 \\ \vdots & Var[Y_2] & & \vdots \\ \vdots & & \ddots & \\ 0 & & & Var[Y_n] \end{bmatrix} = \begin{bmatrix} \sigma^2_{Y_1} & & & 0 \\ \vdots & \sigma^2_{Y_2} & & \vdots \\ \vdots & & \ddots & \\ 0 & & & \sigma^2_{Y_n} \end{bmatrix} \tag{44}$$

then no correlation between any pair og random variables $\bar{Y}$ exists.

A set of uncorrelated variabels $\bar{Y}$ can be obtained by the transformation

$$\bar{Y} = \bar{\bar{A}}^T \bar{X} \tag{45}$$

where $\bar{\bar{A}}$ is an orthogonal matrix with column vectors equal to the orthonormal eigenvalues of $\bar{\bar{C}}_{\bar{X}}$.

The diagonal elements of $\bar{\bar{C}}_{\bar{Y}}$, i.e. $\sigma^2_{Y_1} \cdots \sigma^2_{Y_n}$, are equal to the eigenvalues of $\bar{\bar{C}}_{\bar{X}}$.

After determination of $\bar{Y}$ and $\sigma_{\bar{Y}}$ the following transformation, analog to (27), into uncorrelated and normalized variables $\bar{z}$ is performed

$$z_i = \frac{Y_i - \mu_{Y_i}}{\sigma_{Y_i}} \tag{46}$$

The reliability index β_{HL}, defined in the z-coordinate system as given in Fig. 6 and eq. (28), can be determined by the described iterative procedure of eqs. (35) and (36).

3.2.3 Non-linear failure functions containing non-normal distributed random variables

It is not always a reasonable assumption to consider the random variables normally distributed. This is for example the case for parameters such as H_s characterizing the sea state in long-term wave statistics. H_s will in general follow extreme distributions (e.g. Gumbel and Weibull) quite different from the normal distribution, and cannot be described only by the mean value and the standard deviation.

For such cases it is still possible to use the reliability index β_{HL} but an extra transformation of the non-normal basic variables into normal basic variables must be performed before β_{HL} can be determined as described above.

A commonly used transformation is based on the substitution of the non-normal distribution of the basic variable X_i by a normal distribution in such a way that the density and distribution functions f_{X_i} and F_{X_i} are unchanged at the design point.

If the design point is given by $x_1^d,\ x_2^d,\ \ldots\ ,x_n^d$ then the transformation reads

$$\begin{aligned} F_{X_i}\left(x_i^d\right) &= \Phi\left(\frac{x_i^d - \mu'_{X_i}}{\sigma'_{X_i}}\right) \\ f_{X_i}\left(x_i^d\right) &= \frac{1}{\sigma'_{X_i}}\varphi\left(\frac{x_i^d - \mu'_{X_i}}{\sigma'_{X_i}}\right) \end{aligned} \tag{47}$$

where μ'_{X_i} and σ'_{X_i} are the mean and standard deviation of the approximate (fitted) normal distribution.

From eq. (47) is obtained

$$\begin{aligned} \sigma'_{X_i} &= \frac{\varphi\left(\Phi^{-1}\left(F_{X_i}\left(x_i^d\right)\right)\right)}{f_{X_i}\left(x_i^d\right)} \\ \mu'_{X_i} &= x_i^d - \Phi^{-1}\left(F_{X_i}\left(x_i^d\right)\right)\sigma'_{X_i} \end{aligned} \tag{48}$$

Eq. (47) can also be written

$$F_{X_i}\left(x_i^d\right) = \Phi\left(\frac{x_i^d - \mu'_{X_i}}{\sigma'_{X_i}}\right) = \Phi\left(z_i^d\right) = \Phi\left(\beta_{HL}\alpha_i\right)$$

Solving with respect to x_i^d gives

$$x_i^d = F_{X_i}^{-1}\left[\Phi\left(\beta_{HL}\alpha_i\right)\right] \tag{49}$$

The iterative method presented above for calculation of β_{HL} can still be used if for each step of iteration the values of σ'_{X_i} and μ'_{X_i} given by eq. (48) are calculated for those variables where the transformation (47) has been used.

For correlated random variables the transformation given by eq. (45) is used before normalization.

EXAMPLE 2

The same failure function and non-correlated normal-distributed variable as in Example 1 are considered except that H_s now follows a Gumbel distribution but with the same average and standard deviation as given in Table 2.

The Gumbel distribution function and density function are

$$\begin{aligned} F_G(x_3) &= e^{-e^{-A(x_3-B)}} \\ f_G(x_3) &= \frac{dF_G(x_3)}{dx_3} = A\,e^{\left[-e^{-A(x_3-B)}-A(x_3-B)\right]} \end{aligned} \tag{50}$$

The distribution parameters A and B can be determined by the following expressions for the mean and the standard deviation

$$\begin{aligned} \mu_{x_3} &= B + \frac{0.57722}{A} \\ \sigma_{x_3} &= \frac{\pi}{\sqrt{6}}\frac{1}{A} \end{aligned} \tag{51}$$

Using the Table 2 values $\mu_{x_3} = 4.4$ m amd $\sigma_{x_3} = 0.7$ m gives $A = 1.83\ m^{-1}$ and $B = 4.08$ m.

In the normalized coordinate system the failure surface is then (compared with eq. (41))

$$(1 + 0.18z_1) \cdot 1.6 \cdot (1.5 + 0.1z_2) \cdot 2^{\frac{1}{3}} \cdot 1.59 - \left(\mu'_{x_3} + \sigma'_{x_3} z_3\right) = 0$$

$$0.864z_1 + 0.32z_2 + 0.058z_1z_2 - \sigma'_{x_3} z_3 + \left(4.8 - \mu'_{x_3}\right) = 0$$

$$\beta_{HL} = \frac{-\left(4.8 - \mu'_{x_3}\right)}{0.864\alpha_1 + 0.32\alpha_2 + 0.058\alpha_1\alpha_2\beta_{HL} - \sigma'_{x_3}\alpha_3}$$

By eq. (35)

$$\begin{aligned} \alpha_1 &= -\frac{1}{K}\left(0.864 + 0.058\beta_{HL}\alpha_2\right) \\ \alpha_2 &= -\frac{1}{K}\left(0.32 + 0.058\beta_{HL}\alpha_1\right) \\ \alpha_3 &= \frac{\sigma'_{x_3}}{K} \end{aligned}$$

By eq. (36)

$$K = \sqrt{\left(0.864 + 0.058\beta_{HL}\alpha_2\right)^2 + \left(0.32 + 0.058\beta_{HL}\alpha_1\right)^2 + \left(\sigma'_{x_3}\right)^2}$$

By eq. (49)

$$x_3^d = F_G^{-1}\left[\Phi\left(\beta_{HL}\alpha_3\right)\right]$$

By eq. (48)

$$\begin{aligned} \sigma'_{x_3} &= \frac{\varphi\left(\Phi^{-1}\left(F_G\left(x_3^d\right)\right)\right)}{f_G\left(x_3^d\right)} \\ \mu'_{x_3} &= x_3^d - \Phi^{-1}\left(F_G\left(x_3^d\right)\right) \cdot \sigma'_{x_3} \end{aligned}$$

The results from each step of iteration are shown in Table 6.

Table 6.

	Iteration No.							
	start	1	2	3	4	5	6	7
β_{HL}	3.0	1.717	0.553	0.569	0.463	0.461	0.457	0.457
K		1.295	1.363	1.165	1.155	1.144	1.143	1.143
α_1	−0.5	−0.629	−0.629	−0.735	−0.742	−0.749	−0.749	−0.750
α_2	−0.5	−0.199	−0.220	−0.254	−0.260	−0.262	−0.262	−0.263
α_3	0.5	0.772	0.754	0.627	0.619	0.609	0.608	0.607
x_3^d		5.359	4.568	4.525	4.475	4.471	4.469	4.469
σ'_{x_3}	1.0	1.027	0.731	0.715	0.697	0.695	0.694	0.694
μ'_{x_3}	3.0	4.033	4.139	4.264	4.270	4.275	4.276	4.276

The probability of failure is then

$$P_f = \Phi(-\beta_{HL}) = \Phi(-0.457) = 0.324$$

The coordinates of the design point D in the normalized z-coordinate system are

$$\begin{aligned}\left(z_1^d\ ,\ z_2^d\ ,\ z_3^d\right) &= (\beta_{HL}\alpha_1\ ,\ \beta_{HL}\alpha_2\ ,\ \beta_{HL}\alpha_3)\\ &= (-0.342\ ,\ -0.12\ ,\ 0.277)\end{aligned}$$

Note that $\beta_{HL} = \left(\sum_{i=1}^{3}\left(z_i^d\right)^2\right)^{\frac{1}{2}}$.

The coordinates of the design point D in the original x-coordinate system are calculated by the transformation

$$x_i^d = \mu_{x_i} + \sigma_{x_i} z_i^d \qquad i = 1,\ 2 \qquad \text{(cf. Table 2 for } \mu_{x_i} \text{ and } \sigma_{x_i}\text{)}$$

$$x_3^d = \mu'_{x_3} + \sigma'_{x_3} z_3^d \qquad \text{(cf. Table 6 for } \mu'_{x_3} \text{ and } \sigma'_{x_3}\text{)}$$

to be

$$\left(x_1^d\ ,\ x_2^d\ ,\ x_3^d\right) = (0.934\ ,\ 1.474\ ,\ 4.468)$$

The reliability index is now $\beta_{HL} = 0.457$ which is larger than $\beta_{HL} = 0.341$ from Example 1. However, the failure probability does not change so much (from 36.7% in Example 1 to 32.4% in this example).

A more widely used method of calculating β_{HL} is

1. Select some trial coordinates of the design point in the z-coordinate system

$$\bar{z}^d = \left(z_1^d\ , z_2^d\ ,\ \ldots\ ,\ z_n^d\right)$$

2. Calculate $\alpha_i \qquad i = 1,\ 2,\ \ldots\ ,\ n$ by

$$\alpha_i = \frac{\partial g}{\partial z_i}|_{z=z^d}$$

3. Determine a better estimate of $\bar{z}^d$ by

$$z_i^d = \alpha_i \frac{\sum_{i=1}^{n} \left(\alpha_i\, z_i^d\right) - g|_{z=z^d}}{\sum_{i=1}^{n} (\alpha_i)^2}$$

4. Repeat 2) and 3) to achieve convergence

5. Evaluate β_{HL} by

$$\beta_{HL} = \left[\sum_{i=1}^{n} \left(z_i^d\right)^2\right]^{\frac{1}{2}}$$

The method is based on the assumption of the existence of only one minimum. However, several "local" minima might exist. In order to avoid convergence against such local minima (and thereby overestimation of β_{HL} and the reliability) several different sets of trial coordinates might be tried.

3.2.4 Time-variant random variables

The failure functions within breakwater engineering are generally of the form

$$g = f_1(\bar{r}) - f_2(H_s\ ,\ W\ ,\ T_m) \tag{52}$$

where $\bar{R}$ represents the resistance variables and H_s, W and T_m are the load variables signifying the wave height, the water level and the wave period. The random variables are in general time-variant.

Discussion of Load Variables:

The most important load parameter in breakwater engineering is the *wave height*. It is a time-varying quantity which is best modelled as a stochastic process. Distinction is made between *short-tem* and *long-term* statistics of the wave heights. The first one deals with the distribution of the wave height H during a stationary sequence of a storm, i.e. during a period of constant H_s (or any other characteristic wave height). The short term wave height distribution follows the Rayleigh distribution in case of deep-water waves and some truncated distribution in case of shallow water waves.

The long term statistics deals with the distribution of the storms which are then characterized by the max value of H_s occurring in each storm. The storm history is given

as the sample (H_{s1}, H_{s2}, ... , H_{sn}) covering a period of observation Y. Extreme value distributions like the Gumbel and Weibull distributions are then fitted to the sample. For strongly depth limited wave conditions a normal distribution with mean value as a function of water depth might be considered.

The distribution of H_s can be substituted by the distribution of the maximum value within T years, i.e. the distribution of H_s^T. The calculated failure probability then refers to the period T (which in practice might be the lifetime of the structure) if distribution functions of the other variables in (52) are assumed unchanged during the period T.

As an example consider a sample of n independent storms, i.e. H_{s1}, H_{s2}, ... , H_{sn}, obtained within Y years of observation. Assume that H_s follows a Gumbel distribution

$$F(H_s) = exp\left[-exp\left(-\alpha\left(H_s - \beta\right)\right)\right] \tag{53}$$

i.e. the distribution of H_s within a period of average length between the observations Y/n.

The distribution parameters α and β can be estimated e.g. by the maximum likelihood method or the methods of moments. Moreover, the standard deviations of α and β signifying the statistical uncertainty due to limited sample size can be estimated too.

The sampling intensity is $\lambda = n/Y$. Within a T-years reference period the number of data will be λT. The probability of the maximum value of H_s within the period T is then

$$F\left(H_s^T\right) = \left(F\left(H_s\right)\right)^{\lambda T} = \left[exp\left[-exp\left(-\alpha\left(H_s - \beta\right)\right)\right]\right]^{\lambda T} \tag{54}$$

The expectation (mean) value of H_s^T is given by

$$\mu_{H_s^T} = \beta - \frac{1}{\alpha} ln\left[-ln\left(1 - \frac{1}{\lambda T}\right)\right] \tag{55}$$

and the standard deviation of H_s^T – in case of maximum likelihood estimates – is

$$\sigma_{H_s^T} = \left(\frac{1}{n\alpha^2}\left[1.109 + 0.514\left(-ln\left(-ln\left(1 - \frac{1}{\lambda T}\right)\right)\right)\right.\right.$$
$$\left.\left. + 0.608\left(-ln\left(-ln\left(1 - \frac{1}{\lambda T}\right)\right)\right)^2\right]\right)^{0.5} \tag{56}$$

This expression includes the statistical uncertainty due to limited sample size. Some uncertainty is related to the estimation of the sample values H_{s1}, H_{s2}, ... , H_{sn} due to measurement errors, errors in hindcast models etc. This uncertainty corresponds to a coefficient of variation $\frac{\sigma_{H_s}}{\mu_{H_s}}$ in the order of 5 - 20%. The effect of this might be implemented in the calculations by considering a total standard deviation of

$$\sigma = \left(\sigma_{H_s^T}^2 + \sigma_{H_s}^2\right)^{0.5} \tag{57}$$

In the level II calculation eq. (54) is normalized around the design point and eqs. (55) and (56) or (57) are used for the mean and the standard deviation, cf. the procedure given in Example 2.

Instead of substituting H_s in eq. (52) with H_s^T the following procedure might be used: Consider T in eqs. (54) to (56) to be 1 year.

The outcome of the calculations will then be the probability of failure in a 1 year period, $P_f\,(1\ year)$. If the failure events of each year are assumed independent for all variables then the failure probability in T years is

$$P_f(T\ years) = 1 - [1 - P_f(1\ year)]^T \tag{58}$$

However, for typical resistance variables such as concrete strength it is not realistic to assume the events of each year to be independent. The calculated values of the failure probability in T-years using $H_s^{1\ year}$ and H_s^T will be different. The difference will be very small if the variability of H_s is much larger than the variability of other variables.

The *water level* W is also an important parameter as it influences the structural *freeboard* and limits the wave heights in shallow water situations. Consequently, for the general case it is necessary to consider the joint distribution of H_s, W and T_m. However, in case of deep-water waves W is often almost independent (except for barometric effects) of H_s and T_m and might therefore be taken as a non-correlated variable and might be approximated by a normal distribution with a certain standard deviation. The distribution of W is assumed independent of the length of the reference period T.

The *wave period* T_m is correlated to H_s. As a minimum the mean value and the standard deviation of T_z and the correlation of T_z with H_s should be known in order to perform a level II analysis. However, the linear correlation coefficient is not very meaningful as it gives an insufficient description when the parameters are non-normal distributed. Alternatively the following approach might be used: From a scatter diagram of H_s and T_m a relationship of the form $T_m = Af(H_s)$ is established in which the parameter A is normal distributed (or some other distribution) with mean value $\mu_A = 1$ and a standard deviation σ_A which signifies the scatter. T_m can then be substituted by the variable A in (52). A is assumed non-correlated to all other parameters. Generally, the best procedure to cope with the correlations between H_s, W and T_m is to work on the conditional distributions. Assume the distribution of the maximum value of H_s within the period T given as $F_1\left(H_s^T\right)$. Further, assume the conditional distributions $F_2\left(W|H_s^T\right)$ and $F_3\left(T_m|H_s^T\right)$ to be known. Let Z_1, Z_2 and Z_3 be independent standard normal variables and

$$\Phi(z_1) = F_1\left(H_s^T\right)$$

$$\Phi(z_2) = F_2\left(W|H_s^T\right)$$

$$\Phi(z_3) = F_3\left(T_m|H_s^T\right)$$

The inverse relationships are given by

$$H_s^T = F_1^{-1}\left[\Phi(z_1)\right]$$

$$W = F_2^{-1}\left[\Phi(z_2)\,|H_s^T\right]$$

$$T_m = F_3^{-1}\left[\Phi(z_3)\,|H_s^T\right]$$

Let the resistance variables $\bar{R}$ converted into standard normal variable $\bar{z}_o$. The resistance term is written $f_1(\bar{r}) = f_3(\bar{z}_o)$. Then the failure function eq. (52) becomes

$$g = f_3(\bar{z}_o) - f_2\left(F_1^{-1}\left[\Phi(z_1)\right],\ F_2^{-1}\left[\Phi(z_2)\,\|H_s^T\right],\ F_3^{-1}\left[\Phi(z_3)\,|H_s^T\right]\right) = 0$$

Because g now comprises only independent standard normal variables the usual iteration methods for calculating β_{HL} can be applied.

Discussion of Resistance Parameters

The service life of coastal structures is in most cases a span of years, say 20 to 100 years. During periods of that length a decrease in the structural resistance is to be expected due to various types of material deterioration. Chemical reaction, thermal effect, and repeated loads (fatigue load) can cause deterioration of concrete and natural stone leading to disintegration and rounding of elements. Also the resistance against displacements of armour layers made of randomly placed armour units will decrease with the number of waves (i.e. with time) due to the stochastic nature of the resistance. Consequently, for armour layers it means a reduction of D_n and K_D with time, cf. the Hudson equation.

Although of great importance in some cases, it is not easy to account for the material effects in reliability calculations. The main problem is the assessment of the variation with time which depends a lot on the intrinsic characteristics of the applied rock and concrete. However, only fairly primitive methods are available for assessment of the relevant characteristics. Moreover, the variation with time depends very much on the load-history which can be difficult to estimate for the relevant period of structural life.

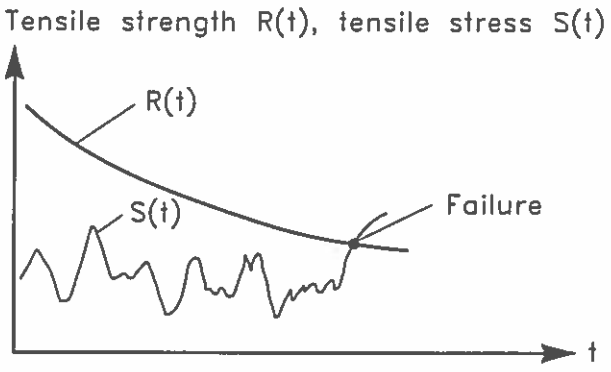

FIG. 7. Illustration of a first-passage problem.

Fig. 7 illustrates a situation where a resistance parameter $R(t)$, e.g. signifying the tensile strength of concrete armour units, decreases with time t. $R(t)$ is assumed to be a deter-

ministic function. The load $S(t)$, e.g. the tensile stress caused by wave action, is assumed to be a stationary process. The probability of failure, i.e. $P(S > R)$, within a period T is

$$P_f(T) \simeq 1 - exp\left[-\int_0^T \nu^+ (R(t))\, dt\right] \tag{59}$$

where $\nu^+ (R(t))$ is the mean-upcrossing rate (number of up-crossings per unit time) of the level $R(t)$ by the process $S(t)$ at time t. ν^+ can be computed by Rice's formula

$$\nu^+ (R(t)) = \int_{\dot{R}}^{\infty} \left(\dot{S} - \dot{R}\right) f_{S\dot{S}} \left(R(t), \dot{S}\right) d\dot{S}$$

in which $f_{S\dot{S}}$ is the joint density function for $S(t)$ and $\dot{S}(t)$.

Implementation of time-variant variables into level II analyses is rather complicated. For explanation reference is given to Wen and Chen, 1987.

4 Failure probability analysis of failure mode systems

It is clear from Fig. 1 that a breakwater can be regarded as a system of components which can either fail or function. Due to interactions between the components, failure of one component may impose failure of another component and even lead to failure of the system. A so-called *fault tree* is often used to clarify the relations between the failure modes.

A fault tree describes the relations between the failure of the system (e.g. excessive wave transmission over a breakwater protecting a harbour) and the events leading to this failure. Fig. 8 shows a simplified example based on some of the failure modes indicated in Fig. 1.

A fault tree is a simplification and a systematization of the more complete so-called cause-consequence diagram which indicates the causes of partial failures as well as the interactions between the failure modes. An example is shown in Fig. 9.

The failure probability of the system, e.g. the probability of excessive wave transmission in Fig. 8, depends on the failure probability of the single failure modes and on the correlation and linking of the failure modes.

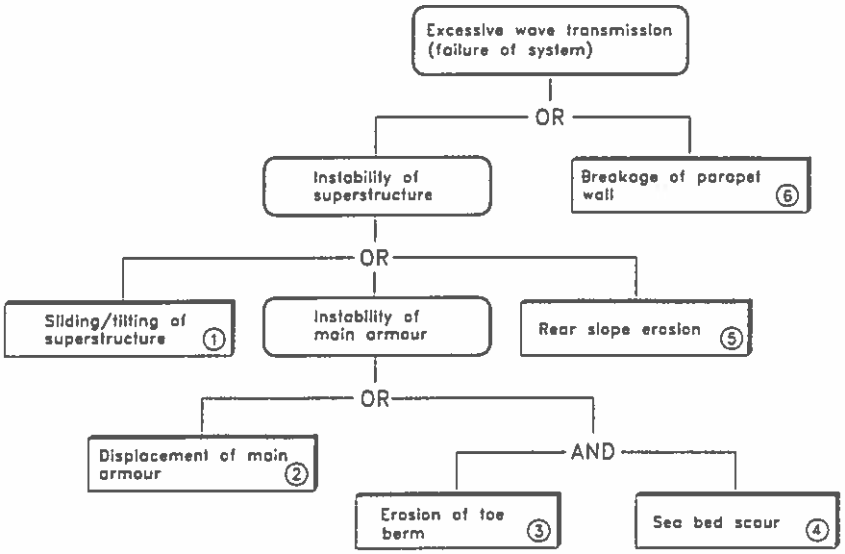

FIG. 8. Example of simplified fault tree for a breakwater.

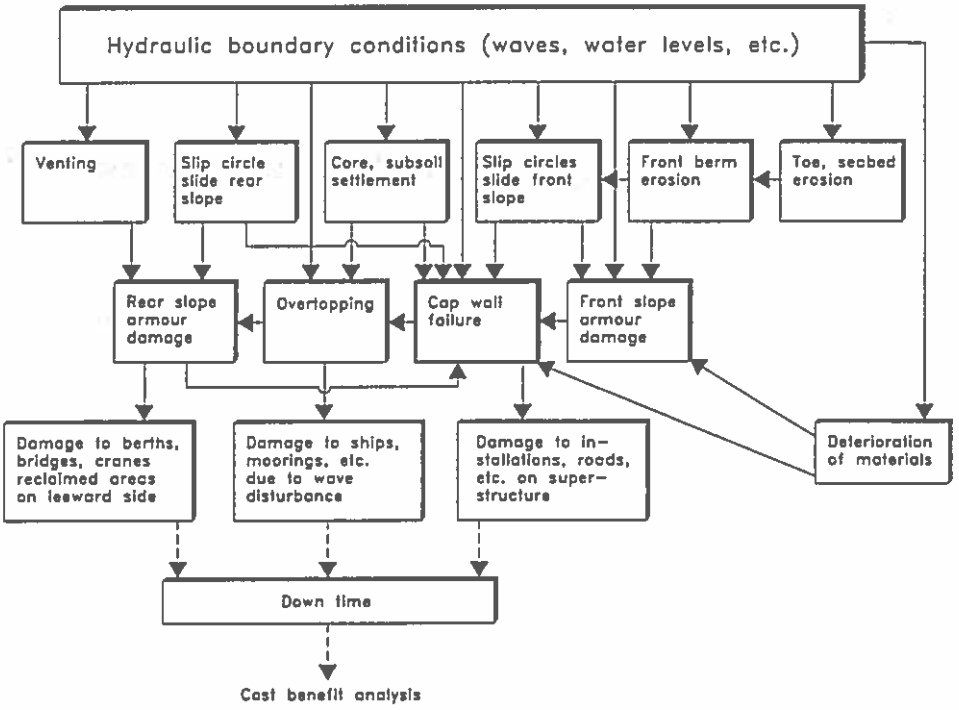

Only hydraulic loads are shown. Other types of loads are for example: SHIP COLLISION – SEISMIC ACTIVITY – AGGRESSIVE HUMAN ACTION (SABOTAGE, WAR, Etc.)

FIG. 9. Example of cause-consequence diagram for a rubble mound breakwater.

The failure probability of a single failure mode can be estimated by the methods described in chapter 3. Two factors contribute to the correlation, namely *physical interaction,* such as sliding of main armour caused by erosion of a supporting toe berm, and *correlation through common parameters* like H_s. The correlations caused by physical interactions are not yet quantified. Consequently, only the common-parameter-correlation can be dealt with in a quantitative way. However, it is possible to calculate upper and lower bounds for the failure probability of the system.

A system can be split into two types of fundamental systems, namely series systems and parallel systems, Fig. 10.

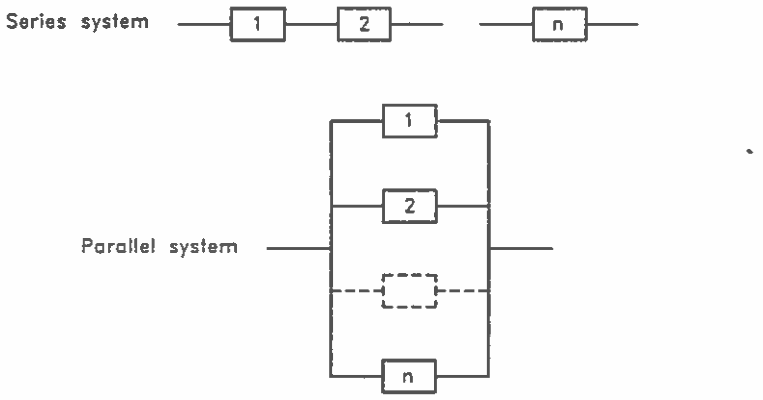

FIG. 10. Series and parallel systems.

Series systems

In a series system failure occurs if any of the elements $i = 1, 2, \ldots, n$ fails. The upper and lower bounds of the failure probability of the system, P_{fS} are

$$\text{Upper bound} \quad P_{fS}^{U} = 1 - (1 - P_{f1})(1 - P_{f2}) \ \ldots \ (1 - P_{fn}) \tag{60}$$

$$\text{Lower bound} \quad P_{fS}^{L} = \max P_{fi} \tag{61}$$

where $\max P_{fi}$ is the largest failure probability among all elements. The upper bound correponds to no correlation between the failure modes and the lower bound to full correlation. Eq. (60) is sometimes approximated by $P_{fS}^{U} = \sum_{i=1}^{n} P_{fi}$ which is applicable only for small P_{fi} because P_{fS}^{U} should not be larger than one.

The OR-*gates* in a fault tree corresponds to series components. Series components are dominating in breakwater fault trees. Really, the AND-gate in Fig. 8 is included for illustration purpose and is better substituted by an OR-gate.

Parallel systems

A parallel system fails only if all the elements fail.

$$\text{Upper bound} \quad P_{fS}^{U} = \min P_{fi} \tag{62}$$

$$\text{Lower bound} \quad P_{fS}^{L} = P_{f1} \cdot P_{f2} \ \ldots \ P_{fn} \tag{63}$$

The upper bound corresponds to full correlation between the failure modes and the lower bound to no correlation.

The AND-*gates* in a fault tree correspond to parallel components.

In order to calculate upper and lower failure probability bounds for a system it is convenient to decompose it into series and parallel systems. Fig. 11 shows a decomposition of the fault tree, Fig. 8.

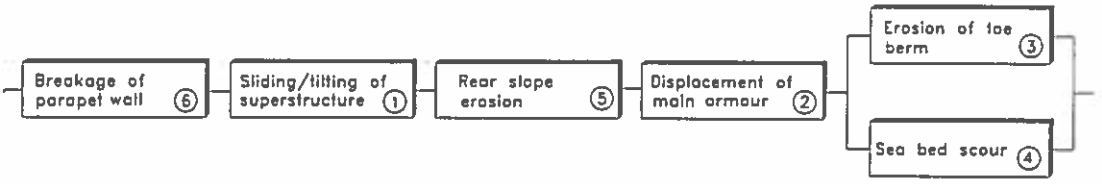

FIG. 11. Decomposition of the fault tree Fig. 8 into series and parallel systems.

EXAMPLE 3

The level II analysis of the single failure modes for a specific breakwater schematized in Figs. 8 and 11 revealed the following probabilities of failure in a 1-year period

i	1	2	3	4	5	6
P_{fi} %	3	6	4	3	0.5	1

Note that these P_{fi}-values cannot be used in general because they relate to a specific structure. However, they are typical for conventionally designed breakwaters with respect to order of magnitude and large variations.

The simple failure probability bounds for the system are, cf. eqs. (60), (61), (62) and (63):

Upper bound (no correlation):

$P_{fS}^{U} = 1 - (1 - P_{f6})(1 - P_{f1})(1 - P_{f5})(1 - P_{f2})(1 - \text{min. of } [P_{f3},\ P_{f4}]) = 12.9\%$

or for small values of P_{fi}

$P_{fS}^{U} = P_{f6} + P_{f1} + P_{f5} + P_{f2} + \text{min. of } [P_{f3},\ P_{f4}] = 13.5\%$

Lower bound (full correlation):

$P_{fS}^{L} = \text{ max of } [P_{f6},\ P_{f1},\ P_{f5},\ P_{f2},\ P_{f3} \cdot P_{f4}] = 6\%$

The simple bounds corresponding to T-years structural life might be approximated by the use of eq. (58) *)

	Structure life in years		
	20	50	100
$P_{fS}^{U}\%$	94	100	100
*) $P_{fS}^{L}\%$	71	95	100

*) It is very important to notice that the use of eq. (58), which assumes independent failure events from one year to another, can be misleading. This will be the case if some of the parameters which contribute significantly to the failure probability are time-invariant, i.e. are not changed from year to year. An example would be the parameter signifying a large uncertainty of a failure mode formula, e.g. A in eq. (2). If all parameters were time-invariant then the correct lower bound would be $P_{fS}^{L} = \max_{i=1-n} [P_{fi}]$ independent of T, i.e. 6% for all T in the example. It follows that use of eq. (58) leads to too large values of P_{fS}^{L} for $T > 1$ year.

In order to obtain correct P_{fS}-values it is very important that the fault tree represents precisely the real physics of the failure development. This is illustrated by Example 4 where a fault tree alternative to Fig. 8 is analysed, however, containing the same failure mode probabilities as given in Example 3.

EXAMPLE 4

Fig. 12 shows the fault tree which differs from the fault tree in Fig. 8 in that in Fig. 12 only failure mode 6 can directly cause system failure, while in Fig. 8 each of the failure modes 6, 5, 1, 2 and (3+4) can cause system failure.

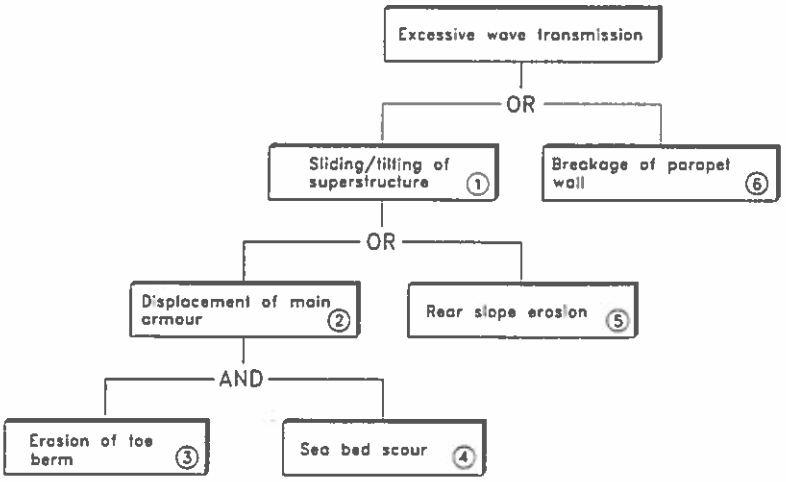

FIG. 12. Example of simplified fault tree for a breakwater.

The decomposition of the fault tree is shown in two steps in Fig. 13. Note that the same failure mode can appear more than once in the decomposed system.

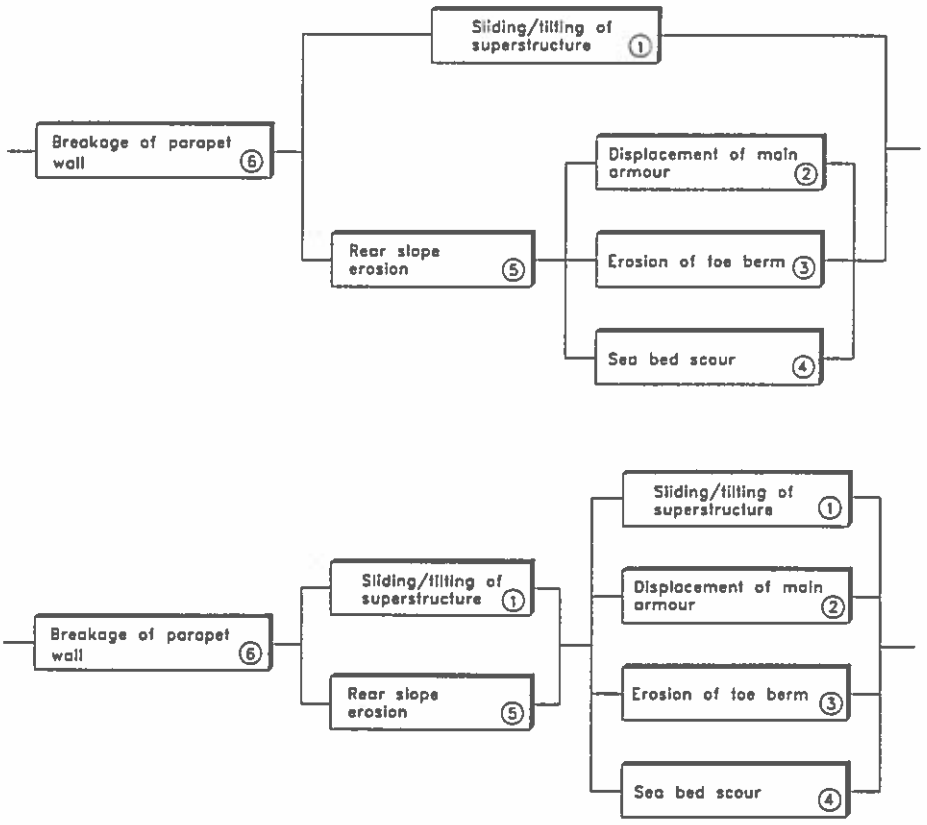

FIG. 13. Decomposition of the fault tree Fig. 12 into series and parallel systems.

The simpel bounds for the system are, cf. eqs. (60), (61), (62) and (63):

Upper bound:

$$P_{fS}^{U} = 1 - (1 - P_{f6})(1 - \text{ min. of } [P_{f1},\ P_{f5}])(1 - \text{ min. of } [P_{f1},\ P_{f2},\ P_{f3}, P_{f4}]) = 4.5\%$$

or for smaller values of P_{fi}

$$P_{fS}^{U} = P_{f6} + \text{ min. of } [P_{f1},\ P_{f5}] + \text{ min. of } [P_{f1},\ P_{f2},\ P_{f3},\ P_{f4}] = 4.5\%$$

Lower bound:

$$P_{fS}^{L} = \text{ max. of } [P_{f6},\ P_{f1} \cdot P_{f5},\ P_{f1} \cdot P_{f2} \cdot P_{f3} \cdot P_{f4}] = 1\%$$

Using the same P_{fi}-values and procedure as given in Example 3 the following system failure probabilities are obtained

	Structure life in years		
	20	50	100
$P_{fS}^{U}\%$	60	90	99
*) $P_{fS}^{L}\%$	18	39	63

These values are quite different from the values of Example 3 which underlines the importance of a correct fault tree. *) see note on page 28.

The real failure probability of the system P_{fS} will always be in between P_{fS}^{U} and P_{fS}^{L} because some correlation exists between the failure modes due to the common sea state parameters, e.g. H_s.

It would be possible to estimate P_{fS} if the physical interactions between the various failure modes were known and described by formulae and if the correlations between the involved parameters were known. However, the procedure for such correlations are very complicated and are in fact not yet fully developed for practical use.

The probability of failure cannot in itself be used as the basis for an optimization of a design. This is because an optimization must be related to a kind of measure (scale) which for most structures is the economy, but other measures such as loss of human life (without considering some cost of a life) are also used.

The so-called *risk*, defined as the product of the probability of failure and the economic consequences is used in optimization considerations. The economic consequences must cover all kind of expenses related to the failure in question, i.e. cost of replacement, down-time costs etc.

5 Uncertainties related to parameters determining the reliability of the structure

Calculation of reliability or failure probability of a structure is based on formulae describing its response to loads and on information about the uncertainties related to the formulae and the involved parameters.

Basically, uncertainty is best given by a probability distribution. Because the distribution is rarely known it is common to assume a normal distribution and a related coefficient of variation

$$\sigma' = \frac{\sigma}{\mu} = \frac{\text{standard deviation}}{\text{mean value}} \tag{64}$$

as the measure of the uncertainty.

The word uncertainty is here used as a general term referring both to errors, to randomness and to lack of knowledge.

5.1 Uncertainty related to failure mode formulae

The uncertainty of a formula can be considerable. This is clearly seen from many diagrams presenting the formula as a nice curve shrouded in a wide scattered cloud of data points (usually from experiments) which are the basis for the curve fitting. Coefficients of variation of 15-20% or even larger are quite normal.

The range of validity and the related coefficient of variation should always be considered when using a formula.

5.2 Uncertainty related to environmental parameters

The sources of uncertainty contributing to the total uncertainties in environmental design values are categorized as:

1. Errors related to instrument response (e.g. from accelerometer buoy and visual observations)
2. Variability and errors due to different and imperfect calculations methods (e.g. wave hindcast models, algorithms for timeseries analysis)
3. Statistical sampling uncertainties due to short-term randomness of the variables (variability within a stochastic process, e.g. two 20 min. records from a stationary storm will give two different values of the significant wave height)

4. Choise of theoretical distribution as a representative of the unknown long-term distribution (e.g. a Weibull and a Gumbel distribution might fit a data set equally well but can provide quite different values of a 200-year event).

5. Statistical uncertainties related to extrapolation from short samples of data sets to events of low probability of occurrence.

6. Statistical vagaries of the elements

Distinction is to be made between *short-term* sea state statistics and *long-term* (extreme) sea statistics. Short-term statistics is related to the stationary conditions during a sea state, e.g. wave height distribution within a storm of constant significant wave height, H_s. Long-term statistics deals with the extreme events, e.g. the distribution of H_s.

Related to the *short-term* sea state statistics the following aspects must be considered:

- The distribution for individual wave heights in a record in *deep water* and *shallow water* conditions, i.e Rayleigh distribution and some truncated distributions, respectively.

- Variability due to short samples of single peak spectra waves in deep and shallow water based on theory and physical simulations.

- Variability due to different spectral analysis techniques, i.e. different algorithms, smoothing and filter limits.

- Errors in instrument response and influence of location of measurement. Floating accelerometer buoys tend to underestimate the height of steep waves. Characteristics of shallow water waves can vary considerably in areas with complex sea bed topography. Wave recordings at positions with depth limited breaking waves cannot produce reliable estimates of the deep water waves.

- Imperfection of deep and shallow water numerical hindcast models and quality of wind input.

Estimates on overall uncertainties for short-term sea state parameters covering items 1 - 3 given above, are presented in Table 7 for use when no more precise site specific information is available.

Table 7. Typical variational coefficients $\sigma' = \sigma/\mu$ (standard deviation over mean value) for measured and calculated sea state parameters (Burcharth, 1989).

Parameter	Methods of determination	Estimated typical values σ'	Bias	Comments
Significant wave height, OFFSHORE	Accelerometer buoy, pressure cell, vertical radar	0.05-0.1	~ 0	
	Horizontal radar	0.15	~ 0	
	Hindcast, num. models	0.1-0.2	0-0.1	Very dependent on quality of weather maps.
	Hindcast, SMB method	0.15-0.2	?	Valid only for storm conditions in restricted sea basins.
	Visual observations from ships	0.2	0.05	
Significant wave height NEARSHORE determined from offshore significant waveheight taking into account typical shallow water effects (refraction, diffraction, shoaling, ...)	Numerical models	0.1-0.20	0.1	σ' can be much larger in some cases
	Manual calculations	0.15-0.35		
Mean wave period offshore on condition of fixed significant wave height	Accelerometer buoy records	0.02-0.05	~ 0	
	Estimates from amplitude spectra	0.15	~ 0	
	Hindcast, num. models	0.1-0.2	~ 0	
Duration of sea state with significant wave height exceeding a specific level	Direct measurements	0.02	~ 0	
	Hindcast, num. models	0.05-0.1	~ 0	
Spectral peak frequency offshore	Measurements	0.05-0.15	~ 0	
	Hindcast, num. models	0.1-0.2	~ 0	
Spectral peakedness offshore	Measurements and hindcast, num. models	0.4	~ 0	
		Degrees		
Mean direction of wave propagation offshore	Pitch - roll buoy	5°		
	Measurements η, u, v or p, u, v *)	10°		
	Hindcast, num. models	15 – 30°		
		σ'		
Astro tides	Prediction from constants	0.001-0.07	~ 0	
Storm surge	Numerical models	0.1-0.25	±0.1	

*) two horizontal velocity components and water level elevation or pressure.

Evaluation of the uncertainties related to the *long-term* sea state statistics and its use for design involves considerations of the following aspects:

- The encounter probability
- Estimation of the standard deviation of a return-period event for a given extreme distribution
- Estimation of extreme distributions by fitting to data sets consisting of uncorrelated values of H_s from
  - frequent measurements of H_s equally spaced in time
  - identification of the largest H_s in each year (annual series)
  - maximum values of H_s for a number of storms exceeding a certain threshold value of H_s (POT, peak over threshold, analysis)

The methods of fitting are the maximum likelihood method, the method of moments, the least square method and visual graphical fit.

- Uncertainty on extreme distribution parameters due to limited data sample size.
- Influence on the extreme value of H_s of the choise of threshold value in the POT analysis. (The threshold level should exclude all waves which do not belong to the statistical population of interest.)
- Errors due to lack of knowledge about the true extreme distribution. Different theoretical distributions might fit a data set equally well, but might provide quite different return period values of H_s. (The error can be estimated only empirically by comparing results from fits to different theoretical distributions.)
- Errors due to applied plotting formulae in case of graphical fitting. Dependent on the applied plotting formulae quite different extreme estimates can be obtained. The error can only be empirically estimated.
- Climatological changes.
- Physical limitations in extrapolation to events of low probability. The most important example might be limitations in wave heights due to limited water depths and fetch restrictions.
- The effect of measurement error on the uncertainty related to an extreme event.

It is beyond the scope of this contribution to discuss in more detail the mentioned uncertainty aspects related to the environmental parameters. Reference is given to Burcharth (1989).

5.3 Uncertainty related to structural parameters

The uncertainties related to material parameters (like density) and geometrical parameters (like slope angle and size of structural elements) are generally much smaller than the uncertainties related to the environmental parameters and to the design formulae.

6 Introduction of a partial coefficient system for implementation of a given reliability in the design

The following presentation explains in short the partial coefficient system developed and proposed by Subgroup-F under the PIANC PTC II Working Group 12 on Rubble Mound Breakwaters. For more details reference is made to Burcharth (1991).

6.1 Introduction to partial coefficients

The objective of the use of partial coefficients is to assure a certain reliability of the structures.

The partial coefficients, γ_i, are related to characteristic values of the stochastic variables, $X_{i,ch}$. In conventional civil engineering codes the charateristic values of loads and other action parameters are often chosen to be an upper fractile (e.g. 5%), while the characteristic values of material strength parameters are chosen to be the mean values. The values of the partial coefficients are uniquely related to the applied definition of the characteristic values.

The partial coefficients, γ_i, are usually larger than or equal to one. Consequently, if we define the variables as either load variables X_i^{load} (as for example H_s) or resistance variables X_i^{res} (as for example the block volume) then the related partial coefficients should be applied as follows to obtain the design values

$$\begin{aligned} X_i^{design} &= \gamma_i^{load} \cdot X_{i,ch}^{load} \\ X_i^{design} &= \frac{X_{i,ch}^{res}}{\gamma_i^{res}} \end{aligned} \tag{65}$$

The magnitude of γ_i reflects both the uncertainty on the related parameter X_i, and the relative importance of X_i in the failure function. A large value, e.g. $\gamma_{H_s} = 1.4$, indicates a relatively large sensitivity of the failure probability to the significant wave height, H_S. On the other hand, $\gamma_i \simeq 1$ indicates no or negligible sensitivity in which case the partial coefficient should be omitted. It is to be stressed that the magnitude of γ_i is not – in a mathematical sense – a stringent measure of the sensitivity of the failure probability to the parameter, X_i.

When the partial coefficients are applied to the characteristic values of the parameters in eq. (2) we obtain the **design equation**, i.e. the definition of how to apply the coefficients.

The partial coefficients can be related either to each parameter or to combinations of the parameters (overall coefficients). In the first case we obtain the design equation

$$G = \frac{Z_{ch}}{\gamma_z}\frac{\Delta_{ch}}{\gamma_\Delta}\frac{D_{n,ch}}{\gamma_{Dn}}\left(K_D\frac{cot\alpha_{ch}}{\gamma_{cot\alpha}}\right)^{1/3} - \gamma_{Hs}H_{s,ch} \geq 0$$

or (66)

$$D_{n,ch} \geq \gamma_z\gamma_\Delta\gamma_{Dn}\gamma_{cot\alpha}^{1/3}\gamma_{H_s}\frac{H_{s,ch}}{Z_{ch}\,\Delta_{ch}K_D\,cot\alpha_{ch}}$$

In the second case we could for example have only γ_{H_s} and an overall coefficient γ_z related to the first term on the right hand side of eq. (2). The design equation would then be

$$G = \frac{Z_{ch}}{\gamma_z}\Delta_{ch}\,D_{n,ch}\,(K_D cot\alpha)^{1/3} - \gamma_{H_s}H_{s,ch} \geq 0$$

or (67)

$$D_{n,ch} \geq \gamma_z\,\gamma_{H_s}\frac{H_{s,ch}}{Z_{ch}\,\Delta_{ch}\,(K_D\,cot\alpha_{ch})^{1/3}}$$

Eqs. (66) and (67) express two different "code formats". By comparing the two equations it is seen that the product of the partial coefficients is independent of the chosen format, other things equal. It is desirable to have a system which is as simple as possible, i.e. as few partial coefficients as possible, but without invalidating the accuracy of the design equation beyond acceptable limits.

Fortunately, it is very often possible to use overall coefficients, like γ_z in eq. (67), without loosing significant accuracy within the realistic range of combinations of parameter values. This is the case for the system proposed in this paper where only two partial coefficients, γ_{H_s} and γ_z, are used in each design formula.

Usually several failure modes are relevant to a design. The relationship between the failure modes are characterized either as series systems or parallel systems. A fault tree can be used to illustrate the complete system. The partial coefficients for failure modes being in a system with failure probability, P_f are different from the partial coefficients for the single failure modes with the same failure probability, P_f. Therefore, partial coefficients for single failure modes and multi failure mode systems are treated separately.

6.2 Overall concept of the proposed partial coefficient system

In existing civil engineering codes of practise, e.g. for steel and concrete structures, it is a characteristic of them that

- partial coefficients are related to combinations of basic variables rather than to each of them in order to reduce the number of coefficients.
- the partial coefficients reflect the safety level inherent in a large number of well proven designs. Two sets of coefficients covering permanent and preliminary structures are usually given, but the related average probabilities of failure are not specified. In other words, it is not possible by means of the normal structural codes to design a structure to a predetermined failure probability.

However, it is not advisable to copy this concept in safety recommendations for rubble mound breakwaters for the following reasons:

- For coastal structures and breakwaters there is no generally accepted tradition which reflects one or more levels of failure probability. On the contrary it is certain that the safety level of existing structures varies considerably and is often very low. Besides, it is very difficult to evaluate the safety level of existing coastal structures and breakwaters because of lack of information, especially on the environmental conditions, e.g. the water level variations and the wave climate. Consequently, it is not possible to produce sets of partial coefficients which, in a meaningful way, are calibrated against existing designs.

- Due to the very nature of coastal engineering where design optimization dictates considerable variations in the safety level of the various structures it is necessary (advisable) to have sets of partial coefficients which correspond to various failure probabilities. In other words the designer and the client decide on the basis of optimization and cost benefit analyses that the structure should be designed for a specific safety level (for example 20% probability of failure ($P_f = 20\%$) within a structural lifetime of $T = 80$ years, where failure is defined as a certain degree damage). The code should then contain a set of partial coefficients corresponding to this failure probability.

- Because the quality of information about the long term wave climate (the dominating load) varies from very unreliable (uncertain) wave statistics based on few uncertain data sets to very reliable statistics based on many years of high quality wave recordings and hindcast values it is necessary that the partial coefficients must be a function of the quality of the available information on the wave climate. This means that the statistical uncertainty due to limited number of wave data and errors in the wave data should be implemented.

Extensive calculations, performed at University of Aalborg, of partial coefficients for armour layer stability formulae demonstrated that it was possible to develop a concept which satisfies these demands.

6.3 Method of determining the partial coefficient

The overall procedure for the development of a partial coefficient system was as follows

- Define the failure modes and the failure element structure
  (single element analysis and/or system analysis)

- Select the code format (design equations)

- Define intervals of the parameters, their statistical properties and combinations

- Select target probabilities of failure

- Calculate the partial coefficients

- Optimize and calibrate the system
- Verify the partial coefficient system against the observed behaviour of existing structures.

The partial coefficients γ_i are determined from a so-called level II reliability analysis. The applied computer programmes BWREL (Break Water RELiability programme) and BWCODE (Break Water CODE) were developed at the University of Aalborg by Dr. John Dalsgaard Sørensen especially for the reliability analysis of breakwaters. For further explanation reference is made to the Sub-group F report.

6.4 Breakwater Types and Failure Modes

The Working Group set out to study five different types of breakwaters and considered a wide range of failure modes. During the work it became clear that sufficiently well documented failure formulae were only available to justify recommendations of partial coefficients for conventional multi-layer rubble mound breakwaters with armour carried over the crest – and for the following Failure modes:

- Hydraulic instability of front face armour
- Instability of low crested rock breakwaters
- Hydraulic instability of rock toe berm
- Run-up on rock armoured slopes

The formulae for these failure modes are given in section 6.8 in the form of design equations, which shows how to apply the partial coefficients.

6.5 Partial Coefficient System Format for Single Failure Modes

For each failure mode only two partial coefficients γ_{H_s} and γ_z are used, cf. the example given by eq. (67). The partial coefficient are determined from formulae. Three different concepts for these formulae have been evaluated and the following were chosen as being acceptable with respect to deviations from the target probability of failure.

$$\gamma_{H_s} = \frac{\hat{H}_s^{T_{P_f}}}{\hat{H}_s^T} + \sigma'_{FH_s} \left(1+\left(\frac{\hat{H}_s^{3T}}{\hat{H}_s^T}-1\right)k_\beta P_f\right) + \frac{k_s}{\sqrt{P_f N}} \tag{68}$$

$$\gamma_z = 1 - k_\alpha ln\, P_f \tag{69}$$

where

$\hat{H}_s^T$ is the central estimate of the T-year return period value of H_s, where T is the structural lifetime (T = 20, 50 and 100 years were used for the code calibration). γ_{H_s} is applied to $\hat{H}_s^T$ (the characteristic value of H_s, cf. the design equations).

$\hat{H}_s^{3T}$ is the central estimate of the $3T$-year return period value of H_s.

$\hat{H}_s^{T_{P_f}}$ is the central estimate of H_s corresponding to an equivalent return period T_{P_f} defined as the return period corresponding to a probability P_f that $\hat{H}_s^{T_{P_f}}$ will be exceeded during the structural lifetime T. T_{P_f} is calculated from the encounter probability formula $T_{P_f} = \left(1-(1-P_f)^{\frac{1}{T}}\right)^{-1}$, cf. Fig. 14.

$\sigma'_{F_{H_s}}$ is the variational coefficient of a function F_{H_s} modelled as a factor on H_s. F_{H_s} signifies the measurement errors and short term variability of H_s and has the mean value 1.0. $\sigma'_{F_{H_s}}$ is equal to σ' for H_s in Table 7. The statistical uncertainty on H_s is not included in F_{H_s}.

N is the number of H_s data, used for fitting the extreme distributions. The statistical uncertainty depends on this parameter. .

k_α, k_β and k_s are coefficients which are determined by optimization. $k_s \simeq 0.05$ for all failure modes. The k_α and the k_β values are given in Tables 9-12.

The first term in eq. (68) gives the correct γ_{H_s} provided no statistical uncertainty and measurement errors related to H_s are present. The middle term in eq. (68) signifies the measurement errors and the short term variability related to the wave data. The last term in eq. (68) signifies the statistical uncertainty of the estimated extreme distribution of H_s. The statistical uncertainty depends on the total number of wave data, N, but not on the length of the period of observation, as might be expected. The 10 largest values of H_s over a 15 years period provides a much more reliable estimate of the extreme distribution than the 10 largest values of H_s over 1 year. However, in the statistical analysis it is assumed that the data samples are equally representative of the true distribution. In other words it is assumed that the data, besides being non-correlated, are sampled with a frequency and over a length of time which ensures that periodic variations (e.g. seasonal) are not biasing the sample. The designer must be aware of these restrictions.

If the extreme wave statistics is not based on N wave data, but for example on estimates of H_s from information about water level variations in shallow water, then the last term in eq. (68) disappears and instead the value of $\sigma'_{F_{H_s}}$ must account for the inherent uncertainty.

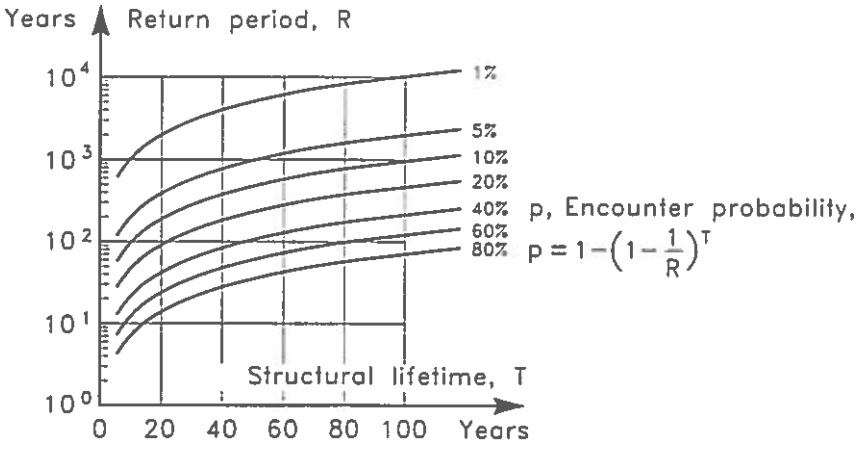

FIG. 14. Encounter probability, i.e. the probability p that the R-year return period event will be exceeded during a T-year structural life.

6.6 Format for Multi Failure Modes

A simple series system is considered, cf. chapter 4. The reliability of the system depends on the correlation between the failure modes. Two factors contribute to the correlation, namely the physical interaction, e.g. the erosion of a toe berm triggering a slide in the main armour layer, and the correlation through common parameters like H_s. The physical correlations are not yet generally known. Consequently, only the common parameter correlations have been implemented in the present work.

A simple system is to treat each failure mode, $i = 1, 2, 3, \ldots, n$ separately using the single failure mode models. The upper and lower bounds of probability of the system, P_f^s could then be estimated as

$$\text{Upper bound} \quad P_f^s = 1 - (1 - P_f^1)(1 - P_f^2)\ldots(1 - P_f^n) \tag{70}$$

$$\text{Lower bound} \quad P_f^s = \max P_f^i \tag{71}$$

Max P_f^i is the largest of the failure probabilities of the failure modes.

Eqs. (70) and (71) correspond to no correlation and full correlation, respectively. Due to the common parameters there will always be a correlation of some size. However, closer bounds must await further work on correlation between failure modes.

6.7 Investigated Ranges of Parameter Variations

The optimization of the partial coefficients is based on calculations where all combinations of realistic values of the failure formula parameters are considered.

The resistance parameters are modelled as normally distributed stochastic variables given by mean values and standard deviations. An example of these values and the related range

of parameter variations is given below for the Hudson equation applied to rock armour

Hudson formula $\frac{H_s}{\Delta D_n} = (K_D cot\alpha)^{1/3}$

Design equation :$G = \frac{1}{\gamma_Z}\hat{Z}\hat{\Delta}\hat{D}_n(K_D cot\hat{\alpha})^{1/3} - \gamma_{H_S}\hat{H}_s^T \geq 0$

Notation

$D(p)$	indicates a deterministic value, p.
$N(x_1, x_2)$	indicates a normally distributed parameter with mean value x_1 and standard deviation, x_2.
z	is the design parameter
$\bar{p}$	defines the ranges of application of the code for this failure mode.
$\hat{X}$	expected value (mean value) of X.
F_{H_s}	error function on H_s.
$\hat{H}_s^T$	central estimate of the significant wave height which on average is exceeded once every T years.

Parameters for the stochastic variables:

parameter	distribution	variation of $\bar{p}$
Δ	N(p_1, p_2)	$(p_1, p_2) = (1.4, 0.03), (1.6, 0.06)$
D_n	N(z, pz)	$p = 0.01, 0.05$
$cot\alpha$	N(p, 0.1)	$p = 1.5, 2, 3$
K_D	D	
F_{H_s}	N(1,p)	$p = \sigma_{FH_s} = (0, 0.10, 0.20)$
Z	N(1.0, 0.18)	
H_s	Extreme distribution fitted to local wave data	

The statistical model for the load parameteer H_s was described by three of the commonly used theoretical extreme distributions: Weibull, Gumbel and Exponential. The distributions are given below expressing the non-exceedence probability within T years. λ is the average number of H_s-data per year and N is the total number of data available for fitting the distribution.

The statistical uncertainty of the distributions is included through the parameters α and β which are modelled as stochastic normally distributed variables with variances based on the maximum likelihood estimates of α and β. It should be noted that no quality

measure (correlation coefficient or X^2-test) of the fit of a distribution to a data sample, is included in the analyses that were carried out.

The considered distribution functions are listed below.
$N(x_1, x_2)$ indicates a normally distributed parameter with mean value x_1 and standard deviation, x_2.

Gumbel $F_{H_s^T}(H_s) = [exp(-exp(-\alpha(H_s - \beta)))]^{\lambda T}$

$$\alpha : N\left(\alpha, \alpha\sqrt{\frac{0.608}{N}}\right) \qquad \beta : N\left(\beta, \frac{1}{\alpha}\sqrt{\frac{1.109}{N}}\right)$$

Weibull $F_{H_s^T}(H_s) = \left[1 - exp\left(-\left(\frac{H_s - H_s'}{\beta}\right)^{\alpha}\right)\right]^{\lambda T}$

$$\alpha : N\left(\alpha, \sqrt{\frac{1}{N}}\right) \qquad \beta : N\left(\beta_1 \left(\frac{\beta^2}{N}\left[\frac{\Gamma(1+2/\alpha)}{\Gamma^2(1+1/\alpha)} - 1\right]\right)^{\frac{1}{2}}\right)$$

$var[\alpha] = \frac{1}{N}$ is an assumption since it has not been possible to find an analytical expression.
Γ is the gamma function.

Exponential $F_{H_s^T}(H_s) = \left[1 - exp\left(-\frac{H_s - H_s'}{\alpha}\right)\right]^{\lambda T} \qquad \alpha : N\left(\alpha, \alpha\sqrt{\frac{1}{N}}\right)$

The H_s data samples used in the analysis are real deep water and shallow water data set from the North Sea, the Atlantic Ocean, the Bay of Biscaya and the Mediterranean Sea. Table 8 shows the distribution parameters for the data sets.

Table 8. Distribution parameters for H_s-data samples.

			Gumbel		Weibull		Exp.	
	N	λ	α	β	α	β	H_s'	α
Bilbao	50	4.17	1.95	5.55	1.39	1.06	4.9	0.97
Sines	15	1.25	0.88	8.75	1.78	2.53	7.1	2.27
Tripoli	15	0.75	0.74	5.06	1.83	3.24	2.9	2.91
North Sea	30	1.88	1.30	6.65	1.28	1.48	5.7	1.39
Follonica	46	5.94	3.14	3.04	1.14	0.58	2.69	0.55
Pozzallo	22	6.94	3.62	2.48	1.05	0.48	2.20	0.47

The statistical uncertainty described through the variance of α and β does not include uncertainties

- lack of knowledge about the true extremal distribution
- climatological changes
- measurement errors
- variability due to imperfect calculations of H_s and short term randomness

The last two points are incorporated in the analysis by the multiplication term F_{H_s} on H_s. F_{H_s} is modelled as a normally distributed variable with a mean value of unity and a specified coefficient of variation, $\sigma'_{F_{H_s}}$, the size of which depends on the quality of the available information, cf. Table 7.

The first two points cannot be treated through F_{H_s}, but in a design situation the designer must try the different models for the extreme wave height and thereby select the most appropriate. A partial coefficient system cannot take these problems into account.

Moreover, it is assumed inherent in the analysis that the N values of H_s represent the statistical population to which H_s belongs. This sets limits to minimum length of the period of observation N/λ and N in order to prevent seasonal changes from biasing the results.

For the calibration of the system the following target values of $\sigma'_{F_{H_s}}$ and P_f were used:

$\sigma_{F_{H_s}}$ = 0.00 , 0.10 and 0.20

P_f = 0.01 , 0.05 , 0.10 , 0.20 and 0.40.

6.8 Example of Design equations and Recommended Values of k_α and k_β

The values of k_α and k_β which have been obtained by carrying out optimization for each failure modes are presented as well as the related design equations in Tables 9 - 12. Note that limitations related to the equations are not given here.

Table 9. Main armour hydraulic stability.

Formula	Design equation	k_α	k_β
Hudson, rock	$\frac{1}{\gamma_z}\,\Delta D_{n50}\,(K_d cot\alpha)^{1/3} \geq \gamma_H, H_s^T$	0.036	151
Van der Meer, rock			
Plunging waves	$\frac{1}{\gamma_z} 6.2 S^{0.2} P^{0.18} \Delta D_{n50} cot\alpha^{0.5} s_m^{0.25} N_z^{-0.1} \geq \gamma_H, H_s^T$	0.027	38
Surging waves	$\frac{1}{\gamma_z} S^{0.2} P^{-0.13} \Delta D_{n50} cot\alpha^{0.5-P} s_m^{-0.5P} N_z^{-0.1} \geq \gamma_H, H_s^T$	0.031	38
Van der Meer Tetrapods $cot\alpha = 1.5$	$\frac{1}{\gamma_z}\left(3.75\frac{N_{od}^{0.5}}{N_z^{0.25}} + 0.85\right) s_m^{-0.2} \Delta D_n \geq \gamma_H, H_s^T$	0.026	38
Van der Meer Cubes $cot\alpha = 1.5$	$\frac{1}{\gamma_z}\left(6.7\frac{N_{od}^{0.4}}{N_z^{0.3}} + 1.0\right) s_m^{-0.1} \Delta D_n \geq \gamma_H, H_s^T$	0.026	38
Burcharth Dolos $cot\alpha = 1.5$	$\frac{1}{\gamma_z} \Delta D_n (47 - 72r) \varphi_{n=2} D^{1/3} N_z^{-0.1} \geq \gamma_H, H_s^T$	0.025	38
	r Dolos waist ratio φ packing density D relative number of units displaced		

Table 10. Hydraulic stability of low crested rock breakwaters.

Formula	Design equation	k_α	k_β
Van der Meer, rock	As for main armour with factor $f_i = \left[1.25 - 4.8\frac{R_c}{H_s^T}\left(\frac{S_m}{2\pi}\right)^{0.5}\right]^{-1}$ applied to D_{n50}	0.035	42

Table 11. Hydraulic stability of rock toe berm.

Formula	Design equation	k_α	k_β
Van der Meer, rock	$\frac{1}{\gamma_z}\, 8.7\left(\frac{h_t}{h}\right)^{1.43} \Delta D_{n50} \geq \gamma_{H_s} H_s^T$	0.087	100

Table 12. Run-up on rock armoured slopes.

Formula		Design equation	k_α	k_β
Hunt	for	$(cot\alpha)^{-1} s_m^{-0.5} < 1.5$ $\frac{1}{\gamma_z}\, R_u\, a^{-1} cot\alpha\, s_m^{0.5} \geq \gamma_{H_s} H_s^T$	0.036	44
	for	$(cot\alpha)^{-1} s_m^{-0.5} > 1.5$ $\frac{1}{\gamma_z}\, R_u\, b^{-1}\, [cot\alpha\, s_m^{0.5}]^c \geq \gamma_{H_s} H_s^T$	0.018	36

6.9 Example of the use of the Partial Coefficient System

The following example will illustrate how the partial coefficient system is applied for design purpose.

Objective:

Determination of the average mass, or the nominal diameter D_{n50}, of quarry rock armour corresponding to the following design conditions:

Case 1. Moderate to severe damage with a probability $P_f = 0.2$ within a structural life of $T = 50$ years.

Case 2. Very severe damage (failure) with a probability $P_f = 0.2$ within a structural life of $T = 100$ years.

Case 3. Moderate to severe damage with a probability $P_f = 0.1$ within a structural life of $T = 100$ years.

The Van der Meer formulae for rock given in Table 9 are assumed valid.

Design parameters:

Densities: Rock 2.8 t/m^3, water 1.03 t/m^3, $\Delta = 1.72$

Slope: $cot\alpha = 1.5$, porosity $P = 0.4$

Wave climate: Weibull distribution of H_s with the site specific coefficients $(\alpha, \beta, H_s') = (1.39, 1.06, 0.44)$ determined by fitting to a hindcasted H_s-data set consisting of the $N = 50$ largest values within a 12 years period, i.e. $\lambda = 50/12 = 4.17$. σ'_{FH_s} is estimated to 0.2 for the hindcasted H_s values. Wave steepness $s_m = 0.04$, number of waves $N_z = 2500$.

Damage: Moderate to severe damage $S = 6$, very severe damage (failure) $S = 14$.

Procedure:

The procedure and the partial coefficent formulae described in section 6.5 are used.

Calculations:

In case of a Weibull distribution the central estimate of the significant wave height with an average return period of T years is given by

$$\hat{H}_s^T = H_s' + \beta\,(exp[ln(ln(\lambda T))/\alpha])$$

$$= 0.44 + 1.06\,(exp[ln(ln(4.17T))/1.39])$$

The equivalent return period is given by

$$T_{P_f} = \left(1 - (1 - P_f)^{\frac{1}{T}}\right)^{-1}$$

From this is obtained

Case	T (year)	P_f	T_{P_f} (year)	$\hat{H}_s^T$ (m)	$\hat{H}_s^{3T}$ (m)	$\hat{H}_s^{T_{P_f}}$ (m)
1	50	0.2	225	3.98	4.49	4.67
2	100	0.2	449	4.30	4.80	4.97
3	100	0.1	950	4.30	4.80	5.29

From Table 9 (for plunging waves)

$k_\alpha = 0.027$, $k_\beta = 38$

From the formulae

$$\gamma_{H_s} = \frac{\hat{H}_s^{T_{P_f}}}{\hat{H}_s^T} + \sigma'_{F_{H_s}} \left(1+\left(\frac{\hat{H}_s^{3T}}{\hat{H}_s^T}-1\right)k_\beta P_f\right) + \frac{0.05}{\sqrt{P_f N}}$$

$$\gamma_Z = 1 - k_\alpha ln\, P_f$$

and the Van der Meer design equation is obtained

Case	γ_{H_s}	γ_Z	D_{n50} (m)	Average mass (t)
1	1.23	1.04	1.58	11.0
2	1.22	1.04	1.43	8.1
3	1.35	1.06	1.91	19.5

The example illustrates how easy it is to calculate the size of the armour for various design conditions. The system facilitates economical optimization of a design.

The system can be used also for the evaluation of the failure probability of existing structures.

6.10 Conclusions

A concept for the calculation of partial coefficients corresponding to given failure probability within given structure life is presented. Two partial coefficients γ_{H_s} and γ_z are applied to a design formula. Two partial coefficients are calculated from formulae (68) and (69) in which two failure mode specific coefficients, k_α and k_β, are used together with characteristic return period values of H_s, extracted from the site specific long term distribution of H_s.

So far the k_α , k_β coefficients have been calculated only for the failure modes which are described by existing uncertainty evaluated formulae . However, it is easy to expand the system as more failure mode formulae appear. It is important to notice that the reliability of the formulae must be documented, e.g. in terms of a standard deviation, in order to implement them in the partial coefficient system.

7 Acknowledgement

The useful comments of Dr. Zhou Liu and Dr. J. Dalsgaard Sørensen are greatly acknowledged.

8 References

BURCHARTH, H.F. (1989) Uncertainties related to environmental data and estimated extreme events. Report of Subgroup-B, PIANC PTCII Working Group 12 on Rubble Mound Breakwaters. (In print by PIANC 1992)

BURCHARTH, H.F. (1991) Introduction of partial coefficients in the design of rubble mound breakwaters. Proc. Conf. on Coastal Structures and Breakwaters. Inst. of Civil Eng., London.

BURCHARTH, H.F. (1991) Development of a partial coefficient system for the design of rubble mound breakwaters. Report of Subgroup-F. PIANC PTC II Working Group 12 on Rubble Mound Breakwaters. (In print by PIANC 1992)

HALLAM, M.G., HEAF, N.I. and WOOTOS, I.R. (1977). Rationalization of Safety and Serviceability factors in Structural Codes. CIRIA report No. 63, London.

THOFT-CHRISTENSEN, P. and BAKER, M.J. (1982). Structural Reliability Theory and its Application. Springer Verlag. Berlin.

WEN, Y.K. and CHEN, H.C. (1987). On fast integration for time variant structural reliability. *Probabilistic Engineering Mechanics,* Vol.2, 1987, pp 156-162.

Scour Around Vertical Pile in Waves

B. Mutlu Sumer, Jørgen Fredsøe and Niels Christiansen

Institute of Hydrodynamics and Hydraulic Engineering
Technical University of Denmark

Scour Around Vertical Pile in Waves

By B. Mutlu Sumer,[1] Jørgen Fredsøe,[2] and Niels Christiansen[3]

Abstract: This paper presents the results of an experimental investigation on scour around piles exposed to waves. In addition to the actual scour tests, bed shear-stress measurements and a flow visualization study are carried out. The effects of lee wake and horseshoe vortex are demonstrated to be the two key elements in the scour process. The development of these flow structures mainly depends on the Keulegan Carpenter (KC) number that hereby becomes the main parameter that governs the equilibrium scour depth on a live bed. Based on the present data, a design equation is established, relating the scour depth to the Keulegan-Carpenter number. For the values of the Keulegan Carpenter number below six, the scour around the pile practically ceases to exist. The scour depth normalized by the pile diameter is found to increase with increasing Keulegan Carpenter number and approaches its steady current value for Keulegan-Carpenter numbers above approximately 100.

Introduction

Scour around piles in steady currents has been investigated extensively in the last decades. The fluid mechanics of the scour process are relatively well understood. The key element in the scour process is the horseshoe vortex, formed around the pile just above the bed. This vortex, which is formed due to the presence of rotation in the incoming velocity profile, is able to erode a significant amount of sediment away from the neighborhood of the pile. The research indicates that the equilibrium scour depth lies in the interval 1 - 1.5 D; D being the pile diameter. A comprehensive review of the subject has been given by Breusers et al. (1977) and Hjorth (1975), the latter also presenting a detailed experimental investigation of the increase in the bed shear stress around a pile exposed to current.

Scour around piles in waves and in combined waves plus current, on the other hand, has attracted much attention in recent years, considering its application to offshore structures.

Some field data have been reported by Palmer (1969) where rate and magnitude of scour developed around obstructions exposed to oscillatory wave-induced flows were measured. Das (1970) presented a few laboratory tests made on local scour around vertical cylinders in an oscillating flume. Kawata and Tsuchiya (1988) made similar tests with real waves and further in combined waves and current.

Herbich and his coworkers [see, for example, Wang and Herbich (1983), Herbich et al. (1984), and Fadle and Herbich (1986)], on the other hand, have made an extensive study of scour around piles in combined waves and current.

---

[1]Assoc. Prof., Inst. of Hydrodynamics and Hydr. Engrg., Tech. Univ. of Denmark, DK-2800 Lyngby, Denmark.

[2]Prof., Inst. of Hydrodynamics and Hydr. Engrg., Tech. Univ. of Denmark, DK-2800 Lyngby.

[3]Grad. Student, Inst. of Hydrodynamics and Hydr. Engrg., Tech. Univ. of Denmark, DK-2800 Lyngby.

Note. Discussion open until June 1, 1992. To extend the closing date one month, a written request must be filed with the ASCE Manager of Journals. The manuscript for this paper was submitted for review and possible publication on July 12, 1990. This paper is part of the *Journal of Waterway, Port, Coastal, and Ocean Engineering*, Vol. 118, No. 1, January/February, 1992. ©ASCE, ISSN 0733-950X/92/0001-0015/ $1.00 + $.15 per page. Paper No. 78.

When the case of waves alone is considered, despite the effort put in the study of scour, even the basic scour-depth data are not fully available, however; the existing data are scarce, consisting of only a few test results reported by the previously mentioned investigators such as Das and as Kawata and Tsuchiya. This might be one reason why the resulting scour depth until now has not been evaluated in a systematic manner even in the simple case of waves alone.

The purpose of the present investigation is to study the scour in waves alone in a systematic manner. An extensive series of laboratory scour tests was conducted with piles subject to real waves. Furthermore, in order to enlighten the underlying mechanisms responsible for the scour, a flow visualization study was made, and also the bed shear stress around the pile was measured.

Experimental Facility

Scour Experiments

Test Series No. 1

These experiments were carried out in a wave flume, 0.6 m in width, 0.8 m in depth, and 26.5 m in length. The mean water depth was held constant at 40 cm. Four model piles were used with diameters D = 10 mm, 20 mm, 30 mm, and 50 mm. In all the tests, the pipe surface acted as a hydraulically smooth surface. Two sizes of sand grain were used with d_{50} = 0.18 mm and 0.58 mm.

Test Series No. 2

These experiments were carried out in a large wave flume, 4 m in width, 1 m in depth, and 28 m in length. The main purpose of these tests was to provide data with relatively larger diameter pile models. Two cylinders were used as pile models with diameters D = 100 mm and 200 mm. The experiments were conducted for only d_{50} = 0.18-mm size sand.

Test Series No. 3

A few tests were carried out in a 2-m-wide current flume in order to supplement the wave-flume experiments with data representing tidal flow situations. In these experiments the flow direction could be reversed with a period that was long enough for the flow to be considered quasi-steady in each half-cycle. Two model piles were used in these experiments with D = 50 mm and 110 mm. Sand grain size was d_{50} = 0.36 mm. One-directional, steady-current experiments were also conducted for reference purpose.

In test series 2, intense suspension of sand in the flume did not allow the continuous video monitoring of the scour process. Instead, the waves were stopped every 5 min, and the scour depth was measured; the scour-depth measurements were made at four points, namely at the upstream edge of the pipe, at the downstream edge of the pipe, and at the two side edges of it.

Velocity measurements were made by a Dantec laser doppler anemometer (LDA) in test series 1 and 3, and by an ultrasonic velocity meter in test series 2.

Test Conditions

The test conditions together with the experimental results regarding the scour depth are listed in Table 1. In the table, the Shields parameter θ is defined by

$$\theta = \frac{U_{fm}^2}{(s-1)gd} \quad \ldots\ldots (1)$$

in which d = the sand grain size; g = the acceleration due to gravity; s = the relative density of sediment; and U_{fm} = the maximum value of the undisturbed bed shear velocity, which is calculated by

$$U_{fm} = \sqrt{\frac{f}{2}}\, U_m \quad \ldots\ldots (2)$$

where f = the friction coefficient; and U_m = the maximum value of the outer oscillatory flow velocity defined by

$$U = U_m \sin(\omega t) \quad \ldots\ldots (3)$$

where ω = the angular frequency of the motion. For steady current situations, U_{fm} and U_m are replaced by U_f and U, respectively, in which U_f = the undisturbed bed shear velocity and U = the mean flow velocity. Also, in the table, the Keulegan-Carpenter (KC) number is defined by

$$\mathrm{KC} = \frac{U_m T}{D} \quad \ldots\ldots (4)$$

and the pile Reynolds number by

$$\mathrm{Re} = \frac{U_m D}{\nu} \quad \ldots\ldots (5)$$

where T = the wave period; and ν = the kinematic viscosity.

Flow-Visualization Experiments

The purpose of the flow visualization experiments was to get an understanding of the near bed flow processes around a pile exposed to waves, such as the horseshoe vortex and the downstream vortex shedding.

These experiments were conducted in the same wave flume as test series 1 scour experiments. The so-called hydrogen-bubble technique was employed in the experiments. A 25-cm-long and 0.050-mm-diameter copper wire was used as the hydrogen bubble wire. It was stretched in the transverse direction between two points in the transverse direction at a streamwise distance of about 1 cm from the edge of the model pile and at a vertical location of y = 2 mm away from the bed. The model pile was a smooth-surface cylinder with a diameter D = 4 cm. The lowermost 1.2-cm portion of the cylinder was made from a transparent material through which the light was spread out.

The KC number range of the experiments was from practically 0 to about 25 where KC was incremented by about 2. The range of pile Re number was from 2×10^3 to 9×10^4, the upper limit corresponding to the test where KC was 25.

Velocity profile measurements were made in the absence of the pile by the same LDA equipment as that used in the scour tests.

TABLE 1 Experimental Data on Scour Around Vertical Pile. All Data Presented in This Table Are for Live-Bed Conditions

Test series (1)	Run number (2)	Sand size d(mm) (3)	Pile diameter D(mm) (4)	Wave frequency f_w(s^{-1}) (5)	Maximum flow velocity (measured) U_m(cm/s) (6)	Maximum shear velocity U_{*m}(cm/s) (7)	Shields parameters θ (8)	Keulegan-Carpenter number KC (9)	Pile Reynolds number Re (10)	Nondimensional equilibrium scour depth S/D (11)
1[a]	1	0.18	50	0.84	20.8	3.3	0.37	4.9	$1.0\cdot10^4$	~0
	2	0.18	50	0.82	22.4	2.3	0.18	5.4	$1.1\cdot10^4$	~0
	3	0.18	50	0.40	11.4	1.3	0.06	5.7	$5.7\cdot10^3$	~0
	4	0.18	50	0.73	23.3	2.2	0.17	6.4	$1.2\cdot10^4$	0.12
	5	0.18	30	0.84	20.8	2.2	0.16	8.2	$6.2\cdot10^3$	0.06
	6	0.18	50	0.68	30.7	2.5	0.22	9.1	$1.5\cdot10^4$	0.22
	7	0.18	50	0.43	19.3	1.8	0.11	9.0	$9.7\cdot10^3$	0.15
	8	0.18	30	0.82	22.4	2.3	0.18	9.1	$6.7\cdot10^3$	0.17
	9	0.18	30	0.40	11.2	1.3	0.06	9.2	$3.4\cdot10^3$	0.08
	10	0.18	30	0.73	23.3	2.2	0.17	10.6	$7.0\cdot10^3$	0.20
	11	0.18	50	0.37	23.7	1.9	0.12	12.9	$1.2\cdot10^4$	0.30
	12	0.18	50	0.50	33.9	2.4	0.20	13.6	$1.7\cdot10^4$	0.30
	13	0.18	30	0.43	19.3	1.8	0.11	15.0	$5.8\cdot10^3$	0.37
	14	0.18	30	0.68	30.7	2.5	0.22	15.1	$9.2\cdot10^3$	0.55
	15	0.18	30	0.32	18.3	1.6	0.09	19.1	$5.5\cdot10^3$	0.25
	16	0.18	30	0.50	30.4	2.3	0.19	20.2	$9.1\cdot10^3$	0.75
	17	0.18	50	0.37	37.8	2.4	0.20	20.4	$1.9\cdot10^4$	0.43
	18	0.18	30	0.37	23.7	1.9	0.12	21.4	$7.1\cdot10^3$	0.42
	19	0.18	20	0.43	19.3	1.8	0.11	22.4	$3.9\cdot10^3$	0.43
	20	0.18	20	0.34	22.2	1.8	0.11	32.3	$4.4\cdot10^3$	0.58
	21	0.18	30	0.28	26.3	1.9	0.12	32.3	$8.0\cdot10^3$	0.42
	22	0.18	50	0.37	37.8	2.4	0.20	34.0	$1.1\cdot10^4$	0.67
	23	0.18	20	0.37	37.8	2.4	0.20	51.0	$7.6\cdot10^3$	0.80
	24	0.18	10	0.37	37.8	2.4	0.20	102	$3.8\cdot10^3$	1.10
	25	0.58	50	0.82	22.4	2.3	0.05	5.4	$1.1\cdot10^4$	~0
	26	0.58	50	0.73	23.3	2.2	0.05	6.4	$1.2\cdot10^4$	~0
	27	0.58	50	0.55	19.9	1.9	0.04	7.2	$1.0\cdot10^4$	~0
	28	0.58	30	0.82	22.4	2.3	0.05	9.1	$7.0\cdot10^3$	0.05
	29	0.58	30	0.73	23.3	2.2	0.05	10.6	$7.0\cdot10^3$	0.04
	30	0.58	30	0.55	19.9	1.9	0.04	12.1	$6.0\cdot10^3$	0.12
	31	0.58	50	0.37	23.7	1.9	0.04	12.9	$1.2\cdot10^4$	0.18
	32	0.58	50	0.50	33.9	2.4	0.06	13.6	$1.7\cdot10^4$	0.20
	33	0.58	20	0.55	19.9	1.9	0.04	18.1	$4.0\cdot10^3$	0.50
	34	0.58	30	0.37	23.7	1.9	0.04	21.4	$7.1\cdot10^3$	0.57
	35	0.58	20	0.43	19.3	1.8	0.04	22.4	$3.9\cdot10^3$	0.72
	36	0.58	20	0.50	33.9	2.4	0.06	22.6	$1.0\cdot10^4$	0.52
	37	0.58	20	0.37	23.7	1.9	0.04	32.1	$4.7\cdot10^3$	0.54
2[b]	38	0.18	100	0.53	23.1	2.0	0.14	4.4	$2.3\cdot10^4$	~0
	39	0.18	200	0.22	30.1	1.8	0.11	6.7	$6.0\cdot10^4$	0.032
	40	0.18	200	0.22	32.6	1.9	0.13	7.3	$6.5\cdot10^4$	0.055
	41	0.18	100	0.33	25.2	1.8	0.11	7.6	$2.5\cdot10^4$	0.12
	42	0.18	200	0.22	39.1	2.0	0.14	8.8	$7.8\cdot10^4$	0.057
	43	0.18	200	0.22	46.9	2.3	0.19	10.5	$9.4\cdot10^4$	0.085
	44	0.18	200	0.22	53.3	2.5	0.22	12.0	$1.1\cdot10^5$	0.11
	45	0.18	100	0.22	30.1	1.8	0.11	13.4	$3.0\cdot10^4$	0.15
	46	0.18	100	0.22	32.6	1.9	0.13	14.6	$3.3\cdot10^4$	0.22
	47	0.18	100	0.22	39.1	2.0	0.14	17.6	$3.9\cdot10^4$	0.25
	48	0.18	100	0.22	46.9	2.3	0.19	21.0	$4.7\cdot10^4$	0.24
	49	0.18	100	0.22	53.3	2.5	0.22	24.0	$5.3\cdot10^4$	0.31
3[c]	50	0.36	100	$3.3\cdot10^{-1}$	47.1	2.4	0.10	1.285	$5.2\cdot10^4$	0.92
	51	0.36	50	$3.3\cdot10^{-1}$	47.1	2.4	0.10	2.826	$2.4\cdot10^4$	1.56
	52	0.36	50	$1.7\cdot10^{-1}$	47.1	2.4	0.10	5.626	$2.4\cdot10^4$	1.20
	53	0.36	50		47.1	2.4	0.10	∞	$2.4\cdot10^4$	1.30

[a]Test series 1: Small wave-flume experiments.
[b]Test series 2: Large wave-flume experiments.
[c]Test series 3: Current flume experiments.

Bed Shear-Stress Measurements

These measurements were carried out in a *U*-shaped oscillatory flow tunnel, 30 cm in width and 29 cm in height. This tunnel is essentially the same as that described by Jensen et al. (1989). The bed shear stress was measured with a flush-mounted Dantec 55R46 hot-film probe. A cylinder, 5 cm in diameter and 29 cm in length, with a smooth surface was placed vertically in the tunnel, extending the whole tunnel height. The bed shear stress was measured at various streamwise and transverse distances of the cylinder from the shear-stress probe. The free-stream velocity at the centerline of the tunnel was measured simultaneously with the bed shear stress, using the LDA equipment.

The ratio of the tunnel width to the pipe diameter was 7.8. According to the potential flow theory, the blockage effect for this value of the width-to-diameter ratio is less than 1%. The range of the KC number in the bed shear-stress measurements was from 4 to 120 and that of the pile Re number from 10^3 to 3×10^4.

The Process of Scour

The scour process around structures occurs because the sediment transport capacity is larger in the vicinity of the structure than away from it. This increase in local transport capacity can be caused by several factors.

If we consider current alone, the increase in the transport capacity is a combination of the local increase in the bed shear stress and the transporting current term.

The local increase in the bed shear stress occurs partly due to contraction in the streamlines and partly due to the occurrence of a complicated three-dimensional vortex system in front of and behind the cylinder. This system partly stems from the downstream vortex shedding and partly from the formation of the horseshoe vortex, which is a secondary vortex formed due to the unbalance between centrifugal forces and pressure forces because of rotation in the incoming flow velocity profile, like the helical flow in a river bend. In current alone, this horseshoe vortex has been described extensively in the literature (Breusers et al. 1977; Hjorth 1975).

It must be mentioned that the presence of the local vortex structures may change the flow pattern tremendously in the neighborhood of the cylinder. For instance, the local increase in the flow velocity due to the contraction of streamlines can no longer be described by the potential flow solution, as indicated by some of the experiments in the present work.

In the case of the combined waves and current, the presence of waves modifies the vortex structure considerably. As an example, if we compare the current-alone situation with the waves-alone case, the extension of the vortex shedding pattern becomes quite different. Also, the horseshoe vortex must be expected to differ very much from that of waves-alone situation as the distribution of rotation in a wave-boundary layer is highly different from that found in a steady-current boundary-layer velocity profile.

In the case of dominating wave-action, the transporting term responsible for carrying the sediment away from the structure also becomes more complex. Even in the case of waves alone, some steady current pattern due to steady streaming (Schlichting 1979, p. 431) around the cylinder must be expected. However, this pattern must also be expected to be quite different from that described by Schlichting when the vortex structures are present around the structure.

However, in the waves-alone case, the most important transporting term is probably the wave-orbital velocities themselves, which, for a slender cylinder, is able to transport sediment several pile diameters away from the structure where the sediment eventually may settle before the flow reversal.

Finally, it must be mentioned that it is common to distinguish between the live bed scour where sediment transport takes place, also far away from the cylinder, and the clear-water scour, in which case sediment transport takes place only close to the structure, due to the increased transport capacity.

Near-Bed Flow Around a Pile

The near-bed flow around a pile partly consists of the horseshoe vortex formed at the seabed and partly of the vortex shedding pattern at the lee side of the pile (Fig. 1), as mentioned previously.

Horseshoe Vortex

The horseshoe vortex is formed at the seabed because of the rotation in the incoming flow velocity (Fig. 1). In waves, this rotation is formed in the wave boundary layer. However, the horseshoe vortex is insignificant when the wave boundary layer is thin.

Fig. 2 presents the flow pictures at the upstream side of the pile for various values of KC number. In the figure, the thickness of the wave boundary layer δ is also given. Here δ is the thickness of the wave boundary layer that develops over the bed in the absence of the pile. The δ values are determined from the measured velocity profiles.

The crescent shape figure in the pictures, designated by A in Fig. 2(*b*), represents the lowermost, transparent portion of the cylinder through which the light spreads out. The existence of the horseshoe vortex manifests itself in the pictures by the absence of the bubbles in the immediate surrounding of the cylinder [Fig. 2(*d*)], while the presence of the bubbles in the immediate

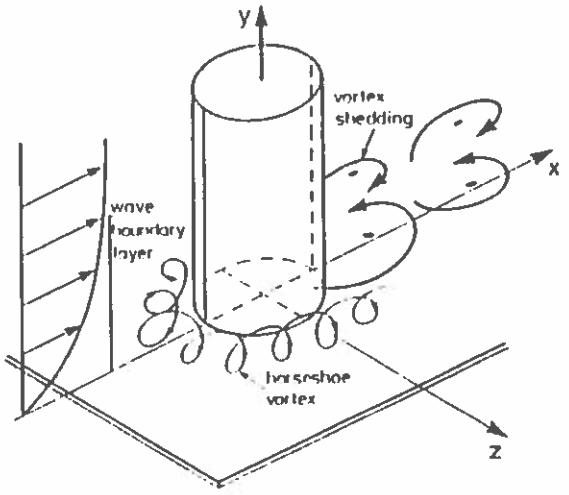

FIG. 1. Near-Bed Flow Around Pile

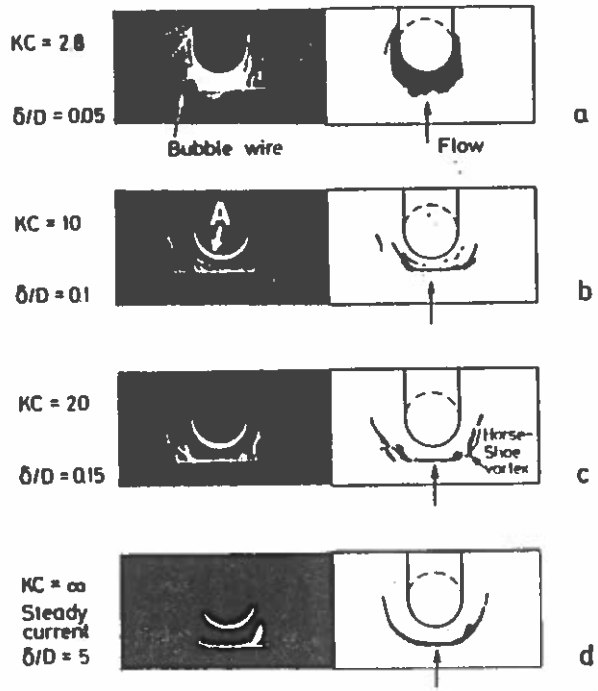

FIG. 2. Near-Bed Flow Picture at Upstream Side of Pile. A: Lowermost Portion of Cylinder (Made of Transparent Material) through which Light Spreads Out. The Horseshoe Vortex for (*b*), (*c*) and (*d*). ωt = 100° in (*a*), 130° in (*b*), and 120° in (*c*)

surrounding of the cylinder means that the horseshoe vortex is nonexistent [Fig. (2*a*)].

As is seen, the horseshoe vortex does not exist for the case where the wave boundary-layer thickness is the smallest [Fig. 2(*a*)]. As the wave boundary-layer thickness increases, however, the horseshoe vortex becomes more and more pronounced, [Figs. 2(*b*)–2(*d*)].

In Fig. 3, results are plotted of the present flow visualization analysis. The figure indicates that no horseshoe vortex exists for KC numbers below 6. The horseshoe vortex first comes into existence when KC becomes 6 and is maintained over a larger and larger span of ωt, thus it becomes more and more pronounced, as the KC number is increased. This is a direct consequence of the effect of the wave boundary layer thickness in relation to the pile diameter. As the KC number increases, the thickness of the wave boundary layer increases, and consequently the horseshoe vortex becomes more pronounced.

Vortex Shedding

The vortex shedding occurs at the lee side of the pile as a result of the interaction between the two shear layers issuing from the side edges of the pile. The vortex shedding pattern in oscillatory flows is governed primarily by the KC number (Williamson 1985).

Fig. 4 shows the vortex shedding pattern at the downstream side of the cylinder obtained for the test where KC = 20. The results of the present flow visualization analysis indicate that no vortex shedding occurs for KC below 6. This result is in agreement with that corresponding to a free cylinder (Williamson 1985). For KC > 6, a vortex street is formed at the lee side of the pile by the vortices shed from the pile. The streamwise extent of this street, L, is increased linearly with KC, corresponding to

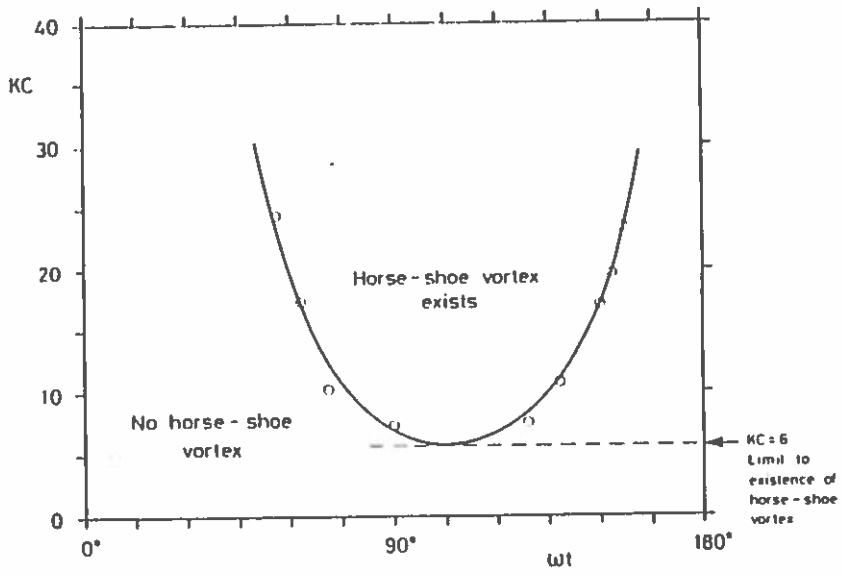

FIG. 3. Diagram Showing at which Value of ωt Horseshoe Vortex Exists

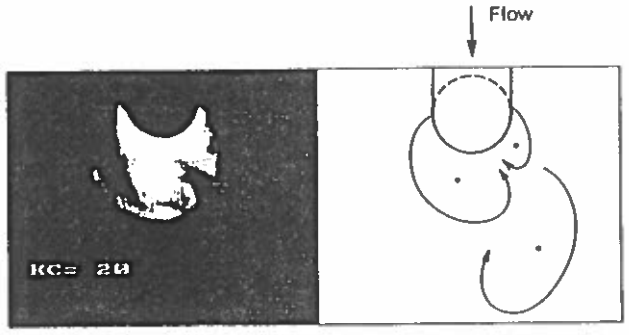

FIG. 4. Near-Bed Flow Picture at Downstream Side of Pile. Vortex Shedding. ωt = 115°

$$\frac{L}{D} = 0.3\mathrm{KC} \qquad (6)$$

The preceding equation is based on the present flow visualization data.

Bed Shear Stress

Figs. 5 and 6 present the bed shear stress data where the bed shear stress is plotted against the streamwise and transverse distances from the pile in the form of the amplification factor defined by

$$\alpha = \frac{\max|\tilde{\tau}_0|}{\tilde{\tau}_{0m}} \quad \ldots\ldots\ldots\ldots\ldots\ldots\ldots\ldots\ldots\ldots\ldots\ldots\ldots\ldots\ldots\ldots\ldots\ldots\ldots\ldots\ldots\ldots (7)$$

in which $\tilde{\tau}_0$ = the mean bed shear stress in the presence of the pile; and $\tilde{\tau}_{0m}$ = the maximum value of the undisturbed mean bed shear stress.

Fig. 7, on the other hand, illustrates how, at a given location, the amplification factor varies with the KC number.

Results of the Scour Experiments and Analysis

Fig. 8 gives a view of the scour hole corresponding to test 17 at stage t = 10 min in which t = the time measured from the instant where the onset of scour occurs. The scour hole has a shape of a truncated cone. As is seen from the figure, the streamwise extents and the transverse extents of the

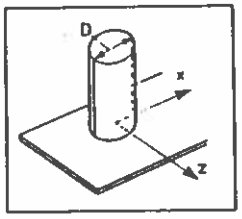

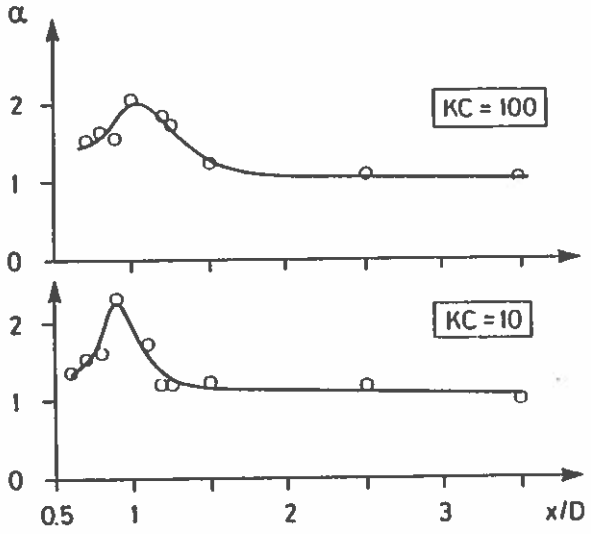

FIG. 5. Bed Shear-Stress Amplification with Respect to Streamwise Distance from Pile Along the x-Axis

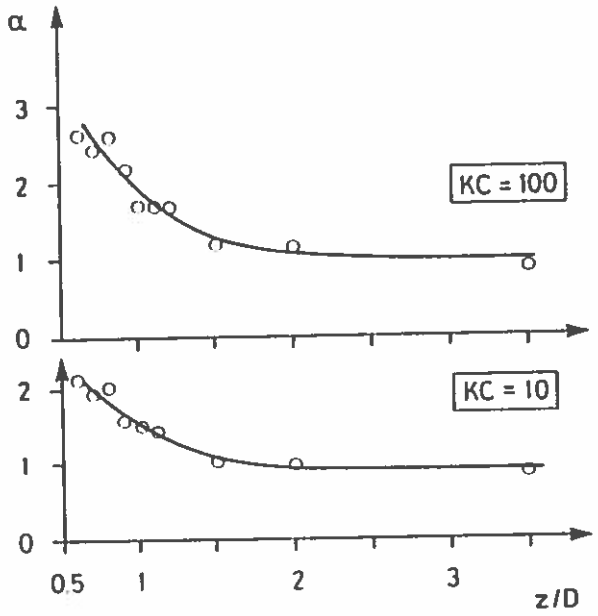

FIG. 6. Bed Shear-Stress Amplification With Respect to Transverse Distance from Pile along z-Axis

scour hole fit quite well with the bed shear-stress picture given in Figs. 5 and 6.

Fig. 9 gives an example, illustrating how the scour depth develops with respect to time. Note that the scaling used to normalize the time, namely $D^2/\sqrt{g(s-1)d^3}$, has been obtained from dimensional considerations.

The equilibrium scour depth S is obtained when the sediment transport in the scour hole is equal to the sediment transport far from the pile. This depth normalized by the pile diameter may depend on the following non-dimensional parameters:

$$\frac{S}{D} = \frac{S}{D}(\theta, \mathrm{Re}, k^*, \mathrm{KC}) \quad \ldots\ldots\ldots\ldots\ldots\ldots\ldots\ldots\ldots\ldots\ldots\ldots\ldots\ldots\ldots\ldots\ldots\ldots\ldots\ldots\ldots\ldots (8)$$

in which $k^* = k/D$, k being the surface roughness of the pile.

Fig. 10 tests the dependence of the normalized equilibrium scour depth upon the Shields parameter θ and the Re number, using the data in Table 1.

As far as the influence of θ is concerned, this should be examined in two different categories: the clear-water case where the sediment far from the pile is not moving, and the live-bed case where it is in motion. It can be argued that, in the case of live bed, the variation of S/D with θ is weak, as has been discussed by the authors in the case of scour below a pipeline (Sumer and Fredsøe, 1990). The data plotted in Fig. 10 correspond to the live-bed category. Examination of Fig. 10 indicates that although there is a very weak tendency that S/D assumes slightly larger values with increasing θ in the upper two diagrams, this dependency does not even exist regarding the rest of the data plotted in the figure.

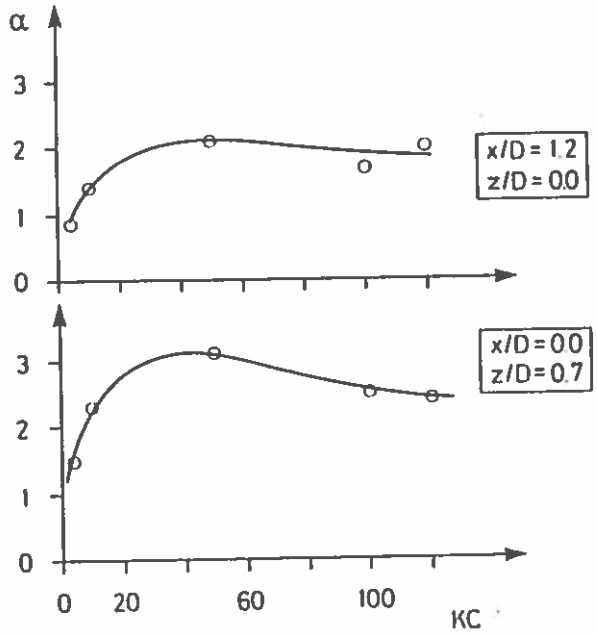

FIG. 7. Bed Shear-Stress Amplification as Function of KC Number

FIG. 8. Photograph of Scour Hole

As for the influence of Re number, this together with the influence of k^+, appear through their effects on the downstream flow of the pile. If the surface of the pile acts as a rough wall, the wake flow is almost unaffected by the Re number, while for a hydraulically smooth-surface pile, some influence of the Re number is expected on the downstream vortex shedding pattern, and thus on the scour depth. However, Fig. 10 indicates practically no Re number dependence, at least for the Re number range of the present data. Nevertheless, the following should be noted. For Re number around $10^5 - 3 \times 10^5$, the transition from subcritical to supercritical flow occurs

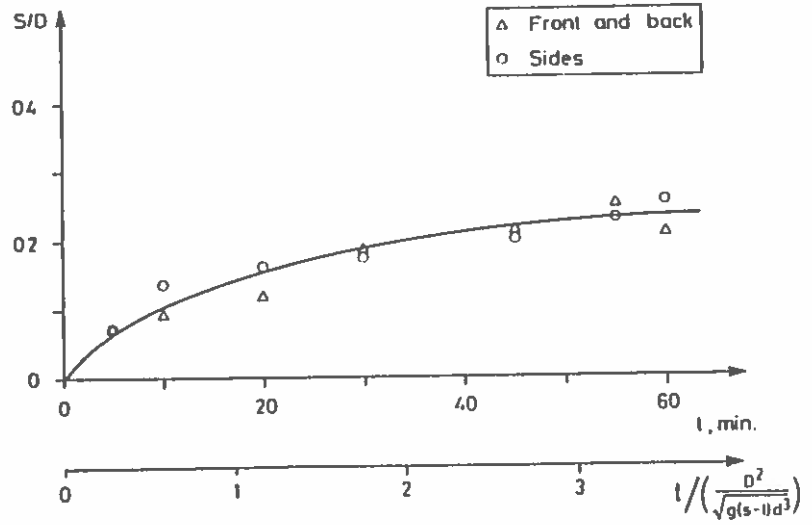

FIG. 9. Time Development of Scour Depth. Test 46

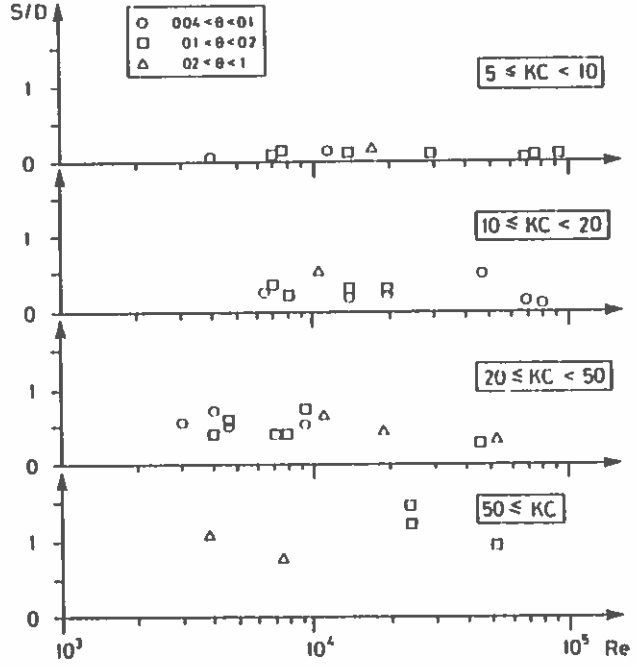

FIG. 10. Equilibrium Scour Depth Normalized with Pile Diameter as Function of θ, Re and KC. Live Bed ($\theta > \theta_{cr}$)

(Schewe 1983; Sumer and Fredsøe 1989). In a previous study (Sumer and Fredsøe 1990), it was demonstrated that this Re number range coincides with the range where a slight decrease in the scour depth occurs for the scour below a pipeline. As in the pipeline situation, a small decrease in the scour depth might be expected for this Re number range for the present case, too. However, it was not possible to verify this by the available experimental facility.

KC Dependence

The KC number in the formulation of the process makes its way through the two effects: (1) The vortex shedding at the lee side of the pile; and (2) the horseshoe vortex formed at the bed at the upstream side of the pile.

Observations show that the vortices shed from the pile erode the bed in such a way that each shed vortex acts like a cyclone, sweeping the sediment grains into its core region where the grains are lifted into the upper portion of the vortex by the updraft. Since the extension of the vortex shedding pattern plus the formation of shed vortices, including their circulation, are governed primarily by the KC number, it might therefore be expected that the resulting scour itself is governed mainly by this parameter, too. It should be noted that there are two other parameters, namely Re and k^*, which are involved in the process of formation and extension of the vortex shedding pattern. However, their role, regarding the formation and extension of the vortex shedding pattern, when compared with that of KC number, appears to be of secondary importance and therefore their influence in the resulting scour is insignificant, as has been demonstrated in the previous subsection.

The horseshoe vortex, on the other hand, is effective in eroding the bed at the upstream side of the pile. It is clear from the previous section that the formation and extension (both in space and in time) of the horseshoe vortex is also governed by the KC number. Thus it might be expected that the scour induced by the horseshoe vortex is governed by the same parameter, namely the KC number.

Fig. 11 shows the variation in the normalized equilibrium scour depth with the KC number. The figure clearly demonstrates that the normalized scour depth correlates remarkably well with the KC number. The figure further demonstrates the following.

1. The scour depth is practically nil for the values of KC number below 6. This is explained as follows. First of all, as mentioned previously, both the vortex shedding and the horseshoe vortex are nonexistent for this range of KC number, thus their contribution to the scour should be zero. The scour may still occur, however, simply because of the increase in the local velocities caused by the apparent contraction of the streamlines around the pile. Yet, for small KC numbers such as KC < 6, Fig. 7 indicates that this increase in the local velocities is insignificant; indeed, the bed shear stress in the immediate neighborhood of the pile appears to be quite close to its undisturbed value for such small KC numbers, so the scour at these low KC numbers should be expected to be insignificant, as observed in Fig. 11.
2. The scour depth increases with increasing KC number. This increase is partly due to the increased extension of the lee wake [(6)] and partly due to the increased presence and strength of the horseshoe vortex with increasing KC number.
3. The scour depth approaches a constant value for large values of KC num-

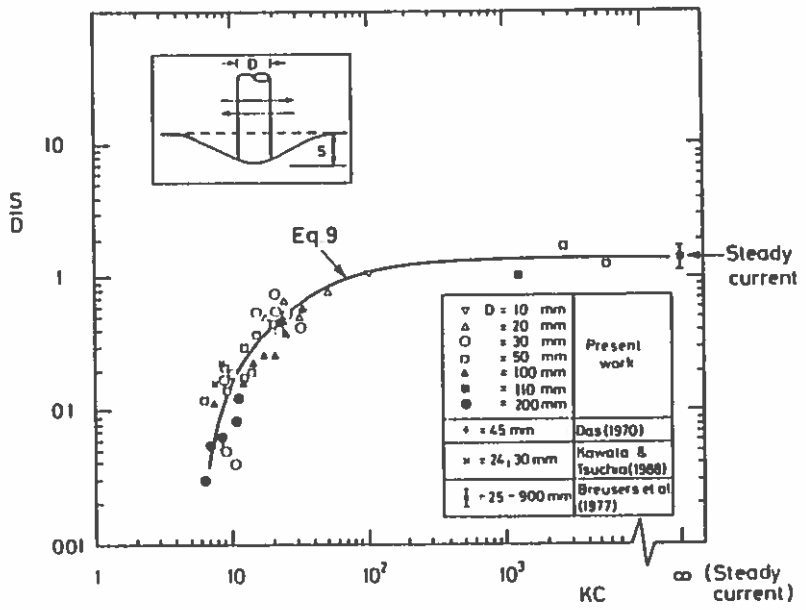

FIG. 11. Equilibrium Scour Depth versus KC Number. Live Bed ($\theta > \theta_c$)

ber. This is expected, because, for large KC numbers: (1) The contribution of the lee-wake vortices to the equilibrium scour depth is expected to approach a constant value, considering the finite lifetime of the vortices; and (2) the contribution of the horseshoe vortex to the equilibrium scour depth is also expected to approach a constant value since the KC dependence of the horseshoe vortex disappears for large values of KC number.

Since the constant value attained by the normalized scour depth S/D is the same as that obtained for steady currents (namely $S/D \rightarrow 1.3$ as KC $\rightarrow \infty$), it can be concluded that the contribution to the equilibrium scour depth for large KC numbers is predominately coming from the horseshoe vortex.

The scour data in Fig. 11 can be represented by the following expression:

$$\frac{S}{D} = 1.3\{1 - \exp[-0.03(\mathrm{KC} - 6)]\} \qquad \mathrm{KC} \geq 6 \quad \ldots\ldots\ldots\ldots\ldots\ldots (9)$$

This equation is valid for the live-bed conditions ($\theta > \theta_c$).

Scale Effects

The effect of θ and Re number has been discussed in the preceding sections. This section will concentrate on the effect of ripple dimensions on the test results. The wave-generated ripples are present for θ values smaller than about 0.8–1. As is seen from Fig. 11, the pile diameter in the experiments was varied from 10 mm to 200 mm. This facilitated a wide range of ripple-length–to–pile-diameter ratio where the ripple length varied from about half a pile diameter to several pile diameters. Fig. 11 shows that the data points corresponding to this range of ripple-length–to–pile-diameter

ratio collapse onto a common curve, confirming that the ripples are not an essential factor in the scour process. This aspect has been observed also for the scour below marine pipelines (Sumer and Fredsøe 1990). As was pointed out in that study, one reason for this may be the absence of ripples in the immediate neighborhood of the pile (where the flow field disturbed by the pile prevents ripple formation).

Summary and Conclusions

1. The scour around a pile in waves is governed by the action of both lee-wake vortices and the horseshoe vortex.
2. The main parameter that determines the equilibrium scour depth on a live bed is the Keulegan-Carpenter (KC) number.
3. The scour data of the present study, which are presented in Table 1 and Fig. 11, have been obtained for live-bed conditions only.
4. The data indicate that:
   a. The scour around the pile practically ceases to exist for KC below 6.
   b. The scour depth monotonously increases, as the KC number is increased. It approaches its steady-current value, namely $S/D = 1.3$, for KC numbers above approximately 100.
5. The data suggest that the relation between the equilibrium scour depth and the KC number is represented by the expression given by (9).

Acknowledgments

This study is partially supported by the program "Marine Technique" for the Danish Technical Research Council (STVF). We thank Peter Roll, Di Yu, Lars Nicolaisen, and Martin Eskholm for their involvements in the conduct of the scour tests and Michael M. Arnskov for his participation in the flow-visualization study.

Appendix I. References

Breusers, H. N. C., Nicollet, G., and Shen, H. W. (1977). "Local scour around cylindrical piers." *J. Hydr. Res.*, 15(3), 211–252.
Das, M. M. (1970). "A literature review on bed-load transport due to wave action and localized scour in non-cohesive sediments." *Final Report HEL 21-6: A Literature Review on Erosion and Deposition of Sediment near Structures in the Ocean*, H. A. Einstein and R. L. Wiegel, eds., Hydraulic Engrg. Lab., Coll. of Engrg., Univ. of California, Berkeley, Calif.
Eadie, IV, R. W., and Herbich, J. B. (1986). "Scour about a single, cylindrical pile due to combined random waves and a current." *Proc. 20th Coastal Engineering Conference*, ASCE Nov. 9–14, 1858–1870.
Herbich, J. B., Schiller, Jr., R. E., Dunlap, W. A., and Watanabe, R. K. (1984). *Seafloor Scour*. Marcel Dekker, Inc., New York, N.Y.
Hjorth, P. (1975). "Studies on the nature of local scour." *Bulletin Series A, No. 46*, Dept. of Water Resour. Engrg., Lund Inst. of Tech., Univ. of Lund, Sweden.
Jensen, B. L., Sumer, B. M., and Fredsøe, J. (1989). "Turbulent oscillatory boundary layers at high Reynolds numbers." *J. Fluid Mech.*, 206(Sept.), 265–297.
Kawata, Y., and Tsuchiya, Y. (1988). "Local scour around cylindrical piles due to waves and currents combined." *Proc. 21st Coastal Engrg. Conf.*, ASCE, 2(June 20–25), 1310–1322.
Palmer, H. D. (1969). "Wave-induced scour on the sea floor." *Proc. of the Civ. Engrg. in the Oceans II*, ASCE (Dec.), 703–716.
Schewe, G. (1983). "On the force fluctuations acting on a circular cylinder in cross-flow from subcritical up to transcritical Reynolds numbers." *J. Fluid Mech.*, 133(Aug.), 265–285.
Schlichting, H. (1979). *Boundary-layer theory*. 7th Ed., McGraw-Hill Book Company.
Sumer, B. M., and Fredsøe, J. (1989). "Effect of Reynolds number on vibration of cylinders." *J. Offshore Mech. and Arctic Engrg.*, 111(May), 131–137.
Sumer, B. M., and Fredsøe, J. (1990). "Scour below pipelines in waves." *J. Waterways, Port, Coastal, and Ocean Engrg.*, ASCE, 116(3), 307–323.
Wang, R.-K., and Herbich, J. B. (1983). "Combined current and wave-produced scour around a single pile." *COE Report No. 269*, Texas Engrg. Experiment Station, Dept. Civ. Engrg., The Texas A&M Univ., College Station, Tex.
Williamson, C. H. K. (1985). "Sinusoidal flow relative to circular cylinders." *J. Fluid Mech.*, 155(June), 141.

Appendix II. Notation

The following symbols are used in this paper:

D = pile diameter;
d = sediment size;
f = friction factor;
f_w = wave frequency;
g = acceleration due to gravity;
k = roughness height of pile surface;
k^* = roughness height of pile surface normalized by pile diamater;
l = length of streamwise extension of lee-wake vortices;
Re = pile Reynolds number [(5)];
S = scour depth;
s = specific gravity of sediment;
T = wave period;
t = time from onset of scour;
U_m = maximum value of outer oscillatory flow velocity;
U_{fm} = maximum value of undistributed bed shear velocity;
x,y,z = coordinates axes (see Fig. 1);
α = bed shear-stress amplification factor [(7)];
δ = boundary layer thickness in absence of pile;
θ = Shields parameter [(1)];
$\tilde{\tau}_0$ = mean bed shear stress in presence of pile;
$\tilde{\tau}_{0m}$ = maximum value of undisturbed mean bed shear stress;
ν = kinematic viscosity; and
ω = angular frequency of the wave motion [(3)].

Time Scale for Wave/Current Scour Below Pipelines

J. Fredsøe, B.M. Sumer and M.M. Arnskov

Institute of Hydrodynamics and Hydraulic Engineering (ISVA)
Technical University of Denmark

International Journal of Offshore and Polar Engineering
Vol. 2, No. 1, March 1992 (ISSN 1053-5381)

Time Scale for Wave/Current Scour Below Pipelines

J. Fredsøe, B.M. Sumer* and M.M. Arnskov
Institute of Hydrodynamics and Hydraulic Engineering (ISVA), Technical University of Denmark, Lyngby

ABSTRACT

A nondimensional formula has been developed for the time scale of the scour process below a marine pipeline, based on the presently available data. The main part of the data originates from ISVA. Both the current case and the pure-wave case are considered. The results indicate that the nondimensional time scale is proportional to the -5/3 power of the Shields parameter. In the study, the time scale of scour, involving a change in the wave climate, has also been investigated. The results indicate that the time scale is governed by the Shields parameter plus the two Keulegan-Carpenter numbers corresponding to the waves before and after the change takes place.

NOMENCLATURE

d	: sand size
D	: pipe diameter
f	: friction factor
f_w	: wave frequency
g	: acceleration due to gravity
KC	: Keulegan-Carpenter number (Eq. 2)
KC_{final}	: KC number following change in wave climate
$KC_{initial}$	: KC number prior to change in wave climate
s	: specific gravity of sediment
S	: scour depth
S_o	: equilibrium scour depth
t	: time
T	: time scale of scour process
T^*	: nondimensional time scale of scour process (Eq. 6)
T_w	: wave period
U	: flow velocity
U_f	: bed shear velocity
U_m	: maximum outer flow velocity in waves
U_{fm}	: maximum bed shear velocity in waves
ν	: kinematic viscosity
θ	: Shields parameter (Eq.1)
θ_{final}	: Shields parameter following change in wave climate
$\theta_{initial}$	: Shields parameter prior to change in wave climate

INTRODUCTION

When a pipeline is laid on an originally plane bed, scour will take place below the pipeline due to the action of waves and current, where the scour process will eventually attain a fully developed stage.

The scour depth corresponding to this fully developed stage has been studied quite extensively for steady currents — Kjeldsen et al. (1973), Bijker and Leeuwestein (1984) and Mao (1986), among others, for a fixed pipe, and Sumer et al. (1988) and Kristiansen (1988) for a vibrating pipe — and more recently for waves — Sumer and Fredsøe (1990).

The purpose of the present study is to investigate the time scale of the scour process. The study covers also the transitional scour processes involving changes in wave climate.

FULLY DEVELOPED STAGE OF SCOUR PROCESS

In steady currents, the fully developed stage of the scour process is governed by three parameters, namely the Shields parameter θ, the relative roughness k/D, and Reynolds number UD/ν. Here U = the flow velocity, D = the pipe diameter, ν = the kinematic viscosity, and the Shields parameter is defined by:

$$\theta=\frac{U_f^2}{g(s-1)d} \tag{1}$$

in which U_f = the friction velocity, g = the acceleration due to gravity, s = the specific gravity of sand, and d = the sand size. However, the data indicate that the dependence on the Shields parameter is quite weak (when the scour takes place on a live bed), while the dependence on the relative roughness and Re number is insignificant. See Sumer and Fredsøe (1990), which collected the data from Kjeldsen et al. (1973), Lucassen (1984), Mao (1986) and Kristiansen (1988). For all practical purposes, the following relation can be used as the design equation, to predict the equilibrium scour depth in steady currents:
$S_o/D = 0.6 \pm 0.1$ in which the second figure indicates the standard deviation.

In waves, on the other hand, there is one additional parameter, namely the Keulegan-Carpenter number, KC. Here KC is defined by:

$$KC=\frac{U_m T_w}{D} \tag{2}$$

in which T_w = the wave period and U_m = the maximum outer flow velocity. Sumer and Fredsøe (1990) present the data plotted as a function of KC number, which indicate that there is a strong correlation between the equilibrium scour depth and the KC number. Based on the data, a design equation was established for the equilibrium scour depth. This equation reads:

$$S_o / D=0.1\sqrt{KC} \tag{3}$$

---

* ISOPE Member.

Received November 27, 1990; revised manuscript received by the editors January 14, 1992. The original version (prior to the final revised manuscript) was presented at The First International Offshore and Polar Engineering Conference (ISOPE-91), Edinburgh, United Kingdom, August 11-16, 1991.

KEY WORDS: Scour, pipeline, time scale.

The equation was found to be applicable from KC numbers around 2 to very large KC numbers, larger than 100.

TIME SCALE

For a pipe originally placed on the seabed, the scour depth develops towards the fully developed stage through a transitional period. Fig. 1 gives two examples, one for the steady-current situation and the other for waves, illustrating how the scour depth develops during this period. It is seen that the time variation of the scour depth can be approximately represented by:

$$S = S_o\left(1 - e^{-\frac{t}{T}}\right) \tag{4}$$

where S_o = the equilibrium scour depth. The quantity T is defined as the time scale of the scour process and represents the time period during which substantial scour develops.

The time scale T can be predicted from the scour-depth-versus-time information, either by calculating the slope of the line to the $S(t)$ curve at $t = 0$ or by integrating $S_o - S(t)$ over time. As Eq. 4 is an approximation only, T has been predicted in both ways in the present analysis. Hereby, the sensitivity in estimating T can be judged.

TIME SCALE FOR STEADY CURRENT

On dimensional grounds, the time scale can be written in the following functional form:

Pipe diameter D (mm)	Sand size d (mm)	Flow velocity U (cm/s)	Shear velocity U_f (cm/s)	Shields parameter θ	Time scale[1] T (s)	T*
500	0.074	25	0.98	0.08	1.1×10^4	0.12
500	0.074	35	1.32	0.15	2.3×10^4	0.23
500	0.074	45	1.64	0.22	2.5×10^4	0.26

[1] Time scale T here is predicted only from area information. No attempt has been made to predict T from slope information due to uncertainty inherent in diagram given in Kjeldsen et al.

Table 1 Experimental data on time scale of scour process in *steady current*. Bed is originally plane, and initial gap between pipe and bed is nil (Kjeldsen et al., 1973).

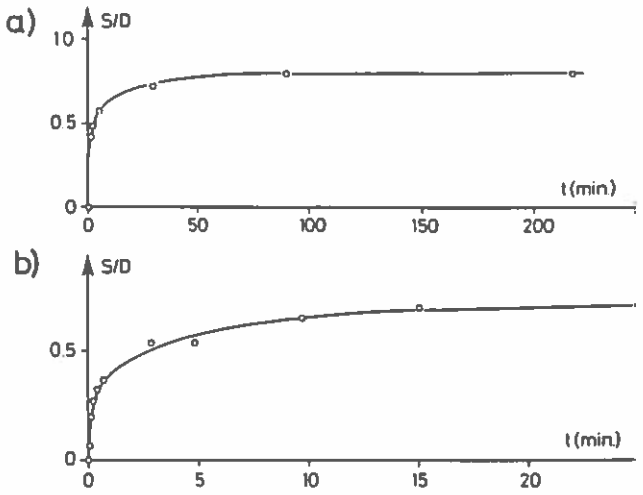

Fig. 1 Time development of scour depth. (a) Steady current. θ = 0.098, D = 100 mm (Mao, 1986). (b) Waves. θ = 0.035, KC = 27 D = 30 mm.

$$T^* = T^*(\theta) \tag{5}$$

in which T^* = the normalized time scale defined by:

$$T^* = \frac{\left[g(s-1)d^3\right]^{1/2}}{D^2} T \tag{6}$$

The time scale predicted from the scour-depth-versus-time information given by Kjeldsen et al. (1973) and Mao (1986) is plotted in the preceding nondimensional form Eq. 5 in Fig. 2. The test conditions and the results are summarized in Tables 1 and 2.

Fig. 2 indicates that the normalized time scale T^* correlates quite well with the Shields parameter. However, one point of the data by Kjeldsen et al. diverges markedly from the general trend observed in the figure, namely the point corresponding to θ = 0.08.

Although no clear explanation has been found for this discrepancy, the following point should be noted.

In the three tests reported in the study by Kjeldsen et al., the flow velocity is increased systematically, while everything else is maintained unchanged. The θ = 0.08 point corresponds to the lowest velocity where the scour process should develop at the slowest tempo. Whereas the test results indicate quite the opposite. Therefore, caution should be taken when considering this particular data point.

Pipe diameter D (mm)	Sand size d_{50} (mm)	Flow velocity U (cm/s)	Shear velocity U_f (cm/s)	Shields parameter θ	Time scale: From the slope T (s)	From the slope T*	From the area T (s)	From the area T*
100	0.36	35.0	1.7	0.048	1142	3.1	1140	3.1
100	0.36	40.0	1.9	0.065	672	1.9	1360	3.7
100	0.36	50.0	2.4	0.098	269	0.74	504	1.4
50	0.36	63.9	3.2	0.18	26	0.29	19	0.2
50	0.36	75.6	3.8	0.25	24	0.26	18	0.2
50	0.36	86.9	4.4	0.33	16	0.18	10	0.11
50	0.36	98.9	5.0	0.43	12	0.13	10	0.11

Table 2 Experimental data on time scale of scour process in *steady current*. Bed is originally plane and initial gap between pipe and bed nil (Mao, 1986).

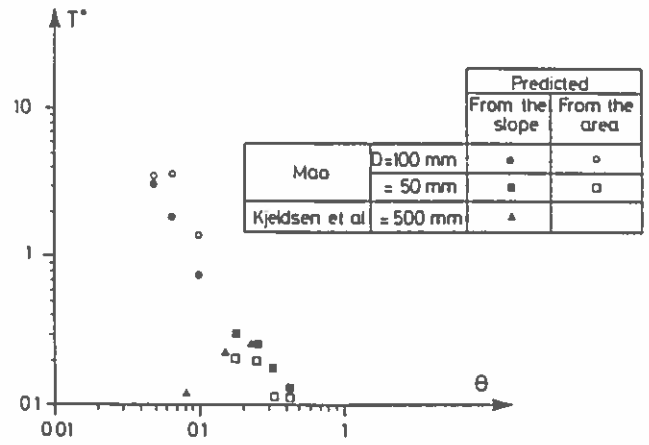

Fig. 2 Nondimensional plot of time scale against Shields parameter. *Steady current.* Note that bed is originally plane, and gap between pipe and bed is nil.

The figure indicates that the larger the Shields parameter, the smaller the time scale. This is in fact what is expected. Because the larger the Shields parameter, the larger the sediment transport due to scouring, therefore the shorter the time period during which a substantial change in the scour depth will occur.

TIME SCALE FOR WAVES

In the case of waves, one additional parameter may be involved in the nondimensional formulation of the time scale in Eq. 5, namely the Keulegan-Carpenter number KC:

$$T^* = T^*(\theta, KC) \tag{7}$$

To study the effect of each parameter on the time scale, the data obtained in our earlier work (Sumer and Fredsøe, 1990) have been analyzed and the time scales have been predicted from both the previously mentioned slope method and the area method, except a few cases where the area method could not be implemented due to uncertainties involved. The test conditions and the results are summarized in Table 3. Although the details of the experiments are given in the preceding reference, the following points about the experimental setup should be mentioned. The experiments were carried out in a 0.6-m-wide wave flume. The mean water depth was held constant at 40 cm. The development of the scour hole in every test was monitored by video. Velocity measurements were made with a DANTEC one-component laser Doppler anemometer.

Fig. 3 gives the nondimensional time scale data plotted against the Shields parameter θ for different groups of KC number. Here, θ is defined by Eq. 1, but U_f is replaced by the maximum bed shear velocity U_{fm}, which is calculated by:

$$U_{fm} = U_m \sqrt{f/2} \tag{8}$$

where f = the friction coefficient for the wave boundary layer. This is calculated by Fredsøe's method (1984).

Fig. 3 indicates that while the final scour depth depends mainly on KC, the normalized time scale is governed by the Shields parameter.

In Fig. 4 are plotted the wave data together with the steady-current data. It is apparent that the two sets of data collapse fairly well. This may be attributed to the fact that the lee-wake scour — the key element in the wave induced scour — is insignificant at the initial stage of the scour process.

Finally, the relation between T^* and θ in Fig. 4 can be represented by the following simple relation:

$$T^* = \frac{1}{50}\theta^{-5/3} \tag{9}$$

CHANGE IN WAVE CLIMATE

In practice, it may be of interest to know the time scale regarding the transitional situations involving changes in wave climate. Fig. 5 gives two examples of scour development in such a situation. In one, the wave climate has changed so that the *KC* number changes from 20 to 6 and θ from 0.092 to 0.13; and in the other,

Pipe diameter D (mm)	Wave frequency f_w (s^{-1})	Maximum outer flow velocity (measured) U_m (cm/s)	Maximum shear velocity U_{fm} (cm/s)	Sand size d_{50} (mm)	Shields parameter θ	Keulegan-Carpenter number KC	Time scale: From the slope T (s)	From the slope T^*	From the area T (s)	From the area T^*
50	0.84	25.2	3.6	0.58	0.13	6	21	0.47	17	0.39
30	0.42	13.7	1.8	0.58	0.035	11	45	2.8	-	-
30	0.81	27.1	3.6	0.58	0.14	11	12	0.75	10	0.64
30	0.82	24.0	2.4	0.18	0.19	11	24	0.25	-	-
30	0.55	22.0	2.7	0.58	0.08	13	24	1.5	56	3.5
30	0.40	17.7	1.7	0.18	0.10	15	138	1.5	-	-
30	0.37	20.9	2.3	0.58	0.06	19	33	2.1	49	3.0
20	0.67	27.1	2.3	0.18	0.18	20	18	0.44	25	0.6
30	0.27	18.4	1.6	0.58	0.03	23	45	2.8	121	7.6
30	0.50	34.7	2.3	0.18	0.19	23	18	0.19	14	0.15
30	0.32	25.7	1.8	0.58	0.035	27	48	3.0	156	9.8
30	0.37	38.8	2.3	0.18	0.19	35	21	0.22	32	0.35
30	0.22	24.0	1.7	0.58	0.03	36	57	3.6	94	5.9
10	0.35	19.5	2.2	0.58	0.05	56	8	4.2	-	-

Table 3 Experimental data on time scale of scour process in *waves*. Bed is originally plane, and initial gap between pipe and bed is nil.

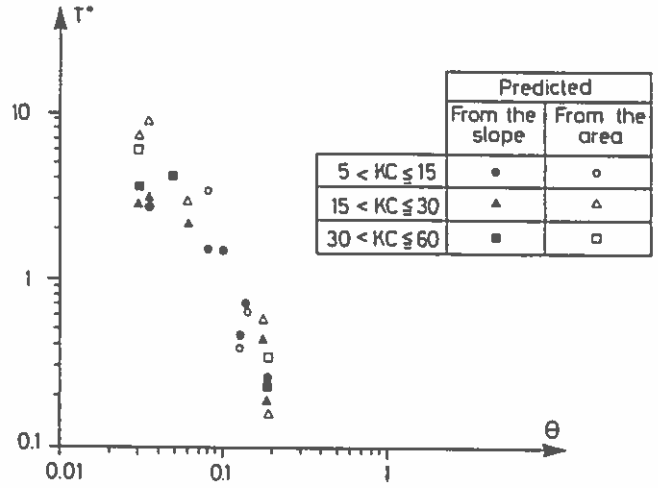

Fig. 3 Nondimensional plot of time scale against Shields parameter. *Waves*. Note that bed is originally plane, and gap between pipe and bed is nil.

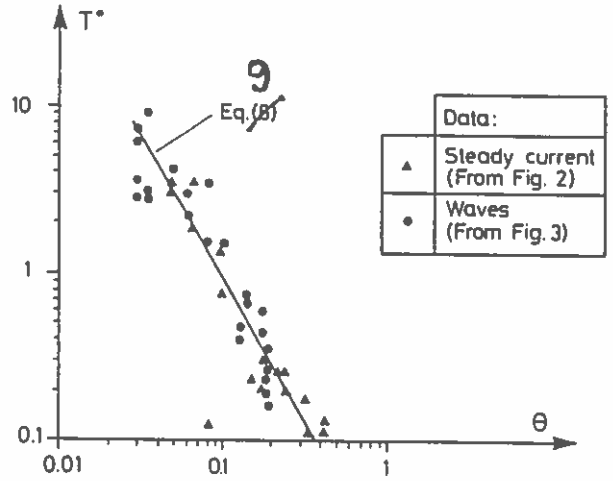

Fig. 4 Nondimensional plot of time scale against Shields parameter. All data. (*Steady-current as well as waves*) Note that bed is originally plane, and gap between pipe and bed is nil.

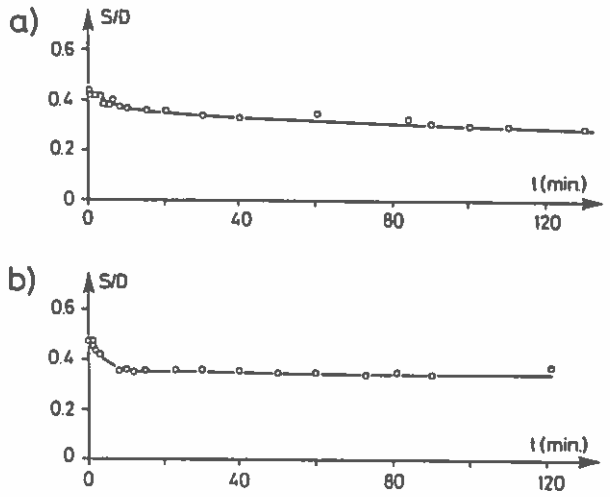

Fig. 5 Time development of scour depth in case of change in wave climate. a) Wave climate is changed suddenly so that KC changes from 19.6 to 5.6 and θ from 0.092 to 0.13. D = 30 mm. d_{50} = 0.19 mm. b) Likewise, KC changes from 19.6 to 9.4 and θ from 0.092 to 0.13. D = 30 mm, d_{50} = 0.19 mm.

KC changes from 20 to 9 and θ from 0.092 to 0.13. These diagrams are taken from a study carried out in the same flume as in the wave experiments described in the previous section. Altogether, eight tests were conducted in that study. The test conditions and the results are summarized in Table 4.

In a typical test, the waves are run with a particular wave period and a particular wave height, and this is done until the scour process reaches an equilibrium situation. The KC number corresponding to this portion of the test is denoted by $KC_{initial}$ and θ by $\theta_{initial}$. Then the wave climate is changed suddenly by changing the wave period and the wave height. The KC number and θ values corresponding to this new portion of the test are denoted by KC_{final} and θ_{final}.

Table 5 compares the equilibrium scour depths with the ones obtained from the expression given in Eq. 3, $S/D = 0.1\sqrt{KC}$, where KC is taken as KC_{final}. As seen, the agreement is quite good. Therefore, it can be concluded that in a transitional situation where the waves change from one climate to another, the equilibrium scour depth is always determined by KC_{final}.

Fig. 6 presents the nondimensional time scale data. The figure clearly shows that the times scale is a function of not only the Shields parameter but also the initial and the final values of the KC number. Obviously the Shields parameter here should be the one imposed on the bed after the wave climate is changed, namely θ_{final}.

The way in which the time scale varies with θ_{final} is exactly the same as in Fig. 4. It is also evident from the figure that the closer the initial and final values of the KC number are, the smaller the time scale will be.

CONCLUSIONS

1) The time scale of the scour process below a pipeline is governed by the Shields parameter, θ. The larger the Shields parameter, the smaller the time scale.

2) The data indicate that the relation between the nondimensional time scale T^* ($= T(g(s\text{-}1)d^3)^{1/2}/D^2$) and the Shields parameter is:

$$T^* = \frac{1}{50}\theta^{-5/3} \tag{10}$$

This relation is applicable to steady currents as well as waves.

3) The time scale in the transitional scour process involving a change in the wave climate is governed by the Shields parameter

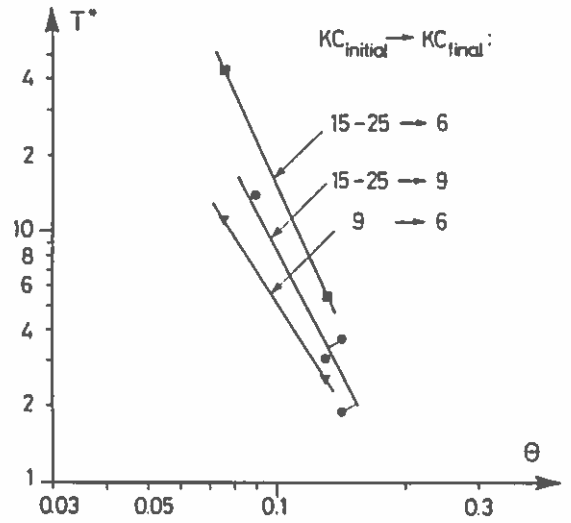

Fig. 6 Nondimensional plot of time scale against Shields parameter. *Change in wave climate*.

Pipe dia. D (mm)	Sand Size d_{50} (mm)	Flow characteristics after the wave climate is changed: Wave freq. f_w (s^{-1})	Max outer flow veloc. U_m (cm/s)	Max shear veloc. U_{fm} (cm/s)	Shields parameter $\theta_{initial}$	θ_{final}	Keulegan-Carpenter number $KC_{initial}$	KC_{final}	Scour depth $(S/D)_{initial}$	$(S/D)_{final}$	Time scale[1] T (s)	Non-dimensional time scale T*
30	0.57	0.88	15.3	2.7	0.053	0.076	15.8	5.8	0.58	0.30	706	43.0
30	0.57	0.88	15.3	2.7	0.077	0.076	9.4	5.8	0.32	0.28	180	11.0
30	0.57	0.69	19.3	2.9	0.053	0.09	15.8	9.4	0.52	0.33	227	13.8
30	0.19	0.91	15.3	2.0	0.092	0.13	19.6	5.6	0.44	0.29	454	5.5
30	0.19	0.91	15.3	2.0	0.12	0.13	9.4	5.6	0.36	0.30	218	2.6
30	0.19	0.59	16.5	2.0	0.092	0.13	19.6	9.4	0.47	0.35	254	3.1
30	0.19	0.70	19.8	2.1	0.094	0.14	25.3	9.2	0.38	0.32	157	1.9
30	0.19	0.70	19.8	2.1	0.12	0.14	21.1	9.2	0.41	0.34	309	3.7

[1] Time scale has been predicted through slope information.

Table 4 Experimental data on time scale of scour process in case of *change* in wave climate

Change in the climate: $KC_{initial}$	KC_{final}	Measured: $(S/D)_{initial}$	$(S/D)_{final}$	Predicted from: $(S/D)_{final} = 0.1\sqrt{KC_{final}}$
15.8	5.8	0.58	0.30	0.24
9.4	5.8	0.32	0.28	0.24
15.8	9.4	0.52	0.33	0.31
19.6	5.6	0.44	0.29	0.24
9.4	5.6	0.36	0.30	0.24
19.6	9.4	0.47	0.35	0.31
25.3	9.2	0.38	0.32	0.30
21.1	9.2	0.41	0.34	0.30

Table 5 Comparison of scour-depth data with expression $S/D = 0.1\sqrt{KC}$

plus the initial and the final Keulegan-Carpenter numbers. The larger the Shields parameter, the smaller the time scale. Also, the closer the initial and the final KC numbers, the smaller the time scale.

ACKNOWLEDGEMENTS

This study is partially supported through the research program Marin Technique of the Danish Technical Research Council (STVF).

REFERENCES

Bijker, EW, and Leeuwestein, N (1984). "Interaction Between Pipelines and the Seabed Under the Influence of Waves and Currents," *Seabed Mechanics*, B. Denness, ed, Graham and Trotman, London, pp 235-242.

Fredsøe, J (1984). "Turbulent Boundary Layer in Wave-Current Motion," *J Hyd Eng ASCE*, Vol 110(8), pp 1103-1120.

Kjeldsen, SP, et al. (1973). "Local Scour Near Offshore Pipelines," *Proc 2nd Int Port and Ocean Eng under Arctic Conditions Conf*, pp 308-331.

Kristiansen, Ø (1988). "Current Induced Vibrations and Scour of Pipelines on a Sandy Bottom," *PhD thesis*, Univ of Trondheim.

Lucassen, RJ (Sept 1984). "Scour Underneath Submarine Pipelines," Rept No PL-4 2A, Netherlands Marine Tech Res, Netherlands Industrial Council for Oceanology, Delft Univ of Tech, pp 117.

Mao, Y (1986). "The Interaction Between a Pipeline and an Erodible Bed," *PhD thesis*, Tech Univ of Denmark, Lyngby.

Sumer, BM, Mao, Y, and Fredsøe, J (1988). "Interaction Between Vibrating Pipe and Erodible Bed," *J Waterway, Port, Coastal and Ocean Eng, ASCE*, Vol 114(1), pp 81-92.

Sumer, BM, and Fredsøe, J (1990). "Scour Below Pipelines in Waves," *J Waterway, Port, Coastal and Ocean Eng, ASCE*, Vol 116(3), pp 307-323.

Influence of Cross Section on Wave Scour Around Piles

B. Mutlu Sumer, Jørgen Fredsøe and
Niels Christiansen

Institute of Hydrodynamics and Hydraulic Engineering
Technical University of Denmark

Influence of Cross Section on Wave Scour around Piles

By B. M. Sumer,[1] N. Christiansen,[2] and J. Fredsøe[3]

Abstract: The study extends the investigation of scour around circular vertical piles in waves, reported in 1992 in two works by Sumer et al. In the present paper, the influence of cross sectional shape of piles on scour is studied. An extensive series of tests was carried out with two kinds of cross sections: a circular cross section, and a square cross section tested at two orientations to the flow (namely, 90° orientation and 45° orientation), therefore giving three different test configurations. The equilibrium scour depth as well as the time scale of the scour process were investigated. Based on the present data, design equations are established relating the equilibrium scour depth, S_e, to the Keulegan-Carpenter number (KC). For a given KC where $KC \gtrsim 100$, the scour depth is the largest for the square pile with 45° orientation and smallest for the square pile with 90° orientation, the circular-cylinder scour lying in between. In all three cases, the equilibrium scour depth normalized by the pile width (S_e/D) increases with increasing KC number. For $KC \gtrsim 100$, however, S_e/D approaches a constant value, which is about 2 for the square piles and about 1.3 for the circular pile. Regarding the time scale of the scour process, this quantity is governed by two parameters, namely the Keulegan-Carpenter number and the Shields parameter. Given the latter two parameters, the time scale was found to be somewhat smaller in the case of the square pile with a 90° orientation than those in the other two cases.

INTRODUCTION

When a pile is placed in an originally plane, erodible bed, scour will take place around it due to the action of waves and current. This process is of importance in connection with the stability of marine structures such as platforms, bridges, subsea templates, and so on. Extensive scour around the structure may reduce its stability, thus leading to its failure.

The process of scour is mainly due to two effects: (1) The structure blocks the flow, leading to increased flow velocity around the structure; and (2) the presence of the structure creates a local system of turbulent vortices (partly the horseshoe vortex, partly downstream vortex shedding), which increases the local transport capacity.

Items 1 and 2 depend strongly on the actual shape of the structure. This can for instance be quite open (like a grid cover of a small subsea structure) leading to only a slight blocking effect, but quite a high level local turbulence. Also, quite often these structures are three-dimensional, which leads to a relative small blocking.

Because the marine structures have a very wide variety of shapes, it is very difficult to give general rules for the expected process of scour in the marine environment.

[1]Assoc. Prof., Tech. Univ. of Denmark, Inst. of Hydrodynamics and Hydr. Engrg., DK-2800 Lyngby, Denmark.

[2]Grad. Student, Tech. Univ. of Denmark, Inst. of Hydrodynamics and Hydr. Engrg., DK-2800 Lyngby, Denmark.

[3]Prof., Tech. Univ. of Denmark, Inst. of Hydrodynamics and Hydr. Engrg., DK-2800 Lyngby, Denmark.

Note. Discussion open until February 1, 1994. To extend the closing date one month, a written request must be filed with the ASCE Manager of Journals. The manuscript for this paper was submitted for review and possible publication on April 6, 1992. This paper is part of the ***Journal of Waterway, Port, Coastal, and Ocean Engineering***, Vol. 119, No. 5, September/October, 1993. ©ASCE, ISSN 0733-950X/93/0005-0477/$1.00 + $.15 per page. Paper No. 3805.

This has been done previously for the special case of scour around cylindrical bridge piers exposed to pure currents, in which the effect of shape and angle of attack has been investigated experimentally; for a review see Breusers et al. (1977) and Hjorth (1975). Hjorth (1977) also measured the bed shear stress distribution around piles with different shapes, as shown in Fig. 1. It is clear that the bed shear-stress distribution (and hence the process of scour) is very different for the three cases considered.

No information, however, exists about the shape effect on scour for structures in the marine environment. Actually, only very few studies are available on wave scour. Oil companies have conducted numerous studies, but unfortunately, they are generally proprietary and not available in the literature. Some field data have been reported by Palmer (1969). Das (1970), Kawata and Tsuchiya (1988), and Chiew (1989) presented a few laboratory tests. In the case of coexisting waves and current, on the other hand, the extensive study made by Herbich and his coworkers [see for example Wang and Herbich (1983), Herbich et al. (1984), and Eadie and Herbich (1986)] can be mentioned.

For the pure wave case, Sumer et al. (1992a) made a detailed experimental investigation of the scour process around a circular pile. In a related work, Sumer et al. (1992b) considered the time scale for the scour around a circular pile. This time scale is of importance with respect to the behavior of the scour depth during a changing wave climate.

The results of these studies have indicated that: (1) The equilibrium scour depth normalized by the pile diameter (S_0/D) is a function of the Keulegan-Carpenter number (KC); (2) S_0/D increases with increasing KC; (3) S_0/D approaches its steady-current value for KC-values above approximately 100; (4) the governing parameters with regard to the time scale of scour are KC and the Shields parameter (θ); and (5) the time scale increases with increasing KC and decreases with increasing θ.

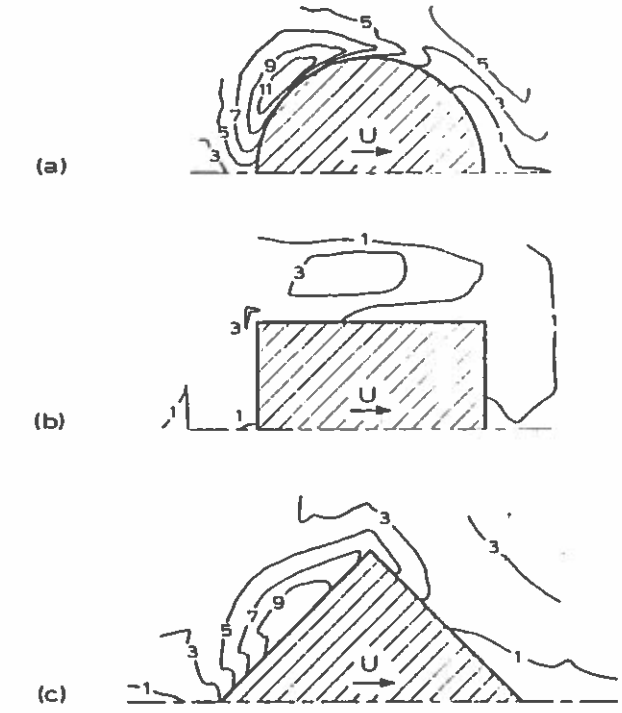

FIG. 1. Amplification in Time-Mean Bed Shear Stress [Flat Bed; Water Depth = 20 cm; Flow Velocity = 30 cm/s; Taken from Hjorth (1975)]

The purpose of the present study is to investigate the simplest extension of the previously studied case of circular pile to that of a pile with a square section [as was done by Hjorth (1975) for the current alone case]. The investigation reveals the importance of this moderate change in the cross-sectional area on the process of scour due to the altered blocking effect and due to the changes in the vortex shedding regime and so on. The study comprises two angles of approach, namely 90° and 45°, the final scour depth, and the time scale for the process are studied.

EXPERIMENTAL FACILITY

Scour Experiments

The experiments of test series No. 1 were carried out in a wave flume (0.6 m in width, 0.8 m in depth, and 26.5 m in length). The mean water depth was maintained constant at 40 cm. Several square-section piles were used, with the size ranging from 9 mm × 9 mm to 40 mm × 40 mm. Also, some additional experiments were carried out with circular piles with the diameter range from 20 mm to 40 mm. One size of sand was used in the tests; namely, with d_{50} = 0.18 mm.

The experiments of test series No. 2 were carried out in a large wave flume, 4 m in width, 1 m in depth, and 28 m in length. The main purpose of these tests was to provide data with a relatively larger size pile model; namely, a 100 mm × 100 mm size pile. The sand size in the tests was d_{50} = 0.18 mm.

A few tests (test series No. 3) were carried out in a 2-m-wide current flume in order to supplement the wave-flume experiments with data representing tidal flow situations. In these experiments the flow direction could be reversed with a period that was long enough for the flow to be considered quasi-steady in each half-cycle. A 40 mm × 40 mm size pile was used in these experiments. Sand-grain size was d_{50} = 0.26 mm. One-directional, steady-current experiments were also conducted for reference purpose.

The development of the scour process was videotaped using two obliquely positioned video cameras in test series 1. This arrangement enabled us to monitor the time development of the scour depth over the whole periphery of the tested pile. In test series 2, intense suspension of sand in the flume and the long distance of the pile from the camera prevented the continuous video monitoring of the scour process. Instead, the waves were stopped every 5 min and the scour depth was measured, again over the whole periphery of the tested pile. In test series 3, the scour process was videotaped as in test series 1; however, only one camera was used, because of experimental constraints. The camera was obliquely positioned and the scour depth over half the periphery of the pile (covering the upstream edge and the side edge of the section) was monitored.

Velocity measurements were made by a DANTEC Laser doppler anemometer (LDA) in test series 1, by an ultrasonic velocity meter in test series 2, and by a propeller in test series 3.

Monochromatic waves were used in the experiments in both test series 1 and test series 2. Waves were produced by a piston-type wave generator.

TABLE 1. Experimental Data

Run Number (1)	Pile (2)	Pile arrangement (degrees) (3)	Sand size d (mm) (4)	Pile width D (mm) (5)	Wave period T_w (s) (6)	Maximum flow velocity (measured) U_m (cm/s) (7)	Maximum shear velocity U_{*m} (cm/s) (8)	Shields parameter θ (9)	Keulegan-Carpenter number KC (10)	Pile Reynolds number R (11)	Nondimensional equilibrium scour depth S_e/D (12)	Nondimensional time scale T^* (13)
(*a*) Test Series 1: Small Wave-Flume Experiments												
1	Square	90	0.18	40	1.6	22	1.9	0.12	9	0.86 × 10^4	0	—
2	Square	90	0.18	40	1.4	31	2.3	0.18	11	1.24 × 10^4	0.05	0.032
3	Square	90	0.18	30	1.6	22	1.9	0.12	12	0.65 × 10^4	0.07	0.022
4	Square	90	0.18	30	2.1	21	1.9	0.11	15	0.63 × 10^4	0.20	0.11
5	Square	90	0.18	20	1.5	20	2.0	0.13	15	0.40 × 10^4	0.23	0.31
6	Square	90	0.18	30	1.4	31	2.3	0.18	15	0.93 × 10^4	0.16	0.21
7	Square	90	0.18	20	1.4	30	2.4	0.19	21	0.59 × 10^4	0.13	—
8	Square	90	0.18	20	2.1	21	1.9	0.11	22	0.42 × 10^4	0.32	0.44
9	Square	90	0.18	20	1.4	31	2.3	0.18	22	0.62 × 10^4	0.35	0.51
10	Square	90	0.18	20	2.7	24	1.9	0.12	33	0.49 × 10^4	0.57	—
11	Square	90	0.18	9	1.4	30	2.4	0.19	46	0.27 × 10^4	0.98	3.2
12	Square	90	0.18	9	2.7	24	1.9	0.12	73	0.22 × 10^4	1.22	2.8
13	Square	45	0.18	57	1.2	33	1.9	0.12	4.5	1.25 × 10^4	0.22	—
14	Square	45	0.18	57	2.0	17	1.6	0.09	6	0.96 × 10^4	0.11	—
15	Square	45	0.18	57	1.6	22	1.9	0.12	9	1.23 × 10^4	0.14	0.036
16	Square	45	0.18	42	2.0	17	1.6	0.09	8	0.71 × 10^4	0.23	—
17	Square	45	0.18	42	1.3	28	2.2	0.17	8	1.16 × 10^4	0.45	0.10
18	Square	45	0.18	42	2.1	21	1.9	0.11	11	0.88 × 10^4	0.42	0.32
19	Square	45	0.18	42	1.4	31	2.3	0.18	11	1.3 × 10^4	0.49	0.18
20	Square	45	0.18	28	1.6	22	1.9	0.12	13	0.60 × 10^4	0.25	0.32
21	Square	45	0.18	28	2.1	21	1.9	0.11	16	0.59 × 10^4	0.45	0.46
22	Square	45	0.18	28	1.4	31	2.3	0.18	16	0.87 × 10^4	0.54	0.24
23	Square	45	0.18	13	2.0	17	1.6	0.09	26	0.22 × 10^4	0.62	—
24	Square	45	0.18	28	2.7	24	1.9	0.12	23	0.68 × 10^4	0.58	0.77
25	Square	45	0.18	13	1.4	30	2.4	0.19	32	0.39 × 10^4	1.0	0.86
26	Square	45	0.18	13	2.7	24	1.9	0.12	51	0.32 × 10^4	1.08	0.71
27	Circular	—	0.18	40	1.4	31	2.3	0.18	11	1.2 × 10^4	—	0.13
28	Circular	—	0.18	20	2.1	21	1.9	0.11	15	0.63 × 10^4	—	0.91
29	Circular	—	0.18	20	1.5	20	2.0	0.13	15	0.40 × 10^4	—	1.34
30	Circular	—	0.18	30	1.4	31	2.3	0.18	15	0.93 × 10^4	—	0.26
31	Circular	—	0.18	20	2.1	21	1.9	0.11	22	0.42 × 10^4	—	1.13
32	Circular	—	0.18	30	2.2	30	2.0	0.14	22	0.90 × 10^4	—	0.48
33	Circular	—	0.18	20	1.4	31	2.3	0.18	22	0.62 × 10^4	—	0.38
(*b*) Test Series 2: Large Wave-Flume Experiments												
34	Square	90	0.18	100	1.9	23.1	2.0	0.14	4.4	2.3 × 10^4	≈0	—
35	Square	90	0.18	100	3.0	25.2	1.8	0.11	7.6	2.5 × 10^4	≈0	—
36	Square	90	0.18	100	4.5	30.1	1.8	0.11	13.5	3.0 × 10^4	0.1	—
37	Square	90	0.18	100	4.5	32.6	1.9	0.13	14.7	3.3 × 10^4	0.1	—
38	Square	90	0.18	100	4.5	39.1	2.0	0.14	17.6	3.9 × 10^4	0.2	—
39	Square	90	0.18	100	4.5	46.9	2.3	0.19	21.1	4.7 × 10^4	0.2	—
40	Square	90	0.18	100	4.5	53.3	2.5	0.22	24.0	5.3 × 10^4	0.2	—
41	Square	90	0.18	100	5.9	50.0	2.4	0.19	29.5	5.0 × 10^4	0.325	—
42	Square	45	0.18	141	1.9	23.1	2.0	0.14	3.1	3.3 × 10^4	0.03	—
43	Square	45	0.18	141	3.0	25.2	1.8	0.11	5.3	3.6 × 10^4	0.06	—
44	Square	45	0.18	141	4.5	30.1	1.8	0.11	9.6	4.2 × 10^4	0.20	—
45	Square	45	0.18	141	4.5	32.6	1.9	0.13	10.4	4.6 × 10^4	0.23	—
46	Square	45	0.18	141	4.5	39.1	2.0	0.14	12.4	5.5 × 10^4	0.3	—
47	Square	45	0.18	141	4.5	46.9	2.3	0.19	21.1	6.6 × 10^4	0.41	—
48	Square	45	0.18	141	4.5	53.3	2.5	0.22	16.9	7.5 × 10^4	0.32	—
(*c*) Test Series 3: Current-Flume Experiments												
49	Square	90	0.26	40	480	40.0	2.6	0.16	4,800	1.6 × 10^4	2.2	—
50	Square	45	0.26	57	480	40.0	2.6	0.16	6,720	2.3 × 10^4	1.74	—
51	Square	90	0.26	40	∞	40.0	2.6	0.16	∞	1.6 × 10^4	2.3	—
52	Square	90	0.26	40	∞	40.0	2.6	0.16	∞	1.6 × 10^4	1.90	—
53	Square	45	0.26	57	∞	40.0	2.6	0.16	∞	2.3 × 10^4	1.88	—
54	Square	45	0.26	57	∞	40.0	2.6	0.16	∞	2.3 × 10^4	1.75	—

A "Dutch-beach" type of wave absorber at the downstream end of the wave flume was used, to handle the reflection.

Before the start of each test the bed was leveled off. The test continued until the scour process attained its equilibrium stage.

Test Conditions

The test conditions, experimental results regarding the scour depth, and the time scale of the scour process are listed in Table 1. In Table 1, the Shields parameter θ is defined by

$$\theta = \frac{U_{fm}^2}{(s-1)gd} \quad \ldots\ldots (1)$$

in which d = sand-grain size; g = acceleration due to gravity; s = relative density of sediment; and U_{fm} = maximum value of the undisturbed bed shear velocity, which is calculated by

$$U_{fm} = \sqrt{\frac{f_w}{2}}\, U_m \quad \ldots\ldots (2)$$

where f_w = wave friction coefficient; and U_m = maximum value of the orbital velocities of water particles at the bed in the absence of the pile, defined by

$$U = U_m \sin(\omega t) \quad \ldots\ldots (3)$$

where ω = angular frequency of waves. For steady-current situations, U_{fm} and U_m are replaced by U_f and U, respectively, in which U_f = undisturbed bed shear velocity; and U = mean flow velocity. Also, in Table 1, the Keulegan-Carpenter number, KC, is defined by

$$KC = \frac{U_m T_w}{D} \quad \ldots\ldots (4)$$

in which T_w = wave period; and D = pile width, i.e. the width of the pile projected on a cross-sectional plane perpendicular to the flow direction. For circular piles, D is obviously the pile diameter.

In Table 1, R = Reynolds number, defined by

$$R = \frac{U_m D}{\nu} \quad \ldots\ldots (5)$$

in which ν = kinematic viscosity; and T^* = normalized time scale defined by

$$T^* = \frac{[g(s-1)d^3]^{1/2}}{D^2}\, T \quad \ldots\ldots (6)$$

where T = time scale of the scour process.

As seen from the table, there are no entries in the column of the equilibrium scour depth in the case of circular cross-section pile (i.e., tests 27–33). The purpose of these latter tests was not to get further scour-depth data [because over 50 test results had been reported in previous work (Sumer et al. 1992a) with regard to the scour depth], but, rather, to get some more data regarding the time scale of scour process, to supplement the time-scale data already reported in Sumer et al. (1992b).

Flow-Visualization Experiments

The objective was to get an understanding of the near-bed flow processes around the pile, such as the horseshoe vortex and the vortex shedding.

The hydrogen-bubble technique was used. The experimental technique was exactly the same as that used in Sumer et al. (1992a). The visualization study made in this latter study for circular piles has in the present study been extended so as to cover the square-section piles for both the 45° and 90° orientations. For these latter experiments a 40 mm × 40 mm size square pile was used. The KC-number range covered was from practically 0 to about 25 where KC was incremented by about 2. The range of pile R number was from 2×10^3 to 9×10^3.

RESULTS OF EXPERIMENTS AND ANALYSIS

Fig. 2 is a sequence of photographs illustrating the time development of the scour holes around the model piles. The sequence indicates that although the scour pattern around the pile is different for different cross sections at the initial stages of the scour process, it eventually attains a constant shape; namely, a truncated cone.

Equilibrium Scour Depth

Fig. 3 depicts the development of the scour depth with respect to time for the square piles. The scour depth in Fig. 3, (and hereafter) is the average scour depth where the average is taken over eight values, four of them corresponding to the scour depth measured at the corners of the pile and the other four corresponding to the scour depths measured at the midpoints of the sides of the pile except in test series 3. In test series 3 the average is taken over four values, covering only half the pile periphery. In the case of circular pile, on the other hand, the average is taken over four values; namely, the downstream and upstream scour depth values, and the two side-edge scour-depth values. As seen from Fig. 3, the scour depth through a transitional period attains an equilibrium value.

Fig. 4 presents the data regarding the equilibrium scour depth for both the 90° arrangement and the 45° arrangement cross sections. The scour depth normalized by the pile width has been plotted in the figure against the Keulegan-Carpenter number following the dimensional considerations in Sumer et al. (1992a). All the tests included in Fig. 4 were carried out under live-bed conditions, i.e. $\theta > \theta_c$, in which θ_c = critical value of θ, corresponding to the initiation of sediment motion on the bed. As seen from the figure, the data are grouped around two different curves; one for the 45° arrangement and the other for the 90° arrangement. Fig. 5, on the other hand, depicts the data in linear scale for small KC numbers, illustrating the behavior of S_0/D, as $KC \to 0$.

Fig. 6 compares the present square-section pile results with the results obtained in Sumer et al. (1992a) for circular piles. To keep the figure relatively simple, the actual data points are not included.

The following observations can be made from the figures.

First, the scour depth is practically nil for very small KC numbers; namely, for $KC < 3$–4 for the square pile with 45° orientation, for $KC < 10$–11 for the square pile with 90° orientation (Fig. 5), and for $KC < 6$–7 for the circular pile [see Sumer et al. (1992a)].

As pointed out in Sumer et al. (1992a), the disappearance of the scour for very small KC numbers is due to the fact that the vortex shedding, the

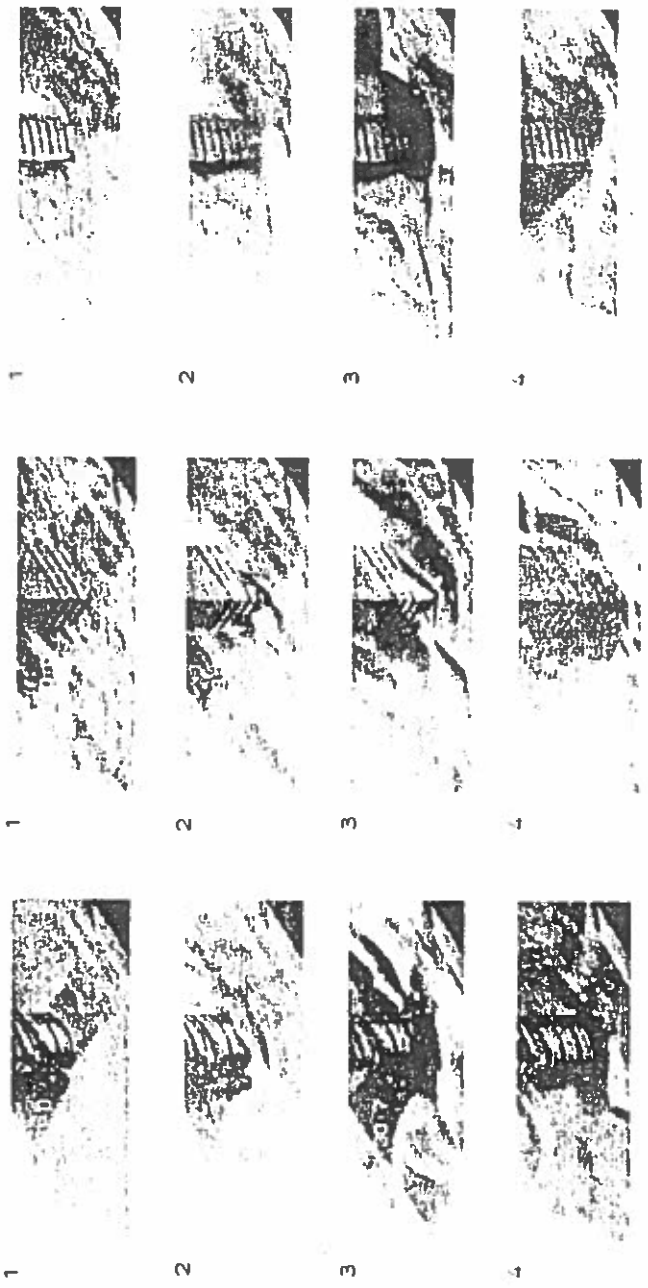

FIG. 2. Time Development of Scour Hole: (a) Circular Pile, D = 3 cm, KC = 15, Run No. 28; (b) Square Pile, 90° Orientation, D = 3 cm, KC = 15, Run No. 4; (c) Square Pile, 45° Orientation, D = 2.8 cm, KC = 15.7, Run No. 21

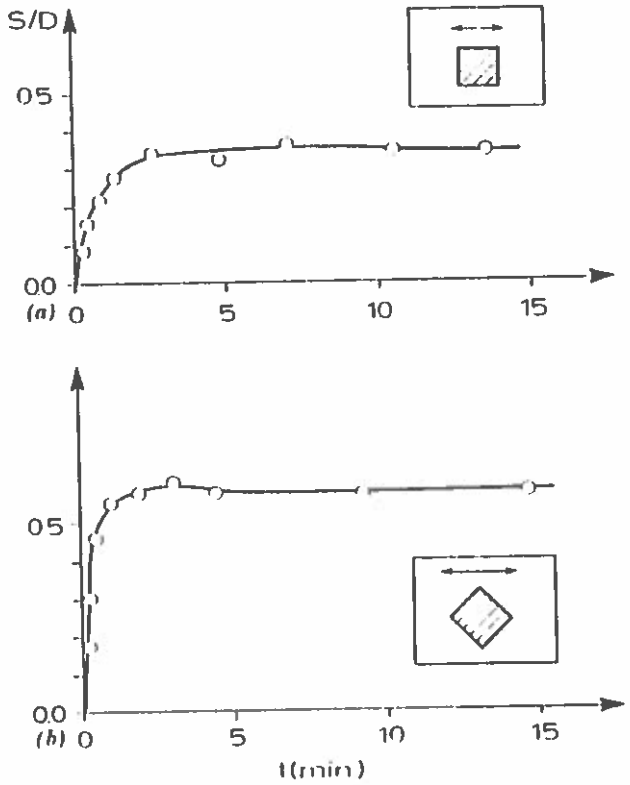

FIG. 3. Time Development of Scour Depth, Run No. 9 for 90° Arrangement Test and Run No. 22 for 45° Arrangement Test

major element in the scour process for small KC numbers, is actually nonexistent in this case. The scour may still occur due to the contraction of streamlines and also due to streaming; yet the bed shear-stress measurements of Sumer et al. (1992a) for circular piles indicated that the bed shear stress in the immediate neighborhood of the pile appears to be quite close to its undisturbed value for such small KC numbers.

The results of the present hydrogen-bubble flow-visualization study has indicated that no vortex shedding occurs for $KC < 4$ in the case of 45° arrangement square pile, for $KC < 6$ in the case of circular pile and for $KC < 11$ in the case of 90° arrangement square pile. The sequences of flow given in Fig. 7, which are taken from video frames, indicates that no vortex shedding occurs for $KC = 10$ and that shedding is existent for $KC = 13$.

The key role of the shedding phenomenon in the scour process is that each shed vortex sweeps the sediment grains into its core region and carries them away from the pile, while it is convected downstream (Fig. 8), thus causing a net scour around the pile. In the absence of shedding, however, the vortices that form behind the pile [Fig. 7(*a*)] sweep the sediment grains into their core region, but do not carry them away from the pile, because they themselves are not removed from the pile due to the absence of the shedding process. Therefore, the end result is that the mean scour around

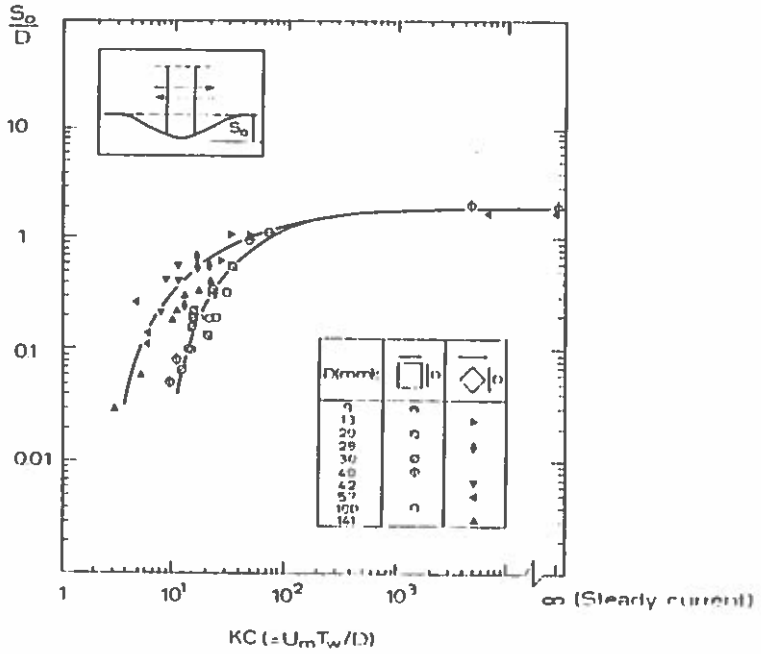

FIG. 4. Equilibrium Scour Depth versus KC Number, Live Bed ($\theta > \theta_{cr}$)

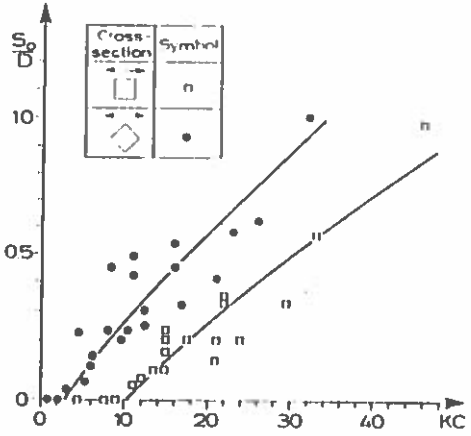

FIG. 5. Equilibrium Scour Depth versus KC Number, Small KC Numbers

the pile will be nil, as is clearly observed from Fig. 6. It is remarkable that the KC numbers at which the scour practically ceases to exist from Fig. 6 (namely, $KC \cong 3$–4 for the 45° arrangement square pile, $KC \cong 6$–7 for the circular pile, and $KC \cong 10$–11 for the 90° arrangement square pile) coincide with the KC numbers at which the vortex shedding disappears.

Second, the scour depth in all the three cases increases with increasing KC number. As demonstrated by Sumer et al. (1992a) for circular piles,

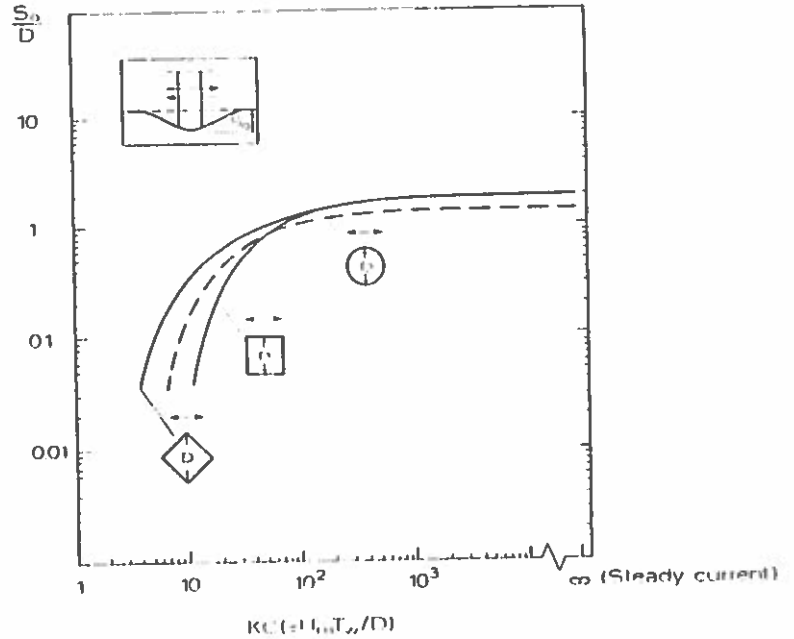

FIG. 6. Equilibrium Scour Depth versus KC Number, Live Bed ($\theta > \theta_{cr}$) [Curve Representing Circular Pile Is Taken from Sumer et al. (1992a)]

this increase is partly due to the increased extension of the lee wake (which is an agglomeration of the shed vortices) and partly due to the increased presence and the increased strength of the horseshoe vortex with increasing KC number.

Third, the difference between the three cases becomes relatively smaller, as KC is increased (Fig. 6). This effect may be attributed to the decreasing importance of the vortex shedding with increasing KC, considering the finite lifetime of the vortices.

Fourth, furthermore, Fig. 6 indicates that the scour depth approaches a constant value (namely, $S_o/D \to 2$ for the square section piles and $S_o/D \to 1.3$ for the circular section piles) for large values of KC number.

Regarding these asymptotic values of the scour depth, there is a substantial decrease in the scour depth in the case of circular piles. This decrease may be linked to the horseshoe-vortex formation. Previous work in connection with circular piles (Sumer et al. 1992a) has indicated that the contribution to the equilibrium scour depth for large KC numbers predominately comes from the horseshoe vortex. The streamwise extent of the horseshoe vortex in the case of circular piles is smaller than in the case of square-section piles (Fig. 9). The smaller the streamwise extent of the horseshoe vortex, the smaller the scour depth. Therefore, the scour depth should be smaller in the case of circular piles.

Finally, the scour data in Fig. 6 can be represented by the following expressions.

Circular pile

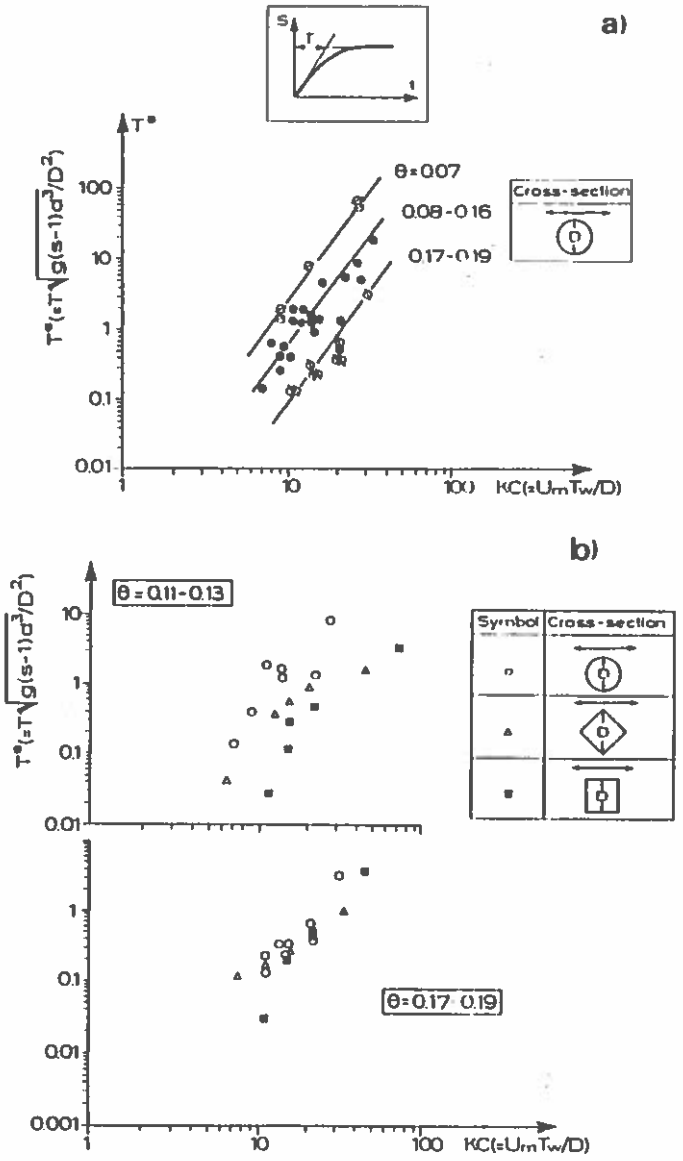

FIG. 10. Time Scale of Scour versus KC, Live Bed ($\theta > \theta_{cr}$): (a) Effect of θ, Circular Pile; (b) Effect of Cross-Sectional Shape

On dimensional grounds, the time scale can be written in the following functional form (Sumer et al. 1992b):

$$T^* = T^*(KC, \theta) \quad \ldots\ldots (11)$$

in which T^* = normalized time scale defined in (6). This relation has been tested against the data obtained for circular piles in Sumer et al. (1992b).

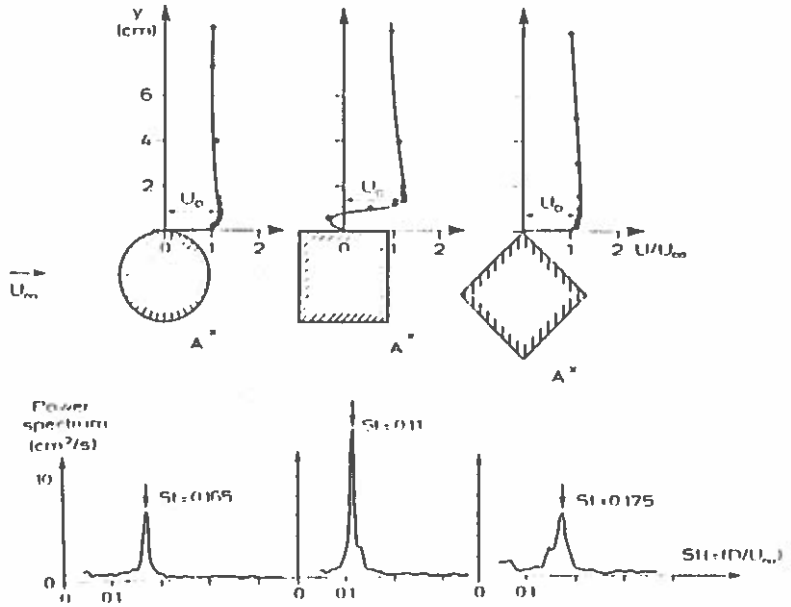

FIG. 11. Velocity Distributions and Power Spectra in Steady Current

The latter data are reproduced in Fig. 10(a), where the present supplementary data (tests 27–33) are also plotted. The following observations can be made from Fig. 10(a).

First, it is seen that the time scale increases with increasing KC. This is related to the fact that the volume of sediment to be eroded increases with increasing KC.

Second, the time scale decreases with increasing θ. This is consistent with the previously obtained knowledge regarding the time scale in scour processes, [e.g. Fredsøe et al. (1992) for time scale of scour process below pipelines]. This behavior is related to the higher capacity of erosion per unit time with increasing θ.

Fig. 10(b) illustrates the cross-section influence on the time scale. The data obtained in the case of square-section piles are plotted in the figure together with the previously mentioned circular-pile data. From the figure, the time scale for the 45° arrangement square pile is not extremely different from that for circular piles, although T^* for the former case appears to be slightly smaller than that for the latter situation. Regarding the 90° arrangement square piles, however, the figure shows that the time scale in this case is somewhat smaller than that for the circular piles. The figure also shows that this discrepancy becomes more pronounced with decreasing θ.

The variation in the time scale with respect to the cross-sectional shape may be related to the strength of the shed vortices. The latter can be approximated by the following relation:

$$\frac{\Gamma}{DU_-} = \frac{1}{4}\left(\frac{U_0}{U_-}\right)^2 \frac{1}{St} \quad \ldots\ldots (12)$$

in which Γ = strength of the vortices shed from a free cylinder, which is

exposed to a steady current; U_c = undisturbed flow velocity, U_0 = potential flow velocity measured at the top of the cylinder boundary-layer at the point of separation in the case of circular and 45° arrangement square sections or, alternatively, at the top of the shear layer issuing from the separation point in the case of 90° arrangement square section (Fig. 11), and S = Strouhal frequency, defined by

$$S = \frac{fD}{U_c} \quad \ldots\ldots (13)$$

in which f = vortex-shedding frequency.

The preceding relation [(12)] stems from

$$\frac{d\Gamma}{dt} = \int_a^b \omega dy = \int_a^b \left(\frac{1}{2} u \frac{\partial u}{\partial y}\right) dy \quad \ldots\ldots (14)$$

in which the right-hand side represents the flux of vorticity, which is fed into a developing vortex behind the pile per unit time and per unit pile length [see Bearman (1984), for instance]. Here the integral limits a and b = levels at which the velocity becomes nil and U_0, respectively.

To estimate the normalized vortex strength $\Gamma/(DU_c)$ from (12) for each cross section, velocity-profile measurements were conducted away from the bed in steady current with U_c = 10.5 cm/s, employing cylinders with D = 4 cm, using a DANTEC one-component laser Doppler anemometer (Fig. 11). Also, the vortex-shedding frequency was measured from the FFT (fast Fourier transform) analysis of the velocity signal received from the cylinder wake (Fig. 11).

The results indicate that U_0/U_c = 1.2–1.3, irrespective of the cross section, while S = 0.165 for circular section and 0.11 for 90° arrangement square section. This will give from (12) the strength of shed vortices as follows: $\Gamma/(DU_c)$ = 2.2 for circular section, while $\Gamma/(DU_c)$ = 3.6 for 90° arrangement square section. In other words, the shed vortices are stronger in the case of 90° arrangement square section than in the case of circular section. The stronger the vortices, the faster the scour process. Therefore, the time scale in the case of 90° square cylinder should be smaller than in the other two cases, as exhibited in Fig. 10.

Furthermore, the previously mentioned velocity measurements have indicated that, in the case of 45° arrangement square section pile, S = 0.175 and $\Gamma/(DU_c)$ = 2.15, meaning that the shed vortices in this case are in almost the same strength as in the case of circular section. This explains why the time scale in the case of 45° arrangement square pile is not extremely different from that of circular pile.

Other Factors Influencing Scour Process

First we consider the equilibrium scour depth. The equilibrium scour depth normalized by the pile width may, in addition to KC and α, depend on the following parameters: θ, R and k^*, where α is the shape factor regarding the cross-sectional shape of the pile, and $k^* = k/D$, k being the surface roughness of the pile. Although the equilibrium scour depth varies with θ strongly in the case of clear-water scour, it can be argued that in the case of a live bed the variation of S_0/D with θ is weak, as has been demonstrated by Breusers et al. (1977) for the current case and by Sumer et al. (1992a) for the wave case.

As for the influence of R and k^*, if the surface of the pile acts as a rough

wall, the wake flow is almost unaffected by the R number, therefore no effect is expected on the scour depth; for a hydraulically smooth-surface pile, a small decrease in the scour depth might be expected for the R number range of 10^5 to 3×10^5 where the transition from subcritical to supercritical flow occurs, as pointed out in Sumer et al. (1992a) in conjunction with scour around circular piles. For square-section piles, however, the flow separation is fixed at the corners, consequently no significant change is expected in the shedding process, thus in the scour depth, with increasing R number.

Regarding the time scale of the scour process, in addition to the studied effects [namely, the effects of KC, α and θ (Fig. 10)] other nondimensional parameters such as R and k^* may influence the end results. As mentioned in the preceding, if the pile is rough, the wake flow will be almost unaffected by the R number, therefore no influence of the R number will be expected on the time scale. If the pile is smooth, however, the wake flow will be influenced by the R number; the Strouhal frequency S will be increased to a value of about 0.45 in the range of $10^5 \lesssim R \lesssim 1.5 \times 10^6$ and then will drop to about 0.15 at $R \simeq 1.5 \times 10^6$, from where it will constantly increase with increasing R, reaching about 0.3 at $R \simeq 7 \times 10^6$ for circular piles (Schewe 1983). This change in S affects the strength of the shed vortices [(12)], therefore the time scale of the scour process might be affected by an increase in R. From (12), it might be anticipated that the time scale may become larger—by a factor of 2 or so for large R numbers ($R \gtrsim 10^6$), particularly for the range $10^5 \lesssim R \lesssim 1.5 \times 10^6$—than Fig. 10 predicts. However, no data are available to verify this. For the square piles, on the other hand, practically no Reynolds-number dependence should be expected because of the fixed separation points at the corners.

Finally, it may be mentioned that the effect of ripple dimensions on the test results has been discussed in Sumer et al. (1992a) in conjunction with the laboratory study of scour around circular piles for a wide range of ripple-length–to–pile-diameter ratio, for which the ripple length varied from about half a pile diameter to several pile diameters; and it was concluded that the ripples are not an essential factor in the scour process.

CONCLUSIONS

The equilibrium scour depth on a live bed normalized by the pile width, S_0/D, is a function of the Keulegan-Carpenter number (KC), based on the pile width. It increases with increasing KC and eventually attains a constant value for large values of KC ($KC \gtrsim 100$).

Given the Keulegan Carpenter number, S_0/D varies with respect to the cross-sectional shape of the pile. For $KC \gtrsim 100$ the scour depth is the largest for the square-section pile with 45° arrangement; and it assumes its smallest value for the square-section pile with 90° arrangement. The scour depth for circular piles lies between the two (Fig. 6). For $KC \gtrsim 100$, the scour depth approaches a constant value, $S_0/D \simeq 2$ for square piles and 1.3 for circular piles.

The empirical relations given in (7)–(9) relating S_0/D to the KC number for the three sections studied may be used as design equations. It is valid only for scour on live beds.

The time scale of the scour process is governed by two parameters, namely the Keulegan-Carpenter number (KC) and the Shields parameter (θ).

Given the Keulegan Carpenter number and the Shields parameter, the time scale varies with the cross-sectional shape of the pile. It is somewhat smaller in the case of square-section pile with 90° arrangement than in the

other two cases studied (the circular pile and the square pile with 45° arrangement).

The study shows the importance of even a moderate change in the cross-sectional shape (such as the one investigated in the present work) on the process of scour.

ACKNOWLEDGMENTS

This study is partially supported by the Marine Technique program of the Danish Technical Research Council (STVF). We thank Di Yu and Jan B. Jakobsen for their involvements in conducting some of the scour tests.

APPENDIX I. REFERENCES

Bearman, P. W. (1984). "Vortex shedding from oscillation bluff bodies." *Ann. Rev. Fluid Mech.*, Vol. 16, 195–222.

Breusers, H. N. C., Nicollet, G., and Shen, H. W. (1977). "Local scour around cylindrical piers." *J. of Hydr. Res.*, 15(3), 211–252.

Chiew, Y. M. (1989). "Local scour at vertical piles under wave action." *9th Australian Conf. on Coast. and Oc. Engrg.*, Adelaide, Australia, 393–396.

Das, M. M. (1970). "A literature review on bed-load transport due to wave action and localized scour in non-cohesive sediments." *A literature review on erosion and deposition of sediment near structures in the ocean: Final Rep. HEL 21-6*, H. A. Einstein and R. L. Wiegel, eds., University of California, Berkeley, Calif.

Eadie, R. W. IV, and Herbich, J. B. (1986). "Scour about a single, cylindrical pile due to combined random waves and a current." *Proc., 20th Coast. Engrg. Conf.*, ASCE, New York, N.Y., 1858–1870.

Fredsøe, J., Sumer, B. M., and Arnskov, M. M. (1992). "Time scale for wave/current scour below pipelines." *Int. J. of Offshore and Polar Engrg.*, 2(1).

Herbich, J. B., Schiller, R. E. Jr., Dunlap, W. A., and Watanabe, R. K. (1984). *Seafloor scour*. Marcel Dekker, Inc., New York, N.Y.

Hjorth, P. (1975). "Studies on the nature of local scour." *Bull. Series A, No. 46*, Univ. of Lund, Lund, Sweden.

Kawata, Y., and Tsuchiya, Y. (1988). "Local scour around cylindrical piles due to waves and currents combined." *Proc., 21st Coast. Engrg. Conf., Vol. 2*, ASCE, New York, N.Y., 1310–1322.

Palmer, H. D. (1969). "Wave-induced scour on the sea floor." *Proc., Civil Engineering in the Oceans II*, ASCE, New York, N.Y., 703–716.

Schewe, G. (1983). "On the force fluctuations acting on a circular cylinder in cross-flow from subcritical to transcritical Reynolds numbers." *J. Fluid Mech.*, 133 (Aug.), 265–285.

Sumer, B. M., Fredsøe, J., and Christiansen, N. (1992a). "Scour around vertical pile in waves." *J. of Wtrwy., Port, Coast., and Oc. Engrg.*, ASCE, 117(1), 15–31.

Sumer, B. M., Christiansen, N., and Fredsøe, J. (1992b). "Time scale of scour around a vertical pile." *Proc., 2nd Int. Offshore and Polar Engrg. Conf.*, International Society of Offshore and Polar Engineers, San Francisco, Calif., Vol. III, 308–315.

Wang, R-K., and Herbich, J. B. (1983). "Combined current and wave-produced scour around a single pile." *COE Rep. No. 269*, Texas A&M University.

APPENDIX II. NOTATION

The following symbols are used in this paper:

D = pile width (see Fig. 6);
d = sediment size;
f = vortex-shedding frequency;
f_w = wave-friction factor;
g = acceleration due to gravity;
KC = Keulegan-Carpenter number (4);
R = Reynolds number for pile (5);
S = scour depth;
S_e = equilibrium scour depth;
S = Strouhal frequency (13);
s = specific gravity of sediment;
T = time scale of scour process;
T^* = normalized time scale of scour process (6);
T_w = wave period;
t = time from onset of scour;
U_m = maximum value of orbital velocity of water particles at bed;
U_{fm} = maximum value of undisturbed bed shear velocity;
U_∞ = undisturbed flow velocity in steady current;
U_0 = potential flow velocity measured at top of pile boundary layer or, alternatively, at top of its related shear layer after separation (Fig. 11);
Γ = vortex strength;
θ = shields parameter (1);
ν = kinematic viscosity; and
ω = angular frequency of wave motion (3).

A Review of Wave/Current-Induced Scour Around Pipelines

B. Mutlu Sumer and Jørgen Fredsøe

Institute of Hydrodynamics and Hydraulic Engineering
Technical University of Denmark

CHAPTER 217

A REVIEW OF WAVE/CURRENT-INDUCED SCOUR AROUND PIPELINES

B.M. Sumer[1] and J. Fredsøe[1]

ABSTRACT

A comprehensive review is presented of scour around pipelines in the case of non-cohesive sediment. The review is organized in four main sections, namely the two-dimensional scour, the three-dimensional scour, the effect of scour on forces on and vibrations of pipelines and the mathematical modelling of scour process. Over sixty works were included in the review.

1. INTRODUCTION

Marine pipelines are used for disposal of industrial and municipal wastewater into the sea, for cooling water in nuclear power plants, and for the transportation of gas and crude oil from offshore platforms. Marine cables, on the other hand, are increasingly used for communication.

Design of marine pipelines and marine cables with regard to their stability is a rather complicated problem. One of the factors which needs to be taken into consideration in the design process is the scour around the pipeline.

The scour around the pipeline is caused by the very presence of the pipeline itself. There are numerous aspects of the problem which need to be addressed during the design process, such as the formation of spans (particularly in determining the maximum extent of spans as well as timing of any remedial action), the self-burial of pipelines, the effect of self-burial on the pipeline stability, just to give a few examples.

A large volume of knowledge has been accumulated on the subject during the last decade or so, as a result of intensive research activities in countries such as Holland, Norway, U.K., U.S.A., Denmark and several others. The purpose of the present paper is to review this research work. Only the non-cohesive sediment bed is considered.

---

[1] Institute of Hydrodynamics and Hydraulic Engineering
Technical University of Denmark

2. TWO-DIMENSIONAL SCOUR

Onset of scour

Consider a pipeline which is laid on an erodible bed. Assume that the bed, soil and flow conditions are the same along the length of the pipe, i.e. the conditions are strictly two-dimensional. If the initial embedment of the pipeline is not very large and if the flow around the pipe is sufficiently strong, scour may break out underneath the pipe. The stage at which the scour breaks out is called the onset of scour.

The onset of scour is directly related to the seepage flow which occurs in the sand beneath the pipe, caused by the pressure difference between the upstream and the downstream of the pipe (Fig. 1c). When the flow velocity is gradually increased, a critical point is approached where the discharge of the seepage flow is increased more rapidly than the driving pressure difference dictates. Simultaneously the surface of the sand at the immediate downstream of the pipe rises and eventually a mixture of sand and water breaks through the space underneath the pipe. This phenomenon is called piping and is well known in soil mechanics in hydraulic structures such as dams, cofferdams etc. (Terzaghi, 1948).

The conditions under which the onset of scour occurs below pipelines have been studied by Mao (1986) and Chiew (1990) in steady currents. Mao described the role of separation vortices that form in front and at the rear of the pipe in the process of the onset of scour. Also, he discussed the seepage flow underneath the pipe in relation to the onset of scour. The latter has been further elaborated by Chiew. Chiew further linked the onset of scour to the phenomenon of piping.

In the case of waves, the piping conditions are created underneath the pipe in the same way as in steady currents. The action is immediate. However, if the conditions are such that the critical condition is not attained immediately, then the action of separation vortices will become important to create scour more early in the wave case. Sumer & Fredsøe (1991) has linked the onset of scour in waves to the latter through the Keulegan-Carpenter number and expressed the critical condition for the onset of scour by the following empirical equation

$$\frac{e_{cr}}{D} = 0.1 \ln(KC) \tag{1}$$

in which e_{cr} = the critical embedment of the pipe beyond which no scour occurs, D = the pipe diameter and KC = the Keulegan-Carpenter number defined by

$$KC = \frac{U_m T_w}{D} \tag{2}$$

in which U_m = the maximum value of the orbital velocity of water particles at the bed, T_w = the wave period. For a sinusoidal motion of water particles KC will obviously be

$$KC = \frac{2\pi a}{D} \tag{3}$$

in which a = the amplitude of the orbital motion of water particles at the bed.

Time development of scour

The onset of scour is followed by the stage of so-called *tunnel erosion* (Leeuwenstein et al., 1985; Hansen et al., 1986). Sumer et al. (1990) present data regarding bed shear stress just under the pipe corresponding to this stage. The data indicate that the bed shear stress is

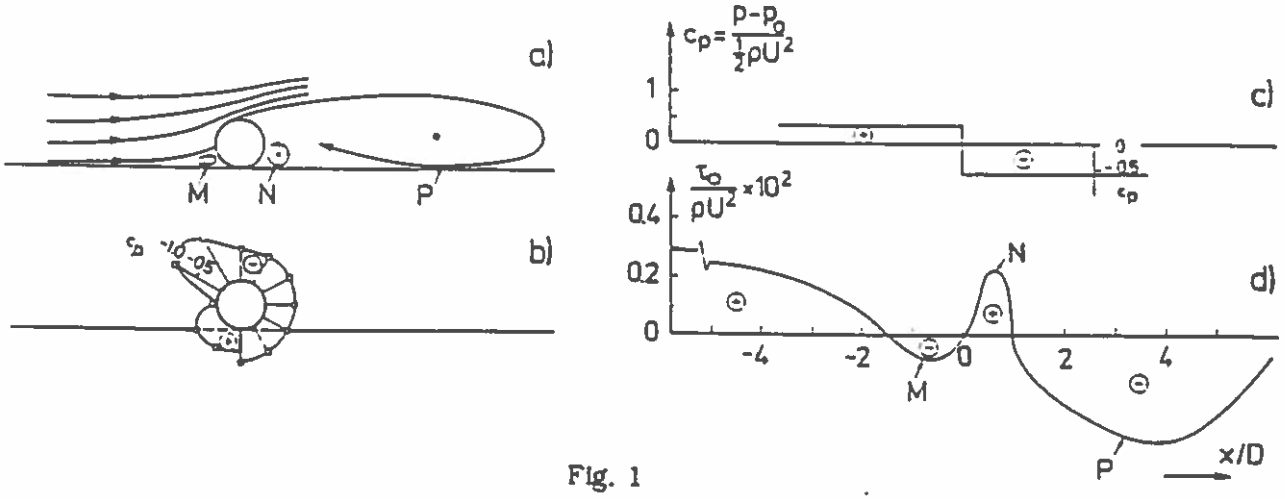

Fig. 1

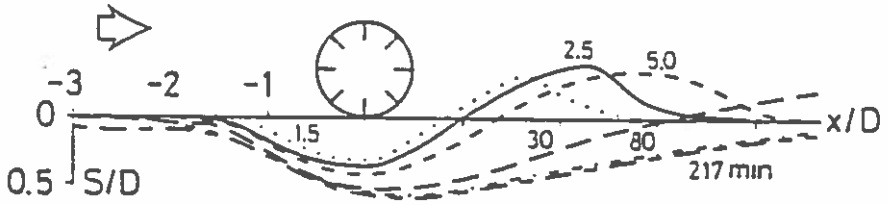

Fig. 2

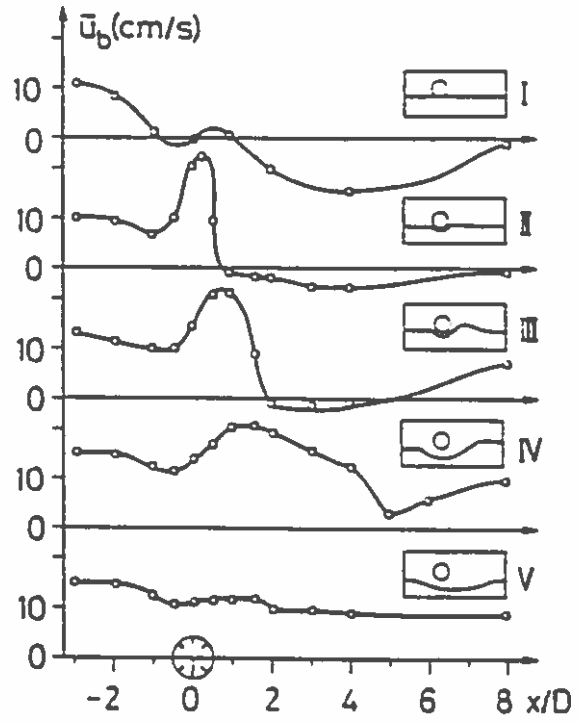

Fig. 3

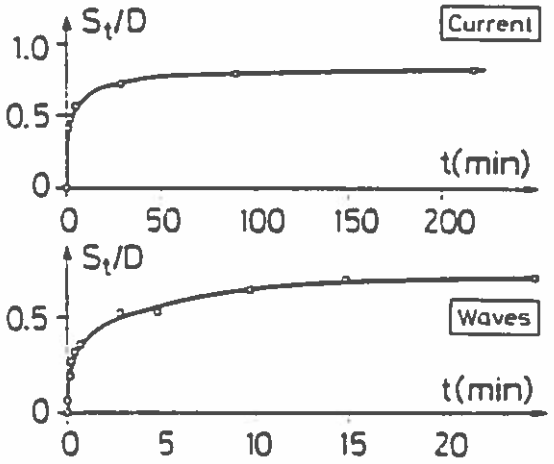

Fig. 4

increased by a factor of 4 with respect to its undisturbed value, resulting in an increase in the sediment transport rate of a factor of 8. This explains why the scour below the pipe occurs so fast and so violently during the tunnel erosion.

The tunnel erosion is followed by the stage called *lee-wake erosion*. In this stage, the scour downstream of the pipe is governed by the lee-wake of the pipe. Sumer et al. (1988b) made an investigation of the effect of lee-wake on scour. This work demonstrates that 1) vortex shedding is present in the lee-wake from rather early stages of the scouring process, and 2) the scour downstream of the pipe is eventually governed by this organized flow.

Fig. 2 shows a typical example where the time development of scour can be seen. The mild slope of the downstream portion of the scour profile is due to the action of the pipe's lee-wake.

As seen from the figure, the scour process attains an equilibrium stage where scouring below the pipe comes to an end. When this stage is reached, the sediment transport will be the same at all sections over the reach of the scour hole, and therefore the amount of sediment which enters the scour hole will obviously be identical to that leaving the scour hole.

Fig. 3 shows the results of Jensen et al.'s (1990) velocity measurements very close to the bed at different stages of the scour process. The figure shows that, while the velocity below the pipe is increased tremendously at the initial stage of the scour process (Profile II), it eventually becomes practically identical to the undisturbed flow velocity, as the scour approaches towards its equilibrium stage (Profile V).

The depth of the scour hole is probably the most significant quantity. Normally, it is taken as the depth of the scour hole just below the pipe.

The scour depth develops towards the fully-developed equilibrium stage through a transitional period, as illustrated in Fig. 4 for a pipe rigidly placed on a bed with initially zero gap. The depth corresponding to the fully-developed stage is called the *equilibrium scour depth*. It is also seen from the figure that a certain period of time must be elapsed for a substantial amount of scour to develop. This time is called the *time scale* of scour process.

The equilibrium scour depth, as well as the time scale of the scour process, constitute two major parameters in scour studies. The remaining part of this section will focus on these two parameters.

Equilibrium scour depth

Scour depth has been studied extensively in the case of *steady currents* (Chao & Hennessy (1972), Kjeldsen et al. (1973), Littlejohns (1977), Herbich (1981), Bijker & Leeuwenstein (1984), Lucassen (1984), Leeuwenstein et al. (1985), Herbich (1985), Herbich et al. (1984), Bijker (1986), Ibrahim & Nalluri (1986), Mao (1986), Kristiansen (1988) and Kristiansen & Tørum (1989)).

Kjeldsen et al. (1973) was the first to conduct scour experiments under controlled conditions. The experiments were done in live-bed situations. Kjeldsen et al.'s data indicated that the equilibrium scour depth can be expressed by the following relation:

$$S = 0.972\left(\frac{V^2}{2g}\right)^{0.2} D^{0.8} \tag{4}$$

in which V = the mean flow velocity. This relation suggests that

$$\frac{S}{D} \propto \theta^{0.2} \tag{5}$$

in which θ = the Shields parameter defined by

$$\theta = \frac{U_f^2}{g(s-1)d} \tag{6}$$

in which U_f = the bed friction velocity, corresponding to the undisturbed flow, g = the acceleration due to gravity, s = the specific gravity of sediment grains and d = the grain size.

Eq. 5 implies that the normalized scour depth S/D is only a weak function of θ. We shall return to this point later in this section.

The exact flow picture created by the presence of the pipe depends on the following quantities: the pipe diameter D, the flow velocity V, the kinematic viscosity of the fluid ν, the pipe roughness k, and the grain diameter d of the bed material. From these quantities, the dimensionless equilibrium scour depth can be found to depend on the following parameters:

$$\frac{S}{D} = \frac{S}{D}(k^*, R, \theta) \tag{7}$$

in which $k^* = k/D$ is the relative roughness, $R = VD/\nu$ is the pipe Reynolds number.

Of the three parameters that appear in Eq. 7, the influence of k^* and the Reynolds number appears through their effect on the downstream flow of the pipe. If the pipe is hydraulically rough, the wake flow is almost unaffected by the Reynolds number, while for a hydraulically smooth pipe some influence of the Reynolds number is expected in the downstream vortex-shedding pattern. Fig. 5 shows a plot of the data by Kjeldsen et al. (1973), Lucassen (1984), Mao (1986) and Kristiansen (1988) on the scour depth below smooth pipes exposed to a current. It is seen in the figure that there is some weak influence of the Reynolds number on the scour depth, because a slight decrease in S occurs for Reynolds number around 10^5 - 3 x 10^5. For a free circular cylinder, this coincides with the transition from subcritical to supercritical flow (Schewe (1983), Sumer and Fredsøe (1988)). In this transition region, the vortex shedding becomes less pronounced, which might lead to a smaller lee-wake erosion and hence less scour depth.

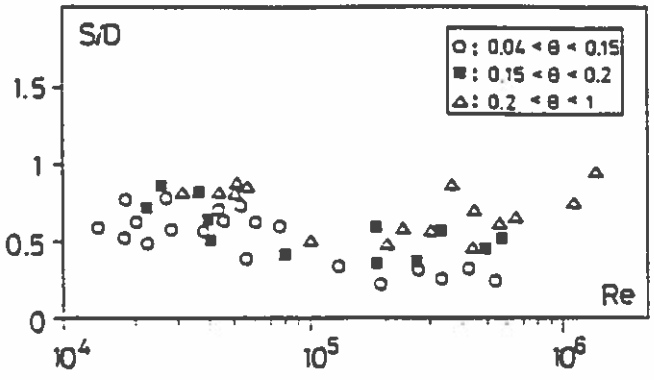

Fig. 5

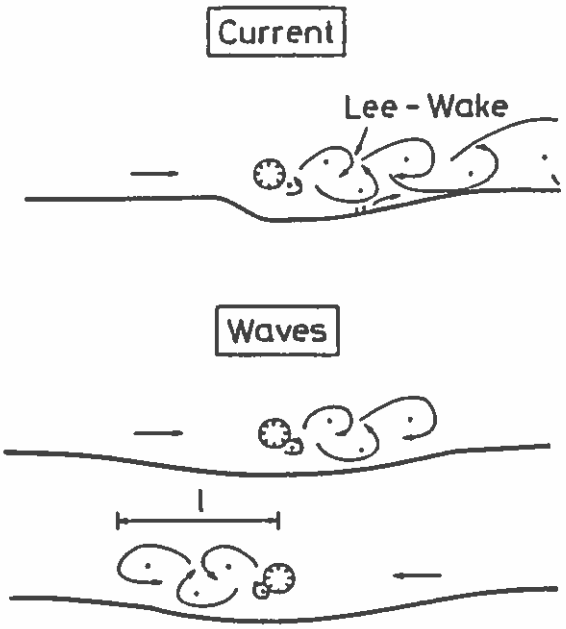

Fig. 6

As far as the influence of θ is concerned, this must be examined in two different categories: the clear-water case, where the sediment far from the pipe is not moving ($\theta < \theta_{cr}$), and the live-bed case, where sediment is transported far from the pipe ($\theta > \theta_{cr}$),in which θ_{cr} = the threshold value of θ for sediment motion. In the clear water case, the variation in scour depth with θ is more pronounced: as S/D increases from 0 at very small θ-values up to values of 0.4 - 1.0 when the θ-value approaches the live-bed case. However, when the live-bed case is obtained, very small variation in S/D is observed, as seen from Fig. 5, as has already been pointed out in conjunction with Kjeldsen et al.'s empirical equation (Eqs. 4 and 5). Ignoring this weak variation it may be suggested that, for all practical purposes, the following relation may be used as the design equation, to predict the equilibrium scour depth in steady currents

$$S/D = 0.6 \pm 0.1 \tag{8}$$

in which the first figure on the right hand side of the equation is the mean of the data plotted in Fig. 5, and the second is the standard deviation.

Regarding the scour in *tidal flows and waves*, the main difference between this case and the steady case is that the downstream-formed wake system now occurs on both sides of the pipeline. Here the strong lee-wake erosion, which gives a much more gentle downstream slope, occurs on both sides of the pipe (Fig. 6). The formation and extension of the wake pattern in oscillatory motion is governed by KC number. Therefore it must be expected that there exists a correlation between the equilibrium scour depth and KC number. Sumer & Fredsøe (1990) demonstrated that this is indeed the case. Based on their experimental data and Lucassen's (1984) data (which were recast in terms of KC number), the following empirical equation was established, relating the equilibrium scour depth to KC number for the live-bed situation ($\theta > \theta_{cr}$) and for a pipe initially in contact with the bed:

$$S/D = 0.1\sqrt{KC} \tag{9}$$

The data suggests that this equation is valid in a very broad range of KC, namely from KC = 2 to about 300. This relation has been confirmed later by Gökçe & Günbak's (1991) experiments and Hansen's (1992) numerical-model results.

Sumer & Fredsøe (1990) discussed also the effect of Shields parameter as well as Re-number dependence plus the effect of the presence of ripples in the wave-flume tests.

Generally, the equations given in the preceding, namely Eqs. 4 or 8 and Eq. 9 may be used as design equations. However, there are several other factors which may influence the scour depth. Of these factors, the following may be mentioned: The pipe position in vertical (Leeuwenstein et al. (1985), Mao (1986), Sumer & Fredsøe (1990)), the roughness of pipe surface (Sumer & Fredsøe (1990)), the angle of attack of the flow (Mao (1988), Hansen (1992)), the current in combined waves and current (Hansen (1992)), the case of multiple pipelines (Westerhorstmann et al. (1992)), the armoring of bed sediment (Sidek & Ibrahim (1992)), vibrations of the pipe (Sumer et al. (1988a)) and the Shields parameter in clear-water scour (Mao (1986), Hansen (1992)).

Time scale

As mentioned previously, the scour depth develops towards its equilibrium stage through a transitional period (Fig. 4), which can be represented by the following relation:

$$S_t = S\left(1 - \exp\left(-\frac{t}{T}\right)\right) \tag{10}$$

The quantity T is defined as the time scale of the scour process and represents the time period during which a substantial scour develops.

Fredsøe et al. (1992) has made a study of this time scale in both steady currents and waves. They found that the time scale normalized as in the following

$$T^* = \frac{[g(s-1)d^3]^{1/2}}{D^2}T \tag{11}$$

is a function of θ, the Shields parameter. Based on their own data as well as the data from Kjeldsen et al. (1973) and Mao (1986), they found that the relation between T^* and θ can be represented by the following simple expression

$$T^* = \frac{1}{50}\theta^{-5/3} \tag{12}$$

for the live bed situation ($\theta > \theta_{cr}$) and for a pipe with an initially zero gap. This equation was found to be valid for both steady currents and waves. Fredsøe et al. (1992) attributed this to the fact that the lee-wake scour -- the key element in the wave induced scour -- is insignificant at the initial stage of the scour process. Therefore the time scale is unable to differentiate whether the flow is a steady-current or a wave-induced flow. In Fredsøe et al. (1992) study, also the effect of change in wave climate has been investigated.

3. THREE-DIMENSIONAL SCOUR

General description

Two-dimensional scour below pipelines, as observed in two-dimensional flume test with a fixed pipe, must in the field turn to three-dimensional scour picture as sketched in Fig. 7 in order to obtain support for the pipeline. Hereby, a three-dimensional scour pattern arises as sketched in Figs. 7a and 7b: a number of scour holes is interrupted by a stretch, where the pipeline is partially or totally buried.

The scour picture in the free-span areas (Section B-B) is two-dimensional, while at other places, particularly in the neighbourhood of span shoulders (Section A-A), it is three-dimensional. See Fig. 8 for a definition sketch.

At Section A-A, the pipe sinks in the soil. This is due to the combined action of three-dimensional scour and soil failure, as will be explained in the following section.

At Section B-B, on the other hand, the scour, after it breaks out, spreads along the length of the pipeline. When the scour hole becomes sufficiently long, the pipe begins to sag into its naturally created trench hole. This may continue until the pipe comes into the neighbourhood of the bottom, which eventually brings an end to the scouring process. From this moment onwards, the backfilling process starts, and later on, the pipeline may partially or fully become covered by sand (self-burial).

Rate of spread of scour along the pipe

The rate of spread of the three-dimensional scour along the pipe is one of the major parameters. Research dealing with this quantity is not extensive. Gravesen & Fredsøe (1983) gave an account of how to deal with the problem when extending the results of model experiments to the nature. Also, various accounts of the spreading process have been given in Leeuwenstein (1985) and Bernetti et al. (1990). Hansen et al. (1991), on the other hand, has presented a semi-empirical model of the process, which can predict the rate of spread of scour along the pipe.

In the case when the current approaches the pipe at an oblique angle, the free span will migrate. This aspect has been investigated by Hansen et al. (1991).

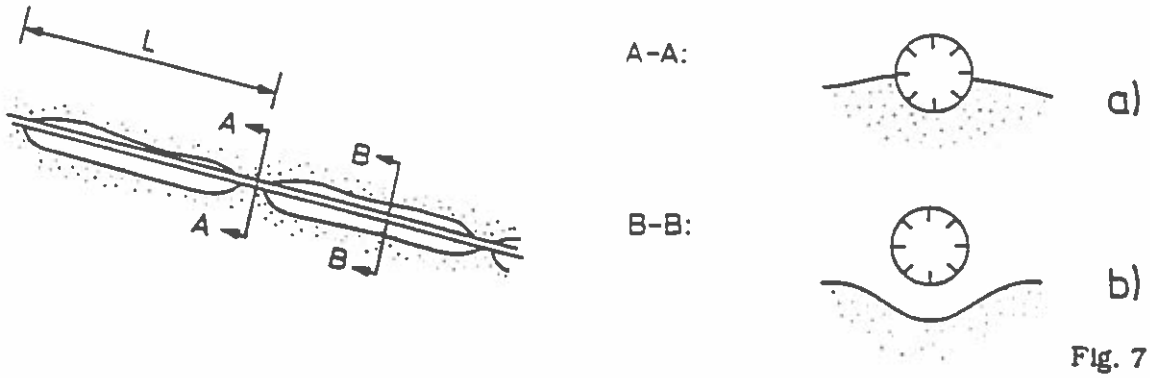

Fig. 7

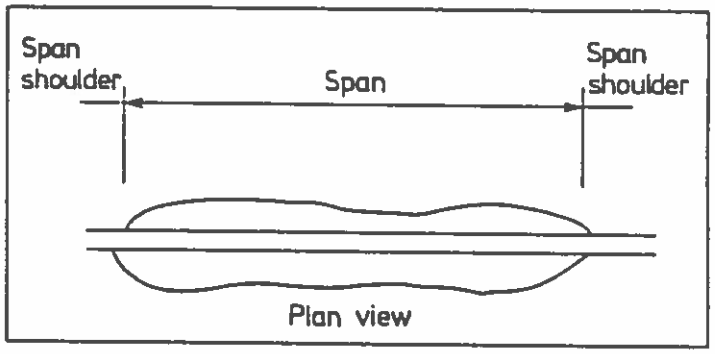

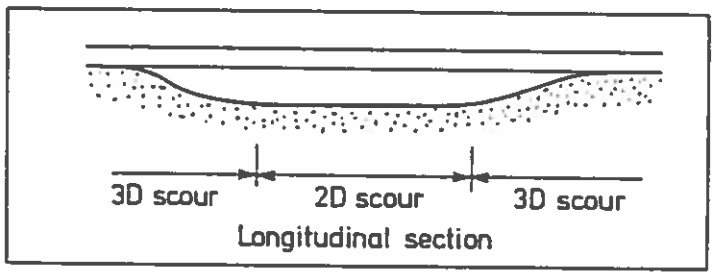

Fig. 8

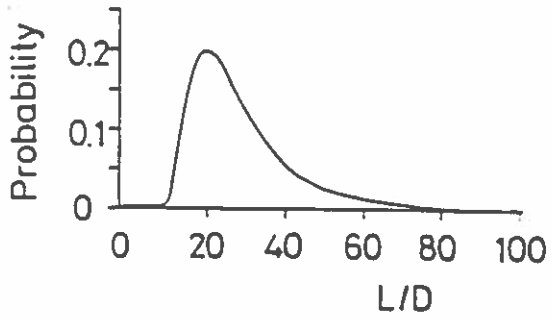

Fig. 9

Fig. 10

Effect of pipe sagging on scour

Normally the time scale of span development, T_h, is large compared with T, the time scale of the two-dimensional scour described in the preceding section, (Eq. 10). Here T_h = the time period during which a substantial span length develops to produce some measurable deflection in the middle of the span. The time scales T_h and T may be estimated using the relations given in Hansen et al. (1991) and Fredsøe et al. (1992) (Eq. 12), respectively. While T_h may be in the order of magnitude of days, T is only in the order of magnitude of hours. This means that the pipe normally begins to sag long after the two-dimensional scour has attained its equilibrium stage. However, the sagging may influence the final scour profile and indeed the final scour depth. Effect of pipe sagging on scour has been investigated by various authors, employing two-dimensional laboratory models (Leeuwenstein et al. (1985), Fredsøe et al. (1988), Gökçe & Günbak (1991)). Backfilling and self-burial in the free-span areas has also been investigated by employing the same two-dimensional models in some of these studies.

Length of free spans

The length of free spans is also of engineering interest. Fig. 9 shows the probability density function of span length obtained by Orgill et al. (1992), based on some limited field data which,

the authors point out, is very site-specific. The figure shows that there is considerable variation in L/D, ranging from 10 to as much as 100 with the mean value of about 20.

Various authors have considered various factors with regard to the assessment of scour-induced free-span lengths (Fredsøe et al. (1988), Brushi et al. (1986), Eide et al. (1988), Bernetti et al. (1990), Bruschi et al. (1991) and Bijker et al. (1992)). In Fredsøe et al. (1988) work, the free-span length has been related to the so-called stiffness-length of the pipe.

Pipe sinking at span shoulders

Pipe sinking is caused by soil failure, as has already been pointed out in the preceding paragraphs. The soil failure itself may be due to a general shear failure or it may be due to liquefaction.

Sumer & Fredsøe (1993) made an investigation of sinking of pipelines at span shoulders employing a rigid pipe in the laboratory in a current flume. Sumer & Fredsøe's investigation was directed towards the understanding of the sinking process of a pipeline in the soil caused by a general shear failure. A simple formula adopted from soil mechanics regarding the bearing capacity of soil was found to give a satisfactory result in relation to the sinking of the pipe at the span shoulder.

The subject liquefaction in relation to pipelines laid on the sea-bed has been investigated by Silvis (1990). Bijker et al. (1991) gives a brief account of the liquefaction potential of seabed with regard to the presence of laid pipelines.

Stimulated self-burial

As has been seen in the preceding paragraphs, pipelines laid on the seabed may bury themselves in the seabed by various mechanisms. This may occur in the free-span areas where the pipe sags into its scour hole and is covered by sand upon the termination of the sagging process. It may also occur at the span shoulders where the pipe sinks in the sand.

After the discovery that a few months after a 12" pipeline (laid in 1980 on the North Sea bottom in the Dutch sector) caused the formation of a trench, 3 pipe diameter deep and then it gradually sank in this trench and buried itself with the thickness of the covering sand layer of more than 30 cm (Kroezen et al. (1982)), the Delft Hydraulic Laboratory has launched an extensive series of research to investigate the feasibility of a method, called stimulated self-burial, to exploit the self-burial potential (Hulsbergen (1984), Hulsbergen (1986), Hulsbergen & Bijker (1989)). This is particularly important in the circumstances where pipelines would not bury themselves fast enough or they would not at all bury themselves. The idea is to stimulate a controlled local scour by using fins (called spoiler) attached to the pipeline as sketched in Fig. 10. From the research carried out by the Delft Hydraulics, it was found that, firstly, the spoiler reduces the time necessary to accomplish a given embedment level by a factor of ten with respect to a plain pipe, and secondly, the final depth of burial is larger than in the case of plain pipelines. The same effects have been observed also in waves (Gökçe & Günbak (1991)).

4. EFFECT OF SCOUR ON FORCES AND VIBRATIONS

Obviously forces on and vibrations of a pipe over a scoured bed will be different from those experienced when the pipe sits on a plane bed. Jensen et al. (1990) has investigated forces on a pipe at different stages of scour process in steady current, using frozen scoured-bed models. Stansby & Starr (1991) has measured forces on a pipe gradually sinking in the bed under flow action in both steady current and waves.

Effect of scour on hydroelastic vibrations of pipelines, on the other hand, has been studied

in steady currents (Sumer et al. (1988a), Kristiansen (1988) and Kristiansen & Tørum (1989)) and in waves (Sumer et al. (1989)).

Forces have been measured also on pipeline models with attached spoilers with different embedment ratios (representing different stages of the self-burial process) (Hulsbergen & Bijker (1989)).

5. MATHEMATICAL MODELLING

The studies concerning mathematical modelling of scouring process may broadly be divided into three categories: 1) the studies dealing with mathematical models based on potential-flow theory, 2) those dealing with k-ε models and 3) those dealing with discrete-vortex models.

Regarding the potential-flow models, Chao & Hennessy (1972) was the first to apply the simple potential solution to the flow in the gap between the pipe and the bed. As a matter of fact, the potential flow around a cylinder placed near a wall was described by von Müller in as early as 1929. Müller's potential flow description was modified by Fredsøe & Hansen (1987) by taking into consideration the actual, measured velocity at the top and bottom edges of the cylinder. This modification is significant particularly in the case of very small gaps where the potential theory overpredicts the velocity in the gap. Hansen et al. (1986) later implemented the same line of thought as in Fredsøe & Hansen, and developed a potential theory for the case of a cylinder over a *scoured* bed. In both models, only the flow upstream of the pipe is described by the potential theory. (Clearly the downstream flow, i.e. the lee-wake, cannot be described by a potential flow model). The results of scour prediction by Hansen et al.'s (1986) potential flow description agreed satisfactorily with the experiments. Recently, Hansen (1992), with a simple representation of the lee wake, extended this model so as to cover waves. His model results give a fairly good agreement with Sumer & Fredsøe's (1990) empirical result (Eq. 9). Using the same model, he also examined the effect of Shields parameter, the effect of current in combined waves and current and the effect of angle of attack. Bernetti et al. (1990) has also developed a mathematical model of scour below pipelines. The model has two main components, namely the two-dimensional scour component and the three-dimensional scour component. The two-dimensional scour component was based on Chao & Hennessy's (1972) potential-flow description. Bernetti et al.'s model is able to predict also the development of the three-dimensional scour, the free-span length and sinking of the pipe at span shoulders. The model has been tested against simple cases where data is available (Mao (1986)). The model performance for these test cases appeared to be quite satisfactory.

The second group of mathematical modelling studies concerns the k-ε simulation of the flow (Leeuwenstein & Wind (1984) and van Beek & Wind (1990)). As is well known, the k-ε model is successfully used in various fields of fluid mechanics (Rodi (1984)). Regarding its application in scour below pipelines, Leeuwenstein & Wind has calculated the flow around the pipe over a scoured bed with such a model and made the morphological calculations by use of sediment continuity equation along with a sediment-transport equation. In the follow-up study, van Beek & Wind extended the model so as to cover also the suspended-load transport in the morphological calculations.

The third group of studies in mathematical modelling of scour concerns the discrete-vortex-model simulation of the flow around pipes (Sumer et al. (1988a), Jensen et al. (1990) and Jensen et al. (1989)). The particular model which has been used in these studies is the so-called cloud-in-cell method. The computational details of the method is well documented in the literature (see for example Stansby & Dixon (1983)). The method is able to predict the gross behaviour of the vortices in the lee wake of the pipe. This enabled Sumer et al. (1988b) to study the effect of lee-wake vortices on the bed shear stress downstream of the pipe over both a plane bed and a scoured bed. The method was later used by the same group to simulate flow around a pipe over a scoured bed in steady currents (Jensen et al. (1990) and in waves (Jensen et al. (1989)).

Finally, it may be mentioned that an integrated approach has been adopted recently by

the Danish Hydraulic Institute and the Delft Hydraulics in a joint study, to develop a computer model which would enable the engineer to decide on occurrence and disappearance of scour along a pipeline/cable, pipeline/cable self-burial, trench backfilling, migrating sand waves exposure and undermining of pipelines or cables. A brief account of this study has been reported by Staub & Bijker (1990).

ACKNOWLEDGEMENT

The study is partially supported by the research programme "Marine Technique" of the Danish Scientific Council (STVF).

REFERENCES

Bearman, P.W. and Zdravkovich, M.M. (1978). Flow around a circular cylinder near a plane boundary. J. Fluid Mech., 89, Part 1, pp. 33-48.

Bernetti, R., Bruschi, R., Valentini, V. and Venturi, M. (1990). Pipelines placed on erodible seabeds. Proceedings of the 9th Int. Conference on Offshore Mechanics and Arctic Engineering, Houston, Texas, ASME, V., pp. 155-164.

Bijker, E.W. (1986). Scour around structures. Proc. 20th Coast. Engrg. Conf., Taipei, Taiwan, pp. 1754-1768.

Bijker, E.W. and Leeuwenstein, N. (1984). Interaction between pipelines and the seabed under the influence of waves and currents. Seabed Mechanics, B. Denness, ed., Graham and Trotman, Gettysburg, Md., pp. 235-242.

Bijker, R., Staub, C., Silvis, S. and Bruschi, R. (1991). Scour-induced free spans. Proceedings of the 23rd Offshore Technology Conference, Houston, Texas, May 6-9, 1991, Paper No. OTC 6762, pp. 583-588.

Bruschi, R., Cimbali, W., Leopardi, G. and Vincenzi, M. (1986). Scour induced free span analysis. Proceedings of the 5th International Offshore Mechanics and Arctic Engineering Symposium, April 13-18, 1986, III, pp. 656-669.

Bruschi, R., Curti, G. Tura, F. (1991).Free spanning pipelines: A Review. Presentation at the First International Offshore and Polar Engineering Conference (ISOPE), 11-16 August, 1991, Edinburgh, U.K.

Chao, J.L. and Hennessy, P.V. (1972). Local scour under ocean outfall pipelines. Jour. Water Pollution Control Fed., 44, No. 7, pp. 1443-1447.

Chiew, Y-M. (1990). Mechanics of local scour around submarine pipelines. J. Hydraulic Engineering, ASCE, 116, No. 4, pp. 515-529.

Eide, L.O., Leopardi, G. and Bruschi, R. (1988). The experience from the Statpipe system on free span development and analysis. Offshore Pipeline Technology Seminar, Stavanger, Norway.

Fredsøe, J. and Hansen, E.A. (1987). Lift forces on pipelines in steady flow. J. Waterway, Port, Coastal and Ocean Engineering, ASCE, 113, No. 2, pp. 139-155.

Fredsøe, J., Hansen, E.A., Mao, Y. and Sumer, B.M. (1988). Three-dimensional scour below pipelines. Trans. ASME, Journal of Offshore Mechanics and Arctic Engineering, 110, pp. 373-379. Also in: Proceedings of the 6th Int. Symp. on Offshore Mech. and Arctic Engrg., ASME,pp. 29-36, 1987.

Fredsøe, J., Sumer, B.M. and Arnskov, M.M. (1992). Time scale for wave/current scour below pipelines. International Jour. Offshore and Polar Engineering, 2, No. 2, pp. 13-17, 1992. Also in Proceedings of the First International Offshore and Polar Engrg. Conf. (ISOPE 91), II, pp. 301-307.

Gökçe, T. and Günbak, A.R. (1991). Self-burial and stimulated self-burial of pipelines by waves. Proc. of the First (1991) International Offshore and Polar Engineering Conf., Edinburgh, U.K. 11-16 August, 1991, II, pp. 308-314.

Gravesen, H. and Fredsøe, J. (1983). Modelling of liquefaction, scour and natural backfilling process in relation to marine pipelines. Offshore oil and Gas Pipeline Technology, European Seminar, Feb. 2-3, 1983, Copenhagen.

Hansen, E.A. (1992). Scour below pipelines and cables: A simple model. Proceedings of 11th Offshore Mechanics and Arctic Engineering Conference (OMAE 92), June 7-11, 1992, V-A, Pipeline technology, ASME, pp. 133-138.

Hansen, E.A., Fredsøe, J., and Mao, Y. (1986). Two dimensional scour below pipelines. Fifth Internat. Symp. on Offshore Mech. and Arctic Engrg., ASME, 3, pp. 670-678.

Hansen, E.A., Staub, C., Fredsøe, J. and Sumer, B.M. (1991). Time-development of scour induced free spans of pipelines. Proceedings of the 10th Offshore Mechanics and Arctic Engineering Conference, Stavanger, Norway, V, Pipeline Technology, ASME, pp. 25-31.

Herbich, J.B. (1981). Scour around pipelines and other objects. Offshore pipeline design elements. Marcell Dekker, Inc., New York, N.Y.

Herbich, J.B. (1985). Hydromechanics of submarine pipelines: Design problems. Can. J. Civ. Engrg., 12(4), pp. 863-887.

Herbich, J.B., Schiller, R.E., Jr., Watanabe, R.K. and Dunlap, W.A. (1984). Scour around pipelines. Sea floor scour-Design guidelines for ocean founded structures (Ocean engineering 4), Marcell Dekker, Inc., New York, N.Y., pp. 203-210.

Hulsbergen, C.H. (1984). Stimulated Self-Burial of Submarine Pipelines. Proceedings of the 16th Offshore Technology Conference, Houston, Texas, May 7-9, 1984, Paper No. OTC 4667, pp. 171-177.

Hulsbergen, C.H. (1986). Spoilers for stimulated self-burial of submarine pipelines. Proceedings of the 18th Offshore Technology Conference, Houston, Texas, May 5-8, 1986, Paper No. OTC 5339, pp. 441-444.

Hulsbergen, C.H. and Bijker, R. (1989). Effect of spoilers on submarine pipeline stability. Proceedings of the 21st Offshore Technology Conference, Houston, Texas, May 1-4, 1989, Paper No. OTC 6154, pp. 337-350.

Ibrahim, A. and Nalluri, C. (1986). Scour prediction around marine pipelines. Proc. 5th Int. Symp. on Offshore and Arctic Engrg., Tokyo, Japan, pp. 679-684.

Jensen, B.L., Sumer, B.M., Jensen, H.R. and Fredsøe, J. (1990). Flow around and forces on a pipeline near a scoured bed in steady current. Trans. of the ASME, Jour. Offshore Mechanics and Arctic Engineering, 112, pp. 206-213. Also in: Proceedings of 7th International Conference on Offshore Mechanics and Arctic Engineering (OMAE), Houston, Texas, Feb. 7-12, 1988, V, pp. 39-48.

Jensen, H.R., Jensen, B.L., Sumer, B.M. and Fredsøe, J. (1989). Flow visualization and numerical simulation of the flow around marine pipelines on an erodible bed. Proc. 8th Int. Conf. on Offshore Mech. and Arctic Engrg., ASME, 5, 1989, pp. 129-136.

Kjeldsen, S.P., Gjörsvik, O., Bringaker, K.G. and Jacobsen, J. (1973). Local scour near offshore pipelines. Second Internat. Port and Ocean Engineering under Arctic Conditions, Conf. Iceland, 1973, pp. 308-331.

Kristiansen, Ø. (1988). Current induced vibrations and scour of pipelines on a sandy bottom. Thesis presented to the University of Trondheim, at Trondheim, Norway, in partial fulfillment of the requirements of the degree of Doctor of Philosophy.

Kristiansen, Ø. and Tørum, A. (1989). Interaction between current induced vibrations and scour of pipelines on a sandy bottom. Proceedings of the 8th Inter. Conference on Offshore Mechanics and Arctic Engineering, ASME, The Hague, the Netherlands, March 19-23, 1989, V., pp. 167-174.

Kroezen, M., Vellinga, P., Lindenberg, J. and Burger, A.M. (1982). Geotechnical and hydraulic aspects with regard to seabed and slope stability. Delft Hydraulics Laboratory, Publication No. 272, June, 13 p.

Leeuwenstein, W. (1985). Natural self-burial of submarine pipelines. MaTS - Stability of pipelines, scour and sedimentation. Coastal Engineering Group, Department of Civil Engineering, Delft University of Technology, Delft, The Netherlands.

Leeuwenstein, W. and Wind, H.G. (1984). The computation of bed shear in a numerical model. Proceedings of 19th International Conference on Coastal Engineering, Chapter 114, pp. 1685-1702.

Leeuwenstein, W., Bijker, E.A., Peerbolte, E.B., and Wind, H.G. (1985). The natural self-burial of submarine pipelines. Proc. 4th Int. Conf. on Behaviour of Offshore Structures (BOSS), Elsevier Science Publishers, pp. 717-728.

Littlejohn, P.S.G. (1977). A study of scour around submarine pipelines. Report No. INT 113, Hydr. Res. Station, Wallingford, England.

Lucassen, R.J. (1984). Scour underneath submarine pipelines. Report No. PL-4 2A, Netherlands Marine Tech. Res., Netherlands Industrial Council for Oceanology, Delft Univ. of Tech., Delft, the Netherlands, Sep. 1984, 117, Student Thesis supervised by E.W. Bijker and W. Leeuwenstein.

Mao, Y. (1986). The interaction between a pipeline and an erodible bed. Series Paper 39, Inst. of Hydrodyn. and Hydraulic Engrg., Tech. Univ. Denmark, in partial fulfillment of the requirements for the degree of Doctor of Philosophy.

Mao, Y. (1988). Seabed scour under pipelines. Proceedings of the 7th International Conference on Offshore Mechanics and Arctic Engineering, Houston, Texas, Feb. 7-12, 1988, V, pp. 33-38.

Müller, W. von. (1929). System von Doppelquellen in der ebenen Strömung, insbesondere die Strömung um zwei Kreiszylinder. Zeitschrift f. angew. Math. und Mech. 9, Heft 3, pp. 200-213.

Orgill, G. Barbas, S.T., Crossley, C.W. and Carter, L.W. (1992). Current practice in determining allowable pipeline free spans. Proceeding of the 11th Offshore Mechanics and Arctic Engineering Conference, June 7-11, 1992, Calgary, Canada, V-A, Pipeline Technology, ASME, pp. 139-145.

Rodi, W. (1984). Turbulence models and their application in hydraulics. IAHR, Delft, the Netherlands, 104 p.

Schewe, G. (1983). On the force fluctuations acting on a circular cylinder in cross-flow from subcritical up to transcritical Reynolds numbers. J. Fluid Mech., 113, pp. 265-285.

Sidek, F.J. and Ibrahim, A.A. (1992). The armouring effects of shell fragments in seabeds beneath pipelines. Proceedings of the 2nd Inter. Offshore and Polar Engineering Conference (ISOPE), San Fransisco, U.S.A., 14-19 June, 1992, II, pp. 92-100.

Silvis, F. (1990). Wave induced liquefaction of seabed below pipelines. 4th Young Geotechnical Engineers' Conference, Delft, the Netherlands, 18-22 June, 1990.

Stansby, P.K. and Dixon, A.G. (1983). Simulation of flows around cylinders by a Lagrangian vortex scheme. Applied Ocean Research, 1983, 5, No. 3, pp. 167-178.

Stansby, P.K. and Starr, P. (1991). Hydrodynamic forces on a horizontal cylinder resting on a sand bed under waves and currents. Proc. of the First (1991) International Conf., Edinburgh, U.K., 11-16 August, 1991, III, pp. 158-163.

Staub, C. and Bijker, R. (1990). Dynamic numerical models for sand waves and pipeline self-burial. Proceedings of 22nd International Conference on Coastal Engineering, Delft, the Netherlands, Chapter 190, pp. 2508-2521.

Sumer, B.M. and Fredsøe, J. (1988). Vibrations of cylinders at high Reynolds numbers. Proc. 7th Int. Offshore Mech. and Arctic Engrg. Symp., ASME, 2, pp. 211-222.

Sumer, B.M. and Fredsøe, J. (1990). Scour below pipelines in waves. Journal of Waterway, Port, Coastal and Ocean Engineering, ASCE, 116, No. 3, May/June 1990, pp. 307-323.

Sumer, B.M. and Fredsøe, J. (1991). Onset of scour below a pipeline exposed to waves. International Jour. of Offshore and Polar Engineering, 1, No. 3, pp. 189-194, 1991. Also in: Proceeding of the First International Offshore and Polar Engrg. Conf. (ISOPE 91), II, pp. 290-295.

Sumer, B.M. and Fredsøe, J. (1993). Self-burial of pipelines at span shoulders. Paper to be presented at the 3rd ISOPE Conference, Singapore 1993.

Sumer, B.M., Mao, Y., and Fredsøe, J. (1988a). Interaction between vibrating pipe and erodible bed. J. Waterway, Port, Coast. and Oc. Engrg., ASCE, 114(1), pp. 81-92.

Sumer, B.M., Jensen, H.R., Mao, Y. and Fredsøe, J. (1988b). The effect of lee-wake on scour below pipelines in current. J. Waterway, Port, Coastal and Ocean Engineering, ASCE, 114, No. 5, pp. 599-614.

Sumer, B.M., Fredsøe, J., Gravesen, H. and Bruschi, R. (1989). Response of marine pipelines in scour trenches. ASCE Jour. Waterway, Port, Coastal and Ocean Engineering, 115, No. 4, 1989, pp. 477-496.

Sumer, B.M., Pedersen, C., Di, Y. and Fredsøe, J. (1990). Bed shear-stress measurements in the vicinity of a pipeline in waves. Prog. Rep. 71, Inst. Hydrodyn. and Hydraulic Engineering, Techn. Univ. Denmark, pp. 61-72.

Sumer, B.M., Jensen, B.L. and Fredsøe J. (1991). Effect of a plane boundary on oscillatory flow around a circular cylinder. J. Fluid Mech., 225, pp. 271-300.

Terzaghi, K. (1948). Theoretical Soil Mechanics. John Wiley and Sons, Inc., New York.

van Beck, F.A. and Wind, H.G. (1990). Numerical modelling of erosion and sedimentation around pipelines. Coastal Engineering, 14, pp. 107-128.

Westerhortmann, J.H., Machemehl, J.L. and Jo, C.H. (1992). Effect of pipe spacing on marine pipeline scour. Proceedings of the 2nd Inter. Offshore and Polar Engineering Conf. (ISOPE), San Francisco, U.S.A., 14-19 June, 1992, II, pp. 101-109.

Spanwise Correlation on a Vibrating Cylinder near a Wall in Oscillatory Flows

A. Kozakiewicz, B. Mutlu Sumer and Jørgen Fredsøe

Institute of Hydrodynamics and Hydraulic Engineering
Technical University of Denmark

Journal of Fluids and Structures (1992) **6**, 371–392

SPANWISE CORRELATION ON A VIBRATING CYLINDER NEAR A WALL IN OSCILLATORY FLOWS†

A. KOZAKIEWICZ,‡ B. M. SUMER AND J. FREDSØE
Institute of Hydrodynamics and Hydraulic Engineering, Technical University of Denmark
DK-2800 Lyngby, Denmark

(Received 16 February 1991 and in revised form 29 July 1991)

Spanwise correlation measurements have been made for a stationary and a transversely vibrating cylinder placed near a wall and exposed to oscillatory flows. The correlation was calculated, based on pressure measurements on the surface of the cylinder. The carriage technique was used in the experiment, to simulate the oscillatory flow. The tests were conducted for three different values of Keulegan-Carpenter number, namely 6, 20 and 65, where the Re number was $3{\cdot}4 \times 10^4$ for KC = 6 and $6{\cdot}8 \times 10^4$ for KC = 20 and 65. The corresponding β number range was from 1,050 to 5,700, the lower end of the range corresponding to KC = 65. The tests were conducted for various values of the gap between the cylinder and the wall, normalized by the cylinder diameter, e/D, covering 0–2·3. The range of double-amplitude of cylinder vibrations, normalized by the cylinder diameter, $2A/D$, was 0–0·7 in the tests. The results indicate that the correlation increases tremendously with the wall proximity, as far as the lift force on the cylinder is concerned. However, the effect of wall proximity appears to be insignificant, when fluctuations in surface pressure, either in the form of organized motion, namely the vortex shedding, in the case of wall-free cylinder or in the form of disorganized wake flow in the case of wall-mounted cylinder are considered. Regarding the influence of vibrations on the correlation, it was found that the correlation coefficient first increases with increasing amplitudes of vibrations. However, the increase in the correlation with increasing amplitudes was found not to be as large as in steady currents. The experiments indicate that the correlation coefficient begins to decrease with further increase of the amplitudes. It was found that this occurs for $2A/D$ larger than about 0·2 for KC = 6 and for $2A/D$ larger than 0·3 for KC = 20 and 65.

1. INTRODUCTION

IT IS KNOWN THAT VORTEX SHEDDING around a cylinder occurs in cells along the length of the cylinder. The spanwise correlation coefficient is one quantity which gives information about the length scale of these cells. It has been recognized that the correlation varies with Reynolds number, surface roughness and turbulence, King (1977). Research has also shown that the vibrations of the cylinder has a significant effect on correlations; the correlation for a transversely vibrating cylinder exposed to a steady current is increased tremendously with increasing amplitudes of vibrations (Koopman 1967; Toebes 1969; Ramberg & Griffin 1976; Novak & Tanaka 1977; Howell & Novak 1979).

† An earlier version of this paper was published in the *Proceedings of the Fifth Conference on Flow Induced Vibrations*. It is reproduced by permission of the Council of the Institution of Mechanical Engineers, London, U.K.

‡ On leave from the Institute of Hydroengineering of the Polish Academy of Sciences, Gdansk, Poland.

0889–9746/92/030371 + 22 $03.00

Correlation measurements have also been made for cylinders exposed to oscillatory flows (Obasaju *et al.* 1988). These measurements have clearly demonstrated that the correlation is strongly dependent on the Keulegan-Carpenter number, KC. The measurements by Obasaju *et al.* (1988) covered the range $10 \leq KC \leq 42$. The highest correlation was obtained for the lowest KC number, namely $KC = 10$. The correlation decreased with increasing KC number, attained its minimum level at around $KC = 20$ and then increased to relatively higher values for a further increase in KC number.

The purpose of the present study is to investigate the effect of (i) transverse vibrations and (ii) the close proximity of a wall on the correlation in oscillatory flows.

The present work has practical relevance to the forces on and hydroelastic vibrations of marine pipelines, where both the effect of transverse vibrations and that of close proximity of a wall (namely, the sea bottom) may be important.

2. EXPERIMENTAL FACILITY

The measurements were made in a water flume which has a test section, 3 m wide, 1 m high and 35 m long. The circular cylinder used was a smooth-surface pipe, 9 cm in diameter and 2 m in length.

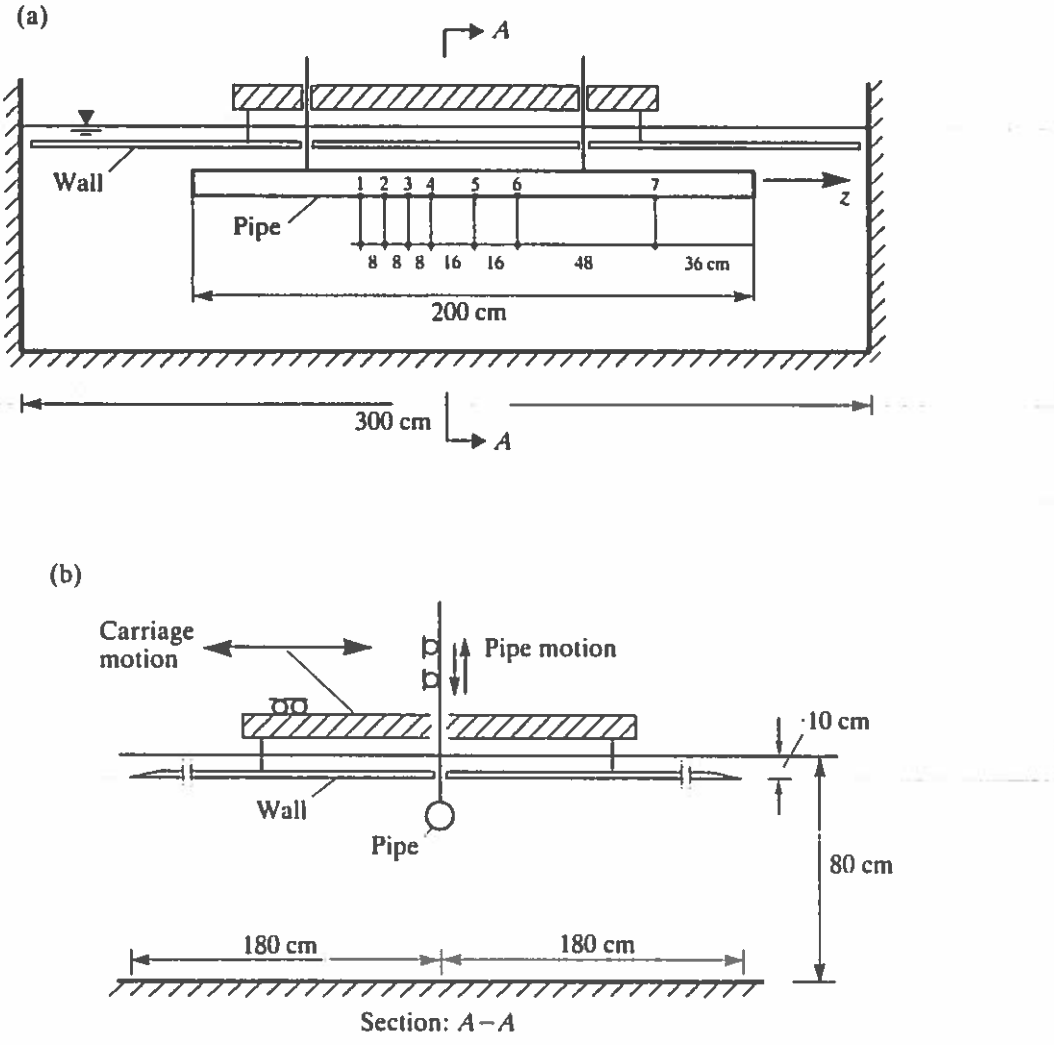

Figure 1. Test set-up: (a) cross-sectional view; (b) section A-A. In (a), the numbers 1, 2, . . . , 7, identify the pressure transducers.

The pipe was mounted to a carriage (Figure 1). The oscillating flow was simulated by driving the carriage back and forth in still water. The relative motion of the pipe to the wall was confined to the vertical direction only. In this direction, the pipe could be oscillated perpendicular to the flow direction, at any distance from the wall, by a hydraulic system. The wall was the bottom surface of a horizontal plate with sharp edges at both ends. The plate, too, was fixed to the carriage. The pipe was free from mechanical vibrations.

In the tests, the cylinder oscillations and the carriage motion were synchronized in such a way that the instants corresponding to the up-zero crossing points in the carriage-velocity time series coincided with those corresponding to the down-zero crossing points in the cylinder-displacement time series. Therefore, the phase between the carriage motion and the cylinder vibration was kept constant for all the tests. No attempt was made to study the effect of this phase difference on the spanwise correlation. We believe, however, that the effect would not be substantial when compared with the effect of the vibrations themselves.

Seven pressure transducers (Endevco Model 8510B-2 with a range of 0–2 psi) were mounted on the surface of the cylinder such that they were aligned in the direction of the cylinder axis as shown in Figure 1(a). The pressure transducers were miniature, high-sensitivity piezoresistive pressure cells with 0·38 cm face diameter. Their sensitivity varied from one transducer to another and was in the range 100–200 mV/psi at 10V dc and 24°C. There was no tubing connecting the surface of the cylinder to the pressure transducers, so no steps were taken to ensure that the measuremens were not contaminated by the acceleration of the fluid in such tubing.

The resonant frequency of the system was measured to be 16·3 Hz.

Most of the experiments were conducted with the pressure transducers positioned at $\alpha = -90°$ (see Figure 2 for the definition sketch). Some experiments were made with $\alpha = +90°$. The correlation measurements appeared to be not very sensitive, however, to the particular position of the pressure transducers, as will be shown later.

Circular, sharp-edged end plates, 39 cm in diameter, were used in some of the stationary-cylinder tests where the cylinder was located from the wall at about 20 cm. The correlation measurements showed that the results are insensitive to the presence of end plates.

Test conditions are summarized in Table 1. In the table, the Keulegan-Carpenter number, KC, is defined by

$$\mathrm{KC} = \frac{U_m T}{D}, \tag{1}$$

where T is the period of the oscillatory flow and U_m is the maximum velocity defined by

$$U = U_m \sin(\omega t), \tag{2}$$

TABLE 1

Test conditions

Keulegan Carpenter number KC	Range of gap ratio e/D	Cylinder Reynolds number Re	β number Re/KC	Range of amplitude $2A/D$
6	0–2·3	$3{\cdot}4 \times 10^4$	5,700	0–0·7
20	0–2·3	$6{\cdot}8 \times 10^4$	3,400	0–0·7
65	0–2·3	$6{\cdot}8 \times 10^4$	1,050	0–0·7

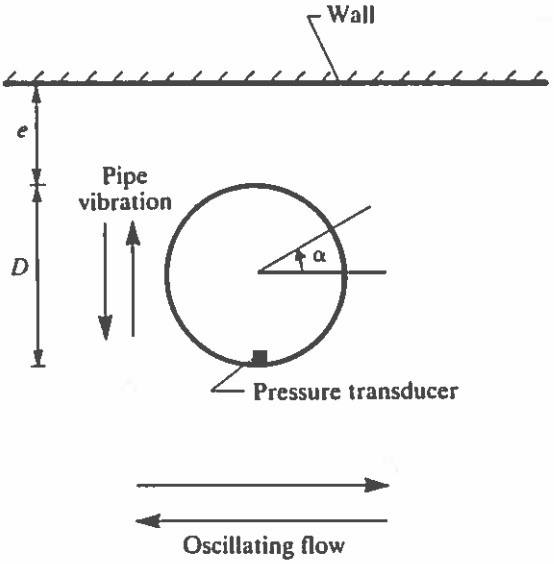

Figure 2. Definition sketch.

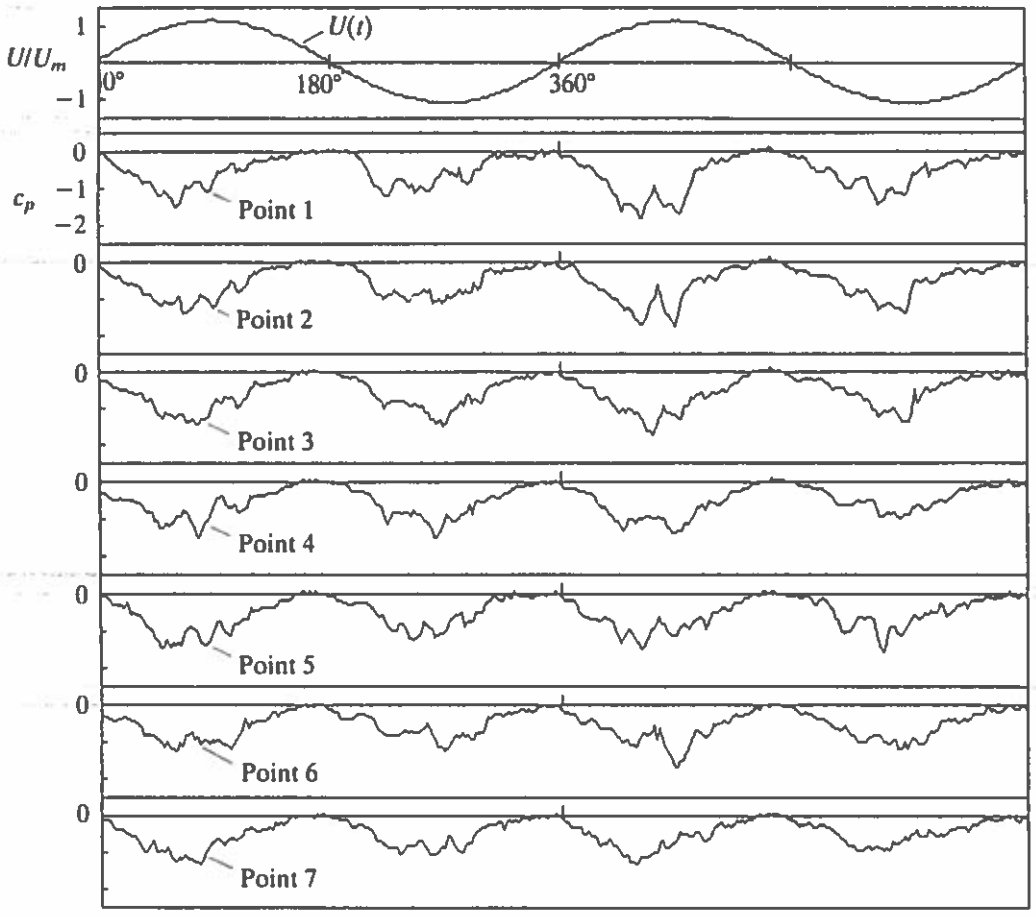

Figure 3. Stationary-cylinder pressure traces. KC = 65, $e/D = 0{\cdot}7$, $\alpha = -90°$. For the points where the pressure is measured, see Figure 1(a).

where U = the flow velocity, t = the time, and $\omega = 2\pi/T$, the angular frequency of the flow. The Reynolds number is defined by

$$\mathrm{Re} = \frac{U_m D}{\nu}. \tag{3}$$

Also, in the table, $2A$ = the double amplitude of the cylinder vibrations perpendicular to the flow direction.

From the table, it is seen that the gap ratio e/D varies in the range 0–2·3, where e is the gap between the pipe and the wall (Figure 2). In the case when the gap ratio is 2·3, the distance between the lower edge of the pipe and the bottom of the flume becomes approximately 40 cm. The ratio of this distance to the pipe diameter would then be 4·4. With this figure, it may be expected that there is some blockage effect. However, no blockage correction was made.

Pressures were measured simultaneously at the previously mentioned seven points, together with the displacement of the carriage, plus the displacement of the cylinder. Figures 3 and 4 give sample pressure traces. Here, c_p is the pressure coefficient defined

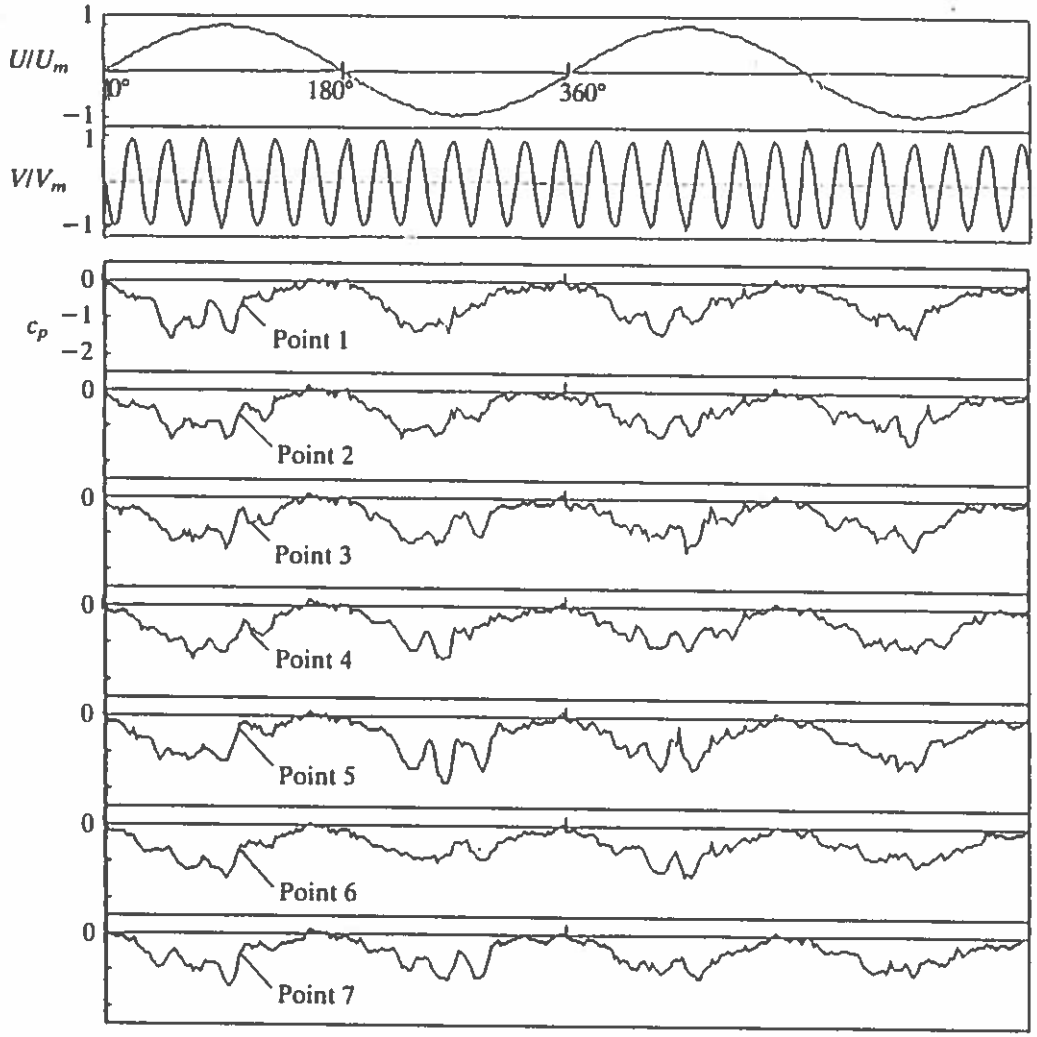

Figure 4. Vibrating-cylinder pressure traces. KC = 65, e/D = 1·5, $2A/D$ = 0·15, N = 13, $\alpha = -90°$. For the points where the pressure is measured, see Figure 1(a).

by

$$c_p = \frac{p - p_0}{(1/2)\rho U_m^2}, \tag{4}$$

in which p is the pressure measured at the point under consideration and p_0 is the hydrostatic pressure measured at the same point.

3. METHODS OF ANALYSIS

The correlation coefficient is calculated through the following equation

$$R(z, \omega t) = \frac{\overline{p'(\zeta, \omega t)p'(\zeta + z, \omega t)}}{[\overline{p'^2(\zeta, \omega t)}]^{1/2}[\overline{p'^2(\zeta + z, \omega t)}]^{1/2}}, \tag{5}$$

in which ζ is the spanwise distance, z is the spanwise separation between two pressure transducers, and p' is the fluctuation in pressure defined by

$$p' = p - \bar{p}. \tag{6}$$

The overbar in the preceding equations denotes ensemble averaging:

$$\bar{p} = \frac{1}{M}\sum_{j=1}^{M} p[\zeta, \omega(t + (j-1)T)], \tag{7}$$

$$\overline{p'^2} = \frac{1}{M}\sum_{j=1}^{M} \{p'[\zeta, \omega(t + (j-1)T)]\}^2, \tag{8}$$

$$\overline{p'(\zeta, \omega t)p'(\zeta + z, \omega t)} = \frac{1}{M}\sum_{j=1}^{M} p'[\zeta, \omega(t + (j-1)T]p'[\zeta + z, \omega(t + (j-1)T], \tag{9}$$

in which M is the total number of cycles. In the tests, the total number of cycles sampled was at least $M = 60$. However, no significant improvement in the consistency of the statistics was obtained with further increase in M.

Most of the results are presented in terms of the period-averaged correlation coefficient, which is defined by

$$R(z) = \frac{1}{2\pi}\int_0^{2\pi} R(z, \omega t)\, \mathrm{d}(\omega t). \tag{10}$$

In one case, however (Section 4.1.3), the correlation coefficient is calculated through the conventional time-averaging according to

$$R_T = \frac{\langle P'(\zeta)P'(\zeta + z)\rangle}{\langle P'^2(\zeta)\rangle^{1/2}\langle P'^2(\zeta + z)\rangle^{1/2}}, \tag{11}$$

where P' is defined by

$$P' = p - \langle p \rangle \tag{12}$$

and the symbol $\langle\ \rangle$ denotes the time-averaging:

$$\langle p \rangle = \lim_{T_0 \to \infty} \frac{1}{T_0}\int_t^{t+T_0} p\, \mathrm{d}t. \tag{13}$$

4. RESULTS AND DISCUSSION

4.1. Stationary Cylinder

4.1.1. *Time variation of correlation coefficient*

Figure 5 illustrates the time evolution of the mean pressure, $\bar{p}$. The instantaneous pressure trace for one cycle corresponding to the same measurement point is plotted on the same diagram to facilitate comparison.

The figure indicates that the fluctuation in pressure, namely p', is caused by the vortex shedding, since these fluctuations occur with the Strouhal period, T_s, which is defined by $\mathrm{St} = D/(U_m T_s)$, an average Strouhal number which is based on the maximum flow velocity, U_m, [see Sumer *et al.* (1991) for a detailed account of Strouhal number in conjunction with a cylinder placed near a wall in oscillatory flows, and note that the Strouhal frequency defined herein is different from any frequency corresponding to the peaks in the power spectrum]. This implies that the correlation coefficient based on these fluctuations [equation (5)] would give information about the length scales of the transverse cell structures associated with the vortex shedding.

Figure 6 illustrates the time evolution of the correlation coefficient, as the flow progresses. Here $\mathrm{KC} = 65$, $e/D = 1{\cdot}5$ and $z/D = 1{\cdot}8$. The figure shows that the correlation coefficient increases towards the end of the deceleration portion of every half period, and attains its maximum at the phase $\omega t \cong 165°$, about 15° before the outer flow reverses. This phase value corresponds to the instant where the flow at the measurement points comes to a standstill, as is seen from the pressure traces in Figure 3. As the flow progresses from this point onwards, however, the correlation is gradually decreased and assumes its minimum value for some period of time. Then it increases again towards the end of the next deceleration period.

Figure 7 shows three video sequences (at the phase values $\omega t = 113°$, 165° and 180°), taken from a video recording made in the present study. A careful inspection of the video film indicated that the flow in the neighbourhood of the cylinder indeed comes to a standstill at $\omega t = 165°$. The flow picture at this instant is given in Figure 7(b): the shear layer marked by the hydrogen bubble has rolled up into its vortex [A in Figure 7(b)] and is standing motionless. As time progresses from this point onwards, however, this vortex begins to move in the reverse direction and is washed over the cylinder as a

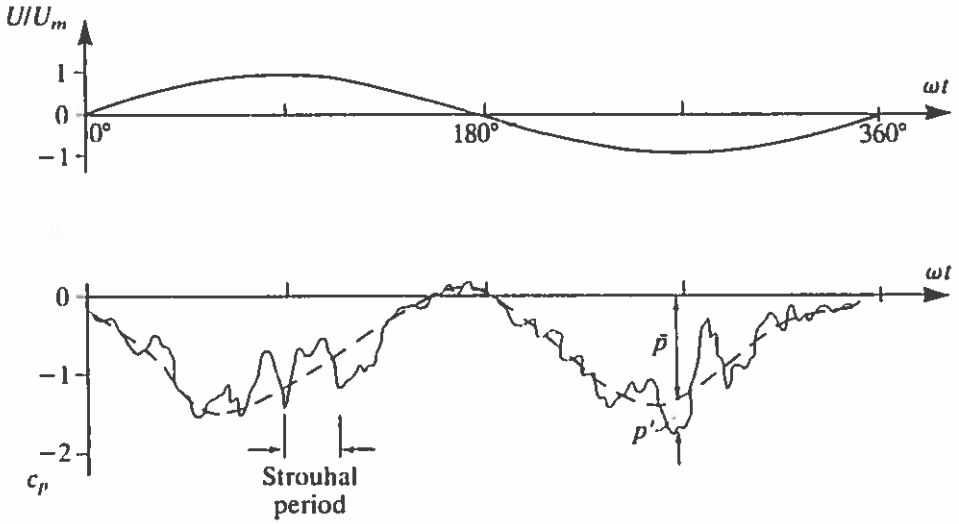

Figure 5. Pressure trace and the mean pressure variation for a stationary cylinder. $\mathrm{KC} = 65$, $e/D = 1{\cdot}5$, $\alpha = -90°$.

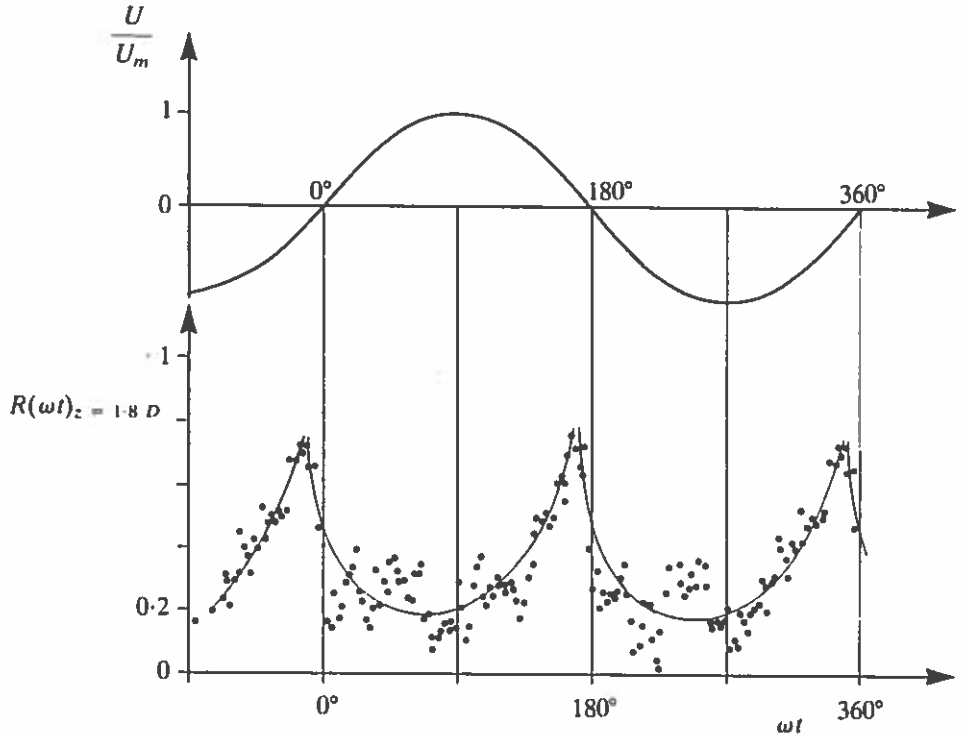

Figure 6. Stationary-cylinder correlation coefficient as a function of phase ωt. KC = 65, $e/D = 1{\cdot}5$, $z/D = 1{\cdot}8$ and $\alpha = -90°$.

coherent entity along the length of the cylinder [Figure 7(c)]. Now, comparison of Figure 7(a) with Figure 7(b) indicates that while spanwise cell structures can easily be identified in the former ($\omega t = 113°$), no such structure is apparent in Figure 7(b) ($\omega t = 165°$), meaning that the spanwise correlation should be distinctly larger in the latter than in the former case. The same is also true for $\omega t = 180°$ where, again, large correlations should be expected. This is indeed the case found in the preceding in relation to Figure 6.

4.1.2. *Period-averaged correlation coefficient*

Figure 8 depicts the period-averaged correlation coefficients. The correlation coefficients presented hereafter in the paper are all the period-averaged ones. In the figure, wall-free cylinder data for oscillatory flows reported by Obasaju *et al.* (1988) are also shown for comparison. In the latter study, the correlation measurements were made by measuring the pressure differential, i.e. the difference between the pressures on the diametrically opposite points at the top and bottom of the cylinder ($\alpha = \pm 90°$). The figure indicates that the present data show exactly the same trend as those of Obasaju *et al.* (1988); namely the correlation coefficient takes very large values when KC is small [KC = 10 in Obasaju *et al.* (1988) and KC = 6 in the present case], while it takes the lowest value when KC is around 20. Obasaju *et al.* (1988) give a detailed account of the behaviour of the correlation coefficient as a function of KC number. They link the low correlation measured at KC = 22 to the fact that KC = 22 lies at the boundary between the two KC-regimes, $15 < KC < 22$ and $22 < KC < 30$, while they argue that the correlation is measured to be high at KC = 10 because KC = 10 lies in the center of the KC-regime $7 < KC < 15$ [see also Bearman (1985)].

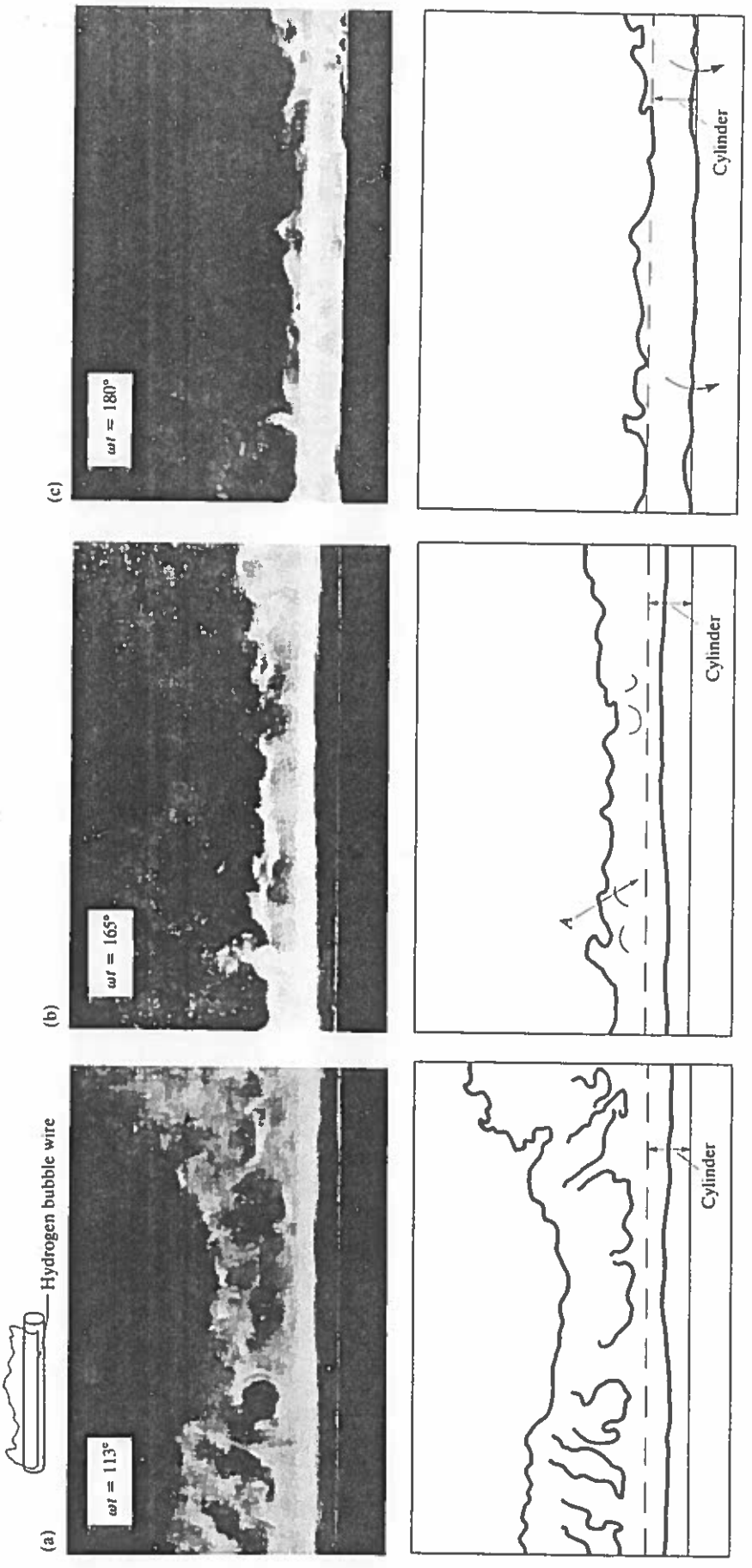

Figure 7. Hydrogen-bubble flow visualization sequence of pictures showing the time development of the spanwise cell structures for a stationary cylinder. $e/D = 3$, $D = 2$ cm, $KC = 40$, $Re = 2 \times 10^3$.

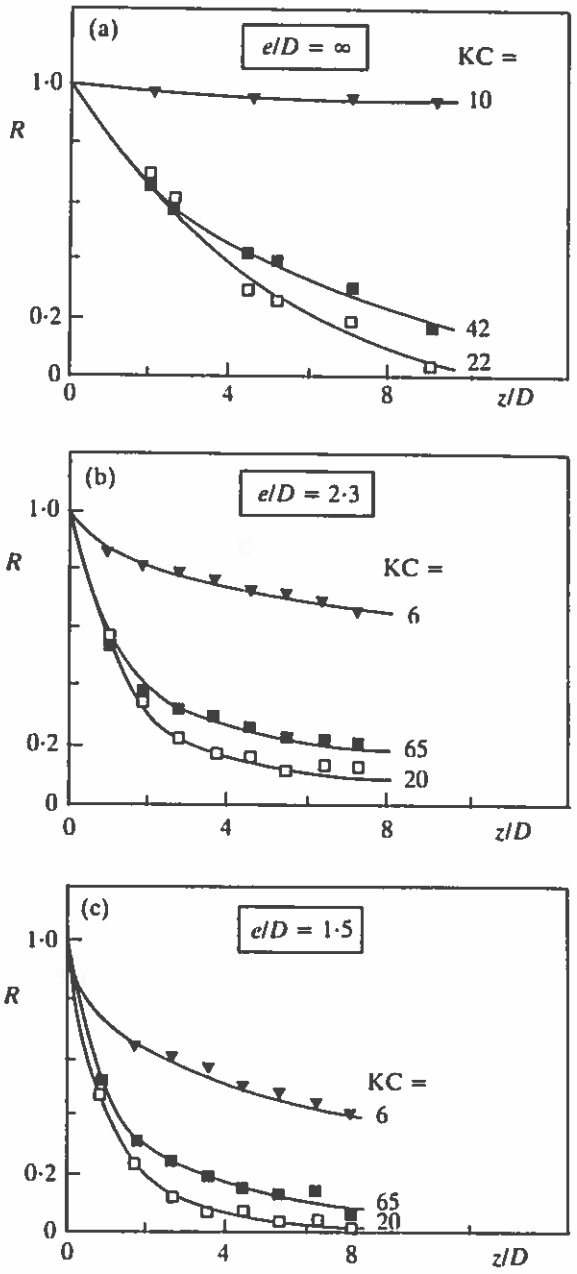

Figure 8. Stationary-cylinder period-averaged correlation coefficient: (a) Obasaju *et al.* (1988) wall-free cylinder $Re = 7 \times 10^3$ for $KC = 10$, $Re = 1{\cdot}5 \times 10^4$ for $KC = 22$, $Re = 3 \times 10^4$ for $KC = 42$; (b) and present experiments, $e/D = 2{\cdot}3$; (c) present experiments, $e/D = 1{\cdot}5$.

In order to see whether or not the present data agree with the steady-current data when KC becomes large, the results regarding the $KC = 65$ tests are plotted together with Toebes' (1969) and Howell & Novak's (1979) steady-current results in Figure 9. In Toebes' study the correlation coefficient was obtained through velocity measurements, while in Howell & Novak's (1979) study it was obtained through measuring the pressure on the cylinder surface. It appears that the present data agree reasonably well with the steady-current data, although there is a tendency for the correlation coefficient to be slightly larger in the oscillatory flow situation for large values of the spanwise distance. This slight increase in the correlation may be attributed to the extremely high values of the correlation coefficient experienced at the times when the flow around the cylinder comes to a standstill during the flow reversals, as described in the previous section.

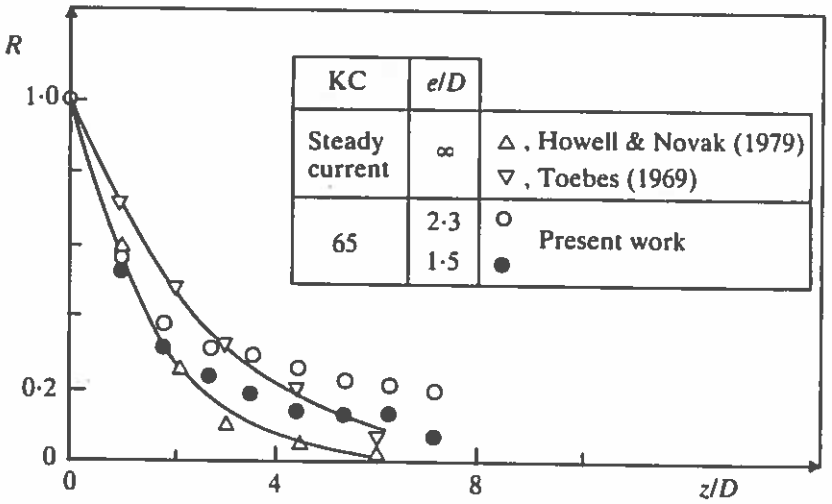

Figure 9. Comparison of present period-averaged correlation coefficients (KC = 65) with steady-current correlation data. $Re = 6{\cdot}8 \times 10^4$ in the present experiments. $Re = 7{\cdot}5 \times 10^4$ in Howell & Novak's (1979) study and $Re = 7 \times 10^4$ in Toebes' (1969) study.

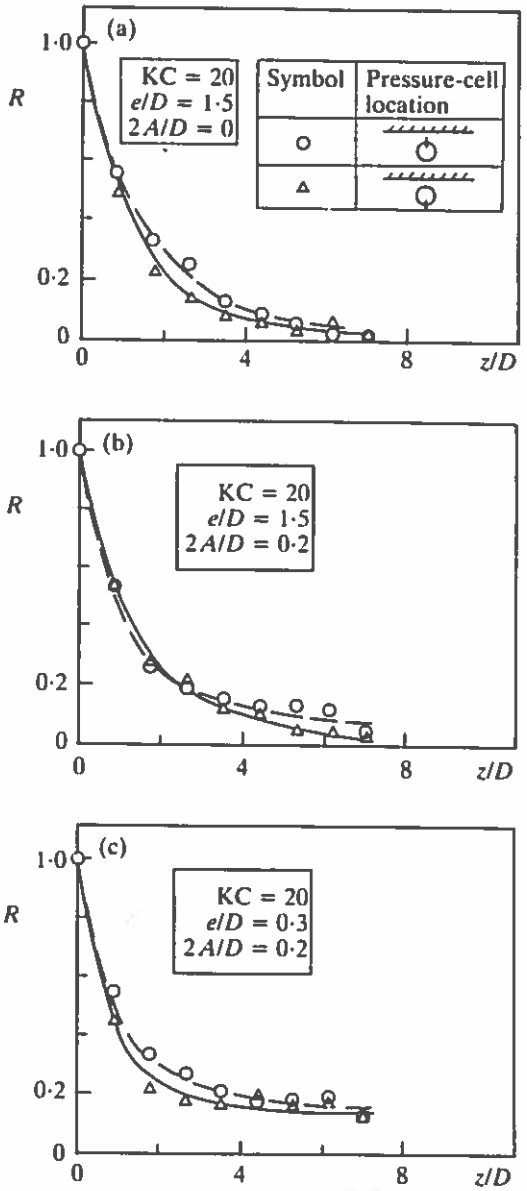

Figure 10. Effect of location of the pressure transducers on period-averaged correlation coefficient. (a) Stationary cylinder; (b) and (c) vibration frequency $N = 4$.

In Figure 10, the correlation diagrams obtained with the pressure cells positioned at $\alpha = -90°$ are compared with those at $\alpha = 90°$. In the figure the vibrating cylinder results are also included for the sake of completeness. The figure indicates that the results are insensitive to the particular position of the transducers, although there is a slight tendency for the correlations to be a little larger when the pressure transducers are located at the wall-side of the pipe ($\alpha = 90°$).

4.1.3. *Influence of wall proximity*

Figure 11 shows the correlation coefficients calculated through equations (5) and (10) for four different test data with $e/D = 2{\cdot}3$, $1{\cdot}5$, $0{\cdot}1$ and 0.

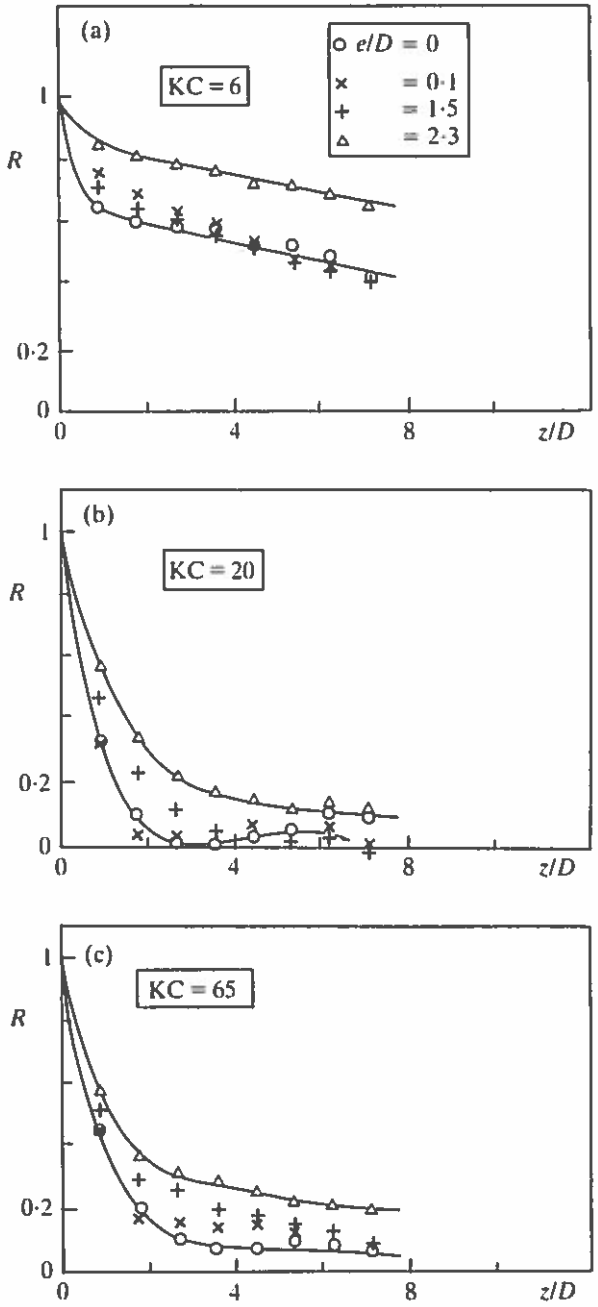

Figure 11. Stationary-cylinder, period-averaged correlation coefficient. Wall proximity effect regarding the pressure fluctuations. See Figure 13 for the wall proximity effect regarding the correlation of the lift force.

The general trend in Figure 11 is that the correlation coefficient decreases with decreasing gap ratio. However, caution must be exercised in interpreting the results in the figure. While R for $e/D = 2{\cdot}3$ and $1{\cdot}5$ can be regarded as the correlation coefficient also for the lift force on the cylinder (since the fluctuations p' for which R is calculated are caused by the vortex shedding), this is not the case for $e/D = 0{\cdot}1$ and 0. First of all, for $e/D = 0$, the vortex shedding is totally absent and the fluctuations in the measured pressure, p', in this case degenerate from those induced by the highly organized vortex-shedding phenomenon ($e/D = 2{\cdot}3$ and $1{\cdot}5$) to those due to disorganized turbulence. So, the correlation, R, for this case, namely $e/D = 0$, only gives information about the length scale in the spanwise direction of this turbulence.

For $e/D = 0{\cdot}1$, on the other hand, the vortex shedding may be maintained, particularly for small KC (Sumer *et al.* 1991). However, the lift in this case consists of two parts, a low frequency portion which is caused by the close proximity of the wall and the superimposed high-frequency fluctuations which are caused by vortex shedding [Figure 12(c)]. As such, the correlation, R, calculated on the basis of fluctuations, p',

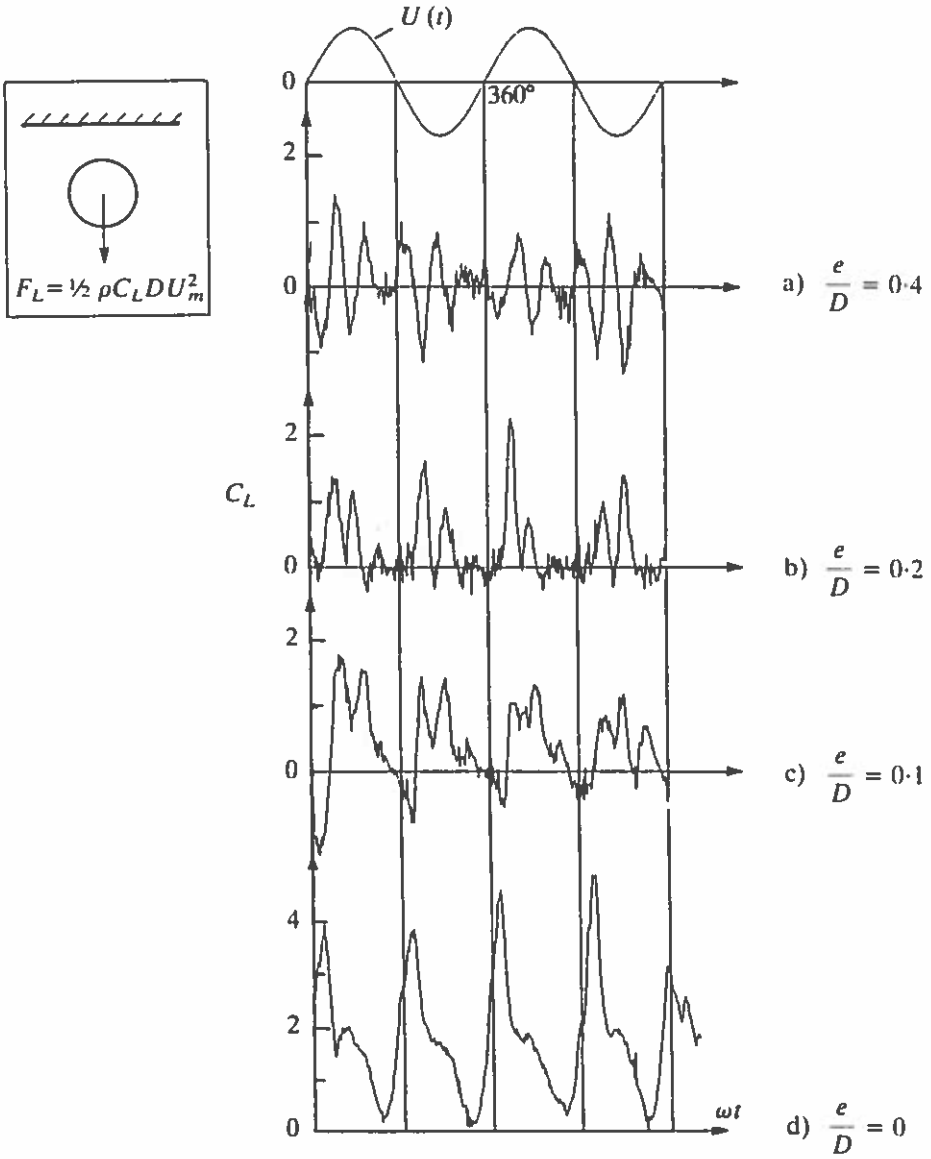

Figure 12. Lift-force traces. KC = 20, positive lift is directed away from the wall. Taken from Sumer *et al.* (1991). $C_L = F_L/(\frac{1}{2}\rho U_m^2 D)$.

which are associated with the vortex shedding only, cannot be regarded as the correlation coefficient also for the lift force for the case of $e/D = 0{\cdot}1$.

Regarding the correlation of the lift force itself, we were unable to study the influence of the wall proximity in a detailed manner with the existing facility. For this, clearly, either the lift force itself or the pressure differential at the top and bottom of the cylinder should be measured. Nevertheless, to give an indication of the kind of change which would take place with regard to the wall proximity, the following analysis has been undertaken.

Only the wall-mounted cylinder situation has been considered, with the pressure transducers positioned on the flow side of the cylinder ($\alpha = -90°$). Clearly, with this arrangement the pressure time-series can be substituted in place of the lift force ones, as far as the correlation calculations are concerned. Regarding the lift force itself, the

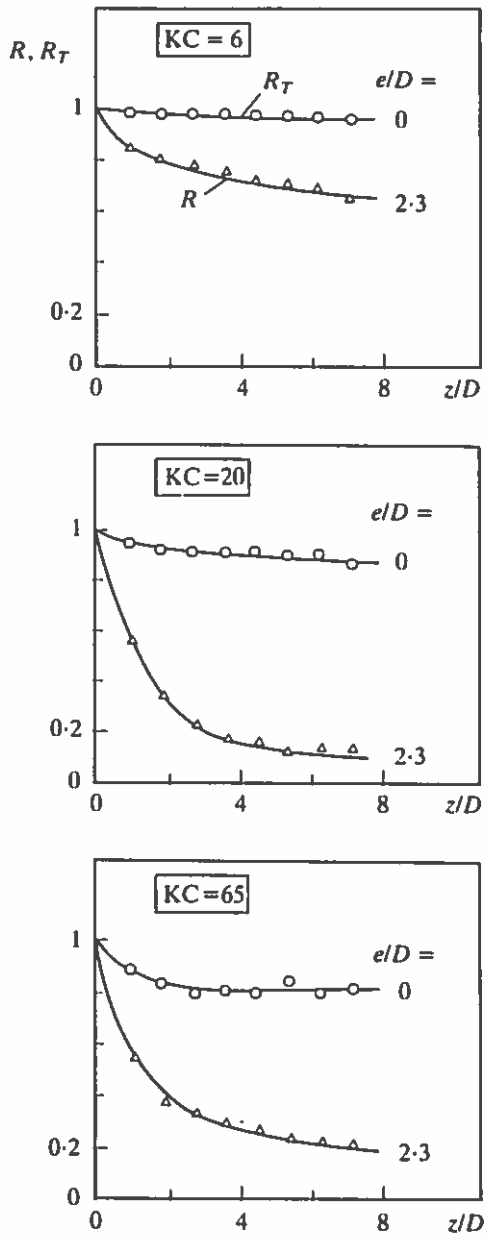

Figure 13. Correlation coefficient for the *lift force* on cylinder, showing wall proximity effect. R_T for the wall-mounted cylinder is computed direct from pressure signals employing time-averaging according to equations (11)–(13).

lift in this case ($e/D = 0$) is not caused by the pressure fluctuations [as opposed to what occurs in the case of wall-free cylinder, Figure 12(a)], but rather by the contraction of the streamlines near the flow side of the cylinder as well as by the movement of the lee-wake vortex over the cylinder, which results in the observed peak in the lift force prior to the flow reversal in each half-cycle of the motion [Figure 12(d) and Sumer *et al.* (1991)]. Hence, the correlation in connection with the lift force in this case cannot be calculated by equation (5) (which is based on the pressure fluctuations rather than on the pressure itself); instead, the usual time-averaging should be employed, i.e. the correlation is calculated by equation (11).

Figure 13 presents the spanwise correlation coefficients obtained for the wall-mounted cylinder, where the results for $e/D = 2{\cdot}3$ of Figure 8 (or Figure 11) are re-plotted to facilitate comparison. The correlations in these diagrams are now all associated with the lift force; therefore comparison can be made on the same basis. The figure indicates that, as expected, the correlation increases tremendously as the gap ratio changes from 2·5 (the wall-free cylinder) to nil (the wall-mounted cylinder). The pressure traces in Figure 14 are quite indicative, in the sense that the pressure-variation pattern at different measurement points is maintained over a long distance along the length of the wall-mounted pipe, revealing the extremely high values of the correlation coefficients found in the analysis.

Figure 15 depicts the maximum value of the standard deviation of the pressure fluctuations, σ_p, together with the lift force as a function of KC and e/D, where σ_p is defined by

$$\sigma_p = \mathrm{Max}[\overline{p'^2(z, \omega t)}]^{1/2}, \tag{14}$$

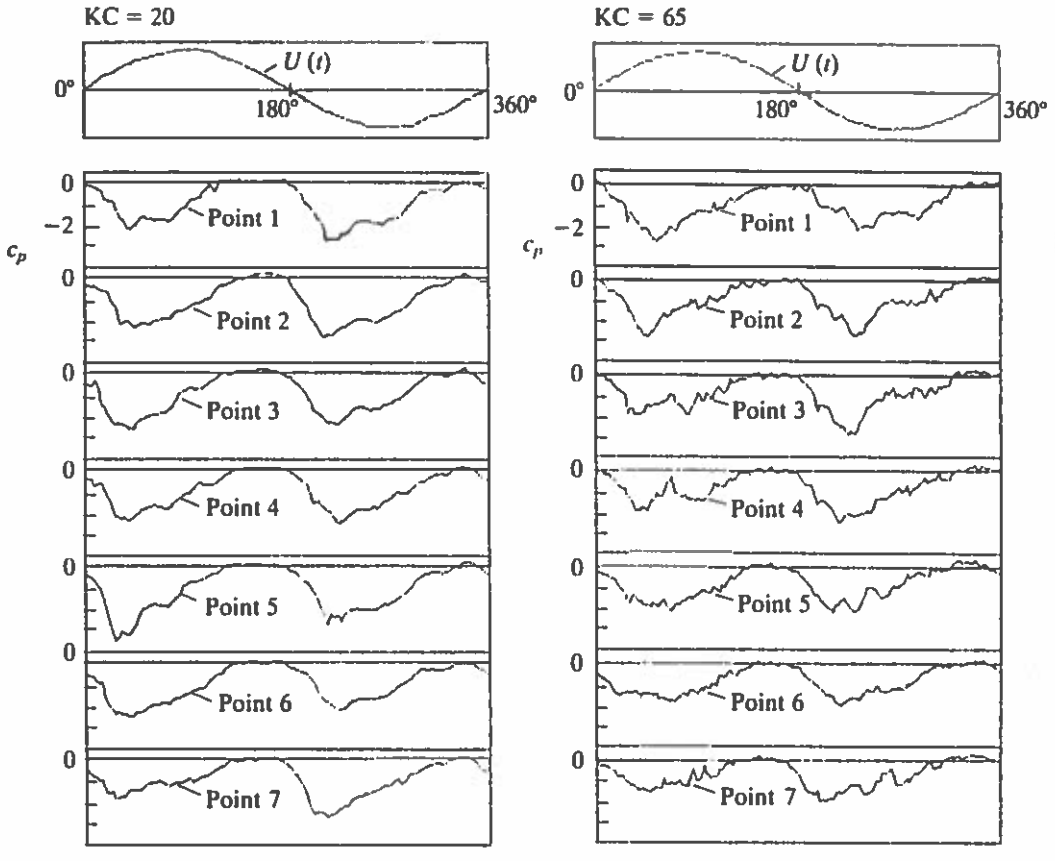

Figure 14. Pressure traces for (a) KC = 20 and (b) KC = 65; $e/D = 0$. Stationary cylinder, with $\alpha = -90°$. For the points where the pressure is measured, see Figure 1(a).

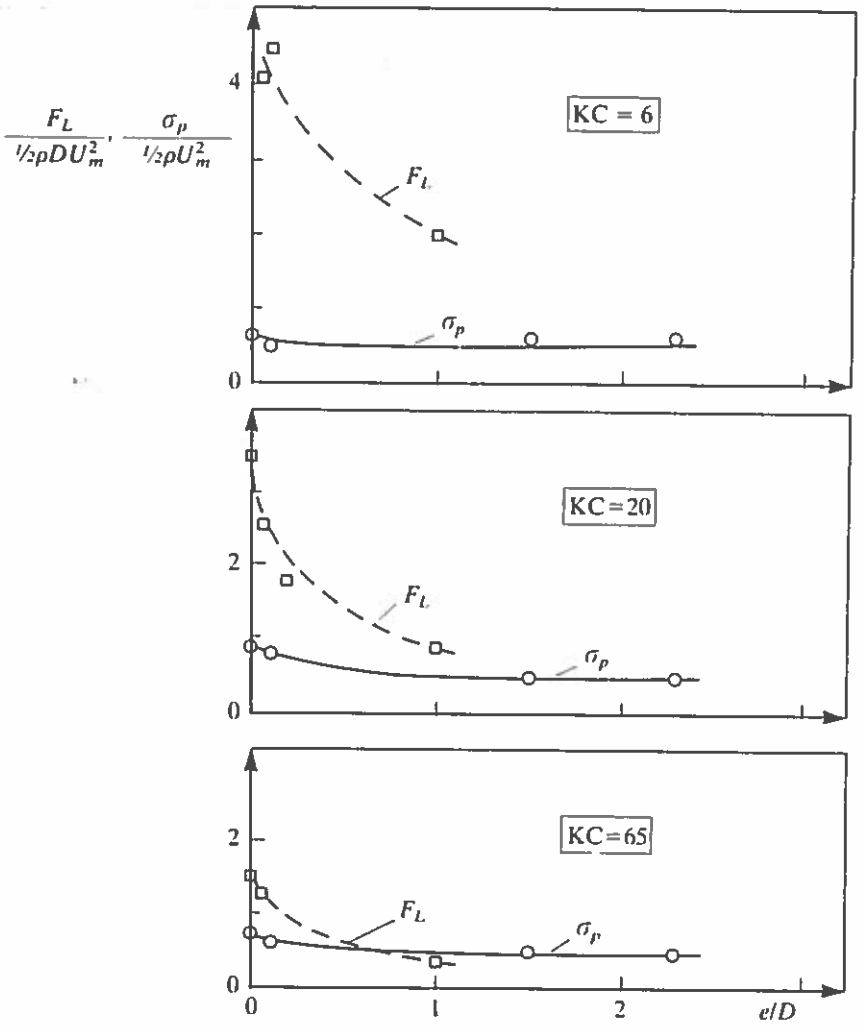

Figure 15. Comparison of turbulence magnitude σ_p with the lift force F_L. The lift force variations are taken from Sumer *et al.* (1991), where Re = $0{\cdot}8 \times 10^5$–$1{\cdot}1 \times 10^5$ and $\beta = 2000$–8000. F_L here is the maximum value of the lift force directed away from the wall.

in which $\overline{p'^2}$ is calculated by equation (8). The quantity σ_p can be regarded as a measure of the magnitude of the previously mentioned turbulence, and the figure illustrates how this turbulence compares with the corresponding lift force. From the figure it may be concluded that the correlation regarding the turbulence must be of secondary importance with respect to the lift force, even for large KC numbers (such as KC = 65) near the wall.

4.2. Vibrating Cylinder

Figure 16 presents the correlation coefficients as functions of the double-amplitude-to-diameter ratio for the three KC numbers studied, plus Howell & Novak's (1979) steady-current data. Note that in Howell & Novak's study the cylinder is vibrated with a frequency equal to its vortex-shedding frequency, which is equal to the frequency of the lift force acting on the cylinder. Likewise, in the present study, the cylinder is vibrated with a frequency equal to the frequency of the lift force. If this frequency is denoted by f_v and the frequency of the oscillatory flow by f_w, then $N = f_v/f_w$ will become the number of oscillations in the lift force for one cycle of the flow. Now, in the present study N was set equal to 13 for KC = 65, to 4 for KC = 20, and to 2 for

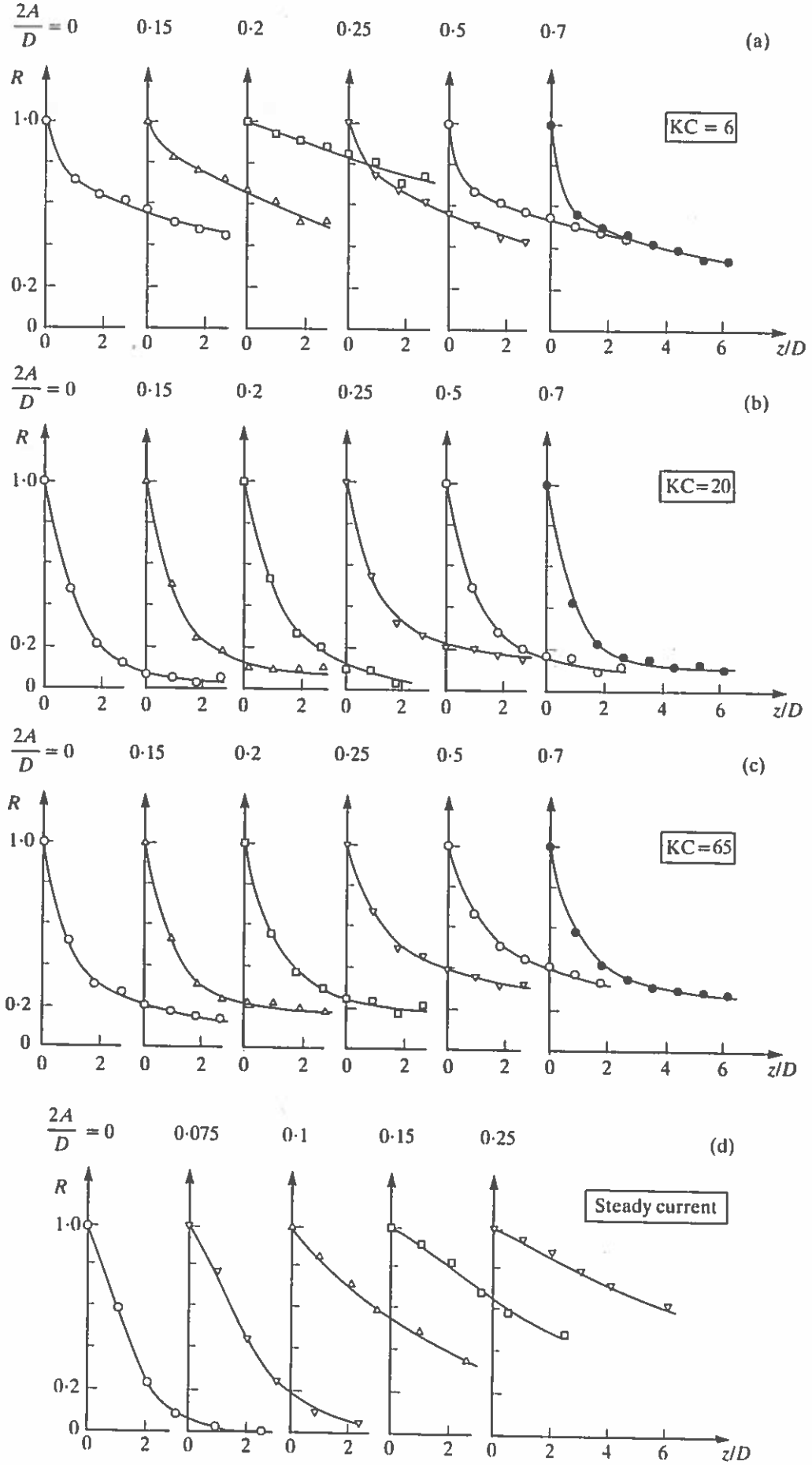

Figure 16. Period-averaged correlation coefficient for vibrating cylinder for $e/D = 1{\cdot}5$. (a) $N = 2$ and $\mathrm{Re} = 3{\cdot}4 \times 10^4$ for $\mathrm{KC} = 6$; (b) $N = 4$ and $\mathrm{Re} = 6{\cdot}8 \times 10^4$ for $\mathrm{KC} = 20$ and (c) $N = 13$ and $\mathrm{Re} = 6{\cdot}8 \times 10^4$ for $\mathrm{KC} = 65$; (d) steady-current data from Howell & Novak (1979), where $e/D = \infty$ and $\mathrm{Re} = 7{\cdot}5 \times 10^4$.

TABLE 2

Sarpkaya's (1976) data on stationary-cylinder lift-force frequency and Sumer & Fredsøe's (1988) data on cross-flow vibration frequency of a flexibly mounted cylinder

	Number of cross-flow vibrations of a flexibly mounted cylinder per flow cycle (for small values of reduced velocity) $N = f/f_w$		Number of oscillations in the lift force on a stationary cylinder per flow cycle	
	Sumer & Fredsøe (1988)		Sarpkaya (1976)	
KC	Experiment I	Experiment II	$N = f_v/f_w$	St$(=f_vD/U_m) = N$/KC
10	2	2	2	0·2
20	4	4–5	4	0·2
30	7	6–7	6	0·2
40	8	8–10	8	0·2
60	13	12	10–15	0·17–0·25
100	21	21	15–?	0·15–?

KC = 6. Note that these figures are in accordance with Sarpkaya's (1976) stationary-cylinder lift-force frequency results and also with Sumer & Fredsøs's (1988) results with regard to the cross-flow vibration frequency of a flexibly mounted cylinder subject to an oscillatory flow (see Table 2). It should be noted that the Strouhal number defined by $\mathrm{St} = f_vD/U_m$, which can be expressed as the ratio of N/KC (see the last column of the table), remains reasonably constant at about 0·2, a point which has already been made by Sarpkaya (1976).

Returning to Figure 16, the following conclusions can be deduced from the figure.

(i) A constant increase in the correlation coefficient with increasing amplitudes takes place up to the values of $2A/D$ of about 0·2 for KC = 6 and up to $2A/D = 0{\cdot}3$ for KC = 20 and 65. This can be seen even more clearly from Figure 17 where the correlation coefficient at the spanwise distance $z = D$ is plotted as a function of $2A/D$. The way in which the correlation coefficient increases with increasing amplitude-to-diameter ratio is in accord with the steady current results (Figures 16 and 17). However, this increase is not as large as in steady currents.

(ii) The correlation decreases, however, for further increase in the value of $2A/D$. This may be attributed to the change in the flow regime with increasing $2A/D$ [this change in the flow regime with increasing $2A/D$ has been demonstrated recently by Williamson & Roshko (1988) for a cylinder exposed to a steady current]. No pressure correlation data are available for the steady-current situation for values of $2A/D$ larger than 0·25. Therefore, no comparison could be made, as far as such high values of $2A/D$ are concerned. There are, however, correlation measurements (Ramberg & Griffin 1976) for $2A/D$ values as large as 0·7, where the correlation coefficient is based on wake velocity signals; these measurements indicate that the correlation coefficient increases in a monotonous manner with increasing amplitudes, which is an obvious consequence of the fact that the correlations in these experiments are based on the wake velocity signal.

Figure 18 illustrates how the vibration frequency influences the correlation coefficient. Here $N = 13$ is the number of vibrations in one cycle of the oscillatory flow and it corresponds to the Strouhal frequency, St, according to $N = \mathrm{St} \times \mathrm{KC}$. As seen from the figure, the correlation decreases as the vibration frequency moves away from

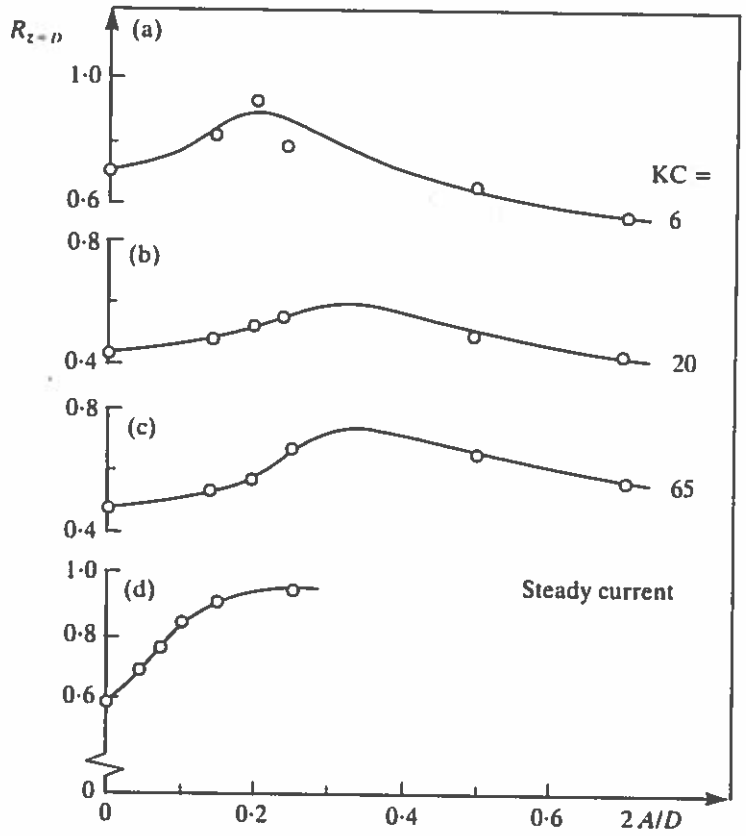

Figure 17. (a), (b) and (c) Period-averaged correlation coefficient for vibrating cylinder for different KC numbers; (d) Steady-current data (Howell & Novak 1979), $e/D = \infty$ and $\mathrm{Re} = 7{\cdot}5 \times 10^4$.

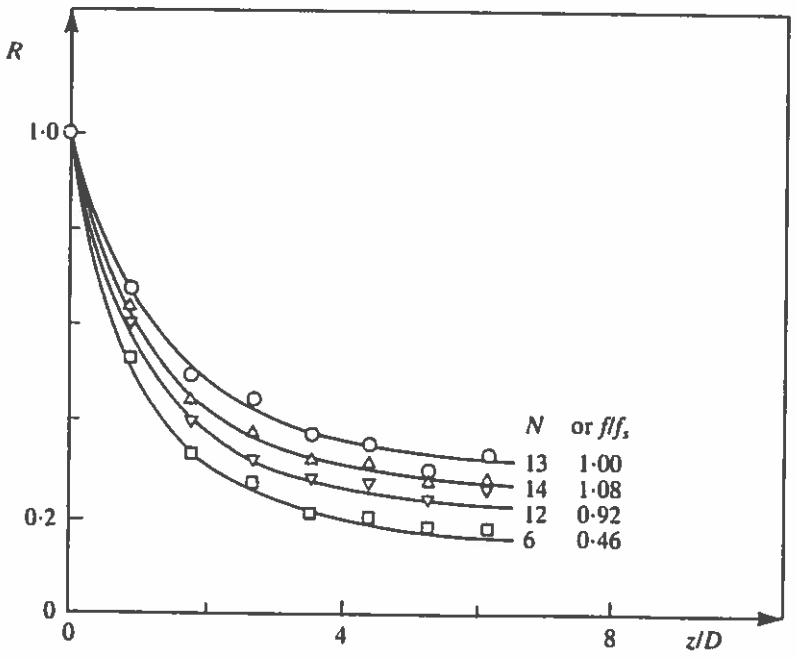

Figure 18. Effect of vibration frequency on period-averaged correlation coefficient for KC = 65, $e/D = 1{\cdot}5$ and $2A/D = 0{\cdot}25$.

the Strouhal frequency. This result is in agreement with the corresponding result obtained in Toebes' (1969) study for the steady-current situation.

Figure 19, on the other hand, illustrates the effect of close proximity of the wall. From the figure, the correlation generally decreases (albeit slightly) with decreasing gap ratio, in accord with the stationary-cylinder results given in Figure 11. For KC = 20 and large values of the separation distance, however, the trend is in the opposite direction. No clear explanation has been found for this behaviour. Again, caution must be exercised in interpreting the results in this figure. As mentioned in Section 4.1.3, while R for $e/D = 1{\cdot}5$ can be regarded as the correlation coefficient also for the lift

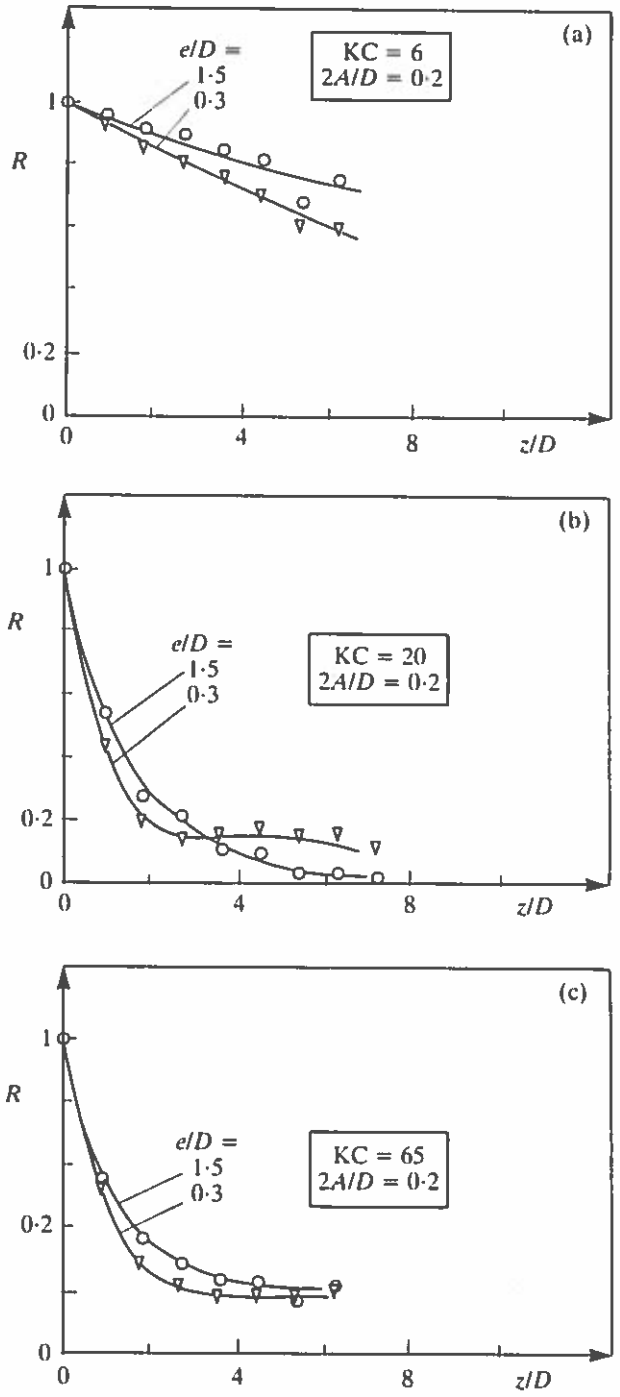

Figure 19. Effect of wall proximity on period-averaged correlation coefficient for vibrating cylinder. Vibration frequencies: (a) $N = 2$ for KC = 6, (b) $N = 4$ for KC = 20 and (c) $N = 13$ for KC = 65.

force, this may not be the case for $e/D = 0{\cdot}3$. So, the variation exhibited in Figure 19 regarding wall proximity does not represent that associated with the lift force on the cylinder.

5. CONCLUSIONS

The main conclusions of this study may be summarized as follows.

(a) The spanwise correlation coefficient evolves in an orderly fashion, as the flow progresses throughout the cycle of the oscillatory motion. It attains its maximum value at the instant when the flow around the cylinder comes to a standstill at the times of flow reversal.

(b) As far as the influence of the wall proximity is concerned, the correlation increases tremendously with wall proximity, regarding the lift force.

(c) The effect of wall proximity becomes insignificant, however, when the turbulence, either in the form of organized motion (namely, vortex shedding in the case of wall-free cylinder) or in the form of disorganized wake flow in the case of wall-mounted cylinder, is considered.

(d) As far as the influence of vibrations is concerned, the correlation coefficient first increases with increasing amplitude of transverse vibrations. The results indicate that this occurs up to the values of $2A/D = 0{\cdot}2$ for $KC = 6$ and $2A/D = 0{\cdot}3$ for $KC = 20$ and 65. For $2A/D$ larger than the preceding figures, the correlation coefficient decreases monotonously with increasing amplitudes.

ACKNOWLEDGMENT

The study is partially supported by the research programme "Marine Technique" of The Danish Scientific Council (STVF). Mr Niels Christiansen, M.Sc., was very helpful in the flow-visualization work.

References

Bearman, P. W. 1985 Vortex trajectories in oscillatory flow. In *Proceedings International Symposium on Separated Flow Around Marine Structures*. p. 133. The Norwegian Institute of Technology, Trondheim, Norway.

Howell, J. F. & Novak, M. 1979 Vortex shedding from a circular cylinder in turbulent flow. In *Proceedings Fifth International Conference on Wind Engineering*, paper V-11

King, R. 1977 A review of vortex shedding research and its application. *Ocean Engineering* **4**, 141–171.

Koopmann, G. H. 1967 The vortex wakes of vibrating cylinders at low Reynolds numbers. *Journal of Fluid Mechanics* **28**, 501–512.

Novak, M. & Tanaka, H. 1977 Pressure correlations on a vibrating cylinder. In *Proceedings Fourth International Conference on Wind Effects on Buildings and Structures*, Heathrow, 1975, U.K. pp. 227–232, Cambridge, Cambridge University Press.

Obasaju, E. D., Bearman, P. W. & Graham, J. M. R. 1988 A study of forces, circulation and vortex patterns around a circular cylinder in oscillating flow. *Journal of Fluid Mechanics* **196**, 467–494.

Ramberg, S. E. & Griffin, O. M. 1976. Velocity correlation and vortex spacing in the wake of a vibrating cable. *ASME Journal of Fluids Engineering* **98**, 10–18.

Sarpkaya, T. 1976 In-line and transverse forces on smooth and sand-roughened cylinders in oscillatory flow at high Reynolds numbers. Naval Postgraduate School Technical Report No. NPS-69SL76062, Monterey, CA, U.S.A.

Sumer, B. M. & Fredsøe, J. 1988 Transverse vibrations of an elastically mounted cylinder exposed to an oscillating flow. *ASME Journal of Offshore Mechanics and Arctic Engineering* **110**, 387–394. Also in *Proceedings 6th Symposium on Offshore Mechanics and Arctic Engineering*, OMAE, Houston, TX, 1987, **2**, 165–173.

SUMER, B. M., JENSEN, B. L. & FREDSØE, J. 1991 Effect of a plane boundary on oscillatory flow around a circular cylinder. *Journal of Fliud Mechanics* **225**, 271–300.

TOEBES, G. H. 1969 The unsteady flow and wake near an oscillating cylinder. *ASME Journal of Basic Engineering* **91**, 493–502.

WILLIAMSON, C. H. K. & ROSHKO, A. 1988 Vortex formation in the wake of an oscillating cylinder. *Journal of Fluids and Structures* **2**, 355–381.

APPENDIX: NOMENCLATURE

c_p	pressure coefficient
C_L	lift coefficient
D	cylinder diameter
f_u	frequency of vortex-shedding induced lift force
f_w	frequency of oscillatory flow
F_L	lift force per unit length of cylinder
KC	Keulegan-Carpenter number
M	number of oscillatory-flow cycles sampled
N	number of transverse vibrations for one cycle of oscillatory flow; also, number of oscillations in lift force for one cycle of oscillatory flow
p	pressure
p_0	hydrostatic pressure
$\bar{p}$	mean pressure
p'	fluctuating pressure
$R(z, \omega t)$	correlation coefficient based on ensemble averaging, equations (5)–(9)
$R(z)$ or R	period-averaged correlation coefficient
R_T	correlation coefficient based on time-averaging, equations (11)–(13)
Re	Reynolds number
St	Strouhal number
t	time
T	period of oscillatory flow
T_s	Strouhal period
U	outer flow velocity
U_m	maximum value of the outer flow velocity
V	velocity of cylinder
V_m	maximum value of the velocity of cylinder
z	separation distance in spanwise direction
α	angular position of pressure transducers
β	Re/KC
ζ	spanwise coordinate
ν	kinematic viscosity
ρ	fluid density
σ_p	maximum value of the root-mean-square of the pressure fluctuations
ω	angular frequency of oscillatory flow

Mathematical Model for Littoral Drift

Rolf Deigaard

Danish Hydraulic Institute
Agern Allé 5
2970 Hørsholm
Denmark

Jørgen Fredsøe and Ida Brøker Hedegaard

Institute of Hydrodynamics and Hydraulic Engineering
Technical University of Denmark

Mathematical Model for Littoral Drift

By Rolf Deigaard,[1] Jørgen Fredsøe,[2] and Ida Brøker Hedegaard[3]

Abstract: The longshore sediment transport along the coast is investigated by use of detailed sediment transport models in the surf zone. Combined with a detailed description of the wave height and longshore current distribution in the surf-zone, the littoral drift along the coast is calculated and presented in dimensionless diagrams for coasts with constant slope. The paper further analyzes the transverse distribution of the longshore sediment transport on a coast with bars. The last case is compared with field measurements.

Introduction

Sediment transport in near-shore areas is a complex three-dimensional phenomenon which often is split up into two parts, the on-off shore transport and the longshore transport. These two processes cannot be considered independently: for instance, the on-off shore sediment transport creates the bars on coasts where the change in water level due to tides only is moderate. Bars are created by onshore movement outside the breaker zone and offshore movement inside the breaker zone, see e.g. Ref. 6. These bars modify the longshore sediment transport distribution across the coast profile, as discussed later in this paper.

The information about on-offshore sediment transport is today very scarce and most research is correlated to the circulation of water under broken waves, see e.g. Ref. 6. Much more research has been done on the longshore sediment transport, where the transport mechanism has been known for several decades. On a coast without any external driven current, the sediment is transported by the longshore current generated in the surf zone due to a decrease in the radiation stresses (20). The sediment is picked up from the bottom due to the orbital wave motion which creates near-bed velocities normally much stronger than the nearbed longshore current velocities.

A first approach to quantify the above mechanism is the well-known CERC-formula (26), which simply relates the longshore sediment transport I_l in terms of the submerged weight to the "longshore energy flux factor" P_{ls} by

$$I_l = KP_{ls} \quad \ldots\ldots (1)$$

By this method, important parameters like grain sizes and the morphology of the coast (bars, slopes) are not taken into account.

A more theoretical approach has been carried out by Bijker (5), who calculated the sediment transport in several steps. First, he calculated

[1]Hydr. Engr., Danish Hydraulic Institute, Agern Alle 5 DK-2970 Horsholm, Denmark.

[2]Assoc. Prof., Inst. of Hydrodynamics and Hydr. Engrg. (ISVA), Tech. Univ., Denmark, DK-2800 Lyngby, Denmark.

[3]ISVA. (Present address: Danish Hydraulic Institute).

Note.—Discussion open until October 1, 1986. To extend the closing date one month, a written request must be filed with the ASCE Manager of Journals. The manuscript for this paper was submitted for review and possible publication on May 2, 1985. This paper is part of the *Journal of Waterway, Port, Coastal and Ocean Engineering*, Vol. 112, No. 3, May, 1986. ©ASCE, ISSN 0733-950X/86/0003-0351/$01.00. Paper No. 20595.

the longshore current induced by the incoming waves. Further on he calculated the variation in wave height perpendicular to the coast, taking into account the breaking of waves. Finally, from this combined wave-current motion he calculated the resulting sediment transport from a sediment transport formula.

The purpose of the present work is to introduce recently developed models for the vertical distribution of suspended sediment in combined wave-current motion in non-breaking waves (14) as well as in broken waves (9), the latter being an extension of Ref. 14. These models are combined with a detailed description of the change in wave height in the surf zone and in the longshore current distribution.

Hydrodynamic Description

The hydrodynamic description can be split up into two parts: (1) A macro scale description giving the gross-behavior of waves (refraction, shoaling, breaking) and current (longshore current distribution); and (2) a detailed description of the flow in a vertical in order to describe the vertical distribution of suspended sediment and the flow-resistance in combined wave-current motion.

Of course items (1) and (2) are interdependent. For instance the longshore current distribution is a function of the friction factor f in combined wave-current motion where f is evaluated under item (2).

In the following, the macro scale description is briefly outlined first. Later on we revert to the detailed flow description.

Variation in Wave Height

In the following, we consider a long straight shore line with parallel bottom contours. From deep water, the waves are refracted and shoaled

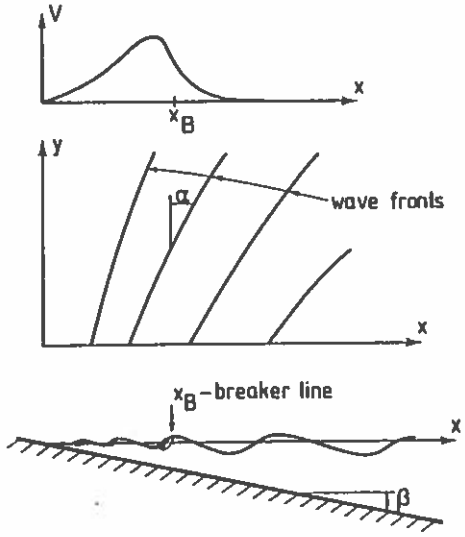

FIG. 1.—Definition of Longshore Current Profile, Wave Crests and Coastal Profile

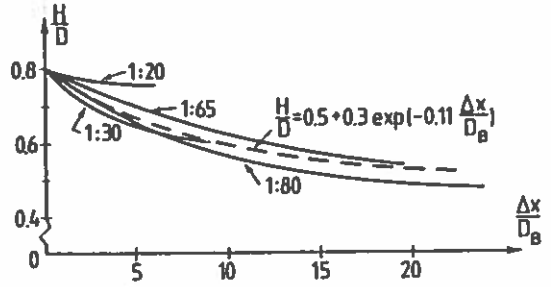

FIG. 2.—Variation in Wave Height after Breaking on Sloping Bottom. Measurements from Horikawa and Kuo (16)

until the breaking point, applying the usual refraction and shoaling theory for linear waves and assuming no energy dissipation. The waves are assumed to break where the wave height becomes equal 0.8 times the water depth, which is a reasonable approximation for small bed slopes. After breaking, the wave height decreases over a certain distance approaching a kind of equilibrium state, where the local wave height H is very close to half the local water depth (16, 24). The transition from breaking to broken state can be approximated by the following expression

$$\frac{H}{D} = \gamma = 0.5 + 0.3 \exp\left(-0.11 \frac{\Delta x}{D_B}\right) \quad \ldots\ldots (2)$$

in which Δx = the distance from the breaking point, D = the water depth referring to mean water level, and D_B = the water depth at the breaking point. Eq. 2 is an analytical approach to the experiments described in Ref. 16, shown in Fig. 2. It is seen that Eq. 2 is a valid approximation for moderate bed slopes (less than about 1:30). Eq. 2 is originally proposed by Andersen and Fredsøe (1).

Longshore Current Distribution

The longshore current driven by the radiation stresses associated with the waves as described by Longuet-Higgins (20) is assumed to be the only current involved in the present study. The important component of the radiation stress tensor in relation to generation of longshore current is the "shear" component S_{xy}, given by

$$S_{xy} = F_m \cos(\alpha) \sin(\alpha) \quad \ldots\ldots (3)$$

in which α = the angle between the wave fronts and the coastline, Fig. 1, and F_m = the momentum flux in the direction of the wave propagation. Longuet-Higgins (20) showed that S_{xy} is constant in refracting waves as long as no energy is dissipated from the waves, i.e. no breaking occurs. When the waves are breaking, S_{xy} decreases towards the shoreline, giving a driving force: $\partial(S_{xy})/\partial x$.

The littoral current can then be found from the equation expressing

equilibrium between the following forces: (1) Radiation stress, gradient of S_{xy}; (2) flow resistance; and (3) transfer of momentum due to velocity gradients in the x-direction, x being the coordinate perpendicular to the coast.

The equation reads:

$$\frac{\partial(S_{xy})}{\partial x} = \tau_b - \frac{\partial}{\partial x}\left(\rho E D \frac{\partial V}{\partial x}\right) \quad \ldots\ldots (4)$$

in which τ_b = the bed shear stress from the current, y = the longshore coordinate, E = the momentum exchange coefficient and V = the current velocity.

The variation in S_{xy} across the surf zone is calculated from the expressions for the wave characteristics given in the section above using the linear wave theory.

To be correct, the shore normal momentum equation should also be included in the flow description in order to calculate set-down and set-up. In the present analysis, this is for reasons of simplicity not taken into account, whereby the longshore current is slightly underestimated very close to the shoreline, where the set-up is largest. However, the maximum sediment transport takes place close to the breaker line, so the above mentioned effect is rather small.

Flow Resistance.—The mean bed shear stress τ_b must be described for the combined three-dimensional wave-current motion, because the flow resistance is increased drastically when waves are superposed the current.

In the present paper, the flow resistance is calculated from Ref. 13, which describes the wave-current flow in arbitrary three-dimensional combinations.

The friction factor will be different for the wave and the current motion due to the large difference between the thicknesses of the wave boundary layer and the current boundary layer. The nonlinear (almost quadratic) relation between the mean bed shear stress and the current velocity gives a weaker relation between the slope and the current velocity than the linear resistance applied by Longuet-Higgins (20): a change in the beach slope of a factor 10 only changes the longshore current strength about a factor 2, as seen from the numerical example with the present model in Fig. 3.

The height of the breaking or broken waves is limited by the depth, γD. γ is a function of the distance from the breaking point (Eq. 2). If the water depth increases towards the coast, as it is the case on a barred coast, the limiting depth is taken as the depth at the crest of the bar. In this case the waves are re-established as non-breaking when the wave height is equal to half the depth over the bar. This model has been shown by Tucker, Carr and Pitt (25) to be in agreement with field measurements.

Momentum Transfer.—The exchange of momentum is described by use of an "eddy viscosity type" of exchange coefficient. Several mechanisms are active in the momentum transfer, such as the turbulent fluctuations in the breaker zone and circulation currents. The exchange coefficient is less important than the bed shear stress, as its effects are more

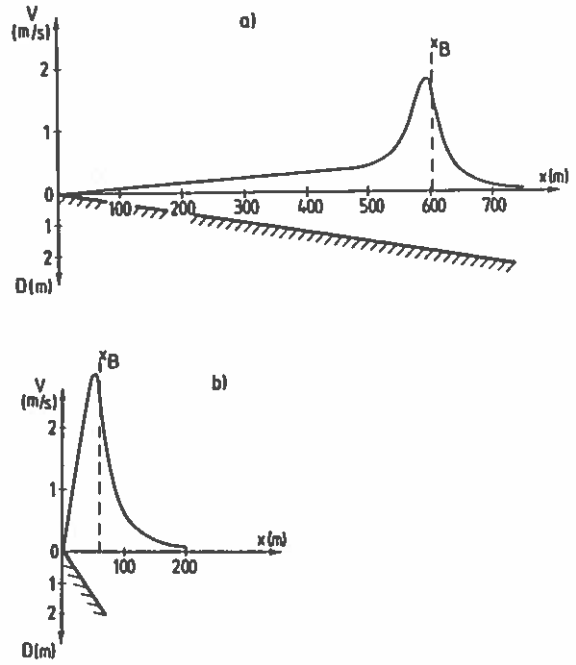

FIG. 3.—Examples of Longshore Current Profiles for Different Bed Slopes. Wave Characteristics: H_0 = 1.5 m, T = 6.2 s, α_0 = 45°. Bed roughness, k = 1.25 mm: (*a*) Bed slope, β = 1:333; (*b*) Bed slope, β = 1:33

to change the distribution of the velocities across the profile than to change the magnitude of the larger velocities close to the breaker line. In the present formulation the expression for E derived by Jonsson, Skovgaard and Jacobsen, Ref. 17,

$$E = \frac{4a^2}{T}\cos^2\alpha \quad \ldots\ldots (5)$$

in which a = the near bed amplitude of the wave orbital motion and T = the wave period.

As shown in Ref. 17, large variations can be allowed in the momentum transfer coefficient E with only moderate changes in the longshore current as a result.

Numerical Solution.—Eq. 4 is solved numerically by a finite difference method with the boundary conditions $V = 0$ at the shore and $V \to 0$ for $x \to \infty$.

An example of a solution for a plane coast with constant slope has already been shown in Fig. 3. Fig. 4 shows how the longshore current is distributed across the coastal profile when bars are present. The profile is taken as the measured one at the Danish North Sea Coast (7). In Fig. 4(*a*) the incoming waves are assumed to be so large that they break at the outer bar. Hereby, a change in S_{xy} occurs at the outer bar until the water depth again becomes sufficiently high, and the waves are re-

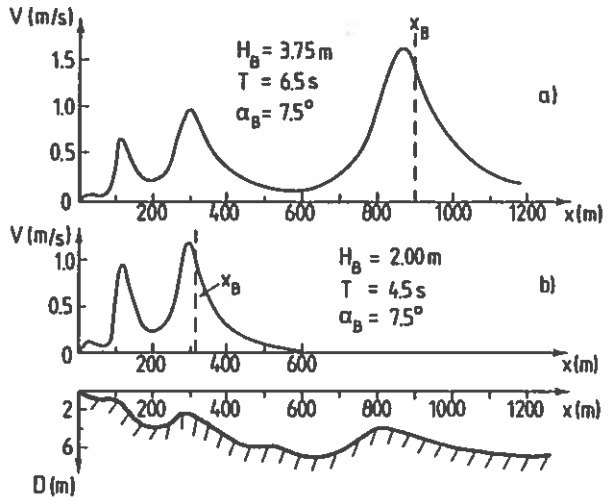

FIG. 4.—Calculated Longshore Current Profiles on Coast with Three Bars. Profile is Taken from (7). Wave Conditions Are Given at Outer Breaking Point: (*a*) Breaking on All Bars; (*b*) Breaking at Two Inner Bars

established at a smaller wave height, after which S_{xy} becomes constant until breaking takes place on bar number two. This means that the longshore current will be concentrated along the bars, as illustrated in Fig. 4(*a*). In case of smaller incoming waves, wave-breaking may not take place at the outer bar, which means that no longshore current will be generated at this bar at smaller wave activity, see Fig. 4(*b*).

Hydrodynamic Description of Turbulence.—In the case of non-breaking waves and no resulting current, the turbulence is restricted to a thin boundary layer just above the sea bed. Several methods are available to calculate this boundary layer, for instance Bakker and van Doorn (3), Grant and Madsen (15) and Fredsøe (13).

In the case of the presence of a current beside the waves, the turbulence is not only restricted to the thin wave boundary layer, but is extended to cover the entire flow depth.

All the three above mentioned models (Refs. 3, 13 and 15) are able to include a resulting current in their flow description in the case where the current is parallel to the direction of wave propagation. Further on, the models by Grant and Madsen (15) and by Fredsøe (13) are able to describe the general three-dimensional case, where the current forms an arbitrary angle with the direction of wave propagation. This is important in description of longshore sediment transport, because the current forms angles up to 90° with the direction of wave propagation in the surf zone.

In breaking and broken waves, turbulent kinetic energy is furthermore produced by the roller in the surface. Deigaard et al. (9) calculated the increase in the turbulent kinetic energy over the entire flow depth formed by the production of turbulent energy in a spilling breaker. The production was assumed to be equal to that of a hydraulic jump, and the

diffusion and dissipation of energy were calculated by a first order turbulence model.

Sediment Description.—With known properties of turbulence—for instance represented by an eddy viscosity ϵ—the distribution of suspended sediment is found from the diffusion equation

$$\frac{\partial c}{\partial t} = w\frac{\partial c}{\partial z} + \frac{\partial}{\partial z}\left(\epsilon_s \frac{\partial c}{\partial z}\right) \quad \ldots\ldots (6)$$

in which c = instantaneous concentration by volume; t = time; w = fall velocity of suspended sediment; z = the vertical coordinate; and ϵ_s = the instantaneous turbulent exchange factor for suspended sediment. ϵ_s is normally taken equal to the eddy viscosity for the flow. In the present model this eddy viscosity is in the case of non-breaking waves evaluated as outlined by Fredsøe et al. (14), applying the flow description by Fredsøe (13). In breaking waves, the description by Deigaard et al. (9) has been applied.

In order to solve Eq. 6, two boundary conditions are needed. One is the requirement of no flux of sediment in the surface or

$$wc + \epsilon_s \frac{\partial c}{\partial z} = 0 \quad \text{at} \quad z = D \quad \ldots\ldots (7)$$

The other boundary condition is correlated to the bed concentration c_b. In the present investigation the bed is assumed plane, so the bed roughness k is scaled to the mean grain diameter d. For the present we have taken $k = 2.5\,d$. This result is known to be valid in uni-directional flow in the plane bed regime at large shear stresses, (12). As pointed out by Dingler and Inman (10), wave generated ripples disappear at large near-bottom flow velocities. Nielsen (22) analyzed the ripple data and found that the disappearance of the ripples took place for the Shields' parameter θ being in the interval $0.8 < \theta < 1.0$. Shields' parameter θ is the dimensionless bed shear stress defined by

$$\theta = \frac{\tau_{b,max}}{\rho(s-1)gd} \quad \ldots\ldots (8)$$

in which $\tau_{b,max}$ = the maximum bed shear stress during a wave-cycle, ρ = fluid density, s = relative density of sand (~2.65), g = acceleration of gravity, and d = mean grain diameter.

By inspection of typical data on wave heights and wave periods during storm situations one finds that typical values of θ are in the range of $1 < \theta < 10$–20. This estimate is of course rough, but indicates that most sediment transport in coastal areas takes place while the bed is plane, i.e. no ripples on the bed.

Keeping this in mind, the bed concentration c_b of suspended sediment can be found by the method suggested by Engelund and Fredsøe (11), who applied the dynamic principles of Bagnold (2) to predict the bed concentration of suspended sediment as function of the instantaneous Shields' parameter θ.

Fig. 5 demonstrates through a numerical example how the models in Refs. 9 and 14 work: in case of non-breaking waves the suspended sed-

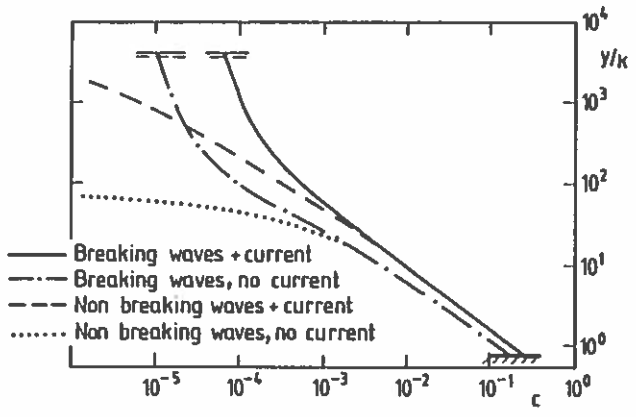

FIG. 5.—Suspended Sediment Concentrations Profiles in Breaking and Non-Breaking Waves. Example is Based on: D = 2 m, H = 1 m, T = 6 sec, d = 0.2 mm, and V = 1 m/s

iment is restricted to the thin turbulent wave boundary layer of thickness some hundred times the bed roughness. If the waves are breaking, the near bed concentration remains nearly the same for a given wave height and wave period. However, farther away from the bed the concentration of suspended sediment increases tremendously due to increase in turbulence intensity. Further on, Fig. 5 demonstrates that the presence of a resulting current also increases the concentration of suspended sediment farther away from the bed.

With known vertical distribution of suspended sediment the longshore transport of sediment per unit width perpendicular to the coast is found by

$$q_s = \frac{1}{T}\int_0^T dt\left[\int_0^D cU\,dz\right] \quad \ldots\ldots (9)$$

U = the instantaneous velocity of the combined wave current motion. The bed shear stress and the depth averaged mean current velocity V are both obtained by an iterative solution of Eq. 4, applying the flow-resistance model by Fredsøe (13). Hereby, the vertical and temporal variation of U is obtained too. The application of Ref. 13 is of course an approximation in the breaker zone where the turbulence generated by the wave breaking will modify the current velocity profile slightly, as seen from the following considerations: the longshore current is driven by the shear component of the radiation stress, whereby the vertical shear stress distribution differs from the normal linear distribution in open channel flow. As an extreme, the driving force can be assumed to be concentrated near the surface (in the roller) whereby the vertical shear stress distribution becomes rectangular. Fig. 6 illustrated through a numerical example the importance of this effect: the dotted line shows the calculated time averaged velocity $\bar{U}$ based on a linear distribution of shear stress, while the dashed shows $\bar{U}$ based on a rectangular shear stress

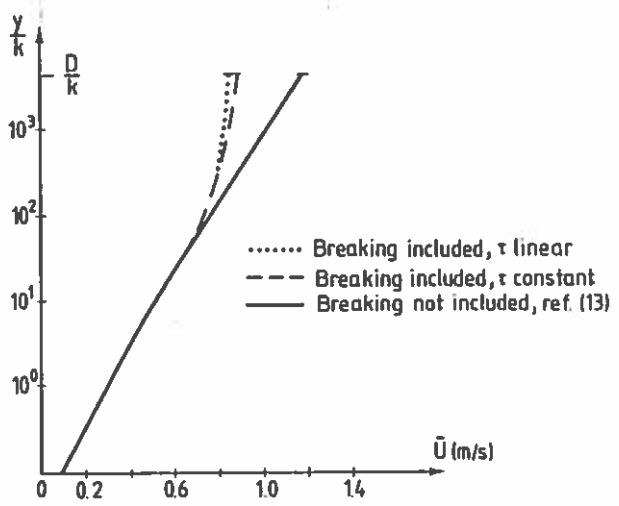

FIG. 6.—Example of Effect of Surface Roller on Mean Current Velocity in Surf Zone for H = 1 m, T = 6 sec, and D = 2 m

distribution. Both profiles include the turbulence generated by wave-breaking applying the eddy viscosity ϵ as calculated in Ref. 9. The deviation between the two calculated profiles is very small. The fully drawn line in Fig. 6 shows the velocity profile obtained by the theory of Ref. 13, neglecting the wave-breaking. It is seen that the effect of surface generated turbulence is most significant far from the bed where the sediment concentrations are smallest. The effect on the suspended load transport is in the present example 12%, which justifies the application of the theory developed in Ref. 13 as an approximation even in the surf zone.

Besides the suspended sediment, the transport of bed load is incorporated in the model. However, at θ-values larger than 1, the bed load transport is negligible compared to the transport of suspended sediment transport.

The total longshore sediment transport Q_S in grain volume is now found by integration perpendicular to the coast to be

$$Q_S = \int_0^\infty q_s\,dx \quad \ldots\ldots (10)$$

Comparison with Field Data

Comparison of the present theory with laboratory experiments has not been carried out. In a laboratory, the bed will normally be covered by wave-ripples, which together with laminar effects in the wave boundary layer may cause large scale errors in the evaluation of the strength of longshore current and in the vertical distribution of suspended sediment. For this reason, we have chosen to compare with a field study instead.

The amount of field data which is required for comparison with a detailed littoral drift model as the present is very comprehensive. Such ideal data should comprise: (1) Wave characteristics; (2) sediment characteristics in the coastal zone; (3) current velocities in the surf zone; (4) bathymetry; and (5) the distribution of the sediment transport rate in the coastal profile. Only very few sets of field data are available which satisfy at least some of the requirements above. Further, in most of the reported field measurements comparison has been made with the CERC-formula, leading to a reduction of the reported data with focus on the "longshore energy flux factor," which is the parameter used in the CERC-formula.

One of the most comprehensive field investigations of longshore sediment transport has recently been reported by the Danish Hydraulic Institute (7,21). Here the complete natural backfilling of a 1,600 m long trench, dredged through a three-bar coastal profile at a straight reach of the Danish West Coast has been monitored. A typical profile is depicted in Fig. 4. The soundings of the trench were made six times during the period of backfilling, and recordings were made of wind, waves and current velocities at 12 m water depth. Unfortunately, no flow measurements could be performed in the surf zone.

It has been chosen to compare results of the theoretical model with the recorded backfilling between March 22nd and April 15th, 1982. This period has been chosen because a significant backfilling occurred in a relatively short time, and this backfilling can be related to a single storm period (April 7th–10th) with significant wave height up to 4.75 m.

At the time of the storm, the trench was only dredged across the outer bar ($x > 400$ m). The distribution of the backfilling is shown in Fig. 7.

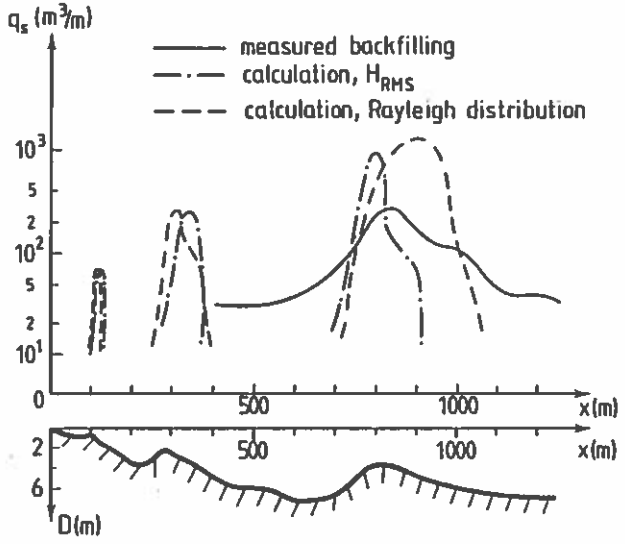

FIG. 7.—Distribution Across Coast Profile of Backfilling of Trench and Calculated Longshore Sediment Transport. The Measured Data Are from (7)

The total backfilling is approx. 90,000 m³ (solid) grain volume.

The width of the trench was 90 m and the depth 10 m, which justify that almost all sediment transported longshore was trapped in the trench.

Storm waves are of course irregular and three-dimensional, and it is not trivial to find the input conditions to the mathematical model which corresponds to the field conditions. Two approaches have been applied:

1. The root mean square, H_{rms}, of the breaking heights has been applied. It has been shown by Rasmussen and Fredsøe (23) that calculations using H_{rms} gave the best agreement with laboratory experiments with sediment transport under irregular waves and a current.

2. It has been assumed that the wave heights follow the Rayleigh distribution, and the sediment transport, Q_s, has been calculated accordingly:

$$Q_s = \int_0^\infty f_r(H) Q_s(H) dH \quad \text{(11)}$$

in which f_r = the probability density function of the Rayleigh distribution. The correlation between wave period and wave height is based on the scatter diagram in Ref. 7. With this approach it has implicitly been assumed that the longshore current always corresponds to the instantaneous wave, i.e. that a single high wave will coincide with a high longshore current velocity. Due to the nonlinear sediment transport relations this could be expected to lead to an over-prediction of the sediment transport.

For both methods the calculation has been performed for the combinations of significant wave heights and wave directions given by Mangor et al. (21) for the period of backfilling. For all situations with waves breaking at the outer bar a south-going sediment transport is predicted, and the backfilling is compared with the total calculated transport.

The total amounts of calculated littoral drift (on the outer bar only) are given in Table 1.

The calculated distributions of sediment transport across the coastal profile are shown in Fig. 7. It is seen that the theory predicts the littoral drift to be concentrated on the bars. This is partly due to the concentration of the longshore current along the bars, cf. Fig. 4, partly due to the smaller water depth above the bars. The latter results in larger near-

TABLE 1.—Comparison between Calculated and Measured Sediment Transport. Mean Grain Diameter Is 0.20 mm

Description (1)	Total amount (m³) (2)	Ratio between calculation and measurement (3)
Measured backfilling	90.000	—
Calculated on basis of H_{rms}	50.000	0.6
Calculated on basis of Rayleigh distribution	205.000	2.3

bed wave induced flow velocities, and therefore larger concentrations of suspended sediment. Finally, the sediment transport capacity is largest in breaking waves, the breaking being concentrated around the bars.

It appears that the calculated distribution is more peaked than the measured backfilling, especially the one based on H_{rms}. This may be partly attributed to the current model which is based on regular waves. It has been shown by Battjes (4) that the longshore current profile will be more smooth for irregular waves, because the wave breaking will be distributed over a wider zone rather than occurring at a breaker line.

Apart from the irregularity of the waves there are some uncertainties involved in the evaluation of the measurements. The most severe uncertainty is probably that the actual coastal profile during the storm is unknown. The sounded profiles after a storm may well be formed by the less severe conditions at the last part of the storm. A small variation in the height or shape of the bar may affect the amount and distribution of the sediment transport. Another unknown factor is the effect of the trench itself on the wave and current pattern.

Diagrams and Formulas of Applications

This section presents diagrams and formulas which can be applied to quantify the littoral drift along a straight coast with constant slope. As the littoral drift is concentrated in a rather narrow zone around the breaking point, the findings may be applicable for a more complicated bed profile by putting the slope equal to the slope around the point of breaking.

As seen from Fig. 3, the longshore current velocity increases slightly with increasing bed slope. On the other hand, the width of the transport zone decreases. These two items result totally in an increase in the total sediment transport, Q_s, which is found to be approximately proportional to $\sqrt{\beta}$. This can be seen from Fig. 8, which shows the variation of the dimensionless total sediment transport, Φ, with β for four different combinations of wave height and sediment size. Here Φ is defined by

$$\Phi = \frac{Q_s}{H_0 \sqrt{\beta} \sqrt{(s-1) g d^3}} \qquad (12)$$

in which H_0 = the deep waterwave height. Φ will be a function of the following dimensionless parameters: bed slope β, deep water wave height H_0/d, deep water wave steepness H_0/L_0, where L_0 = deep water wave length, the angle α_0 between coast and deep water wave crest, and finally sediment settling velocity w^*, defined by

$$w^* = \frac{w}{\sqrt{gd}} \qquad (13)$$

in which w = fall velocity of sediment.

Fig. 8 shows that Φ is almost constant for a variation in β over one decade. In the following the influence of the bed slope on the transport will be taken into account through the definition of Φ.

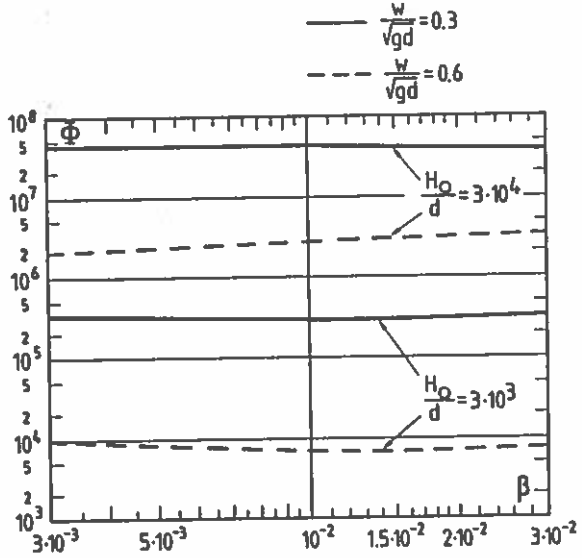

FIG. 8.—Variation in Φ with Bed Slope β, $\alpha_0 = 45°$

The variation in different parameters with the deep water wave direction is shown in Fig. 9 for a single combination of wave height, wave steepness, and settling velocity. Besides the sediment transport, the variation in the maximum current velocity and in the "longshore energy flux factor" at breaker line, P_{ls}, is shown. The latter indicates the variation in littoral drift according to the CERC-formula (26).

The variation in Q_s with deep water wave angle depicted in Fig. 9(*a*) is typical for a large range of H_0/d, w^* and H_0/L_0. A curve fitted to this variation is

$$\frac{Q_s}{Q_{s,max}} = \left(\sin \left\{ 2\alpha_0 \left[1 - 0.4 \frac{\alpha_0}{90°} \left(1 - \frac{\alpha_0}{90°} \right) \right] \right\} \right)^{5/2} \qquad (14)$$

which can be used as an approximation for the variation of the sediment transport with the wave direction.

The sediment transport at $\alpha_0 = 45°$, Φ_0, is shown in Fig. 10 as a function of H_0/d, w^* and H_0/L_0. As described earlier, the model is only valid for a flat bed without ripples, which corresponds to a minimum wave height, H_0, of approximately 2,000 d.

The curves shown in Fig. 10 can for $H_0/d < 3 \times 10^4$ be approximated by the following expression with an accuracy within 10%:

$$\Phi_0 = \left(\frac{\frac{H_0}{d}}{10^4} \right)^P 1.8 \times 10^7 \left(\frac{H_0}{L_0} \right)^{0.42} \exp \left\{ \left(-8.9 + 65 \frac{H_0}{L_0} \right) (w^* - 0.3) + \left[4.0 - 65 \left(\frac{H_0}{L_0} \right) \right] (w^* - 0.3)^2 \right\} \qquad (15)$$

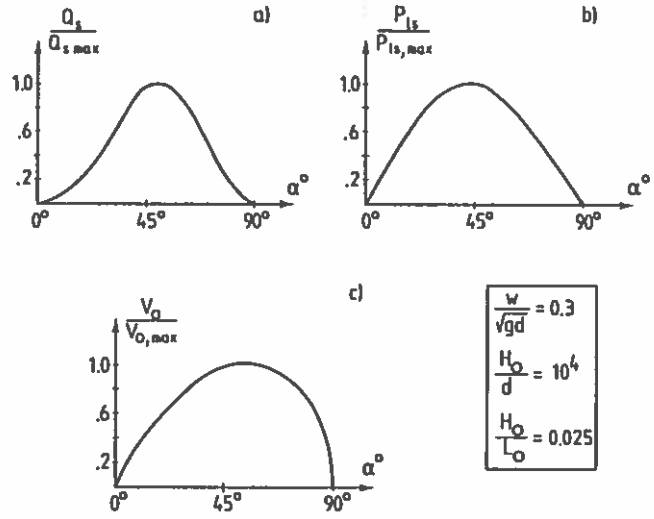

FIG. 9.—(*a*) Variation in Littoral Drift; (*b*) "Longshore Energy Flux Factor"; (*c*) Maximum Littoral Current Velocity with α_o

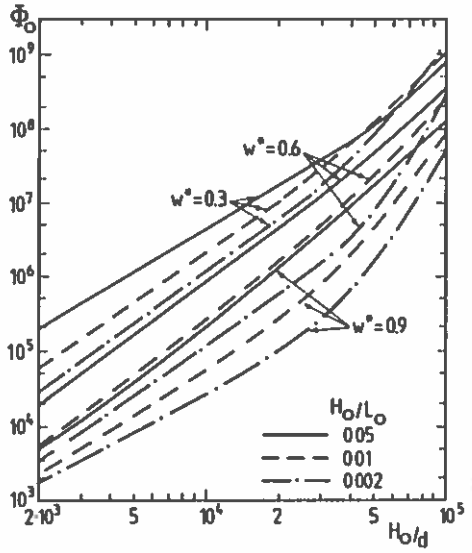

FIG. 10.—Variation of Longshore Transport with Grain Size, Wave Steepness and Wave Height, $\alpha_o = 45°$

in which

$$P = 2.79 + 0.069 \ln\left(\frac{H_o}{L_o}\right) - 1.67\left[1.46 + 0.187 \ln\left(\frac{H_o}{L_o}\right) - w^*\right]^2 \quad \ldots\ldots (16)$$

A less elaborate expression than Eqs. 15 and 16 is

$$\Phi_o = 0.1\left(\frac{H_o}{d}\right)^{2.3}\left(\frac{H_o}{L_o}\right)^{1/2} \exp(-6.1\, w^*) \quad \ldots\ldots (17)$$

which produces the curves in Fig. 10 within 50%.

These expressions can be combined with Eq. 14 to obtain estimates for other wave directions than $\alpha_o = 45°$.

As mentioned in the introduction, the CERC-formula is the most commonly used littoral drift formula. This is partly because of its simplicity, but also because it is supported by a lot of field measurements, although with large scatter. It is therefore relevant to compare the present model to the CERC-formula.

The variation with the wave direction has been illustrated in Fig. 9, where it is noticed that the transport according to this model is relatively

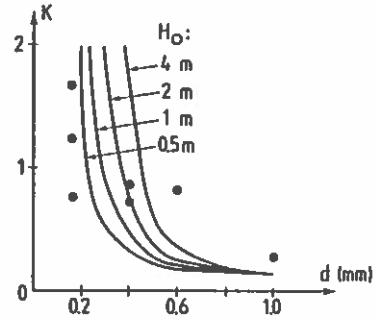

FIG. 11.—Variation in *K*-Factor with Grain Size. Theoretical Prediction is Based on $H_o/L_o = 0.025$, $\beta = 0.01$, and $\alpha_o = 45°$. The Measured Values (Filled Circles) Are from Ref. 8

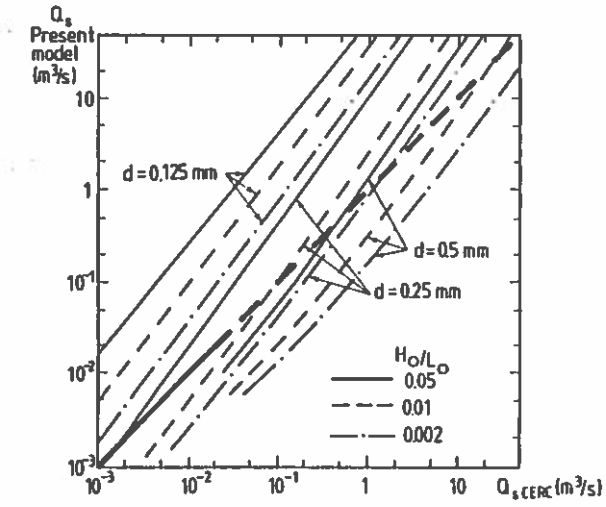

FIG. 12.—Comparison Between Present Model and CERC-Formula for $\alpha_o = 45°$

smaller for small and large values of α_0 than predicted by the CERC-formula.

Another important parameter in the CERC-formula is the wave height, and the littoral drift is approximately proportional to the wave height in a power 2.5. The dependency of the wave height is stronger in this model, where the power on the wave height is about 3–3.5.

The grain size is a very important parameter in the present model, as in all sediment transport models. No sediment characteristics enter the CERC-formula, which may be because of a small variation in the grain size between the different sites where data have been obtained for the CERC-formula.

Komar and Inman (19) suggest a value of $K = 0.77$ in Eq. 1. Based on measurements, Dean, Berek, Gable and Seymour (8) have proposed a relation between the grain size of the beach sediment and the factor K. An example of the variation obtained by the present model is shown in Fig. 11, together with the points forming the basis for Dean's relation. The tendency is the same, namely increasing transport with decreasing grain size.

A comparison between the present mathematical model and the CERC-formula is shown in Fig. 12 for $\alpha_0 = 45°$ and $\beta = 0.01$. The line of perfect agreement is shown as a fully drawn line in the region where the CERC-formula is supported by empirical data. The two models can be seen to predict littoral drifts of the same order of magnitude for a grain size of about 0.2 mm. Changes in α_0 or β would result in a displacement of the curves in Fig. 12, but not a change in their shape.

Conclusion

A mathematical model for littoral drift is presented which includes a detailed hydrodynamic as well as a detailed sediment behavior description.

The paper first describes the littoral drift along a bar coast. The model predicts that the littoral drift is concentrated on the bars. This is partly due to smaller local water depth, partly due to large longshore current on the bars, and finally due to larger transport capacity under broken waves.

This model has been compared with a field study at the Danish North Sea coast, and the agreement has been found to be satisfactory, taking into account the complexity of the treatment of an irregular wave climate.

In case of a coast with constant slope, dimensionless diagrams have been worked out for calculation of the littoral drift.

The present theory suggests that the littoral drift not only is a function of the "longshore energy flux factor," but also of the slope of the coast and the sediment properties: the littoral drift increases nearly by the square root of the slope, and increases very much with decreasing grain size.

For grain sizes around 0.2 mm, which is very common on beaches, the present theory does not deviate much from the CERC-formula. The present theory further on predicts the transverse distribution of the longshore sediment transport on the coastal profile.

Acknowledgment

One of the writers (Rolf Deigaard) is supported by the Danish Technical Research Council (STVF).

Appendix I.—References

1. Andersen, O. H., and Fredsøe, J., "Transport of suspended sediment along the coast," Institute of Hydrodynamics and Hydraulic Engineering, Technical Univ. of Denmark, Prog. Rep. 59, 1983, pp. 33–46.
2. Bagnold, R. A., "Experiments on a gravity-free dispersion of large solid spheres in a Newtonian fluid under shear," Proceeding Royal Society, London (A) 225, 49, 1954.
3. Bakker, W. T., and van Doorn, T., "Near-bottom velocities in wave with current," Coastal Engineering Conference, 1978, pp. 1394–1413.
4. Battjes, J. A., "Computation of set-up. Longshore currents, run-up and over topping due to wind-generated waves," Delft Technishe Hogeschool, 1974, 244 pp.
5. Bijker, E. A., "Longshore Transport Computations," *Journal of the Waterways, Harbors and Coastal Engineering Division*, ASCE, Vol. 97, No. WW4, Nov., 1971, pp. 687–701.
6. Dally, W. R., and Dean, R. G., "Suspended sediment transport and beach profile evolution," *Journal of Waterway Port Coastal and Ocean Engineering*, ASCE, Vol. 110, No. 1, 1984.
7. Danish Hydraulic Institute, "North Sea shore approach, monitoring of sedimentation in a dredged trench," Research report, Copenhagen, 1984.
8. Dean, R. G., Berek, E. P., Gable, C. G., and Seymour, J., "Longshore transport determined by an efficient trap," Coastal Engr. Conf., 1982, pp. 954–968.
9. Deigaard, R., Fredsøe, J., and Hedegaard, I. B., "Suspended sediment in the surf zone," Vol. 112, No. 1, 1986, pp. 115–128.
10. Dingler, J. R., and Inman, D. L., "Wave-formed ripples in nearshore sands," 15, Coastal Engineering Conference, 1976, pp. 2109–2126.
11. Engelund, F., and Fredsøe, J., "A sediment transport model for straight alluvial channels," *Nordic Hydrology*, 7, 1976, pp. 293–306.
12. Engelund, F., and Hansen, E., "A monograph on sediment transport in alluvial streams," Technical Press, Copenhagen, Denmark, 1972.
13. Fredsøe, J., "The turbulent boundary layer in combined wave-current," *Journal of Hydraulic Engineering*, ASCE, Vol. 110, No. HY8, 1984, pp. 1103–1120.
14. Fredsøe, J., Andersen, O. H., and Silberg, S., "Distribution of suspended sediment in large waves," *Journal of the Waterway Port Coastal and Ocean Engineering*, ASCE, Vol. 111, No. 6, 1985, pp. 1041–1059.
15. Grant, W. D., and Madsen, O. S., "Combined wave and current interaction with a rough bottom," *Journal of Geophysical Research*, Vol. 84, 1979, pp. 1797–1808.
16. Horikawa, K., and Kuo, C.-T., "A study on wave transformation inside surf zone," Coastal Engineering Conference, Vol. 1, 1966, pp. 217–233.
17. Jonsson, I. G., Skovgaard, O., and Jacobsen, T. S., "Computation of longshore currents," Proc. Coastal Engineering Conference, 1974, pp. 699–714.
18. Komar, P. D., *Beach processes and sedimentation*, Prentice Hall, Inc., Englewood Cliffs, N.J., 1976.
19. Komar, P. D., and Inman, D. L., "Longshore sand transport on beaches," *Journal of Geophysical Research*, Vol. 75, No. 30, 1970, pp. 5914–5927.
20. Longuet-Higgins, M. S., "Longshore currents generated by Obliquely Incident Sea Waves, 1 and 2," *Journal of Geophysical Research*, Vol. 75, 1970, pp. 6778–6801.
21. Mangor, K., Sørensen, T., and Navntoft, E., "Shore approach at the Danish North Sea Coast, monitoring of sedimentation in a dredged trench," Proc.

Onshore/Offshore Sediment Transport and Morphological Modelling of Coastal Profiles

Rolf Deigaard

Danish Hydraulic Institute
Agern Allé 5
2970 Hørsholm
Denmark

Jørgen Fredsøe and Ida Brøker Hedegaard

Institute of Hydrodynamics and Hydraulic Engineering
Technical University of Denmark

ONSHORE/OFFSHORE SEDIMENT TRANSPORT AND MORPHOLOGICAL MODELLING OF COASTAL PROFILES

Ida Brøker Hedegaard[1], Rolf Deigaard[2], and Jørgen Fredsøe[3]

ABSTRACT: This paper presents a deterministic model for the morphological evolution of a coastal profile for direct incoming waves. The model contains description of waves across the coastal zone, current profiles, sediment transport and the corresponding morphological evolution. A discussion is given of the sensitivity of the model to a number of parameters and phenomena: Wave transformation after breaking, currents driven by density differences on a sloping bed, onshore transport in the non-broken waves, irregularity of waves, tidal variation.

INTRODUCTION

A morphological model includes the interaction between hydrodynamic conditions and bed level evolution, i.e. the hydrodynamic conditions adjust themselves to the actual bed topography which in turn is developing as a function of the hydrodynamics and the sediment transport. The present model reflects this interaction. Firstly, the hydrodynamic conditions, wave and current profiles, across the coastal zone are calculated corresponding to the initial bathymetry. Afterwards, the cross shore sediment transport rates and the initial bed level changes are determined. The bathymetry is updated correspondingly and the calculation is repeated. This procedure is sketched in Fig. 1.

The repeated calculations and especially the feed-back from topography to sediment transport makes the model very sensitive, and makes it difficult to predict the effect of a small change to the model. The sensitivity of the model has therefore been investigated by:
a) changing the key parameters in the model and b) considering the effect of specific physical mechanisms, such as currents driven by density differences on a sloping bed, onshore transport in nonbroken waves, irregular waves, tide. A definition sketch for the coastal profile model is presented in Fig. 2.

---

1) Hydraulic Engineer, Ph.D., Danish Hydraulic Institute, Agern Alle 5, DK-2970 Hørsholm, Denmark; 2) Associate Professor, Institute of Hydrodynamics and Hydraulic Engineering (ISVA), Technical University of Denmark, DK-2800 Lyngby, Denmark; 3) Professor, ISVA.

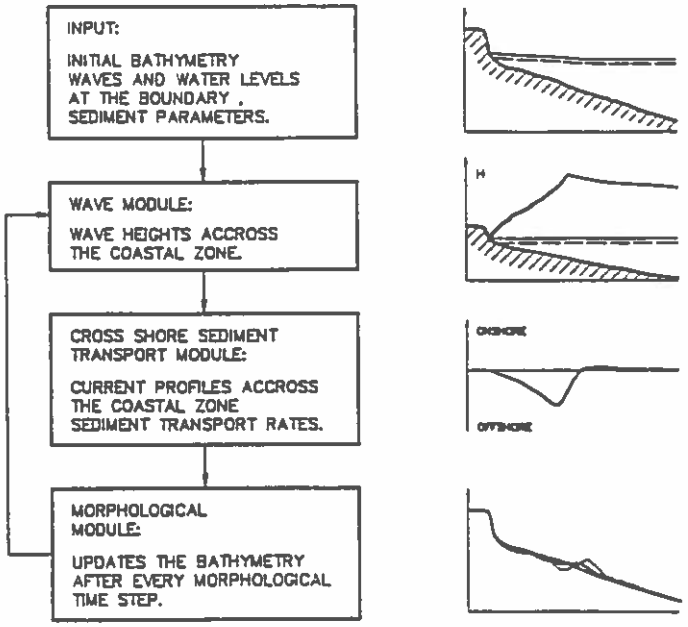

Figure 1. Sketch of Modules in the Morpholgical Model

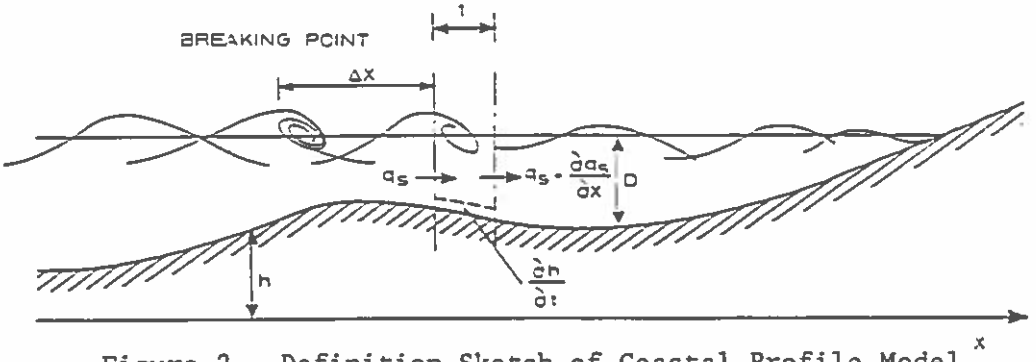

Figure 2. Definition Sketch of Coastal Profile Model

WAVE HEIGHTS ACROSS THE PROFILE

The variation of the wave heights across the profile are determined from the criteria that the wave has either constant energy flux - the shoaling non-broken wave - or looses energy in accordance with an empirical relation first suggested by Andersen and Fredsøe (1983):

$$\frac{H}{D} = \gamma = 0.5 + 0.3 \exp\left(-0.11 \frac{\Delta x}{D_B}\right) \qquad (1)$$

where H is the wave height, D is the depth, Δx is the distance from breaking point and D_B is the depth at the breaking point.

Eq. (1) is a valid approximation for moderate slopes (< 1:30), but for more steep slopes the relative wave height will probably not decrease as indicated by the above given relation. The effect of the formulation of the decrease of wave heights on the morphological development of the profile is discussed later on.

CROSS-SHORE SEDIMENT TRANSPORT

Modelling of the sediment transport in the cross-shore direction is an important element in the description of profile development. It is a complicated process because in the two-dimensional case there is no net flow in the transport direction and many different mechanisms contribute to the resulting transport. In the following the model for cross-shore sediment transport is described. Firstly, the hydrodynamics are considered, and secondly, the effects on the sediment transport modelling are described.

Hydrodynamic Modelling

Outside the surf zone the energy dissipation and the turbulence are mainly located in the near-bed wave boundary layer, and the main effort is concentrated on describing the conditions in this boundary layer and its influence on the mean flow. The basis for the model is the combined wave-current boundary layer model of Fredsøe (1984) which describes the development of the wave boundary layer during each half wave cycle.

Streaming. The wave boundary layer is non-uniform, as it varies along the wave length. The non-uniformity causes small vertical velocities which give vertical convection of horizontal momentum when averaged over a wave period. In order to obtain a stationary force balance this momentum flux must be compensated by a mean shear stress. A perfect force balance can be obtained with zero shear stress outside the wave boundary layer (Deigaard and Fredsøe, 1989), i.e. with potential flow outside the boundary layer. The shear stress associated with the streaming is determined by the same principles as applied by Longuet-Higgins (1953), but taking the velocity distribution in the turbulent wave boundary layer into account. A typical example of the shear stress due to streaming is shown in Fig. 3.B.

Non-Linear Waves. As we approach the shore the waves become increasingly non-linear and the variation of the near bed orbital velocity deviates from the sinusoidal one. A requirement for potential flow outside the boundary layer is that the mean shear stress is zero. If the wave boundary layer is laminar this causes no problems as the different harmonic components can simply be superposed to give the shear stress variation. In the case of a turbulent wave boundary layer the non-linearity is treated as follows: The potential wave motion outside the wave boundary layer can in principle be combined with any small net flow that is constant over the depth. The model determines the potential flow that is consistent with the turbulent boundary layer by finding the mean flow velocity outside the boundary layer, which corresponds to zero mean shear stress in the wave boundary layer.

The wave orbital motion can e.g. be calculated by second order Stokes theory or by Cnoidal wave theory. The mean flow corresponding to zero mean shear stress is illustrated in Fig. 3.A, using second order Stokes wave theory.

Wave Drift. The wave motion in itself implies a net flux of water - the wave drift q_d. It can be determined by calculating the instantaneous discharge through a cross section and then average over a wave period. For linear, shallow water waves this gives:

$$q_d = \frac{1}{T}\int_0^T U(D+\eta)dt = \overline{U\eta} = \frac{D}{C}\overline{U^2} \qquad (2)$$

where T is the wave period, U is the horizontal orbital velocity, D is the mean water depth and η is the water surface elevation and C is the celerity.

As an alternative the wave drift can be calculated by Lagrangian considerations, following the paths of the individual water particles. The two calculation principles give the same results, but while the Eulerian calculation gives a discharge concentrated between the wave trough and crest, the Lagrangian considerations give an even distribution over the vertical.

There appears to be some confusion as to whether the Lagrangian drift velocity shall be included when calculating the suspended load transport, and a discussion of this question is therefore relevant.

The sediment concentration field, c, is determined by the convection-diffusion equation

$$\frac{dc}{dt} = \frac{\partial c}{\partial t} + u\frac{\partial c}{\partial x} + w\frac{\partial c}{\partial z} = \frac{\partial}{\partial z}\left(\epsilon\frac{\partial c}{\partial z}\right) - w_s\frac{\partial c}{\partial z} \qquad (3)$$

where u and w are the horizontal and vertical flow velocities, ϵ is the turbulent exchange coefficient and w_s is the settling velocity of the sediment.

If the convection terms are included in the description and the vertical and horizontal flow velocities are determined correctly, then the wave drift of the suspended sediment q_{sd} will be determined correctly by an Eulerian analysis because the vertical motion of the sediment is included and the Lagrangian drift velocity must not be included in the analysis. In the present sediment transport model, as in most others, the convective terms in eq. (3) is, however, neglected, and the sediment concentrations are calculated as if the wave boundary layer were generated under uniform conditions. With this simplification the wave sediment drift determined by Eulerian analysis becomes zero, which is incorrect. A good first approximation can be obtained by using the Lagrangian drift velocity u_1, taking the velocity distribution in the wave boundary layer into account when calculating u_1:

$$q_{sd} = \int_0^D u_1\bar{c}\, dz \qquad (4)$$

The Mean Turbulent Flow. We have now three contributions to the net flow, which all have been determined under the assumption of potential flow outside the wave boundary layer. In order to fulfil the continuity equation, which in this case states that the net flux is zero, the mean water surface must have a slope S that can drive a mean current to compensate for the three contributions from the potential wave motion. The slope of the mean water surface gives a shear stress distribution of

$$\bar{\tau} = \rho g S(D-z) \qquad (5)$$

which is included in the hydrodynamic model in order to obtain a turbulent wave-current boundary layer that includes the effect of all three wave phenomena and fulfils the continuity equation.

The resulting mean velocity profile is shown in Fig. 3.C as the full drawn line. The dotted line shows the velocity profile with the Lagrangian drift added.

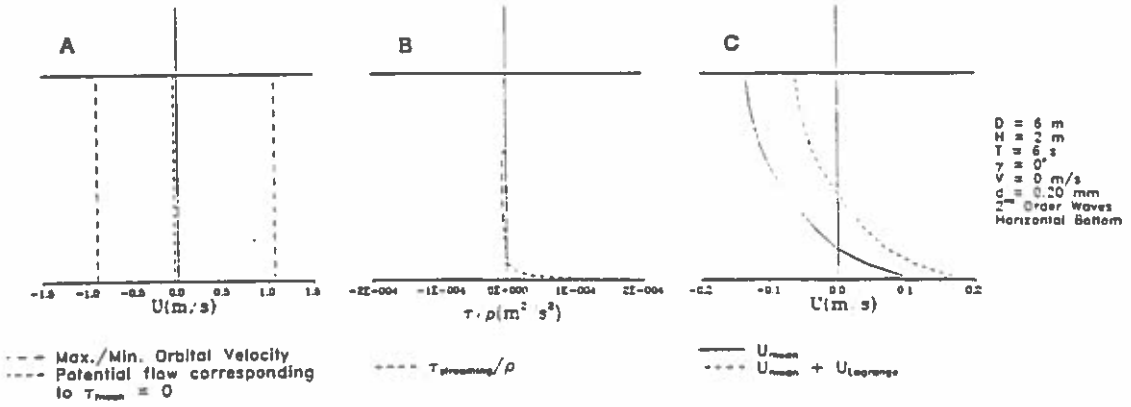

Figure 3. A. Orbital Velocity and Potential Flow Corresponding to $\bar{\tau} = 0$
B. $\tau_{streaming}$
C. Mean Velocity and Mean Langrangian Drift

The Surf Zone. The conditions in the surf zone are characterized by the strong production of turbulence and energy dissipation caused by the wave breaking. All the mechanisms described above are also relevant for the surf zone, but their significance is much less here as the energy dissipation in the wave boundary layer is small compared to the wave breaking.

When the energy loss occurs close to the water surface it is not possible to obtain a force balance without introducing shear stresses over the entire water depth, which are important for the mean velocity distribution, Deigaard and Fredsøe (1989). There is an extra contribution to the continuity and momentum equation from the water carried shoreward by the surface rollers that follow each wave front of the broken waves in the surf zone, Svendsen (1984).

The mean velocity profile and suspended sediment concentrations are influenced by the high turbulence level from the wave breaking. The turbulence is calculated by the transport equation for turbulent kinetic energy, describing the production, diffusion, and dissipation of the turbulence, Deigaard et al. (1986).

The continuity equation and the distribution of the shear stresses in the surf zone give the circulation current known as the undertow with a strong offshore directed flow near the bed and an onshore flow near the surface. The result is an offshore directed net sediment transport in the surf zone. The model is valid for spilling breakers and the inner surf zone, but the complex flow pattern near the plunge point of plunging breakers is not described.

Sediment Transport Modelling

When a satisfactory hydrodynamic description has been obtained, the sediment transport is determined as bed- and suspended load transport. In addition to the mean velocity profile determined above the transport model gives some contributions to the net sediment transport. The asymmetry of the bed shear stress gives a net sediment transport because the bed load transport and the near bed sediment concentration are non-linear functions of the bed shear stress.

Another effect is due to the time-variation of the eddy viscosity and the sediment concentration at different levels. It is important to have the correct phases of the concentration and the flow velocity in order to calculate the net sediment transport.

The presence of wave ripples can be of significance in this respect. The sediment brought into suspension during one half wave period is carried in the vortex at the lee side of each ripple crest. Only in the next half wave period the vortex and the sediment is lifted into the flow over the ripples, at the same time new vortices are formed and entrains suspended sediment. This mechanism can give a large phase lag between the maximum of the flow velocity and the sediment transport, but is not yet included in the cross-shore sediment transport model.

The Bed Slope. A slope of the bed ß also gives contributions to the net transport. The increased density due to suspended sediment gives an additional mean shear stress contribution of:

$$\bar{\tau} = \int_z^D \tan\beta(s-1)\rho g\bar{c}\, dz' \qquad (6)$$

which is included in the flow description to calculate the mean flow. s is the specific density of the sediment, ρ is the density of water and g the acceleration of gravity.

Other effects of a bed slope are that the wave boundary layer flow becomes convergent/divergent during each wave period, which was

analyzed by Justesen (1988), and that the wave profile is deformed by the shoaling. These two effects are not included in the present model.

THE MORPHOLOGICAL MODULE

The bed level changes are described by the continuity equation for the sediment:

$$\frac{\partial h}{\partial t} = - \frac{1}{1-n} \frac{\partial q_s}{\partial x} \qquad (7)$$

where h is the bed level, n is the porosity of the bed material, and t is the time. A definition sketch is given in Fig. 1.

The numerical solution of continuity equation is explicit. A modified Lax-Wendroff scheme has been applied to reduce the numerical diffusion and to obtain a stable solution.

The cross-shore sediment transport model gives the relation between the local hydraulic parameters (wave height, energy dissipation etc.) and the sediment transport. The sediment transport model is, however, formulated for quasi-uniform conditions, and the actual sediment transport rate cannot be expected to adjust itself to abrupt changes in the hydraulic conditions as for example at the point of wave breaking for regular waves, where the present simple models predict a large discontinuity in the energy dissipation and the radiation stress gradient.

The calculated sediment transport is therefore smoothed before being used for the morphological calculations. There is a number of physical mechanisms that will smooth out the sediment transport compared to the variation in the input parameters: a) the main part of the sediment transport is suspended load which in the surf zone can be far away from the bed. It takes some time for the sediment to be entrained into the concentration profile or to settle out from it. b) It takes some time and distance for the turbulence generated near the surface in the wave breaking process to diffuse down to the bed. c) The forcing of the undertow is mainly attacking near the water surface, and it takes some distance for the mean velocity profile to be fully developed. d) Inshore of the break point the near bed flow is directed offshore while it is directed onshore outside the surf zone. This gives a complex flow pattern with vertical flow velocities due to the gradual transition from the undertow in the surf zone to the much weaker current outside the surf zone.

Today no theory exists which describes the actual cross-shore variation of the near-bed wave averaged velocities and sediment transport. In the present model two types of adjustment functions between transport capacity as function of the local waves and the actual transport capacity have been applied. Firstly, the calculated transport rates are smoothed by a running average, and secondly, a response function is introduced:

$$\frac{dq_m}{dx} = \frac{q_s - q_m}{L_r} \qquad (8)$$

where q_s is transport capacity as function of local parameters smoothed by a running average and q_m is actual transport. The length scale, L_s, used for the running average and for the above given response function is proportional with the local water depth. An example of the calculated transport as function of the local parameters, q, q_s, and q_m are given in Fig. 4.

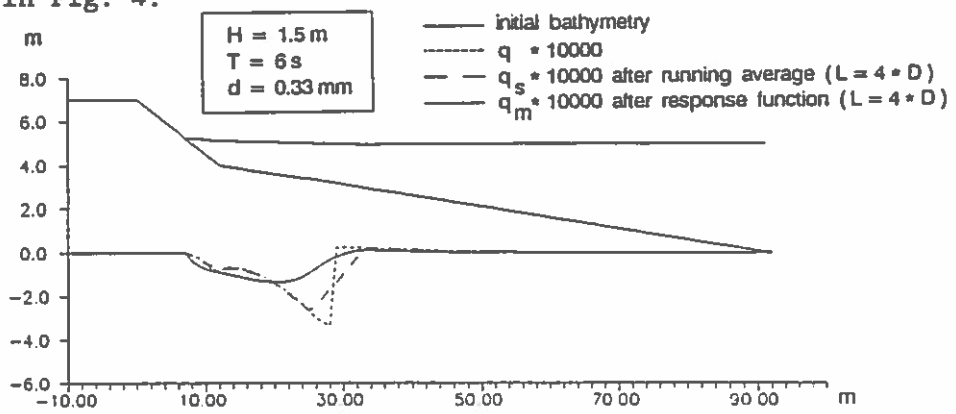

Figure 4. Illustration of the Transport Capacity from the Local Parameters, q, the smoothed transport, q_s, and the actual transport, q_m.

Comparison with Measurements

Simulated evolutions of a breaker bar have been compared to measurements for two cases: 1) Saville, 1957 and 2) Dette and Uliczka, 1986. Both tests were carried out in large wave flumes with regular waves. Figs. 5 and 6 show comparison of measured and simulated evolutions.

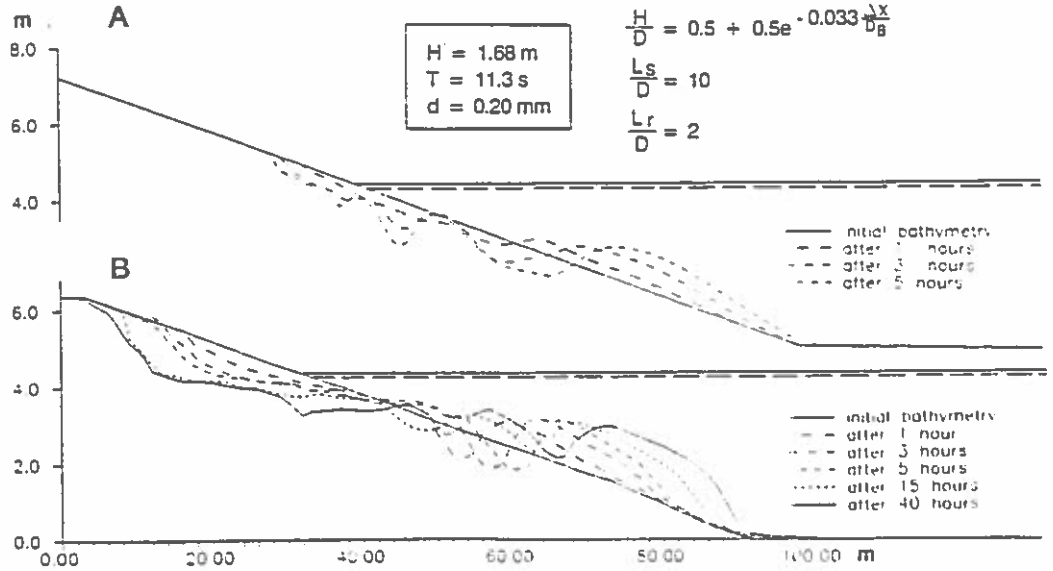

Figure 5. A. Simulated Evolution (only the first 5 hours)
B. Measured Evolution, Saville (1957)

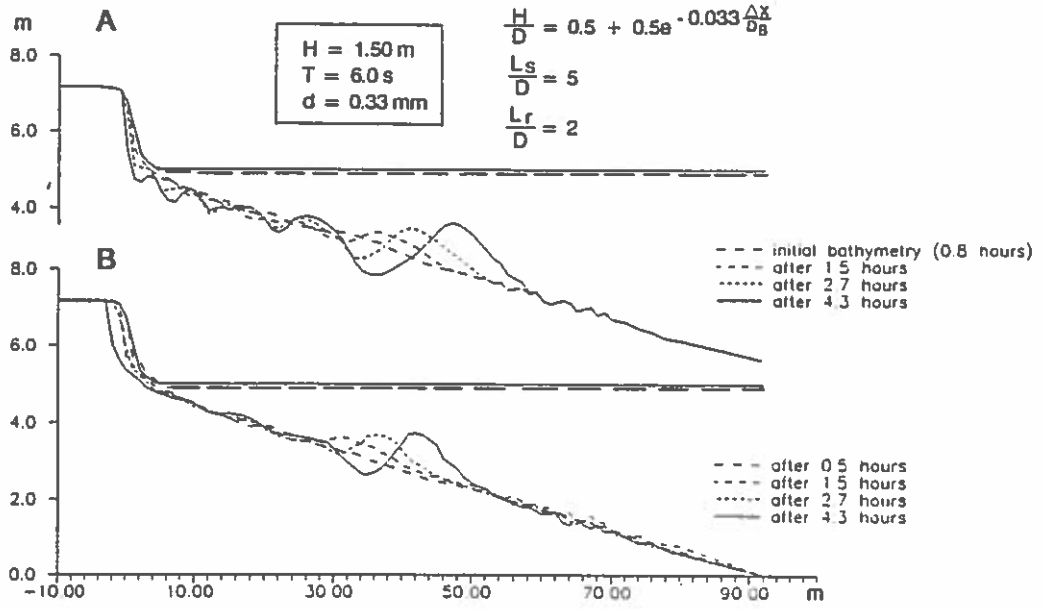

Fig. 6 A. Simulated Evolution
B. Measured Evolution, Dette and Uliczka (1986)

In Figs. 5 and 6 L_s is length scale for the running average and L_r is the length scale for the response function.

In both cases the initial slope was steep 1:14 and 1:20. In the simulation the decay of the waves after breaking, see Eq. (1), has therefore been modified as shown in the Figures. The length scales for the running average and the response function for these simulations are given in the Figures.

SENSITIVITY OF THE MORPHOLOGICAL MODEL

From Figs. 5 and 6 it appears that the model can be calibrated to simulate the evolution of a breaker bar under regular waves. However, there are still discrepancies between the calculated and measured evolutions. Further, the simulated evolution does not reach a stable profile. This seems to be in contradiction with observations. It is therefore relevant to discuss the influence on the calculated morphological evolution of both parameters applied in the model and phenomena described by the model.

Effect of the Length Scale

The effect on the morphological evolution of the length scales, L_s and L_r, is pronounced. This is illustrated in Fig. 7 where the calculated evolution is shown with three different length scales, here $L=L_s=L_r$. It is seen that the shorter the length scale, i.e. the larger gradients in transport rate, the steeper and higher the breaker bar.

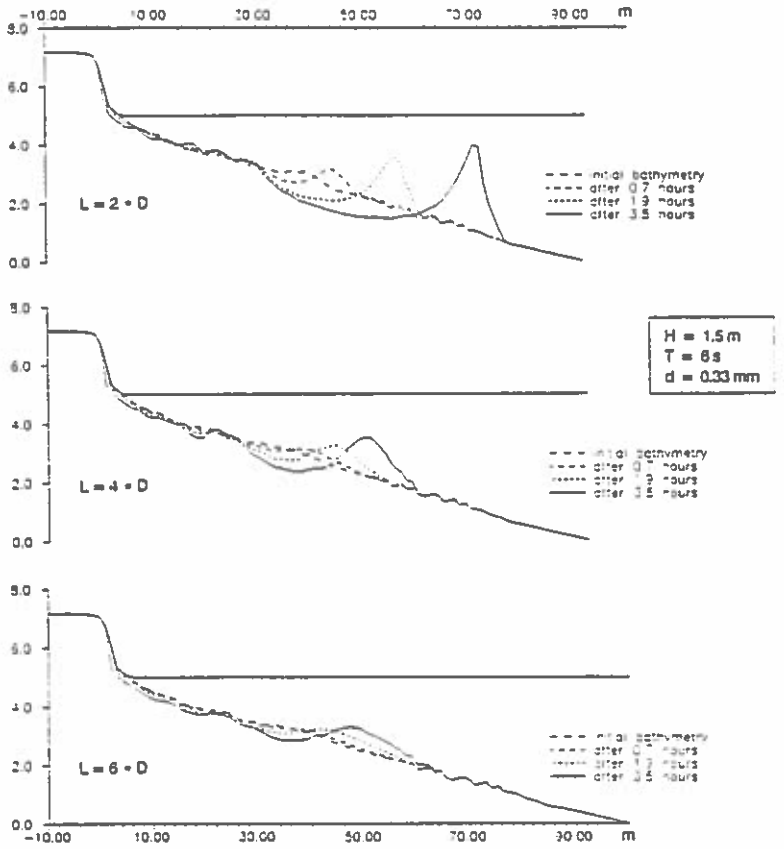

Figure 7. Illustration of the Influence of the Length Scales, $L=L_s=L_r$, on the Morphological Evolution

The effect of the response function is to introduce a shift between the maximum transport and the breaking point. If the running average is ignored a breaker bar will be formed, but the offshore side becomes very steep. The running average smoothes the offshore side. This is illustrated in Fig. 8.

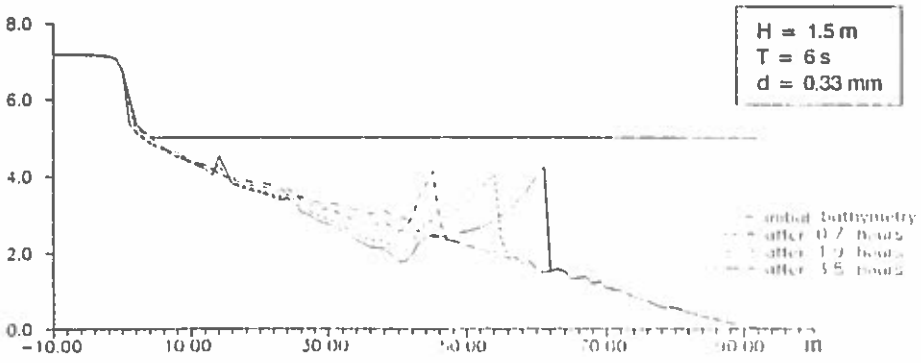

Figure 8. Morphological Evolution without the Running Average (L_r=4D)

Effect of Description of Wave Heights after Breaking

In Fig. 9 the influences on the bar formation of the decay of the waves after breaking are illustrated. The difference is reached by variation of the parameters in Eq. (1). It is noted that the loss of energy strongly influences the undertow which increases with increasing loss of energy. From Fig. 9 the following is noted: The size of the bar increases with increasing relative height of the waves at the breaking point. The length of the trough between the bars depends on the rate of energy loss after breaking. If the wave looses its energy very quickly a steep, high bar will be formed. The near-shore waves are limited in height by the first bar. In this case the next bar will therefore start to grow at relatively low water depths.

If the wave looses its energy more slowly the transport capacity becomes more evenly distributed, e.g. the bar becomes a little lower. The next breaker bar can then be formed at larger depths than in case of the very rapid decrease in wave heights just after breaking.

Effect of Density Driven Currents and Gravitation on Bed Load/Bed Concentrations

The present model includes the mechanism that the suspended sediment increases the density of the fluid which means that in case of sloping bed there is a downhill contribution to the near-bed mean current.

Further, the model includes an adjustment to the bed concentrations and bed load in case of sloping bed. These adjustments are described by Fredsøe (1979). The effect on the morphological evolution of these down-hill contributions to the transport rates are illustrated in Fig. 10a and b. Fig. 10a shows a simulated breaker bar after 3.5 hours with and without density driven currents and gravitation on the bed load and concentrations. It is clearly seen that these effects increase the seaward (downhill) motion of the bar. Fig. 10b shows an example of the calculated deformation by smaller waves (i.e. non-breaking) of the storm bar with and without inclusion of bed slope effects. Again it is clear that these effects pull the bar downhill, i.e. offshore.

Effect of Onshore Transport

In the numerical experiments presented in Figs. 7 and 9 the transport under the non-broken waves has been included. However, in the case of development of a breaker bar the transport rates under the non-broken waves are two orders of magnitude smaller than in the surf zone. The effect of the onshore transport during a short storm period is therefore insignificant.

The examples in Fig. 10b with small waves show that the transport under the non-broken waves smooth out the storm bar, and a significant onshore transport takes place inside the storm bar. (In these examples the onshore transport is calculated corresponding to first order Stokes waves taking into account, streaming, Lagrangian drift, and bed slope effects.)

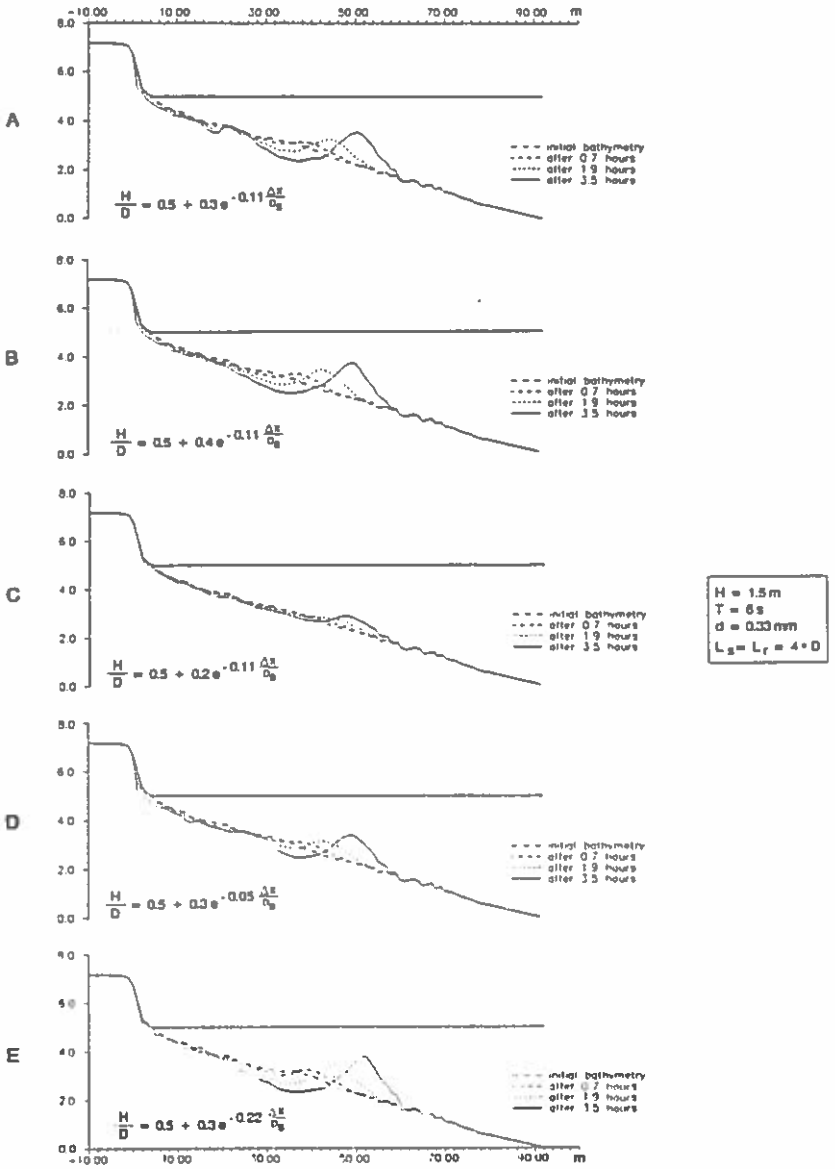

Figure 9. Illustration of the Effects of Description of the Wave Heights after Breaking on the Evolution of the Profile.

Effect of Irregular Waves

The above examples on calculated profile evolutions have been carried out with regular waves. Evidently, the effect of irregular wave heights is to smooth out the bar formation. In the present model the effect of irregularity is included by calculation of the transport rate along the profile as the average of the transport rates for a number of wave components, i.e. there is no interaction between the waves included in this model. The smoothing of the profile is illustrated in Fig. 11, where the test presented in Fig. 9b is repeated, but now with Rayleigh distributed wave heights and H_s = 1.5 m.

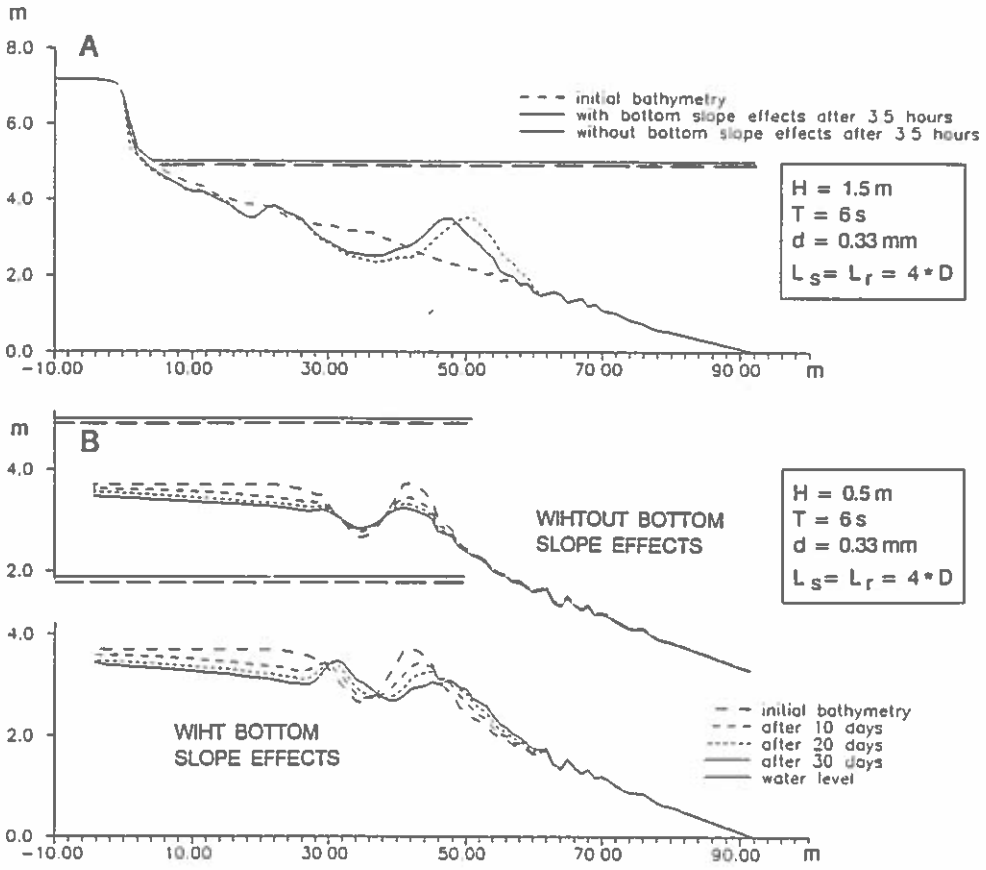

Figure 10a Storm Bar after 3.5 Hours. Calculated with and without Bottom Slope Effects.

10b Deformation of Storm Bar by small Waves with and without Bottom Slope Effects.

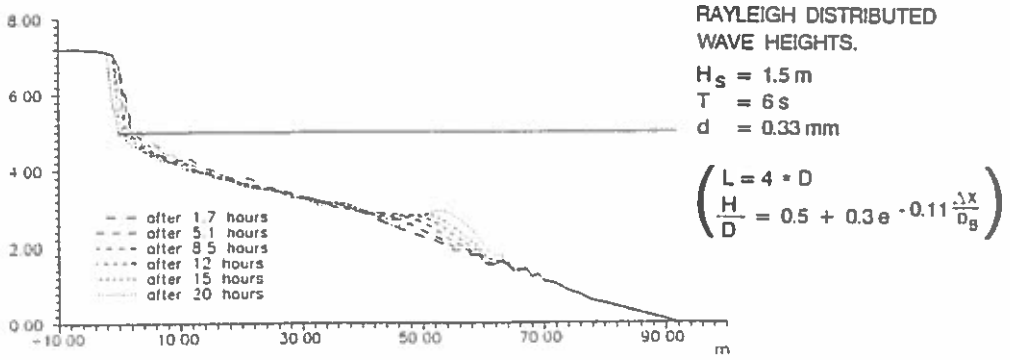

Figure 11. Illustration of the Effect on the Bar Formation of Irregular Waves.

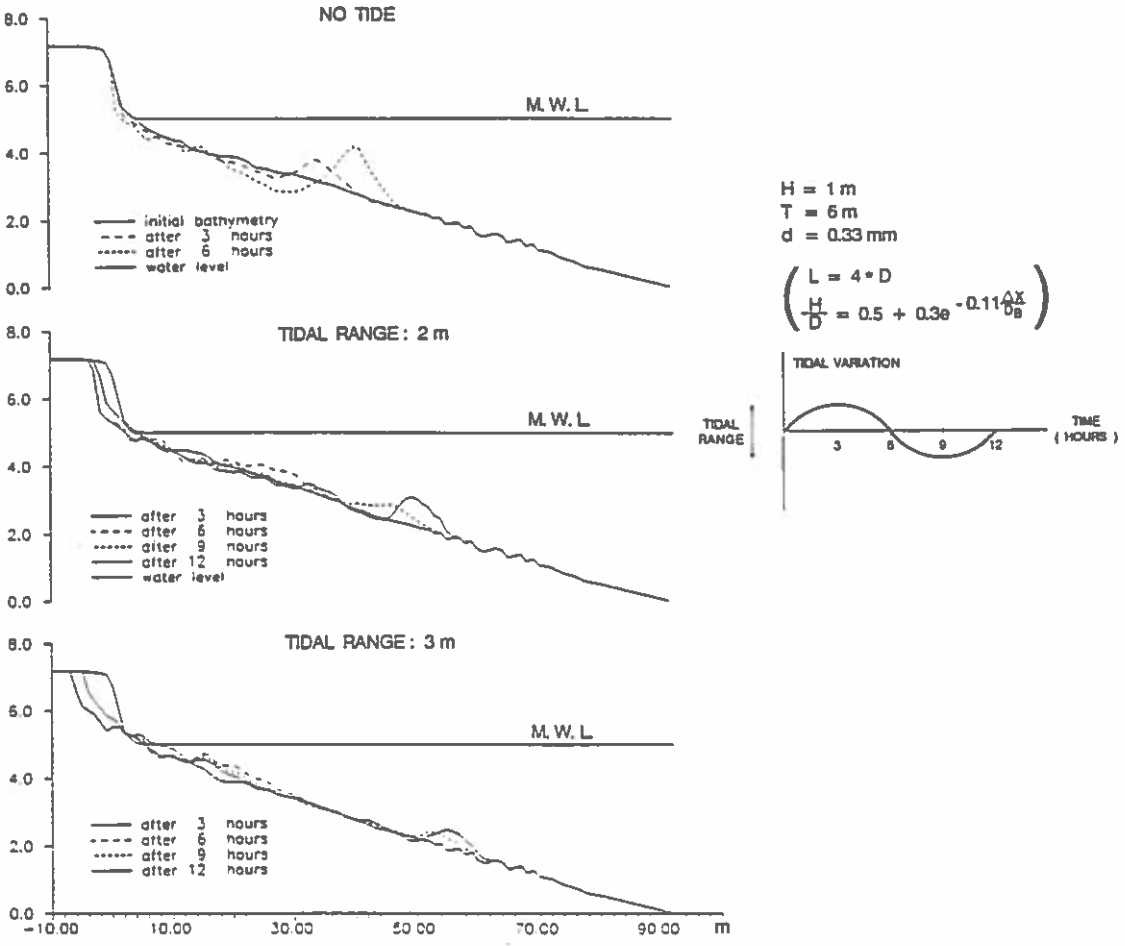

Figure 12. Illustration of the Effect of Tidal Variation on Bar Formation

Effect of Tidal Variation on Bar Formation

It is well known that tidal variation hinders the formation of bars. This phenomenon can be illustrated by the present model. In Fig. 12 is shown simulated evolution of the profile for regular waves, no tide and two different tidal ranges. The formation of bars depends of the time scale for development of the bar under steady conditions, the period of the tide and the tidal range. In the present case, see Fig. 12 for specifications, the formation of the bar is strongly decreased for tidal range larger than three times the wave height.

CONCLUSIONS

A deterministic model which describes the morphological evolution of a coastal profile has been presented. The model includes detailed description of the hydrodynamics and sediment transport across the profile.

The model is able to simulate the growth of a breaker bar formed by regular waves and to give indications of the modifications of the evolution due to phenomena as irregularity of the waves and tide.

ACKNOWLEDGEMENTS

This work was undertaken as part of the MAST G6 Coastal Morphodynamic research programme. It was funded jointly by the Danish Technical Research Council (STVF) and by the Commission of the European Communities, Directorate General for Science, Research and Development under MAST contract No. 0035.

REFERENCES

Andersen, O.H., Fredsøe, J. (1983): Transport of Suspended Sediment along the Coast. Inst. of Hydrodynamics and Hydraulic Engineering, Techn. University of Denmark. Prog. Rep. 59.

Brøker Hedegaard, I., Rønberg, J.K., Deigaard, R. (1991): Net Transport in Non-Broken Waves. MAST G6, Coastal Morphodynamics, Edinburgh, U.K.

Brøker Hedegaard, I, Deigaard, R. (1988): A Model for Cross-Shore Sediment Transport and Coastal Profile Development. Presented at 2nd International Symposium on Wave Research and Coastal Eng., Hannover, Germany.

Deigaard, R., Fredsøe J. (1989): Shear Stress Distribution in Dissipative Water Waves. Coastal Engineering Vo. 13, p. 357-378.

Deigaard, R., Fredsøe, J., and Hedegaard, I.B. (1986): Suspended Sediment in the Surf Zone. J. Waterway, Port, Coastal, and Ocean Engineering, ASCE, Vol. 112, No. 3.

Dette, H., Uliczka, K. (1986): Seegangsserzeugte Wechselwirkung zwischen Vorland und Vorstrand sowie Küstenschutzbauwerk. Technischer Bericht Nr. 3 - SBF 205/TP A6. Universität Hannover.

Engelund, F. and Fredsøe, J. (1976): A Sediment Transport Model for Straight Alluvial Channels. Nordic Hydrology, Vol. 7.

Fredsøe, J. (1979): Natural Backfilling of Pipeline Trenches. J. Petroleum Tech. Vol 31.

Fredsøe, J. (1984): Turbulent Boundary Layer in Wave and Current Motion, J. Hydraulic Engineering, ASCE, Vol. 110, No. 8.

Justesen, P. (1988): Turbulent Wave Boundary Layers. Inst. of Hydrodynamics and Hydraulic Engineering. Techn. University of Denmark. Series Paper No. 43.

Longuet-Higgins, M.S. (1953): Mass Transport in Water Waves, Philos. Trans. R. Soc. London, Ser. A, 245.

Saville, T. (1957): Scale Effects in Two-Dimensional Beach Studies. Trans. 7th Meeting, IAHR, Lisbon.

Svendsen, I.A. (1984): Mass Flux and Undertow in a Surf Zone. Coastal Engineering, Vol. 8, No. 4.

Intercomparison of Coastal Profile Models

Ida Brøker Hedegaard
Danish Hydraulic Institute
Agern Allé 5
2970 Hørsholm
Denmark

J.A. Roelvink
Delft Hydraulics

Howard Southgate
HR Wallingford Ltd.

Philippe Rechon
Laboratoire National d'Hydrulique

John Nicholson
University of London

Luc Hamm
Sogreah

INTERCOMPARISON OF COASTAL PROFILE MODELS

Ida Brøker Hedegaard[1], J.A. Roelvink[2], Howard Southgate[3]
Philippe Pechon[4], John Nicholson[5], Luc Hamm[6]

Abstract

The present paper briefly presents 6 different models for short term coastal profile modelling for direct incoming waves. The models have been tested against measured profile evolutions from a large wave flume. Features such as wave height distribution, cross shore current profiles and sediment transport are compared and discussed.

Introduction

The described models are all established with the same structure of modules for hydrodynamics, sediment transport and bed level evolution but with different degrees of determinism/empiricism and refinement. The basic structure of the modules and a definition sketch for the coastal profile models are presented in Fig. 1.

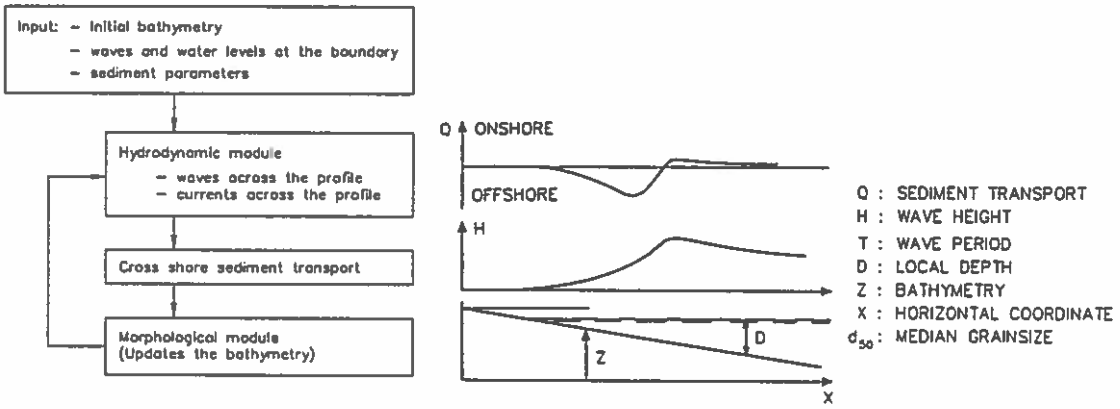

Fig. 1. Basic Structure of the Morphological Models and Definition Sketch.

---

1) Danish Hydraulic Institute, 2) Delft Hydraulics, 3) HR Wallingford Ltd., 4) Laboratoire National d'Hydraulique, 5) University of Liverpool, 6) Sogreah

Description of the Models

LITCROSS, Danish Hydraulic Institute.

The variation of the wave heights across the profile is determined from the criteria that the wave has either constant energy flux or wave heights decreases in accordance with an empirical relation first suggested by Andersen and Fredsøe (1983):

$$\frac{H}{D} = 0.5 + 0.3 \exp\left(-0.11 \frac{\Delta x}{D_B}\right)$$

where Δx is the distance from breaking point and D_B is the depth at the breaking point. The areas of the surface roller of the breaking waves are assumed to correspond to hydraulic jumps apart from a zone just inside the breaker point where the area is assumed to vary according to measurements by Buhr Hansen (1991). Random waves are treated as individual waves with no interaction.

Hydrodynamic modelling. The vertical distributions of currents and turbulence are assumed to be determined by the local depth, wave conditions and sediment properties. The basis for the model is the combined wave current boundary layer model of Fredsøe (1984). In breaking waves a major contribution to the turbulence comes from the loss of energy in waves and surface rollers. This contribution is calculated by the vertical transport equation for turbulent energy, Deigaard et al. (1986). The vertical distribution of the wave period averaged velocities is derived from the distributions of shear stresses and wave period averaged eddy viscosity. The shear stresses include the contributions from breaking waves, Deigaard and Fredsøe (1989), from streaming, determined as outlined by Longuet Higgins (1953), from the increased density due to suspended sediment in case of sloping bed and from a setup of the water surface which is determined such that the total flux including the wave drift and the water carried in the surface rollers equals zero, Svendsen (1984).

The net sediment transport is calculated as bed and suspended load. The instantaneous bed load and nearbed boundary condition for the vertical distribution of suspended sediment are determined as functions of the instantaneous shear stress, Engelund and Fredsøe (1976). The time varying vertical distribution of suspended concentrations is calculated by the vertical diffusion equation, Deigaard et al. (1986). The total wave period averaged net transport is found from

$$q_s = \frac{1}{T} \int_{\text{period}} \int_{\text{depth}} c \cdot u \, dz \, dt + \int_{\text{depth}} u_l \cdot \bar{c} \, dz$$

where u_l is Lagrangian drift. The last term is included to compensate the omission of convective terms in the solution of the concentration field.

The bed level evolutions are determined by the continuity equation for the sediment.
The numerical solution is explicit. A modified Lax-Wendroff scheme has been applied to reduce the numerical diffusion and to obtain a stable solution. LITCROSS is described in more detail in Brøker Hedegaard, Deigaard and Fredsøe (1991).

UNIBEST, Delft Hydraulics.

UNIBEST-TC stands for UNIform BEach Sediment Transport, Time-dependent Cross-shore. It is a direct descendant of the models OSTRAN (Stive and Battjes, 1984) and COSTRAN (Stive, 1986). In Roelvink and Stive (1989), the model has been tested against wave flume measurements and improved on some points. The model aims at predicting long-term development of the profile of beaches that are approximately uniform in alongshore direction, and which are subjected to obliquely incident wave fields, varying water levels and tidal currents. The morphodynamic behaviour due to cross-shore transport only is considered, however, effects of longshore currents on cross-shore transport are accounted for.

For the present study, cross-shore effects only are considered, and the formulations as given in Roelvink and Stive (1989) are used. Mechanisms included here are:

- Wave shoaling and breaking and associated set-up according to Battjes and Janssen (1978);
- Cross-shore current description according to de Vriend and Stive (1987);
- Transition zone effects on the return flow according to Roelvink and Stive (1989); Short wave velocity moments based on Rienecker and Fenton's (1981) Fourier approximation of the stream function method;
- Long wave effects according to the same paper;
- Sediment transport according to Bailard (1981);
- A Fully implicit scheme for the bed evolution.

For the case of regular waves, the wave decay model is adapted simply by setting the fraction of breaking waves to 1 after the wave height exceeds a given fraction of the water depth.

NPM, Hydraulic Research.

NPM (Nearshore Profile Model) is a model for waves, longshore and cross-shore current and sediment transport on uniform beaches for obliquely or direct incoming waves. A brief summary of the physical processes represented in the NPM is given below.

- Wave transformation by refraction (by depth variations and currents), shoaling, Doppler shifting, bottom friction and wave breaking. For random waves, a Battjes and Janssen (1978) framework is used for determining the distribution of wave height and the fraction of time that waves are breaking at any point.
- Wave setup determined from the gradient of wave radiation stress.
- Driving forces for longshore wave-induced currents, determined directly from the spatial rate of wave energy dissipation.
- Longshore currents from pressure-driven tidal forces and wave-induced forces, and the interaction between the two types of current.
- Cross-shore undertow velocities using a three-layer model of the vertical distribution of cross-shore currents (de Vriend and Stive, 1987).
- Transition zone effects (the transition zone is the distance between where a wave starts to break and where turbulence becomes fully developed).

- Cross-shore and longshore sediment transport rates using an 'energetics' approach (Bailard, 1981; Stive, 1986).
- Seabed level changes due to cross-shore sediment transport using a Lax-Wendroff scheme.

Tests (Southgate, 1991) have shown that the model results are particularly sensitive to the transition zone length and to the height above the seabed at which the undertow velocity is taken for input to the sediment transport calculations. Recent improvemnets to the NPM therefore include:

- A reanalysis of transition zone data (O'Shea et. al., 1991) to give a more accurate formula for the transition zone length.
- The use of a concentration-weighted average undertow velocity in the sediment transport calculations.

NPM is described in detail in Southgate and Nairn (1993) and Nairn and Southgate (1993).

WATAN 3, University of Liverpool.

The model WATAN3 consists of a wave sub-model and a sediment sub-model. The wave sub-model (Watanabe and Dibajnia, 1988) comprises a set of two equations which are equivalent to a time-dependent version of the mild-slope equation and contain an additional term to allow for energy dissipation in the surf zone. The latter term represents the rate at which energy is dissipated by breaking and is set to zero wherever the broken waves have reformed inside the surf zone, as well as outside the surf zone. An empirical criterion (Watanabe et al, 1984) is used to determine the point of breaking, and setup and setdown are computed by solving the momentum balance equation.

The sediment sub-model (Ohnaka and Watanabe, 1990) is based on the sediment transport rate due to wave action:

$$Q = (A_W (\tau_B - \tau_C) + A_{WB} \tau_T) F_D \hat{u}_B / (\rho g)$$

where Q is the sediment transport rate, A_W and A_{WB} are coefficients, τ_B is the maximum nearbed shear stress due to wave action, τ_C is the threshold of movement shear stress. τ_T is the shear stress generated by breaker turbulence, F_D is a dimensionless directional function and $\hat{u}_B$ is the maximum nearbed orbital velocity. Having derived the transport rates throughout the computational domain, the former are then modified to allow for bed slope effects, so that:

$$Q_M = Q - \epsilon |Q| \tan \beta$$

where Q_M is the modified transport rate, ϵ is a coefficient and tan β is the local bed slope. Finally, the bed level changes are computed using the sediment mass conservation equation.

An additional feature of the present version of the sediment sub-model is the inclusion of a breaker transition length, within which turbulence generated by the post-breaking surface roller is distributed throughout the water column. A re-analysis of work

carried out by Nairn et al (1990) yielded the following expression for the transition length (O'Shea et al, 1991):

$$L_T = L_B \ (0.56 \ \xi^{-1.47}) \ \tan \beta$$

where L_T is the transition length, L_B is the wave length at breaking and ξ is the Iribarren No. The effects of the transition length are incorporated into the sub-model by switching off the breaker turbulence contribution to the transport rate within the transition length.

SEDITEL, Laboratoire National d'Hydraulique.

SEDITEL computes the wave refraction and shoaling, wave height decay in the surf zone, time-averaged three-dimensional currents (2DV currents here) induced by breaking waves, sediment transport rates, bed evolution.

The wave refraction is derived from the classical Snell's law. The wave height is deduced from the equation of the flux of energy where the dissipation is supposed to be similar to the one of a hydraulic jump in the surf zone. In order to have a good estimation of the wave characteristics in shallow water, non-linear effects are considered in the calculation of the flux of energy, see Péchon (1987).

The time-averaged currents induced by breaking waves are computed with the three-dimensional model TELEMAC-3D outlined in Lepeintre et al. (1991). In order to establish the equations the instantaneous velocity is separated into three contributions: an unknown mean current, a purely periodic current corresponding to the wave motion, and turbulent fluctuations. In the time-averaged equations some closures are required to express the velocity correlations (see details in Péchon, 1992). They are given by previous works of Svendsen (1984), De Vriend and Stive (1987), Deigaard and Fredsøe (1989).

The sand transport is computed using Bailard's formula, Bailard (1981), but the suspended load efficiency factor is increased in the surf zone to take the breaking effect into account. The proposed expression is:

$$\varepsilon_s' = \left(1 + a \frac{|u_b|}{\sqrt{gD}}\right) \varepsilon_s \quad ;$$

ϵ_s : efficiency factor, non breaking
ϵ'_s: efficiency factor, breaking
a : constant
u_b : mean velocity at the bottom

The bed evolution is computed by solving the continuity equation for the sediment. To reproduce the process of avalanching of dune in the application presented here, the measured amount of sediment is distributed between the crest of the bar and the shoreline before each hydrodynamic computation. Moreover a maximum stability slope of 15/100 is specified out of the breaking zone.

The wave and current patterns are updated when the bottom evolution becomes significant. However, in order to reduce the number of iterations, an additional treatment is performed during the computation of the bottom evolution: considering the bed evolution

at the breaking point, its location is moved along the coastal profile and the wave and current characteristics are moved the same way.

REPLA, SOGREAH.

REPLA is a wave-averaged, finite amplitude, current-depth shoaling and refraction model to simulate regular or random wave propagation from deepwater to the shoreline.

The formulation is detailed in Fornerino et al (1992). A set of four equations is to be solved with an iterative procedure because of the influence of the wave height on the wave celerity.

Stokes third order theory is used for small Ursell numbers. For large Ursell numbers a cnoidal second order theory is used. The model can, however, also be run with Stokes first order waves.

The wave breaking criteria derived by Weggel (1972) is used. In presence of an adverse current, this expression is modified following Sakai et al.(1988). The bore model is used to express the energy dissipation. In order to simulate wave reformation after breaking on a bar, the dissipation rate is put to zero when the wave height is less than half the local maximum wave height.

For random waves, two methods are implemented. The parametric approach of Battjes and Janssen (1978) and the individual wave method Mase and Iwagaki (1982); Mizuguchi (1982) in which each class is propagated independently with the regular wave model.

Results from the various Models

The models have been tested against experimental results obtained from the large wave flume in Hannover in 1986 and 1987, Dette and Uliczka (1986) and Dette and Oelerich (1991). The experiment from 1986 was carried out with regular waves. The 1987 experiment was run with irregular waves and included a comprehensive measuring program focusing on waves.

Regular Wave Case

The experiment with regular waves constitutes a severe test of the models due to the fact that all waves are breaking nearly at the same position. This first test gives the opportunity to tune the possible model parameters in the various models. Results in the form of calculated and measured profiles from this first test are presented in Fig. 2.

The calculated profile evolution is the integrated result of the modelling of several physical mechanisms. The interpretation of the differences between the modelled evolutions can therefore only be pointed out after comparison of each individual element in the various models. These comparisons are carried out for a similar case,but now the initial profile is a plane beach with an initial slope of 1:20. Below, the initial wave heights, current fields and sediment transport along this plane beach are considered.

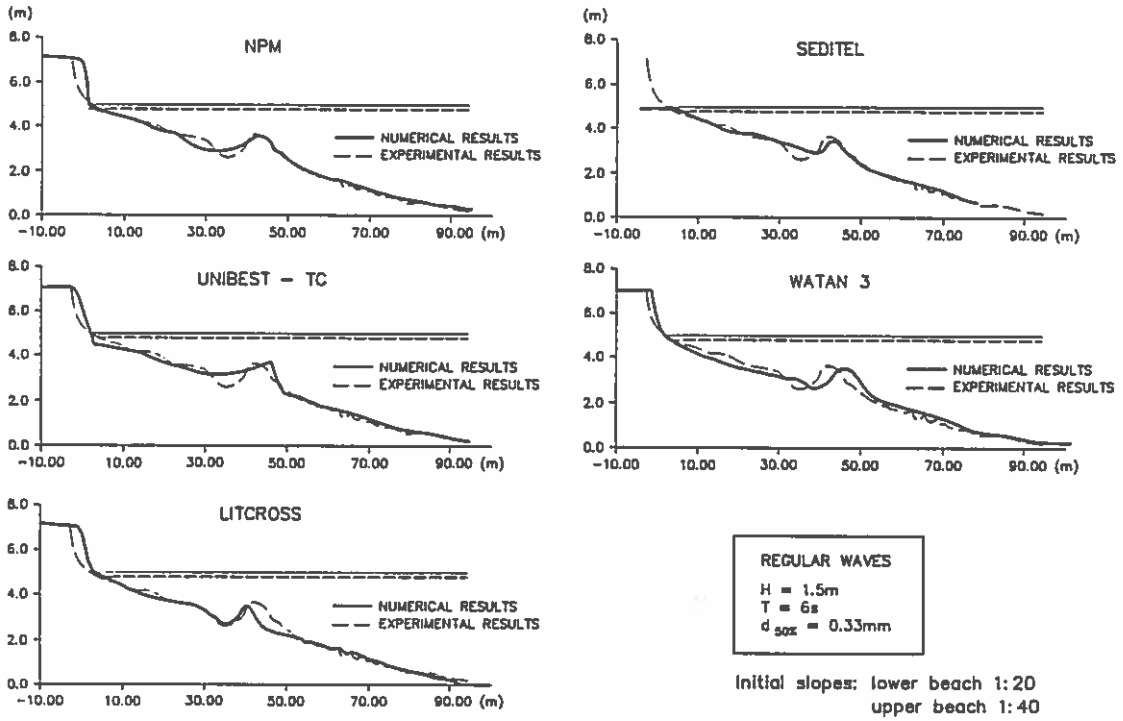

Fig. 2. Comparison of Measured and Calculated Coastal Profiles after 4.3 hours of Exposure.

The figures 3, 4, and 5 show wave heights across the plane profile, vertical distribution of horizontal wave averaged velocities, for Seditel also the vertical velocity component just shoreward of the breaker point and the vertical flow pattern, and the initial cross shore sediment transport. Already the comparison of wave heights show large spreading across the surf zone. This spreading is reflected in deviations in the assumed cross section area of the surface rollers. The differences in the vertical distribution of horizontal velocities exist due to differences in the formulation of the vertical distribution of shear stresses, eddy viscosities and the area of surface rollers.

The above comparisons illustrates differences in the models, but suffer unfortunately from lack of measured data. The calculated initial transport rates highlight the fact that the bar forms at a 'critical' position, seen from a model view point where the onshore transport under the non breaking waves turn into offshore transport inside the surf zone.

Further, although discrepancies exist between the distribution of horizontal velocities calculated by the one DV models and the 2 DV model, Seditel, the 2 DV results indicate that the order of magnitude of vertical velocities shoreward of the breaker point are comparable with the settling velocity of sand. Therefore, in a narrow zone inside the breaker point, the sediment transport models which take into account only velocities parallel to the bottom might underestimate the amount of suspended sediment.

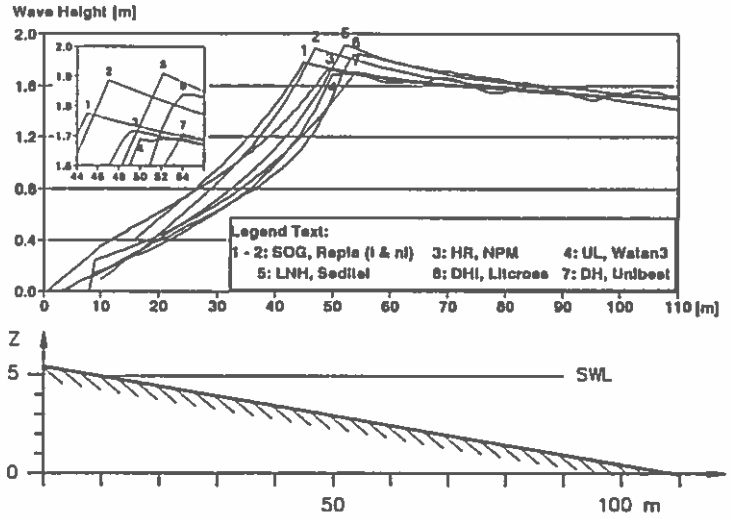

Fig. 3. Wave heights as calculated by 6 different models.

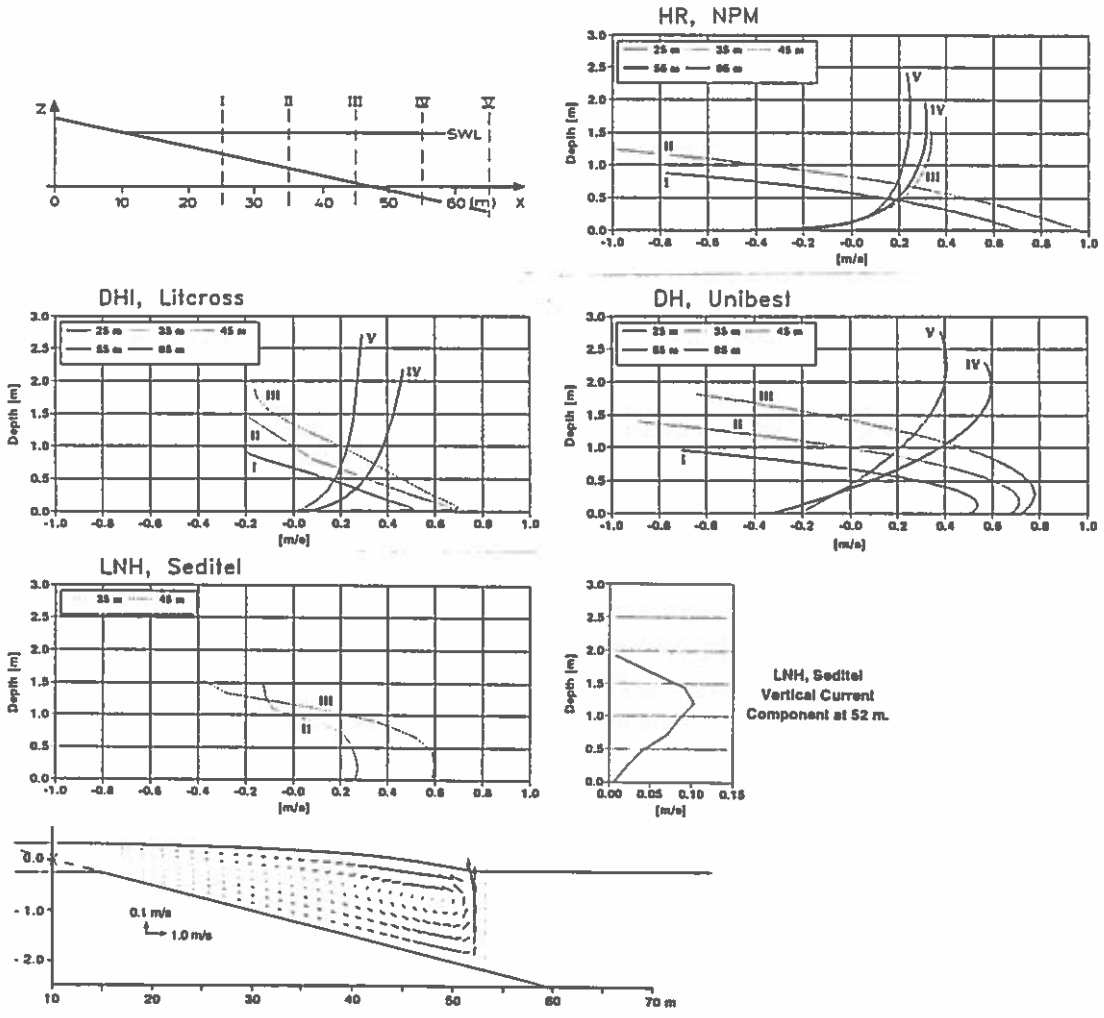

Fig. 4. Velocity components and the 2 DV current field as calculated by Seditel.

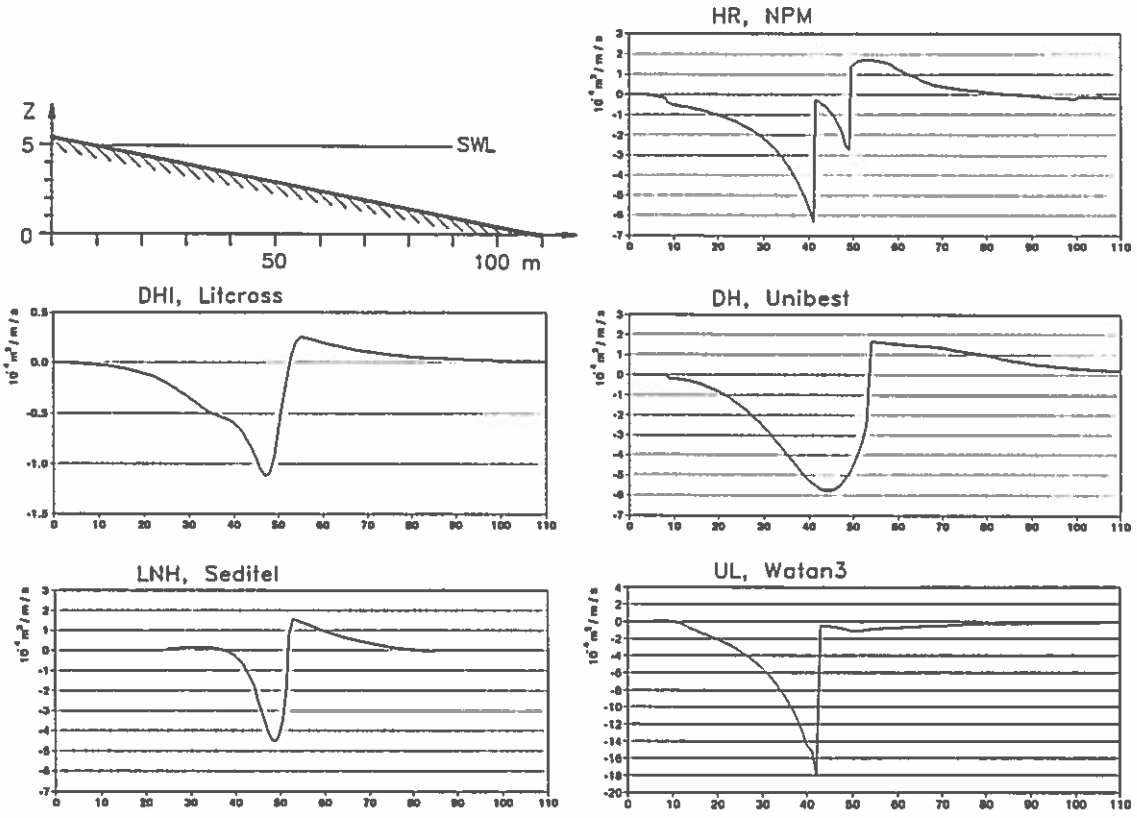

Fig. 5. Cross shore sediment transport calculated by NPM, Unibest, LITCROSS, Seditel and Watan 3.

It appears that the cross shore transport models when applied in a morphological calculation sequence in combination with more or less smoothing, either on the calculated transport or on the bed levels between updates, are able to reproduce to a certain extent the evolution of a breaker bar. In the case of regular waves it seems clear that the mechanisms just shoreward of the breaker point are essential for the bar evolution.

For irregular waves these complex mechanisms are expected to be less important for the profile evolution. In the following the models are compared with measurements in the case of irregular waves.

Irregular Waves Case

This test was carried out with irregular waves, Jonswap spectrum, with H_s = 1.5m and T_p = 6 s at 5 m depth in front of the wavemaker. The profile was built out of natural well sorted sand with a mean diameter of 0.22 mm. The test was subdivided into 45 runs of 780 s each. The wavemaker was stopped after each run. The wave generation was first order with no long waves reflection compensation. The observed bathymetry, the wave heights (H_{RMS}), the sediment transport derived from successive observations of the bed evolution and the wave energy spectrum as measured at three positions are presented in Fig. 6.

In this case a pronounced bar is not formed but the relatively steep profile is flattened out. The wave heights in the surfzone decrease concurrently with the flattening of the profile, i.e. the energy is dissipated further and further offshore. These tendencies are reflected in the cross-shore transport rates which are largest at the beginning of the test. From the spectral analysis of wave energy it appears that the spectra become double-peaked while the waves approach the beach, i.e. in the nearshore area low frequency waves become more important, see figure 6. From analysis of correlations between bound long waves and the observed low frequency waves it seems clear that the major part of the low frequency energy come from reflections in the flume.

In figures 7 and 8 measured and simulated variations of the wave heights across the profile for the observed bathymetries in runs 2, 14 and 32 are compared. These results are produced by REPLA applying both the parametric approach and the individual wave method with both linear and non linear wave theory. With the first approach it appears that when γ is adjusted corresponding to the highest wave heights, the heights inside the surf zone are underestimated for runs 2 and 14. The individual wave method is seen also to underestimate the near shore wave heights. It might be necessary to include mechanisms as the extra variations of the water level and flow due to the long waves and the opposing undertow in the wave modules.

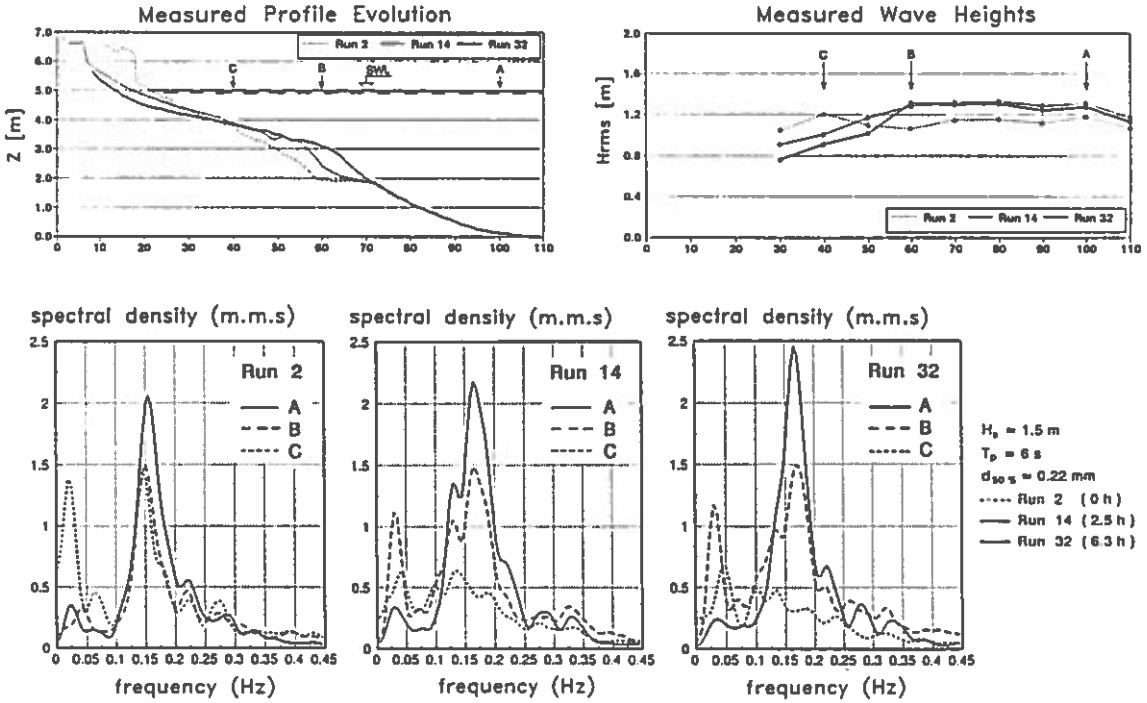

Fig. 6. Observed bathymetries, measured H_{RMS}, and wave energy spectrum at 3 positions.

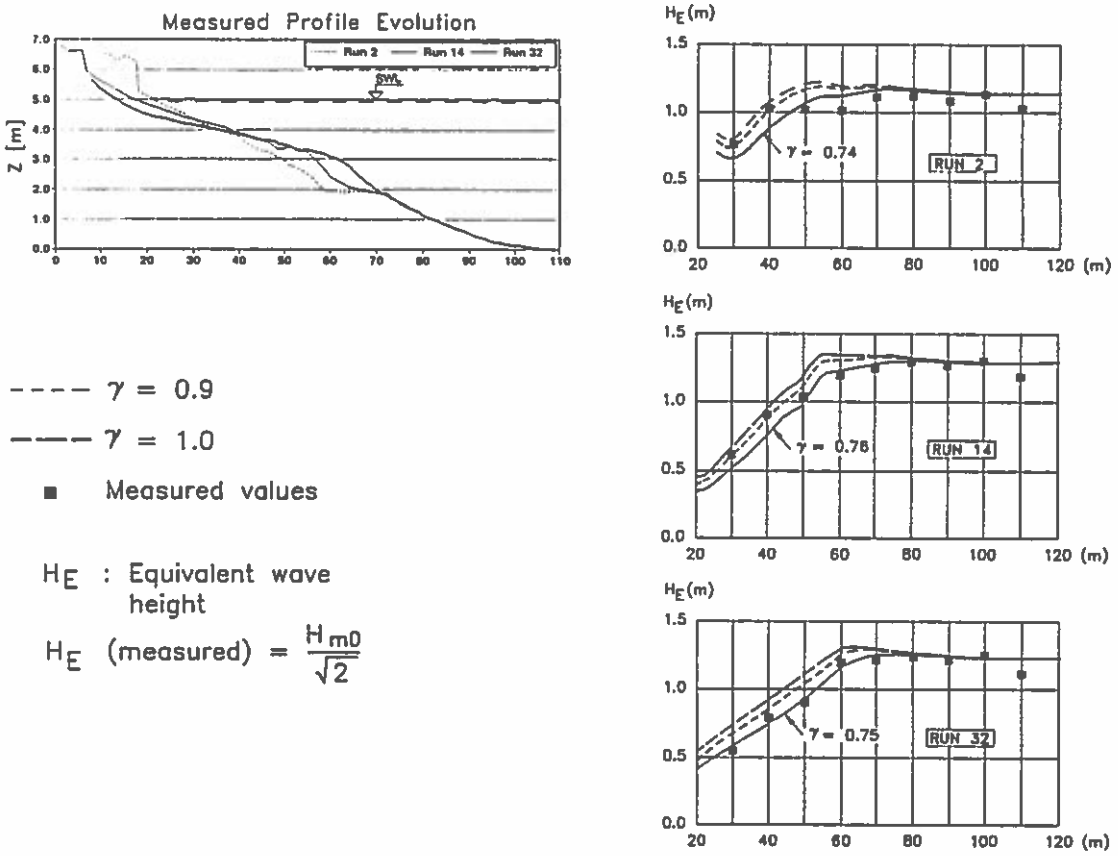

Fig. 7. Measured and calculated equivalent wave heights. Calculations by REPLA applying Battjes and Janssen's parametric approach.

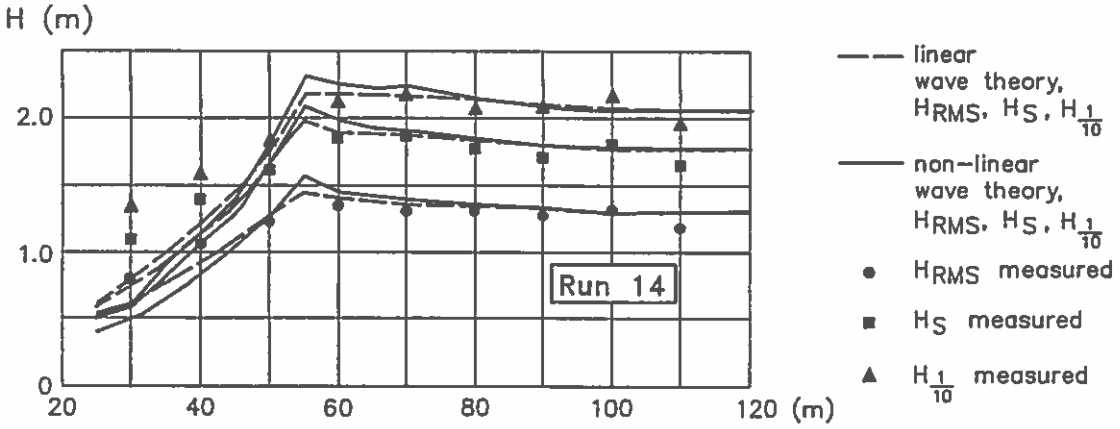

Fig. 8. Measured and calculated H_{RMS}, H_S and $H_{1/10}$. Calculations by REPLA applying the individual wave approach with linear and non linear wave theories.

Figure 9 shows the measured and calculated cross-shore transport. It is seen that the models are very sensitive to even small humps in the bed and that the observed relatively

large initial offshore transport is not very well reproduced. The Watan 3 model has been run with 5 wave components only which obviously gives a very scattered transport pattern.

Figure 10 shows results of morphological modelling of the coastal profile. The modelled evolutions obviously suffer from the underestimation of the initial offshore transport capacity and the lack of description of the erosion in the steep dune front.

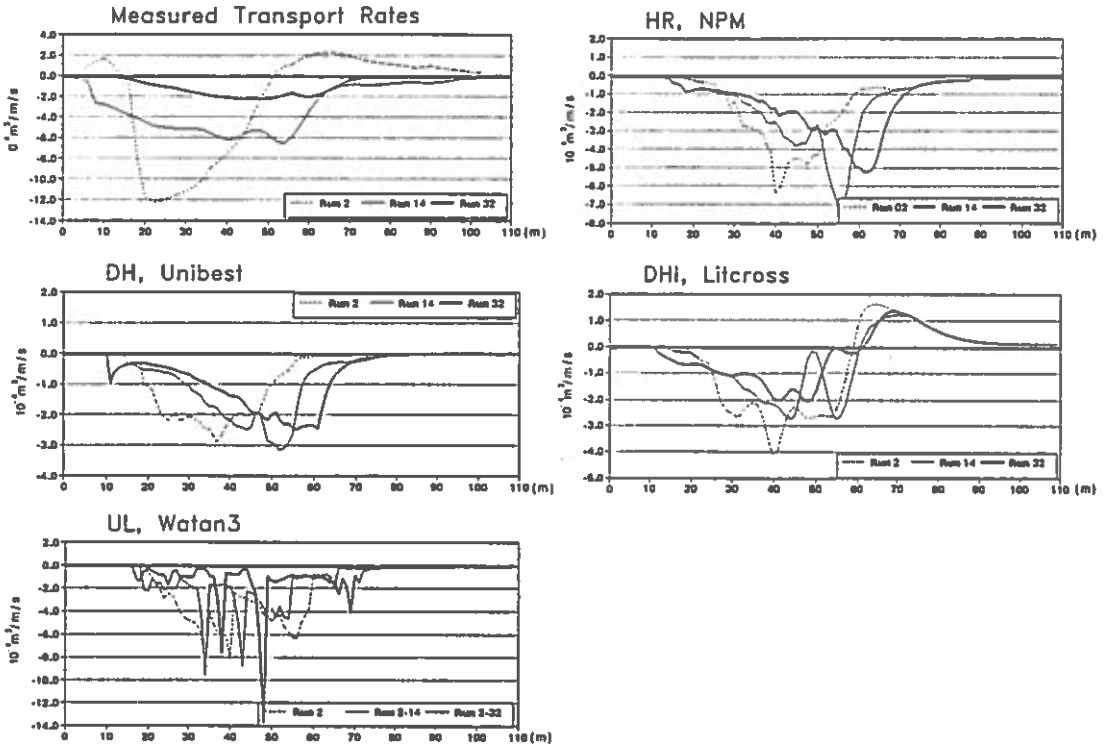

Fig. 9. Measured and calculated cross-shore transport rates. These calculations are carried out with the observed bathymetries.

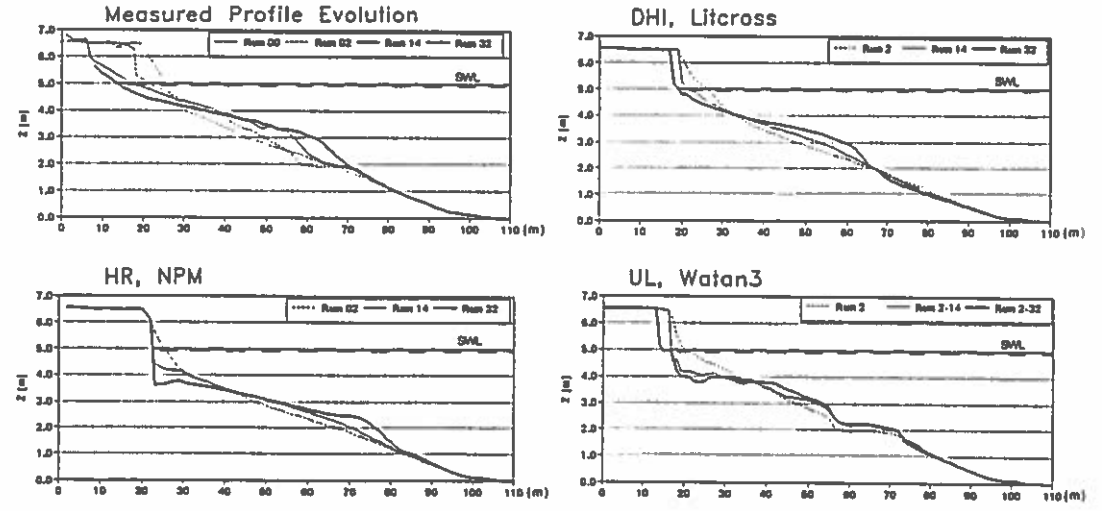

Fig. 10. Measured profile evolution. Simulated evolution. HR, NPM and DHI, LITCROSS from 'initial' to Run 32. UL, WATAN 3 from Run 2 to Run 32.

Concluding remarks

Large differences exist between the coastal profile models presented above. However, based on the experience gained through the comparisons with experimental data the following general comments are given:

- The models generally underestimate the offshore transport on relatively steep profiles. One reason seems to be related to poor wave description in cases where reflections and long waves, free and bound, exist.
- The swash zone processes and dune erosion are not described in the models. In combination with the above mentioned underestimation of transport on steep slopes the exchange of material from the dune to the bar is too slow in the case of a steep, initial profile.
- The vertical velocities close to the breaker point seem to reach a significant order of magnitude and might influence the bar formation, at least in the case of a closed flume. Generally, the velocity field in the area just before and after the (average) break point is still understood rather poorly.

It is noted that with the outlined concept of a coastal profile model the pronounced breaker bar in regular waves and the flattening of a steep profile in irregular waves can be modelled. In nature the coastal profiles are formed by 3D phenomena. It seems that the understanding of cross-shore processes has now reached a stage where it is relevant to extend the models into 3D to be able to judge where the 'weakest point' appears and where most effort in the future should be spent.

Acknowledgements

This work has been undertaken as part of the MAST G6 Coastal Morphodynamic Research Programme. It was funded partly by the Commission of European Communities, Directorate General for Science, Research and Development under MAST Contract No. 0035-C and partly by national fundings, among these The Danish Technical Research Council (STVF), Service technique Central des Ports Maritimes et des Voies Navigables (Compiègne, France), The Netherlands 'Coastal Genesis Programme' (Kustgenese).

The authors would like to thank Dr. Dette and Dr. Oelerich, Hannover University, for the delivery of processed data from the experiments in the large wave flume.

References

Andersen, O.H. and Fredsøe, J. (1983): Transport of sediment along the coast. Prog. Rep. 59, ISVA, Techn. Univ. of Denmark, pp. 33-46.

Bailard, J.A. (1981). An Energetics Total Load Sediment Transport Model for Plane Sloping Beach, J. Geophys. Res., Vol. 86, No. CII.

Battjes, J.A. and Janssen J.P.F.M. (1978) Energy Loss and Set-up due to Breaking of Random Waves, Proc. 16th Int. Conf. on Coastal Eng, ASCE, Hamburg.

Brøker Hedegaard, I., Deigaard, R., Fredsøe, J. (1991). Onshore/Offshore Sediment Transport and Morphological Modelling of Coastal Profiles. Proc. Coastal Sediments '91, Seattle.

Buhr Hansen, J. (1991). Air entrainment in surf zone waves, 3rd Int. conf. on Coastal and Port Eng. in Dev. Countries, Mombasa, 1991.

Deigaard, R., Fredsøe, J. (1989). Shear Stress Distribution in Dissipative Water Waves. Coastal Eng. Vol. 13, pp. 357-378.
Deigaard, R., Fredsøe, J., and Hedegaard, I.B. (1986). Suspended Sediment in the Surf Zone. J. Waterway, Port, Coastal, and Ocean Eng., ASCE, Vol. 112, No. 3.
Dette, H., Uliczka, K. (1986). Seegangsserzeugte Wechselwirkung zwischen Vorland und Vorstrand sowie Küstenschutzbauwerk. Technischer Bericht Nr. 3-SBF 205/TP A6. Universität Hannover.
Dette, H. and Oelerich (1991): Internal MAST-G6M report.
De Vriend, H.J. and Stive M.J.F. (1987). Quasi-3D Modelling of Nearshore Currents, Coastal Engineering, Vol II, pp. 565-601.
Engelund, F. and Fredsøe, J. (1976). A Sediment Transport Model for Straight Alluvial Channels. Nordic Hydrology, Vol. 7.
Fornerino, M., P. Sauvaget and L. Hamm (1992). Numerical modelling of finite amplitude wave shoaling in presence of currents in Hydraulic Engineering Software IV, Fluid flow modelling, eds. W.R.Blain and E. Cabrera, Computational Mechanics publ., Southhampton, pp. 587-598.
Fredsøe, J. (1984). Turbulent Boundary Layer in Wave and Current Motion, J. Hydraulic Engineering, ASCE, Vol. 110, No. 8.
Lepeintre, F., Gest, B., Hervouet, J-M., Péchon, Ph., (1991), 'MITHRIDATE (former name for TELEMAC-3D): a finite element code to solve 3D free surface flow problems'. 2nd International Conference on Computer Modelling in Ocean engineering, Barcelone.
Longuet-Higgins, M.S. (1953). Mass Transport in Water Waves, Philos. Trans. R. Soc. London, Ser. A, 245.
Mase, H. and Y. Iwagaki (1982). Wave height distributions and wave grouping in surf zone 'Proc. Int. Conf. on Coastal eng., ASCE, 58-76.
Mizuguchi, M. (1982). Individual wave analysis of irregular wave deformation in the nearshore zone. Proc. Int. Conf. on Coatal Eng., ASCE, 485-504.
Nairn, R.B. and Southgate, H. N. (1993). "Deterministic profile modelling of nearshore processes. Part 2. Sediment transport and beach profile development", Coastal Engineering (to appear).
Nairn, R.B., Roelvink, J.A. and Southgate, H.N. (1990), Transition Zone Width and Implications for Modelling Surfzone Hydrodynamics, Proc. Twenty-Second Coastal eng. Conf., ASCE, pp 68-81.
O'Shea, K., Nicholson, J. and O'Connor, B.A. (1991). The Transition Zone Length in Cross-Shore Sediment Transport Modelling, Report CE/1/91. Department of Civil Eng., University of Liverpool.
Ohnaka, S. and Watanabe, A. (1990), 'Modeling of Wave-Current Interaction and Beach Change', Proc. Twenty-Second Coastal Engineering Conf., ASCE, pp. 2443-2456.
Péchon, P. (1987), 'Modelling of longshore currents with a non-linear wave theory'. ASCE Speciality Conference on Coastal Hydrodynamics, Delaware, 1987.
Péchon, P., (1992), Numerical modelling of wave-driven currents and sediment transport in the surfzone. Internal report EDF-LNH HF.42/92.15.
Rienecker, M.M. and J.D. Fenton (1981). A Fourier approximation method for steady water waves. J. Fluid Mech., Vol. 104, pp. 119-137.
Roelvink, J.A. and Stive M.J.F. (1989). Bar-generating Cross-shore Flow Mechanisms on a Beach, JGR Vol. 94, No. C4, pp. 4785-4800.
Sakai, S., K. Hirayama and H. Saeki (1988). A new parameter for wave breaking with opposing current on sloping bed. Proc. Int. Conf. on Coastal Eng., ASCE, 1035-1044.
Southgate, H.N. and Nairn, R. B. (1993). "Deterministic profile modelling of nearshore processes. Part 1. Waves and Currents", Coastal Engineering (to appear).
Southgate, H.N. (1991) Beach Profile Modelling: Flume Data Comparisons and Sensitivity Tests, coastal Sediments '91, Seattle, USA.
Stive, M.J.F. and Battjes, J.A. (1984). 'A Model for Offshore Sediment Transport'. Proc. 19th Int. Conf. Coastal Eng., pp. 1420-1436, ASCE, New York.
Stive, M.J.F. (1986). A Model for Cross-shore Sediment Transport, Proc. 20th ICCE, ASCE, Taiwan.
Svendsen, L.A. (1984). Mass Flux and Undertow in a Surf Zone. Coastal Engineering, Vol.8, No.4.
Watanabe, A., Hara, T. And Horikawa, K. (1984). Study on Breaking Condition for Compound Wave Trains, Coastal Entineering in Japan, vol. 27, pp. 71-82.
Watanabe, A. and Dibajnia, M. (1988). A Numerical Model of Wave Deformation in Surf zone, Proc. Twenty-First Coastal Engineering Conf., ASCE, pp. 578-587.
Weggel, J.R. (1972) 'Maximum breaker height for design', Proc. Int. Conf. on Coastal Eng., ASCE, 419-432.

Applications of Mathematical Models for Coastal Sediment Transport and Coastline Development

Ann Skou and I.B. Hedegaard

Danish Hydraulic Institute
Agern Allé 5
2970 Hørsholm
Denmark

Jørgen Fredsøe and Rolf Deigaard

Institute of Hydrodynamics and Hydraulic Engineering
Technical University of Denmark

Presented at COPEDEC III, 1991 Mombassa

APPLICATIONS OF MATHEMATICAL MODELS FOR COASTAL SEDIMENT TRANSPORT AND COASTLINE DEVELOPMENT

by

Ann Skou[1]
I.B.Hedegaard[1]
Jørgen Fredsøe[2]
Rolf Deigaard[2]

ABSTRACT

The structure of the numerical modelling system LITPACK is described by an example, wherein the process of calculating a given coastline evolution is followed step by step. The theoretical background the calculations is given with a more detailed description of each of the models.

The applications of the model are shown by a presentation of two actual cases, for which the LITPACK models have been used to simulate historical and present transport conditions.

INTRODUCTION

During the last 20 years, the theoretical background for a complex of deterministic models of the processes in the coastal zone has been developed at Danish Hydraulic Institute and at the Technical University of Denmark, Institute of Hydrodynamics and Hydraulic Engineering.

The central element in the model complex is a detailed intra wave period model for description of sediment transport as function of the local conditions, i.e. combined breaking or non-breaking waves, current and bed material.

Further, models for wave-driven currents along the coast and undertow along the coastal profile have been developed. The current and sediment transport models have been combined to form a tool for calcula-

[1] Danish Hydraulic Institute (DHI), Agern Alle 5, DK-2970 Hørsholm, Denmark

[2] Inst. of Hydrodynamics and Hydraulic Engineering (ISVA), Technical University of Denmark, Building 115, DK-2800 Lyngby, Denmark

tion of littoral drift, cross-shore transport and the corresponding coastline and coastal profile evolutions.

The establishment of the numerical model complex has been carried out by DHI in collaboration with ISVA.

THE PHILOSOPHY BEHIND THE STRUCTURE OF THE MODEL COMPLEX.

The entire model complex, named **LITPACK**, consists of a number of individual models each describing one or more of the processes in the nearshore zone along a sandy beach.

Consider the calculation of the littoral drift along a sandy beach for given off-shore wave conditions. In this case the following calculations are carried out:

1: Calculation of wave conditions across the surf zone (in the model LITCURR).

2: Calculation of longshore current (in LITCURR).

3: Calculation of the longshore sediment transport across the profile (in the model STP).

4: Calculation of total longshore sediment transport (in the model LITLONG).

The structure of this part of the model complex is illustrated in Fig. 1.

Each of the models (STP,LITCURR,LITLONG) is structured such that interconnected series of modules describes the physical mechanisms involved.

An advantage of such a structure, is that results from ongoing research may be implemented in the individual modules without effecting other modules.

Consider the calculation of the coastline development along the same sandy beach :

1: Calculation of the littoral drift for all wave incidents (in the model LITLONG).

2: Calculation of annual drift along the shore (in the model LITTOT).

3: Calculation of the sediment transport relations for different coastline orientations (in the model LITLINE).

4: Calculation of sheltering effects due to structures (in LITLINE).

5: Calculation of coastline evolution (in LITLINE).

The structure of this part of the model complex is illustrated in Fig. 2.

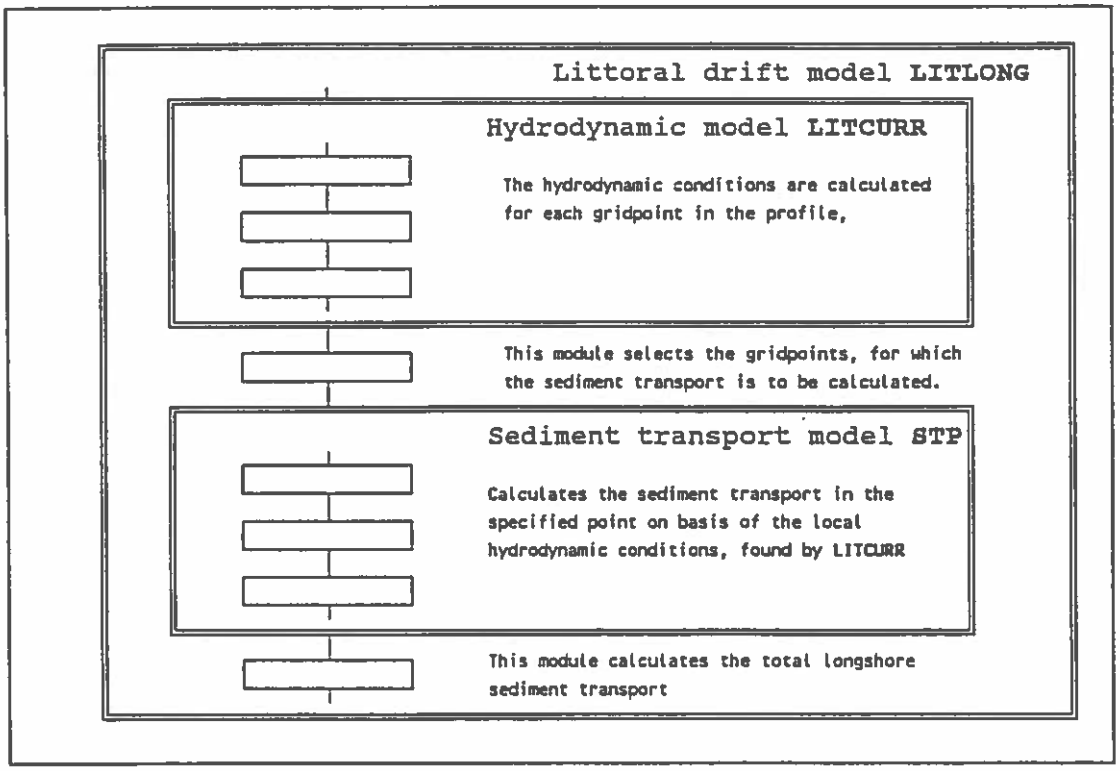

Fig. 1 Structure of the littoral drift model LITLONG.

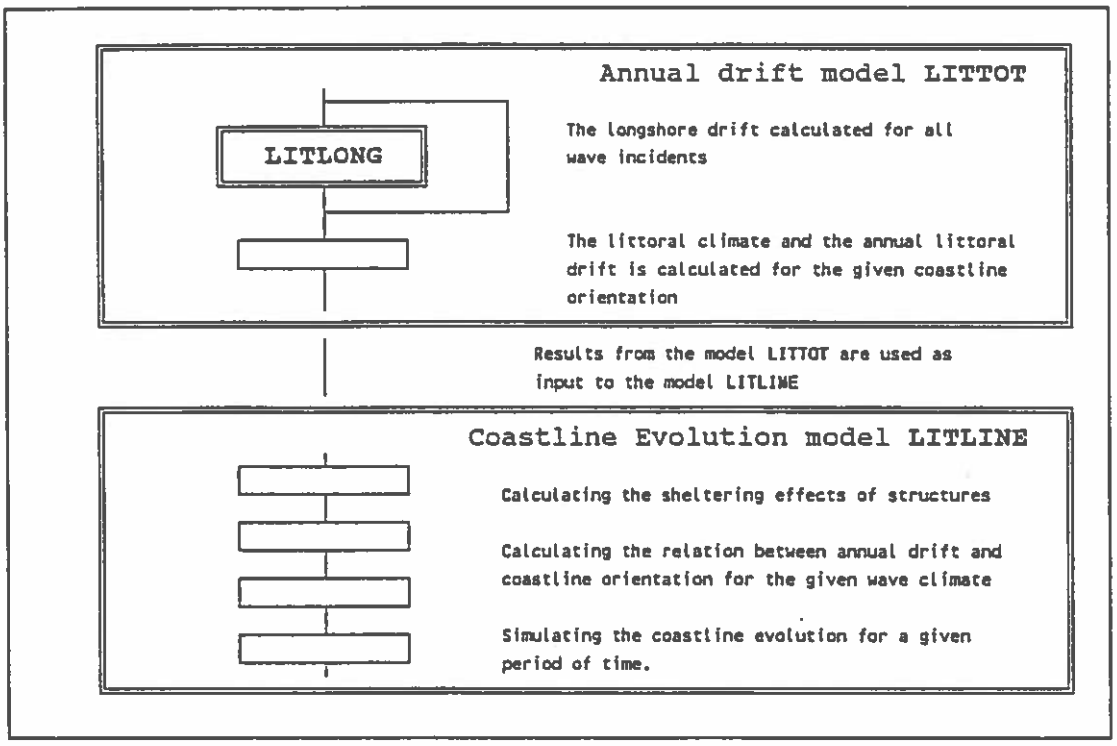

Fig. 2 Structure of the annual drift model LITTOT and coastline evolution model LITLINE.

THEORETICAL BACKGROUND

The sediment transport model

The transport of non-cohesive material is calculated according to the model presented by Engelund and Fredsøe (1976). Through subsequent developments this model has been extended to cover combined waves and current, and conditions in the surf zone.

Inside the surf zone, the wave energy is dissipated due to breaking, and the production of turbulence is very intense. This has been taken into account by applying a one-equation turbulence model, Deigaard et al. (1986).

The basis for the sediment transport description is the model for turbulent wave-current boundary layers of Fredsøe (1984). The boundary layer is composed of two regions:

- Close to the bed, the turbulence and the shear stress in the wave boundary layer vary with the wave period, giving rapidly changing bed concentration and turbulent diffusion coefficients.

- Outside the wave boundary layer the mean velocity is described by a log-profile. The increased turbulence level in the wave boundary layer retards the mean current, an effect which is expressed through an apparent wave roughness, k_w, which is larger than the natural bed roughness k.

The total sediment load can be divided into bed load and suspended load. The bed load transport is calculated as a function of the bed shear stress through the dimensionless bed shear stress, θ

$$\theta = U_f^2/(s-1)gd \qquad (1)$$

where s is the relative sediment density, g the acceleration due to gravity, d the grain size and U_f is the shear velocity. The bed load transport is assumed to correspond to the instantaneous bed shear stress under unsteady conditions, e.g. under wave action.

The suspended load transport, q_s, is described through the sediment concentration c, which is determined from the vertical turbulent diffusion equation:

$$\frac{\partial c}{\partial t} = \frac{\partial}{\partial z}\left(\epsilon_s \frac{\partial c}{\partial z}\right) + w\frac{\partial c}{\partial z} \qquad (2)$$

where t is time, z the vertical coordinate (zero at the bed) ϵ_s the turbulent diffusion coefficient and w is the settling velocity of the sediment. ϵ_s is taken to be equal to the turbulent eddy viscosity of the flow field. The near-bed boundary condition for (2) is given as bed concentration C_b at the level z = 2d. C_b is determined as a function of θ using the dynamic considerations of Bagnold (1954), that a certain sediment concentration is required near the bed in order to transfer the shear stress to the bed through grain-grain interaction.

The bed concentration, C_b, is only valid for the plane bed case, i.e. sheet flow, which is found for θ larger than about 0.8. At smaller θ-values the bed is covered by wave ripples. The sediment transport model by Fredsøe et. al. (1985) has been modified to take the effect of wave ripples into account. The modification involves the bed concentration, turbulent diffusion and the bed roughness. The values of C_b and ϵ are based directly on the laboratory measurements of Nielsen (1979). The roughness is expressed through the ripple dimensions as given by Raudkivi (1988). The sediment transport model converges gradually towards a plane bed description with increasing bed shear stress or mean current velocity.

Fig. 3 shows the vertical mean sediment concentration profile calculated by the sediment transport model, compared to full scale field measurements.

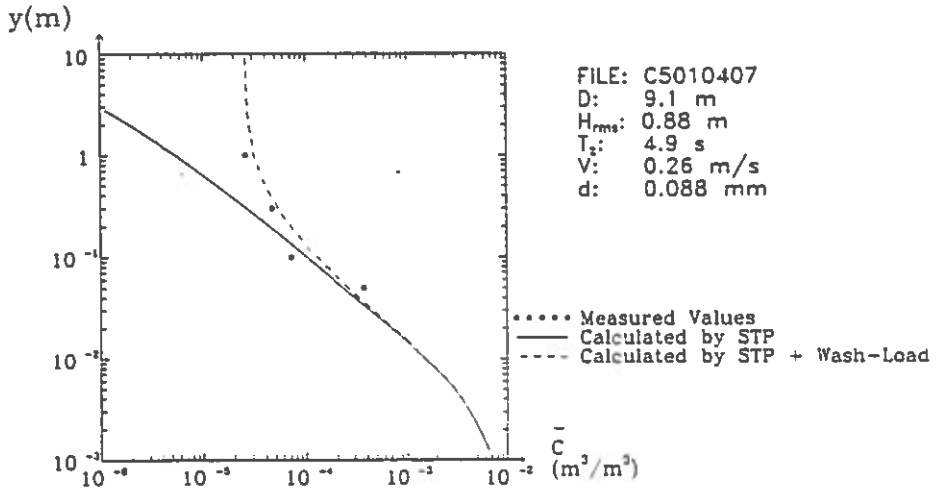

Fig. 3 Vertical Profiles of Mean Sediment Concentrations

The longshore current model

It is assumed in the model that conditions are uniform along a straight coast.

The hydrodynamic model includes a description of propagation, shoaling and breaking of waves, calculation of the driving forces due to radiation stress gradients, momentum balance for the cross-shore and longshore direction giving the wave set-up and the longshore current velocities. The model can be applied on complex coastal profiles with longshore bars. In the case of a longshore bar the broken waves can reform at the trough onshore of the bar. The waves treated can be regular or irregular, and the effect of directional spreading can be included.

The equation for shore-parallel momentum balance determines the longshore current velocity profile:

$$\tau_b - \frac{d}{dy}(\rho E D \frac{du}{dy}) = - \frac{ds_{xy}}{dy} + \tau_w + \tau_{cur}. \qquad (3)$$

τ_b is the bed shear stress due to the longshore current, ρ is the density of water, E is the momentum exchange coefficient, D is the water depth, u the longshore current velocity, y the shore-normal coordinate, s_{xy} is the shear component of the radiation stress and τ_w and τ_{cur} are the driving forces due to wind and coastal current. The relation between u and τ_b is established by the model of Fredsøe (1984).

The longshore drift model

The littoral drift model uses as input the wave and current conditions calculated by LITCURR. The sediment transport model is applied as a submodule to calculate the sediment transport at selected points.

The total longshore sediment transport across the profile is dominated by contributions from areas where wave breaking occurs. The point selection procedure therefore gives preference to points in this area. In the case of a bar-profile, the sediment calculation points will thus be located on the bars, where the waves break.

Fig. 4 shows littoral current and littoral drift across a profile with bars.

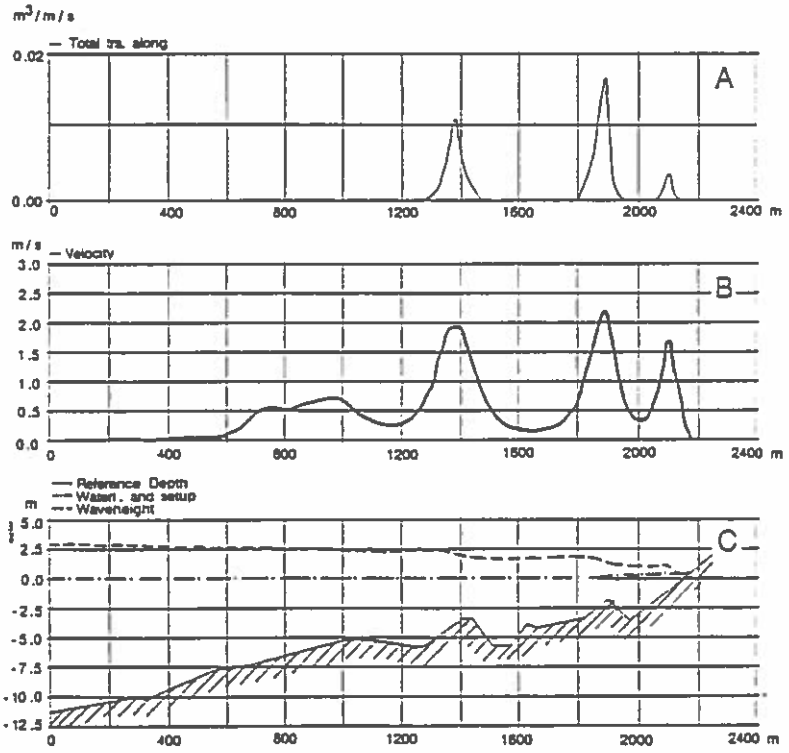

Irregular waves:

H_s = 4.1 m, T = 8.6 s, incoming wave angle $\alpha = 58^o$
bed material: $d_{50\%}$ = 0.25 mm.

A : Solid transport along profile.
B : Wave driven currents along profile.
C : Coastal profile, water level and wave heights along profile.

Fig. 4. Calculated Sediment Transport, Velocities, Wave Heights and Water Levels along a Profile.

The coastline evolution model

The annual littoral drift model LITTOT outputs the means for calculating the correlation between coastline orientation and net sediment drift.

The coastline evolution model uses this to model the coastline development taking the sheltering and blocking effects of structures into consideration.
The model solves the continuity equation for the coastline:

$$\frac{\partial Y}{\partial t} = \frac{-1}{h(1-n)} \frac{\partial Q_s}{\partial X} \qquad (4)$$

where Y is the distance from a baseline to the coastline, h is the height of the coastal profile affected by the changes, n is the porosity of the sediment. Q_s is the net littoral drift, and X is a longshore coordinate.

The change in the transport conditions caused by a coastal structure is modelled by introducing internal boundary conditions. If the structure blocks the littoral drift, the condition is $Q_s = 0$ at the site of the structure. If the accretion on the updrift side of the structure after some years reaches the seaward limit of the structure, the bypassing of sand will begin gradually. Large structures change the transport relations close to the structure due to the sheltering effect from the structure itself. This effect is included by introducing modified transport correlations close to the structure.

Fig. 5 shows the result of an application of the coastline development simulation close to a breakwater.

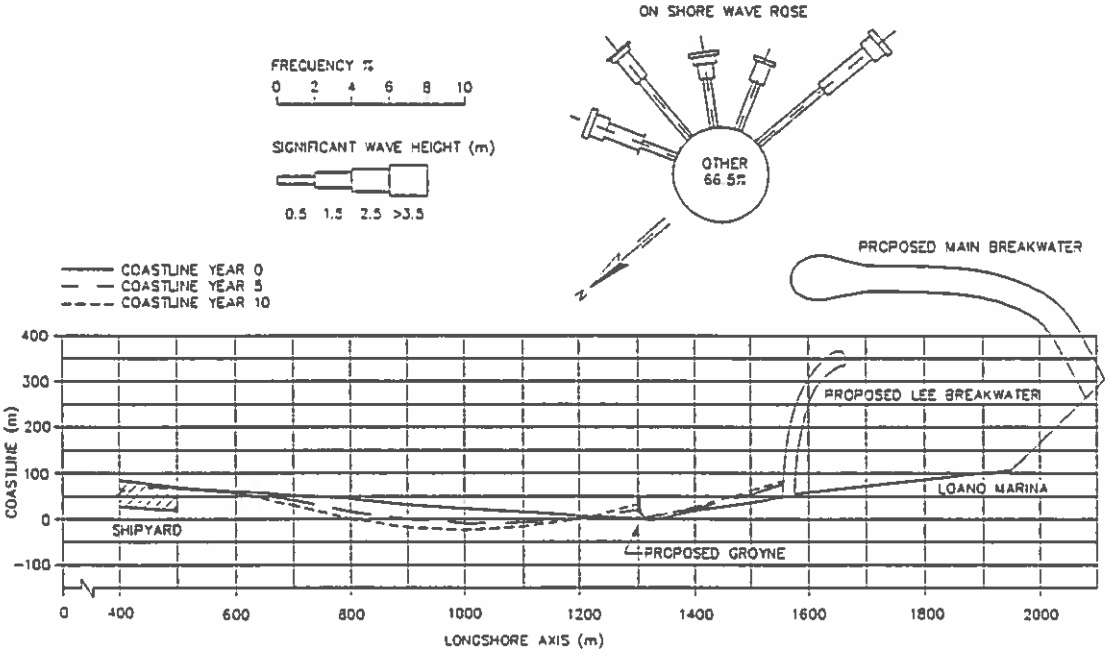

Fig. 5 Coastline Development Close to a Harbour.
Site: Loano, Italy, 1990.

APPLICATIONS

The model complex has been applied in several projects carried out by DHI in the recent years. In the following, two case studies are described, illustrating the aim of the investigation, data processing techniques and results.

Loano Harbour

This investigation concerned the hydraulic conditions and coastline development resulting from an extension of the Loano Harbour in Italy.

The site inspections indicated that the net sediment transport was to the north. This was also found by the numerical simulations.

Having analyzed the wave climate, the existing longshore sediment transport field was calculated using the littoral drift model. By calculating the annual drift for various sections along the coast using the annual drift model, the existing overall sediment budget was found, indicating erosion and accretion areas. These were found to agree well with observed transport patterns. Fig. 6 shows the existing sediment budget, together with the proposed extension of the harbour.

The construction of the new marina and underwater breakwaters will alter the transport field along the coast. The sediment budget along the coast was found for the new conditions. Fig. 7 shows the sediment budget after construction of the new marina and underwater breakwaters.

These sediment budgets were used to simulate the coastline evolution, taking into account the new structures. By use of the coastline evolution model, the changes to erosion and accretion rates were found, giving valuable information about necessary beach nourishment at specific positions in order to prevent erosion of the coastline.

Fig. 5 shows the expected change of the coastline over 10 years.

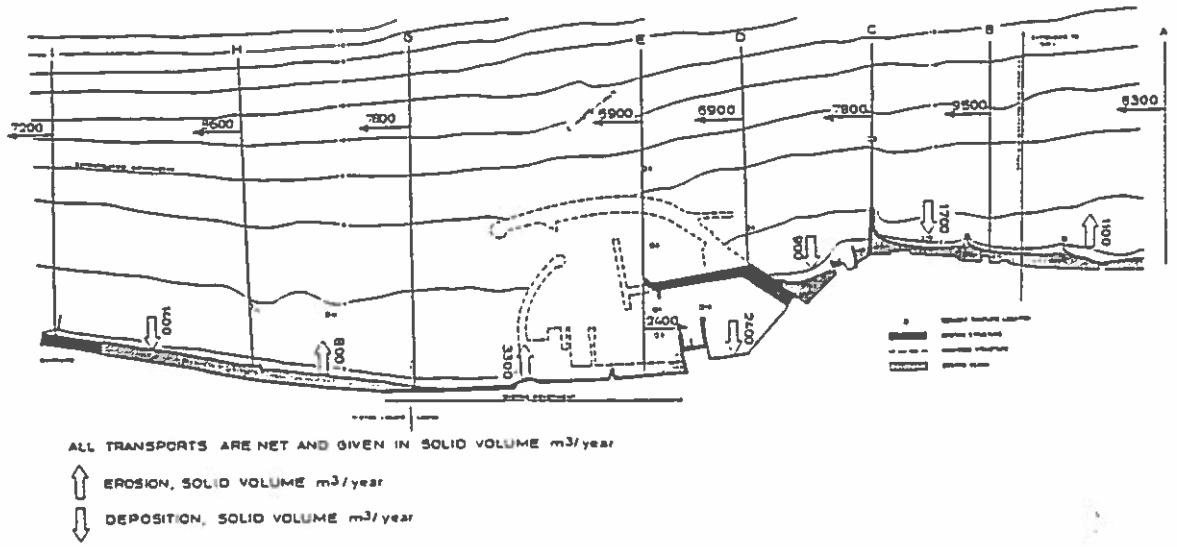

Fig. 6 Existing sediment budget.

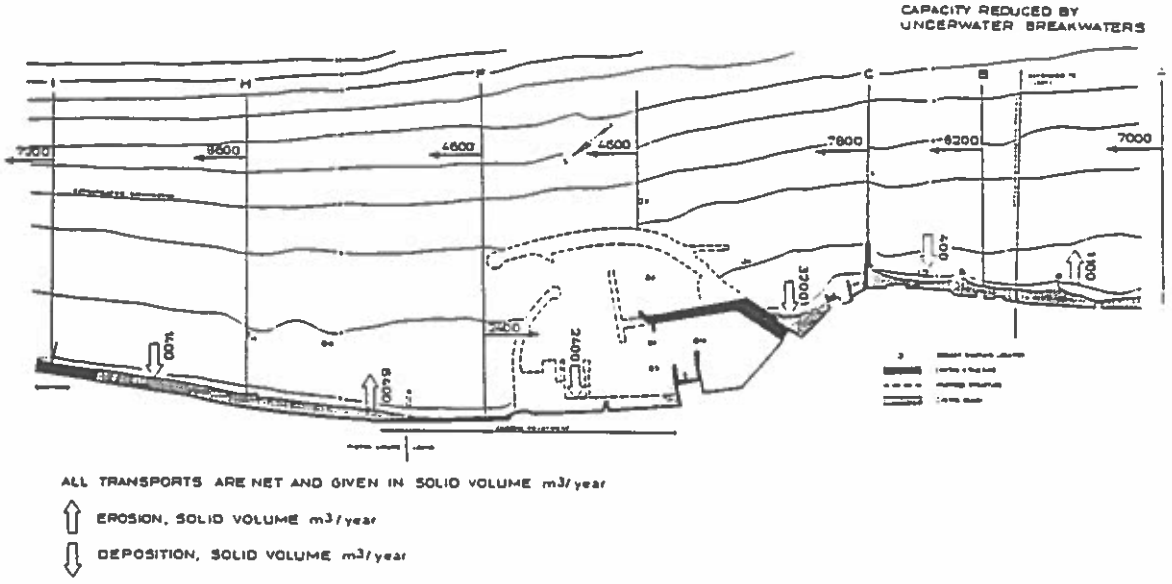

Fig. 7 Sediment budget after construction of the new Marina and underwater breakwaters.

Cavallino

As part of a larger study, the historical development of Cavallino beach, Italy, was investigated.

The beach is located updrift a large jetty at the northern inlet of the Venice Lagoon.

The conditions for the development of the coastline have changed significantly during the period from the construction of the jetty to the present day. Furthermore in the later period 1950-1990 the transport rate has decreased partly due to changes in coastline orientation and partly due to the establishment of short groynes.

The development of the coastline was simulated by the coastline evolution model with the purpose of verifying the order of magnitude of the estimated littoral drift along Cavallino beach.

Based on the analysed wave climate, the littoral drift model was used to simulate the transport field for all wave incidents.

The coastline evolution model then calculated the net average transport rate as a function of beach orientation. This relation is used in LITLINE, simulating the coastline development over a given period. Fig. 8 shows the result of 30 years of simulation together with the actual measured coastline accretion. A relatively good agreement is found between simulated and observed coastline development. From these results, the annual drift north of the Lido Inlet was estimated to be 290,000 m^3/year.

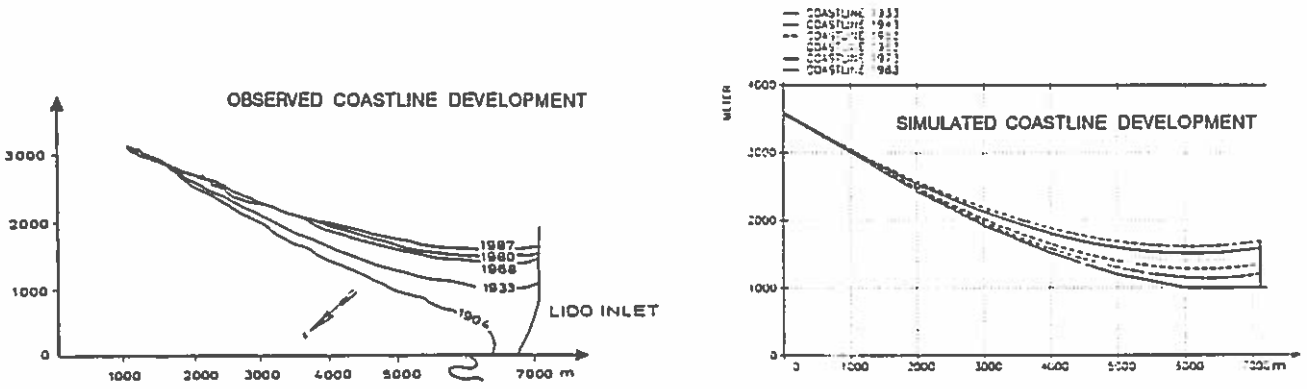

Fig. 8

A : Simulated coastline development.

B : Observed coastline development.

List of References

Bagnold, R.A., "Experiments on a gravity-free dispersion of large solid spheres in a Newtonian fluid under shear", Proceedings of the Royal Society, London (A), 49, 1954.

Deigaard, R., Fredsøe, J. and Hedegaard, I.B. (1986) "Suspended sediment in the surf zone". J. of Waterway, Port, Coastal and Ocean Engineering, ASCE, Vol. 112, No. 1.

Engelund, F. and Fredsøe, J. (1976) "A sediment transport model for straight alluvial channels", Nordic Hydrology, 7.

Fredsøe, J. (1984) "The turbulent boundary layer in combined wave-current motion". J. of Hydraulic Engineering, ASCE, Vol. 110, No. HY8.

Fredsøe, J., Andersen, O.H. and Silberg, S. (1985) "Distribution of suspended sediment in large waves". J. of Waterway, Port, Coastal and Ocean Engineering, ASCE, vol. 111, No. 6.

Nielsen, P. (1979) "Some basic concepts of wave sediment transport". Int. Hydrodynamics and Hydraulic Engineering. Tech. Univ. of Denmark. Ser. Paper 20.

Raudkivi, Arved J. (1988) "The roughness heights under water". J. Hydraulic Research, Vol. 26, No. 5.

ACKNOWLEDGEMENT

This work was undertaken as part of the MAST G6 Coastal Morpho-dynamics research programme. It was funded jointly by the Danish Technical Research Council (STVF) and by the Commission of the European Communities, Directorate General for Science, Research and Development, under MAST contract no. 0035-C.

Sediment Transport behind an Offshore Breakwater Using Different Wave Model

H.K. Johnson, I. Brøker and P.A. Madsen

Danish Hydraulic Institute
Agern Allé 5
2970 Hørsholm
Denmark

Sediment Transport behind an Offshore Breakwater Using Different Wave Models

by
H.K. Johnson, I. Brøker and P.A. Madsen[1]

Abstract
With the intention of finding the optimal wave model to use for morphological investigations in areas dominated by diffraction, three wave models, an elliptic mild slope model (Madsen and Larsen, 1987), a parabolic mild slope model and a spectral wind-wave model are applied in the computation of waves, wave-induced currents and sediment transport behind a single detached breakwater. The results are presented and the differences between the model results are discussed.

Introduction

In order to model the morphological evolution behind an offshore breakwater subjected to wave action, it is necessary to have a good description of the wave field. Various wave models are available for this purpose depending on complexity (generally increasing with accuracy) and cost. In a morphological model requiring many repetitive calculations of the wave field, there is a need to find an optimal balance between accuracy and cost. This paper presents an investigation into the use of three different wave models for the calculation of sediment transport and hence morphological response behind an offshore breakwater. The wave models are 1) the elliptic mild slope model, MIKE 21 EMS; 2) Parabolic mild slope model, MIKE 21 PMS and 3) Spectral nearshore wind wave model, MIKE 21 NSW.

Wave Models

MIKE 21 EMS is a linear refraction-diffraction wave model including back scattering and wave breaking. The model includes a general formulation of radiation stresses which applies in crossing wave trains and in areas of strong diffraction. Of the three models, this is the most accurate for monochromatic linear waves, and it is chosen as our reference model. However, it is the most expensive.

MIKE 21 PMS is based on a simplification of the mild slope equations assuming wave propagation in one predominant direction (x-dir), neglecting diffraction in this direction and back scattering in the opposite direction. Using the approach of Kirby(1986), this model is made to allow large-angle (up to 60 deg.) propagation to the x-dir. Furthermore, MIKE 21 PMS includes the effect of a frequency spectrum and directional spreading. The model is extremely cost-efficient and requires a very low computational effort, being approximately 50 times faster than the elliptic mild slope model for the same setup.

MIKE 21 NSW is a stationary directionally decoupled parametric model based on the wave action conservation equations as formulated by Holthuijsen et. al.(1989). It describes the propagation, growth and decay of short period waves in nearshore areas. The model takes into account the effects of refraction and shoaling due to varying depth, wind generation, energy dissipation due to bottom friction and wave breaking plus the effect of current on these phenomena. Although this model does not include diffraction (an important phenomenon behind the breakwater), it is nevertheless included in the analysis to illustrate the relative importance of this limitation.

In the wave models, wave breaking is formulated using the theory of Battjes and Jansen(1978).

Model Setup

A hypothetical offshore breakwater was used. The breakwater is 300m long, located at a distance of 280m from the shoreline. The nearshore contours are straight and parallel with a slope of 1:50. The offshore wave height is 2m with a period of 8 secs. on the 10m contour. The wave crests are parallel

[1] Danish Hydraulic Institute, Agern Allé 5, DK 2970, Hørsholm, Denmark.

to the coastline.

A grid spacing of 5m was used in the EMS and PMS models. Furthermore, the front face of the breakwater is assumed to have zero reflection in the EMS model. This is achieved by placing a 5-line sponge layer inside the breakwater. The incident wave field is assumed to be monochromatic and unidirectional in the EMS and PMS models. For the NSW model, the grid spacing was chosen as DX=2m, DY=10m and a $\cos^2$ directional spreading function was used. The bed roughness in the wave models was chosen as 1.5mm.

The radiation stresses from the wave models are interpolated to a square grid with DX=10m used for the hydrodynamic simulations. The hydrodynamic time step is 6 secs. and a bed roughness corresponding to a Manning number of 32 is used.

Results

Figure 1 shows the contours of wave heights, wave-induced currents and sediment transport vectors from the three models. Figure 2 shows comparisons of the wave heights and the x- and y- sediment transport components along the 4m contour (line A) and 2m contour (line B). The x-direction is normal to the shoreline.

Although, the NSW model does not include diffraction, some wave energy can be observed behind the breakwater due to the use of a broad-banded ($\cos^2$) directional spectrum. However, the computed NSW wave heights in the diffraction zone are smaller than corresponding EMS waves by up to a factor of 2, while the PMS wave heights are generally closer to the EMS waves.

With all the three models, two eddies were established between the breakwater and the shoreline. The maximum current speed in the EMS model is slightly greater than 1m/s, which is nearly the same as obtained with the PMS model. However, the current speeds are generally lower for the NSW model, the maximum in this case being about 0.8m/s. The difference in wave induced currents between NSW and the others is partly due to directional spreading in NSW. The directional spreading results in a smoothing of the radiation stress field, and hence a reduction in the radiation stress gradients.

The combined wave and current fields are used for calculating the sediment transport field using DHI's STP model. As can be expected from a comparison of the waves and current fields, the sediment transport rates computed using the NSW model is about a factor of 3 smaller than calculated using the EMS model. In contrast, the PMS model results are generally much closer to the EMS values, except that the alternating high and low transport rates computed close to the shoreline behind the breakwater are not reproduced in the PMS results. This is because of the crossing wave trains behind the breakwater, resulting in alternating bands of high and low wave heights (constructive/destructive interference) which is modelled in the EMS model, but only partially modelled in the PMS model.

Conclusion

It can be concluded that the PMS model is an optimal choice for computing the sediment transport field and hence the morphology response behind the given offshore breakwater, since it gives comparable results to the EMS model at a much lower cost.

The NSW model is found to be unsuitable as a basis for computing sediment transport rates for the given offshore breakwater setup, i.e. a setup in which diffraction is an important phenomenon.

References

Holthuijsen, L.H., N. Booij and T.H.C. Herbers(1989): "A prediction model for stationary, short-crested waves in shallow water with ambient current", Coastal Engrg. Vol. 13, pp. 23-54.

Kirby, J.T.(1986): "Rational approximations in the parabolic equation method for water waves", Coastal Engrg. Vol. 10, pp. 355-378.

Madsen, P.A. and J. Larsen(1987): "An efficient finite difference approach to the mild-slope equation", Coastal Engrg. Vol. 11, pp. 329-351.

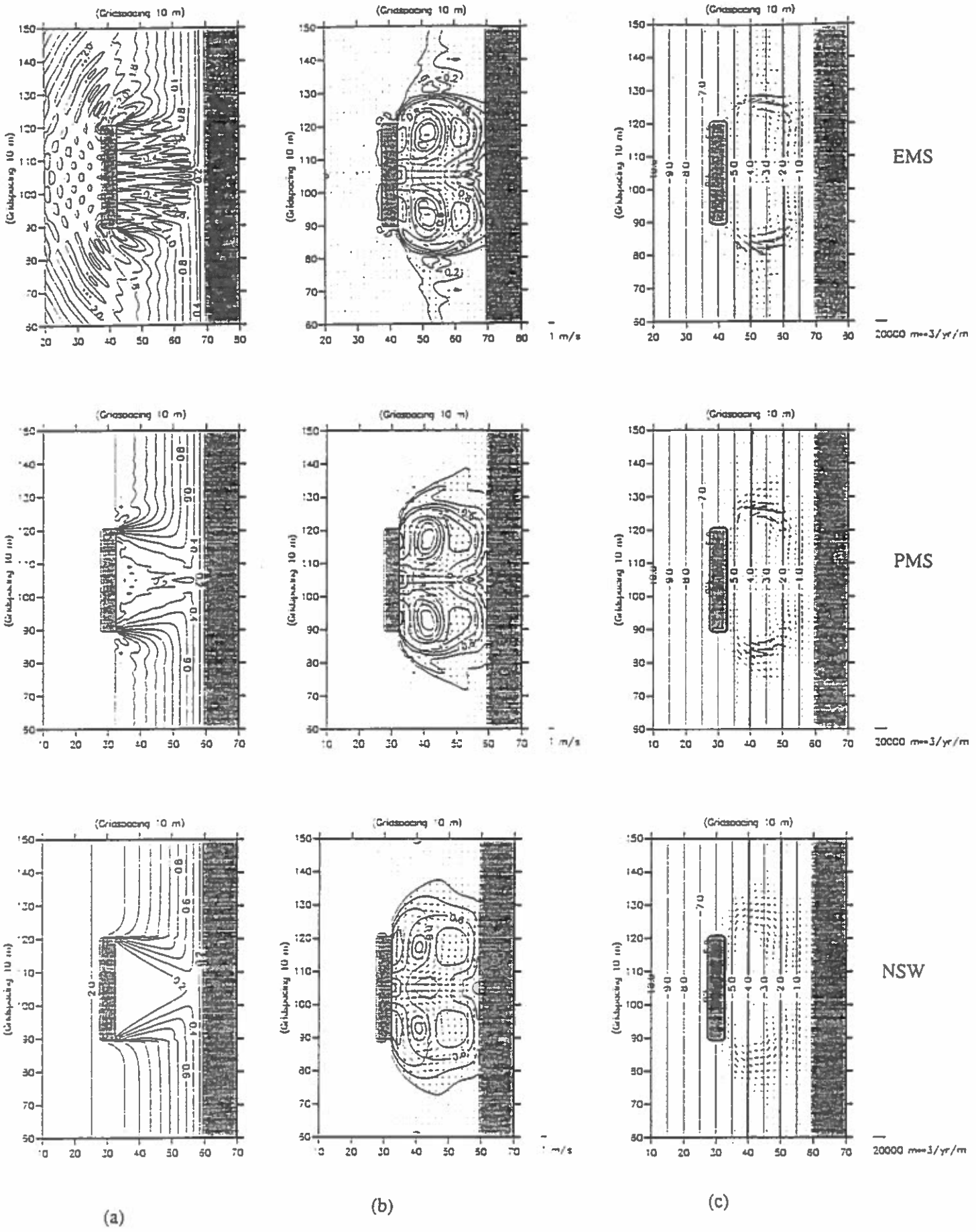

Fig. 1 Contours of wave heights (a), current speeds (b) and sediment transport field (c)

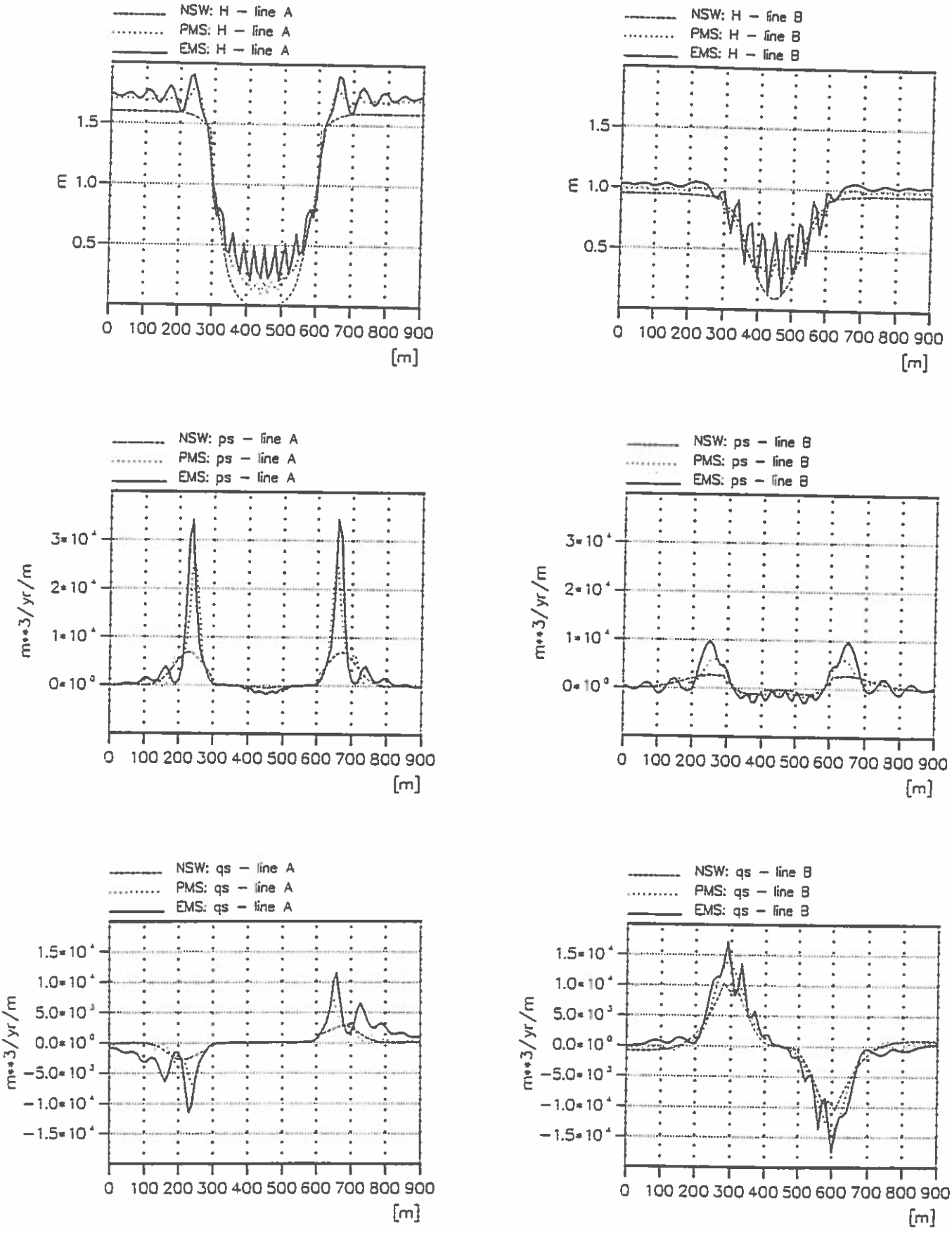

Fig. 2 Comparison of wave heights, x- and y- sediment transport components on 4m contour(line A) and 2m contour(line B).

A New Approach to 2DH Morphological Modelling

H.K. Johnson, I. Brøker, J.A. Zyserman and P.Justesen

Danish Hydraulic Institute
Agern Allé 5
2970 Hørsholm
Denmark

A New Approach to 2DH Morphological Modelling

by
H.K. Johnson, I. Brøker, J.A. Zyserman and P. Justesen[1]

Abstract
This paper presents a coastal morphology modelling system, M21MORF based on the MIKE 21 system of models. M21MORF is based on a new approach using an explicit forward time integration scheme for the morphological evolution involving the following stages: a) Initialisation, b) Sediment transport computation using DHI's STP model, c) wave computation using an arbitrary wave model, d) Hydrodynamic computation assuming a mobile bed evolving at dz/dt, with optional use of a module to determine the apparent roughness in combined wave-current motion and e) Bed level update scheme using an improved second order Lax Wendroff scheme.

An example application to the case of a detached breakwater is also presented.

Introduction

The morphological evolution of coastal areas subjected to waves and currents due to the impact of engineering works is an important factor in the design and implementation of such works. At the present state-of-the-art, so-called 1-line models are generally used for predicting the long term morphological evolution of the coast. Although this approach yields useful results, it oversimplifies the processes occurring in the coastal zone (in some cases), and hence, some significant details of the morphological response can not be observed. In order to predict the 2D morphological response, a 2D modelling system incorporating waves, currents and sediment transport models is required. This type of model was developed at DHI in the eighties, see Andersen et.at.(1988). A new approach to this method of modelling morphological evolution is described in this paper.

Modelling Scheme

A block flow chart showing the morphological modelling scheme is shown in Figure 1. This figure is explained as follows: Given the initial bathymetry and time series of boundary wave and current conditions, the initial wave and current fields are first computed, before entering the morphological loop. Then, the loop is entered and the sediment transport, rates of bed level changes, dz/dt and the allowable maximum morphological time step, DTsedi (based on the stability condition for the bed update scheme) are computed. Next the wave field is updated if necessary (since this is done every k-th update of the sediment transport field, where k is an integer $\geq$ 1). Next the bed resistance map is updated taking into account the apparent roughness in combined wave-current motion using a boundary layer model and lastly using the hot output from the previous HD simulation, the hydrodynamic calculation is continued from present time, T, to T+DTsedi where the sediment transport field is updated. Using the given dz/dt, the bed level is gradually updated during the hydrodynamic computation. The whole process is then repeated in a cyclical loop until the prescribed length of simulation is completed.

Description of Component Models

The wave models presently built into the system are: a) the parabolic mild slope model and b) a spectral nearshore wave model. Both models include refraction, shoaling, directional spreading, wave breaking and bottom dissipation. In addition, the parabolic mild slope model includes wave diffraction and frequency spectrum.

A wave-current roughness module based on Fredsøe's boundary layer theory is included for the

[1] Danish Hydraulic Institute, Agern Allé 5, DK 2970, Hørsholm, Denmark.

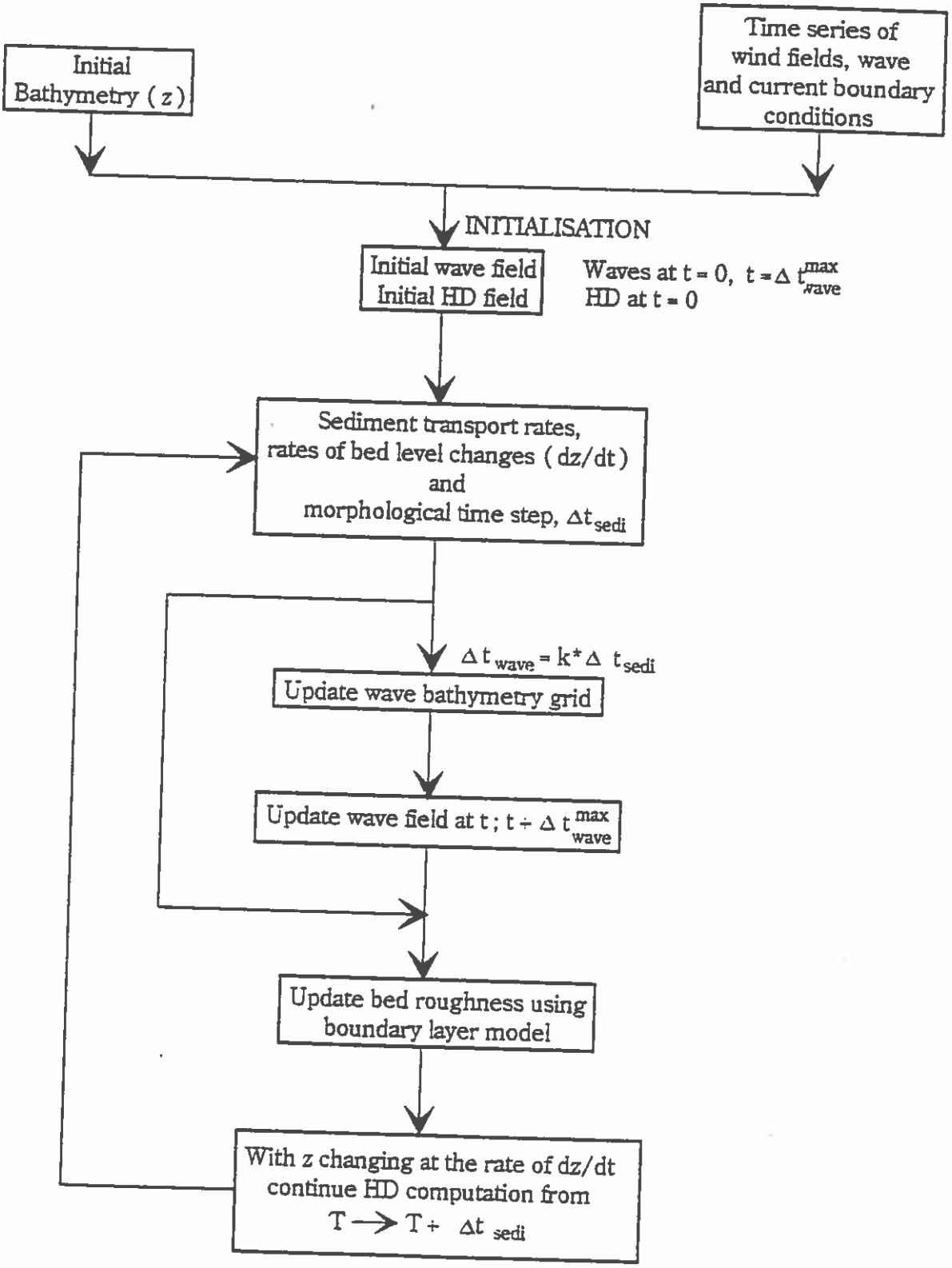

Fig. 1: Block flow chart for morphological model.

computation of the enhanced roughness for the current due to the interaction of waves and current in the bottom boundary layer.

The hydrodynamic model is based on MIKE 21 HD and extended to include the effect of bed level changes (dz/dt) in the equation for conservation of mass. For a mobile bed, it was found that this term is of the same order of magnitude as other terms in the conservation of mass equation, and thus it is not negligible when simulating currents for morphological investigations.

The sediment transport rates are calculated using DHI's STP model and a recently improved explicit second order Lax-Wendroff scheme is used for the bed level update calculations. A Courant criterion for propagating bed disturbances is used to determine the maximum allowable morphological time step for the stability of the scheme.

Furthermore, the following time steps are used in the model: a) the hydrodynamic time step - this is the time step used in the computation of the hydrodynamic field; b) the maximum morphological time step, (DTsed)max - this is a user-specified absolute maximum time step before updating the sediment transport field. The actual time step before updating the sediment transport field is the smaller of this time step and the time step obtained from Courant criterion for the bed level update scheme; c) the maximum wave time step, (DTwave)max - this is a user-specified absolute maximum time step before updating the wave field. The actual time step used is every k-th update of the sediment transport field, where k equals (DTwave)max/(DTsed)max.

Example Application

In order to test the modelling system, a hypothetical offshore breakwater was used. The breakwater is 300m long, located at a distance of 280m from the shoreline. The nearshore contours are straight and parallel with a slope of 1:50, and the beach grain size is 0.25mm. A monochromatic wave train with wave crests parallel to the breakwater is allowed to attack the coast continuously for a period of 72 hours. The wave height is 2m, with period 8 seconds at a depth of 10m.

The maximum morphological time step is specified as 1 hour, while the maximum wave time step is 3 hours. Thus, the wave climate is updated after every third {k=(Dtwave)max/(DTsed)max} update of the sediment transport field. The hydrodynamic time step was chosen as 6 secs. Furthermore, the parabolic mild slope model is used, and a bed resistance corresponding to a Manning number of 32 is specified for the HD model.

The vectors of sediment transport rates and contours of bed level at 24 hrs and 72 hrs are shown in Figures 2a and 2b respectively. Important features to note in these figures are the significant erosion at the leeward edges of the breakwater accompanied with significant deposition closer to the shoreline in the diffraction zone. This deposition area forms a double-peaked salient. It can be seen from Figures 2a and 2b that the peaks gradually become closer as the simulation progress, possibly forming a single peak after a sufficiently long time. This type of morphological response has also been observed in laboratory experiments by Suh and Dalrymple(1987). A small amount of deposition can also be observed immediately behind the breakwater.

The observed morphological response is explained by the two eddies which form behind the breakwater, in combination with the wave field characterized by low waves in the diffraction zone and higher waves in the exposed zone. The eddies move in opposite directions and join to form a pointed jet towards the breakwater at the centre line. This gives a sediment transport field generally in the same direction as the eddies, however with relatively small sediment transport close to the centreline of the breakwater. As the salient form, the local current speed increases over the salient, leading to increased sediment transport towards the centreline of the breakwater. Further tests are planned to investigate the case of waves approaching at an angle, combination of waves from different directions and the influence of irregular waves. The influence of bed resistance used in the hydrodynamic

simulation and the choice of wave model are discussed in companion papers in this volume, see Johnson et.al.(1993)a,b.

Conclusions

A morphological model based on a new approach for calculating the impact of engineering works on coastal areas subjected to waves and currents has been set up. Although only the case of an offshore breakwater has been tested, the results obtained are realistic and commends this approach to further investigations.

References

Andersen, O.H., I.B. Hedegaard, R. Deigaard, P. Girolamo and P. Madsen (1988): "Model for Morphological Changes Under Waves and Current", Proc. IAHR Symp. on Math. Modelling of Sediment Transport in the Coastal Zone, Copenhagen.

Fredsøe, J.(1983): The turbulent boundary layer in combined wave-current motion", Danish Centre for Applied Mathematics and Mechanics, Rep. No. 259, 1983.

Johnson, H.K., I. Brøker and J.A. Zyserman(1993a): "Influence of Bed Resistance on Morphological Response behind Breakwaters", Extended abstract, Proc. Workshop of the MAST G8-M Project, Grenoble, September 1993.

Johnson, H.K., I. Brøker and P.A. Madsen(1993b): "Sediment Transport behind an Offshore Breakwater using different Wave Models", Extended abstract, Proc. Workshop of the MAST G8-M Project, Grenoble, September 1993.

Suh, K. and Dalrymple, R.A.(1987): Offshore Breakwaters in Laboratory and Field", Journal of Waterway, Port Coastal and Ocean Engrg., Vol. 113, No.2, Mar 1987, pp. 105-121.

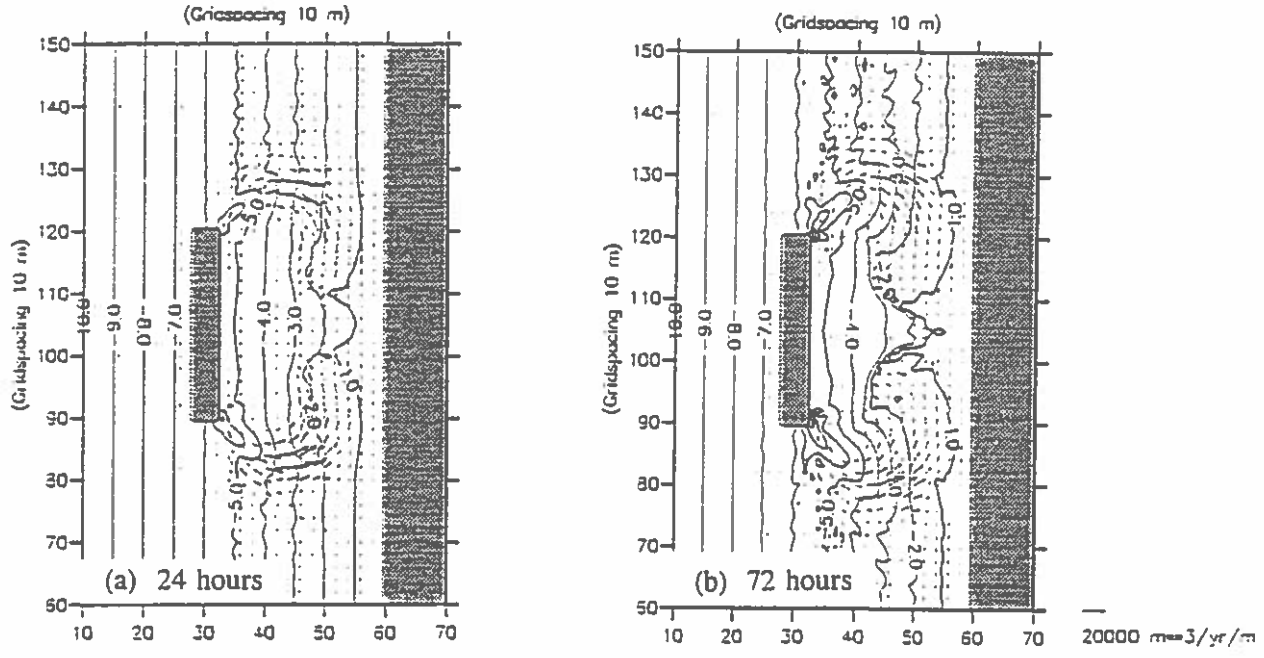

Fig. 2 Bathymetry and vectors of sediment transport rates.

Influence of Bed Roughness on Morphological Response behind Breakwaters

H.K. Johnson, I. Brøker and J.A. Zysermann

Danish Hydraulic Institute
Agern Allé 5
2970 Hørsholm
Denmark

Influence of Bed Roughness on Morphological Response behind Breakwaters

by
H.K. Johnson, I. Brøker and J.A. Zyserman[1]

Abstract
The morphological response behind a single detached breakwater is investigated using DHI's morphology modelling system, M21MORF (see Johnson et.al., 1993). For the setup investigated with a bed roughness corresponding to Manning number of 32, the morphological response behind the breakwater can be characterised by a double-peaked salient in the initial stages, tending towards a single-peaked salient in the later stages plus severe erosion at the leeward tips of the breakwater. A change in the bed roughness specified in the hydrodynamic model has a significant influence on the distribution of sediment transport field, and hence on the morphological response. Results available from these tests are presented and discussed.

Introduction

The morphological evolution of a given coastal area is dependent on the gradients of the sediment transport field, which in turn depends on the hydrodynamic and wave fields. For a given wave field, the computed hydrodynamic field is quite dependent on the specified bed roughness. The bed roughness in the hydrodynamic model has been specified with and without considering the feedback effect due to wave-current interaction in the boundary layer which leads to enhanced bed roughness for the current compared to the geometric roughness. Furthermore, the sensitivity to the geometric bed roughness is investigated.

Model Setup

A hypothetical breakwater was used. The breakwater is 300m long, located at a distance of 280m from the shoreline. The nearshore contours are straight and parallel with a beach slope of 1:50. Regular unidirectional waves with a wave height of 2m and a period of 8 secs approach the 10m contour with parallel wave crests. The initial bathymetry is shown in Fig. 1.

For the wave simulations, a parabolic mild slope model (MIKE 21 PMS) is used. The bed roughness used in the wave simulation is chosen as 1.5mm. A grid spacing of 5m is used in the wave model and the radiation stress results interpolated onto the 10m grid used in the hydrodynamic simulations.

The time step for the hydrodynamic simulation is chosen as 6 secs, and the eddy viscosity is specified using the Smagorinsky formulation, with a Smagorinsky factor of 0.5.

Three morphological simulations were carried out corresponding to different specifications for the bed roughness used in the hydrodynamic computations. The bed roughness specifications are: (1) Manning number, M=32; (2) computed bed roughness map from the boundary layer model, in which a geometrical roughness, k_N=10cm (corresponding to a Manning number, M=32) is specified and (3) computed bed roughness map from the boundary layer model, in which a geometrical roughness k_N=0.625mm (corresponding to a flat bed with 0.25mm sand) is specified. The boundary layer model accounts for an increase in apparent bed roughness due to combined wave-current motion. The simulations corresponding to these bed roughness specifications are referred to as tests 1, 2 and 3 respectively.

Results

The initial wave field for all three simulations is shown in Fig. 2. The initial current vectors and contours of current speeds are shown in Figures 3a, 4a and 5a for tests 1, 2 and 3 respectively. Furthermore, the sediment transport vectors and bathymetry after 12 hours of wave action are shown

[1] Danish Hydraulic Institute, Agern Allé 5, DK 2970, Hørsholm, Denmark

in Figures 3b, 4b and 5b for tests 1, 2 and 3 respectively.

A comparison of Figs. 3a and 4a shows that there is no significant difference in the current fields, hence, there is no significant difference in the morphological response as can be seen in Figs. 3b and 4b. This result is quite unexpected since the effect of including wave-current interaction in the boundary layer is to increase the apparent bed roughness. However, a closer look reveals that the areas with appreciable currents corresponds to the areas with low waves (i.e. the diffraction zone), in which case the effect of wave-current interaction in the boundary layer would be small. Conversely, the areas with relatively high waves correspond to the areas with low currents, in which case there would be a substantial increase in the apparent roughness, however, since the currents are small in these areas, the increase in apparent roughness will not have a significant effect on the current field. This explains why no significant difference between tests 1 and 2 can be seen. It should be noted that this situation is unique to the case where the wave crests are parallel to the shoreline. In the case of waves approaching at an angle, there would be longshore currents in the area with relatively high waves which can potentially lead to a significant influence of wave-current interaction. This situation will be investigated in the near future.

A comparison of Figs. 4a and 5a shows quite appreciable difference in the current flows. The maximum current speed in Fig. 4a is about 1 m/s occuring at a water depth of 1 to 2m, some distance away from the centre-line before the eddies join together to form a jet towards the breakwater. However in Figure 5a, the maximum current speed of 1.6 m/s occurs at a water depth of 3 to 5m along the centre-line of the breakwater. The increase in current speeds is to be expected because of the reduction in bed roughness. The change in the flow pattern is due to the non-linear relationship between roughness and flow.

Furthermore, a comparison of Figs. 4b and 5b shows a significant difference in the distribution of sediment transport. In Fig. 4b, there is relatively small sediment transport along the centre-line compared to the leeward edges of the breakwater. In contrast, Fig 5b shows a significant sediment transport along the centre-line compared to leeward edges of the breakwater. This difference in sediment transport distribution results in reduced erosion at the leeward edges of the breakwater in Fig. 5b compared to Fig. 4b. Furthermore, there is increased deposition immediately behind the breakwater in Fig. 5b.

Conclusions

A change in the specified bed roughness in the hydrodynamic model used in morphological simulations will not only affect the current field, but can alter the distribution of sediment transport and hence the morphological response.

In the particular case of waves propagating normally to offshore breakwaters, the influence of wave-current interaction in the boundary layer on the bed roughness used in hydrodynamic simulations does not significantly affect the hydrodynamic results and hence the morphological response. A different response can be expected for waves approaching at an angle.

References

Johnson, H.K., I. Brøker, J.A. Zyserman and P. Justesen(1993): "A new approach to 2DH Morphological Modelling", Extended abstract, Proc. Workshop on the MAST G8-M Project, Grenoble, September 1993.

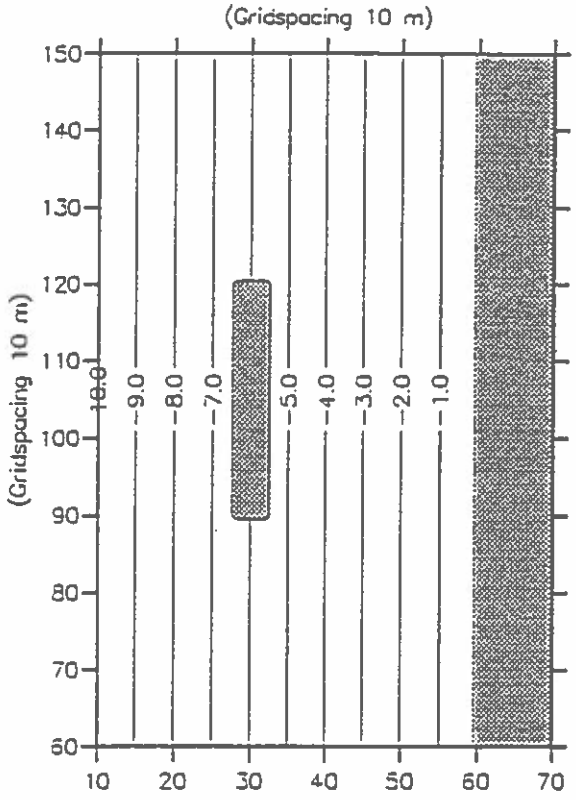

Fig. 1 Initial bathymetry

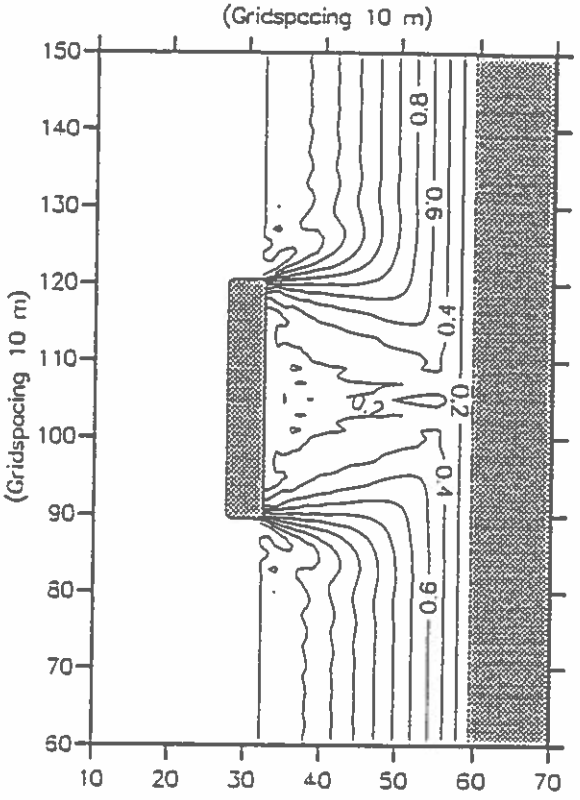

Fig. 2 Initial wave field

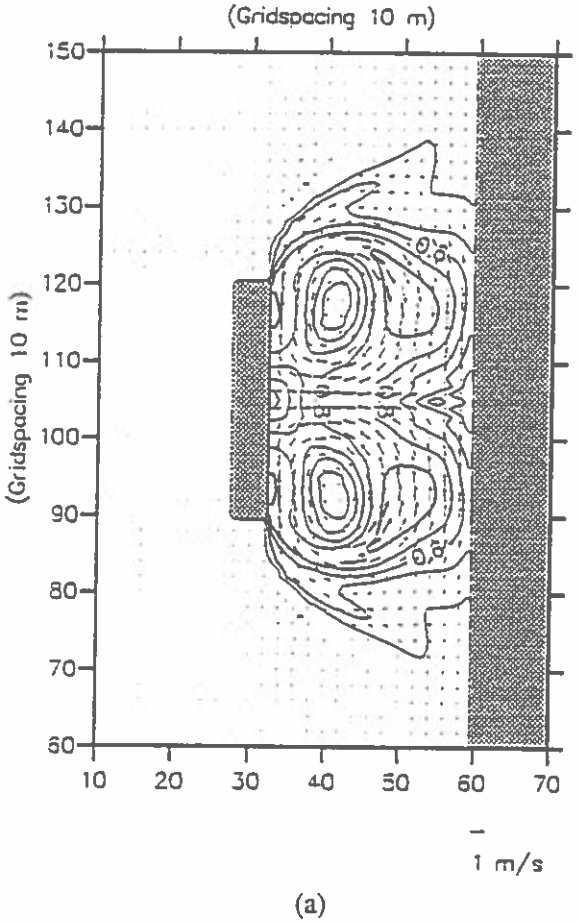

(a)

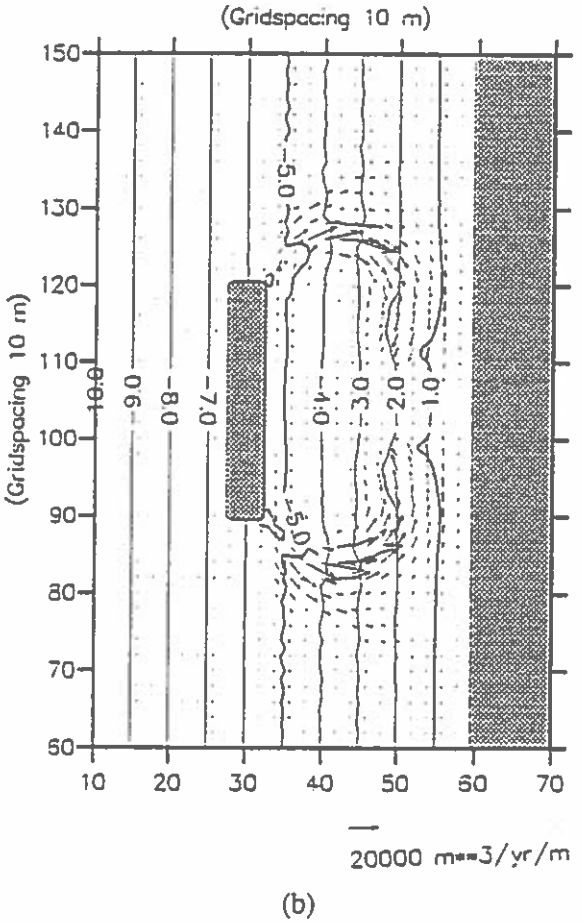

(b)

Fig. 3 Test 1 results. (a) Initial current field, (b) bathymetry & sediment transport field after 12 hrs.

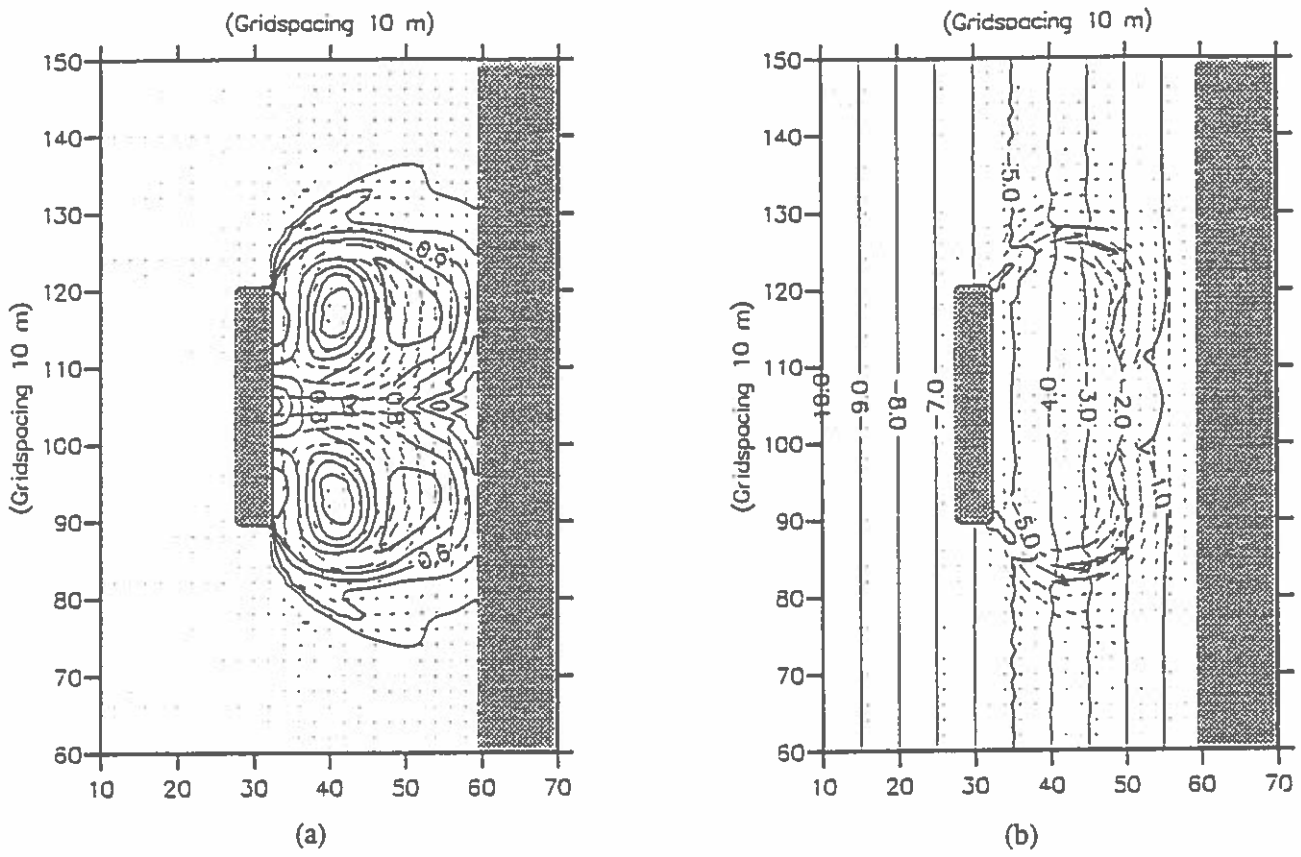

Fig. 4 Test 2 results. (a) Initial current field, (b) bathymetry & sediment transport field after 12 hrs.

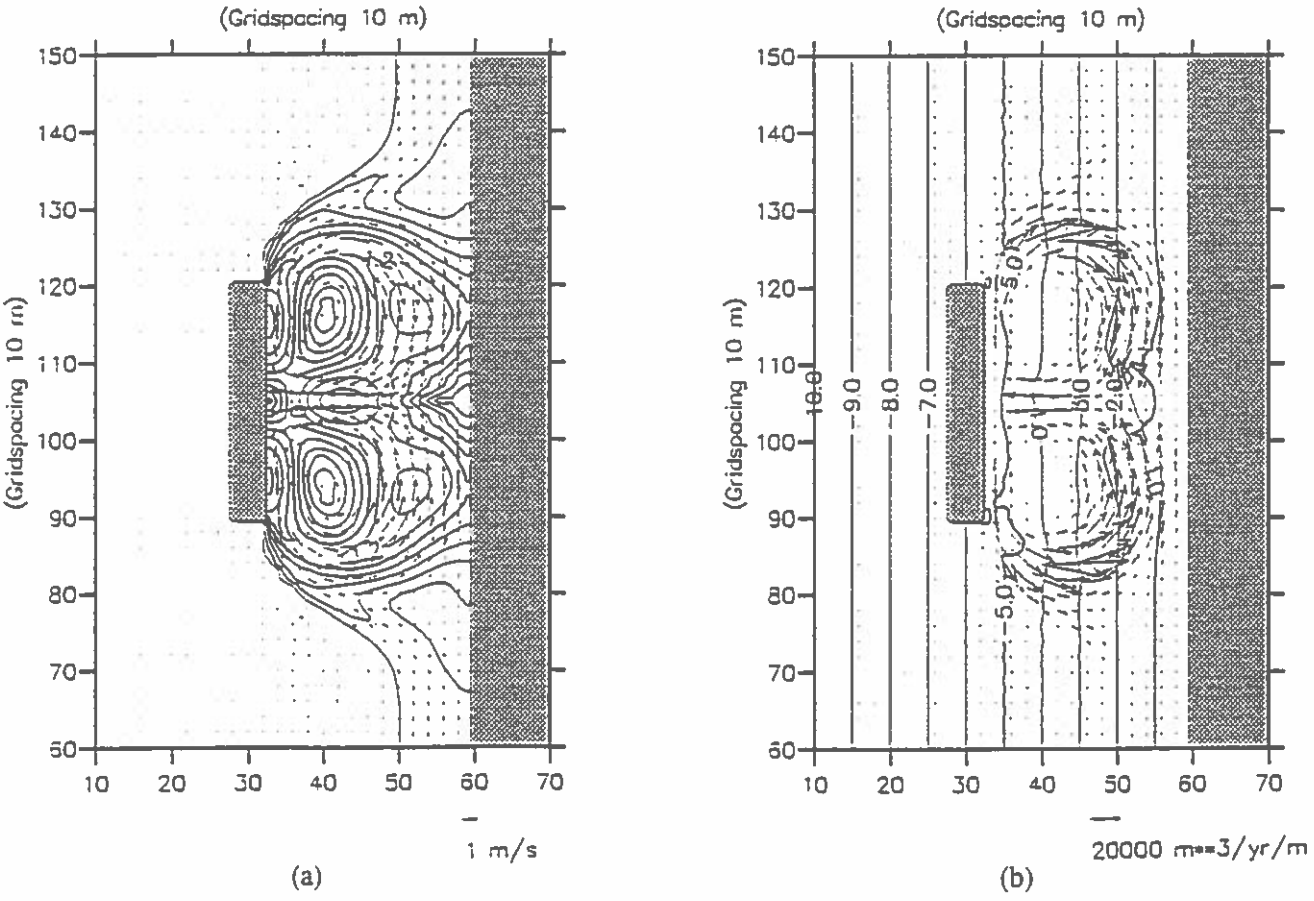

Fig. 5 Test 3 results. (a) Initial current field, (b) bathymetry & sediment transport field after 12 hrs.

Errata to Fig. 5b, page 4 of "Influence of Bed Roughness on Morphological Response behind Breakwaters" by Johnson, Brøker and Zyserman.

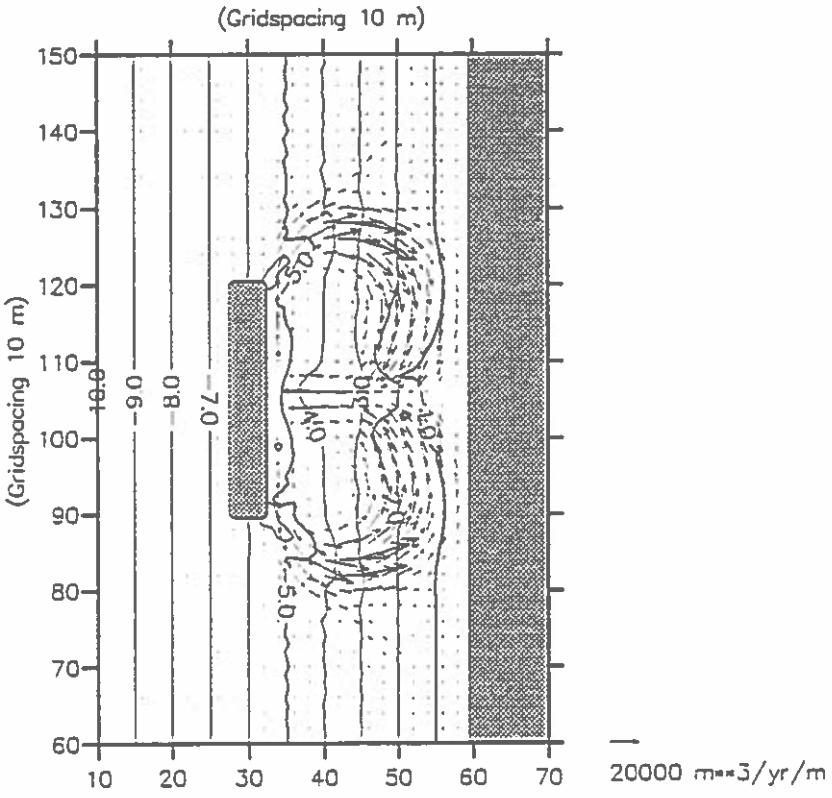

Udvalgte publikationer fra

Rammeprogrammet "Marin Teknik" (STVF).

Dansk Selskab
Mødt i Vandbygningsteknisk ~~Forening~~

November 1993